Fall 12-15-2017

SYNTHESIS, CHARACTERIZATION, AND SPECTROSCOPY OF DONOR-ACCEPTOR CHARGE TRANSFER COMPLEXES

DOMINIC K. KERSI
University of New Mexico

Dominic Kofi Kersi
Candidate

Chemistry and Chemical Biology
Department

This dissertation is approved, and it is acceptable in quality and form for publication:

Approved by the Dissertation Committee:

Professor Martin. L. Kirk, Chairperson

Dr. Yang Qin

Dr. C. Feng

Dr. R. Giri

SYNTHESIS, CHARACTERIZATION, AND SPECTROSCOPY OF DONOR-ACCEPTOR CHARGE TRANSFER COMPLEXES

by

DOMINIC KOFI KERSI

B. Sc. Chemistry, Kwame Nkrumah University of Science & Technology, 2003

M.Sc. Chemistry, University of Minnesota, 2006

DISSERTATION

Submitted in Partial Fulfillment of the

Requirements for the Degree of

Doctor of Philosophy

Chemistry

The University of New Mexico

Albuquerque, New Mexico

December, 2017

DEDICATION

To my beloved wife, Rebecca Mawutor Kersi, and our three children: Courtney-Dona Kersi, Carlaney Kersi, and Rebecca Kersi. To my deceased grandmother Gertrude Kersi, and parents (Anthony Kersi and Doris Arthur).

ACKNOWLEDGEMENTS

First and foremost, I would like to give thanks to the Almighty God for His favor, strength and blessings. I wholeheartedly acknowledge Prof. Martin L. Kirk, my research advisor and dissertation chairperson, for his guidance, support, patience and encouragement throughout the course of my Ph.D. program. I thank my wife, Rebecca Kersi who gave me incalculable support over the fourteen years of our marriage. Your love is magnificent.

I also want to express my profound acknowledgment to the University of New Mexico, Department of Chemistry and Chemical Biology for the study opportunity, teaching and research assistanceship granted to me during my Ph.D. studies at the Department of Chemistry and Chemical Biology.

I would like to express my appreciation to the current and former Prof. Kirk's research group members; Dr. Abebe, Antonio William, Meita Fulton, Dr. Regina Peter Mtei, Dr. Joseph Sempombe, Dr. Chao Dong, Dr. Benjamin Stein, Dr. Jing Yang, Dr. Diana Habel-Rodriguez, Dr. Logan J. Giles, Dr. Benjamin Richard Williams, Ju Chen, Dr. Ezra Depperman, Shiyne Gao, Khadanand Kc, Laura Jane Ingersol, Amrit Pokhrel, Randjana Dangi, and Sangita Paudel for their help, encouragement, contributions and assistance. I thank Dr. Diane Dickie, Ken Sherrell, and Dr. Karen Ann Smith for their indispensable support with X-ray

crystallography, Mass spectrometry, and nuclear magnetic resonance spectroscopy (NMR) respectively. I thank all the workers at Chemical & Research Laboratory Supplier (CRLS) for providing me with laboratory equipment and chemicals. I thank Dr. Jing Yang and Dr. C. Feng for their help with time resolved spectroscopy data acquisition.

Finally, I would like to acknowledge my committee members; Dr. Yang Qin, Dr. C. Feng, and Dr. R. Giri for their comments and suggestions.

SYNTHESIS, CHARACTERIZATION, AND SPECTROSCOPY OF DONOR-ACCEPTOR CHARGE TRANSFER COMPLEXES

by

Dominic Kofi Kersi

B. Sc. Chemistry, Kwame Nkrumah University of Science & Technology, 2003

M.Sc. Chemistry, University of Minnesota, 2006

Ph.D. Chemistry, University of New Mexico, 2017

ABSTRACT

A series of square-planar metal (diimine)(dichalcogenolene) chromophoric complexes have been synthesized, characterized and studied spectroscopically. Studies conducted on diiminеplatinum(II) dichalcogenolene complexes (LPtL') using time resolved spectroscopic techniques such as transient absorption and emission, reveal a charge-separated excited state of the type dichalcogenolene → diimine charge-transfer (LL'CT) [(dichalcogenolene$^{\bullet+}$)Pt(diimine$^{\bullet-}$) with an open shell donor-acceptor biradical character. This makes the low-energy ligand-to-ligand charge-transfer (LL'CT), or the mixed-metal ligand-to-ligand charge-transfer (MMLL'CT), transitions of diiminеplatinum(II) dichalcogenolene complexes particularly interesting to us in facilitating our knowledge of biradical charge-separated states. Long-live excited state lifetimes were observed for these complexes upon visible photoexcitation of the LL'CT or MMLL'CT band. These complexes are abbreviated as (E,E') in this dissertation, with

Pt(dbbpy)(bdt), (S,S), Pt(dbbpy)(bds), (Se,Se), Pt(dbbpy)(bSO), (S,O), Pt(dbbpy)(bSSe), (S,Se), Pt(dbbpy)(bSeO), (Se,O), and Pt(dbbpy)(CAT), (O,O). The excited-state lifetimes observed for these d^8 platinum (II) compounds shows no periodic dependence on the heteroatoms of the donor ligand, i.e. no direct relationship was observed between the principal quantum number of dichalcogenolene donor atoms and excited-state lifetime. The relationship between observed lifetimes and principal quantum number can be explained by using heteroatom-dependent singlet-triplet (S—T) energy gaps and anisotropic covalency contributions to the M—E (where the donor atom, E= O, S, Se and M= Pt) bonding scheme that direct the rates of intersystem crossing between the singlet (S) and the triplet (T) states. For O,O; no emissive behavior was observed due to the very rapid relaxation to the ground state within 0.63 ns. This behavior was ascribed to the fact that the energy of the T_2 state lies above that of the S_1 excited state [$E(T_2) > E(S_1)$] and hence a rapid nonradiative (nr) decay is observed from the S_1 excited state to the S_0 ground state. In contrast, long-lived photoluminescence was observed for S,S; S,Se; S,O; Se,O; and Se,Se due to the fact that $E(T_2) \leq E(S_1)$ and this helps to direct S→T intersystem crossing. Diimineplatinum(II) dichalcogenolene complexes (LPtL') with mixed E donor atoms display excited state lifetimes values between that of O,O; and S,S.

In the two-level approximation, spin-orbit coupling (SOC) controls the rate constant for intersystem crossing (k_{ISC}) in C_{2v} symmetry according to

$$k_{ISC} \propto \langle S_n|L_x|T_n\rangle^2 / \Delta E_{ST}^2$$

$\langle S_1|L_i|T_1\rangle = \langle A_1|L_i|A_1\rangle = 0$……..……(1)

$\langle A_1|L_x|B_2\rangle \neq 0$ ……..……..…(2)

where L_i are the orbital angular momentum operators, which transform as a_2, b_1, and b_2 in C_{2v} symmetry. Intersystem crossing (ISC) from $S_1 \rightarrow T_1$ and $T_1 \rightarrow S_0$ is symmetry-forbidden in C_{2v} symmetry (equation 1) and the observed rates of ground state recovery are often slow. Conversely, ISC from $S_1 \rightarrow T_2$ is symmetry-allowed according to equation 2 and the observed rates are highest when the energies of T_2 and S_1 are very close.

A direct linear relationship is observed to exist between photoluminescence rates, calculated SOC matrix elements, and ^{13}C-NMR chemical shifts. These heteroatom effects have modulated the excited-state lifetimes by not less than three orders of magnitude. The non-radiative decay rates (k_{nr}) for Pt(diimine)(dichalcogenolene) complexes show a direct relationship between the differences in ^{13}C-NMR chemical shifts. A closer inspection of the non-radiative decay rates (k_{nr}) for the series suggests that Se,Se; does not follow the linear trend exhibited by S,S; S,Se; Se,O; and S,O, as it possesses a shorter lifetime than S,S. The shorter lifetime ($T_1 \rightarrow S_0$ ground-state recovery) is likely due to vibronic SOC contributing to T_1 depoulation. A linear correlation was found to exist between the squares of the differences in ^{13}C-E-E'-^{13}C' ligand ^{13}C NMR chemical shifts $(\Delta\delta)^2$ and the observed excited state lifetimes. This same relationship was found to exist between the square of the SOC matrix elements ($\langle T_1|L_i|S_0\rangle^2$) and ground-state recovery lifetimes. The computed $\langle T_1|L_i|S_0\rangle$ matrix

elements from DFT SOC calculations shows an exceptional linear relationship with the $T_1 \rightarrow S_0$ lifetime. Anisotropic covalency in the E-Pt-E' bonding scheme induces an orbital rotation in the HOMO (Pt d_{xy} and d_{zx}) and this increases the SOC. The Pt d-orbital rotation is therefore the dominant source of non-zero $\langle T_1|L_i|S_0\rangle$ matrix elements. For O,O; S,S; and Se,Se there is no d-orbital rotation and $\langle T_1|L_i|S_0\rangle = 0$. Chapter 1 details the theory used in this dissertation. Chapter 2 describes the synthetic scheme, and the methods used to characterize the systems studied. Chapter 3 provides spectroscopic and computational studies of diimineplatinum(II) dichalcogenolene complexes. Finally, chapter 4 describes the solvatochromic shifts observed for the LL'CT band of Pt(II), Pd(II) and Ni(II) diimine dichalcogenolene complexes.

A series of M(diimine)(dichalcogenolene) complexes were tested against the electric field of widely used organic solvents such as acetone, acetonitrile, dimethylsulfoxide (DMSO), dichloromethane (DCM), chloroform, tetrahydrofuran (THF), dichloroethane (DCE), dimethylformamide (DMF), toluene and benzene. First and foremost, it was observed that an increase of the polarity of the solvent remarkably stabilizes the occupied orbitals (HOMO) and destabilizes the virtual orbitals of the complexes. Thus, the HOMO-LUMO gap is observed to increase, and the LL'CT band is blue shifted. This trend is in total accordance with the experimental results. From TD-DFT calculations, it was determined that the HOMO orbitals are localized on both the metal and the dichalcogenolene atoms, and the LUMO is of diimine character. The solvent field stabilizes the orbitals that

are localized on both the dichalcogenolene ligand and metal and destabilizes the orbitals which are mainly diimine in character. The electron density difference map (EDDM) plots of these model systems shows that electron density is always lost from the HOMO and gained by the LUMO during the vertical transition. The observed trend in the increasing energy of the LL'CT band as the solvent polarity increases can be explained based on the charge distribution in the ground state. A linear relationship was observed when the energy of the LL'CT band maxima was plotted versus the solvent parameter, E^*_{MLCT}. This same trend was also observed when the energy of the LL'CT band maxima was plotted against the calculated dipole moment.

TABLE OF CONTENTS

LIST OF FIGURES

LIST OF TABLES

Chapter 1 Methodology, Background, and Statement of the Research Problem

1.1 Introduction/Spectroscopic Methodologies

1.1.1 Introduction

Group VIII transition metal complexes of the form M(diimine)(dithiolate) have attracted the attention of a vast number of researches due to their distinct properties that include solution luminescence, photocatalysis, large excited-state oxidation potential ls, solvatochromism, and large molecular hyperpolarizabilities. They have been recognized as artificial photosynthetic receptors, photoluminescent nuclei acid probes, and building blocks for molecular photonic devices.[1-15]

Preceding reports in this field have mainly focused on d^6 $Ru(bpy)_3^{2+}$ diimine systems and various derivative molecules. The examination of fluid-solution photoluminescence from Pt(II) diimine dithiolates and Cu(I) bis-diimines led to the tuning and maximizing of their photophysical and electronic structure properties for particular applications. The use d^8 metal chromophores has been of interest since they possess open coordination sites, while their d^6 counterparts does not. These open coordination sites enhance chemical reactions such as photoreactivity, cross-quenching, and self-quenching.[1]

Multichromophoric complexes have been explored extensively in regard to their photochemical and photophysical properties due to their capacity for applications

in developing synthetic systems with light harvesting and storage capacity in optoelectronic devices.[3]

Pt(II)(diimine)(dithiolate) complexes have been explored widely due to the presence of a low-energy MMLL'CT (mixed metal ligand-to-ligand charge transfer) band in the visible region of their optical spectra, which results in a long-lived charge-transfer excited state. These excited states give rise to luminescence in the visible and NIR (near infrared) regions of their spectra. Photocurrent generation can be observed via these long-lived excited states because of its reductive nature, and the complexes are able to transfer electrons

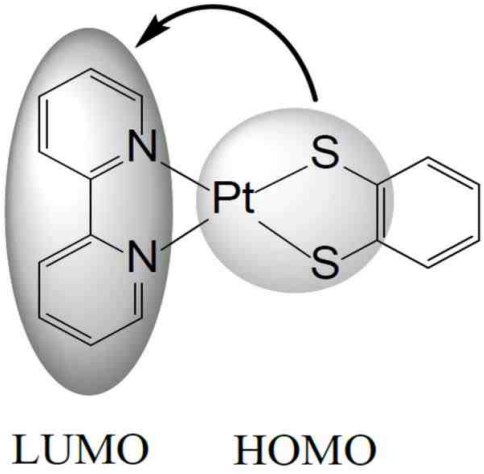

Figure 1.0: Pt(bpy)(dithiolate) complex displaying its Mixed-Metal Ligand-to-Ligand Charge transfer (MMLL'CT) transition.

to nanocrystalline TiO_2.[19] The long-lived excited states of these complexes also exhibit capabilities evidence of electron transfer quenching, which can lead to the generation of hydrogen from water by initiating the photocatalytic cycle in the presence of sacrificial donor.[3] In the field of nonlinear optical (NLO) materials, these complexes have studied extensively for use in nonlinear optical materials

such as laser technologies, optical switches, data storage devices, and telecommunications devices.[2]

The long-lived excited states of these complexes also exhibit evidence of electron transfer quenching, which can be used in the field of nonlinear optical (NLO) materials, these complexes have been studied extensively for use in laser technologies, optical switches, data storage devices, and telecommunications devices.[2]

Based on extensive studies performed by Eisenberg and co-workers on mixed-ligand Pt(II)(diimine) complexes, the excited states are known to involve a charge transfer from the highest occupied molecular orbital (HOMO), which is a combination of platinum d orbital and dithiolate orbital character, to the lowest

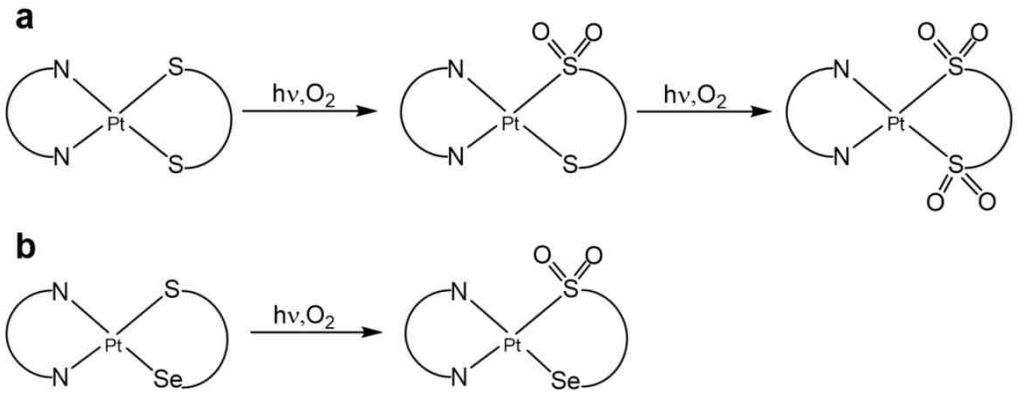

Figure 1.1: Photochemical reactions depicting the formation of **(a)** monosulfinate and disulfinate photoproducts from Pt(diimine)(dithiolate) **(b)** monosulfinate photoproduct from Pt(diimine)(2-selenylbenzenethiolate).

unoccupied molecular orbital (LUMO), which purely involves the π^* orbitals of the diimine ligand (see Figure 1.0). The π^* LUMO orbital of the diimine ligand is a good π acceptor orbital and is antibonding in nature.[2]

Pt(II) and Pd(II) dithiolene-α-diimine complexes have also been shown to undergo photoinduced decomposition in the presence of atmospheric oxygen (equation 1.0). The photoproducts include monosulfinate, monosulfenate, disulfenate, disulfinate and mixed sulfinate/sulfonate complexes.

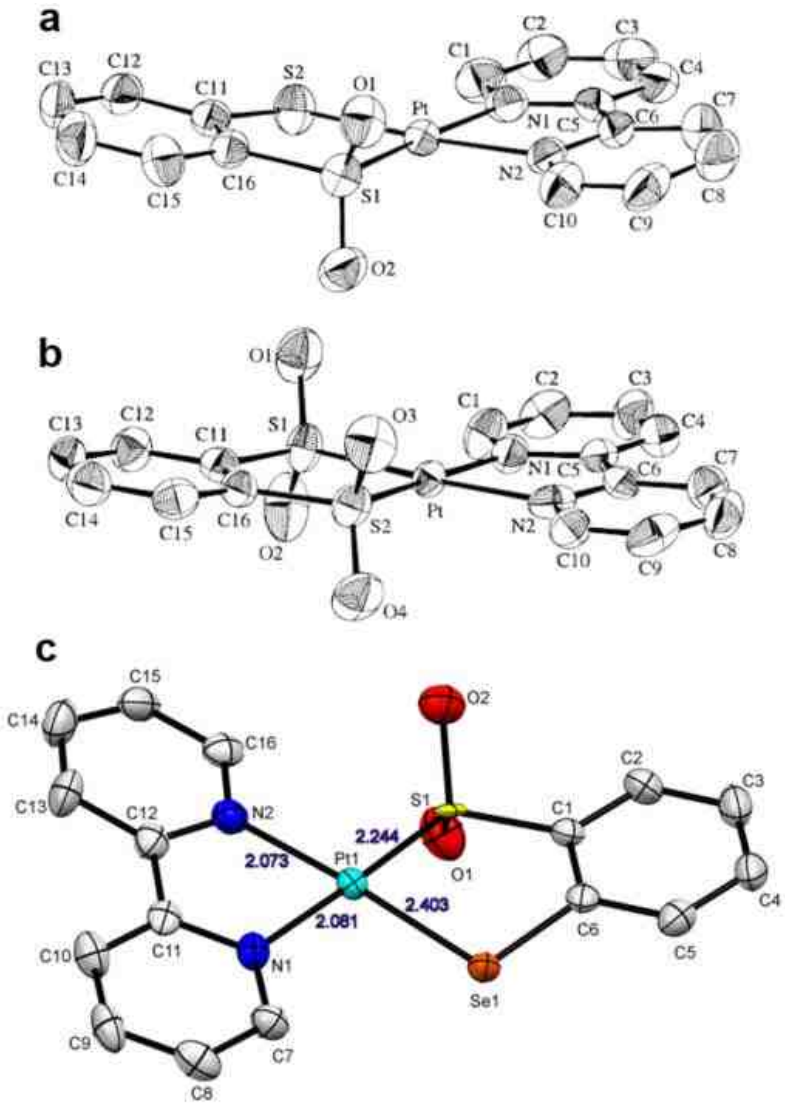

Figure 1.2: ORTEP diagrams of the photooxidation products (a) monosulfinate, [Pt(bpy)(bdtO_2)][15] (b) disulfinate, [Pt(bpy)(bdtO_4)][15] (c) monosulfinate, Pt(bpy)(b$SeSO_2$).

For example, Pt(bpy)(bdt) has been observed to undergo photochemical

oxidation in the presence of atmospheric oxygen in polar aprotic solvent such as acetonitrile, dimethyl sulfoxide (DMSO), and N, N'-dimethylformamide (DMF). Both monosulfinate [Pt(bpy)($bdtO_2$)] and disulfinate Pt(bpy)($bdtO_4$)] were obtained as the photoproduct (see Figure 1.2), and the reaction was probe using ^{1}H NMR and UV-Vis spectroscopies. The photochemical reaction occurs in the presence of singlet oxygen that is generated by energy transfer from the excited complex. The formation of sulfinated photoproduct was deduced from thermodynamic data to be strongly exergonic (see Equation 1.0). Gray and co-workers[15] proposed that the photooxidation chemistry of Pt(diimine)(dithiolate) complexes follow similar reaction mechanism of organic sulfides based on the data obtained from the mono- and disulfinate photoproducts.

$O_2 + (CH_3)_2S \rightarrow (CH_3)_2SO_2 \qquad \Delta G^0 = 64.7$ kcal/mol…….…. (1.0)

Nickel dithiolate complexes have also been demonstrated to react thermally with both $^3O_2$ and $^1O_2$ to form sulfinate and sulfenate photoproducts. Darensberg and co-workers demonstrated that disulfinate nickel dithiolate complex results only from the reaction of its monosulfinate with reactive singlet oxygen ($^1O_2$) but not the ground-state triplet oxygen ($^3O_2$).[15,21-26]

Ligand substitution in Pt(diimine)(dithiolate/diselenoate) complexes can be performed on both the diimine and dithiolate/diselenoate ligands in other to tune excited-state energy transfer processes and photoluminescent properties. The principal purpose of this investigations detailed in this thesis is to understand the

molecular design components that control the excited state lifetime, emission quantum yield, transition energy and redox potentials of these complexes.[27]

For the use of M(diimine)(dithiolate/diselenoate) and related complexes as primary components of dyes, dyes used in solar cells, and for catalyzing light-driven reactions, having an idea of the electronic structure contributions of the rates of intersystem crossing (K_{ISC}), non-radiative decay (k_{nr}) and radiative decay (k_r) is very important. Based on the above-mentioned properties, a series of Pt(II) diimine dichalcogenolene complexes have been synthesized and characterized by NMR, Mass spectrometry, X-ray crystallography, and elemental analysis. The lifetimes of these complexes were analyzed using transient absorption and emission spectroscopies. These studies yielded excited-state to ground-state lifetimes, which derive from a low-energy charge-separated dichalcogenolene to diimine charge-transfer (LL'CT) state. The excited-state lifetimes exhibit an extraordinary and nonperiodic dependence on the type of dichalcogenolene heteroatoms that are chelated to the Pt ion. This non-linear relationship between the excited-state lifetimes and the principle quantum number of the dichalcogenolene ligand donors can be explained in terms of singlet-triplet (S-T) energy gaps and anisotropic covalency contributions to the metal-dichalcogenolene bonding scheme that controls intersystem crossing rates (k_{ISC}).[28]

This chapter introduces the principles underlying the important spectroscopic techniques used in this dissertation. The spectroscopic techniques employed in

this dissertation includes electronic absorption spectroscopy (EAS), emission spectroscopy, Infrared (IR) spectroscopy, and transient absorption (TA) spectroscopy. These spectroscopic techniques were employed to understand electronic structure contributions to the rates of intersystem crossing (k_{ISC}), non-radiative decay (k_{nr}), and radiative decay (k_r).

1.1.2 Electronic Absorption Spectroscopy (EAS)

1.1.2.1 The Beer-Lambert Law, and the Transition Dipole moment

Electronic absorption spectroscopy uses the principle of absorption of electromagnetic radiation by a molecule and is registered as a function of the wavelength (λ) or energy of the electronic transition. The Beer-Lambert absorption law shows the correlation between the absorption of electromagnetic radiation by a sample molecule to the properties of the medium through which this radiation is travelling. This relationship is depicted in equation 1.1 below,[29-31] where A is the absorbance, I_0 is the incident light intensity, I is the intensity of the transmitted light, ε is the molar absorptivity or molar extinction coefficient in units of $Lmol^{-1}cm^{-1}$ at the probing wavelength.

$$A = \log_{10}\left(I_0 / I\right) = \varepsilon c l \quad \text{..... (1.1)}$$

The molar concentration in units of $molL^{-1}$ is given as c and the light pathlength, l is in centimeters. Equation 1.1 depicts the general formula used in spectroscopic applications. From equation 1.1, the absorbance (A) is directly proportional to the path length l. Therefore, an increase in absorbance A is observed if the

path length is increased and therefore results in a reduction in the intensity of light at the detector. Equation 1.1 also shows a direct relationship between absorbance A and the molar concentration. The molar extinction coefficient ε is an intrinsic property of the sample and quantifies how strongly a chemical species absorbs light at specific wavelength, and this is a unique property of a specific compound.

A molecule that absorbs electromagnetic radiation in the form of a photon is excited to a higher energy level. The occupied energy level from which the electron is coming from derives from the ground state, and the higher level to which the electron is being promoted is called the excited state. The one-electron promotion to the excited state can result in population of either a half occupied or unoccupied orbital. Charge transfer (CT) transitions in metal complexes can be referred to as intramolecular or intermolecular charge transfers. When the transitions involve orbitals on the same molecule, it called intramolecular charge transfer. However, if the CT process involves promotion of an electron from one orbital in one molecule to another orbital in a different molecule, it is called intermolecular charge transfer.

Transition-metal complexes typically display electronic transitions that are ligand field (d-d transitions), ligand to metal charge transfer (LMCT), and metal to ligand charge transfer transitions (MLCT)[32] in nature as depicted in Figure 1.3. Ligand to metal charge transfer transitions (LMCT) occur in complexes where the metal is in a high oxidation state and the ligands contain lone pairs of electrons, whereas the metal to ligand charge transfer transitions (MLCT) are observed in

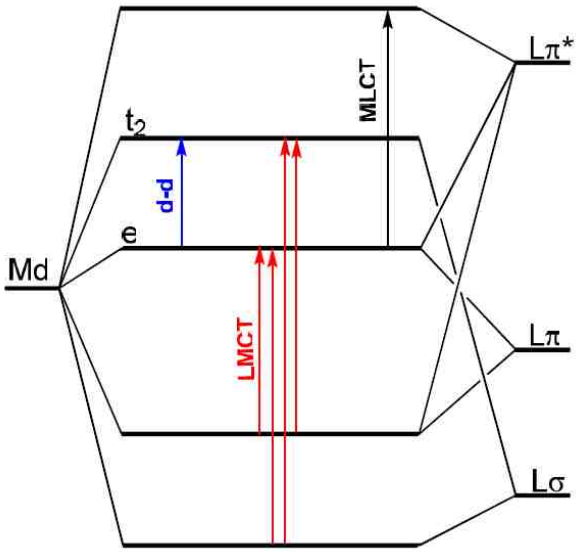

Figure 1.3: A summary of electronic transitions observed in a tetrahedral complex.

complexes having ligands with low lying π* orbitals like 2,2'-bipyridine(bpy),1,10-phenanthroline (phen), SCN^-, CN^- and CO [33]. Electronic transitions that result from charge transfer processes are typically more intense than ligand field transitions. Additionally, if a transition involves the promotion of an electron from an orbital that is predominantly ligand in character to an orbital that also possesses predominantly ligand character, the transition is referred to as a ligand to ligand charge transfer (LLCT) or interligand charge transfer (ILCT). These CT transitions can also be very intense. The relative allowedness of a transition is designated by the oscillator strength ($f_{\psi_e\psi_g}$) which is dimensionless quantity that is given in equation 1.2. The quantity $\bar{\nu}$ represents the frequency in wavenumbers and ε is the molar extinction coefficient.

$$f_{\psi_e\psi_g} = 4.32\ x\ 10^{-9} \int \varepsilon(\bar{\nu}) d\bar{\nu} \quad \text{..... (1.2)}$$

This transition moment integral is defined in equation 1.3 and the oscillator strength, $f_{\psi_e\psi_g}$, depicted in equation 1.2 is proportional to the square of the transition dipole moment integral (equation 1.4). This yields the strength of the coupling between the ground state and excited state wavefunctions.[33-34]

$$\mu_{eg} = \langle \psi_e \left| \mu \right| \psi_g \rangle \quad \text{..... (1.3)}$$

$$f_{\psi_e\psi_g} = \frac{2m_e}{\hbar^2}\left(E_{\psi_e} - E_{\psi_g}\right)\left|\langle \psi_e \left| \mu \right| \psi_g \rangle\right|^2 \quad \text{..... (1.4)}$$

In these equations, ψ_e and ψ_g are the ground state and the excited state wavefunctions respectively, m_e represent the free electron mass, $\hbar$ is the reduced Planck constant, E_{ψ_e} and E_{ψ_g} are the excited and ground state wavefunction energies respectively, and μ represents the electric dipole moment operator and transforms as x, y and z in a given point group. If the triple product of the symmetries for the ground state, excited state, and transition dipole moment operator transform as the total symmetric representation, then the transition dipole moment integral is non-zero and the transition is allowed. Conversely, if the transition dipole moment integral is zero the transition is said to be forbidden. This happens when the integral does not belong the the totally symmetric representation as part of its integrand.[7-9] Nonetheless, allowed transitions are always observed when at least one of the following integrals, equation 1.5 to equation 1.7, have a non-zero value. Forbidden transitions occur if equations 1.5 to 1.7 have a zero-value integral.

$$\mu_{eg} = \langle \psi_e \left| \mu_x \right| \psi_g \rangle \quad \text{..... (1.5)}$$

$$\mu_{eg} = \langle \psi_e \left| \mu_y \right| \psi_g \rangle \quad \text{..... (1.6)}$$

$$\mu_{eg} = \langle \psi_e \left| \mu_z \right| \psi_g \rangle \quad \text{..... (1.7)}$$

However, dipole forbidden transitions can gain allowedness through vibronic and spin-orbit coupling.

1.1.2.2 Selection Rules

Transition metal complexes have two selection rules that govern the allowedness of their electronic transitons:

The spin selection rule, $\Delta S = 0$.

The spin selection rule states that transitions are only allowed if the initial and final states have the same multiplicity, otherwise the transition is said to be spin-forbidden. Spin allowed transitions occur when an electron is promoted from one state to other without a change in the total spin of the system. Thus, triplet to singlet (T-S) or singlet-triplet (S-T) transitions are formally spin-forbidden, and when they are observed they will be very weak.

The orbital selection rule (Laporte), $\Delta l = \pm 1$.

The Laporte (orbital) selection rule applies to molecules that are centrosymmetric, i.e. molecules that possess an inversion center. The rule states if a molecule is centrosymmetric, transitions within p and d orbitals are forbidden because the electronic transition must conserve parity. That is whether the transition is symmetric or asymmetric with respect to the inversion center.

Henceforth, g (gerade) to g or u (ungerade) to u transitions are Laporte forbidden. Transitions involving a change in parity i.e. $g \rightarrow u$ or $u \rightarrow g$ in such molecules are allowed. The s and d orbitals are symmetric with respect to inversion, so they are represented by g whereas p orbitals are antisymmetric with respect to inversion, so they denoted by u. Thus, in octahedral O_h complexes, ligand field transitions (i.e. $d \rightarrow d$ transitions) are forbidden by the orbital selection rule and are observed to be very weak because O_h complexes have center of inversion. However, in tetrahedral complexes ligands field transitions are allowed by the Laporte rule since no center of symmetry is present. Therefore, a more intense $d \rightarrow d$ transition is observed.

Both the spin and orbital rules can can be relaxed by spin-orbit coupling, vibronic coupling (interaction between vibrational electronic wavefunctions), and low symmetry mixing of states. Molecular vibrations can remove the center of inversion and hence ligands bound to the metal atom can change its perfect centrosymmetry, leading to the relaxation of the Laporte selection rule. This result in some allowedness gained for forbidden transitions since the orbital selection rule is relaxed. Transition metal complexes of metalloproteins have spin and orbitally forbidden bands that can be very intense due substantial spin orbital coupling and low symmetry distortions which contribute to a mixing of the states. Broadly speaking, allowed transitions are much stronger in intensity than forbidden transitions (see Table 1.1)[32].

Table 1.1: Types of electronic transitions and their relative intensities.[32]

Band type	**ε ($M^{-1}cm^{-1}$)**
Spin forbidden	< 1
Laporte forbidden	100 – 200
Larporte allowed	ca. 500
Symmetry allowed	1000 - 50000

1.1.2.3 Transition Dipole Intensities

Generally, allowed transitions are orders of magnitude more intense compared to forbidden transitions. Table 1.1 shows allowed and forbidden transitions with their respective band intensities (molar extinction coefficients).[32] In molecules that possess a center of inversion, vibronic coupling involving antisymmetric (ungerade) vibrations allow the d-orbital wavefunctions on the metal to mix with the p-orbital wavefunctions on the metal to relax this orbital selection rule. In non-centrosymmetric molecule, there is a greater mixing of the d- and p-orbitals. This results in a larger relaxation of the Laporte selection rule and it leads to more intense ligand field transitions.

1.1.2.4 Band Shape

Broadness in an absorption band is always observed in electronic absorption spectra. The main factors that contribute to this broadness include the solvatochromic effect, vibronic coupling, a distortion relative to the ground state geometry, spin-orbit coupling, and the Jahn-Teller effect.[13]

1.1.3 Transient Absorption Spectroscopy (TAS)

1.1.3.1 Introduction

Transient absorption (TA) spectroscopy is an extension of electronic absorption spectroscopy. It is useful in probing and characterizing the electronic and structural properties of photochemical and photobiological molecules. It is similar to absorption spectroscopy, but with the exception that the species probed are short-lived (i.e., transient). The resulting excited state and reaction intermediate lifetimes may range from femtoseconds for the primary excited states, to kiloseconds for very slow reaction intermediates.

Transient absorption spectroscopy provides information related to the electronic properties of metastable (i.e. transient) states, rate constants of the processes where these species participate, excited-state lifetimes, and the kinetic profiles for the formation and decay processes that can be generated through various stages of a photophysical pathway.[36] It is a useful method for the studies of photoinduced electron transfer reactions. Measuring the absorption spectrum of a transient species often requires the use two independent pulsed laser sources.

In transient absorption spectroscopy, an excitation (or pump) pulse is used to promote a fraction of molecules to an electronically excited state. This fraction typically ranges from 0.1% - 10% depending on the type of experiment. A weak probe pulse is sent through the sample with a delay, τ, relative to the pump pulse. The weaker probe beam is used to monitor the temporal evolution of the system by monitoring the absorption signal. Figure 1.4 shows an example of a

simple schematic diagram for a pump-probe measurement of a charge transfer state.

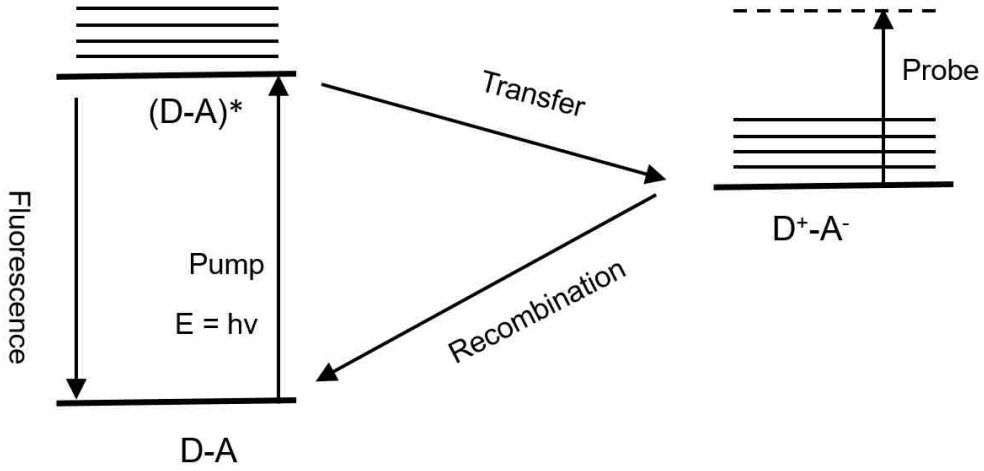

Figure 1.4: Schematic diagram for pump-probe measurements of charge-transfer (CT) transitions.[36]

1.1.3.2 Definitions Used

A sample with concentration *c* in a cuvette of thickness *l* can be irradiated with a light beam of intensity I_0. According to the Beer-Lambert Law, the absorbance is related to the incident intensity I_0 and transmitted intensity *I* by

$$\left(I_0 / I\right) = \exp(\varepsilon c l) \quad \text{(1.8)}$$

Here ε is the molar extinction coefficient of the sample, which is dependent on the wavelength of the incident light and thus shows the individual wavelength characteristic of the molecules.

The total absorption, A_{total}, is calculated by the sum of several absorbing molecules in the sample:

$$A_{total} = \sum_{i=1}^{n} A_i = \sum_{i=1}^{n} \varepsilon_i c_i \, l \quad \text{(1.9)}$$

When there is no overlap of the absorption bands for the different species in the sample, the absorption varies directly with the population of the state under observation. The time trace of a state involved in a chemical reaction (e.g. electron transfer) can be followed under this condition. Optimal performance for ultrafast studies are achieved when time resolutions down to the sub-picosecond regime are used. Today's conventional detectors cannot achieve such resolution, so the method of choice is the time-resolved pump-probe-method for ultrafast studies.

1.1.3.3 The Pump-Probe Setup

This setup uses a pump laser at a given excitation wavelength and a probe laser tuned to the characteristic wavelength of the absorbing state. A strong pump beam is used to photoexcite, or pump, the sample from the ground state to the excited state, and thus the system is brought out of thermal equilibrium. The excited state will decay to various other states with a characteristic decay time.

By measuring the absorption of the weaker probe beam, which is delayed relative to the excitation pulse, the time evolution of the state under study (ground state, excited state, radical pair) can be monitored. The time resolution is now dependent on the temporal convolution of pump and probe pulses (instrument function) and the precision of the variable time delay, whereas the time resolution of the detector has no influence. The importance of a precise and reproducible time delay between pump and probe is obvious.

1.1.3.4 The Differential Absorption Spectrum

The difference absorption, ΔA, spectrum is calculated by taking the difference

between the measured absorption of the sample without excitation and with excitation at a given delay time τ

$$\Delta A = A_{with}(\tau) - A_{without} \quad \text{(2.0)}$$

By varying the time delay τ between the probe and the pump pulses, and recording the differential absorption spectrum at each time delay, a ΔA profile as a function of τ and wavelength λ, i.e., ΔA(λ,τ) is obtained. This ΔA(λ, τ) data gives information on the dynamic processes that occur in the photochemical or photophysical system such as excited state energy migration, electron and/or proton transfer processes, isomerization, internal conversion, fluorescence, phosphorescence, and intersystem crossing. Contributions from various processes can be obtained from the differential absorption spectrum and these include:

(1) **Ground-state bleaching**: Following excitation the fraction of molecules in the ground state decreases. This causes the ground state absorption in the excited sample to be less than that in the non-excited sample, and hence the differential absorption spectrum becomes negative (bleaching) in the wavelength region of ground state absorption, as shown in Figure 1.5 (dashed line).

(2) **Stimulated emission:**

Populating the excited state by promoting a fraction of molecules from the ground state with a pulse pump allows stimulated emission from the excited state to the ground state to occur if the probe pulse proceeds through the excited volume. Stimulated emission is observed for transitions that are optically allowed and

their spectral profile is like that of a fluorescence spectrum. During the process, a photon generated by the probe pulse generates emission of another photon from the molecules in the excited state. The probe photon and photon generated by stimulated emission are emitted in the same direction and both are observed at the detector. This results in a light intensity increase at the detector and hence a negative ΔA signal is observed (Figure 1.5, dotted line)

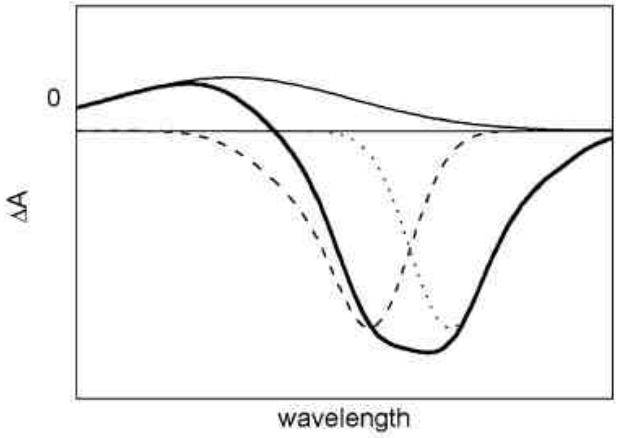

Figure 1.5: Contributions to a ΔA spectrum: ground-state bleach (dashed line), stimulated emission (dotted line), excited-state absorption (solid line), sum of these contributions (thin gray line).[37]

(3) **Excited state absorption:** Excited-state absorption occurs when a fraction of molecules in the lower excited states are promoted to higher excited states through the action of a pump beam. A positive signal is always observed for excited-state absorption (Figure 1.5, solid line). Excited-state absorption is observed for transitions that are optically allowed and the probe pulse absorption occurs at these wavelengths. The excited-state population does not change significantly by the excited-state absorption process because the probe pulse

intensity is very weak.

(4) **Product absorption:**

The excitation of a chromophore may result in products that have a short-lived (transient) or long-lived molecular state. These include triplet states, charge-separated states, and photoisomerized states. A positive signal in the ΔA spectrum will be observed for the absorption of such transient species. Ground-state bleach (GSB) will always occur in the chromophore if the product has a ground-state absorption (GSA).[37]

1.1.4 Laser Flash Photolysis

1.1.4.1 Introduction

The LP920 laser flash photolysis spectrometer is depicted in Figure 1.6. It is used to obtain transient absorption spectra and transient absorption kinetics of compounds using the laser flash photolysis principle. Based on the modular construction and flexibility of the LP920, it can be used to study both chemical

Figure 1.6: A Laser Flash Photolysis Spectrometer, the LP920.[38]

and/or biological species. It also allows users to measure TA in either kinetic or spectral mode. The LP920 is available in three configurations, namely Kinetic (LP920-K), Spectral (LP920-S), and Combined (LP920-KS). The Kinetic (LP920-K) is used mainly for lifetime transient decay measurements at a single wavelength by using a single detector and oscilloscope. The Spectral (LP920-S) on the other hand, is used primarily for spectral measurements of the decay process by making use of a CCD camera.[38] The Combined (LP920-KS) system is made from the combination of two versions of LP920-K and LP920-S into a single system and is used for both kinetic and spectral measurements. The experiments in this dissertation were performed using the Combined (LP920-KS) system.

Laser Flash Photolysis Spectrometer

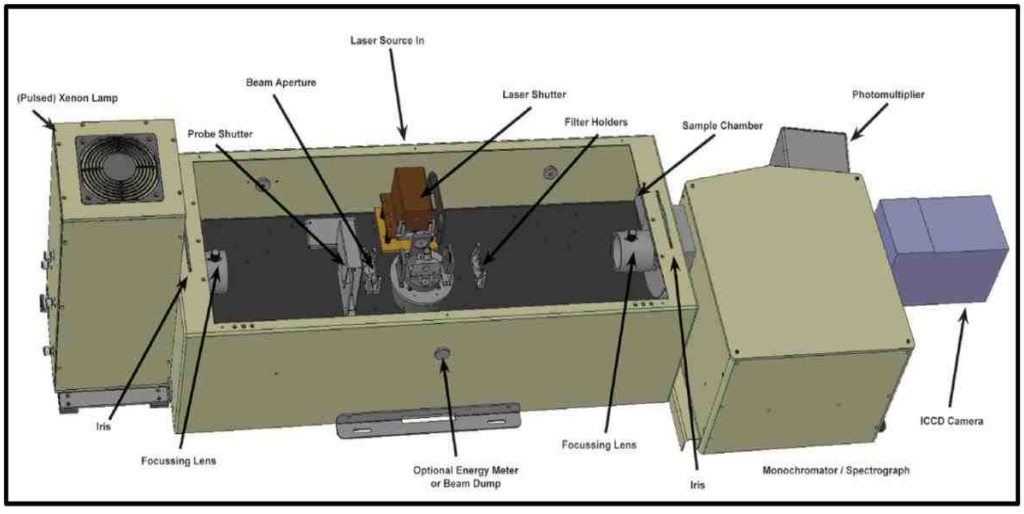

Figure 1.7: Laser flash photolysis spectrometer (LP920) showing all the individual components.

The laser flash photolysis spectrometer is like a single beam UV-VIS absorption spectrometer with some added distinct features. The additional features include pulsed excitation, and the pump source (Figure 1.7). These features help in the generation of the transient species. Figure 1.8 depicts the principal layout of a laser flash spectrometer. Excited-state (ES) species are generated using an intense pulse of the pump source, i.e. using a laser source. The analyzing light from a xenon lamp passes through the sample at right angles to the path of the exciting pulse, and the light is then directed to the monochromator/spectrograph. For kinetic analysis at a single wavelength, the transmitted probe light is measured by a single detector and, for spectral analysis at a given time, the transmitted probe light is measured by an array detector. The detector then converts the transmission properties of the sample during, before, and after laser excitation pulse into electrical signals.

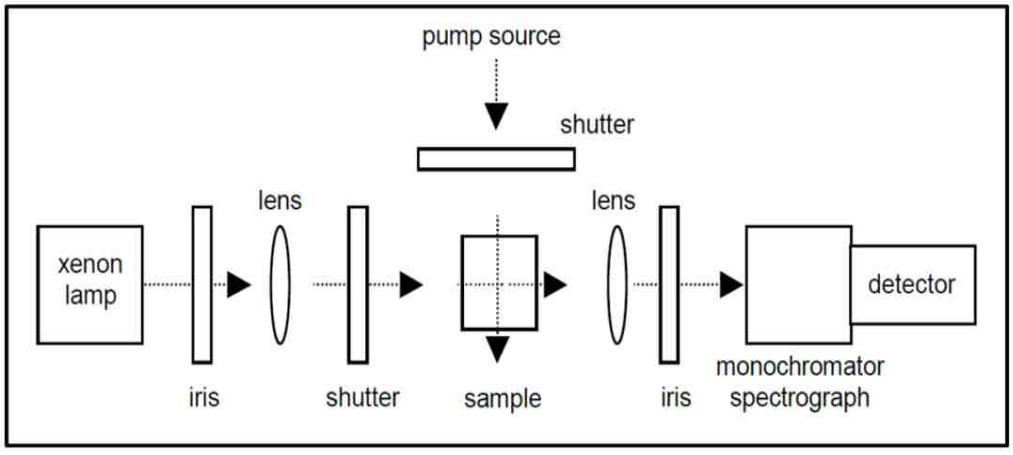

Figure 1.8: Principal layout of a laser flash spectrometer.[38]

These electrical signals are measured by an oscilloscope for kinetic analysis at a single wavelength and by a CCD camera for time-dependent spectral analysis.

The changes of optical density are generated from the changes in the transmission properties. For kinetic analysis using laser flash photolysis, the time scale for the measurements using this instrumentation are in the microsecond to the upper nanosecond regions. A background level is required for this analysis like other absorption measurements to enable the observation of changes in transmission and hence changes in optical density. The background photon flux provided by either a xenon or tungsten lamp is inadequate, so the probing xenon lamp is operated in a pulsed mode (see Figure 1.7). This pulsed mode provides a larger background level for the kinetic analysis time scale. The photon flux for the time of the pulse duration is increased by ~2 orders of magnitude using the pulsed mode operation. The signal-to-noise ratio is remarkably improved using

Sample Geometries

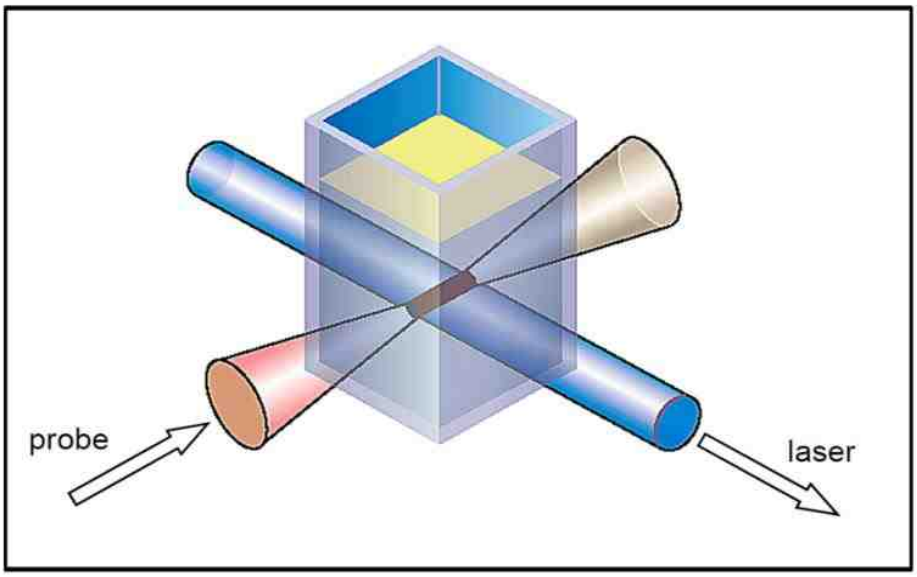

Figure 1.9: Standard cross-beam sample geometry[38]

the pulsed mode operation in this time scale region. The LP920 incorporates a probe shutter and laser shutter to protect the sample from continuous high probe light levels in between experimental measurements. The experimental spectral range for the LP920-KS is 200-870 nm.[38]

In a laser flash photolysis experiment, the alignment between the probe beam and laser beam plays a vital role. To attain the largest changes in the absorbance and to reduce scattered light and fluorescence, the two beams must overlap each other perfectly when using fluid sample solutions. This is known as a cross-beam or perpendicular geometry (see Figure 1.9). In the standard LP920 instrument, with a fluid solution sample, a relatively low concentration of the transient species is generated when a right-angle excitation geometry is used. The only drawback to employing a right-angle excitation is that, at the wavelength where the starting material absorbs, the monitoring light can be greatly reduced. This drawback can be minimized by using fluid solutions of low absorbance or by narrowing the entrance slits where an iris is employed.[38]

1.1.4.2 Energy Scheme

The photochemical and photophysical properties of compounds can be studied using the flash photolysis technique. This technique is used to study absorption and kinetic characteristics of excited state species. Excited state species in molecules are created by light irradiation. The ground state absorption of the sample is triggered by means of a pulsed excitation source, such as a laser or flash lamp. With the use of a laser as an excitation source, a significant amount

of the excited state species can be generated.[38] Once the excited state species is generated, there are several ways that this excited state energy may be

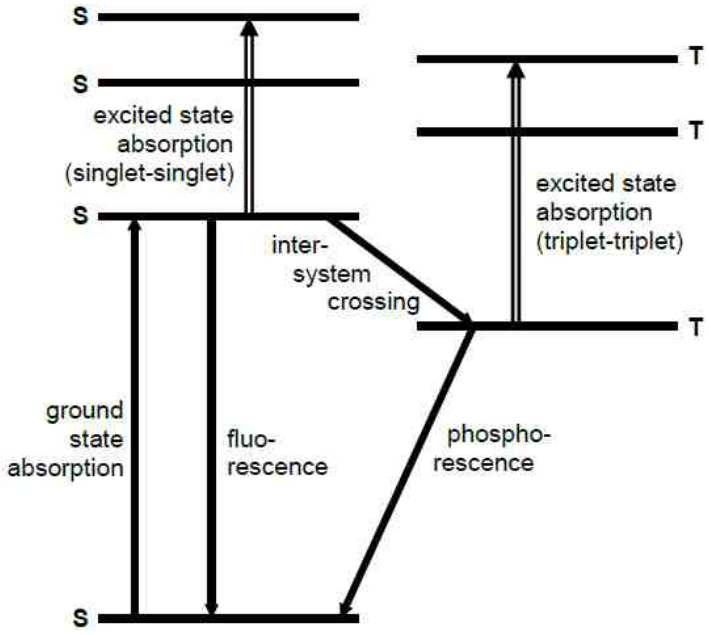

Figure 2.0: Jablonski Energy Diagram[38]

dissipated, and this is depicted in the Jablonski energy diagram of Figure 2.0. Energy dissipation can occur through both radiative and non-radiative processes. Radiative transitions can be absorptive or emissive depending on whether the transition is to a higher energy level or to a lower energy level. Non-radiative processes include vibrational relaxation, internal conversion (IC), and intersystem crossing (ISC). Non-radiative processes can occur through several different mechanisms. [39,40]

Vibrational relaxation occurs when there is a relaxation of an excited state from high vibrational quanta to the lowest vibrational level. Since this relaxation occurs only between vibrational energy levels, this process occurs within the same excited electronic state and is in the form of kinetic energy (heat). Vibrational

relaxation occurs on very fast time scale, between 10^{-14} to 10^{-11} seconds but slower than absorbance, which occurs on a time scale of ~10^{-15} seconds. Since vibrational relaxation occurs on a very fast time scale, it is highly likely to occur instantly after absorption. However, if an overlap exists between electronic and vibrational energy levels, there is a possibility that the molecule may relax from a vibrational level in one state to a vibrational level in another electronic state. If this process occurs without a change in spin, this is referred to as internal conversion, and it is similar to vibrational relaxation mechanistically. Intersystem crossing (ISC) is a distinctly different pathway for a molecule to dissipate energy during excited state relaxation. The process is radiationless and involves two electronic states with different spin multiplicity (e.g. from S→T). Since ISC processes violates the spin selection rule, ISC is the slowest process in the Jablonki energy diagram.[41] This is a forbidden transition but is made partially allowed by spin-orbit coupling. ISC may lead to the observation of phosphore-scence and delayed fluorescence as depicted in Figure 2.1.

Phosphorescence is a radiative process where an electron transitions from an excited state (e.g. T_1) to a ground state (e.g. S_0) of different spin multiplicity. Delayed fluorescence occurs as a result of thermal equilibrium between states, for example S_1 and T_n with the emissive transition being $S_1 \rightarrow S_0$ to the ground electronic state. Phosphorescence emission occurs on a longer time scale than fluorescence emission due to a spin forbidden ISC from an excited state to the ground state. In phosphorescence, the emitted photon has lower a energy

compared to that of fluorescence (i.e. S_1 is higher in energy than T_1) and hence the emitted photons are observed to have longer wavelength.[40]

Fluorescence is another pathway whereby energy can be dissipated after

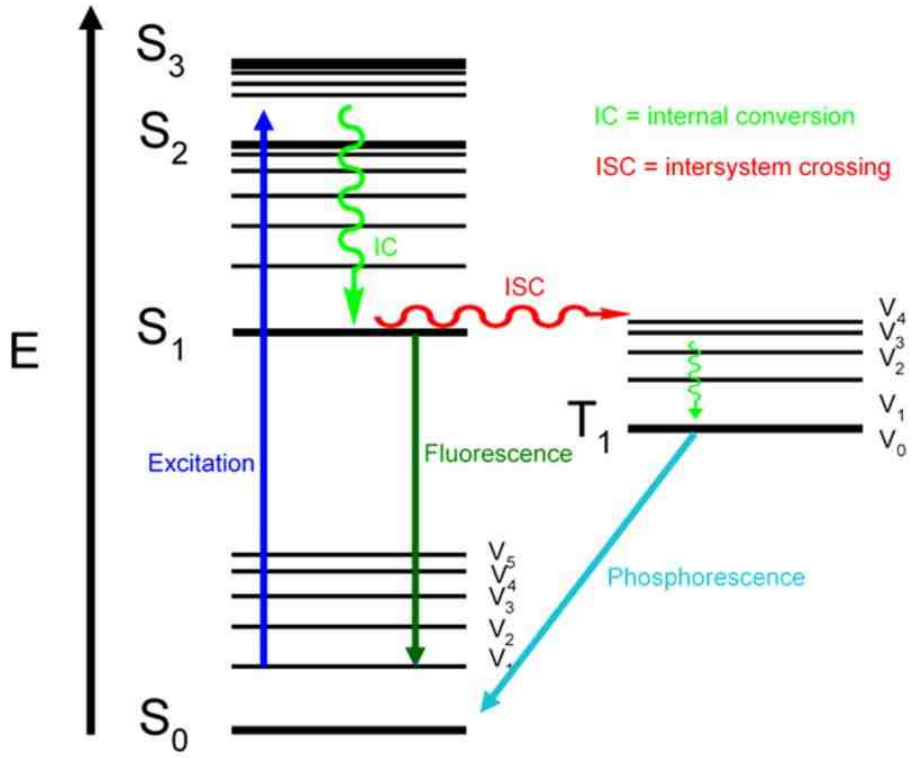

Figure 2.1: Energy scheme showing excited state absorption

photoexcitation, and this is indicated in Figure 2.1. It occurs if an excited molecule occupies the lowest singlet excited state for a period of about 10^{-8} seconds before dissipating energy to the ground state. Fluorescence occurs if the relaxation from the long-live state is associated with the emission of a photon. Fluorescence is detected as emission intensity over a range of wavelengths rather than a single sharp line. The emission intensity occurs due to the coupling of the closely spaced vibrational energy levels to the thermal motion of the molecule, and this results in the production of a variety of photon energies during

emission. Fluorescence is a spin allowed transition. This radiative transition occurs frequently between the first excited singlet (S_1) state and the ground state for any given molecule. The quantum of radiation given off during fluorescence is lower in energy than the quantum absorbed. This difference in energy can be attributed to vibrational relaxation after absorption. Moreover, the fluorescence spectrum is observed at a longer wavelength than the corresponding absorption spectrum. The energy difference is known as the Stokes Shift.[39]

Table 1.2: Non-radiative and radiative processes time scales.[39,40]

Transition	**Time Scale (s)**	**Radiative Process?**
Intersystem Crossing (ISC)	$10^{-8} – 10^{-3}$	No
Internal Conversion (IC)	$10^{-14} – 10^{-11}$	No
Vibrational Relaxation	$10^{-14} – 10^{-11}$	No
Absorption	10^{-15}	Yes
Fluorescence	$10^{-9} – 10^{-7}$	Yes
Phosphorescence	$10^{-4} – 10^{-1}$	Yes

Table 1.2 depicts the average time scale for radiative and non-radiative processes. By knowing the time scales for each process, one can understand which process is more probable. All the processes listed in Table 1.2 can be incorporated into a single Jablonski diagram for any given molecule of interest to showcase all the processes that occur after irradiation of a molecule with light energy.[39,40] Species generated in the excited state can be grouped into long-lived (ranging from 100’s of ns to s) and short-lived excited species (usually from ps to

10's of nanoseconds). Singlet to singlet ($S_n \rightarrow S_m$) transitions always generate short-live excited state species. Laser flash photolysis usually probes the long-lived triplet excited state and triplet→triplet excitations.

1.1.4.3 The Observable ΔOD

In laser flash photolysis, the change in absorption can be calculated in units of differential optical density (ΔOD) because of the change in sample transmission as illustrated in equation 2.1. I_{100} is the light measured prior to the generation of the excited state species and I_T represents the transmitted (probe) light through the sample, at times during and shortly after the generation of the excited state species when the laser pump beam converts a significant amount of the molecules in the electronic ground state to the excited state.

$$\Delta OD(t,\lambda) = log\ \frac{I_{100}}{I_T(t,\lambda)} \quad \text{..... (2.1)}$$

The change in optical density, ΔOD is given by equation 2.2 when the singlet-singlet transition is disregarded. The singlet-singlet transition is often disregarded because the singlet excited state is deactivated very rapidly by fluorescence and other processes. Moreover, species in the excited singlet state do not undergo further absorption into higher singlet state because they are so short-lived.

$$\Delta OD(t,\lambda) = \mathcal{E}_T(\lambda)C_T(t)d - \mathcal{E}_G(\lambda)[C_T(t) + C_S(t)]d - \phi(\lambda)C_S(t) \quad \text{..... (2.2)}$$

$\mathcal{E}_G$ denotes the extinction of the ground state, $\mathcal{E}_T$ is the extinction of the transient, d is the probe beam path length, ϕ is the fluorescence spectrum of the sample, C_S and $\mathcal{E}_T$ are the concentrations of excited singlet species and triplet species,

respectively. The true triplet-triplet features are divulged by the observable ΔOD if the spectra have no ground state absorption contribution ($\mathcal{E}_G = 0$) as depicted in equation2.3. Under these conditions, the observable ΔOD is positive. In Figure

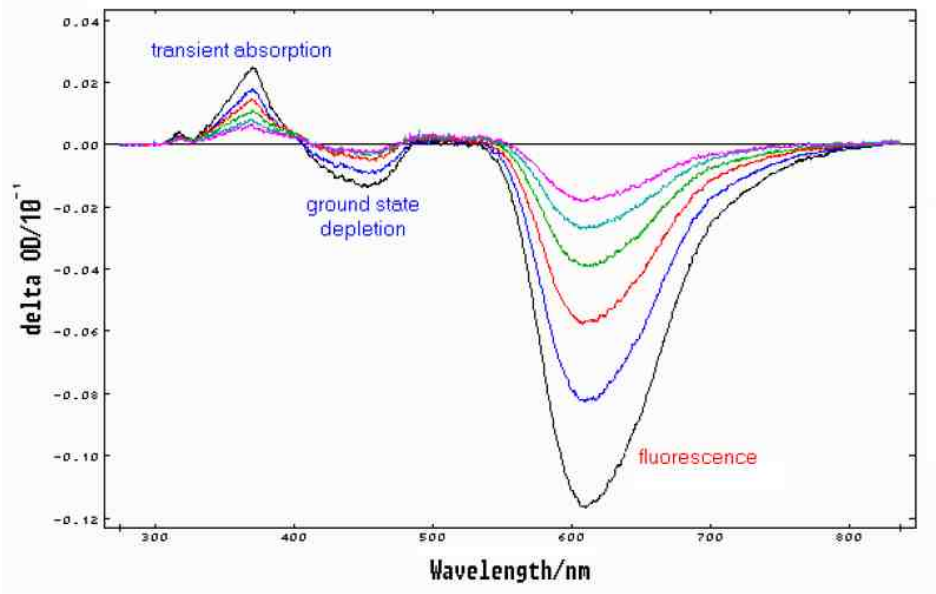

Figure 2.2: Spectral Features of the observable ΔOD against the ground state absorption and fluorescence.[38]

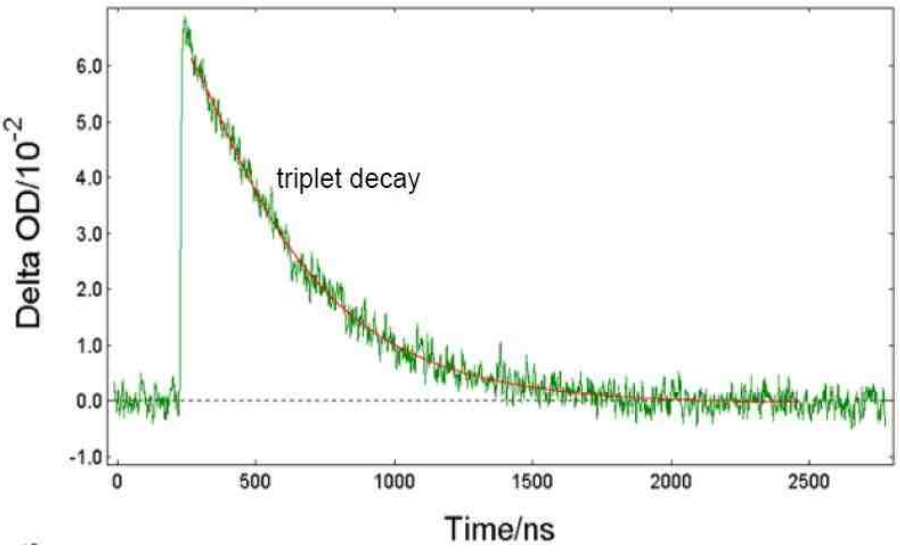

Figure 2.3: Kinetic features of the observable ΔOD showing triplet decay.[38]

$\Delta OD(t,\lambda) = \mathcal{E}_T(\lambda)C_T(t)d$ ..... (2.3)

2.2, the top left portion of the spectrum shows a positive ΔOD (this can be overlying with ground state depletion) that decays (see Figure 2.2). The change in optical density (ΔOD) is negative if spectral measurements are obtained in areas where ground state absorption (GSA) is the dominant as depicted in equation 2.4. This is shown in the center region of Figure 2.2, and in Figure 2.4. The ΔOD can cancel out to be zero in areas with both ground state and triplet absorption, although the triplet absorption is the strongest. The change in optical density can also be negative if the spectral regions have contributions from fluorescence. The decay kinetics associated with fluorescence are very fast since it involves the spin allowed decay of a short-live singlet species.[38]

$\Delta OD(t,\lambda) = -\mathcal{E}_G(\lambda)c_T(t)d$ ..... (2.4)

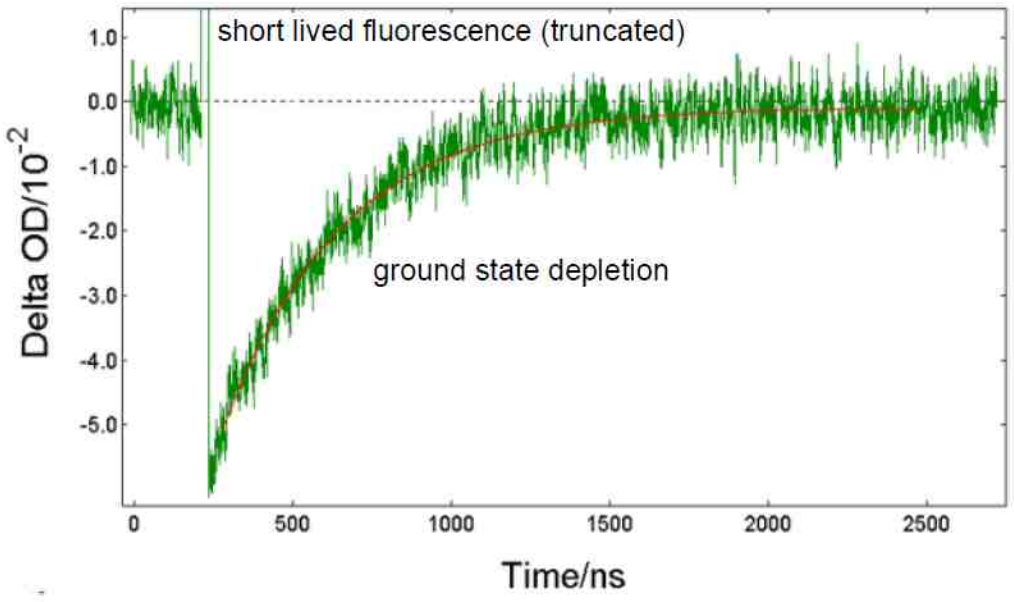

Figure 2.4: Kinetic features of the ΔOD showing ground state depletion.[38]

1.1.4.4 Kinetics in Laser Flash Photolysis

The kinetics of excited state processes can be revealed by the observable ∆OD. The equations detailed below will briefly summarize the decay rate laws related to the kinetics of various molecular excited state processes.

First order decays

An example of first order (unimolecular) decay occurs when a sample is excited to the triplet state, ^{3}M*, with a low intensity laser pulse. In the absence of a quencher, the triplet state molecule decays by non-radiative collisional deactivation because of its interaction with solvent molecules. The low intensity laser pulse always results in ≲10% transformation to the triplet state. This decay process yields a unimolecular first order decay rate constant, k_1, given below:

$$\frac{-d[^3M^*]}{dt} = k_1 \ [^3M^*] \ldots\ldots\ldots\ldots\ldots\ldots\ldots\ldots\ldots\ldots\ldots\ldots\ldots\ldots\ldots\ldots\ldots\ldots\ldots\ldots\ldots\ldots\ldots (2.5)$$

$$\ln[^3M^*] = \ln\,[^3M_0^*] - k_1 t \ldots\ldots\ldots\ldots\ldots\ldots\ldots\ldots\ldots\ldots\ldots\ldots\ldots\ldots\ldots\ldots\ldots\ldots\ldots\ldots (2.6)$$

Here, $[^3M_0^*]$ represent the initial concentration of $^3M^*$. Equation 2.6 can be rewritten in the form of equation 2.7 by replacing the sample triplet concentration $^3M^*$ by the time-dependent concentration c(t).

$$c(t) = c_0 \ e^{-k_1 t} \ldots\ldots\ldots\ldots\ldots\ldots\ldots\ldots\ldots\ldots\ldots\ldots\ldots\ldots\ldots\ldots\ldots\ldots\ldots\ldots\ldots\ldots\ldots\ldots (2.7)$$

In terms of the change in optical density (∆OD), equation 2.7 becomes:

$$\Delta\mathrm{OD(t)} = \Delta\mathrm{OD}_0 \ e^{-k_1 t} \ldots\ldots\ldots\ldots\ldots\ldots\ldots\ldots\ldots\ldots\ldots\ldots\ldots\ldots\ldots\ldots\ldots\ldots\ldots\ldots\ldots (2.8)$$

Where ΔOD_0 and ∆OD(t) represent the initial differential absorbance and the differential absorbance at time, t respectively. From the single exponential fits of

the measured temporal dependence of ΔOD, the first order rate constant, k_1, for the decay process can be determined.

Pseudo-first order decays

In the presence of a quencher, such as molecular oxygen, $O_2(^3\sum)$, this triplet state can be quenched, and its rate of decay would increase relative to a first order decay process. In this approximation, the comprehensive rate of decay of $[^3M^*]$ can be written as:

$$\frac{-d[^3M^*]}{dt} = k_1\ [^3M^*] + k_q\ [^3M^*][O_2]\ \ldots\ldots\ldots\ldots\ldots\ldots\ldots\ldots\ldots\ldots\ldots\ldots\ldots\ldots (2.9)$$

Pseudo-first order kinetics are observed because the ground state oxygen concentration (10^{-3} to 10^{-4} mol•L^{-1}) is far greater than the concentration of the triplet state (10^{-6} to 10^{-7} mol•L^{-1}). Thus, the rate of decay can be rewritten as:

$$k_2 = k_1 + k_q[O_2] \ldots\ldots\ldots\ldots\ldots\ldots\ldots\ldots\ldots\ldots\ldots\ldots\ldots\ldots\ldots\ldots\ldots\ldots\ldots\ldots\ldots\ldots (2.10)$$

Thus, the decay rate law and exponential decay are the same as that predicted by equations 2.7 and 2.8 respectively, but with a faster decay time due to an increase in the rate constant.

Second order decays (triplet-triplet annihilation)

With a high intensity laser pulse, a notable concentration of the triplet species can be created, and this increases the probability of collisions between triplets. This results in what is called triplet-triplet annihilation.

$[^3M^*] + [^3M^*] \xrightarrow{k_q}$ cts …… (2.11)

Products obtained under this condition can be two ground state species, a combination of S_1 and S_2, dimers, and the creation of S_1 excited states resulting in P-type delayed fluorescence. The overall rate of decay for $[^3M^*]$ at high laser pulse energies is given by:

$$\frac{-d[^3M^*]}{dt} = k_1\ [^3M^*] + k_a\ [^3M^*]^{\,2} \quad \ldots\ldots\ldots\ldots\ldots\ldots\ldots\ldots\ldots\ldots\ldots\ldots\ldots\ldots\ldots\ldots (2.12)$$

Replacing $[^3M^*]$ by c(t), the mathematical solution for the second order kinetic is:

$$c(t) = \frac{c_0}{(1 + k_2 t)} e^{-k_1 t} \quad \ldots\ldots\ldots\ldots\ldots\ldots\ldots\ldots\ldots\ldots\ldots\ldots\ldots\ldots\ldots\ldots\ldots\ldots (2.13)$$

$$\Delta OD(t) = \frac{\Delta OD_0}{(1 + k_2 t)} e^{-k_1 t} \quad \ldots\ldots\ldots\ldots\ldots\ldots\ldots\ldots\ldots\ldots\ldots\ldots\ldots\ldots\ldots\ldots\ldots\ldots (2.13)$$

with $k_2 = c_0\ k_a$

The triplet-triplet annihilation decay law is non-exponential, and is characterized by a fast, dramatic signal intensity reduction due to the first part of Eqn. 2.13. The second part of Eqn. 2.13 is characterized by an exponential decay that goes to zero asymptotically. Triplet-triplet annihilation is very common in laser flash photolysis when both sample concentrations and laser pulse energies are high. Second order decays (e.g. triplet-triplet annihilation) are normally applied in laser flash photolysis when a single exponential decay function provides an unacceptable result.

1.1.4.5 Analysis of Kinetic Data

Kinetic data can be analyzed using exponential sample decay (or growth) models given in equation 2.14. The kinetic data usually involves time resolved

transient ΔOD curves or time resolved emission measurements and it demands the use of numerical analysis for obtaining the rate constants or intrinsic lifetime parameters. The growth or decay processes can be single exponential, multi exponential, or non-exponential as observed in second order kinetics.

Mathematically, an exponential growth or decay process is given by:

$$\boldsymbol{R}(\boldsymbol{t}) = \boldsymbol{A} + \sum_{i=1}^{4} B_i \quad e^{-t/\tau i} \ldots\ldots\ldots\ldots\ldots\ldots\ldots\ldots\ldots\ldots\ldots\ldots\ldots\ldots\ldots\ldots\ldots\ldots\ldots..\ldots\ldots\ldots\ldots\ldots.(2.14)$$

where B_i is pre-exponential factor, τ_i is the intrinsic lifetime, and A is an additional background. R(t) represents the sample decay model. This is a theoretical expression that represents the sample response to an infinitely short excitation pulse. The amplitude of the curves at zero time is given by the pre-exponential factors (B_i). The values of B_i can either be positive or negative. For exponential decay process, B_i is positive, and it is negative when the process involves growth of a spectroscopic feature in the time domain. The intrinsic lifetime, τ_i, is the most important of the lifetime parameters. The intrinsic lifetime is specific for a particular growth or decay processes and is also equal to the inverse of the rate constant (k^{-1}) for that process. It represents the time it takes for the number of the excited molecules to decay to 1/e or 37% of the original value. For kinetic data involving changes in the optical density [ΔOD(t)], B_i defines the optical density at time t = 0. These values can be positive for transient absorption features or negative if the feature represents a ground state depletion.

1.1.4.6 Numerical Fitting

The numerical data fit allows the extraction of decay or growth parameters such

as B$_i$ and τ_i from the experimental data, raw emission data, or calculated ΔOD curves. By using a Marquardt-Levenberg, or similar function minimization algorithm, the best-fit B$_i$ and τ_i values can be obtained. The Marquardt-Levenberg algorithm is an iterative procedure that searches for the best B$_i$ and τ_i by a managed and regulated minimization of the “goodness of fit” parameter, χ_g^2, which is given by:

$$\chi_g^2 = \sum_k W_k^2 \ (S_k - F_k)^2 \ldots\ldots\ldots\ldots\ldots\ldots\ldots\ldots\ldots\ldots\ldots\ldots\ldots\ldots\ldots\ldots\ldots\ldots\ldots\ldots\ldots (2.15)$$

Here, F$_k$ represents the raw measured data, S$_k$ is the curve fitted data points, and the W$_k$ are the weighting factors for the individual data points. By using the Marquardt-Levenberg algorithm, two sets of linear equations can be obtained and solved simultaneously by taking the partial derivatives of χ_g^2 with respect to B$_i$ and τ_i, respectively, and setting them both to zero. The values obtained for B$_i$ and τ_i from the two simultaneous equations yield the fit best to the raw data. The Marquardt-Levenberg algorithm can also be used to generate the standard deviation for each of the fitted parameters, in addition to the best intrinsic lifetime parameters.[38]

1.2 Brief Literature Review

1.2.1 Donor-Acceptor (D-A) Interactions

The use of Donor-Acceptor (D-A) and Donor-Bridge-Acceptor (D-B-A) molecules have played a vital role in obtaining insight into photoinduced electron transfer (PET), electronic coupling (H$_{DA}$), ligand spin-orbit coupling, anisotropic covalency, molecular conductance and rectification.[28,41-58] Complexes of the type

diimineplatinum(II)dichalcogenolene, depicted in Figures 2.5 and 2.6, have played a prominent role in electronic structure studies due to their tunable electronic structures. The flexibility inherent to their electronic structures results in modification and tuning of the observed long wavelength interligand charge

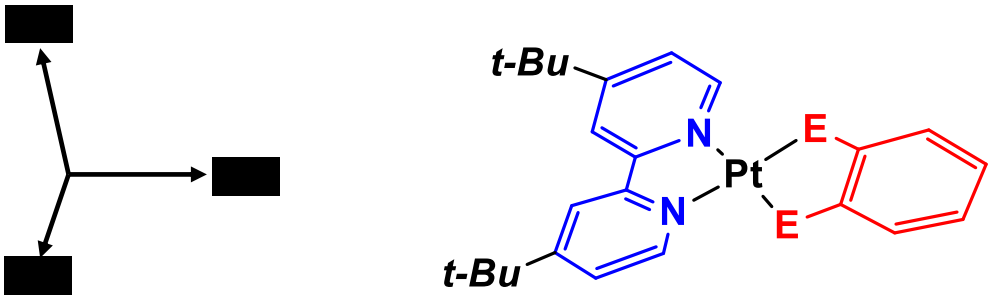

Figure 2.5: Structure of (dbbpy)Pt(E,E) complexes where E,E = O,S; O,Se; S,S; S,Se; and Se,Se. Blue and red fragments represent acceptor and donor ligands respectively. dbbpy represent the diimine ligand 4,4'-di-tert-butyl-2,2'-bipyridine.

transfer (CT) band in the visible to the near infrared region of the electronic spectrum. This interligand CT band is also referred to as a ligand-to-ligand charge-transfer (LL'CT) band or a mixed metal-ligand-to-ligand charge-transfer (MMLL'CT).[1-8,13-18,28,59-60]

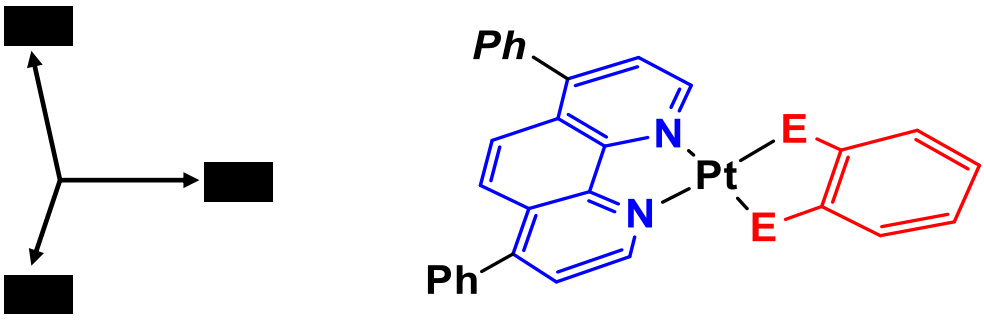

Figure 2.6: Structure of (dpphen)Pt(E,E) complexes where E,E = O,S, O,Se, S,S, S,Se, and Se,Se. Blue and red fragments represent the acceptor and donor ligands, respectively. The dpphen abbreviation represents the diimine ligand 4,7-diphenyl-1,10-phenanthroline

The LL'CT excited state of these complexes is marked by a substantial degree of charge separation along the z- or long axis of the complex, as depicted in figures 2.5 and 2.6. The LL'CT transitions in these complexes are of paramount importance in facilitating our understanding of biradical charge-separated states. The LL'CT excited state thus created is of the form (dichalcogenolene)$^{\bullet+}$Pt(diimine)$^{\bullet-}$ with an open shell D-A biradical character. [21]

1.2.2 Statement of Research Problem

To regulate excited state (ES) processes such as the rate constant for intersystem crossing (K_{ISC}), rate constant for radiative processes (K_r), and the rate constant for non-radiative process (K_{nr}) of the photogenerated (dichalcogenolene)$^{\bullet+}$Pt(diimine)$^{\bullet-}$ biradical states, attempts have been to made to synthetically alter the electronic structure of the dithiolene, dioxolene and diimine ligands of these D-A molecules. Nonetheless, there is an appreciable gap in the knowledge base regarding how the donor atom spin orbit coupling (SOC), anisotropic covalency in the metal-ligand (M-L) bonding scheme, and the concept of added spin controls critical excited state processes. These key factors can greatly affect ES processes by supplying a way to control charge and spin transfer in molecular systems. The (dichalcogenolene)Pt(diimine) complexes have accumulated intense interest because of their photoluminescent (PL) behavior (which is derived from the low energy, long-lived triplet LL'CT excited state) and electrochromic properties. Modulating the ES processes in these molecules are of prime importance due to the ability of these processes to store

energy in a photoexcited state, facilitate interconversions between specific states, control the relative rates of the ES processes, and avert electron-hole recombination to form the ground state. The key questions that I would examine in this chapter include the

following:

1. How can M-L (metal-ligand) anisotropic covalency be used in a prognostic way to manage the lifetimes of excited state (ES) process?
2. Does the ligand spin-orbit coupling (SOC) modulate the ES lifetimes?
3. How can the introduction of a mixed donor ligand set such as O,S; O,Se; S-Se, with a variable donor atom SOC constant (ζ_O = 154, ζ_S = 365, ζ_{Se} = 1659 cm^{-1}) affect excited state processes?
4. How can the use of new Donor-Acceptor chromophores enrich our understanding of the role of spin in CT excited states to the extent of modifying intersystem crossing (ISC) rates and the regulation of ES lifetimes? [20,21]

1.2 Hypotheses

I hypothesize that ligand spin-orbit coupling (SOC) and metal-ligand (M-L) anisotropic covalency can be used in systematic way to discern the excited state lifetime processes in these D-A molecules that possess low-energy LL'CT excited states. The diimine ligands I proposed for this study are depicted in figure 2.7 and the dichalcogenolene ligands are depicted in Figure 2.8.

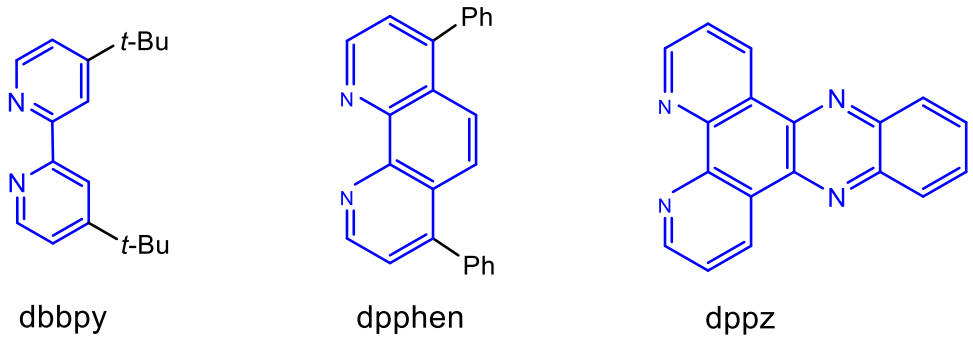

Figure 2.7: The diimine ligands used for this study.

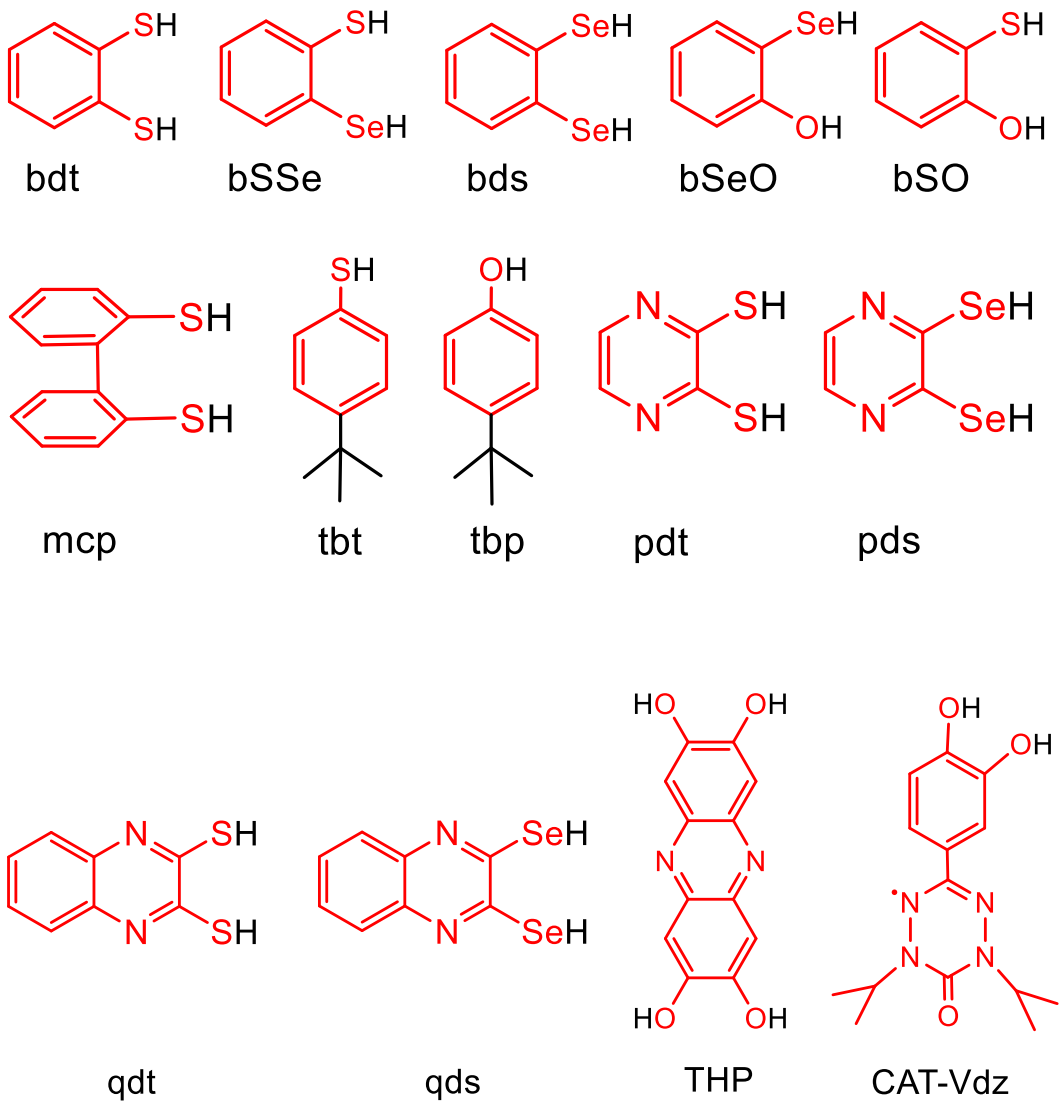

Figure 2.8: The dichalcogenolene ligands used in this study.

1.4 References

(1) Weinstein, J. A; Tierney, M. T.; Davies E. S.; Base, K.; Robeiro, A. A.; Grinstaff, M. W. *Inorg. Chem.* **2006**, 45, 4544-4555.

(2) Makedonas, C.; Mitsopoulou, C. A.; Lahoz, F.J.; Balana, A. I. *Inorg. Chem.* **2003**, 42, 8853-8865.

(3) Miller, T. R.; Dance, I.G.; *J. Am. Chem. Soc.* **1973**, 95, 6970.

(4) Hissler, M.; McGarrah, I. E.; Connick, W.B.; Geiger, D. K.; Cummings, S. D.; Eisenberg, R. *Coord. Chem. Rev.* **2000**, 208,115.

(5) Paw, W.; Cummings, S. D.; Mansour, M. A.; Connick, W. B.; Geiger, D. K.; Eisenberg, R. *Coord. Chem. Rev.* **1998**, 171,125.

(6) Cummings, S. D.; Cheng, L. T.; Eisenberg, R. *Chem. Mater.* **1997**, 9, 440.

(7) Cummings, S. D.; Eisenberg, R. *J. Am. Chem. Soc.* **1996**, 118, 1949.

(8) Cummings, S. D.; Eisenberg, R. *Inorg. Chem.* 1995, 34, 2007.

(9) Kubo, K.; Nakano, M.; Tamura, H.; Matsubayashi, G. E. *Inorg. Chim. Acta* **2002**, 336, 120.

(10) Islam, A.; Sugihara, H.; Hara, K.; Singh, L. P.; Katoh, R.; Yanakida, M.; Takahashi, Y.; Murata, S.; Arakawa, H. *Inorg. Chem.* **2001**, 40, 5371.

(11) Chen, C. -T.; Liao, S. -Y.; Lin, K. -J.; Chen, C. -H.; Lin, T. -Y. *J. Inorg. Chem.* **1999**, 38, 2734.

(12) Base, K.; Grinstaff, M. W., *Inorg. Chem.* 1998, 37, 1432.

(13) Makedonas, C.; Mitsopoulou, C. -A., *J. Inorg. Biochem.* **2001**, 86, 326.

(14) Cocker, T. M.; Bachman, R. E., *Inorg. Chem.* **2001**, 40,1550.

(15) Connick, W. B.; Gray, H. B., *J. Am. Chem. Soc*. **1997**, 119, 11620.

(16) Makedonas, C; Mitsopoulou, C.-A., *Spectrochim. Acta* **2006**, 64, 918.

(17) Makedonas, C.; Mitsopoulou, C.-A.; Lahoz, F.J.; Balana, A.I. *Inorg. Chem.* **2003**, 42, 8853.

(18) Lazarides, T.; McCormick, T. M.; Wlison, K. C.; Lee, S.; MaCamant, D. W.; Eisenberg R. *JACS* **2011**, 133, 350-364.

(19) Islam, A.; Sugihara, H.; Hara, K.; Singh, L. P.; Katoh, R.; Yanagida, M; Takahashi, Y.; Murata, S.; Arakawa, H., *Inorg. Chem.* **2001**, 40, 5371-5380.

(20) Connick, W. B.; Gray, H. B. *J. Am. Chem. Soc.* **1997**, 119, 11620-11627.

(21) Farmer, P. J.; Solouki, T.; Mills, D. K.; Soma, T.; Russell, D. H.;Reibenspies, J. H.; Darensbourg, M. Y. *J. Am. Chem. Soc.* **1992**, *114*, 4601.

(22) Darensbourg, M. Y.; Tuntulani, T.; Reibenspies, J. H. *Inorg. Chem.* **1995**, *34*, 6287.

(23) Farmer, P. J.; Solouki, T.; Soma, T.; Russell, D. H.; Darensbourg, M. Y. *Inorg. Chem.* **1993**, *32*, 4171.

(24) Buonomo, R. M.; Font, I.; Maguire, M. J.; Reibenspies, J. H.; Tuntulani, T.; Darensbourg, M. Y. *J. Am. Chem. Soc.* **1995**, *117*, 963.

(25) Buonomo, R. M.; Font, I.; Maguire, M. J.; Reibenspies, J. H.; Tuntulani, T.; Darensbourg, M. Y. *J. Am. Chem. Soc.* **1995**, *117*, 5427.

(26) Grapperhaus, C. A.; Darensbourg, M. Y.; Sumner, L. W.; Russell, D. H. *J. Am. Chem. Soc.* **1996**, *118*, 1791.

(27) Cummings, S. D.; Eisenberg, R. *Luminescence and Photochemistry of Metal Dithiolene Complexes*, **2004**, 339-340.

(28) Yang, J.; Kersi, K. K.; Giles, L. J.; Stein, B. W.; Feng, C.; Tichnell, C. R.; Shultz, D. A.; Kirk, M. L. *Inorg. Chem.* **2014,**53, 4791-4793.

(29) Que L Jr; *Physical Methods in Bioinorganic Chemistry: Spectroscopy and Magnetism*. University Science Books, Sausalito, California, **2000**.

(30) Solomon EI, Lever ABP; *Inorganic Electronic Structure and Spectroscopy: Volume I, Methodology*. John Wileys and Sons, Inc, **2006**.

(31) Drago R.S.; *Physical Methods for Chemists:* Second Edition. Surfside Scientific Publishers, **1992**.

(32) Shriver DF, Atkins PW; *Inorganic Chemsitry*: Third Edition. Oxford University Press, **1999**.

(33) Shriver DF, Atkins PW; *Inorganic Chemsitry*: Third Edition. Oxford University Press, **1999**.

(34) Hens Z*.; Chemical Physics Letters* **2008**, *463*, 391-395.

(35) Ed, J. L.; Joint Ed, R. G. W. Modern *Coordination Chemistry*; **1967.**

(36) www.andor.com/learning-academy/transient-spectroscopy-an-introduction-to-pump-probe-spectroscopy*.*

(37) Berera, R.; Grondelle, R. V.; Kennis, J. T. M. *Photosynth. Res., **2009**,101:105–118.*

(38) Operating instructions, LP920 Laser Flash Photolysis Spectrometry.

(39) Miller, A. L.; Jaffe, H. H. *J. Chem. Education,***1966**, 43, 469.

(40) Haug, A.; Priestley, E. B*. J. Chem. Phys.* **1968**, 49, 622.

(41) Barbara, P. F.; Meyer, T. J.; Ratner, M. A. *J. Phys. Chem.* **1996**, *100*, 13148-13168.

(42) Marcus, R. A. *Chem. Phys. Lett.* **1987**, *133*, 471-477.

(43) Gray, H. B.; Walther, R.; Ellis, J. Electron Transfer. In *Bioinorganic Chemistry*; Bertini, I., Gray, H. B., Lippard, S. J., Valentine, J. S., Eds. University Science Books: Sausalito, CA, 1994; pp 315-364.

(44) Nakamoto, T.; Yoshida, M.; Kitagawa, S.; Katada, M.; Endo, K.; Sano, H. *Polyhedron* **1996**, *15*, 2131-2139.

(45) Wall, M. H.; Basu, P.; Buranda, T.; Wicks, B. S.; Findsen, E. W.; Ondrias, M.; Enemark, J. H.; Kirk, M. L. *Inorg. Chem.* **1997**, *36*, 5676-5677.

(46) Sekiguchi, S.; Kobori, Y.; Akiyama, K.; Tero-Kubota, S. *J. Am. Chem. Soc.* **1998**, *120*, 1325-1326.

(47) Bleuzen, A.; Lomenech, C.; Dolbecq, A.; Villain, F.; Goujon, A.; Roubeau, O.; Nogues, M.; Varret, F.; Baudelet, F.; Dartyge, E.; Giorgetti, C.; Gallet, J. J.; Moulin, C. C. D.; Verdaguer, M. *Mol. Cryst. Liq. Cryst. Sci. Technol., Sect. A* **1999**, *334*, 965-974.

(48) Nelsen, S. F.; Ismagilov, R. F.; Gentile, K. E.; Powell, D. R. *J. Am. Chem. Soc.* **1999**, *121*, 7108-7114.

(49) Kuciauskas, D.; Liddell, P.; Lin, S.; Stone, S.; Moore, A.; Moore, T.; Gust, D. *J. Phys. Chem. B* **2000**, *104*, 4307-4321.

(50) Lewis, F.; Wu, T.; Liu, X.; Letsinger, R.; Greenfield, S.; Miller, S.; Wasielewski, M. *J. Am. Chem. Soc.* **2000**, *122*, 2889-2902.

(51) Miller, S.; Lukas, A.; Marsh, E.; Bushard, P.; Wasielewski, M. *J. Am. Chem. Soc.* **2000**, *122*, 7802-7810.

(52) Sato, O.; Hayami, S.; Gu, Z.; Seki, K.; Nakajima, R.; Fujishima, A. *Chem. Lett.* **2001**, 874-875.

(53) Davis, W. B.; Ratner, M. A.; Wasielewski, M. R. *Chem. Phys.* **2002**, *281*, 333-346.

(54) Tachikawa, T.; Kobori, Y.; Akiyama, K.; Katsuki, A.; Usui, Y.; Steiner, U. E.; Tero-Kubota, S. *Mol. Phys.* **2002**, *100*, 1413-1420.

(55) Lukas, A. S.; Bushard, P. J.; Weiss, E. A.; Wasielewski, M. R. *J. Am. Chem. Soc.* **2003**, *125*, 3921-3930.

(56) Goldsmith, R. H.; Sinks, L. E.; Kelley, R. F.; Betzen, L. J.; Liu, W. H.; Weiss, E. A.; Ratner, M. A.; Wasielewski, M. R. *Proc. Natl. Acad. Sci. U.S.A.* **2005**, *102*, 3540.

(57) Kirk, L. M.; Shultz, D. A.; Depperman, E. C.; Brannen, C. L. *J. Am. Chem. Soc.* **2007**, *129*, 1937-1943.

(58) Turro, N. J.; Ramamurthy, V.; Scaiano, J. Modern Molecular Photochemistry of Organic Molecules; University Science Books: Mill Valley, CA, 2010.(59) Best, J.; Sazanovich, I. V.; Adams, H.; Bennett, R. D.; Davies, E. S.; Meijer, A. J. H. M.; Towrie, M.; Tikhomirov, S. A.; Bouganov, O. V.; Ward, M. D.; Weinstein, J. A. *Inorg. Chem.* **2010**, *49*, 10041-10056.

(60) Kirk, M. L. NSF Proposal, Donor-Acceptor interactions and their relationship to molecular electronics and excited state processes.

CHAPTER TWO

Materials, Methods, and Protocols

2.1 Reagents

Analytical reagent (AR) grade 4,7-Diphenyl-1,10-phenanthroline (dpphen), potassium tetrachloroplatinate(II) [K_2PtCl_4], N,N,N',N'-tetramethylethane-1,2-diamine (TMEDA), dichloromethane-d_2 (CD_2Cl_2-d_2), DMSO-d_6, chloroform-d ($CDCl_3$), 4,4'-di-tert-butyl-2,2'-bipyridine(dbbpy), Palladium(II)dichloride ($PdCl_2$), benzenedithiolate (bdt), *n*-butyllithium solution in hexane(2.5M), *sec*-butyllithium solution in cyclohexane (1.4M), phenylmagnesium bromide solution in THF(1.0M), potassium tert-butoxide, selenium powder, benzenethiol, 2,3-dichloropyrazine, potassium borohydride (KBH_4), sodium borohydride ($NaBH_4$), 2,3-dichloroquinoxaline, thiourea, selenourea, 1,2-dimethoxybenzene, hydrazine monohydrate ($N_2H_4.H_2O$), glacial acetic acid (CH_3CO_2H), 2,2'-biphenol, 4-tert-butylphenol, 4-tert-butylbenzenethiol, sodium hydride (NaH), hexamethylphosphoric triamide (HMPA), 1,2-dibromobenzene, and dimethylthiocarbamoyl chloride were supplied Sigma-Aldrich Chemicals. 2,5-dihydroxy-1,4-benzoquinone and 2-Bromophenol were supplied by Alfa Aesar Johnson Matthey Company.

2.2. Physical measurements and instrumentation

2.2.1 NMR Spectroscopy

^1H NMR spectra and decoupled ^{13}C NMR spectra were obtained on Bruker

Avance 500 MHz and Avance III 300 MHz NMR spectrometers, both of which are standard bore systems. ^{1}H and ^{13}C NMR chemical shifts (δ) are referenced to external tetramethylsilane (TMS) at δ 0.0. All NMR spectra were acquired at an ambient probe temperature of ~298 K.

2.2.2 Electronic Absorption Spectroscopy

Solution electronic absorption spectra of all the compounds were collected using a Hitachi-3501 UV-vis-NIR double beam spectrophotomer and 1 cm path length black-masked quartz cuvettes at room temperature. Samples were collected using these solvents: 1,2-dichloromethane (DCM), 1,2-dichloroethane (DCE), tetrahydrofuran (THF), toluene, benzene, acetonitrile, dimethylsulfoxide (DMSO), N,N-dimethylformamide (DMF), acetone, and chloroform.

2.2.3 X-ray Crystallography

Crystal structure determinations were performed in the Department of Chemistry and Chemical Biology at The University of New Mexico. The X-ray laboratory possesses a Kippa Apex II, Bruker top-of-line sealed tube chemical crystallography system. The instrument combines a 4-circle Kappa goniometer available with the APEX II CCD detector. The instrument can handle a wide range of samples from strongly diffracting to weakly diffracting due to the low dark noise and high gain obtained with CCD chip cooling. The instrument is equipped with a molybdenum fine focus sealed tube, graphite monochromator, and a low temperature attachment for collecting data down to $-75^{0}C$.

2.3 General synthetic procedures

All syntheses were carried out under dry argon and dinitrogen using standard Schlenk techniques. The organic solvents used were appropriately dried and purified using standard procedures and stored under an atmosphere of dry dinitrogen.

Transition metal diimine complexes have received significant attention over the past three decades due to their distinctive electrochemical and photophysical properties.[1-15] In this chapter, I will focus on general procedures for the synthesis of structurally similar Pt(II), Pd(II) and Ni(II) diimine complexes with different chalcogen donor ligands. The goal is to understand the impact of systematically varying the electronic structure of these compounds using the following parameters: (i) changing solvent polarity; (ii) substitution of sulfur for oxygen; (iii) substitution of oxygen for selenium; and (iv) substitution of sulfur for selenium. In these new transition metal complex chromophores, the lowest excited state is designated as a mixed metal/ligand-to-ligand charge transfer (MMLL'CT) state. The lowest energy spin allowed optical transition arises from a one-electron promotion from the HOMO of mixed Pt/S (or Pt/Se, Pt/O) character. The MMLL'CT state has been characterized using a combination of electronic absorption spectroscopy, emission spectroscopy, and Time Dependent Density Functional Theory (TD-DFT) calculations.

2.4 Description of synthetic schemes

2.4.1 Ligand Synthesis

2.4.1.1 2-selenylphenol (bSeO)

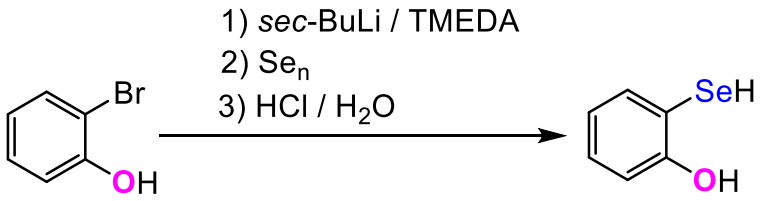

2-selenylphenol (bSeO) was prepared by a modification of the published literature procedure.[16] 2-Bromophenol (8.66 g, 50 mmol) dissolved in 10 mL of dry and degassed cyclohexane was added dropwise over 30 min to a stirred mixture of sec-butyllithium (1.3 M, 150 mmol) in cyclohexane, N,N,N',N'-tetramethylethane-1,2-diamine (11.62 g, 100 mmol), and cyclohexane (100 mL) at -40^{0}C. The reaction mixture was allowed to warm to room temperature over a period of 2 h and then stirred at this temperature for an additional 6 h.

The reaction mixture was cooled to 0^{0}C and selenium powder (3.94 g, 50 mmol) was added in one portion. The reaction mixture was allowed to warm to room temperature over an hour and stirred at this temperature for 1 day. The mixture was then cooled to 0 ^{0}C and acidified using hydrochloric acid (3 M, 200 mL), the organic layer separated, and the aqueous layer was extracted with pentane. The combined organic layer was dried with magnesium sulfate and the solvent was removed by vacuum. The product was obtained by vacuum distillation as a colorless oily liquid with an unpleasant odor. Yield 4.52 g, 52%. High-resolution electrospray ionization (ESI) mass spectrometry (m/z): calcd for C_6H_6OSe: 173.96; Found: 172.94 $[M]^-$. ^{1}H NMR spectrum (300 MHz, $CDCl_3$, 298 K, ppm): δ 1.22-1.28 (m, ^{77}Se satellites), 6.03 (br. s, 1H; OH), 6.80-6.88, 6.92-7.00, and 7.52-7.63 (m, 6H), 7.65 (m, 4H; SeC_6H_4O). ^{13}C NMR ($CDCl_3$, 300 MHz): δ 156.5

ppm, 136.9 ppm, 108.7 ppm 131.2 ppm, 121.5 ppm, 115.3 ppm, 108.7 ppm. ^{1}H NMR and ^{13}C NMR data were consistent with literature reported values.

2.4.1.2 2-selenylbenzenethiol (bSSe)

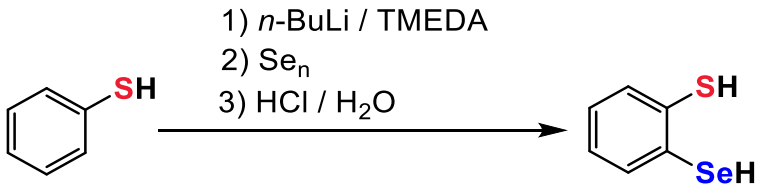

To a mixture of benzenethiol (3.07 g, 27.9 mmol) and N,N,N',N'-tetramethylethane-1,2-di-amine (3.6 g, 30.7 mmol) in hexane (60 mL) at 0 ^{0}C, was added a solution n-butyllithium (2.5 m, 61 mmol) in hexanes (25.0 mL) over a period of 20 min and the resulting mixture was allowed to warm to room temperature and stirred at this temperature for an additional 3 days. Thereafter, the mixture was cooled to 0 ^{0}C and then selenium powder (2.20 g, 27.9 mmol) was added in one portion. The reaction mixture was then allowed to warm to room temperature over a period of 2 h and stirred at this temperature for an additional 2 days. The mixture was cooled to 0 ^{0}C and acidified with hydrochloric acid (3 M, 100 mL), the organic layer separated, and the aqueous layer was extracted with diethyl ether (3 x 40 mL). The combined organic layer was dried with magnesium sulfate and the solvent was removed under vacuum. The product was obtained by vacuum distillation as a colorless oily liquid with an unpleasant odor. Yield 3.52 g, 67%. High-resolution electrospray ionization (ESI) mass spectrometry (m/z): calcd for C_6H_6SSe: 189.94; Found: 188.92 $[M]^{-}$.^{1}H NMR spectrum (300 MHz, $CDCl_3$, 298 K, ppm): δ 1.90–1.94 (m, ^{77}Se satellites), 3.90–3.93 (m, 1H; SH), 6.95–7.05, 7.09–7.18, 7.32–7.41, and 7.50–7.56 ppm (m,

4H; SeC_6H_4S). ^{13}C NMR ($CDCl_3$, 300 MHz): δ 127.1 ppm, 127.6 ppm, 127.8 ppm, 131.3 ppm, 133.4 ppm, 134.5 ppm. ^{1}H NMR and ^{13}C NMR data were consistent with literature reported values.[16]

2.4.1.3 Benzene-1,2-diselenol (bds)

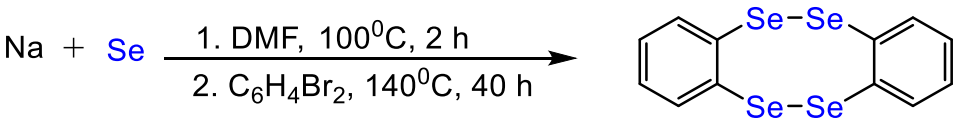

Benzene-1,2-diselenol(bds) was prepared by a modification of the literature procedure.[17] Sodium diselenide reagent was prepared from selenium powder (7.90 g, 0.1 mol) and sodium (2.30 g, 0.1 mol) in anhydrous DMF (100) at 100 ^{0}C under a dinitrogen atmosphere. The mixture was stirred for 2 h under these conditions, and then 1,2-dibromobenzene (11.8 g, 50 mmol) was added dropwise and the temperature of the bath raised to 140 ^{0}C. The mixture was kept at this temperature for 40 h, cooled to room temperature, and then diluted with 100 mL methanol. Brine solution (300 mL) was added and the mixture was washed with water, sodium sulfide solution, tetrahydrofuran (THF) and diethyl ether. 2.86 g of poly(o-diselenobenzene) was obtained as a brown solid after vacuum drying. Experimental mp is 116-122 ^{0}C and reported mp is 117-124 ^{0}C. The yield was 32%. The infrared (IR) spectrum and melting point data were consistent with the literature reported values. The oxidized poly(*o*-diselenobenzene) dimer was converted to the monomeric form by reacting it with excess sodium borohydride ($NaBH_4$) in methanol under an atmosphere of dinitrogen. The solid-state infrared (IR) spectrum was consistent with the literature reported values.

2.4.1.4 Pyrazine-2,3-diselenol (pds)

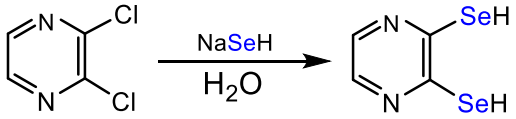

Pyrazine-2,3-diselenol (pds) was prepared by a modification of the literature procedure.[18] Sodium hydrogen selenide (NaHSe) was prepared with a 2:1 molar ratio of sodium borohydride ($NaBH_4$) to selenium in water. To an aqueous solution of NaHSe prepared from Se (3.45 g, 44 mmol) and $NaBH_4$ (3.45 g, 91 mmol) was added 2,3-dichloropyrazine (3 g, 20 mmol) in one portion under a dinitrogen atmosphere. The mixture was heated to reflux for 1 h and then cooled to 0 ^{0}C. The precipitate that formed was filtered off and the brown filtrate was treated with 30 mL of glacial acid to give the product. The product was filtered off and washed with water before being air dried. The solid state infra-red (IR) spectrum was consistent with the literature reported spectrum.

2.4.1.5 Pyrazine-2,3-dithiol (pdt)

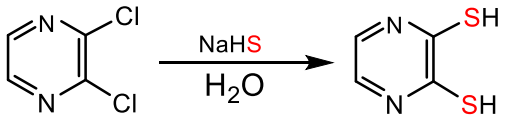

Pyrazine-2,3-dithiol (pdt) was prepared by a modification of the literature procedure.[19] To a mixture of 2,3-dichloropyrazine (4.96 g, 33 mmol) and NaHS (2.21 g, 39 mmol) in 50 mL of H_2O was stirred and reflux under the atmosphere of dinitrogen. The mixture was cooled to room temperature and the yellow precipitate that formed was filtered and washed with H_2O. The solid was added to water and then dissolved by the addition of a concentrated NaOH solution to a

pH >10. The solution was extracted with dichloromethane (3 x 25 mL) and the aqueous phase (top layer) was filtered and acidified with glacial acetic acid to pH< 3. The yellow solid that was formed was filtered off and washed with water, acetone, and diethyl ether. It was dried in a vacuum to give pure analytical yield. Yield 1.41 g, 30%. IR (KBr pellet): $\tilde{\nu}$ =3130, 3091, 2902, 2780, 1586, 1538, 1392, 1255, 1150,1040, 785, 645, 499 cm^{-1}. The solid-state infrared (IR) spectrum was consistent with the literature reported spectrum.

2.4.1.6 2,2'-dimercaptobiphenyl (mcp)

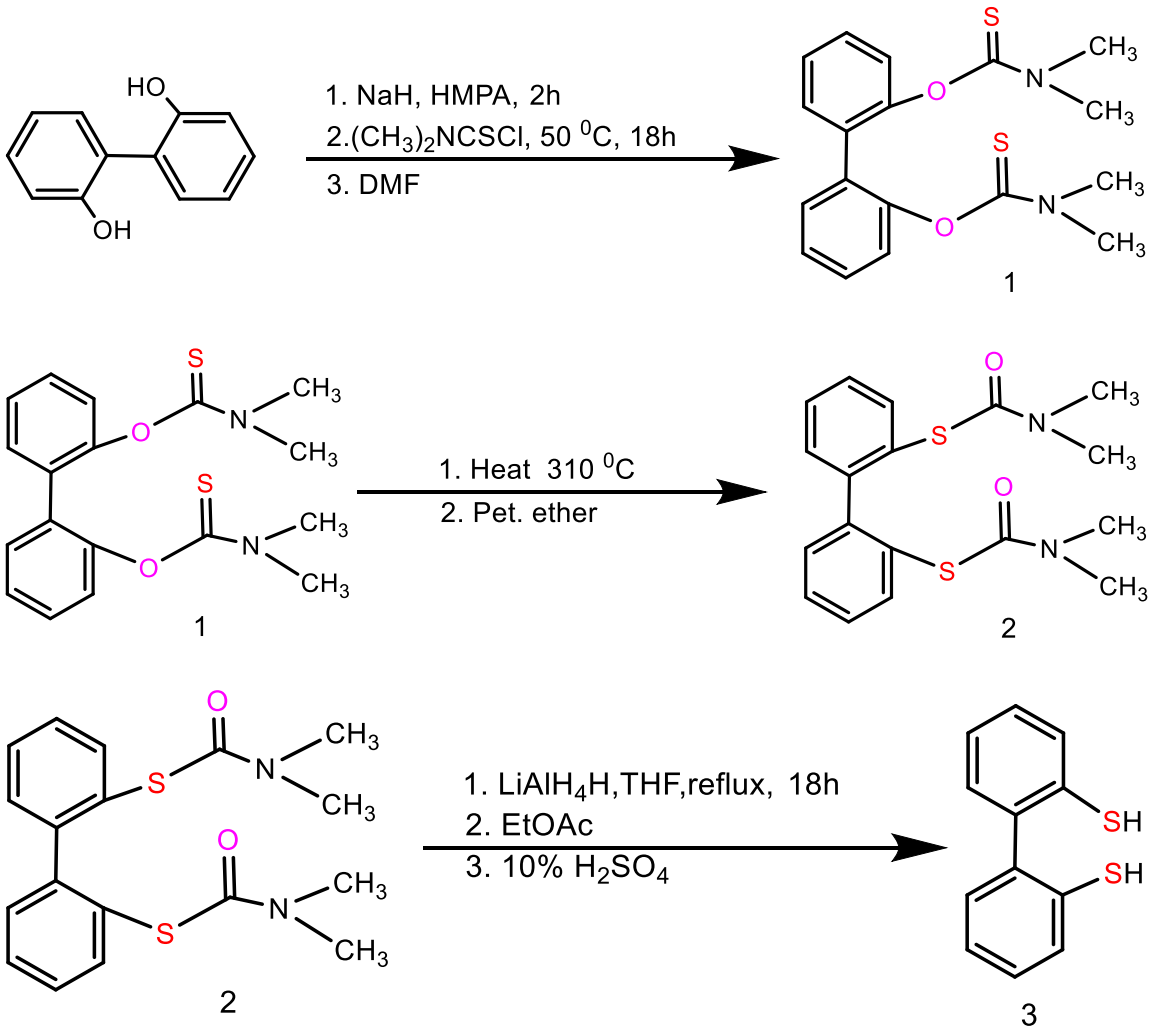

The synthesis of precursor 1 [2,2'-Bis(O-dimethylthiocarbamato) biphenyl] has been reported.[20] 2,2'-biphenol (9.88 g, 53 mmol) was dissolved in 100 mL of dry dimethylformamide (DMF), and sodium hydride (2.6 g, 106 mmol) was added in portions. Afterwards, 25 mL of hexamethylphosphoric triamide (HMPA) was added and the mixture was stirred for 3 h. Subsequently, N,N-dimethylthiocarbamoyl chloride (18 g, 145 mmol) was added in a single portion and the mixture stirred at 45-50 ^{0}C for 20 h. The mixture was added to 200 mL of H_2O and then extracted three times with 50 mL of 4:1 chloroform – petroleum ether. The combined organic layers were washed with saturated brine solution and dried over magnesium sulfate ($MgSO_4$). The solvent was remove under vacuum and the product was recrystallized from methanol. The yield was 18 g (89%). ^{1}H NMR spectrum (300 MHz, $CDCl_3$, 298 K, ppm): δ 3.04 (s, 6H), 3.28 (s, 6H), 7.34 (m, 8H). The ^{1}H NMR was consistent with the literature reported values.

The synthesis of precursor 2, [2,2'-Bis(S-dimethylthiocarbamato) biphenyl] was prepared from 2,2'-Bis(O-dimethylthiocarbamato) biphenyl (4.5 g, 13 mmol) placed in a 100 mL round bottom flask equipped with a dinitrogen gas inlet and outlet. The flask was heated at 310 ^{0}C in a salt-bath (40% $NaNO_2$, 7% $NaNO_3$, 53% KNO_3) for 30 min under the atmosphere of dinitrogen gas. The melt was cooled to room temperature and then washed with petroleum ether to give the crude brown solid. Recrystallization from a toluene-petroleum ether solvent mixture yielded 3.8 g (86 %) of product. ^{1}H NMR spectrum (300 MHz, $CDCl_3$, 298K, ppm): δ 2.82 (s, 12H), 7.45 (m, 6H), 7.65 (m, 2H). The ^{1}H NMR was

consistent with the literature reported values.

2,2'-dimercaptobiphenyl (mcp) was prepared from a solution of 2,2'-bis(S-dimethylthiocarbamato) biphenyl (5.6 g, 16 mmol) in 100 mL THF. Under an atmosphere of dinitrogen gas, $LiAlH_4$ (1.3 g, 34 mmol) in 80 mL of THF was added dropwise and the mixture was refluxed for 18 h. The excess $LiAlH_4$ was removed by treating the mixture with ethyl acetate, followed by the addition of 100 mL of 10% sulfuric acid. The two layers were separated with a separatory funnel and the aqueous layer extracted three times with 60 mL ether per extraction. The combine organic layers were dried over $MgSO_4$, and the filtrate was evaporated under reduced pressure to give a yellow oil. The crude product was then washed with petroleum ether and air dried to give a pale-yellow solid (2.5 g, 75%), mp 77^0 (lit, 78-79^0). ^{1}H NMR spectrum (300 MHz, $CDCl_3$, 298 K, ppm): δ 3.5 (s, 2H), 7.68-7.22 (m, 8H). ^{13}C NMR ($CDCl_3$, 300 MHz, 298 K, ppm): δ 138.1 ppm, 136.1 ppm, 128.9 ppm, 128.5 ppm, 127.9 ppm. The ^{1}H NMR was consistent with the literature reported values.[20]

2.4.1.7 Quinoxaline-2,3-dithiol (qdt)

Quinoxaline-2,3-dithiol (qdt) was prepared by a modification of the literature procedure.[21] 2,3-dichloroquinoxaline (2 g, 10 mmol) was dissolved in 60 mL of absolute ethanol, and thiourea (4 g, 53 mmol) was added in a single portion. The

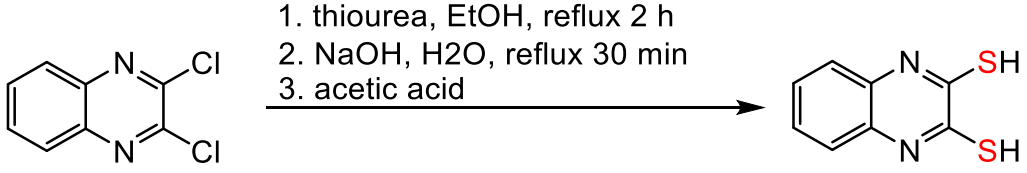

mixture was then refluxed for 4 h and the volume of the mixture was reduced. The remaining slurry was diluted with 50 mL of H_2O and treated with a solution of 13 g of NaOH in 80 mL of H_2O. The orange mixture was refluxed for 1 h and immediately filtrated. The filtrate was then acidified with glacial acetic acid to give a brown-red solid. The product was then filtered off and was washed several times with H_2O and ethanol. ^1H NMR spectrum (300 MHz, DMSO-d_6, 298 K, ppm): δ 1.90 (s, 2H), 7.26 (m, 2H), 7.42 (m, 2H).

2.4.1.8 Quinoxaline-2,3-diselenol (qds)

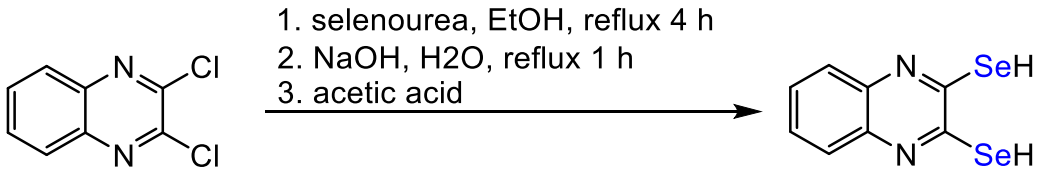

Quinoxaline-2,3-diselenol (qds) was prepared by a modification of the literature procedure[21] for the synthesis quinoxaline-2,3-dithiol (qdt). Selenourea was used in place of thiourea for the synthesis of quinoxaline-2,3-diselenol.

2.4.2 Synthesis of 4,4'-di-*tert*-butyl-2,2'-bipyridineplatinum(II) dichloride [Pt(dbbpy)Cl_2]

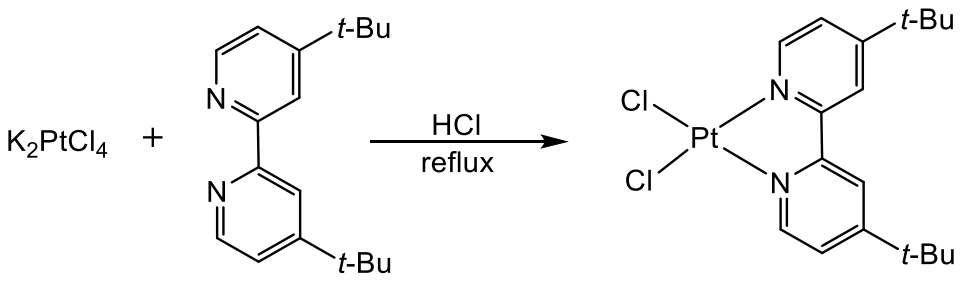

4,4'-di-*tert*-butyl-2,2'-bipyridine (0.26 g, 0.968 mmol) was added to a stirred solution of $K_2[PtCl_4]$ (0.400g, 0.968 mmol) in 6 M HCl (100 mL). The red suspension was refluxed for 1 day and the color changed to bright-yellow. The bright yellow precipitate was then isolated by filtration (0.480 g, 93.2%) and washed with distilled water, ethanol, hexane, and diethyl ether. The solid was dried in vacuo for 1 day and it was then used in the next reaction sequence without further purification. ^{1}H-NMR (CD_2Cl_2, 300 MHz, 298 K, ppm): δ 9.52 (d, 2H, *J*= 6.3 Hz), 7.92 (d, 2H, *J*= 2.0 Hz), 7.57 (dd, J_1= 6.3 Hz, J_2= 2.2 Hz), 1.45 (s, 18H, ***tert*-butyl** groups). ^{13}C NMR ($CDCl_3$, 300 MHz): δ 164.9, 157.1, 149.3, 124.8, 120.0, 36.2 (***tert*-butyl** groups), 30.3 (***tert*-butyl** groups).[2] Spectroscopic data agree with literature values.[22]

2.4.3 Synthesis of 4,7-Diphenyl-1,10-phenathrolineplatinum(II) dichloride, [Pt(dpphen)Cl_2]

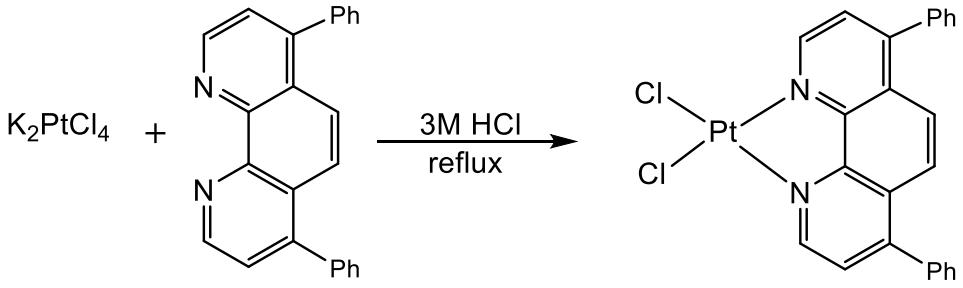

Pt(dpphen)Cl_2 was prepared by modification of a literature procedure.[23] Here, 4,7-diphenyl-1,10-phenathroline (1.019 g; 3.064 mmol) was added to a stirred solution of $K_2[PtCl_4]$ (1.278g; 3.080 mmol) in 3 M HCl (100 ml). The red suspension was refluxed under an atmosphere of dinitrogen (N_2) for 12 hours with a color change to bright-yellow. The bright yellow precipitate that formed was filtered and washed with water and diethyl ether. Column chromatography

on silica gel (3:1 dichloromethane/hexane mixture) yielded a bright yellow solid. Yield: 1.22 g; 66.7 %.^{1}H-NMR (CD_2Cl_2, 300 MHz, 298 K, ppm): δ9.97 (d, 2H, *J*= 6.0 Hz), 7.82 (d, 2H, *J*= 6.0 Hz), 8.05 (s, 2H), 7.60 (m, 10H, **phenyl** groups). ^{13}C NMR (CD_2Cl_2, 300 MHz, 298 K, ppm): δ 149.34, 126.35, 125.87, 151.18, 129.30, 148.58, 136.51 (**phen**), 129.52 (**phen**), 129.87 (**phen**), 130.00 (**phen**).

2.4.4 Synthesis of 4,4'-di-tert-butyl-2,2'-bipyridinepalladium(II) dichloride, [(Pd(dbbpy)Cl_2]

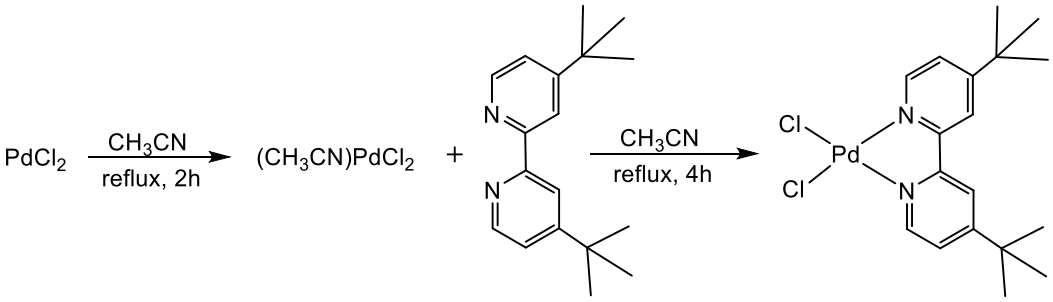

Pd(dbbpy)Cl_2 was prepared by modification of a literature procedure.[24] $PdCl_2$ (2.128 g, 12 mmol) was refluxed in 250 mL of acetonitrile for 2 h to form a reddish-brown solution of $(CH_3CN)_2PdCl_2$. A 150 mL solution of 4,4'-di-tert-butyl-2, 2'-bipyridine (2.128 g, 12 mmol) in acetonitrile was added in portions to the reaction flask over a period of 20 min, producing an instant bright orange precipitate with each addition. The suspension was refluxed for 4 h and then cooled to room temperature. The bright orange precipitate was isolated by filtration and washed with hexane followed by diethyl ether and an air-dry. Column chromatography on silica gel (4:1 dichloromethane/hexane mixture) yielded a bright orange solid (4.83 g, 90.4%). ^{1}H NMR (300 MHz, $CDCl_3$, 298 K,

ppm): δ 9.08 ppm (d, 2H, *J*= 6.2 Hz), 7.93 ppm (d, 2H, *J*= 2.0 Hz), 7.46,7.43 ppm (dd, 2H, J_1= 2.0 Hz J_2= 2.0 Hz), 1.43 (s, 18H, ***tert*-butyl** group).

2.4.5 Synthesis of 4,7-Diphenyl-1,10-phenathrolinepalladium (II) dichloride, [Pd(dpphen)Cl_2]

Pd(dpphen)Cl_2 was prepared by refluxing $PdCl_2$ (2.500 g, 14 mmol) in 200 mL of acetonitrile for 2 h to form a reddish-brown solution of $(CH_3CN)_2PdCl_2$. A 150-mL solution of 4,7-diphenyl-1,10-phenathroline (4.654 g, 14 mmol) in acetonitrile was

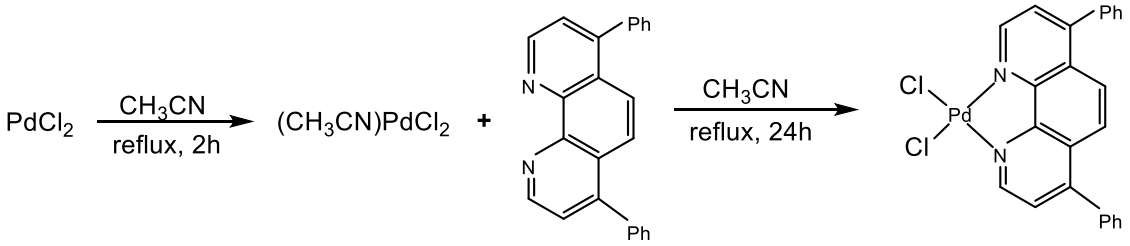

added in portions to the reaction flask over a period of 30 min, producing a yellow precipitate with each addition. The suspension was refluxed for 24 h and then cooled to room temperature. The yellow precipitate was isolated by filtration, washed with water, methanol, hexane and diethyl ether and then dried under vacuum. Column chromatography on silica gel (4:1 dichloromethane/ hexane mixture) yielded a yellow solid. Yield: 90%. ($CDCl_3$, 300 MHz, 298 K, ppm): δ9.95 (d, 2H, *J*= 6.0 Hz), 7.80 (d, 2H, *J*= 6.0 Hz), 8.03 (s, 2H), 7.60 (m, 10H**, phenyl** groups). ^{13}C NMR (CD_2Cl_2, 300 MHz, 298 K, ppm): δ 149.24, 126.26, 125.76, 151.10, 129.19, 148.47, 136.50 (**phen**), 129.51 (**phen**), 129.85 (**phen**), 130.01 (**phen**).

2.4.6 Synthesis of 4,4'-di-*tert*-butyl-2,2'-bipyridineplatinum(II)benzenedithiolate, [Pt(dbbpy)(bdt)]

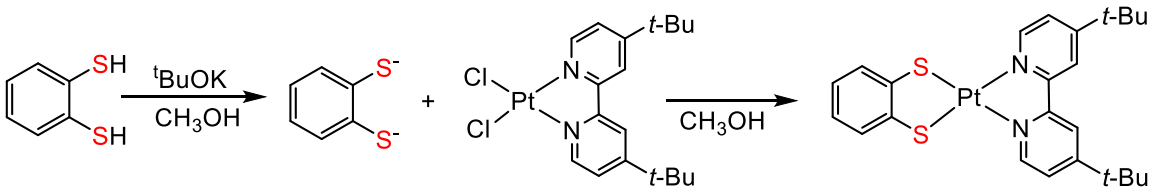

To a suspension of $Pt(dbbpy)Cl_2$ (0.20 g, 0.38 mmol) in 30 ml of deaerated dry methanol, was added a mixture of 1,2-benzenedithiol (bdt) (0.054 g, 0.38 mmol) and potassium *tert*-butoxide (0.09 g, 0.8 mmol) in 30 ml of deaerated dry methanol. The suspension instantly changed from yellow to purple and the mixture was stirred at room temperature under an atmosphere of nitrogen for a day. The solid was collected by filtration and purified by column chromatography on silica gel using hexane/CH_2Cl_2 1:1 as eluent. The purple band was collected, and the solvent removed affording a purple crystalline solid. Yield 0.192 g (84%). ^{1}H NMR ($CDCl_3$, 300 MHz, 298 K, ppm): 9.04 ppm (d, 2H, *J*=6.1 Hz, **dbbpy** aromatic), 7.87 ppm (d, 2H, *J*=1.7 Hz, **dbbpy** aromatic), 7.40 ppm (m, 4H, **dbbpy** and **bdt** aromatic), 6.78 ppm (m, 2H, **bdt**),1.42 ppm (s, 18H, ***tert*-butyl** groups). ^{13}C-NMR ($CDCl_3$, 300 MHz, 298 K, ppm): 162.6ppm (**dbbpy**), 155.6 ppm (**dbbpy**), 148.3 ppm (**dbbpy**), 142.5 ppm (**bdt**), 128.1 ppm (**bdt**), 124.6 ppm (**dbbpy**), 121.7 ppm (**bdt**), 119.5 ppm (**dbbpy**), 35.7 ppm (***tert*-butyl** groups), 30.1 ppm (***tert*-butyl** groups). High-resolution electrospray ionization (ESI) mass spectrometry (m/z): calcd for $C_{24}H_{28}N_2PtS_2$: 603.13; Found: 604.14 $[M+H]^+$. Absorption spectrum for Pt(dbbpy)(bdt): $\lambda_{max}(CH_2Cl_2)$ = 545 nm (18350 cm^{-1}). $\epsilon(CH_2Cl_2)$ = 7700 $M^{-1}cm^{-1}$.

2.4.7 Synthesis of 4,4'-di-*tert*-butyl-2,2'-bipyridineplatinum(II) benzenediselenolate, [Pt(dbbpy)(bds)]

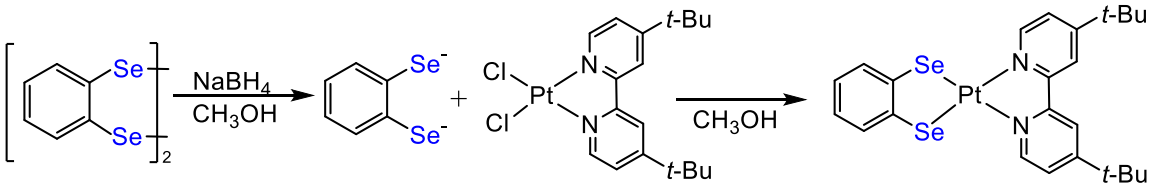

[Pt(dbbpy)(bds)] was synthesized following a literature procedure,[25] using $Pt(dbbpy)Cl_2$ instead of $[(bpy)PtCl_2]$. The crude product was purified by column chromatography on silica gel using hexane/CH_2Cl_2 1:1 as eluent. The purple band was collected, and the solvent removed affording a purple crystalline solid. Yield 220 mg (86% based on Pt). ^{1}H NMR (CD_2Cl_2, 300 MHz, 298 K, ppm): 8.99 ppm (d, 2H, *J*=6.1 Hz, **dbbpy** aromatic), 7.99 ppm (d, 2H, *J*=1.9 Hz, **dbbpy** aromatic), 7.53,7.51 ppm (dd, 2H, J_1=1.9 Hz, J_2=2.0 Hz **dbbpy** aromatic), 7.49-7.46 ppm (m. 2H, bds), 6.81-6.78 ppm (m, 2H, bds), 1.44 ppm (s, 18H, ***tert*-butyl** groups). ^{13}C-NMR ($CDCl_3$, 300 MHz):163.5 ppm (**dbbpy**), 156.3 ppm (**dbbpy**), 149.3 ppm (**dbbpy**), 136.4 ppm (**bds**), 131.0 ppm (**bds**), 125.6 ppm (**dbbpy**), 123.0 ppm (**bds**), 120.2 ppm (**dbbpy**), 36.1 ppm (***tert*-butyl** groups), 30.2 (***tert*-butyl** groups). High-resolution electrospray ionization (ESI) mass spectrometry (m/z): calcd for $C_{24}H_{28}N_2PtSe_2$: 698.02; Found: 698.03 $[M]^+$, 721.01 $[M+Na]^+$. Absorption spectrum for Pt(dbbpy)(bds): $\lambda_{max}(CH_2Cl_2)$ = 553 nm (18080 cm^{-1}). $\epsilon(CH_2Cl_2)$ = 9100 $M^{-1}cm^{-1}$. [2]

2.4.8 Synthesis of 4,4'-di-t*ert*-butyl-2,2'-bipyridineplatinum(II) (2-mercaptophenolate), [Pt(dbbpy)(bSO)]

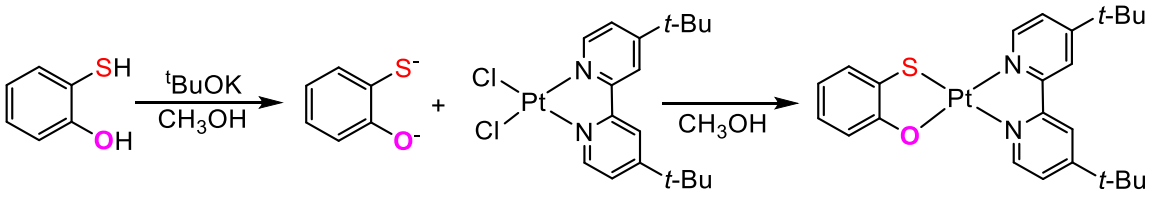

To a solution of $Pt(dbbpy)Cl_2$ (0.50 g, 1.12 mmol) in 30 ml of degassed dry dichloromethane (CH_2Cl_2), was added a mixture of 2-mercaptophenol (184.22 mg, 1.46 mmol), and potassium *tert*-butoxide (0.38 g, 3.36 mmol) in 30 ml of degassed dry methanol. The mixture instantly changed from yellow to purple and was stirred at room temperature under an atmosphere of nitrogen for a day. Addition of 50 ml of methanol afforded a violet precipitate. The product was filtered and washed with cold MeOH and then redissolved in 20 ml of CH_2Cl_2. After gravity filtration and removal of the solvent from the filtrate yielded a violet solid. Yield 620.0 mg (94% based on Pt). ^{1}H NMR ($CDCl_3$, 300 MHz, 298 K, ppm): 8.99 ppm (d, 1H, *J* =5.8 Hz, **dbbpy** aromatic),8.53 ppm (d, 1H, *J* =6.0 Hz, **dbbpy** aromatic), 7.94 ppm (s, 1H, **dbbpy** aromatic), 7.89 ppm (s, 1H, **dbbpy** aromatic), 7.66 ppm (d, 1H, *J* =5.8 Hz, **dbbpy** aromatic), 7.35 ppm (d, 1H, *J* =6.1 Hz, **dbbpy** aromatic), 7.12 ppm (d, 1H, *J* =7.8 Hz, **bSO**), 6.84-6.79 ppm (m, 1H, **bSO**), 6.58 ppm (m, 1H, **bSO**), 6.49 ppm (d, *J* = 8.1 Hz, 1H, **bSO**), 1.47 ppm (s, 9H, ***tert*-butyl** group), 1.41 ppm (s, 9H, ***tert*-butyl** group). ^{13}C-NMR ($CDCl_3$, 300 MHz, 298 K, ppm): 171.1, 162.4, 162.2, 156.8, 153.9, 151.9, 146.0, 129.6, 128.2, 124.5, 124.2, 122.8, 119.6, 118.9, 116.5, 115.9, 35.8, 35.6, 30.3, 30.1 ppm. High-resolution electrospray ionization (ESI) mass spectrometry (m/z): calcd for $C_{24}H_{28}N_2OPtS$: 587.16; Found: 588.16 $[M+H]^+$, 610.15 $[M+Na]^+$. Absorption spectrum for Pt(dbbpy)(bSO): $\lambda_{max}(CH_2Cl_2)$ = 563 nm (17760 cm^{-1}). $\epsilon(CH_2Cl_2)$ =

6700 $M^{-1}cm^{-1}$.

2.4.9 Synthesis of 4,4'-di-*tert*-butyl-2,2'-bipyridineplatinum(II)(2-selenylbenzenethiolate), [Pt(dbbpy)(bSSe)]

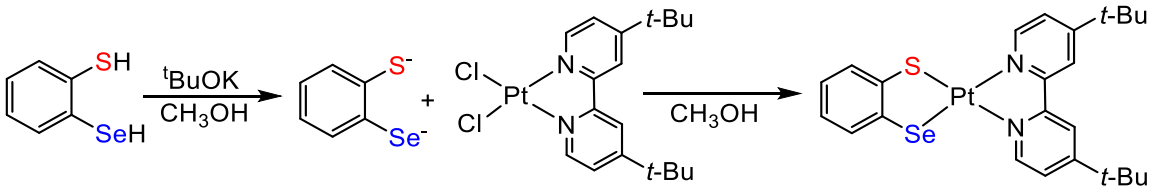

To a suspension of $Pt(dbbpy)Cl_2$ (0.40 g, 0.74 mmol) in 20 ml of degassed dry methanol (MeOH) was added a mixture of 2-selenylbenzenethiol (bSSe) (0.14 g, 0.74 mmol) and potassium *tert*-butoxide (0.18 g, 1.56 mmol). The suspension instantly changed from yellow to purple and the mixture was stirred at room temperature under an atmosphere of nitrogen for 1 day. The solid was collected by filtration and purified by column chromatography on silica gel using hexane/CH_2Cl_2 1:1 as eluent. The purple band was collected, and the solvent removed affording a purple crystalline solid. Yield 390.0 mg (81% based on Pt). ^{1}HNMR (CD_2Cl_2, 300 MHz, 298 K): 9.11 ppm (d, 1H, J=6.1 Hz, **dbbpy** aromatic), 9.01 ppm (d, 1H, J=6.1 Hz, **dbbpy** aromatic), 8.00 ppm (s, 1H, **dbbpy** aromatic),7.99 ppm (s, 1H, **dbbpy** aromatic), 7.57 ppm (dd, 1H, J_1=6.1 Hz**,** J_2=2.0 **dbbpy** aromatic), 7.47 ppm (m, 2H, **dbbpy** aromatic and **bSSe**), 7.33 ppm (d, 1H, J=7.0 Hz, **bSSe**), 6.82 ppm(m, 1H, **bSSe)**, 6.73 ppm (m, 1H, **bSSe**), 1.44 ppm (s, 18H, ***tert*-butyl** groups). High-resolution electrospray ionization (ESI) mass spectrometry (m/z): calcd for $C_{24}H_{28}N_2PtSSe$: 651.08; Found: 651.09 $[M+H]^+$, 673.07 $[M+Na]^+$. ^{13}C-NMR (CD_2Cl_2, 300 MHz, 298 K, ppm): 162.5, 162.3, 155.9, 155.5, 149.5, 146.9, 144.9, 132.6, 130.20, 128.5, 124.9, 124.4, 122.4,

121.5, 119.8, 119.7, 35.6, 30.0. Absorption spectrum for Pt(dbbpy)(bSSe): $\lambda_{max}(CH_2Cl_2)$ = 554 nm (18050 cm^{-1}). $\epsilon(CH_2Cl_2)$ = 6900 $M^{-1}cm^{-1}$. [2]

2.4.10 Synthesis of 4,4'-di-*tert*-butyl-2,2'-bipyridineplatinum(II)(2-selenyl-phenolate), Pt(dbbpy)(bSeO)]

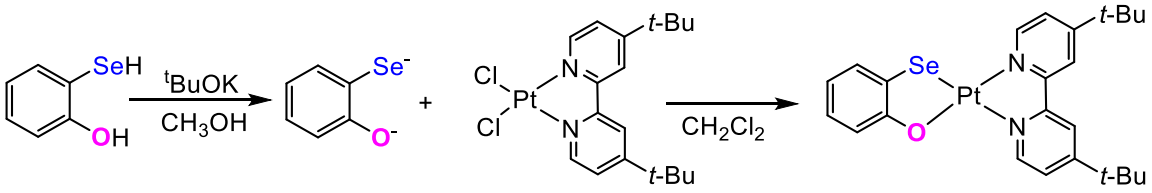

To a solution of $Pt(dbbpy)Cl_2$ (330 mg, 0.62 mmol) in 50 ml of deaerated dry dichloromethane was added a mixture of 2-selenylphenolate (bSeO) (140.20 mg, 0.81 mmol) and potassium *tert*-butoxide (208.7 mg, 1.86 mmol) in 50 ml of deaerated dry methanol. The mixture changed from yellow to blue after 2 h and was stirred at 50 ^{0}C under a nitrogen atmosphere for 24 h. The product was filtered and washed with MeOH, dissolved in 20 ml of CH_2Cl_2, and then filtered. Removal of solvent by evaporation yielded a deep blue solid. Yield 410.0 mg (92% based on Pt). ^{1}H NMR ($CDCl_3$, 300 MHz, 298 K, ppm): 9.25 ppm (d, 1H,J=6.0 Hz), 8.79 ppm (d, 1H,J=6.2 Hz), 7.90 ppm (d, 1H,J=1.7 Hz), 7.77 ppm (d, 1H, J=2.0 Hz), 7.66, 7.64 ppm (dd, 1H, J=1.9, 2.0 Hz), 7.41, 7.39 ppm (dd, 1H, J=1.1, 1.3 Hz), 7.15, 7.13 ppm (dd, 1H, J=2.1, 2.1 Hz), 6.78 ppm (m, 2H, **bSO** aromatic), 6.49 ppm (m, 1H, **bSO** aromatic), 1.36 ppm (s, 9H, ***tert*-butyl** groups),1.48 ppm (s, 9H, ***tert*-butyl** groups). ^{13}C NMR ($CDCl_3$, 300 MHz, 298 K, ppm) δ 171.8, 162.5, 162.1, 157.0, 153.8, 145.3, 130, 124.8, 124.1, 123.8,

119.78, 118.87, 116.6, 35.9 (***tert*-butyl** groups), 35.6 (***tert*-butyl** groups), 30.3 (***tert*-butyl** groups), 30.0 (***tert*-butyl** groups) ppm. High-resolution electrospray ionization (ESI) mass spectrometry (m/z): calcd for $C_{24}H_{28}N_2OPtSe$: 635.10; Found: 634.10 $[M]^+$. Absorption spectrum for Pt(dbbpy)(bSeO): $\lambda_{max}(CH_2Cl_2)$ = 565 nm (17700 cm^{-1}).

2.4.11 Synthesis of 4,4'-ditert-butyl-2,2'-bipyridineplatinum(II)(2,2'-dimercaptobiphenyl), [Pt(dbbpy)(mcp)]

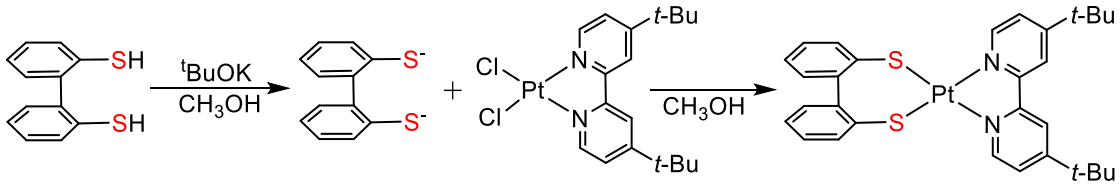

To a suspension of $Pt(dbbpy)Cl_2$ (0.20 g, 0.38 mmol) in 50 ml of deaerated dry methanol, was added a mixture of 2,2'-dimercaptobiphenyl (mcp) (0.081 g, 0.38 mmol) and potassium *tert*-butoxide (0.09 g, 0.8 mmol) in 50 ml of deaerated dry methanol. The suspension instantly changed from yellow to orange and the mixture was stirred at room temperature under an atmosphere of nitrogen for 2 days. The solid was collected by filtration and purified by column chromatography on silica gel using 10% CH_3OH in CH_2Cl_2 as eluent. The bright orange band was collected and the solvent removed affording a bright orange crystalline solid. Single crystals suitable for X-ray diffraction studies of Pt(dbbpy)(mcp) were obtained by layering a solution of each compound in dichloromethane with hexane. Yield: 0.206 g (90%). ^1H NMR ($CDCl_3$, 300 MHz, 298 K): 9.72 ppm (d,

J=6.1 Hz), 7.93 ppm (d, J=1.9 Hz), 7.89 ppm (d, J=1.1 Hz), 7.86 ppm (d, J=1.2 Hz), 7.60, 7.58 ppm (dd, J=2.0,2.0 Hz), 7.16-7.32 ppm (m), 7.13, 7.12, 7.08 ppm (dt, J=1.6, 1.6, 1.7 Hz), 1.45 ppm(s, 18H, ***tert*-butyl** groups). ^{13}C NMR ($CDCl_3$, 300 MHz, 298 K, ppm): δ 162.9 ppm, 155.9 ppm, 152.2 ppm, 148.9 ppm, 148.4 ppm, 148.2 ppm, 138.2 ppm, 135.4 ppm, 129.8 ppm, 127.9 ppm, 126.70 ppm, 126.8 ppm, 124.2 ppm, 120.3 ppm, 118.8 ppm, 42.6 ppm (***tert*-butyl** groups), 35.7 ppm (***tert*-butyl** groups), 30.9 ppm (***tert*-butyl** groups), 30.3 ppm (***tert*-butyl** groups). High-resolution electrospray ionization (ESI) mass spectrometry (m/z): calcd for $C_{24}H_{28}N_2PtSe_2$: 679.17; Found: 680.34 $[M+H]^+$. Absorption spectrum for Pt(dbbpy)(mcp): $\lambda_{max}(CH_2Cl_2)$ = 463 nm (21600 cm^{-1}). $\epsilon(CH_2Cl_2)$ = 7810 $M^{-1}cm^{-1}$.

2.4.12 Synthesis of 4,4'-di-*t*-butyl-2,2'-bipyridineplatinum(II)(2,2'-dihydroxy-biphenyl), [Pt(dbbpy)(hbp)]

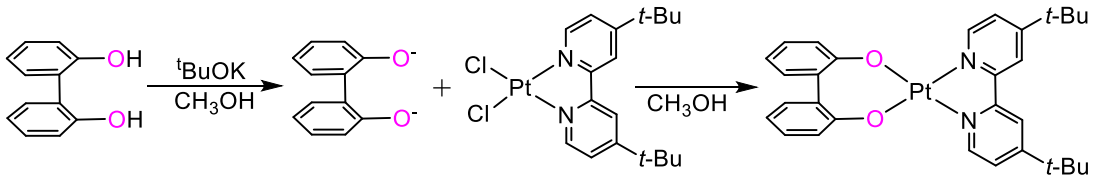

To a suspension of $Pt(dbbpy)Cl_2$ (0.400 g, 0.74 mmol) in 70 ml of deaerated dry methanol, was added a mixture of 2,2'-dihydroxybiphenyl (hbp) (0.138 g, 0.74 mmol) and potassium hydroxide (KOH) (0.051 g, 0.9 mmol) in 20 ml of degassed dry methanol (MeOH). The suspension instantly changed from yellow to deep orange and the mixture was stirred at room temperature under a nitrogen atmosphere for 24 h. The solid was collected by filtration and purified by column

chromatography on silica gel using 10% CH_3OH in CH_2Cl_2 as eluent. The bright orange band was collected, and the solvent removed affording a bright orange crystalline solid. Yield 0.386 g (90% based on Pt). High-resolution electrospray ionization (ESI) mass spectrometry (m/z): calcd for $C_{30}H_{32}N_2O_2Pt$: 647.21; Found: 648.22 $[M+H]^+$.^{1}H NMR ($CDCl_3$, 300 MHz, 298 K, ppm): 9.18 ppm (d, 2H, J=6.2 Hz, **dbbpy**), 7.76 ppm (d, 2H, J=1.9 Hz, **dbbpy**), 7.50, 7.48 ppm (dd, 2H, J_1=1.9, J_2=1.9 Hz, **dbbpy**), 7.26-7.14 ppm (4H, m, **dihydroxybiphenyl**), 6.99-6.87 ppm (4H, m, **dihydroxybiphenyl**), 1.40 ppm (s, 18H, **tert-butyl** groups). ^{13}C NMR ($CDCl_3$, 300 MHz, 298 K): 164.1 ppm, 161.8 ppm, 161.1 ppm, 156.6 ppm, 153.2 ppm, 148.1 ppm, 134.6 ppm, 131.5 ppm, 129.1 ppm, 128.7 ppm, 125.9 ppm, 124.2 ppm, 121.8 ppm, 121.3 ppm, 120.8 ppm, 119.1 ppm, 117.2 ppm, 35.8 ppm (***tert*-butyl** groups), 30.1 ppm (***tert*-butyl** groups). Absorption spectrum for Pt(dbbpy)(hbp): $\lambda_{max}(CH_2Cl_2)$ = 505 nm (19805 cm^{-1}).

2.4.13 Synthesisof4,4'-ditert-butyl-2,2'-bipyridineplatinum(II)(quinoxaline-2,3-diselenolate), [Pt(dbbpy)(qds)]

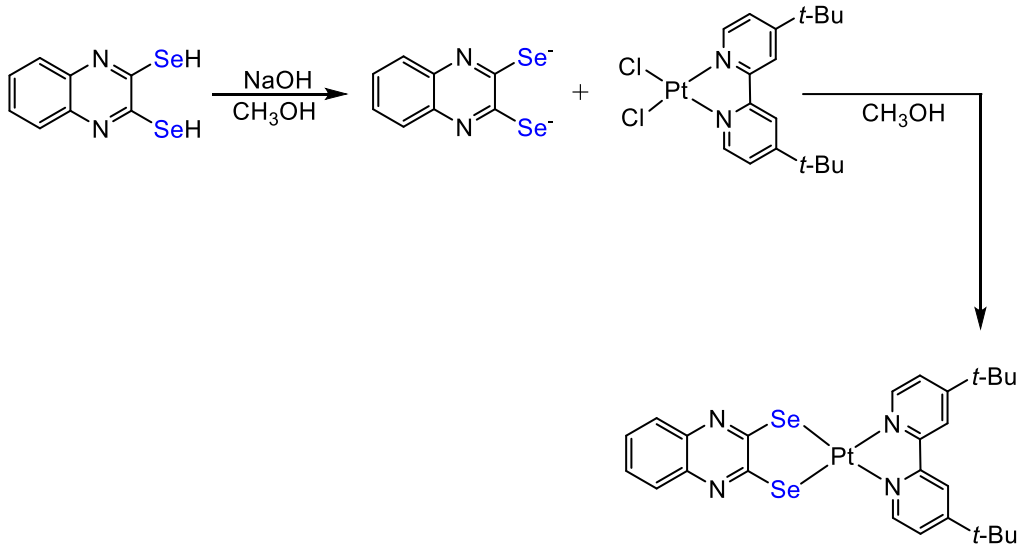

To a suspension of Pt(dbbpy)Cl_2 (0.20 g, 0.38 mmol) in 30 ml of deaerated dry methanol was added a mixture of quinoxaline-2,3-diselenolate (qds) (0.107 g, 0.38 mmol) and excess NaOH (0.038 g, 0.95 mmol) in 30 ml of deaerated dry methanol. The suspension instantly changed from yellow to the bright orange-red color of the product, and the mixture was stirred at room temperature under an atmosphere of nitrogen for 24 h. The solid was collected by filtration and purified by column chromatography on silica gel using hexane/CH_2Cl_2 1:1 as eluent. The orange-red band was collected, and the solvent removed affording an orange-red crystalline solid. Yield is 245.6 mg (96% yield based on Pt). The solid was collected by filtration and purified by column chromatography on silica gel using 10% CH_3OH in CH_2Cl_2 as eluent. The bright orange band was collected, and the solvent removed affording a bright orange crystalline solid. High-resolution electrospray ionization (ESI) mass spectrometry (m/z): calcd for $C_{26}H_{28}N_4PtSe_2$: 751.03; Found: 751.04 $[M+H]^+$. ^{1}H NMR ($CDCl_3$, 300 MHz, 298 K): 8.66 ppm (d, 2H, *J*=6.0 Hz), 7.93-7.90 ppm (m, 2H), 7.89 ppm (d, 2H, *J*=1.8 Hz), 7.54-7.50 (m, 4H, **qds** aromatic), 1.33 (s, 18H, ***tert*-butyl** groups).^{13}C NMR ($CDCl_3$, 300 MHz, 298 K, ppm): δ 163.3, 159.9, 156.2, 147.6, 138.2, 127.4, 126.9, 125.2, 120.1, 35.8 (***tert*-butyl** groups), 30.1 (***tert*-butyl** groups). Absorption spectrum for Pt(dbbpy)(qds): $\lambda_{max}(CH_2Cl_2)$ = 485 nm (20620 cm^{-1}).

2.4.14 Synthesis of 4,4'-ditert-butyl-2,2'-bipyridineplatinum(II)(quinoxaline-2,3-dithiolate) [Pt(dbbpy)(qdt)]

This complex was prepared by the method described for Pt(dbbpy)(qds) using 200 mg (0.38 mmol) of Pt(dbbpy)Cl_2 and 72 mg (0.38 mmol) of quinoxaline-2,3-

dithiolate(qdt) and excess NaOH. 302.1 mg of a bright orange-red product was isolated (96% yield based on Pt). The NMR and elemental analysis data are consistent with literature reported values.[26] High-resolution electrospray ionization (ESI) MS (m/z): calcd for $C_{26}H_{28}N_2PtS_2$: 655.14; Found: 656.15 $[M+H]^+$. EA spectrum for Pt(dbbpy)(qdt): $\lambda_{max}(CH_2Cl_2)$ = 473 nm (21140 cm^{-1}).

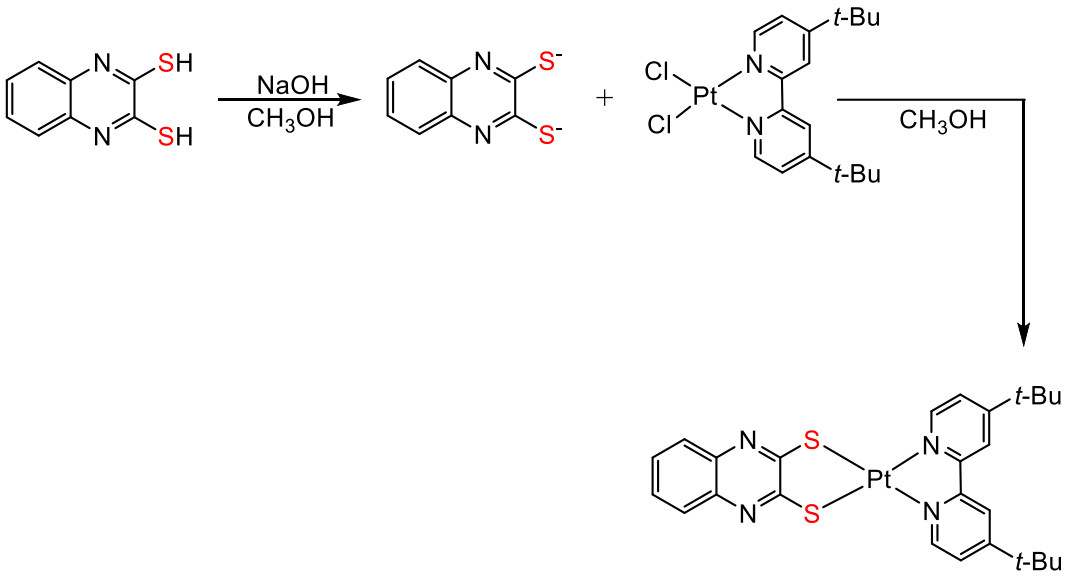

2.4.15 Synthesis of 4,4'-ditert-butyl-2,2'-bipyridineplatinum(II)(pyrazine-2,3-dithiolate), [Pt(dbbpy)(pdt)]

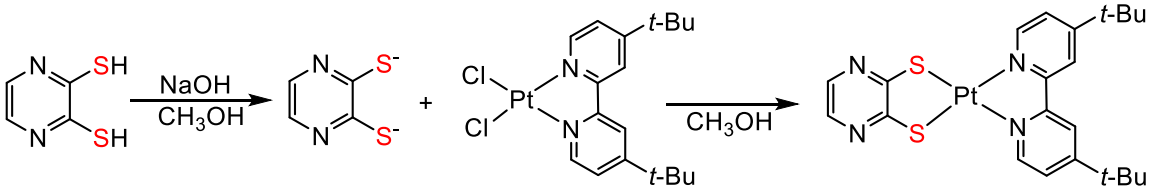

To a 200 mg (0.37 mmol) of Pt(dbbpy)Cl_2 suspension in 50 mL of CH_2Cl_2 was added to a solution of 53 mg (0.37 mmol) of pdt and 120 mg of NaOH in 25 mL of MeOH. The reaction mixture was stirred at room temperature for 6 h, during

which time a bright red-orange precipitate was formed. The product was filtered off and washed with diethyl ether followed by pentane. The solid was purified by column chromatography on silica gel using 5% MeOH in dichloromethane as eluent. The product was vacuum dried at 40 ^{0}C. Yield is 145.6 mg (65% yield based on Pt). High-resolution electrospray ionization (ESI) mass spectrometry (m/z): calcd for $C_{22}H_{26}N_4PtS_2$: 605.12; Found: 606.13 $[M+H]^+$. ^{1}H NMR ($CDCl_3$, 300 MHz, 298 K): 9.21 ppm (d, 1H, *J*=6.3 Hz), 8.70 ppm (d, 1H, J=6.1 Hz), 8.00 ppm (d, 1H, *J*=1.6), 7.89 ppm (d, 1H, *J*=1.8) 7.81 (s, 2H), 7.49,7.47 ppm(dd, 1H, J_1=1.9 Hz, J_2= 1.9 Hz), 7.40,7.38 ppm (dd, 1H, J_1=2.0 Hz, J_2=2.0 Hz), ^{13}C NMR ($CDCl_3$, 300 MHz, 298 K): δ 164.0 ppm, 163.4 ppm, 160.6 ppm, 156.9 ppm, 155.9 ppm, 148.3 ppm, 147.0 ppm, 141.9 ppm, 135.1 ppm, 125.0 ppm, 123.8 ppm, 120.4 ppm, 120.1 ppm, 35.8 ppm (***tert*-butyl** groups), 30.2 ppm (***tert*-butyl** groups). Absorption spectrum for Pt(dbbpy)(pdt): $\lambda_{max}(CH_2Cl_2)$ = 487 nm (20530 cm^{-1}).

2.4.16 Synthesis of 4,4'-di-*tert*-butyl-2,2'-bipyridineplatinum(II)(pyrazine-2,3-diselenolate), [Pt(dbbpy)(pds)]

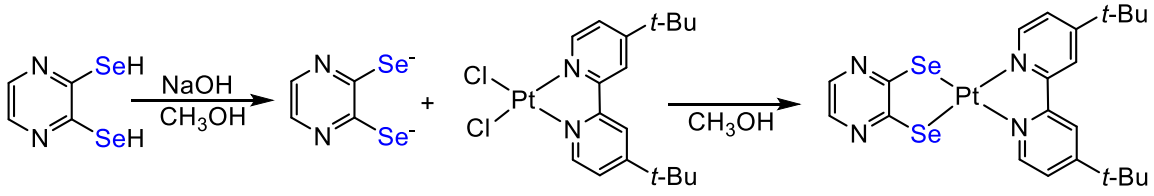

To a 200 mg (0.37 mmol) Pt(dbbpy)Cl_2 suspension in 50 mL of CH_2Cl_2 was added to a solution of 88 mg (0.37 mg) of pds and 140 mg of NaOH in 25 mL of MeOH. The reaction mixture was stirred at room temperature for 12 h, during

which time a bright red-orange precipitate was formed. This product was filtered off and washed with diethyl ether followed by pentane. The solid was purified by column chromatography on silica gel using 10% MeOH in CH_2Cl_2 as eluent. The product was vacuum dried at 40 ^{0}C. Yield is 165.6 mg (68% yield based on Pt). High-resolution electrospray ionization (ESI) mass spectrometry (m/z): calcd for $C_{22}H_{26}N_4PtSe_2$: 701.01; Found: 701.02 $[M+H]^+$. ^{1}H NMR $CDCl_3$, 300 MHz, 298 K): 8.89 ppm (d, 2H, J=6.1 Hz), 7.94 ppm (s, 2H), 7.55,7.53 ppm (dd, 2H, J_1=2.0 Hz, J_2=2.0 Hz), 6.94 ppm (d, 2H, J=6.1 Hz), 1.42 ppm (s, 18H). NMR ($CDCl_3$, 300 MHz): δ 163.4 ppm, 157.5 ppm, 156.1 ppm, 148.3 ppm, 136.5 ppm, 125.2 ppm, 119.6 ppm, 35.9 ppm (***tert*-butyl** group), 30.1 ppm (***tert*-butyl** group). Absorption spectrum for Pt(dbbpy)(pds): $\lambda_{max}(CH_2Cl_2)$ = 504 nm (19840 cm^{-1}).

2.4.17 Synthesis of 4,4'-di-*tert*-butyl-2,2'-bipyridineplatinum(II)(3,5-di-*t*-butylbenzene catecholate), [Pt(dbbpy)(dtbCAT)]

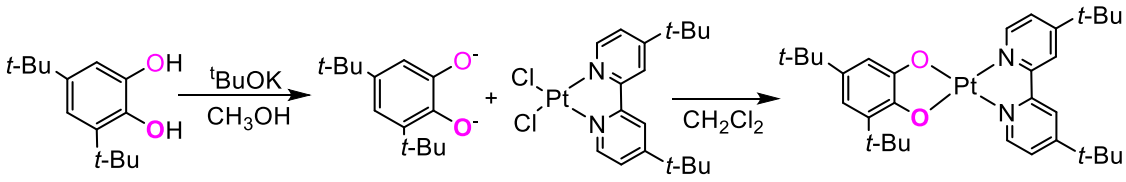

4,4'-di-tert-butyl-2,2'-bipyridineplatinum(II) dichloride (0.40 g, 0.75 mmol) was suspended in 200 mL of dichloromethane. A solution of 3,5-di-*t*-butylbenzene catecholate (0.17 g, 0.75 mmol) in 40 ml of deaerated dry methanol was added to potassium *tert*-butoxide (0.17 g, 1.50 mmol) under an atmosphere of dinitrogen to form a blue solution of the mixture. The blue mixture was then

added to the bright yellow solution of 4,4'-di-tert-butyl-2,2'-bipyridineplatinum(II) dichloride in dichloromethane and the resulting mixture immediately turned from bright yellow to green. The mixture was heated to reflux for 12 h under an atmosphere of dinitrogen, during which time the solution turned to dark purple. The solvent was removed under vacuum and yielded a dark blue solid. Column chromatography on silica gel using 1% methanol in dichloromethane yielded a dark blue solid. Yield is 1.043 g (85% yield based on Pt). Calcd for $C_{32}H_{44}N_2O_2Pt\cdot(H_2O)_{0.5}$ (MW 692.79): C, 55.48; H, 6.55; N, 4.04. Found: C, 55.23; H, 6.55; N, 4.04. High-resolution electrospray ionization (ESI) mass spectrometry (m/z): calcd for $C_{32}H_{44}N_2O_2Pt$: 683.31; Found: 683.4 $[M+H]^+$. The elemental analysis and electrospray ionization (ESI) mass spectrometry data are consistent with those reported previously.[27,28] ^1H NMR ($CDCl_3$, 300 MHz, 298 K): 9.32 ppm (d, 1H, *J*=6.1 Hz), 9.25 ppm (d, 1H, *J*=6.1 Hz), 7.96 ppm (d, 2H, *J*=1.8 Hz), 7.62 ppm (dd, 1H, J_1=2.0 Hz, J_2=2.0 Hz), 7.57 ppm (dd, 1H, J_1=1.9 Hz, J_2=2.0 Hz), 6.70 ppm (d, 1H, *J*=2.2 Hz), 6.49 ppm (d, 1H, *J*=2.2 Hz), 1.60 ppm (s, 9H, **dtbCAT dbbpy *tert*-butyl group**), 1.50 ppm (s, 9H, **dbbpy *tert*-butyl group**), 1.49 ppm (s, 9H, **dbbpy *tert*-butyl group**), 1.35 ppm (s, 9H, **dtbCAT dbbpy *tert*-butyl group**). ^{13}C NMR ($CDCl_3$, 300 MHz, 298 K): δ 162.5, 162.4, 162.1, 158.9, 156.1, 155.9, 148.9, 148.6, 137.7, 133.9, 127.9, 127.6, 124.8, 124.4, 124.3, 120.5, 119.5, 119.3, 110.3, 110.2, 35.8 (***tert*-butyl group**), 34.6 (***tert*-butyl group**), 33.8 (***tert*-butyl group**), 31.9 (***tert*-butyl group**), 29.9 (***tert*-butyl group**), 29.7 (***tert*-butyl group**).

2.4.18 Synthesis of 4,4'-di-*tert*-butyl-2,2'-bipyridineplatinum(II)(bis-4-*tert*-butylphenolate), [Pt(dbbpy)(tbp)$_2$]

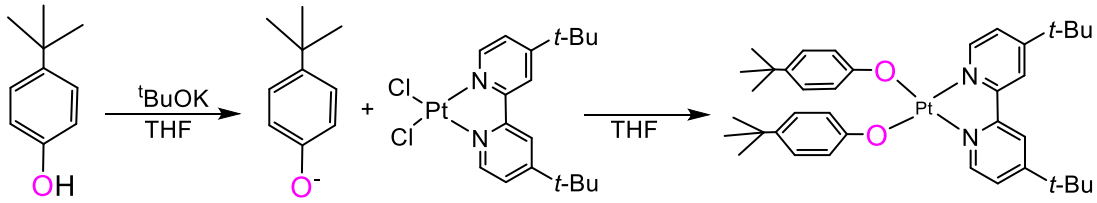

To a suspension of Pt(dbbpy)Cl_2 (0.20 g, 0.37 mmol) in 60 mL of degassed dry THF, was added a mixture of 4-*tert*-butyl phenolate (tbp) (0.112 g, 0.75 mmol) and potassium *tert*-butoxide (0.0834 g, 0.75 mmol) in 15 mL of degassed dry THF. The suspension instantly changed from yellow to orange and the mixture was refluxed under an atmosphere of nitrogen for 15 h. The solid was collected by filtration and purified by column chromatography on silica gel using 10% CH_3OH in CH_2Cl_2 as eluent. The red orange band was collected and the solvent removed affording an orange red crystalline solid. Yield 0.183 g (80% based on Pt). High-resolution electrospray ionization (ESI) mass spectrometry (m/z): calcd for $C_{38}H_{50}N_2O_2Pt$: 761.35; Found: 762.36 $[M+H]^+$, $[M+Na]^+$: 784.34. ^{1}H NMR ($CDCl_3$, 300 MHz, 298 K): 9.04 ppm (d, 2H, J=6.1 Hz), 7.80 ppm (d, 2H, J=1.6 Hz), 7.47,7.45 ppm (dd, 2H, J=1.8,1.8 Hz), 7.20 ppm (d, 2H, J=8.6 Hz), 7.12 ppm (d, 2H, J=8.6 Hz), 7.02 ppm (d, 2H, J=8.6 Hz), 6.84 ppm (d, 2H, J=8.6 Hz), 1.40 ppm (s, 18H,), 1.23 ppm (s, 18H,). ^{13}C NMR ($CDCl_3$, 300 MHz, 298 K): δ 164.8, 163.5, 156.8, 154.9, 149.2, 141.4, 137.8, 125.9, 125.1, 123.9, 118.7, 115.5, 35.8 (***tert*-butyl** groups), 33.7 (***tert*-butyl** groups), 31.8 (***tert*-butyl** groups) ,30.2 (***tert*-butyl** groups). Absorption spectrum for Pt(dbbpy)$(tbp)_2$: $\lambda_{max}(CH_2Cl_2)$ = 535 nm (18700 cm^{-1}).

2.4.19 Synthesis of 4,4'-di-*tert*-butyl-2,2'-bipyridineplatinum(II)(bis-4-*tert*-butylbenzenethiolate), [Pt(dbbpy)(tbt)$_2$]

To a suspension of Pt(dbbpy)Cl_2 (0.200 g, 0.37 mmol) in 40 mL of degassed dry CH_2Cl_2 was added a mixture of 4-*tert*-butylbenzenethiolate (tbt) (0.123 g, 0.74

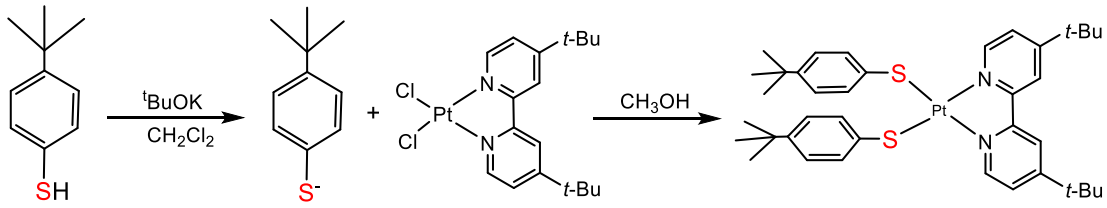

mmol) and potassium *tert*-butoxide (0.0834 g, 0.75 mmol) in 10 mL of degassed dry MeOH. The suspension instantly changed from yellow to purple and the mixture was refluxed under an atmosphere of nitrogen for 24 h. The solid was collected by filtration and purified by column chromatography on silica gel using 3% CH_3OH in CH_2Cl_2 as eluent. The dark purple band was collected, and the solvent removed affording a dark purple crystalline solid. Yield 0.187 g (78% based on Pt). High-resolution electrospray ionization (ESI) mass spectrometry (m/z): calcd for $C_{38}H_{50}N_2PtS_2$: 793.31; Found: 793.31 $[M]^+$. ^{1}H NMR ($CDCl_3$, 300 MHz): 9.79 ppm (d, 2H, J=6.1 Hz), 7.95 ppm (d, 1H, J=1.8 Hz), 7.54 ppm (d, 1H, J=8.5 Hz), 7.51, 7.49 ppm (dd, 2H, J_1=2.0, J_2=2.0 Hz), 6.98-6.93 ppm (m, 8H), 1.41 ppm (s, 18H, *tert*-butyl groups), 1.24 ppm (s, 18H, *tert*-butyl groups). ^{13}C-NMR ($CDCl_3$, 300 MHz): 163.4 ppm, 156.3 ppm, 148.9 ppm, 144.9 ppm, 139.5 ppm, 131.7 ppm, 124.2 ppm, 118.6 ppm, 35.7 ppm (***tert*-butyl** groups), 34.2 ppm (***tert*-butyl** groups), 31.0 ppm (***tert*-butyl** groups), 30.1 ppm (***tert*-butyl** groups). Absorption spectrum for Pt(dbbpy)(tbt)$_2$: $\lambda_{max}(CH_2Cl_2)$ = 545 nm (18350 cm^{-1}).

$\epsilon(CH_2Cl_2)$ = 7700 $M^{-1}cm^{-1}$.

2.4.20 Synthesis of 4,4'-di-*tert*-butyl-2,2'-bipyridineplatinum(II) (1,5-diiso-propyl-3-(3',4'-dihydroxyphenyl)-2-yl-6-oxoverdazyl, [Pt(dbbpy)(CAT-Vz)]

4,4'-di-tert-butyl-2,2'-bipyridineplatinum(II) dichloride, $Pt(dbbpy)Cl_2$ (0.200 g, 0.37 mmol) was suspended in 60 mL of tetrahydrofuran (THF). A solution of 1,5-diisopropyl-3-(3',4'-dihydroxyphenyl phenyl)-6-oxoverdazyl (CAT-Vz)[29] (0.108 g, 0.37 mmol) in 15 mL of deaerated dry THF was added to potassium *tert*-butoxide (0.0461 g, 0.41 mmol) under an atmosphere of dinitrogen to form a reddish-brown solution of the mixture. The reddish-brown mixture was then added to the yellow solution of 4,4'-di-tert-butyl-2,2'-bipyridineplatinum(II) dichloride in THF

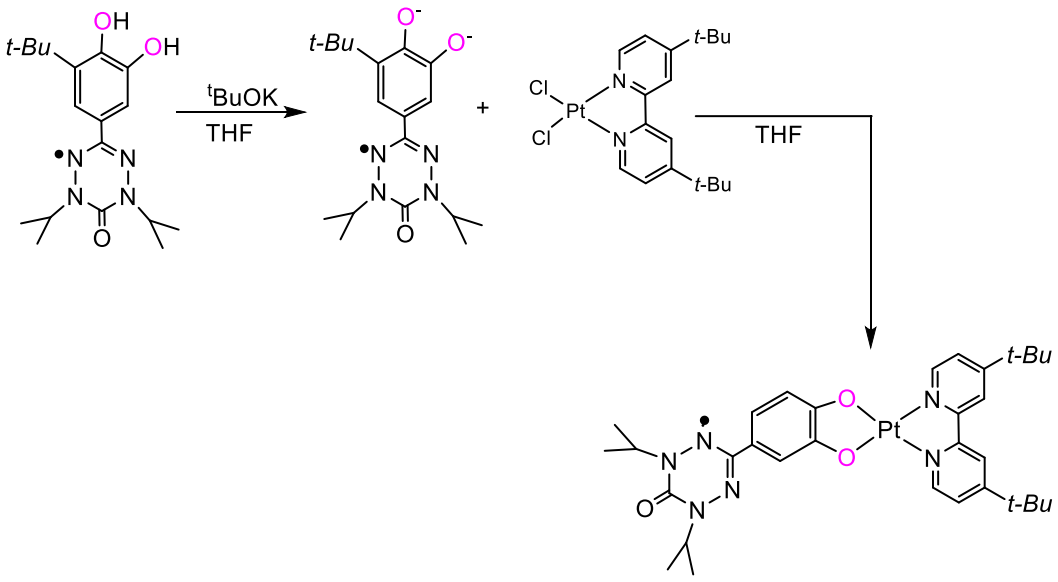

and the mixture was heated to reflux for 24 h under the atmosphere of dinitrogen, during which time the solution turned to purple. The solvent was removed under

vacuum, yielding 0.187 g dark purple solid (80% based on Pt). The dark purple solid was purified by column chromatography on silica gel using 2% CH_3OH in CH_2Cl_2 as eluent. High-resolution electrospray ionization (ESI) mass spectrometry (m/z): calcd for $C_{32}H_{41}N_6O_3Pt$: 752.29; Found: 752.29 $[M]^+$. Anal. Calculated for $C_{32}H_{41}N_6O_3Pt$: C, 51.06; H, 5.49; N, 11.16; O, 6.38; Pt, 25.91 Found: C, 50.73; H, 5.24; N, 11.33. Absorption spectrum for Pt(dbbpy)(CAT-Vz): $\lambda_{max}(CH_2Cl_2)$ = 540 nm (18500 cm^{-1}). $\epsilon(CH_2Cl_2)$ = 6110 $M^{-1}cm^{-1}$.

2.4.21 Synthesis 4,7-diphenyl-1,10-phenathrolineplatinum(II)(benzenedithiolate), [Pt(dpphen)(bdt)]

To a suspension of $Pt(dpphen)Cl_2$ (0.20 g, 0.34 mmol) in 40 ml of degassed dry methanol, was added a mixture of benzene-1,2-dithiolate (bdt) (0.048 g, 0.34

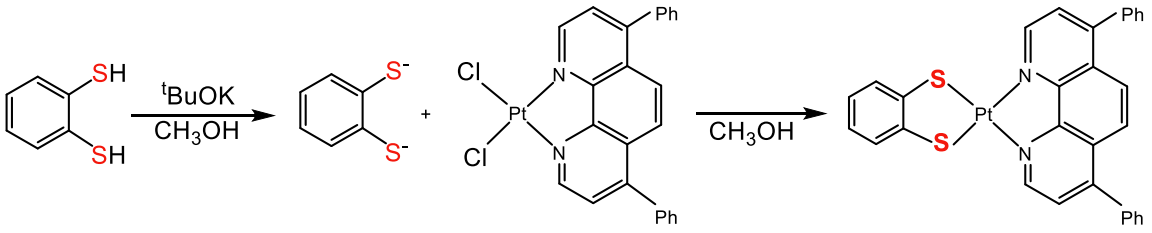

mmol) and potassium *tert*-butoxide (0.09 g, 0.8 mmol) in 15 ml of degassed dry methanol. The suspension instantly changed from yellow to blue and the mixture was stirred at room temperature under an atmosphere of nitrogen for 24 hr. The solid was collected by filtration and purified by column chromatography on silica gel using 0.5% CH_3OH in CH_2Cl_2 as eluent. The blue band was collected, and the solvent removed affording a dark blue crystalline solid. Yield 0.173 g (74%).

High-resolution electrospray ionization (ESI) mass spectrometry (m/z): calcd for $C_{30}H_{20}N_2PtS_2$: 667.07; Found: 667.07 $[M]^+$. The NMR and elemental analysis data are the same as those reported previously.[21]

2.4.22 Synthesis 4,7-diphenyl-1,10-phenathrolineplatinum(II)(benzenediselenolate), [Pt(dpphen)(bds)]

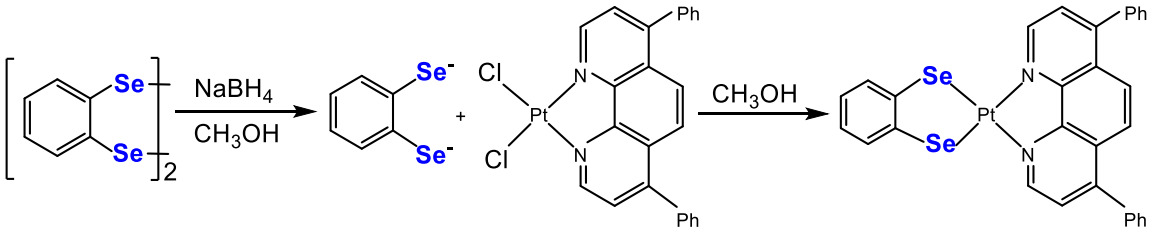

Pt(dpphen)(bds)

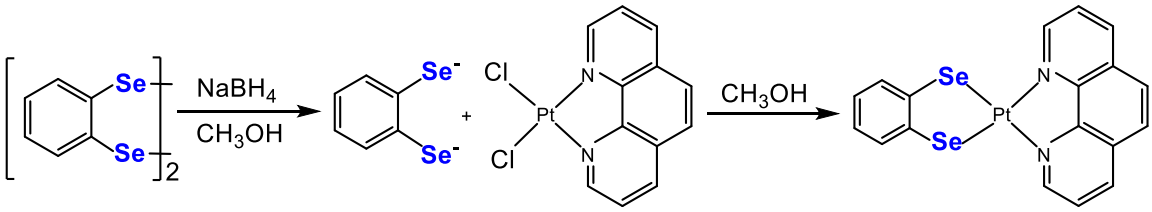

Pt(phen)(bds)

Pt(dpphen)(bds) and Pt(phen)(bds) were synthesized following the procedure used for the synthesis of Pt(dbbpy)(bds), by using Pt(dpphen)Cl_2 and Pt(phen)Cl_2 respectively for Pt(dpphen)(bds) and Pt(phen)(bds) in place of Pt(dbbpy)Cl_2. The crude products were purified by column chromatography on silica gel using 5% MeOH in CH_2Cl_2.). For Pt(dpphen)(bds), High-resolution electrospray ionization (ESI) mass spectrometry (m/z): calcd for $C_{30}H_{20}N_2PtSe_2$: 762.96; Found: 761.96

$[M]^+$. For Pt(phen)(bds), High-resolution electrospray ionization (ESI) mass spectrometry (m/z): calcd for $C_{18}H_{12}N_2PtSe_2$: 610.90; Found: 609.89 $[M]^+$. ^1H NMR (DMSO-d_6, 300 MHz, 298 K): 9.38 ppm (d, 2H, *J*=5.6 Hz, **dpphen**), 9.19 ppm (d, 2H, *J*=4.2 Hz, **dpphen**), 8.11 ppm (s, 2H, **dpphen**), 7.72-7.67 ppm (m, 10H, **dpphen**), 7.46-7.43 ppm (m, 2H, **bds**), 6.84-6.80 ppm (m, 2H, **bds**). Absorption spectrum for Pt(dpphen)(bds): $\lambda_{max}(CH_2Cl_2)$ = 580 nm (17240 cm^{-1}). Absorption spectrum for Pt(phen)(bds): $\lambda_{max}(CH_2Cl_2)$ = 573 nm (17450 cm^{-1})

2.4.23 Synthesis 4,7-diphenyl-1,10-phenathrolineplatinum(ll)(2,2'-dimercaptobiphenyl), [Pt(dpphen)(mcp)]

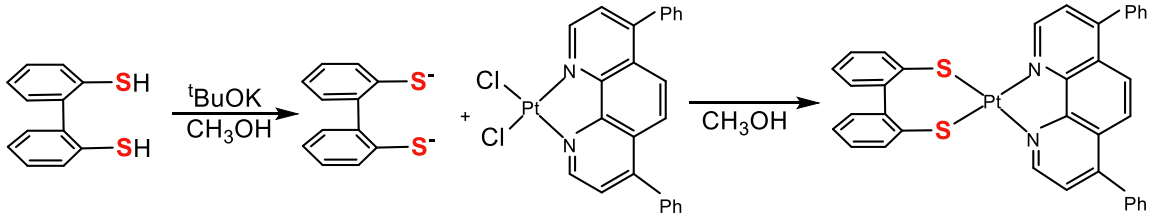

To a suspension of $Pt(dpphen)Cl_2$ (0.20 g, 0.34 mmol) in 60 ml of degassed dry methanol was added a mixture of 2,2'-dimercaptobiphenyl (mcp) (0.073 g, 0.34 mmol) and potassium *tert*-butoxide (0.09 g, 0.8 mmol) in 50 ml of degassed dry methanol. The suspension instantly changed from yellow to orange and the mixture was stirred at room temperature under an atmosphere of nitrogen for 24 hr. The solid was collected by filtration and purified by column chromatography on silica gel using 5% CH_3OH in CH_2Cl_2 as eluent. The bright orange band was collected, and the solvent removed affording a bright orange crystalline solid. Yield 0.183 g (80% based on Pt). ^1H NMR ($CDCl_3$, 300 MHz): 10.12 ppm (d, 2H, J=5.5 Hz), 8.01 ppm (s, 2H), 7.91, 7.84 ppm (dd, J=7.6, 5.5 Hz), 7.61-7.55 (m,

Ar-H), 7.32, 7.29, 7.27 ppm (dt, J=1.3, 1.3, 1.8 Hz), 7.20, 7.18 ppm (dd, J=1.6, 1.5 Hz), 7.13, 7.11, 7.08 ppm (dt, J=1.6, 1.6, 1.7 Hz). High-resolution electrospray ionization (ESI) mass spectrometry (m/z): calcd for $C_{36}H_{24}N_2PtS_2$: 743.10; Found: 744.11 $[M+H]^+$. Absorption spectrum for Pt(dpphen)(mcp): $\lambda_{max}(CH_2Cl_2)$ = 468 nm (21360 cm^{-1}).

2.4.24 Synthesis 4,7-diphenyl-1,10-phenathrolineplatinum(II)(bis-4-*tert*-butylphenolate), [Pt(dpphen)(tbp)$_2$]

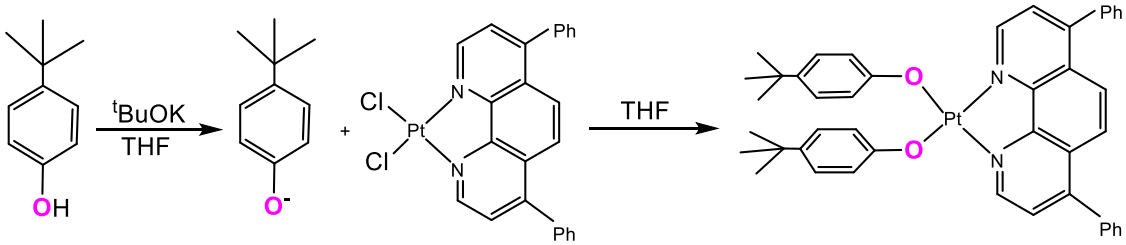

To a suspension of $Pt(dpphen)Cl_2$ (0.22 g, 0.37 mmol) in 50 mL of degassed dry THF, was added a mixture of 4-*tert*-butyl phenolate (tbp) (0.112 g, 0.74 mmol) and potassium *tert*-butoxide (0.0834 g, 0.74 mmol) in 20 mL of degassed dry THF. The suspension instantly changed from yellow to red and the mixture was refluxed under an atmosphere of nitrogen for 12 h. The solid was collected by filtration and purified by column chromatography on silica gel using 5% CH_3OH in CH_2Cl_2 as eluent. The red band was collected, and the solvent removed affording a dark red crystalline solid. Yield 271.10 mg (89% based on Pt). High-resolution electrospray ionization (ESI) mass spectrometry (m/z): calcd for $C_{44}H_{42}N_2O_2Pt$: 825.29; Found: 825.29 $[M]^+$. ^1H NMR ($CDCl_3$, 300 MHz): 9.50 ppm (d, 2H, J=5.5 Hz), 8.03 ppm (s, 2H), 7.76 ppm (d, 2H, J=5.5 Hz), 7.61-7.58 ppm (m, 10H), 7.28

ppm (d, 4H, J=8.5 Hz), 7.07 ppm (d, 4H, J=8.6 Hz), 1.25 ppm (s, 18H). ^{13}C NMR ($CDCl_3$, 300 MHz): δ 165.4, 150.1, 149.4, 149.2, 137.4, 135.4, 129.9, 129.3, 129.3, 128.5, 125.5, 125.3, 125.2, 118.9, 33.7 (*tert*-butyl groups), 31.7 (*tert*-butyl groups). Absorption spectrum for Pt(dpphen)(tbp)$_2$: $\lambda_{max}(CH_2Cl_2)$ = 575 nm (17390 cm^{-1}).

2.4.25 Synthesis 4,7-diphenyl-1,10-phenathrolineplatinum(II)(2-mercaptoph-enolate), [Pt(dpphen)(bSO)]

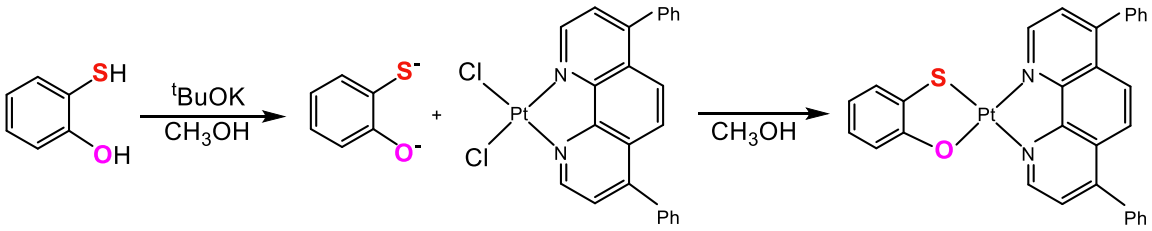

Pt(dpphen)(bSO)

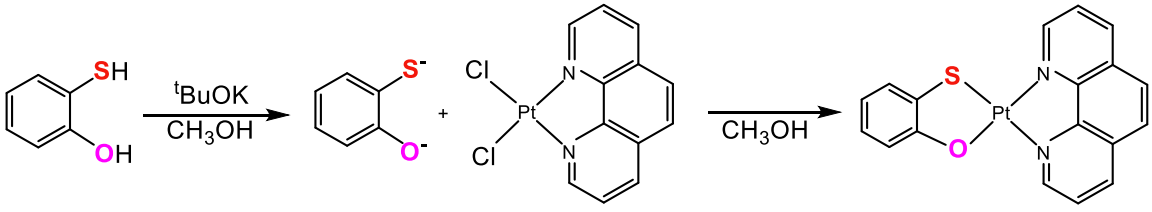

Pt(phen)(bSO)

To a suspension of Pt(dpphen)Cl_2 (0.30 g, 0.502 mmol) in 30 mL of degassed dry methanol, was added a mixture of 2-mercaptophenolate (bSO) (0.063 g,

0.502 mmol) and potassium *tert*-butoxide (0.08 g, 0.8 mmol) in 20 mL of degassed dry methanol. The suspension instantly changed from yellow to purple and the mixture was stirred at room temperature under an atmosphere of nitrogen for 24 hr. The solid was collected by filtration and purified by column chromatography on silica gel using 1% CH_3OH in CH_2Cl_2 as eluent. The purple band was collected, and the solvent removed affording a dark purple crystalline solid. A dark purple rod-like specimen of Pt(dpphen)(bSO) with an approximate dimension of 0.162 mm x 0.253 mm x 0.331 mm was obtained by slow evaporation of saturated solution of dichloromethane (CH_2Cl_2) and benzene in the dark for 3 weeks. Yield for Pt(dpphen)(bSO) 0.280 g (88% based on Pt). Pt(phen)(bSO) was synthesized using Pt(phen)Cl_2 instead of Pt(dpphen)Cl_2 yielding 0.2150 g (68% based on Pt) a dark purple crystalline solid. For Pt(phen)(bSO), high-resolution electrospray ionization (ESI) mass spectrometry (m/z): calcd for $C_{18}H_{12}N_2OPtS$: 499.03; Found: 499.03 $[M]^+$. For Pt(dpphen)(bSO), high-resolution electrospray ionization (ESI) mass spectrometry (m/z): calcd for $C_{30}H_{20}N_2OPtS$: 651.09; Found: 651.09 $[M]^+$. ^1H NMR ($CDCl_3$, 300 MHz) for Pt(dpphen)(bSO): 9.54 ppm (d, 1H, *J*=5.5 Hz, **dpphen** aromatic), 9.28 ppm (d, 1H, *J*=5.6 Hz, **dpphen** aromatic), 7.94 ppm (d, 1H, *J*=9.4 Hz, **dpphen** aromatic), 7.86 ppm (d, 1H, *J*=9.5 Hz, **dpphen** aromatic), 7.50 ppm (d, 1H, *J*=5.6 Hz, **dpphen** aromatic), 7.25 ppm (d, 1H, *J*=7.9 Hz, **dpphen** aromatic), 7.70-7.63 (m, 10H, dpphen **phenyl**), 6.81-6.71 ppm (m, 2H, **bSO**), 6.53-6.48 ppm (m, 2H, **bSO**). Absorption spectrum for Pt(dpphen)(bSO): $\lambda_{max}(CH_2Cl_2)$ = 586 nm (17070 cm^{-1}).

2.4.26 Synthesis 4,7-diphenyl-1,10-phenathrolineplatinum(II)(2-selenylbenzenethiolate), [Pt(dpphen)(bSSe)]

Pt(dpphen)(bSSe) and Pt(phen)(bSSe) were synthesized using the procedure forPt(dbbpy)(bSSe) with dpphen and phen acceptor ligands, respectively, being substituted for dbbpy. The yield for Pt(dpphen)(bSSe) and Pt(phen)(bSSe) were

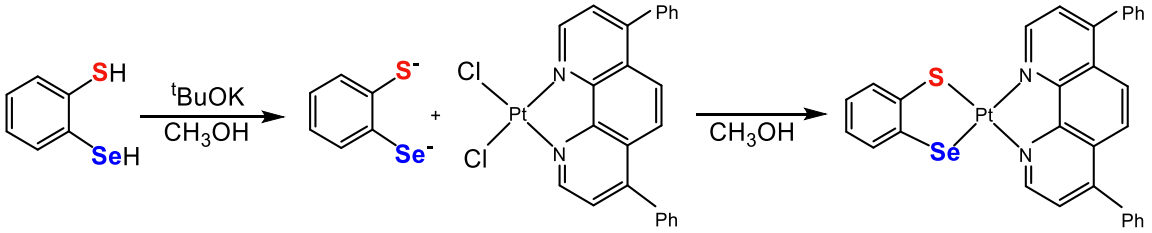

Pt(dpphen)(bSSe)

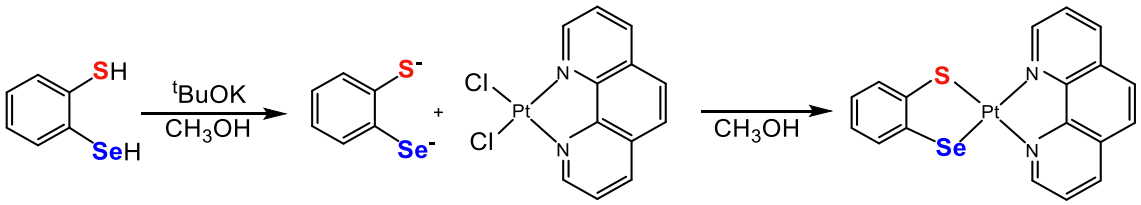

Pt(phen)(bSSe)

240 mg (75% based on Pt) and 210 mg (65% based on Pt) respectively. ForPt(phen)(bSSe), high-resolution electrospray ionization (ESI) mass spectrometry (m/z): calcd for $C_{18}H_{12}N_2PtSSe$: 561.95; Found: 561.95 $[M]^+$. For Pt(dpphen)-(bSSe), high-resolution electrospray ionization (ESI) mass spectrometry (m/z): calcd for $C_{30}H_{20}N_2PtSSe$: 714.01; Found: 714.02 $[M]^+$. ^1H NMR [DMSO-d_6, 300 MHz, [Pt(phen)(bSSe)]: 9.41, 9.36 ppm (dd, 2H, J_1 =1.5 Hz, J_2 =5.1 Hz, **phen**), 9.05-8.98 ppm (m, 2H, **phen**), 8.28 ppm (s, 2H, **phen**), 8.18-8.14 ppm (m, 1H, **phen**), 8.09-8.05 ppm (m, 1H, **phen**), 7.43 ppm (d, 1H, *J*

=7.6 Hz, **bSSe**), 7.27 ppm (d, 1H, *J* =7.8 Hz, **bSSe**), 6.85-6.80 ppm (m, 1H, **bSSe**), 6.75-6.70 ppm (m, 1H, **bSSe**). Absorption spectrum for Pt(dpphen)(bSSe): $\lambda_{max}(CH_2Cl_2)$ = 580nm (17230 cm^{-1}).

2.4.27 Synthesis 4,7-diphenyl-1,10-phenathrolineplatinum(II)(2-selenylphenolate), [Pt(dpphen)(bSeO)]

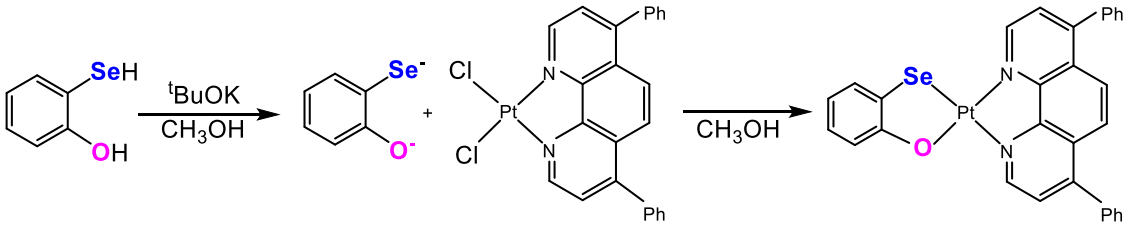

To a suspension of $Pt(dpphen)Cl_2$ (0.200 g, 0.33 mmol) in 40 mL of degassed dry methanol was added a mixture of 2-selenylphenolate (bSeO) (0.057 g, 0.33 mmol) and potassium *tert*-butoxide (0.045 g, 0.4 mmol) in 20 mL of degassed dry methanol. The suspension instantly changed from yellow to purple and the mixture was stirred at room temperature under an atmosphere of nitrogen for 24 hr. The solid was collected by filtration and purified by column chromatography on silica gel using 5% CH_3OH in CH_2Cl_2 as eluent. The purple band was collected, and the solvent removed affording a dark purple crystalline solid. Yield 195.10 mg (85% based on Pt). A dark purple rod-like specimen of Pt(dpphen)(bSeO) with an approximate dimension of 0.170 mm x 0.217 mm x 0.420 mm mm was obtained by slow evaporation of saturated solution of dichloromethane (CH_2Cl_2), hexane and dimethylacetamide in a 1:1:1 mixture in the dark for a month. High-resolution electrospray ionization (ESI) mass spectrometry (m/z): calcd for $C_{30}H_{20}N_2OPtSe$: 699.04; Found: 699.04 $[M]^+$. ^1H

NMR ($CDCl_3$, 300 MHz, 298 K): 9.57 ppm (d, 1H, *J*=5.7 Hz, **dpphen** aromatic), 9.30 ppm (d, 1H, *J*=5.9 Hz, **dpphen** aromatic), 7.96 ppm (d, 1H, *J*=9.6 Hz, **dpphen** aromatic), 7.96 ppm (d, 1H, *J*=9.8 Hz, **dpphen** aromatic), 7.54 ppm (d, 1H, *J*=7.8 Hz, **dpphen** aromatic), 7.29 ppm (d, 1H, *J*=8.0 Hz, **dpphen** aromatic), 7.75-7.68 (m, 10H, dpphen **phenyl**), 6.83-6.74 ppm (m, 2H, **bSeO**), 6.51-6.45 ppm (m, 2H, **bSeO**). Absorption spectrum for Pt(dpphen)(bSeO): $\lambda_{max}(CH_2Cl_2)$ = 595 nm (16800 cm^{-1}).

2.4.28 Synthesis of 4,4'-di-*tert*-butyl-2,2'-bipyridinepalladium(II)(benzenedithiolate), [Pd(dbbpy)(bdt)]

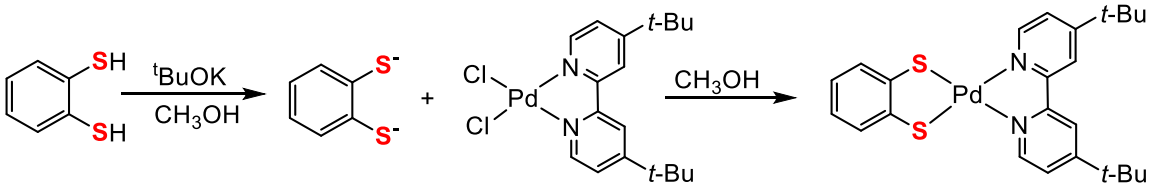

Pd(dbbpy)(bdt) was prepared by the modification of a literature procedure.[26]. To a suspension of Pd(dbbpy)Cl_2 (0.20 g, 0.60 mmol) in 40 mL of deaerated dry methanol was added a mixture of 1,2-benzenedithiol (bdt) (0.085 g, 0.60 mmol) and potassium *tert*-butoxide (0.146 g, 1.3 mmol) in 20 mL of deaerated dry methanol. The suspension instantly changed from orange to dark red and the mixture was stirred at room temperature under an atmosphere of nitrogen for 24 h. The dark-red solid was collected by filtration and purified by column chromatography on silica gel using hexane/CH_2Cl_2 1:1 as eluent. The brown band was collected, and the solvent removed affording a reddisd-brown crystalline solid. Yield 0.160 g (66% based on Pd). High-resolution electrospray

ionization (ESI) mass spectrometry (m/z): calcd for $C_{24}H_{28}N_2PdS_2$: 514.07; Found: 514.07 $[M]^+$. ^1H NMR ($CDCl_3$, 300 MHz): 8.53 ppm (d, 2H, *J*=5.9, **dbbpy** aromatic), 7.92 ppm (d, 2H, *J*=1.7, **dbbpy** aromatic), 7.44,7.42 ppm (dd, 2H, J_1=1.9, J_2=1.9, **dbbpy** aromatic), 7.14-7.11 ppm (m, 2H, **bdt**), 6.83-6.80 ppm (m, 2H, **bdt**), 1.41 ppm (s, 18H, *tert*-butyl groups). ^{13}C-NMR ($CDCl_3$, 300 MHz): 163.5 ppm,155.4 ppm, 148.7 ppm, 142.9 ppm, 127.8 ppm, 123.9 ppm, 121.7 ppm, 119.2 ppm, 35.6 ppm (*tert*-butyl groups), 30.3 ppm (*tert*-butyl groups). Absorption spectrum for [Pd(dbbpy)(bdt)]: $\lambda_{max}(CH_2Cl_2)$ = 478 nm (20900 cm^{-1}).

2.4.29 Synthesis 4,7-diphenyl-1,10-phenathrolinepalladium(II)(2-selenylbenzenethiolate), [Pd(dpphen)(bSSe)]

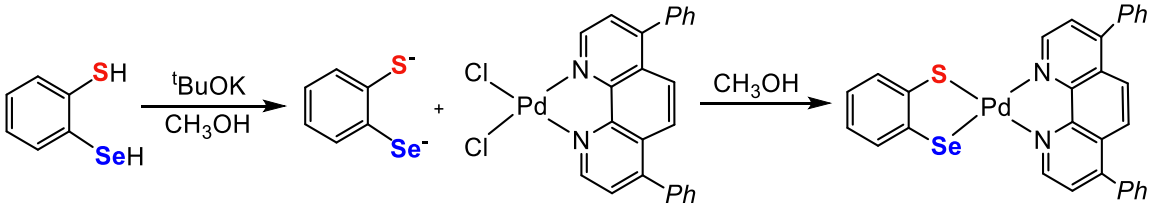

Pd(dpphen)(bSSe)

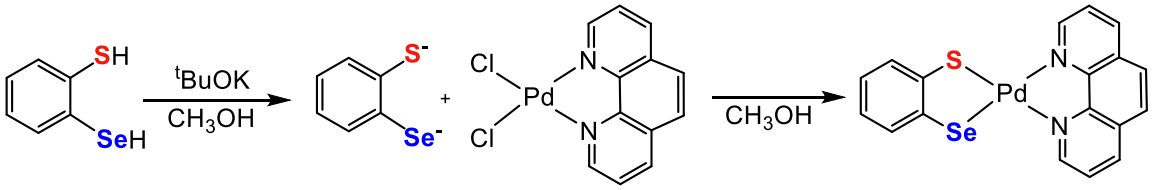

Pd(dpphen)(bSSe)

To a suspension of $Pd(dpphen)Cl_2$ (0.200 g, 0.4 mmol) in 50 mL of degassed dry

methanol was added a mixture of 2-selenylbenzenethiol (bSSe) (0.076 g, 0.4 mmol) and potassium *tert*-butoxide (0.08 g, 0.8 mmol) in 20 mL of degassed dry methanol. The suspension instantly changed from yellow to deep red and the mixture was stirred at room temperature under an atmosphere of nitrogen for 24 hr. The solid was collected by filtration and purified by column chromatography on silica gel using 2% CH_3OH in CH_2Cl_2 as eluent. The yield for Pd(dpphen)(bSSe) and Pd(phen)(bSSe) were 204 (82% based on Pd) and 198 mg (75% based on Pd) respectively. High-resolution electrospray ionization (ESI) mass spectrometry (m/z) for Pd(phen)(bSSe): calcd for $C_{18}H_{12}N_2PdSSe$: 473.89; Found: 473.89 $[M]^+$ and for Pd(dpphen)(bSSe): calcd for $C_{30}H_{20}N_2PdSSe$: 625.95; Found: 625.95 $[M]^+$. ^1H NMR ($CDCl_3$, 300 MHz, 298 K [Pd(dpphen)(bSSe]): 9.18 ppm (d, 1H, J=5.3 Hz), 9.09 ppm (d, 1H, J=5.3 Hz), 7.98 ppm (S, 2H), 7.82 ppm (d, 1H, J=5.3 Hz), 7.74 ppm (d, 1H, J=5.3 Hz), 7.58-7.54 (m, 10H), 7.40 ppm (d, 1H, J=7.4 Hz), 7.22 ppm (d, 1H, J=7.9 Hz), 6.98-6.84 (m, 2H). Absorption spectrum for [Pd(dpphen)(bSSe)]: $\lambda_{max}(CH_2Cl_2)$ = 524 nm (19070 cm^{-1}).

2.4.30 Synthesis 4,7-diphenyl-1,10-phenathrolinepalladium(II)(2-mercapto-phenolate), [Pd(dpphen)(bSO)]

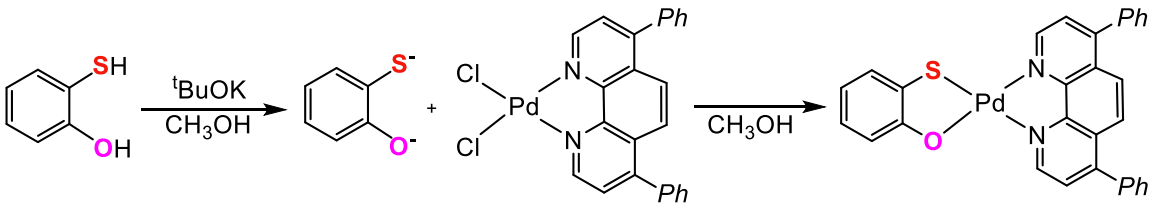

Pd(dpphen)(bSO)

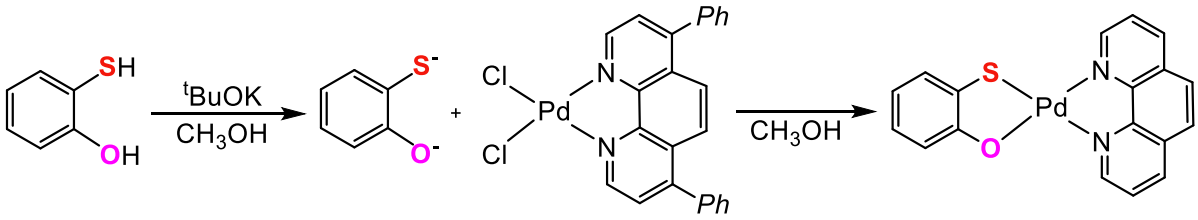

Pd(dpphen)(bSO)

To a suspension of $Pt(dpphen)Cl_2$ (0.200 g, 0.502 mmol) in 40 mL of degassed dry methanol was added a mixture of 2-mercaptophenolate (bSO) (0.050 g, 0.4 mmol) and potassium *tert*-butoxide (0.08 g, 0.8 mmol) in 20 mL of degassed dry methanol. The suspension instantly changed from yellow to reddish brown and the mixture was stirred at room temperature under an atmosphere of nitrogen for 24 hr. The solid was collected by filtration and purified by column chromatography on silica gel using 1% CH_3OH in CH_2Cl_2 as eluent. The yield for Pd(dpphen)(bSO) and Pd(phen)(bSO) were 192 mg (68% based on Pd) and 175 mg (85% based on Pd) respectively. High-resolution electrospray ionization (ESI) mass spectrometry (m/z) for Pd(phen)(bSO): calcd for $C_{18}H_{12}N_2PdSO$: 409.97; Found: 409.97 $[M]^+$ and for Pd(dpphen)(bSO): calcd for $C_{30}H_{20}N_2PdSO$: 562.03; Found: 562.04 $[M]^+$. ^1H NMR ($CDCl_3$, 300 MHz, 298 K, [Pd(dpphen)(bSO]): 9.27 ppm (d, 1H, J=4.5 Hz, **dpphen**), 9.06 ppm (d, 1H, J=5.1 Hz, **dpphen**), 8.75 ppm (d, 1H, J=4.3 Hz), 7.75 ppm (d, 1H, J=5.2 Hz, **dpphen**), 7.59 ppm (S, 2H, **dpphen**), 7.92-7.82 ppm (m, 5H, **dpphen**), 7.64-7.55 ppm (m, 5H, **dpphen**), 6.95-6.92 (m,1H, **bSO**), 6.73-6.69 (m,1H, **bSO**), 6.47-6.39 (m,2H, **bSO**). Absorption spectrum: Absorption spectrum for Pd(phen)(bSO): $\lambda_{max}(CH_2Cl_2)$ = 566 nm (17670 cm^{-1}).

2.4.31 Synthesis 4,7-diphenyl-1,10-phenathrolinepalladium(II)(3,5-di-*t*-butyl-benzene catecholate), [Pd(dpphen)(dtbCAT)]

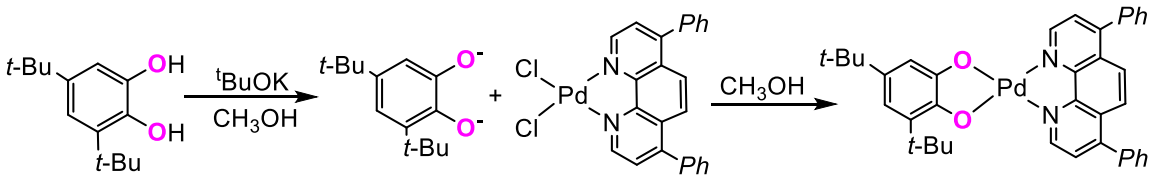

4,7-diphenyl-1,10-phenathrolinepalladium(II) dichloride (1.000 g, 0.20 mmol) was suspended in 50 mL of MeOH. A solution of 3,5-di-*t*-butylbenzene catecholate (0.045 g, 0.20 mmol) in 10 ml of deaerated dry methanol was added to potassium *tert*-butoxide (0.0461 g, 0.41 mmol) under an atmosphere of dinitrogen to form a blue solution of the mixture. The blue mixture was then added to an orange solution of 4,7-diphenyl-1,10-phenathrolinepalladium(II) dichloride in methanol and the resultant combined mixture immediately turned from yellow to blue. This mixture was then heated to reflux for 12 h under an atmosphere of dinitrogen, during which time the solution turned to dark blue. The solvent was removed under vacuum and yielded a dark blue solid, 857.33 mg (85% based on Pd). High-resolution electrospray ionization (ESI) mass spectrometry (m/z): calcd for $C_{38}H_{36}N_2O_2Pd$: 658.18; Found: 658.18 $[M]^+$, Anal. Calcd for $C_{38}H_{36}N_2O_2Pd$: C 69.24; H 5.51; N 4.25; O 4.85. Found: C 68.91; H 5.26; N 4.43; O 4.65. ^1H NMR ($CDCl_3$, 300 MHz, 298 K): 8.93 ppm (d, 1H, J=4.5 Hz, **dpphen**), 8.80 ppm (d, 1H, J=5.1 Hz, **dpphen**), 8.36 ppm (d, 1H, J=8.2 Hz, **dpphen**), 8.30 ppm (d, 1H, J=8.1 Hz, **dpphen**), 7.82 ppm (s, 2H, **dpphen**), 7.74-7.70 ppm (m, 5H, **dpphen phenyl**), 7.67-7.63 ppm (m, 5H, **dpphen phenyl**), 6.48 ppm (m, 2H, **dtbCAT**), 1.55 ppm (s, 9H), 1.34 ppm (s, 9H). ^{13}C NMR

($CDCl_3$, 300 MHz, 298 K): δ 148.9 ppm, 148.2 ppm, 144.9 ppm, 144.1 ppm, 141.8 ppm, 141.6 ppm, 137.1 ppm, 135.4 ppm, 129.5 ppm, 129.4 ppm, 127.0 ppm, 126.6 ppm, 125.2 ppm, 124.6 ppm, 114.7 ppm, 112.1 ppm, 34.9 ppm (***tert*-butyl** groups), 34.7 ppm (***tert*-butyl** groups), 30.1 ppm (***tert*-butyl** groups), 29.9 ppm (***t*-butyl** groups). Absorption spectrum: $\lambda_{max}(CH_2Cl_2)$ = 611 nm (16360 cm^{-1}).

2.4.32 Synthesis of 4,7-diphenyl-1,10-phenathrolinepalladium(II)(1,5-diiso-propyl-3-(3',4'-dihydroxy-5'-*t*-butylphenyl)-2-yl-6-oxoverdazyl, [Pd(dpphen)-(tbCAT-Vz)]

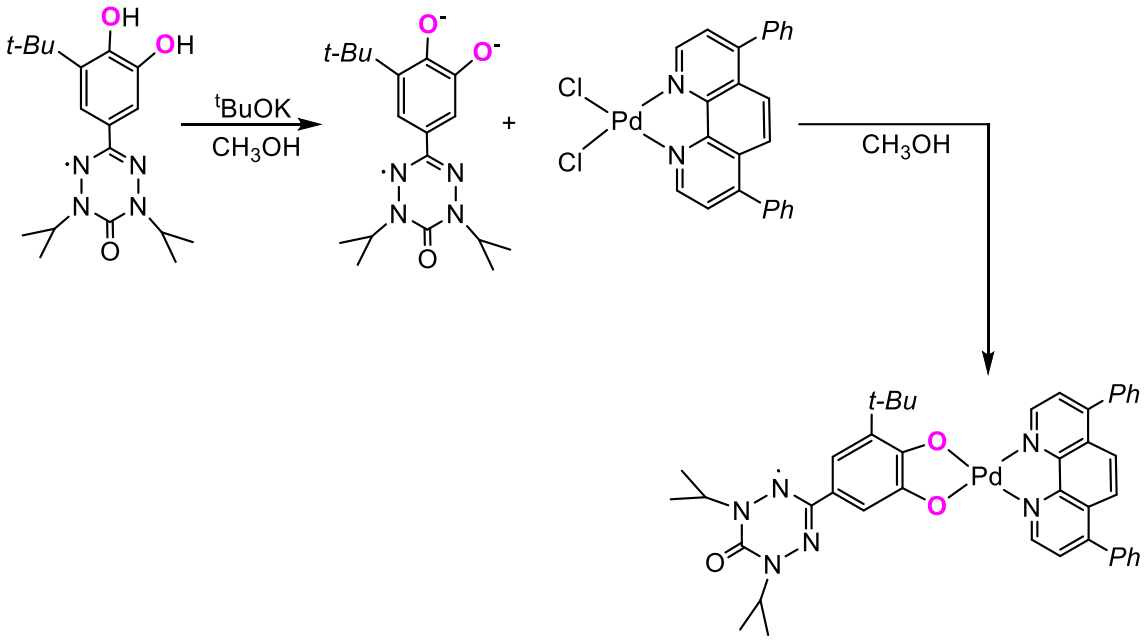

4,7-diphenyl-1,10-phenathrolinepalladium(II) dichloride (0.200 g, 0.40 mmol) was suspended in 60 mL of MeOH. A solution of 1,5-diisopropyl-3-(3',4'-dihydroxy-5'-*t*-butylphenyl)-6-oxoverdazyl (0.139 g, 0.40 mmol) in 20 mL of deaerated methanol was added to potassium *tert*-butoxide (0.0461 g, 0.41 mmol) under an

atmosphere of dinitrogen to form a reddish-brown solution of the mixture. The reddish-brown mixture was then added to the yellow solution of 4,7-diphenyl-1,10-phenathrolinepalladium(II) dichloride in methanol and the mixture immediately turned from orange to blue. The mixture was heated to reflux for 12h

under the atmosphere of dinitrogen, during which time the solution turned to dark blue. The solvent was removed under vacuum to yield a dark blue solid, 185.56 mg (Yield: 80% based on Pd). High-resolution electrospray ionization (ESI) mass spectrometry (m/z): calcd for $C_{42}H_{41}N_6O_3Pd$: 783.23; Found: 783.20 $[M]^+$. Anal. calculated for $C_{42}H_{41}N_6O_3Pd$: C, 64.32; H, 5.27; N, 10.72; O, 6.12; Pd, 13.57. Found: C, 64.01; H, 5.02; N, 10.90. Absorption spectrum: $\lambda_{max}(CH_2Cl_2)$ = 589 nm (16980 cm^{-1}).

2.4.33 Synthesis of 4,4'-di-*tert*-butyl-2,2'-bipyridinenickel(II)(1,2-benzenedi-thiolate), [Ni(dbbpy)(bdt)]

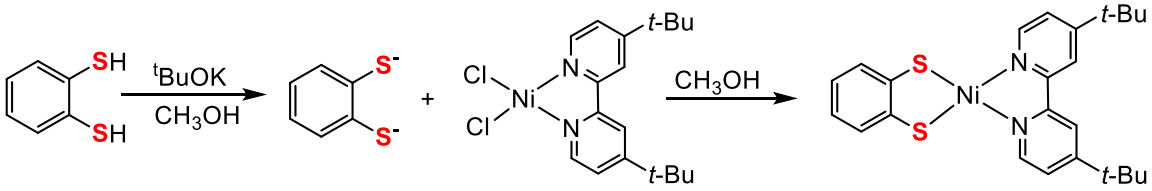

$Ni(dbbpy)Cl_2$ was synthesized according to the method described by Awad and Peter Strauch[30]. An ethanolic solution of 4,4'-di-*tert*-butyl-2,2'-bipyridine was added slowly to a well-stirred ethanolic solution of $NiCl_2.6H_2O$. The reaction mixture was then stirred for 2 h at 70 ^{0}C, after which it was cooled to room temperature. The pale green product was filtered off, washed with ethanol, and

vacuum dried. To a suspension of $Ni(dbbpy)Cl_2$ (0.20 g, 0.50 mmol) in 40 ml of deaerated dry methanol was added a mixture of 1,2-benzenedithiol (bdt) (0.072 g, 0.50 mmol) and potassium *tert*-butoxide (0.09 g, 0.80 mmol) in 20 ml of deaerated dry methanol. The suspension instantly changed from pale green dark to purple and the mixture was stirred at room temperature under an atmosphere of nitrogen for a day. The solid was collected by filtration and purified by column chromatography on silica gel using hexane/CH_2Cl_2 1:1 as eluent. The purple band was collected, and the solvent removed affording a purple crystalline solid. Yield 145.48 mg (77% based on Ni). High-resolution electrospray ionization (ESI) mass spectrometry (m/z): calcd for $C_{24}H_{28}N_2Ni_2$: 466.10; Found: 466.11 $[M]^+$. ^1H NMR ($CDCl_3$, 300 MHz, 298 K): 8.56 ppm (d, 2H, *J*=6.1 Hz, **dbbpy** aromatic), 7.81 ppm (d, 2H, *J*=1.6 Hz, **dbbpy** aromatic), 7.34,7.32 ppm (dd, 2H, J_1=1.8 Hz, J_2=1.8 Hz, **dbbpy** aromatic), 7.17-7.14 ppm (m, 2H, **bdt**), 6.79-6.76 ppm (m, 2H, **bdt**), 1.37 ppm (s, 18H, **dbbpy *tert*-butyl** group). ^{13}C-NMR ($CDCl_3$, 300 MHz, 298 K): 163.3 ppm, 155.0 ppm, 148.4 ppm, 143.9 ppm, 126.9 ppm, 123.2 ppm, 121.4 ppm, 117.9 ppm, 35.5 ppm (***tert*-butyl** groups), 30.3 ppm (***tert*-butyl** groups). Absorption spectrum: $\lambda_{max}(CH_2Cl_2)$ = 530 nm (18870 cm^{-1}).

2.4.34 Synthesis of 4,4'-di-*tert*-butyl-2,2'-bipyridinenickel(II)(3,5-di-*t*-butyl-benzene catecholate), [Ni(dbbpy)(dtbCAT)]

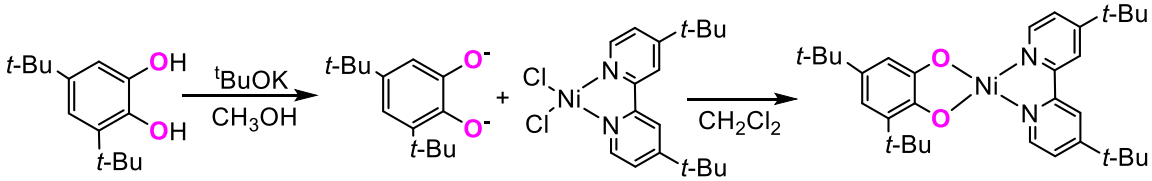

Ni(dbbpy)(dtbCAT) was prepared by following the synthetic procedure for the synthesis of Ni(dbbpy)(bdt). Here, 3,5-di-*t*-butylbenzene catecholate was used in place of 1,2-benzenedithiol (bdt). Yield: 185.70 mg (85% based on Ni). High-resolution electrospray ionization (ESI) mass spectrometry (m/z): calcd for $C_{32}H_{44}N_2NiO_2$: 546.28; Found: 546.28 $[M]^+$. ^{1}H NMR ($CDCl_3$, 300 MHz, 298 K): 8.66 ppm (d, 2H, *J*=25.3 Hz, **dbbpy** aromatic), 7.76 ppm (s, 2H, **dbbpy** aromatic), 7.45 ppm (d, 2H, *J*=22.7 Hz **dbbpy** aromatic), 6.59 ppm (s, 1H, **dtbCAT**), 6.38 ppm (s, 1H, **dtbCAT**), 1.50 ppm (s, 9H, **dtbCAT *tert*-butyl** group), 1.43 ppm (s, 18H, **dbbpy *tert*-butyl** group), 1.29 ppm (s, 9H, **dtbCAT *tert*-butyl** group). ^{13}C-NMR ($CDCl_3$, 300 MHz, 298 K): 163.2 ppm, 154.7 ppm, 148.8 ppm, 144.0 ppm, 126.9 ppm, 123.4 ppm, 121.2 ppm, 117.9 ppm, 35.5 ppm (***tert*-butyl** groups), 30.2 ppm (***tert*-butyl** groups). Absorption spectrum: $\lambda_{max}(CH_2Cl_2)$ = 571 nm (17500 cm^{-1}).

2.4.35 References

(1) Weinstein, J. A; Tierney, M. T.; Davies E. S.; Base, K.; Robeiro, A. A.; Grinstaff, M. W. *Inorg. Chem.* **2006**, 45, 4544-4555.

(2) Yang, J.; Kersi, D. K.; Giles, L. J.; Stein, B. W.; Feng, C.; Tichnell, C. R.; Shultz, D. A.; Kirk, M. K. *Inorg. Chem.* **2014**, 53, 4791-4793.

(3) Miller, T. R.; Dance, I. G.; *J. Am. Chem. Soc.* **1973**, 95, 6970.

(4) Hissler, M.; McGarrah, I. E.; Connick, W.B.; Geiger, D. K.; Cummings, S. D.; Eisenberg, R. *Coord. Chem. Rev.* **2000**, 208,115.

(5) Paw, W.; Cummings, S. D.; Mansour, M. A.; Connick, W. B.; Geiger, D. K.; Eisenberg, R. *Coord. Chem. Rev.* **1998**, 171,125.

(6) Makedonas, C.; Mitsopoulou, C. A.; Lahoz, F.J.; Balana, A. I. *Inorg. Chem.* **2003**, 42, 8853-8865.

(7) Cummings, S. D.; Eisenberg, R. *J. Am. Chem. Soc.* **1996**, 118, 1949.

(8) Cummings, S. D.; Eisenberg, R. *Inorg. Chem.* **1995**, 34, 2007.

(9) Kubo, K.; Nakano, M.; Tamura, H.; Matsubayashi, G. -E. *Inorg. Chim. Acta* **2002**, 336, 120.

(10) Islam, A.; Sugihara, H.; Hara, K.; Singh, L. P.; Katoh, R.; Yanakida, M.; Takahashi, Y.; Murata, S.; Arakawa, H. *Inorg. Chem.* **2001**, 40, 5371.

(11) Chen, C. -T.; Liao, S. -Y.; Lin, K. -J.; Chen, C. -H.; Lin, T. -Y. *J. Inorg. Chem.* **1999**, 38, 2734.

(12) Base, K.; Grinstaff, M. W., *Inorg. Chem.* **1998**, 37, 1432.

(13) Makedonas, C.; Mitsopoulou, C. -A., *J. Inorg. Biochem.* **2001**, 86, 326.

(14) Cocker, T. M.; Bachman, R. E., *Inorg. Chem.* **2001**, 40,1550.

(15) Connick, W. B.; Gray, H. B., *J. Am. Chem. Soc*. **1997**, 119, 11620.

(16) Theis, B.; Metz, S.; Burschka, C.; Bertermann, R.; Maisch, S.; Tacke, R. *Chem. Eur. J.* **2009**, 15, 7329-7338.

(17) Sandman, D. J.; Allen, G. W.; Acampora, L. A.; Stark, J. C.; Jansen, S.; Jones, M. T.; Ashwell, G. J.; Foxman, B. M. *Inorg. Chem.* **1987,** 26, 11,1664-1669.

(18) Papavassiliou, G.; Yiannopoulos, S.; Zambounis, J.; Kobayashi, K.; Umemoto, K. *Chemistry Letters* **1987**, 1279-1282.

(19) Ribas, X.; Joào C. Dias, J. C.; Morgado, J.; Wurst, K.; Molins, E.; Ruiz, E.; Almeida, M.; Veciana, J.; Rovira, C. *Chem. Eur. J.* **2004**, 10, 1691-1704.

(20) Sorrell, T.; Cheesman, E. *Syn. Comm.* **1981**, 909-912.

(21) Schwartx, L.; Singh, P.; Eriksson, L.; Lomoth, R.; Ott, S. *C.R. Chimie* **2008**, 11, 875-889.

(22) Shavaleev, N. M.; Davies, S. E.; Adams, H.; Best, J.; Weinstein, J.A., *Inorg. Chem. **2008,** 47,1532-1547*.

(23) Weinstein, J. A; Tierney, M. T.; Davies E. S.; Base, K.; Robeiro, A. A.; Grinstaff, M. W. *Inorg. Chem.* **2006**, 45, 4544-4555.

(24) Choi, Y. S.; Moschetta, E. G.; Miller, J. T.; Fasulo, M.; McMurdo, M. J.; Rioux, R. M.; Tilley, T. D., *ACS Catal.* **2011**, 1, 1166-1177.

(25) Sandman, D.; Allen, G.; Acampora, L.; Stark, J.; Jansen, S.; Jones, T.; Ashwell, G.; Foxman, B. *Inorg. Chem.* **1987**, 26,1664.

(26) Cummings, S. D.; Eisenberg, R., *J. Am. Chem. Soc.* **1996**, 118, 1949-1960.

(27) Best, J.; Sazanovich, I. V.; Adams, H.; Bennett, R. D.; Davies, E. S.; Meijer, A. J. H. M.; Towrie, M.; Tikhomirov, S. A.; Bouganov, O. V.; Ward, M. D.; Weinstein, J. A., *Inorg. Chem.* **2010**, 49, 10041-10056.

(28) Shavaleev, N. M.; Davies, E. S.; Adams, H.; Best, H.; Weinstein, J. A. *Inorg. Chem.* **2008**, 47, 1532-1547.

(29) Chemistruck, V.; Chambers, D.; Brook, D. J. R., *J. Org. Chem.* **2009**, 74, 1850-1857.

(30) Awad, D. J.; Conrad, F.; Koch, A.; Schilde, U.; Poppl, A.; Strauch, P., *Inorganica Chimica Acta,* **2010**, 363, 1488-1494.

Chapter 3: Spectroscopic, Structural and Computational studies of Pt(II) Diimine Dichalcogenolene Complexes

3.1 Introduction

Donor-acceptor transition metal diimine complexes have received significant attention over the past three decades due to their distinctive electrochemical and photophysical properties.[1-38] These complexes are typically strongly absorbing visible chromophores and are used in applications such as artificial photosynthethetic receptors,[1-3,13] supramolecular assemblies,[39-41] photoluminescent nucleic acid probes,[2,8,42,43] and molecular photonic devices.[39-43] Transition metal diimne complexes have been shown to display solvatochromic effects,[26] solution and solid-state photoluminescence,[2,14-26,39] molecular hyper-polarizabilities,[33,34] and unusual redox behavior.[40] These extensive properties have made Pt(II) chromophores potentially useful as tunable materials for nonlinear optical, light-emitting diode,[35] photochemical sensing[44-49] applications, and solar cell[36,50] applications, in addition to sensitization of singlet oxygen.[27,37,38] Coordinately unsaturated d^8 transition metal chromophores are also of importance since they have open coordination sites for chemical reactions such as cross- and self-quenching,[16,27-30] photoreactivity[31] and photocatalysis.[32]

Research on transition metal diimine complexes continues with vigor since these complexes possess long-lived excited states that can be used in bimolecular energy transfer, in electron transfer reactions, and as efficient lumiphores. Synthetically, modified ground state properties include a high degree of stability, with excited-state properties that can be modified by systematic variations in their

molecular structure. The intense color of these complexes and other physical properties are due to the nature of their charge transfer excited states. Various terms have been used to assign the nature of the charge transfer (CT) transitions. These include intraligand charge transfer (ILCT), metal-to-ligand charge transfer (MLCT), charge-transfer-to-diimine, ligand-to-ligand charge transfer (LLCT) and mixed metal/ligand-to-ligand charge transfer (MMLL'CT).[2,3] But throughout this dissertation, the term mixed metal/ligand-to-ligand charge transfer (MMLL'CT) will be used. This designation was originally employed by Eisenberg to highlight the role of mixed metal/ligand character in the HOMO, while the LUMO is a pure π* orbital of the diimine.

We have examined the influence of several parameters, such as the identity of the transition metal ion (Pt versus Ni versus Pd) and the inclusion of accepting or donating groups on the ligands in order to develop structure-property relationships for these complexes. Little work has been done using heavier dichalcogenolene such as diselenolene, ditellurene, and mixed dichalcogenolene chelating ligands (O,S; O,Se; S,Se), despite the fact that sulfur donor atoms play a significant role in the physical properties of these complexes.[3]

Different types of luminescent platinum(II) complexes of the type Pt(diimine)(dithiolate), Pt(diimine)(diselenolate), Pt(diimine)(selenylbenzenethiolate), Pt(diimine)(selenylphenolate), Pt(diimine)(mercaptophenolate), and Pt(diimine)(cateholate) have been prepared, characterized, and spectroscopically studied. The diimine ligands that we use here are of the type 4,4'-di-tert-butyl-2,2'-bipyridine (dbbpy), and 4,7-diphenyl-1,10-phenathroline (dpphen). The

dithiolate, diselenolate, cateholate, selenylbenzenethiolate, selenylphenolate, and mercaptophenolate ligands are all chelating dianions. In this chapter, we perform studies of these complexes that involve systematic ligand variations to assign and understand their rich emission and absorption spectra.

The emission lifetimes and quantum yield of various forms of the Pt(diimine)(dichalcogenolene) chromophore can be influenced by using different diimine and dichalcogenolene ligands.[1-3,17,51] The Pt(diimine)(dichalcogenolene) complexes studied here have ground state recovery and luminescence lifetimes that range from ns to μs, and this indicates the influence of the diimine and dichalcogenolene ligands on their underpinning excited state electronic structure. Interestingly, the emission maxima for Pt(diimine)(dichalcogelene) complexes is independent of solvent polarity, which contrasts with their respective absorption band maxima.

3.2 Spectroscopic Studies of Pt(II) Diimine Complexes

3.2.1 [Pt(dbbpy)(bdt)]

3.2.1.1 Electronic Absorption Spectroscopy

The electronic absorption spectrum of Pt(dbbpy)(bdt) was collected in dichloromethane at room temperature and is shown in Figure 3.1. The MMLL'CT absorption band maximum (λ_{max}^{Abs}) is located at 18350 cm^{-1} in CH_2Cl_2 with a molar extinction coefficient of 7700 $M^{-1}cm^{-1}$. The absorption maximum is recorded only

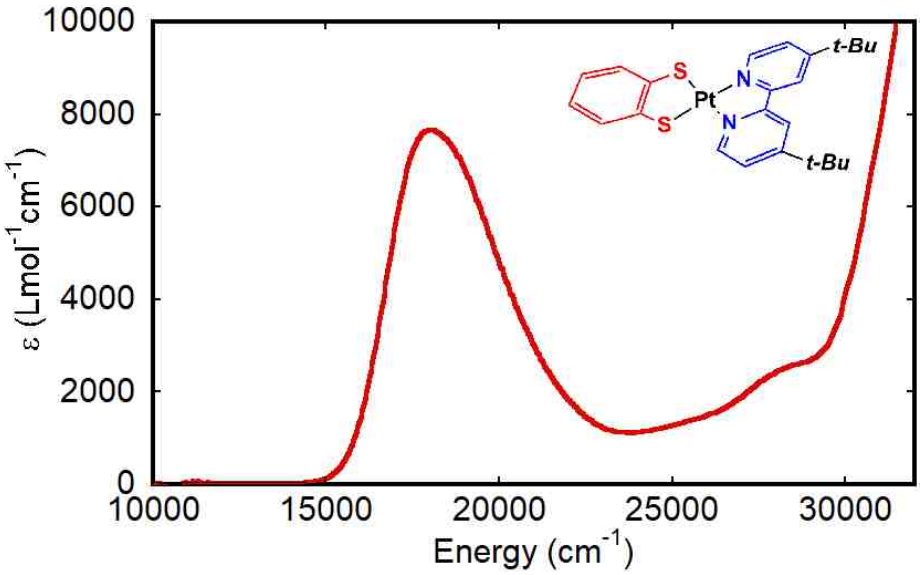

Figure 3.1: Absorption spectrum of Pt(dbbpy)(bdt) in CH_2Cl_2. Inset: Compound structure.

for the lowest-energy band, even though additional absorption features occur at higher energies. The lowest-energy absorption maxima for all the complexes under study exhibit a strong solvent dependency.

3.2.1.2 Transient Absorption Spectra, Emission Spectra, and Excited State Lifetimes

Solution emission spectra for all complexes were performed on deoxygenated samples using an LP920 laser flash photolysis spectrometer. The photoluminescence properties of Pt(dbbpy)(bdt) were observed at room temperature in degassed dichloromethane solution. The ambient temperature (298 K) emission spectrum of Pt(dbbpy)(bdt) is depicted in figure 3.2. The emission maxima (λ_{max}^{Em}) of Pt(dbbpy)(bdt) is at 702 nm (14250 cm^{-1}) and the

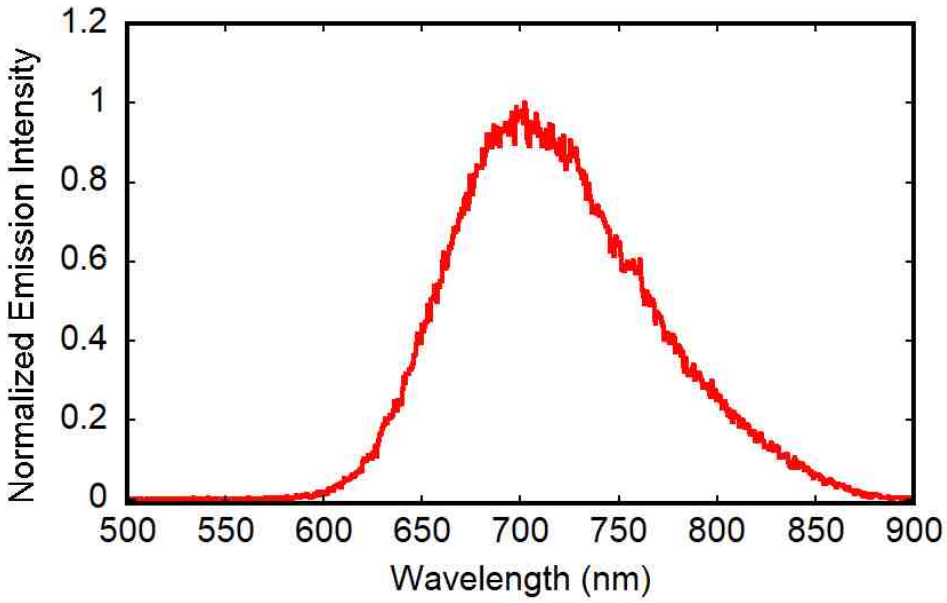

Figure 3.2: Emission spectrum of Pt(dbbpy)(bdt) in degassed CH_2Cl_2 solution at 298 K, the excitation wavelength is 550nm.

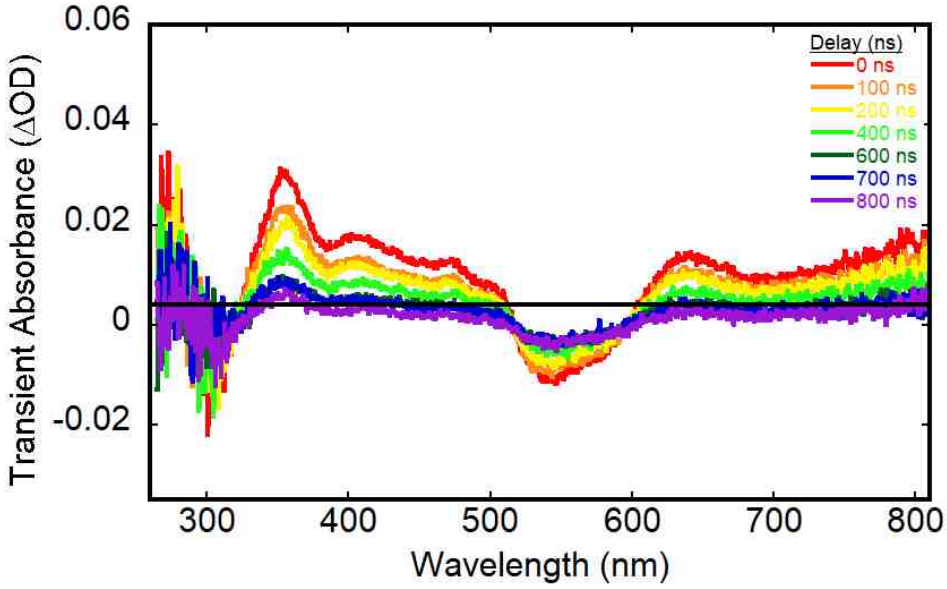

Figure 3.3: Transient Absorption (TA) difference spectra for Pt(dbbpy)(bdt) obtained in degassed CH_2Cl_2 fluid solution following 550 nm excitation, pump: 5 mJ/pulse at the MMLL'CT absorption maximum, recorded at 0, 100, 200, 400, 600, 700, and 800 ns time delays.

Stokes shift is 4100 cm^{-1}. The photoluminescence based emission of Pt(dbbpy)(bdt) is due to a MMLL'CT transition back to the electronic ground state. Transient Absorption (TA) difference spectra for (dbbpy)Pt(bdt) obtained with a 550 nm pump pulse is shown in Figure 3.3. The spectrum depicted in Figure 3.4 shows the various peak positions observed in the transient absorption spectra. The TA spectra for Pt(dbbpy)(bdt) are marked by a broad transient absorption (Excited- State Absorption) signal starting from 515 nm and extending to the blue region of the spectrum. Pt(dbbpy)(bdt) is characterized by a ground-state (GS) bleach between 515 to 600 nm. Additional transient absorption features are observed at wavelengths greater than 600 nm. The kinetic emission spectrum of (dbbpy)Pt(bdt) is depicted in Figure 3.5. The spectrum decays monoexponentially between 0-1500 ns and then remain static. The emission feature is observed in spectral regions with no ground state absorption or fluorescence. The change in optical density is positive and the emission is

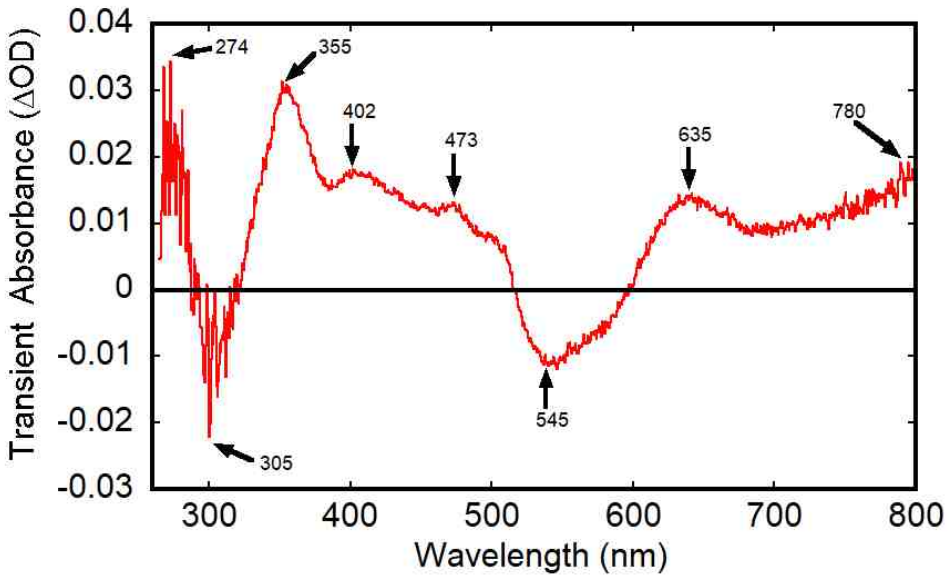

Figure 3.4: Transient Absorption (TA) difference spectra for Pt(dbbpy)(bdt) obtained in degassed CH_2Cl_2 fluid solution following excitation with 550 nm, pump: 5 mJ/pulse at the MMLL'CT absorption maximum, recorded at 0 ns time gate delay.

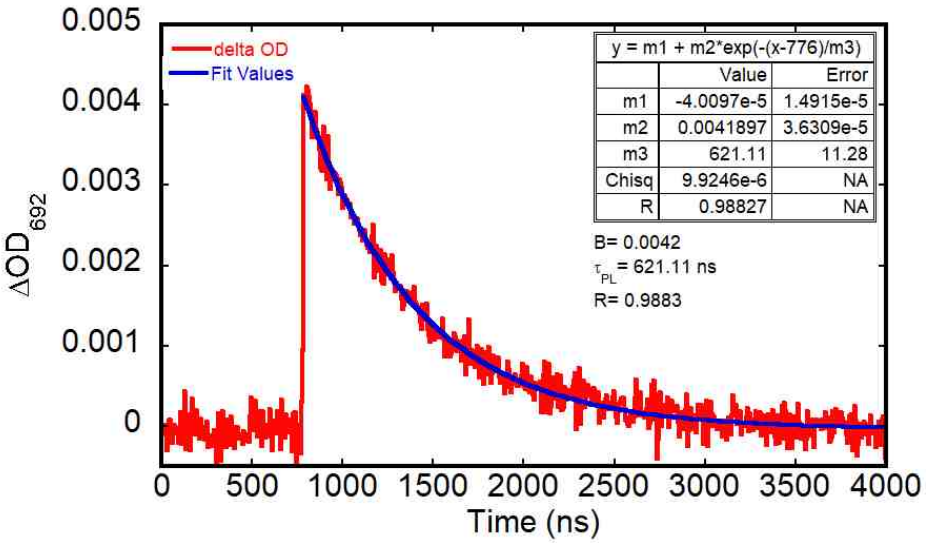

Figure 3.5: Kinetic emission trace (red) and fit (blue) for Pt(dbbpy)(bdt) in degassed CH_2Cl_2 at 692 nm excited at 550 nm.

assigned as a $T_1 \rightarrow S_0$ phosphorescence decay to the ground state. The kinetic emission trace for Pt(dbbpy)(bdt) in degassed fluid CH_2Cl_2 solution at ambient temperature is depicted in Figure 3.5. The trace was monitored at 692 nm and excited at 550 nm. The overall photoluminescence profile decays with a lifetime (τ_{PL}) of 621 ± 10 ns which is ascribed to the regeneration of the ground state after decay from the triplet MMLL'CT excited state. The kinetic absorption trace for Pt(dbbpy)(bdt) depicted in Figure 3.6 was obtained by monitoring the transient absorbance at 473 nm. The overall transient absorption profile decays with a lifetime (τ_{TA}) of 614 ± 10 ns, in good agreement with the photoluminescence lifetime results. This strongly suggests that non-radiative processes dominate the

ground sate recovery in solution at room temperature as observed by Eisenberg and coworkers.[2,51-53]

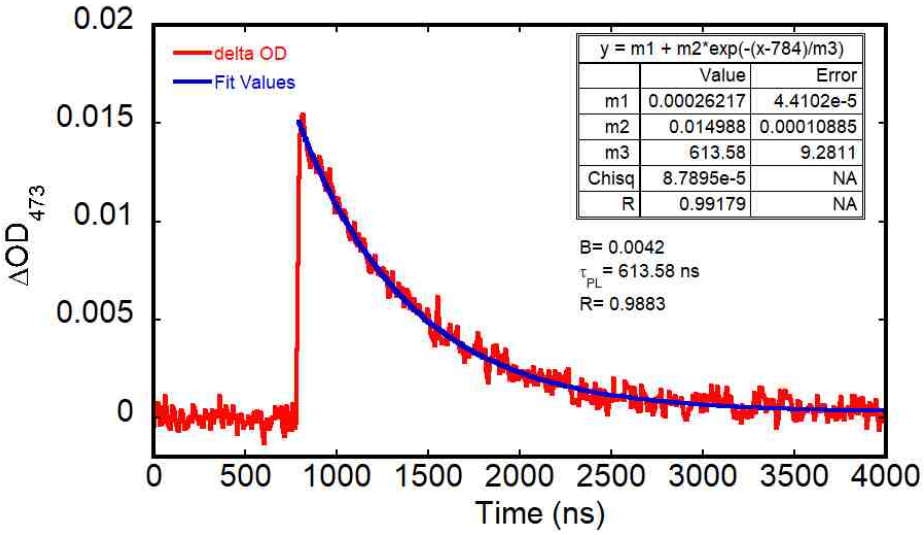

Figure 3.6: Kinetic absorption trace (red) and fit (blue) for Pt(dbbpy)(bdt) in degassed CH_2Cl_2 at 473 nm excited at 550 nm.

3.2.2 [Pt(dbbpy)(bds)]

3.2.2.1 Electronic Absorption Spectroscopy

The electronic absorption spectrum for Pt(dbbpy)(bds) was collected in dichloromethane solution at ambient temperature and is shown in Figure 3.7. The low-energy charge transfer (CT) absorption maximum is observed at 18080 cm^{-1} (553 nm) with a molar extinction coefficient of 9040 $M^{-1}cm^{-1}$. The absorption maximum is shown only for the lowest-energy band, but other absorption features occur at higher energies. The CT band is assigned as a MMLL'CT

(bds/Pt → diimine) absorption band in analogy with Pt(dbbpy)(bdt). The MMLL'CT absorption band maximum (λ_{max}^{Abs}) for Pt(dbbpy)(bds) is red shifted

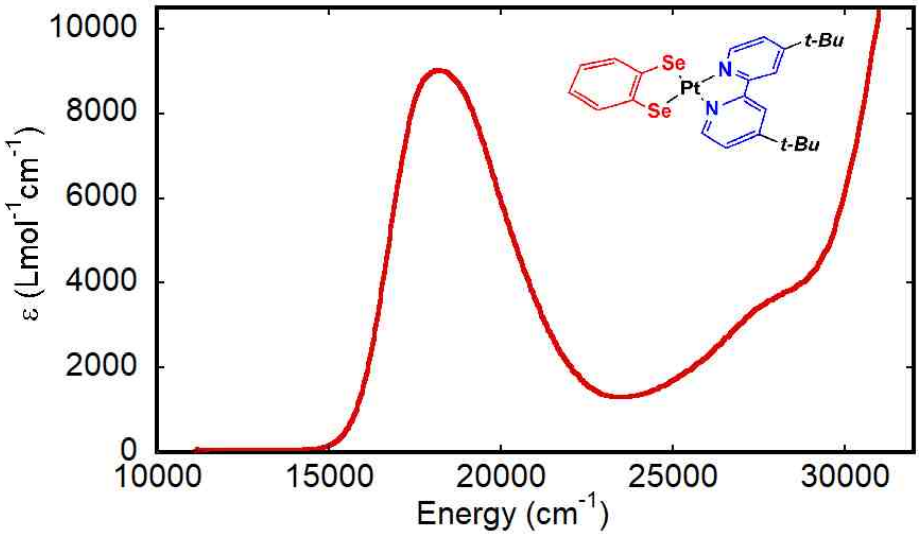

Figure 3.7: Absorption spectrum of Pt(dbbpy)(bds) in CH_2Cl_2. Inset: Compound structure.

(lower energy) compared to the MMLL'CT absorption band maximum of Pt(dbbpy)(bdt) (i.e. 545 nm).

3.2.2.2 Transient Absorption Spectra, Emission Spectra, and Excited State Lifetimes

The Pt(dbbpy)(bds) compound is emissive in fluid solution at ambient temperature upon excitation into the lowest energy absorption band. The 298 K emission spectrum of Pt(dbbpy)(bds) was collected in deoxygenated dichloromethane solution and is shown in Figure 3.8. The emission band is featureless and is observed at 702 nm (14250 cm^{-1}), yielding a Stokes shifts of 3830 cm^{-1}. The transient absorption (TA) difference spectra of Pt(dbbpy)(bds)

were collected in degassed dichloromethane solution using a 570 nm pump

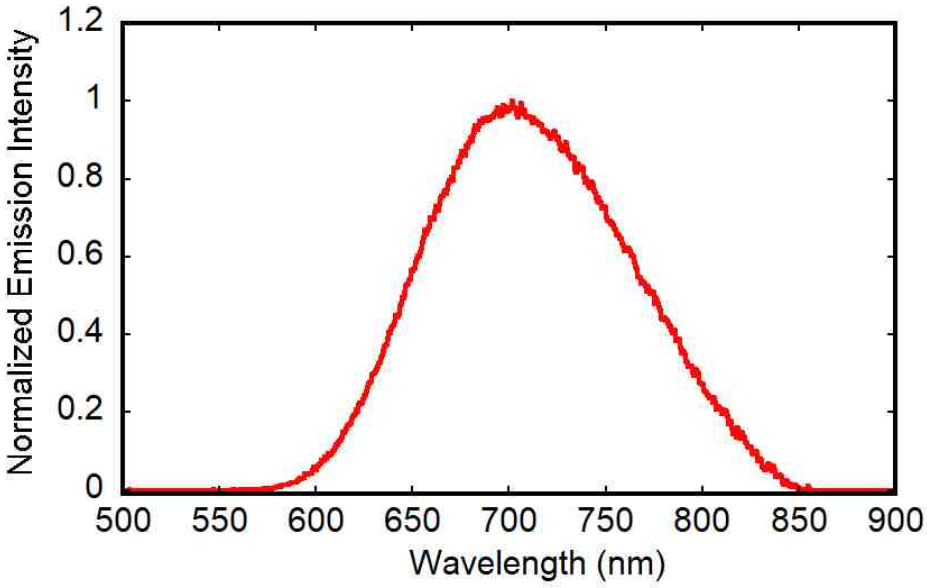

Figure 3.8: Emission spectrum for Pt(dbbpy)(bds) in degassed CH_2Cl_2 solution at 298 K, excited at 570 nm.

pulse with time delays that extend to 250 ns after the pump pulse. Following excitation at 570 nm, the observed transient absorption spectra for Pt(dbbpy)(bds) possess broad transient absorption (Excited-State Absorption) features between 300 – 510 nm and 600 – 800 nm with a ground-state (GS) bleach observed in the 510 - 600 nm region where the ground state MMLL'CT absorption occurs. The spectrum shown in Figure 3.10 highlights the band positions for the various peaks. The kinetic emission trace for Pt(dbbpy)(bds) was monitored at 709 nm and excited at 555 nm, and the data is shown in Figure 3.11. The blue line is the best fit to the kinetic emission trace and correspond to a biexponential decay. A Marquardt- Levenberg algorithm was used to fit this model to the data. From Figure 3.11, the pre-exponential factors (B), which

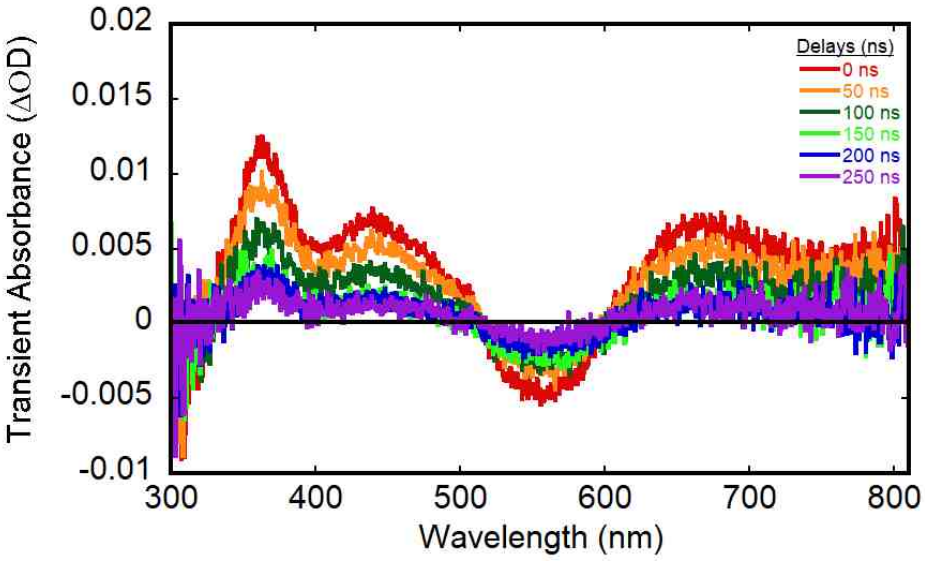

Figure 3.9: Transient Absorption (TA) difference spectra for Pt(dbbpy)(bds) obtained in aerated CH_2Cl_2 fluid solution following 570 nm excitation, pump: 5 mJ/pulse at the MMLL'CT absorption maximum, recorded at 0, 50, 100, 150, 200, and 250 ns time delays.

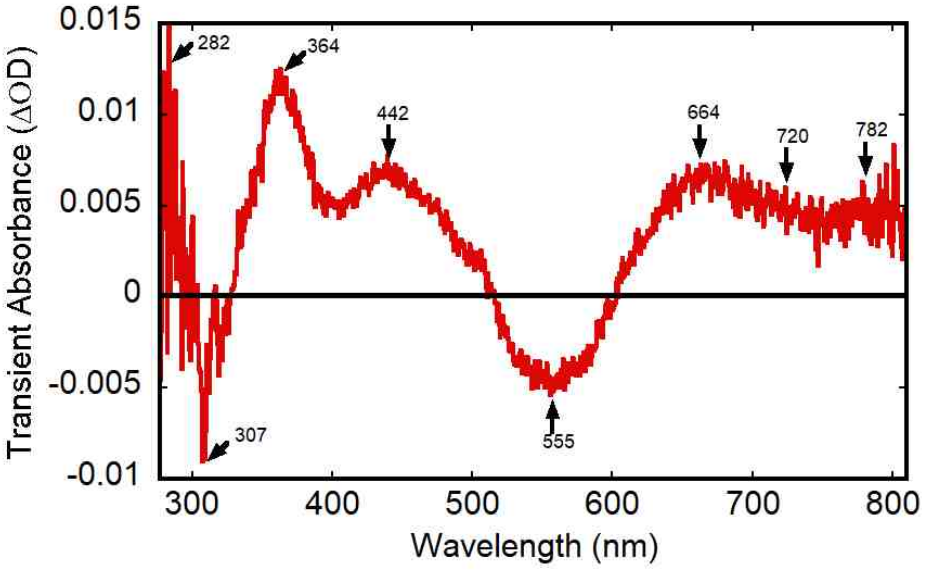

Figure 3.10: Transient Absorption (TA) difference spectra for Pt(dbbpy)(bds) obtained in degassed CH_2Cl_2 fluid solution following excitation with 570 nm, pump: 5 mJ/pulse at the MMLL'CT absorption maximum, recorded at 0 ns time gate delay.

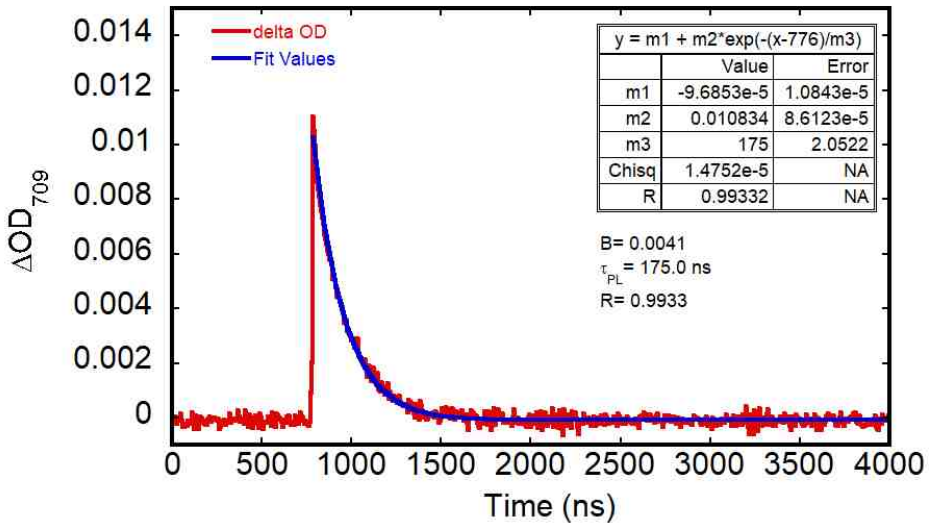

Figure 3.11: Kinetic emission trace (red) and fit(blue) for Pt(dbbpy)(bds) in degassed CH_2Cl_2 at 709 nm excited at 555 nm.

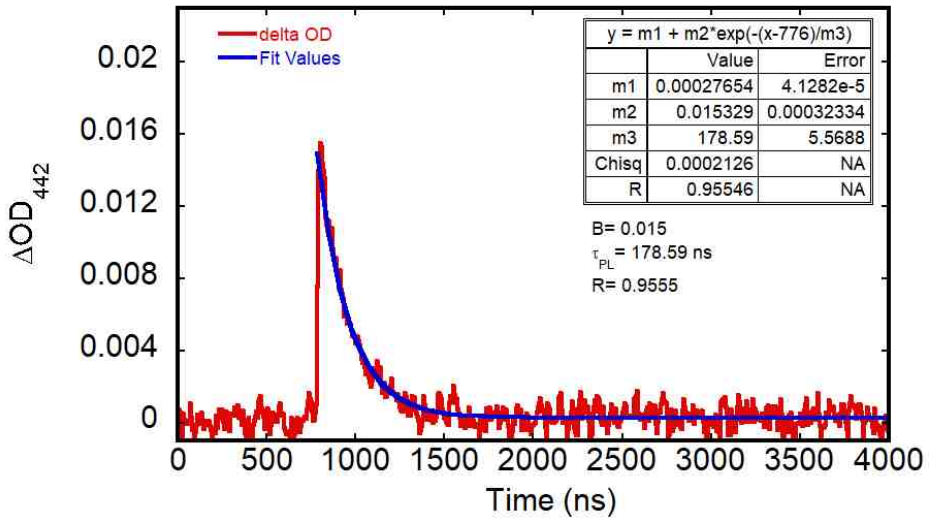

Figure 3.12: Kinetic absorption trace (red) and fit (blue) for Pt(dbbpy)(bds) in degassed CH_2Cl_2 at 442 nm excited at 570 nm.

represent the amplitude of the curve under study at time zero, is 0.0041. The positive value of B signifies a decay process. For growth processes, the pre-exponential value is always negative. The kinetic emission lifetime (τ_{PL}) for Pt(dbbpy)(bds) under these conditions is 175 ± 2 ns. An additional kinetic absorption trace for Pt(dbbpy)(bds) in degassed CH_2Cl_2 is shown in Figure 3.12. Here, the transient absorbance was monitored at 442 nm and excited at 570 nm. The overall transient absorption profile decays with a lifetime (τ_{TA}) of 179 ± 6 ns, in complete agreement with kinetic emission trace at 709 nm.

3.2.2.3 X-ray Crystallography

Pt(dbbpy)(bds)

The crystal structure of 4,4'-di-tert-butyl-2,2'-bipyridineplatinum(II)(benzenedise-

lenolate), Pt(dbbpy)(bds), was performed at the UNM X-ray Laboratory. A red rod-like specimen of $C_{24}H_{28}N_2PtSe_2$, approximate dimensions 0.106 mm x 0.141 mm x 0.199 mm, was coated with Paratone oil and mounted on a MiTiGen support that had been previously attached to a metallic pin using epoxy for the X-ray crystallographic analysis. The X-ray intensity data were measured on a Bruker Kappa APEX II CCD system equipped with a graphite monochromator and a Mo Kα fine-focus tube (λ = 0.71073 Å). The frames were integrated with the Bruker SAINT software package using a narrow-frame algorithm. The final

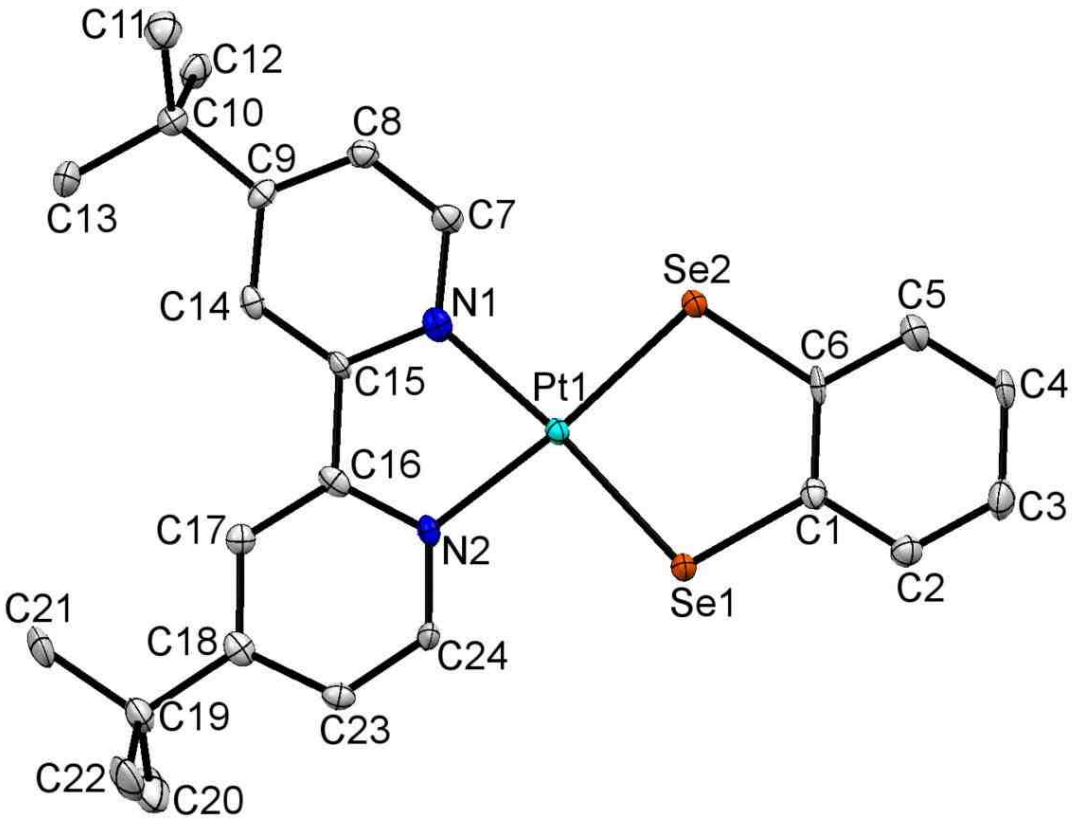

Figure 3.13: Crystal structure of (dbbpy)Pt(bds).

cell constants of a = 15.2900(7) Å, b = 11.5607(6) Å, c = 13.5519(7) Å, β = 103.904(3)°, volume = 2325.3(2) $Å^3$, are based upon the refinement of the XYZ-centroids of reflections above 20 σ(I). Data were corrected for absorption effects using the multi-scan method (SADABS). The calculated minimum and maximum transmission coefficients (based on crystal size) are 0.2620 and 0.4430 respectively.

The structure was solved and refined with the Bruker SHELXTL Software Package, using the space group P 1 21/c 1, with Z = 4 for the formula unit, $C_{24}H_{28}N_2PtSe_2$. Non-hydrogen atoms were refined anisotropically. Hydrogen

atoms were placed in geometrically calculated positions with U_{iso} = 1.2U_{equiv} of the parent atom (U_{iso} = 1.5U_{equiv} for methyl groups). The final anisotropic full-matrix least-squares refinement on F^2 with 268 variables converged at R1 = 3.77% for the observed data and wR2 = 8.31% for all data. The goodness-of-fit was 1.073. The largest peak in the final difference electron density synthesis was 1.806 $e^-/Å^3$ and the largest hole was -1.641 $e^-/Å^3$ with an RMS deviation of 0.210 $e^-/Å^3$. Based on the final model, the calculated density was 1.992 g/cm^3.

Pt(bpy)(bSSe) and Pt(bpy)(bSeO$_2$)

A red plate-like specimen of $C_{16}H_{12}N_2PtSSe$ and $C_{16}H_{12}N_2O_{1.50}PtSSe$, was cut to the approximate dimensions 0.059 mm x 0.145 mm x 0.152 mm, coated with Paratone oil and mounted on a CryoLoop that had been previously attached to a metallic pin using epoxy for the X-ray crystallographic analysis. The X-ray intensity data were measured on an APEX II CCD system equipped with a

graphite monochromator and a Mo Kα sealed tube (λ = 0.71073 Å). The frames were integrated with the Bruker SAINT software package using a narrow frame algorithm. The integration of the data using a monoclinic unit cell yielded a total of 12285 reflections to a maximum θ angle of 26.36° (0.80 Å resolution), of which 3080 were independent (average redundancy 3.989, completeness = 99.7%, R_{int} = 7.20%, R_{sig} = 6.34%) and 2126 (69.03%) were greater than $2\sigma(F^2)$. The final cell constants of a = 8.0461(16) Å, b = 14.472(3) Å, c = 13.353(3) Å, β = 102.472(12)°, volume = 1518.2(6) $Å^3$, are based upon the refinement of the XYZ-centroids of reflections above 20 σ(I). The calculated minimum and maximum

transmission coefficients (based on crystal size) are 0.2675 and 0.5432 respectively.

The structure was solved and refined using the Bruker SHELXTL Software Package, using the space group P 1 21/c 1, with Z = 4 for the formula unit, $C_{16}H_{12}N_2PtSSe$. Non-hydrogen atoms were refined anisotropically. Hydrogen atoms were placed in geometrically calculated positions with U_{iso} = 1.2U_{equiv} of the parent atom. The final anisotropic full-matrix least-squares refinement on F^2 with 220 variables converged at R1 = 3.57%, for the observed data and wR2 = 8.83% for all data. The goodness-of-fit was 0.998. The largest peak in the final difference electron density synthesis was 1.830 $e^-/Å^3$ and the largest hole was -1.843 $e^-/Å^3$ with an RMS deviation of 0.259 $e^-/Å^3$. On the basis of the final model, the calculated density was 2.461 g/cm^3. The disorder in the Se/S atoms was modeled as a 75/25 mixture of $SeSO_2$/SSe with distance constraints applied to the Pt-S, Pt-Se, Se-C and S-C distances.

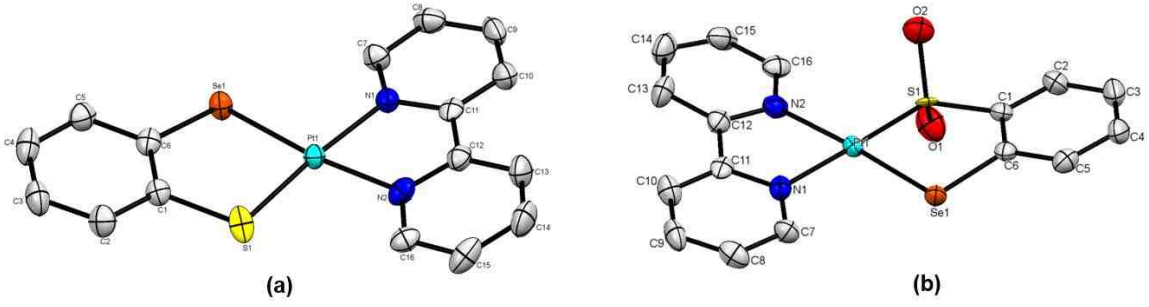

Figure 3.14: Crystal structure of (bpy)Pt(bds) and (bpy)Pt(b $bSeSO_2$).

Results

Molecular Crystal Structure

The X-ray crystal structures of (dbbpy)Pt(bds), and (bpy)Pt(bSeS)/(bpy)Pt(bSeSO$_2$) are depicted in Figure 3.12 and Figure 3.14 respectively. A red rod-like specimen of (dbbpy)Pt(bds) with an approximate dimensions 0.106 mm x 0.141 mm x 0.199 mm was obtained by room temperature evaporation of a saturated solution of dichloromethane (CH_2Cl_2), hexane, and benzene in a 1:1:1 mixture in the absence of light for several weeks. On the other hand, red plate-like crystals of (bpy)Pt(bSeS) and (bpy)Pt(bSeSO$_2$) with approximate dimensions of 0.059 mm x 0.145 mm x 0.152 mm, were obtained by slow evaporation of saturated solution of dichloromethane and toluene in the air for a couple of weeks.

Table 3.0 and Table 3.1 depict the crystallographic data for Pt(dbbpy)(bds) and Pt(bpy)(bSSe)/Pt(bpy)(bSeO$_2$) respectively. For comparison, the calculated selected bond lengths (Å) from optimized structures of Pt(bpy)(bds) and Pt(bpy)(bSSe) computed from DFT using B3LYP hybrid functional and LANL2DX basis set have been included in Table 3.0 and Table 3.1 respectively. Tables 3.0 and 3.1 also illustrate the selected bond lengths (Å) of (dbbpy)Pt(bds) and Pt(bpy)(bSSe)/Pt(bpy)(bSeO$_2$) respectively from single crystal X-ray analysis. Figure 3.14 and Figure 3.15 show an ORTEP diagram using 50% probability thermal ellipsoids for Pt(dbbpy)(bds) and (dbbpy)Pt(bSeSO$_2$) respectively. These plots display the key bond lengths around the central Pt ion and the numbering

Table 3.0: X-ray Crystallographic Data for (dbbpy)Pt(bds).

Crystallographic Data	(dbbpy)Pt(bds)
empirical formula	$C_{24}H_{28}N_2PtSe_2$
fw, $gmol^{-1}$	697.49
crystal system	monoclinic
crystal habit	red rod
space group	P 1 21/c 1
a, Å	15.290(7)
b, Å	11.561(6)
c, Å	13.552(7)
α, deg	90
β, deg	103.90(3)
γ, deg	90
V, $Å^3$	2325.3(2)
Z	4
T, K	100(2)
R1[a]	0.0377
wR2[a]	0.0790
GOF *(F^2)*[a]	1.073

[a] R1 = $\sum ||F_0 - |F_c||/\sum |F_0|$ (55926 reflections collected, $I > 2\sigma(I)$);

wR2 =$[\sum[w|F_0^2 - F_c^2|^2]/w(F_0^2)^2]^{½}$; GOF = $[\sum[w|F_0^2 - F_c^2|^2]/(n-p)]^{½}$, where n and p represent the number of data and number of parameters refined respectively.

scheme of all the non-hydrogen atoms present in the complex. The platinum (Pt) metal at the center of these two complexes possesses a square planar geometry with both structures having similar torsional deformation.

Table 3.1: X-ray Crystallographic Data for (bpy)Pt(bSSe) and (bpy)Pt(bSeSO$_2$).

Crystallographic Data	**(bpy)Pt(bSSe)**	**(bpy)Pt(bSeSO$_2$)**
empirical formula	**$C_{16}H_{12}N_2PtSSe$**	**$C_{16}H_{12}N_2O_{1.50}PtSSe$**
fw, gmol^{-1}	538.39	562.39
crystal system	monoclinic	monoclinic
crystal habit	red plate	red plate
space group	P 1 21/c 1	P2(1)/c
a, Å	8.046(16)	8.046(16)
b, Å	14.472(3)	14.472(3)
c, Å	13.353(3)	13.353(3)
α, deg	90	90
β, deg	102.47(12)	102.47(12)
γ, deg	90	90
V, Å^3	1518.2(6)	1518.2(6)
Z	4	4
T, K	173(2)	173(2)
R1[a]	0.0357	0.0357
wR2[a]	0.0743	0.0743
GOF *(F^2)*[a]	0.998	0.998

[a] R1 = $\sum||F_0 - |F_c||/\sum|F_0|$ (55926 reflections collected, $I > 2\sigma(I)$); wR2 =$[\sum[w|F_0^2 - F_c^2|^2]/w(F_0^2)^2]^{½}$; GOF = $[\sum[w|F_0^2 - F_c^2|^2]/(n-p)]^{½}$, where n and p represent the number of data and number of parameters refined respectively.

As shown in Figure 3.16, all the three structures display an upward bend in the molecule about dichalogenolene donor atoms. The upward bending of these structures is absent in the DFT geometry optimized structures because this

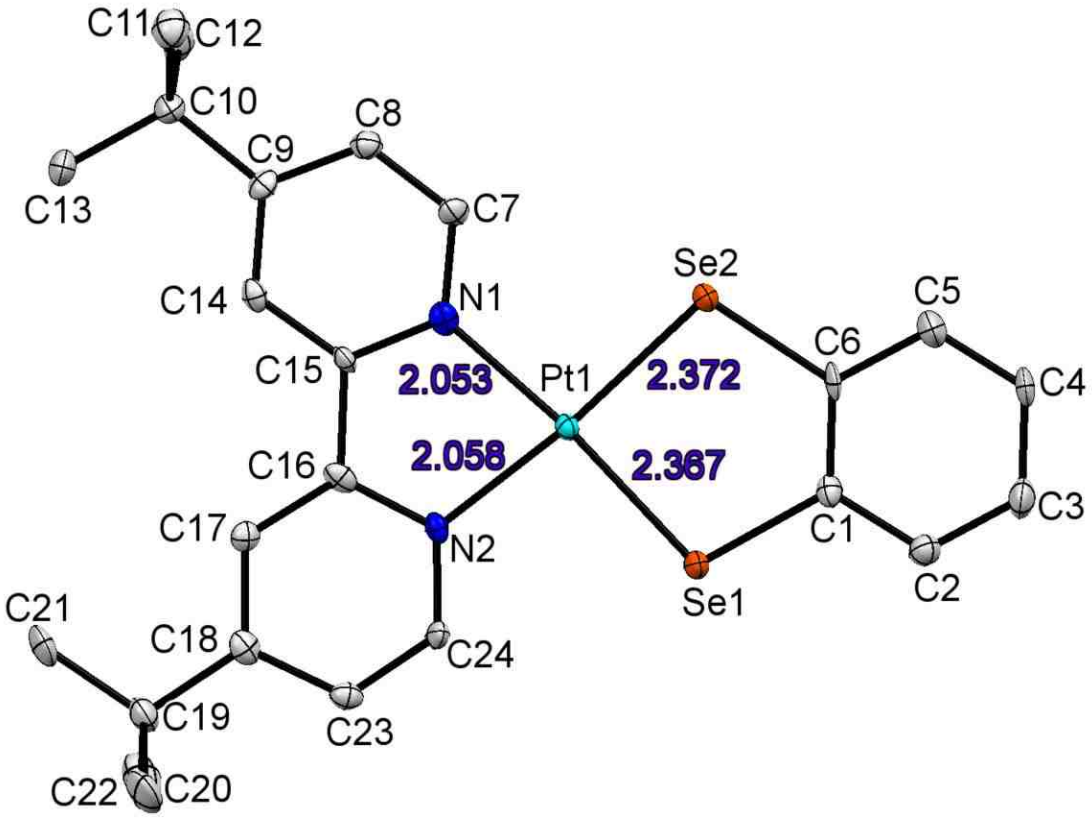

Figure 3.15: Crystal structure and atomic numbering system (ORTEP diagram) for (dbbpy)Pt(bds). Thermal ellipsoids are at 50% probability level.

observation is due to crystal packing effect. The upward bending effect is more intense in (a), Pt(bpy)(bSSe) and (b), Pt(bpy)($bSeO_2$) than in (c), (dbbpy)Pt(bds). Pt(II) ion in Figures 3.12 and 3.13 depict slightly distorted square planar geometry with the four coordination sites been occupied by two nitrogen atoms from 4,4'-di-tert-butyl-2,2'-bipyridine (dbbpy) or 2,2'-bipyridine (bpy), two selenium atoms in Pt(dbbpy)(bds), a sulfur and selenium atom in Pt(bpy)(bSSe)/ Pt(bpy)(bSSe). The selected bond lengths and bond angles for Pt(dbbpy)(bds),

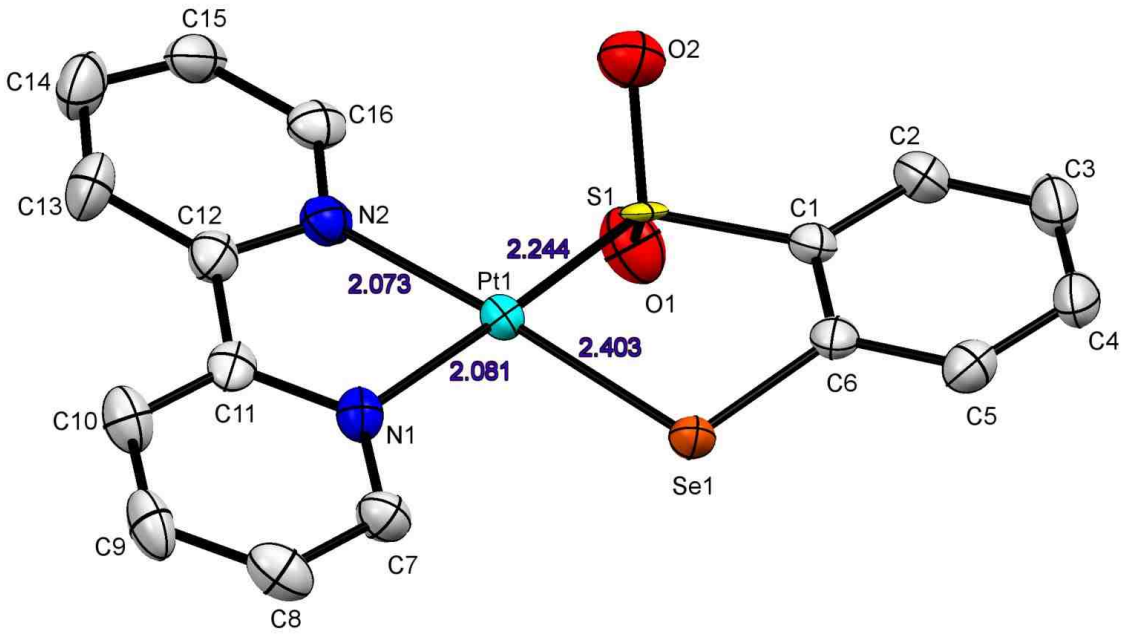

Figure 3.16: Crystal structure and atomic numbering system (ORTEP diagram) for (bpy)Pt(bSeSO$_2$). Thermal ellipsoids are at 50% probability level.

and (bpy)(bSeS)/ Pt(bpy)(bSeSO$_2$) are presented in Table 3.2 and Table 3.3 respectively. The dbbpy/bpy chelate results in a N1-Pt-N2 bond angles of 79.1(19) and 79.1(3)^0 for Pt(dbbpy)(bds), and (bpy)(bSeS)/ Pt(bpy)(bSeSO$_2$) depicted in Figure 3.17 and Figure 3.18 respectively. These values deviate significantly from the ideal square planar geometry of 90^0. Based on the asymmetric unit cells of the two complexes, Pt(dbbpy)(bds), and (bpy)(bSeS)/ Pt(bpy)(bSeSO$_2$), each is made of one crystallographically independent molecule which is comprised of one Pt(II) atom, one dbbpy/ bpy ligand, and one molecule of benzenediselenolate or 2-selenylbenzenethiolate for (dbbpy)Pt(bds) and (bpy)(bSeS) respectively. Molecular crystal π stacking was not present in these complexes, even though Pt(II) complexes are known to under intermolecular π

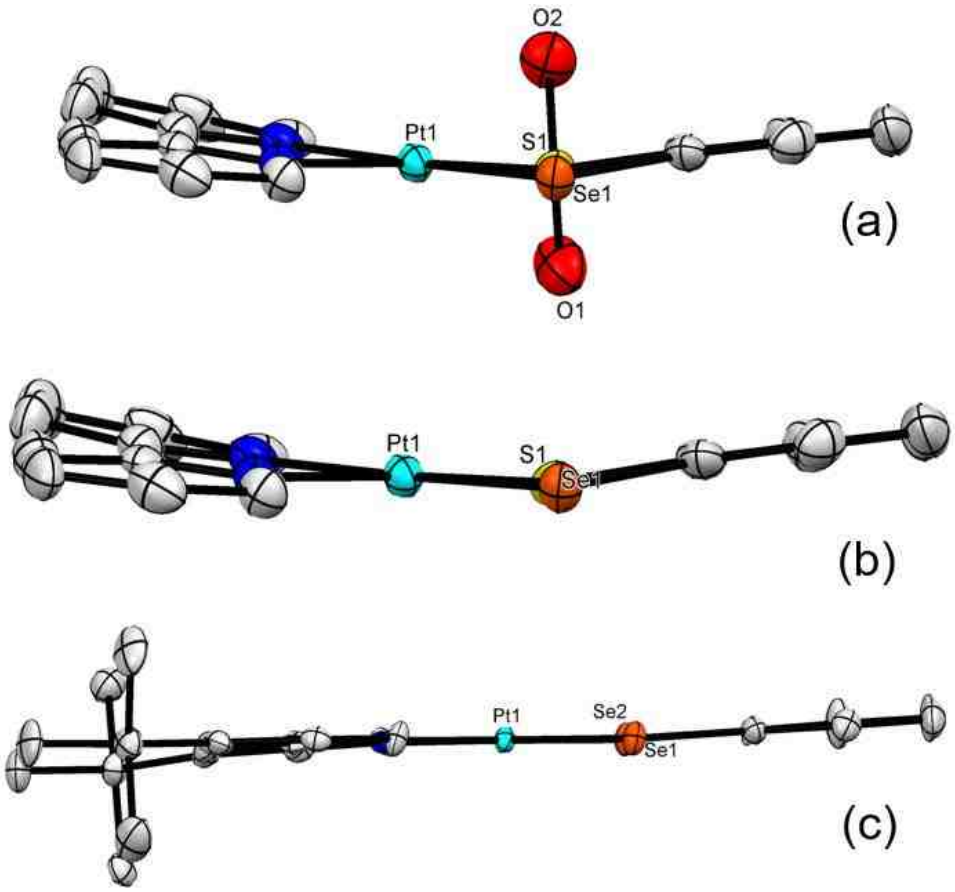

Figure 3.17: ORTEP diagram of (a) Pt(bpy)(bSeSO$_2$), (b) Pt(bpy)(bSeS), (c) Pt(dbbpy)(bds) displaying the upward bend in the molecule about the dichalogenolene donor atoms. H atoms are omitted for clarity.

stacking with a Pt-Pt distance of 3.24 Å and π-π distance of 3.51 Å. No Pt—Pt interactions were observed in the crystal packing of these complexes. The average Pt—Pt distances for (dbbpy)Pt(bds) and (bpy)(bSeS)/ Pt(bpy)(bSeSO$_2$) are 8.74 and 9.11 Å, as depicted in depicted in Figure 3.20 and Figure 3.21 respectively. Hence the Pt—Pt distances in these structures are too long to experience any type of molecular crystal stacking. This π-π molecular stacking was also not observed in (dbbpy)Pt(bds) due to the bulky substituents on the acceptor ligand. Shown in Table 3.2 are the X-ray crystallography bond lengths

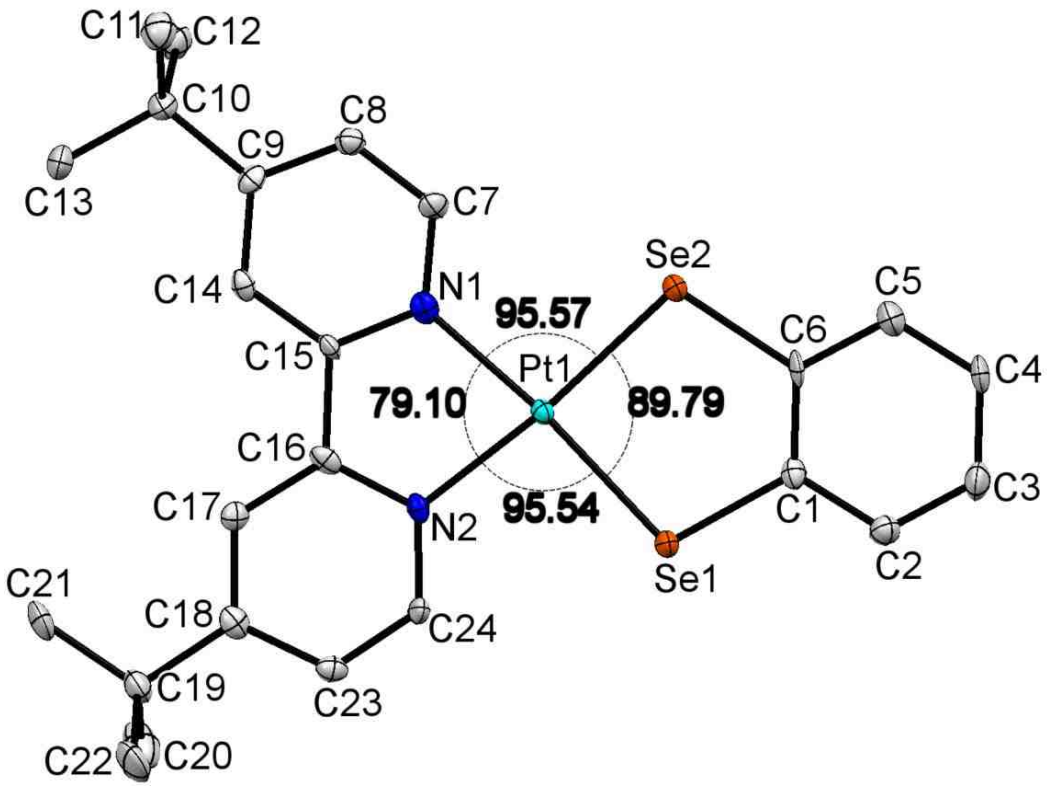

Figure 3.18: Crystal structure and atomic numbering system (ORTEP diagram) for (dbbpy)Pt(bds) showing selected key bond angles.

for Pt(dbbpy) (bds). The Pt-N1, Pt-N2, Pt-Se1, and Pt-Se2 bond lengths for Pt(dbbpy)(bds) are 2.053(5), 2.058(5), 2.367(6) and 2.372(6) Å, respectively. The experimental bond lengths values compare well with the calculated values of 2.094, 2.094, 2.397 and 2.397 Å, respectively, which are slightly longer. The calculated bond length values were obtained from DFT geometry optimized structures of (dbbpy)Pt(bds) and (bpy)Pt(bSSe). The experimental bond length values for the Pt-N bonds are in the range of bonds lengths common to other Pt(diimine)(dithiolate) complexes[2] and Pt(diimine)(diselenolate)[6]. The Pt-N bond lengths in Pt(bpy)(bds) are 2.065(8) and 2.049(7) Å, these values compare well with the Pt-N bond lengths found in Pt(dbbpy)(bds). The Pt-Se bond distances in

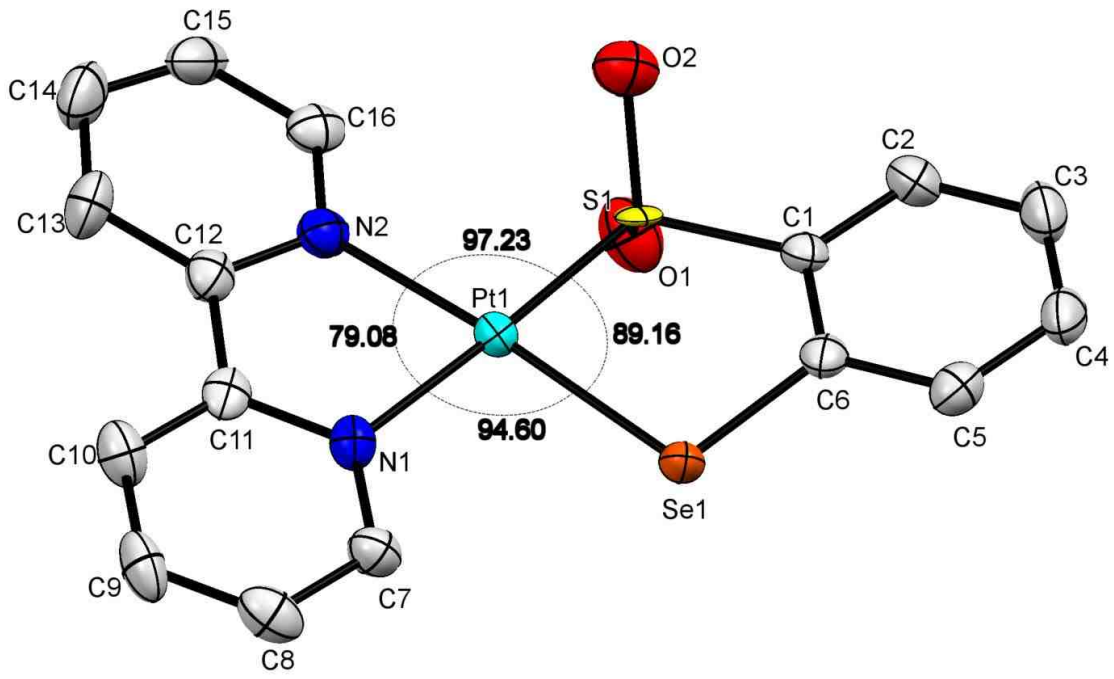

Figure 3.19: Crystal structure and atomic numbering system (ORTEP diagram) for (bpy)Pt(bSeSO$_2$) showing selected key bond angles.

Pt(bpy)(bds) are 2.3740(10) and 2.3701(10) Å. These bond distances are very similar to those obtained for Pt(dbbpy)(bds). Pt(bpy)(bSSe) and Pt(bpy)(bSeSO$_2$) Pt-N bond lengths are in the range of bond lengths common to Pt(diimine)(dithiolate) complexes[2,3] and Pt(diimine)(diselenolate)[54] complexes. The Pt-Se bond length (2.403 Å) is much greater than the Pt-S bond distance (2.245 Å), consistent with selenium having a larger atomic radius than the sulfur atom. The Pt-Se bond is approximately 0.16 Å longer than the Pt-S bond distance depicted in Figure 3.15. Nonetheless, the concomitant increment in the C-Se bond compared to C-S bond lengths leaves the bite angle (e.g. E1-Pt-E2) relatively unaltered: 89.0(1)^0 for Pt(bpy)(bdt)[6], 89.2(2)^0 for Pt(bpy)(bSSe), and 89.8(2)^0 Pt(dbbpy)(bds), where E1=E2=S for bdt, E1=S, E2=Se for bSSe, and E1=E2=Se

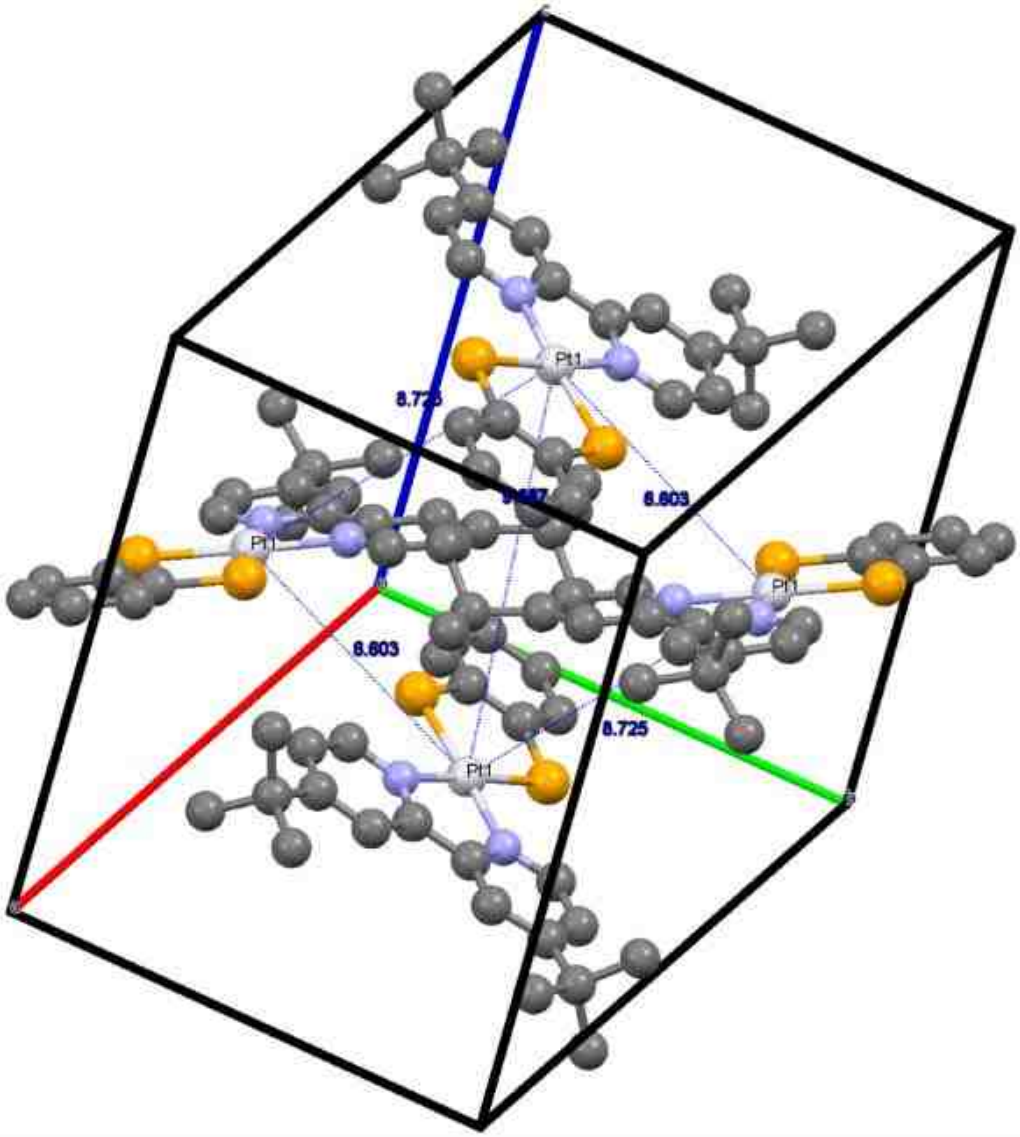

Figure 3.20: Pt(dbbpy)(bds) crystal packing arrangement.

bds. The N-Pt-N bond angles for Pt(dbbpy)(bds) and Pt(dbbpy)(bSSe) are 79.1(19) and 79.1(3)^0, which compare very well with the calculated values of 78.0 and 78.1^0 respectively. The experimental N-Pt-N bond angles are markedly less than the idealized value of 90^0 for a perfect square planar geometry. The experimental Se-Pt-Se and Se-Pt-S bond angles are 89.8(2) and 89.2(3)^0,

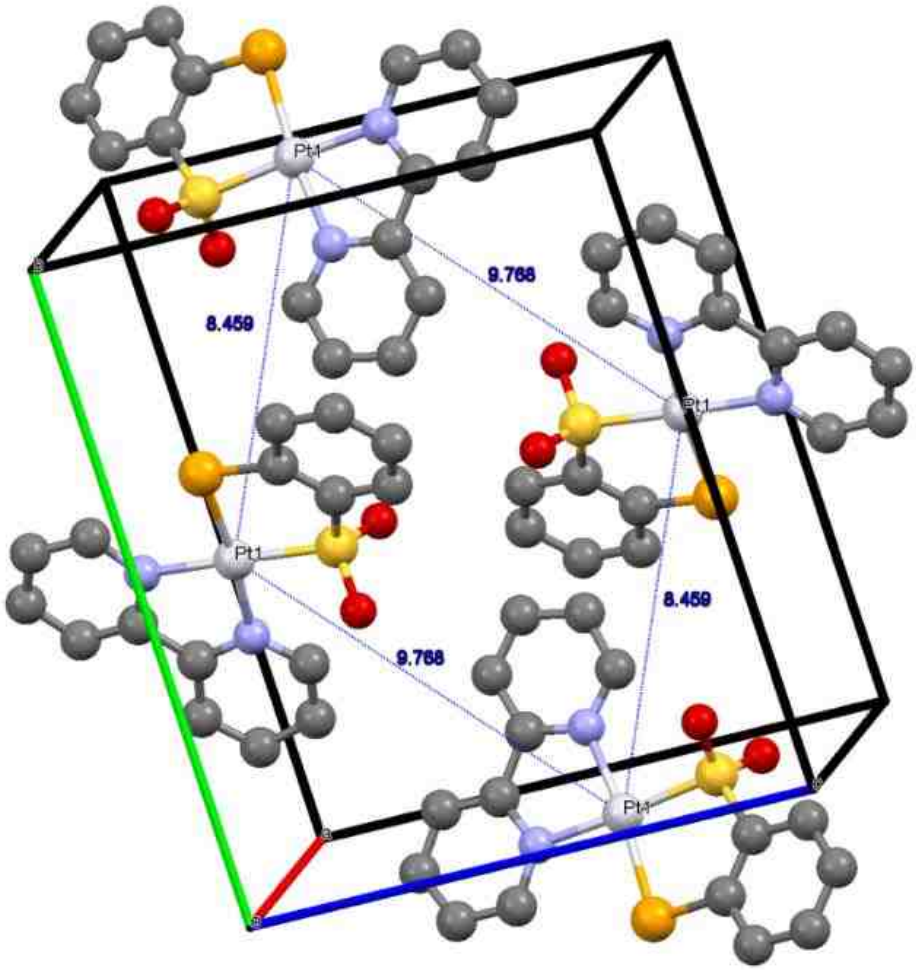

Figure 3.21: Pt(dbbpy)(bSeSO$_2$) crystal packing arrangement.

Table 3.2: Comparison of calculated selected bond lengths (Å) with experimental values from X-ray analysis for (dbbpy)Pt(bds).

	Experimental	**Calculated**
Pt1-N1	2.053(5)	2.094
Pt1-N2	2.058(5)	2.094
Pt1-Se1	2.367(6)	2.397
Pt1-Se2	2.372(6)	2.397

N1-C15	1.343(7)	1.359
N1-C7	1.344(7)	1.344
N2-C24	1.342(7)	1.344
N2-C16	1.359(8)	1.359
Se1-C1	1.907(6)	1.911
Se2-C6	1.909(6)	1.911
C1-C6	1.370(8)	1.393
C15-C16	1.479(8)	1.463
C1-C2	1.403(8)	1.398
C5-C6	1.404(9)	1.398

Table 3.3: Comparison of Calculated Selected Bond Lengths (Å) with experimental values from X-ray analysis for (bpy)Pt(bSSe) and (bpy)Pt(bSeSO$_2$).

	Experimental	**Calculated**
Pt1-N1	2.081(7)	2.083
Pt1-N2	2.072(7)	2.092
Pt1-S1	2.245(11)	2.273
Pt1-Se1	2.403(2)	2.396
N1-C11	1.354(10)	1.360
N1-C7	1.333(11)	1.345
N2-C12	1.373(10)	1.358
N2-C16	1.344(11)	1.343
S1-C1	1.785(12)	1.758

Se1-C6	1.895(8)	1.909
C1-C6	1.379(11)	1.396
C11-C12	1.454(12)	1.462
C1-C2	1.414(11)	1.402
C5-C6	1.426(11)	1.400
S1-O1	1.363(16)	1.442(5)[a]
S1-O2	1.535(12)	1.460(5)[a]

[a] Bond lengths obtained from Pt(bpy)(bdtO_2) [7]

respectively, and 88.8 and 88.5^0 for the calculated angles. The experimental bond angles agree well with the calculated angles for the two complexes. The key bond angles around the central platinum atom in Pt(bpy)(bSSe) are 79.1(3), 97.2(3), 94.6(2), and 89.2(3)^0 for N2-Pt1-N1, N2-Pt1-S1, N1-Pt1-Se1, and S1-Pt1-Se1 respectively. These bond angles deviate significantly from those anticipated for a perfect square planar geometry. The upward bending due to crystal packing effect is consistent with the deviation from the perfect square planar angle of 90^0.

On the other hand, the key bond angles recorded around the central platinum atom in (dbbpy)Pt(bds) are 79.1(19), 95.6(14), 95.6(13), and 89.8(2), respectively, for N2-Pt1-N1, N2-Pt1-Se1, N1-Pt1-Se2 and Se1-Pt1-Se2. The dihedral angle between the N1-Pt-N2 and Se1-Pt-Se2 planes is 0.37^0 for Pt(dbbpy)(bds), while that of Pt(bpy)(bSSe) is 3.30^0 for N1-Pt-N2 and S1-Pt-Se1 planes. The large difference in dihedral angles between these two complexes is a direct consequence of an increase in the upward bending effect observed in

Pt(bpy)(bSSe) depicted in figure Figure 3.17.

3.2.3 [Pt(dbbpy)(bSO)]

3.2.3.1 Electronic Absorption Spectroscopy (EAS)

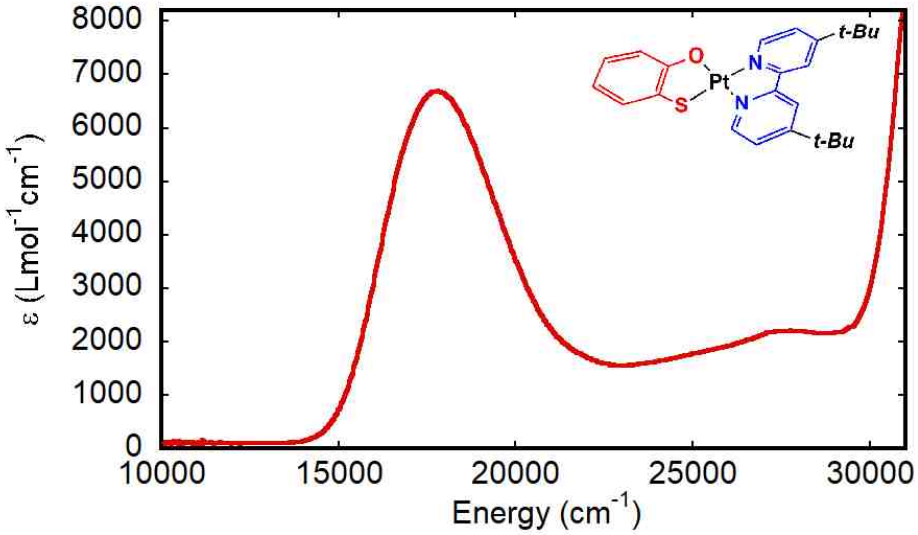

Figure 3.22: Absorption spectrum of Pt(dbbpy)(bSO) in CH_2Cl_2. Inset: Compound structure.

The electronic absorption spectrum for Pt(dbbpy)(bSO) is depicted in Figure 3.21, and the data was collected in dichloromethane (CH_2Cl_2) at ambient temperature. The MMLL'CT absorption maximum (λ_{max}^{Abs}) was observed at 17800 cm^{-1} with a molar extinction coefficient of 6700 $M^{-1}cm^{-1}$. The absorption maximum is shown only for the lowest-energy band, even though additional absorption features occur at higher energies. The charge-transfer-to-diimine absorption band maximum is at 563 nm.

3.2.3.2 Transient Absorption Spectra, Emission Spectra, and Lifetimes

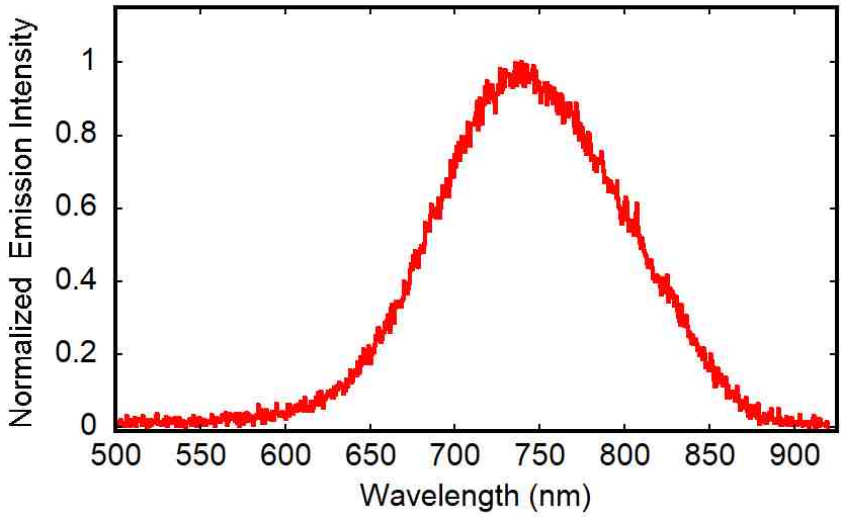

Figure 3.23: Emission spectrum for Pt(dbbpy)(bSO) in degassed CH_2Cl_2 solution at 298 K, excited at 556 nm.

The photoluminescence spectrum of Pt(dbbpy)(bSO) was measured at ambient temperature by exciting into MMLL'CT absorption band. The emission spectrum was taken in a degassed dichloromethane solution at 298 K. The emission

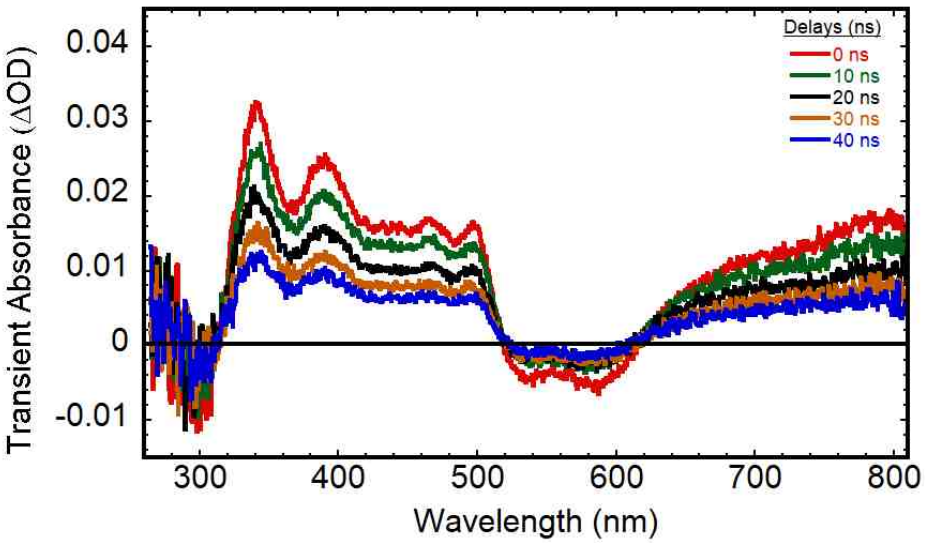

Figure 3.24: Transient Absorption (TA) difference spectra for Pt(dbbpy)(bSO) obtained in degassed CH_2Cl_2 fluid solution following 564 nm excitation, pump: 5 mJ/pulse at the MMLL'CT absorption maximum, recorded at 0, 10, 20, 30, and 40 ns time delays.

spectrum of Pt(dbbpy)(bSO) has emission maxima (λ_{max}^{Em}) at 740 nm (13510 cm^{-1}), and this is shown in Figure 3.23. The calculated stokes shift is 4250 cm^{-1}. Figure 3.24 depicts the transient absorption (TA) difference spectra for Pt(dbbpy)(bSO) in degassed dichloromethane solution obtained with a 570 nm pump pulse. After excitation at 564 nm, the TA difference spectra for Pt(dbbpy)(bSO) shows a broad transient absorption signal starting from 520 nm and extending to the blue region of the electromagnetic spectrum. The ground state depletion is observed from ~ 520 to 620 nm for Pt(dbbpy)(bSO). Additional signals are observed at wavelengths greater than 620 nm. Depicted in Figure

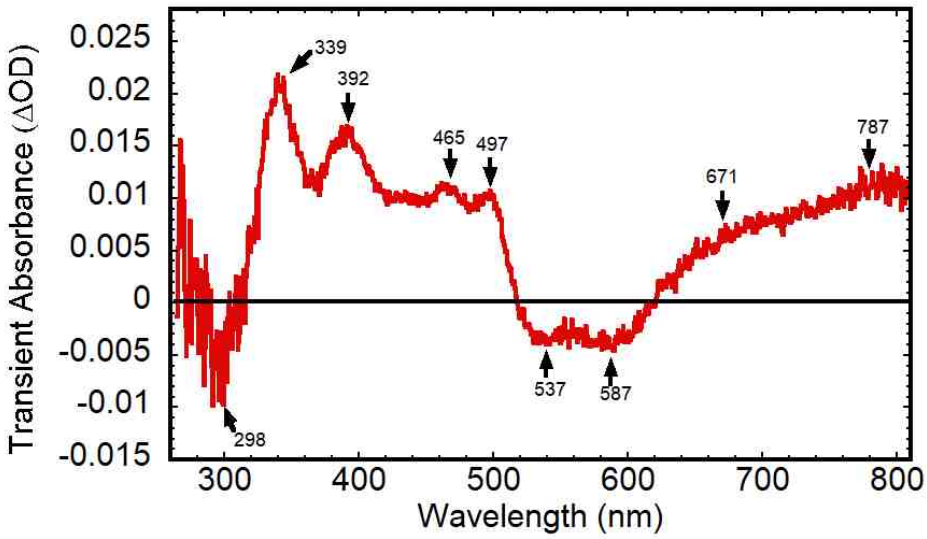

Figure 3.25: Transient Absorption (TA) difference spectra for Pt(dbbpy)(bSO) obtained in degassed CH_2Cl_2 fluid solution following excitation with 564 nm, pump: 5 mJ/pulse at the MMLL'CT absorption maximum, recorded at 0 ns time gate delay.

3.25 is the transient absorption difference spectrum recorded at 0 ns time gate delay. It clearly shows the numerous peaks used in the kinetic absorption analysis. The ground state depletion (i.e. ground-state bleach) is represented by a negative ΔOD as shown in Figure 3.25. Depicted in Figure 3.26 is the kinetic emission trace for Pt(dbbpy)(bSO). The kinetic trace was monitored at 746 nm and excited at 564 nm. The decay was observed to be very rapid and then remain static afterwards. The blue trace in Figure 3.26 depicts the best biexponential fits using a Marquardt-Levenberg algorithm. From Figure 3.26, the pre-exponential factor (B) is 0.0019 which represent a decay process. The kinetic emission lifetime (τ_{PL}) for Pt(dbbpy)(bSO) is 32 ± 3 ns. Figure 3.27 depicts the kinetic absorption trace for Pt(dbbpy)(bSO) in degassed dichloromethane solution at ambient temperature. The overall transient absorption profile decays

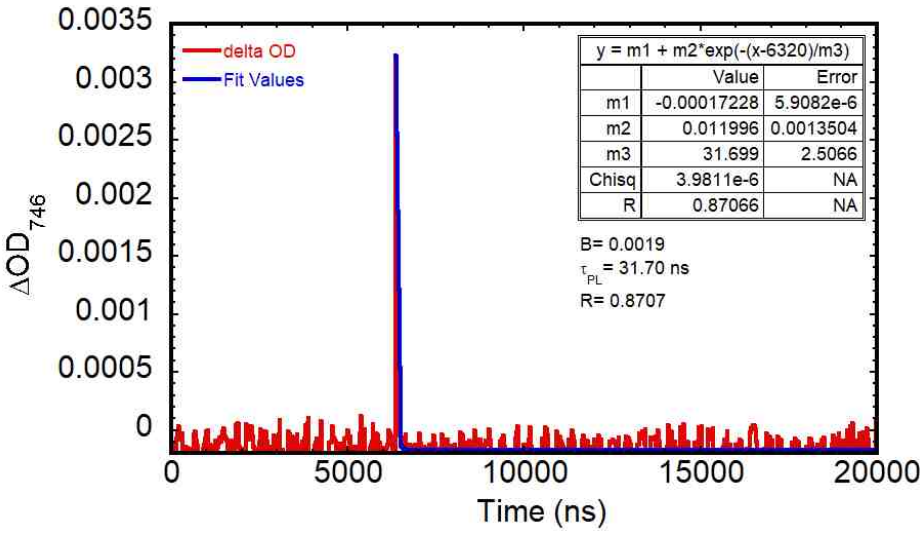

Figure 3.26: Kinetic emission trace (red) and fit (blue) for Pt(dbbpy)(bSO) in degassed CH_2Cl_2 at 746 nm excited at 564 nm.

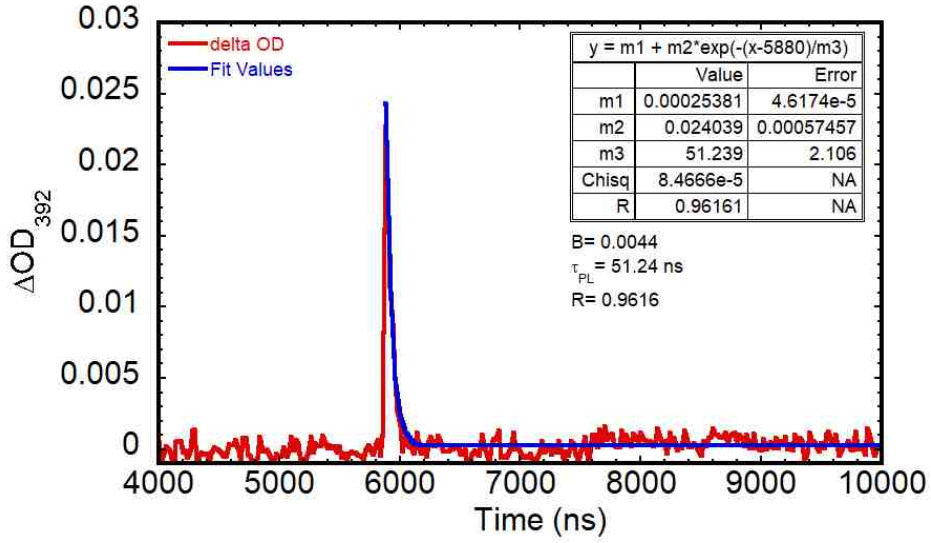

Figure 3.27: Kinetic absorption trace (red) and fit (blue) for Pt(dbbpy)(bSO) in degassed CH_2Cl_2 at 339 nm excited at 564 nm.

with a lifetime (τ_{TA}) of 51 ± 2 ns. The emission lifetimes and TA lifetimes for Pt(dbbpy)(bSO) are observed to be very short compared to that of Pt(dbbpy)(bdt) and Pt(dbbpy)(bds).

3.2.4 [Pt(dbbpy)(bSSe)]

3.2.4.1 Electronic Absorption Spectroscopy

The electronic absorption spectrum for Pt(dbbpy)(bSSe) depicted in Figure 3.28 was taken in dichloromethane (CH_2Cl_2) solution at room temperature. The CT absorption maxima is at 18050 cm^{-1} (554 nm) with a molar extinction coefficient of 6890 $M^{-1}cm^{-1}$. The absorption maximum is recorded only for the lowest-energy band, even though additional absorption features occurs at higher energies.

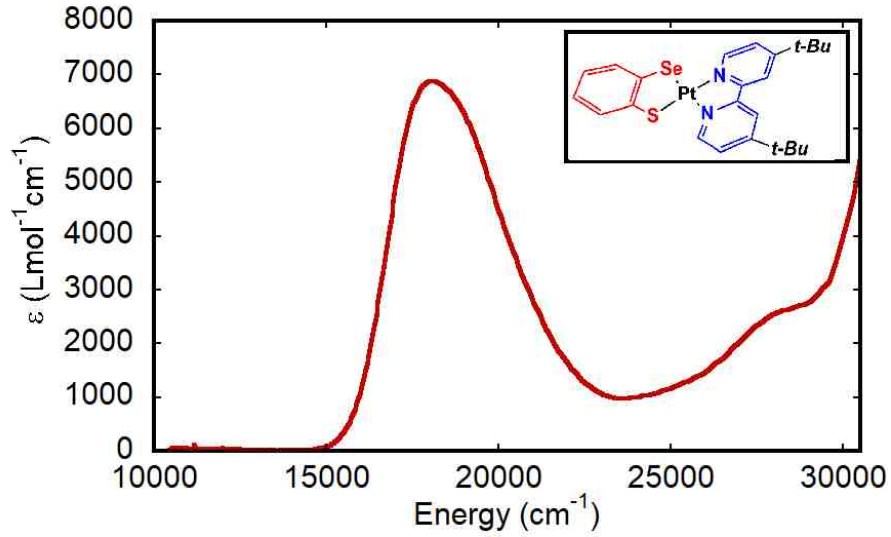

Figure 3.28: Absorption spectrum of Pt(dbbpy)(bSSe) in CH_2Cl_2 . Inset: Compound structure.

3.2.4.2 Transient Absorption Spectra, Emission Spectra, and Lifetimes

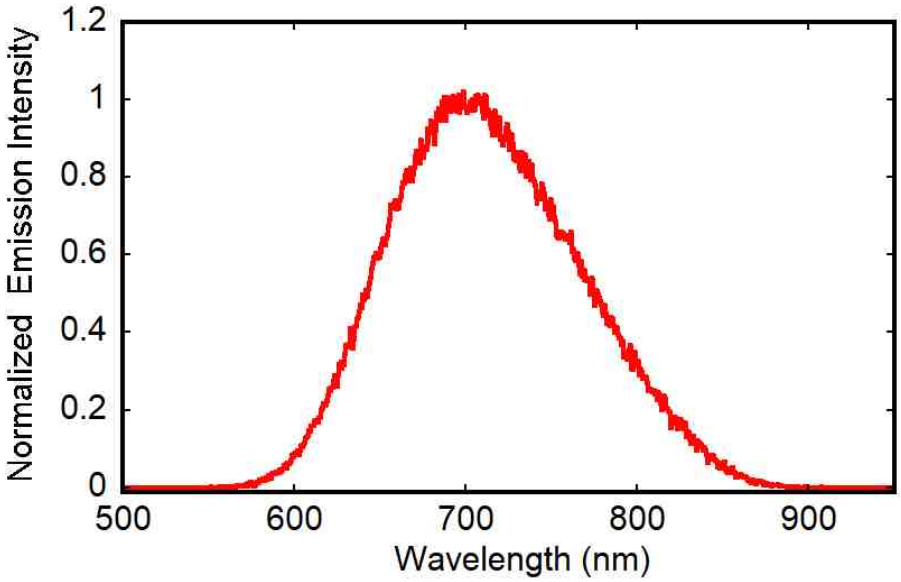

Figure 3.29: Emission spectrum for Pt(dbbpy)(bSSe) in degassed CH_2Cl_2 solution at 298 K, excited at 556 nm.

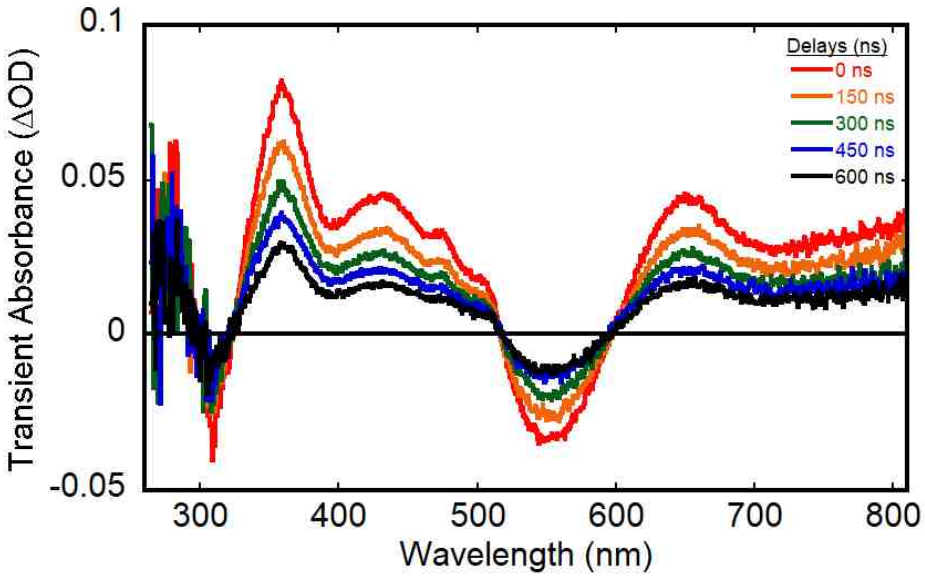

Figure 3.30: Transient Absorption (TA) difference spectra for Pt(dbbpy)(bSSe) obtained in degassed CH_2Cl_2 fluid solution following 564 nm excitation, pump: 5 mJ/pulse at the MMLL'CT absorption maximum, recorded at 0, 150, 300, 450, and 600 ns time delays.

Pt(dbbpy)(bSSe) exhibit a broad emission band in degassed dichloromethane fluid solution with emission maxima (λ_{max}^{Em}) at 700 nm. The emission spectrum for Pt(dbbpy)(bSSe) is depicted in Figure 3.29 and the calculated stokes shift is 3760 cm^{-1}. The TA spectra of Pt(dbbpy)(bSSe) in CH_2Cl_2 recorded at 0, 150, 300, 450, and 600 ns time delays after initial excitation with a 564 nm pump is depicted in Figure 3.30. The TA spectra of Pt(dbbpy)(bSSe) shows similar features displayed by other Pt(diimine)(dichalcogelene) complexes. A transient absorption signal is observed starting from 520 nm and lengthening to the blue region of the spectra. The ground state depletion is observed from 520 to 600 nm with minima centered at 549 nm (see Figure 3.31). The ground state depletion observed in the TA spectra corresponds well to the ground state

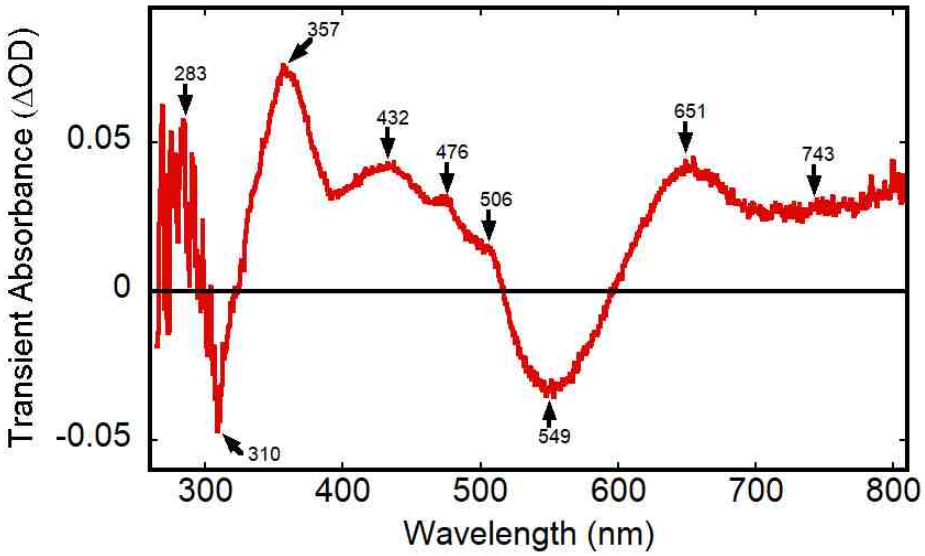

Figure 3.31: Transient Absorption (TA) difference spectra for Pt(dbbpy)(bSSe) obtained in degassed CH_2Cl_2 fluid solution following excitation with 564 nm, pump: 5 mJ/pulse at the MMLL'CT absorption maximum, recorded at 0 ns time gate delay.

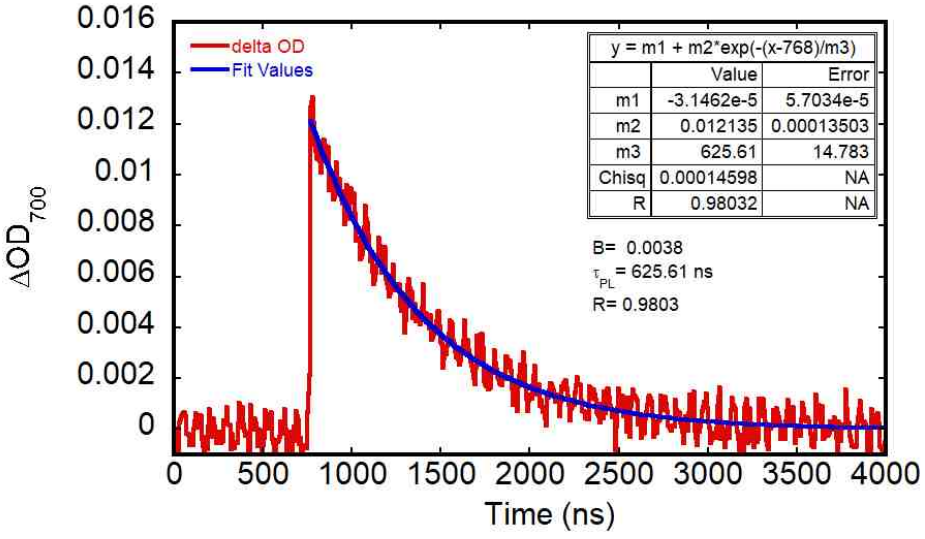

Figure 3.32: Kinetic emission trace (red) and fit (blue) for Pt(dbbpy)(bSSe) in degassed CH_2Cl_2 at 700 nm excited at 555 nm.

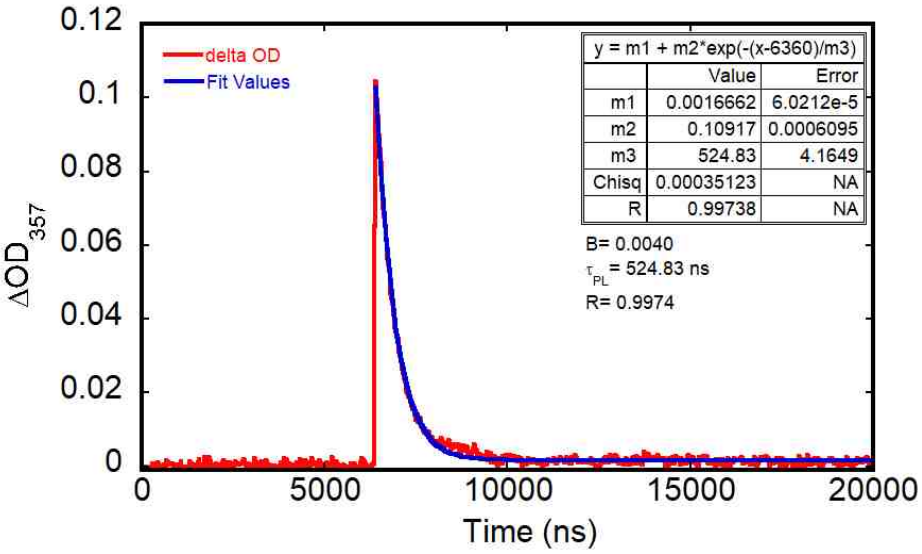

Figure 3.33: Kinetic absorption trace (red) and fit (blue) for Pt(dbbpy)(bSSe) in degassed CH_2Cl_2 at 357 nm excited at 555 nm.

absorption recorded in the electronic absorption spectroscopy (EAS). The TA spectrum presented in Figure 3.31 shows the various peak for the kinetic absorption trace of Pt(dbbpy)(bSSe). Figure 3.32 depicts the kinetic emission traces for Pt(dbbpy)(bSSe) in degassed CH_2Cl_2 at 700 nm excited at 555 nm. The spectra decay rapidly from 0 to about 2500 ns and then remains static. By using Marquardt-Levenberg algorithm fit (blue line on the kinetic emission trace), the kinetic emission lifetime (τ_{PL}) for Pt(dbbpy)(bSSe) was calculated as 626 ± 15 ns. The kinetic absorption trace for Pt(dbbpy)(bSSe) is presented in Figure 3.33. The spectrum was collected in degassed CH_2Cl_2 solution at ambient temperature by monitoring the transient absorbance at 357 nm. The overall transient absorption profile decays with a lifetime (τ_{TA}) of 525 ± 4 ns.

3.2.5 [Pt(dbbpy)(bSeO)]

3.2.5.1 Electronic Absorption Spectroscopy

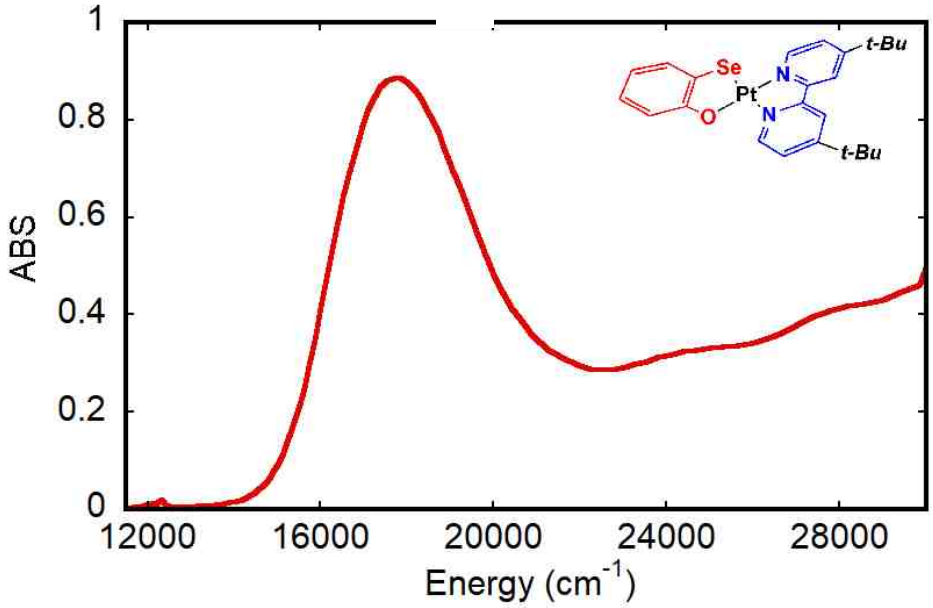

Figure 3.34: Absorption spectrum of Pt(dbbpy)(bSeO) in CH_2Cl_2. Inset: Compound structure.

Figure 3.34 depicts the electronic absorption spectrum (EAS) of Pt(dbbpy)(bSeO) in dichloromethane fluid solution at ambient temperature. The charge-transfer-to-diimine absorption band maxima is at 565 nm (17700 cm^{-1}). The lowest-energy CT absorption band for Pt(dbbpy)(bSeO) exhibit solvent dependency.

3.2.5.2 Transient Absorption Spectra, Emission Spectra, and Lifetimes

The photoluminescence measurements for Pt(dbbpy)(bSeO) was monitored upon excitation into the lowest energy charge transfer (CT) absorption band. The

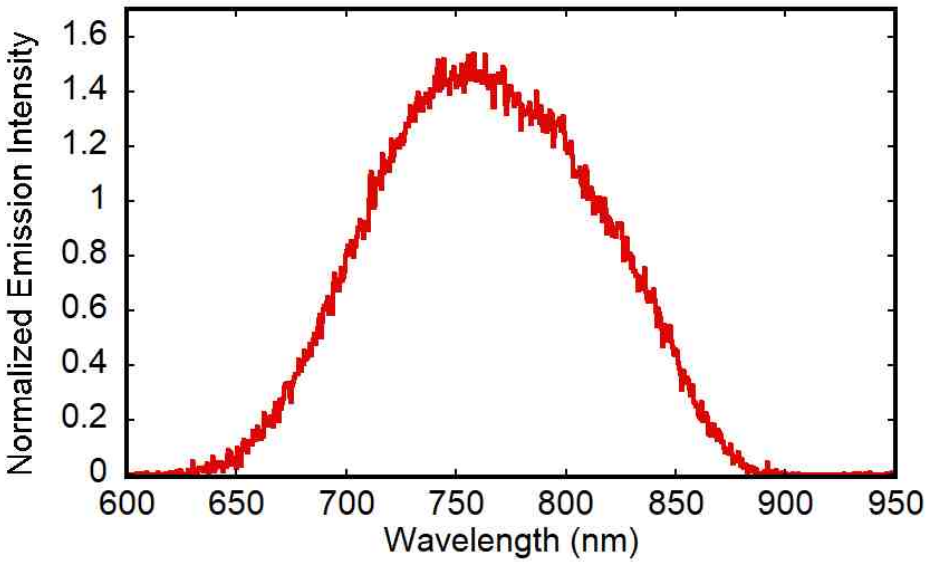

Figure 3.35: Emission spectrum for Pt(dbbpy)(bSeO) at 755 nm, in degassed CH_2Cl_2 solution at 298 K, excited at 567 nm.

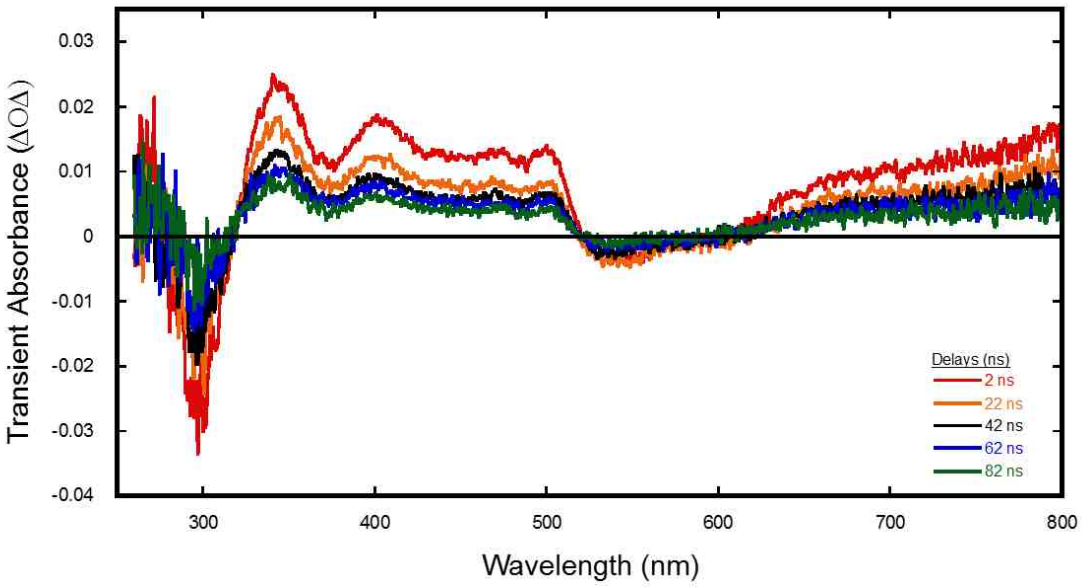

Figure 3.36: Transient Absorption (TA) difference spectra for Pt(dbbpy)(bSeO) obtained in aerated CH_2Cl_2 fluid solution following 567 nm excitation, pump: 5 mJ/pulse at the LL'CT absorption maximum, recorded at 2, 22, 42, 62, and 82 ns time delays.

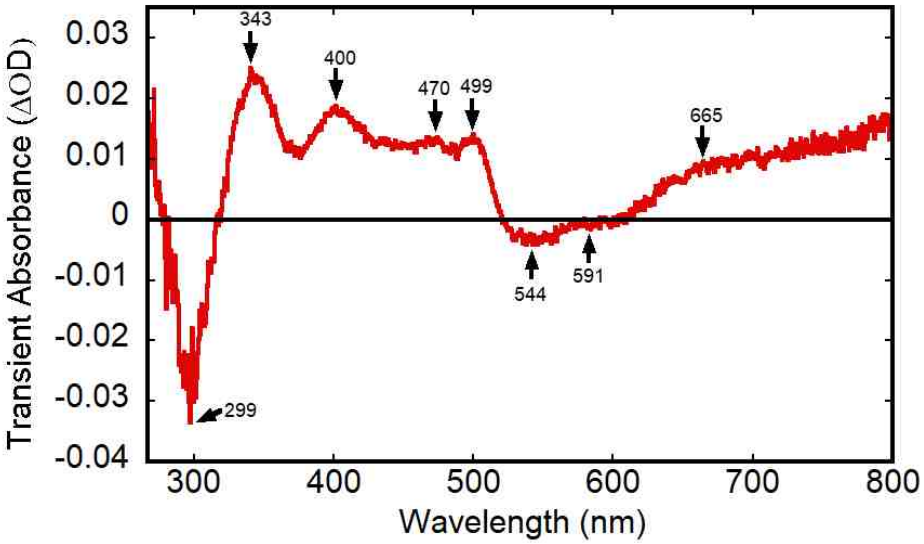

Figure 3.37: Transient Absorption (TA) difference spectra for Pt(dbbpy)(bSeO) obtained in degassed CH_2Cl_2 fluid solution following excitation with 564 nm, pump: 5 mJ/pulse at the LL'CT absorption maximum, recorded at 2 ns time gate delay.

emission spectrum was recorded in degassed dichloromethane (CH_2Cl_2) fluid solution at ambient temperature. The pictorial presentation of the emission spectrum of Pt(dbbpy)(bSeO) is depicted in Figure 3.35. The emission maxima (ε_{max}) recorded for Pt(dbbpy)(bSeO) is 755 nm (13250 cm^{-1}) and the calculated stoke shift is 4450 cm^{-1}. Figure 3.36 depicts the TA difference spectra for Pt(dbbpy)(bSeO) in degassed CH_2Cl_2 solution obtained with 567 nm pump pulse, recorded at 2, 22, 42, 62, and 82 ns time delays. After photoexcitation at 567 nm, the TA spectra for Pt(dbbpy)(bSeO) display a wide excited-state absorption signal beginning from 510 nm extending to the lower wavelength. From Figure 3.36, the ground- state (GS) bleach is recorded from 510 to 600 nm. Figure 3.37 shows the TA difference spectrum recorded at 2 ns time delay with labelled peaks for the kinetic traces analysis. Figure 3.38 shows the kinetic emission

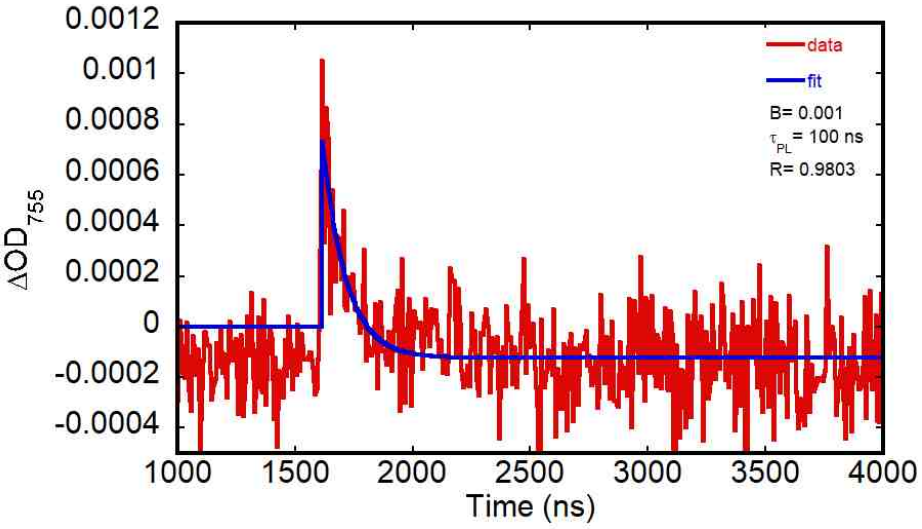

Figure 3.38: Kinetic emission trace (red) and fit (blue) overlay for Pt(dbbpy)(bSeO) at 755 nm, excited at 567 nm.

traces for Pt(dbbpy)(bSeO). The kinetic traces were monitored at 755 nm and excited a 567 nm. The exponential decay evolves quickly from 0 to 2000 ns and remains completely constant. Marquardt-Levenberg algorithm was used for the curve fitting and the kinetic parameters were calculated. The kinetic emission

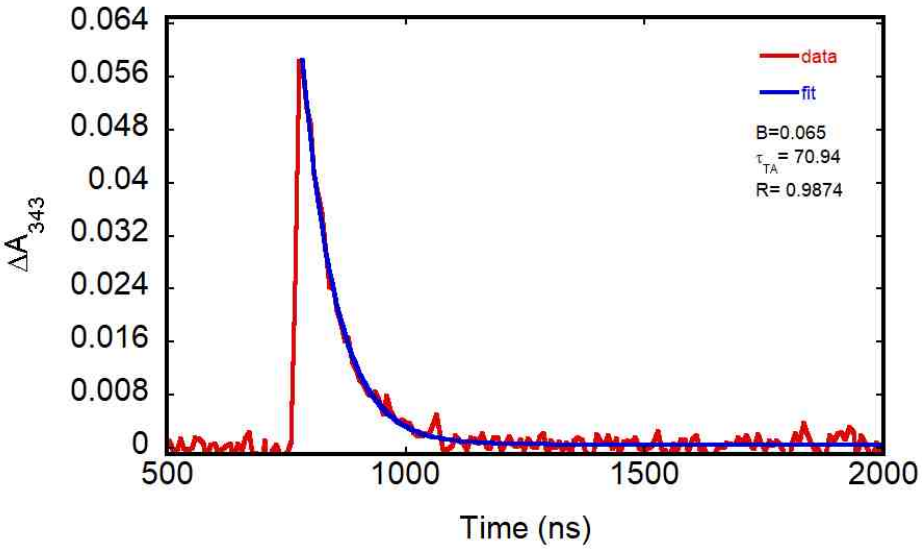

Figure 3.39: Kinetic absorption trace (red) and fit (blue) overlay for Pt(dbbpy)(bSeO) at 343 nm, excited at 567 nm.

lifetime (τ_{PL}) for Pt(dbbpy)(bSeO) was calculated as 100 ± 5 ns. Figure 3.39 depicts the kinetic absorption traces for Pt(dbbpy)(bSeO) in degassed dichloromethane solution at 298 K. The overall transient absorption profile decays with a lifetime (τ_{TA}) of 71 ± 5 ns. The kinetic emission- and absorption lifetimes for Pt(dbbpy)(bSeO) and Pt(dbbpy)(bSO) are very similar but differs from that of Pt(dbbpy)(bdt) and Pt(dbbpy)(bds).

3.2.6 Overlay of (dichalcogenolene)Pt(diimine)

3.2.6.1 Electronic Absorption Spectroscopy

The electronic absorption spectra overlay for Pt(dbbpy)(bSSe), Pt(dbbpy)(bSO), Pt(dbbpy)(bdt), Pt(dbbpy)(bds), and Pt(dbbpy)(tbuCAT) are depicted in Figure 3.40, where Pt(dbbpy)(tbuCAT) is 4,4'-di-*tert*-butyl-2,2'-bipyridineplatinum(II)(3,5-di-*tert*-butylbenzene-1,2-catecholate). The spectra were taken in fluid solution of dichloromethane at 298 K. The lowest energy ligand-to-ligand charge-transfer (LL'CT) or mixed-metal ligand-to-ligand charge-transfer (MMLL'CT) absorption maxima for Pt(dichalcogenolene)(diimine) complexes ranges from the visible to the near-infrared (NIR) region of the electromagnetic spectrum with molar extinction coefficient of the order of 10^3 (Table 3.4, Figure 3.40). The energy and the molar extinction coefficient of the LL'CT band depends on the nature of the donor atom. Pt(dbbpy)(tbuCAT) has the lowest energy LL'CT band, and Pt(dbbpy)(bds) possesses the highest energy LL'CT band (see Table 3.4). By changing the donor atom from oxygen to sulfur within the same structure, shifts

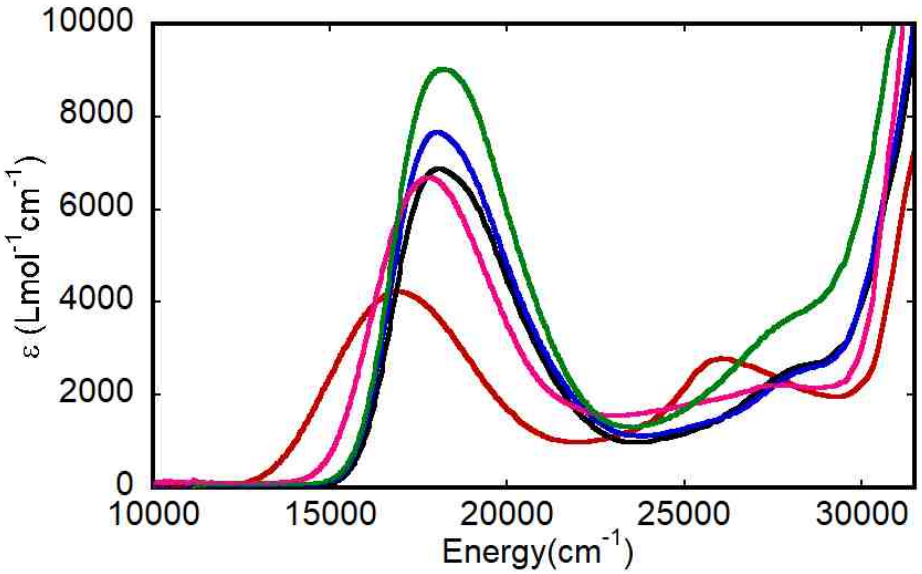

Figure 3.40: Overlay of electronic absorption spectra for Pt(dbbpy)(bSSe) (black), Pt(dbbpy)(bSO) (pink), Pt(dbbpy)(bdt) (blue), Pt(dbbpy)(bds) (green), and Pt(dbbpy)(tbuCAT) (red) in CH_2Cl_2 at 289 K.

the visible absorption band to a higher energy by 1430 cm^{-1}. Pt(dbbpy)(tbuCAT) has the lowest energy MMLL'CT absorption band with the smallest molar extinction coefficient (4300 $M^{-1}cm^{-1}$). On the other hand, Pt(dbbpy)(bds) exhibit the largest molar extinction coefficient (9100 $M^{-1}cm^{-1}$).

3.2.6.2 Transient Absorption Spectra, Emission Spectra, and Lifetimes

The photoluminescence properties of Pt(diimine)(dichalcogenolene) complexes were observed in degassed fluid solutions at ambient temperature. The room temperature (298 K) emission spectra overlay of Pt(dbbpy)(bSSe) (red), Pt(dbbpy)(bSO) (blue), Pt(dbbpy)(bdt) (black), and Pt(dbbpy)(bds) (green) is presented in Figure 3.41. Upon photo-excitation into the lowest energy absorption band, Pt(dbbpy)(bSeO) has the most red-shifted emission maxima

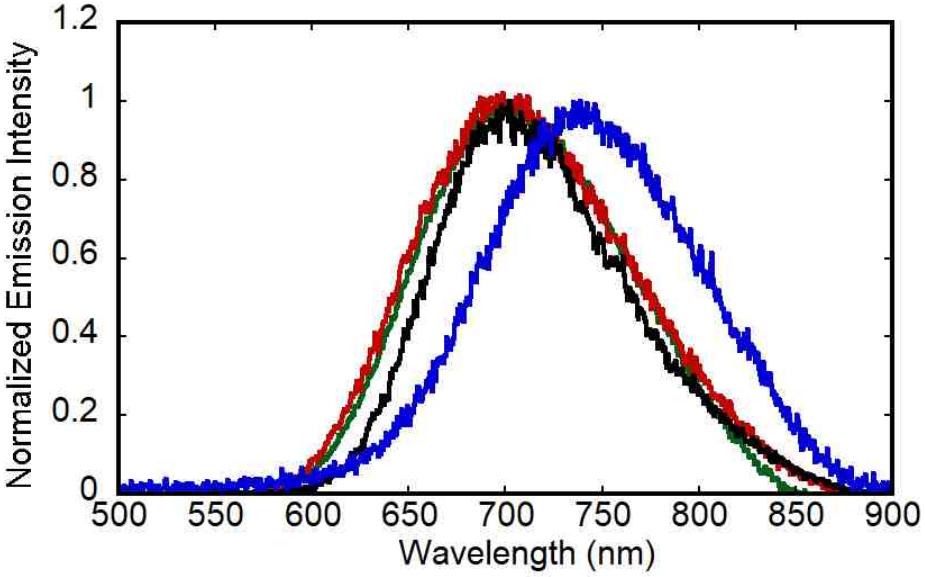

Figure 3.41: Overlay of the emission spectra of Pt(dbbpy)(bSSe) (red), Pt(dbbpy)(bSO) (blue), Pt(dbbpy)(bdt) (black), and Pt(dbbpy)(bds) (green) in degassed CH_2Cl_2 at 298 K.

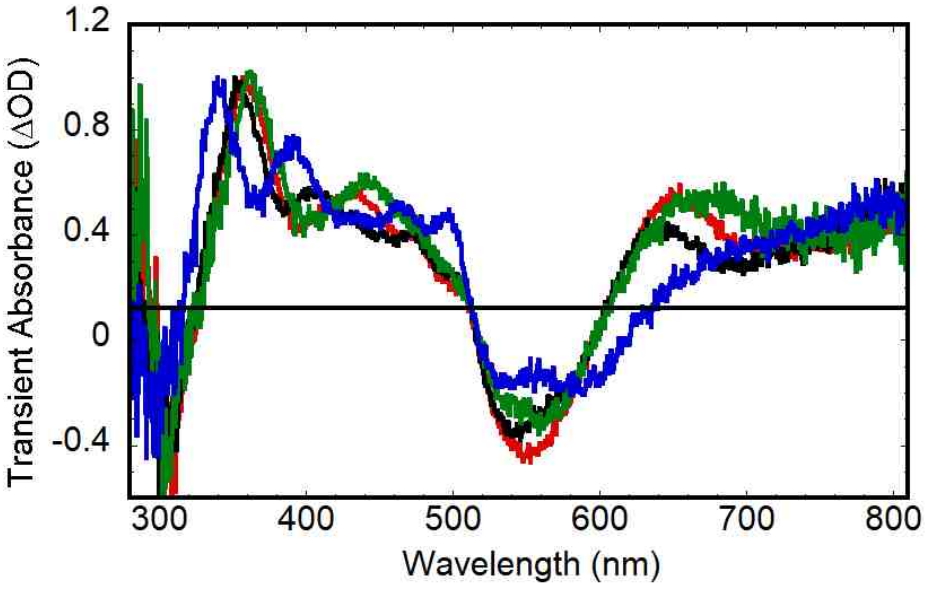

Figure 3.42: Transient Absorption (TA) difference spectra overlay for Pt(dbbpy)(bSSe) (red), Pt(dbbpy)(bSO) (blue), Pt(dbbpy)(bdt) (black), and Pt(dbbpy)(bds) (green) recorded instantly following a 5 ns gate delay (pump: 5 mJ/ pulse at the CT band maxima).

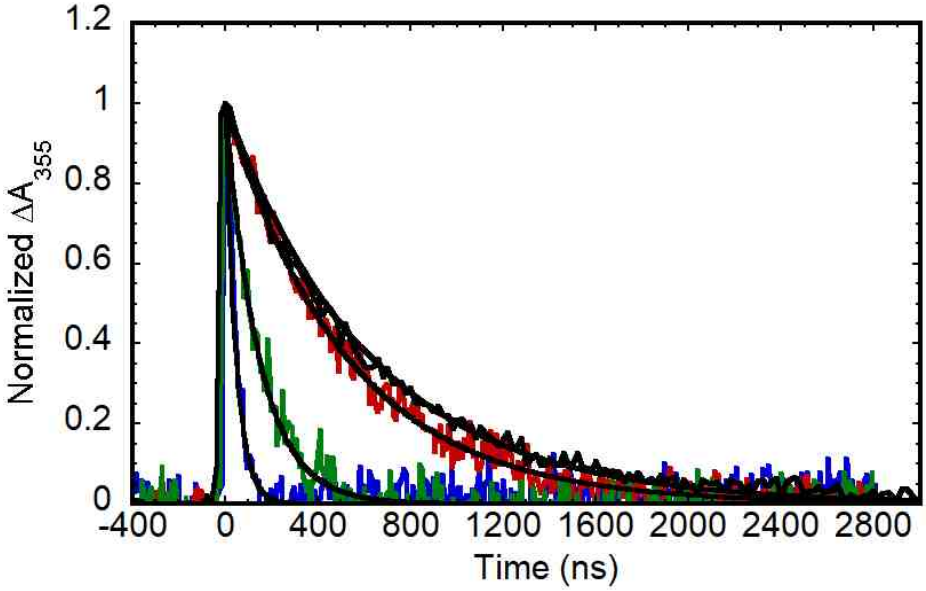

Figure 3.43: Overlay of Kinetic Absorption traces for Pt(dbbpy)(bSSe) (red), Pt(dbbpy)(bSO) (blue), Pt(dbbpy)(bdt) (black), and Pt(dbbpy)(bds) (green) in degassed CH_2Cl_2 at 298 K.

stokes shift (3760 cm^{-1}) and the most blue-shifted emission maxima (700 nm). (755 nm) and the largest stokes shift (4450 cm^{-1}). As the emission maxima decreases, the Stokes shift also decreases. Thus, Pt(dbbpy)(bSSe) has smallest the emission energies of Pt(diimine)(dichalcogenolene) complexes follows the same trend as the absorption energies, i.e. as the emission energies increases, so as the absorption energies (see Table 3.4). These results support the argument that both the emissive and absorbing state originate from the same source, thus the emissive state originates from a charge-transfer-to-diimine excited state.[2] Transient Absorption (TA) difference spectra overlay for Pt(dbbpy)(bSSe) (red), Pt(dbbpy)(bSO) (blue), Pt(dbbpy)(bdt) (black), and Pt(dbbpy)(bds) (green) are depicted in Figure 3.42. The similarity in the transient absorption (TA) difference spectra of Pt(diimine)(dichalcogenolene) complexes

depict their electronic structure similarity among these complexes.[37] The transient absorption (TA) difference spectra of Pt(diimine)(dichalcogenolene) complexes shows an excited-state absorption (ESA) of the LL'CT band from 310 – 520 nm and from wavelength greater than 620 nm. The negative signal which correspond to a ground-state bleach of the LL'CT band is observed from 520 to 620 nm. The kinetic absorption spectra of Pt(diimine)(dichalcogenolene) complexes are depicted in Figure 3.43. The spectra decay is most rapid for Pt(dbbpy)(bSO), followed by Pt(dbbpy)(bds), and then Pt(dbbpy)(bSSe) and Pt(dbbpy)(bdt) (Figure 3.43). Thus, Pt(dbbpy)(bSO) has the shortest ground-

Table 3.4: Photophysical Properties of Pt(diimine)(dichalcogenolene) Complexes.

	O,O	**O,S**	**O,Se**	**S,S**	**S,Se**	**Se,Se**
λ_{abs} (nm)	591	563	565	545	554	553
E_{abs} (cm^{-1})	16920	17760	17700	18350	18050	18080
ε_{max} (nm)		740	755	702	700	702
ε_{max} (cm^{-1})		13510	13250	14250	14290	14250
Stokes shift (cm^{-1})		4250	4450	4100	3760	3830
τ_{PL} (ns)[a]		32 ± 3	100 ± 5	621± 10	626± 15	175± 2
$\tau_{trip\ abs}$ (ns)[b]	0.63[d]	51 ± 2	71 ± 5	614 ± 10	525± 4	179± 6
$\tau_{GS\ dep}$ (ns)[c]		41± 2	68 ± 2	587± 10	465± 4	181+10
ϵ ($Lmol^{-1}cm^{-1}$)	4300	6700		7700	6900	9100

[a]PL = photoluminescence, [b]Trip abs = triplet absorption, [c]GS dep = ground state depletion, [d]Reference 1, ε_{max} = emission maxima, E_{abs} = Energy of the absorption maxima, λ_{abs} = wavelength of maximum absorption. O,O= Pt(dbbpy)(tbuCAT), O,S= Pt(dbbpy)(bSO), O,Se= Pt(dbbpy)(bSeO), S,S= Pt(dbbpy)(bdt), S,Se= Pt(dbbpy)(bSSe), and Se,Se= Pt(dbbpy)(bds)

state recovery or triplet absorption time constant among Pt(diimine)(dichalcoge-nolene) complexes (see Figure 3.43). Pt(dbbpy)(bSSe) and Pt(dbbpy)(bdt) have

the longest ground-state recovery or triplet absorption time constants. By closely inspecting Table 3.4, it can be deduced that the ground-state recovery or triplet absorption time constants differ by almost three orders of magnitude with Pt(dbbpy)(tbuCAT) having the fastest ground-state recovery time constant of 0.63 ns.

3.2.7 [Pt(dbbpy)(pdt)] and [Pt(dbbpy)(pds)]

3.2.7.1 Electronic Absorption Spectroscopy (EAS)

The UV-Vis absorption spectra of Pt(dbbpy)(pdt) and Pt(dbbpy)(pds) are presented in Figure 3.44. The spectra were taken in dichloromethane solution at

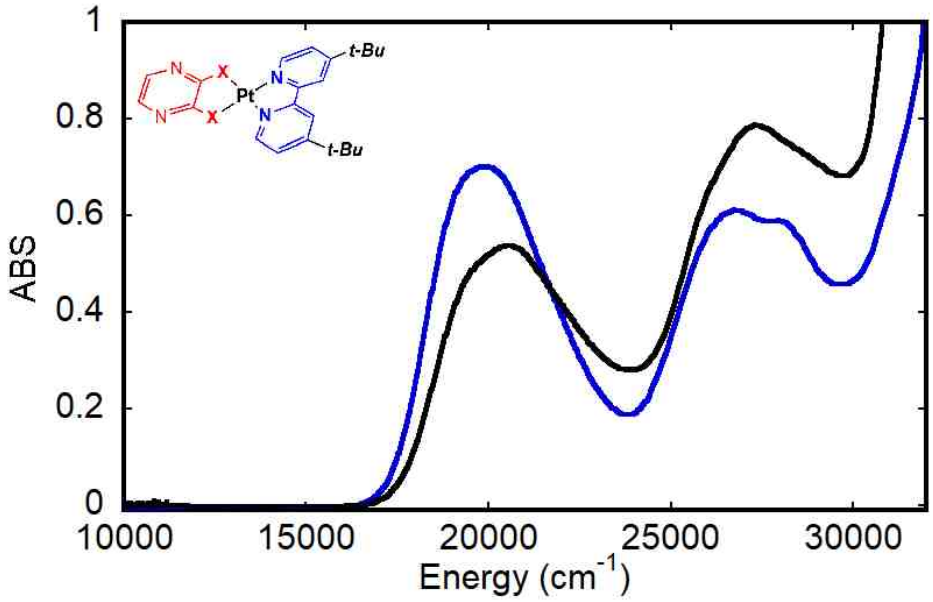

Figure 3.44: Electronic absorption overlay for Pt(dbbpy)(pdt) (black) and Pt(dbbpy)(pds) (blue) in CH_2Cl_2 at 298 K. Inset: Compound structure: X=S for Pt(dbbpy)(pdt) and X=Se for Pt(dbbpy)(pds).

ambient temperature. The MMLL'CT absorption band maxima (λ_{max}^{Abs}) for Pt(dbbpy)(pdt) and Pt(dbbpy)(pds) are 20530 cm^{-1} (487 nm) and 19840 cm^{-1} (504 nm) respectively. The MMLL'CT band represent the lowest energy absorption band even though additional absorption features occur at higher energies. The higher energy feature in Pt(dbbpy)(pds) has two resolved maxima while that of Pt(dbbpy)(pdt) shows only one maxima in dichloromethane. The feature which lies at higher energy in Pt(dbbpy)(pdt) and Pt(dbbpy)(pds) are solvent dependent. Their band energies have been observed to shift in different solvents. (see Figure 4.0).

3.2.7.2 Transient Absorption Spectra, Emission Spectra, and Lifetimes

The 298 K emission spectra in deoxygenated dichloromethane fluid solution for Pt(dbbpy)(pdt) and Pt(dbbpy)(pds) are presented in Figure 3.45. The emission spectra for Pt(dbbpy)(pdt) and Pt(dbbpy)(pds) has a featureless band with

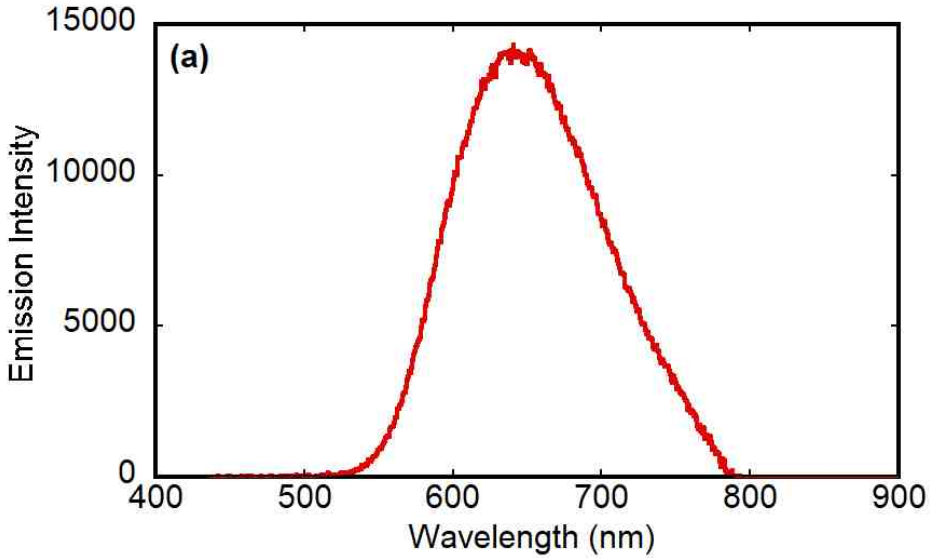

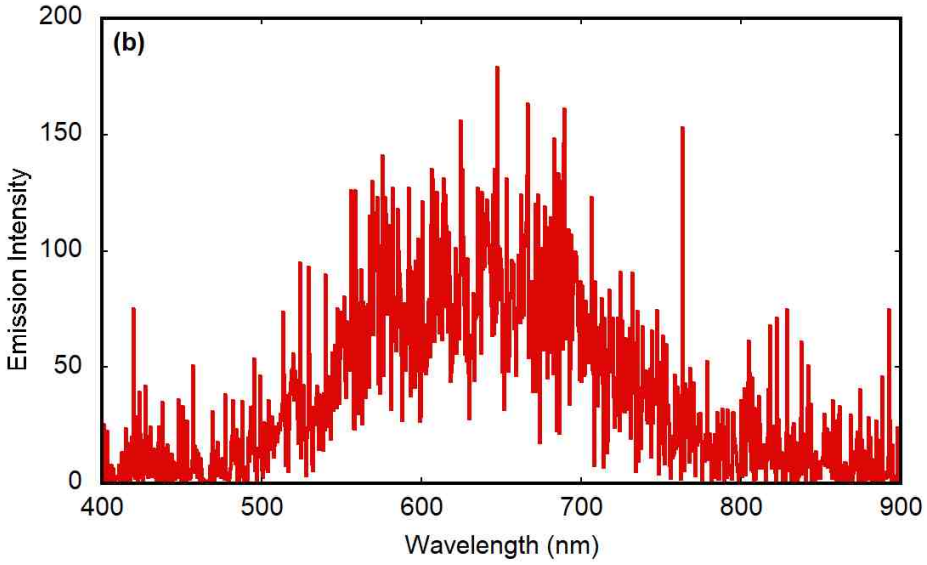

Figure 3.45: Emission spectra for **(a)** Pt(dbbpy)(pdt) at 642 nm, excited @ 487 nm, power 20 Mw **(b)** Pt(dbbpy)(pds) at 630 nm, excited @ 500 nm, power: 25 mW in degassed CH_2Cl_2 solution at 298 K.

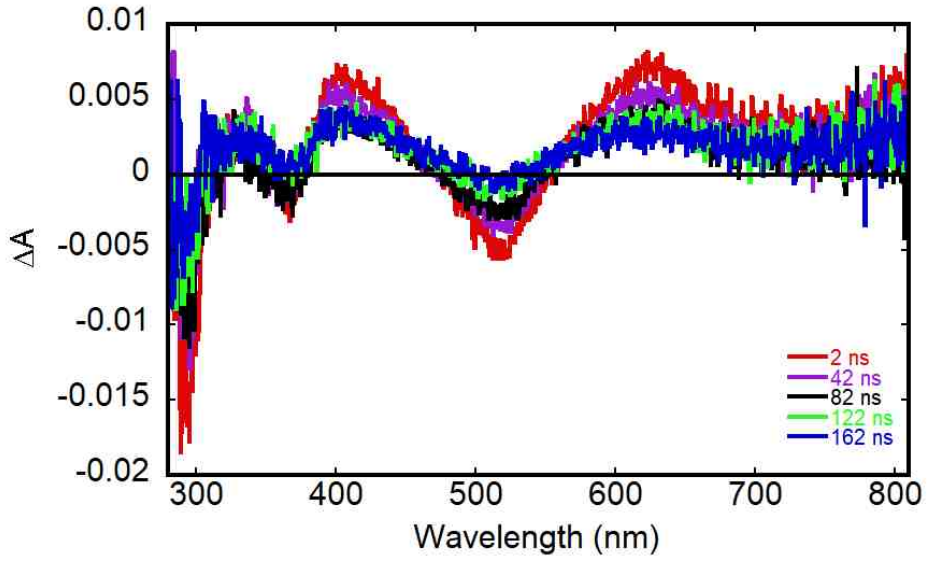

Figure 3.46: Transient Absorption (TA) difference spectra for Pt(dbbpy)(pdt) obtained in aerated CH_2Cl_2 fluid solution following 487 nm excitation, pump: 20 Mw, recorded at 2, 42, 82, 122, and 162 ns time delays.

emission maxima (ε_{max}) at 642 nm (15580 cm^{-1}) and 630 nm (15870 cm^{-1}) respectively. A very weak emission was observed for the two complexes. The calculated stokes shifts are 4950 and 3970 cm^{-1} for Pt(dbbpy)(pdt) and Pt(dbbpy)(pds) respectively. Transient Absorption (TA) difference spectra for Pt(dbbpy)(pdt) in degassed dichloromethane solution obtained with a 487 nm pump pulse, starts at 2 ns and ends at 162 ns are depicted in Figure 3.46. After excitation at 487 nm, the transient absorption spectra of Pt(dbbpy)(pdt) are marked by positive signal from 315 to 350 nm, 380 to 480 nm, and at $\lambda > 550$ nm. These positive signals represent excited state absorption (ESA). Pt(dbbpy)(pdt) is characterized by a ground-state bleach (GSB) from ~ 480 to 550 nm. The kinetic emission traces for Pt(dbbpy)(pdt) presented in Figure 3.47(a) was monitored at 642 nm and excited at 487 nm. The spectra decay rapidly from 750 to 1000 ns and then remains static signifying that the species formed at 750 to 1000 ns are long-lived. The kinetic emission lifetime (τ_{PL}) for Pt(dbbpy)(pdt) is 105 ± 10 ns. The kinetic absorption traces for Pt(dbbpy)(pds) depicted in Figure

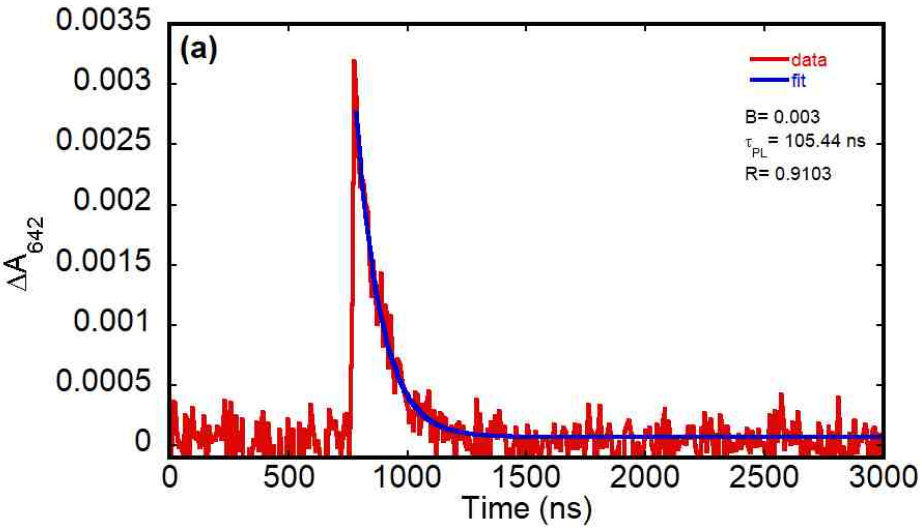

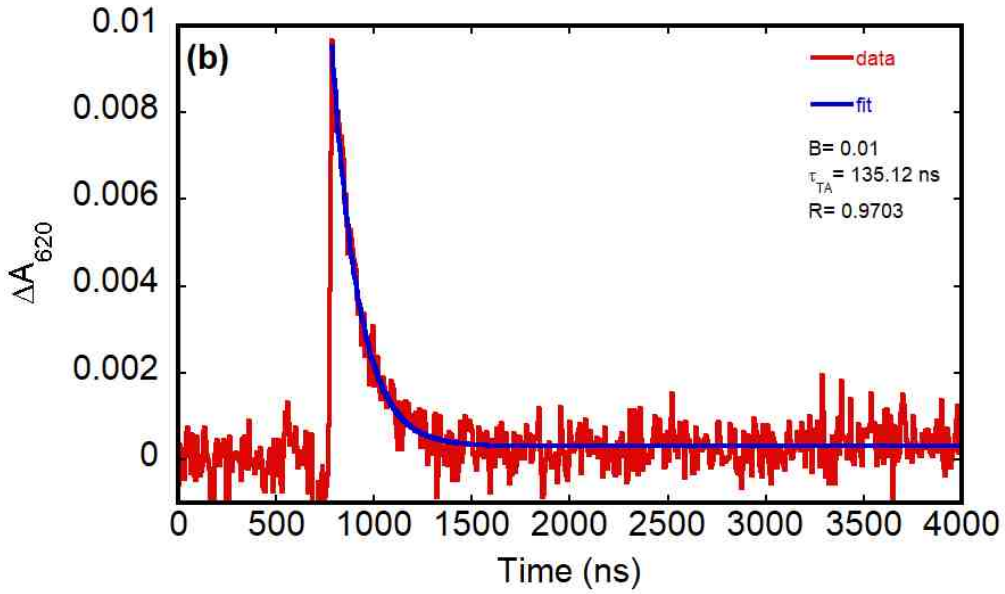

Figure 3.47: (a) Kinetic emission trace at 642 nm trace for Pt(dbbpy)(pdt) in CH_2Cl_2, excited at 487 nm **(b)** kinetic absorption trace at 620 nm for Pt(dbbpy)(pdt) in CH_2Cl_2, excited at 487 nm.

3.47(b) in aerated CH_2Cl_2 solution at 298 K was obtained by monitoring transient absorbance at 620 nm. The overall transient absorption profile decays with a lifetime (τ_{TA}) of 135 ± 10 ns.

3.2.8 [Pt(dbbpy)(qdt)] and [Pt(dbbpy)(qds)]

3.2.8.1 Electronic Absorption Spectroscopy (EAS)

The electronic absorption spectra of Pt(dbbpy)(qds) and Pt(dbbpy)(qdt) are depicted in Figure 3.48. The spectra were taken in fluid solution of dichloromethane at ambient temperature. The lowest energy MMLL'CT

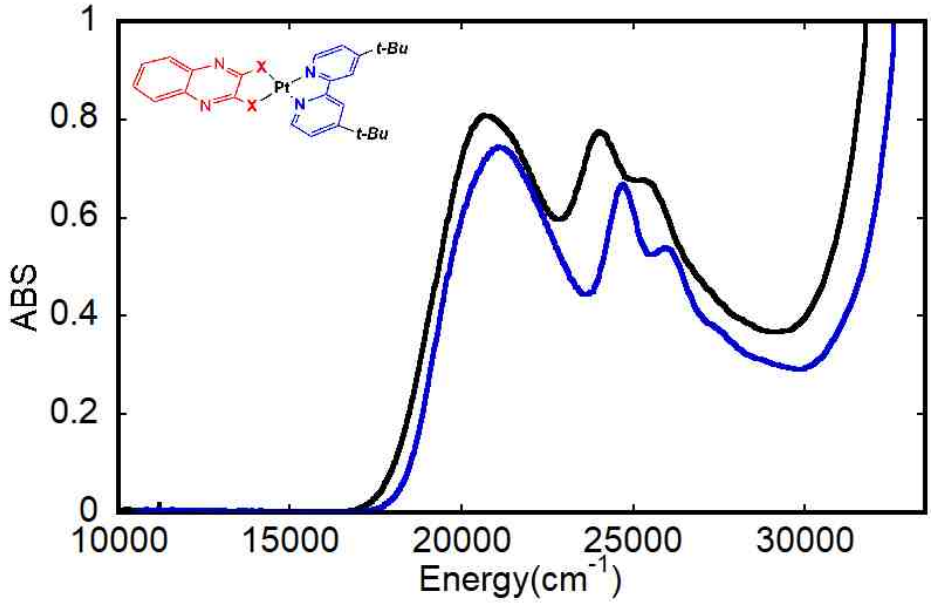

Figure 3.48: Electronic absorption overlay for Pt(dbbpy)(qds) (black) and Pt(dbbpy)(qdt) (blue) in CH_2Cl_2 at 298 K. Inset: Compound structure: X=S for Pt(dbbpy)(qdt) and X=Se for Pt(dbbpy)(qds).

absorption band maxima for Pt(dbbpy)(qds) and Pt(dbbpy)(qdt) are 20620 cm^{-1} (485 nm) and 21140 cm^{-1} (473 nm) respectively. The absorption maxima are recorded only for the lowest-energy CT band, even though additional absorption features occur at higher energies (see Figure 3.48). The absorption features which lies at higher energies of the spectra have two resolved maxima at 25970 cm^{-1} (385 nm) and 24690 cm^{-1} (405 nm) for Pt(dbbpy)(qdt), 25380 cm^{-1} (394 nm) and 23980 cm^{-1} (417 nm) for Pt(dbbpy)(qds). The lowest energy CT absorption maxima for both Pt(dbbpy)(qds) and Pt(dbbpy)(qdt) are solvent dependent, while the absorption features at higher energies are solvent independent. The difference in energy of the two higher energy bands are 1280 and 1400 cm^{-1} for Pt(dbbpy)(qdt) and Pt(dbbpy)(qds) respectively. The energy difference obtained

for both Pt(dbbpy)(qdt) and Pt(dbbpy)(qds) are very similar to those obtained for other Pt(diimine)(dithiolate) such as [Pt(qdt)$_2$] (1219 cm^{-1}), [Pt(phen)(qdt)] (1215 cm^{-1}) and [Pt(COD)(qdt)] (1156 cm^{-1}) where COD is 1,5-cyclooctadiene. In these complexes, the higher energy band was assigned as charge-transfer-to-dithiolate in which the acceptor orbital was qdt π* orbital instead of the diimine phen ligand[8].

3.2.8.2 Transient Absorption Spectra, Emission Spectra, and Lifetimes

Figure 3.49 (a) depicts the ambient temperature emission spectrum for Pt(dbbpy)(qds) in degassed CH_2Cl_2 solution. Centered at 683 nm is the emission maximum (λ_{max}^{Em}) for Pt(dbbpy)(qds) with energy of 14640 cm^{-1}. The calculated stokes shifts is 5980 cm^{-1}. The kinetic emission traces for Pt(dbbpy)(qds) depicted in figure 3.49 (b) was monitored at 683 nm and excited at 470 nm. The kinetic emission lifetime (τ_{PL}) for Pt(dbbpy)(qds) is 4 ± 2 ns. The 298 K overlay of absorption spectrum (red), solid-state emission spectrum (green), and fluid solution emission spectrum (blue), excited @ 470 nm for Pt(dbbpy)(qdt) are presented pictorially in Figure 3.50. The emission maxima (λ_{max}^{Em}) in the fluid solution and the solid-state are 604 nm (16560 cm^{-1}) and 573 nm (17450 cm^{-1}) respectively. The fluid solution emission spectrum is red shifted relative to the solid-state emission spectrum by 900 cm^{-1}. The calculated stokes shift for the fluid solution is 4580 cm^{-1}. Pt(dbbpy)(qdt) is emissive in both fluid solution and solid-state at 298 K upon excitation into the lowest energy absorption band.

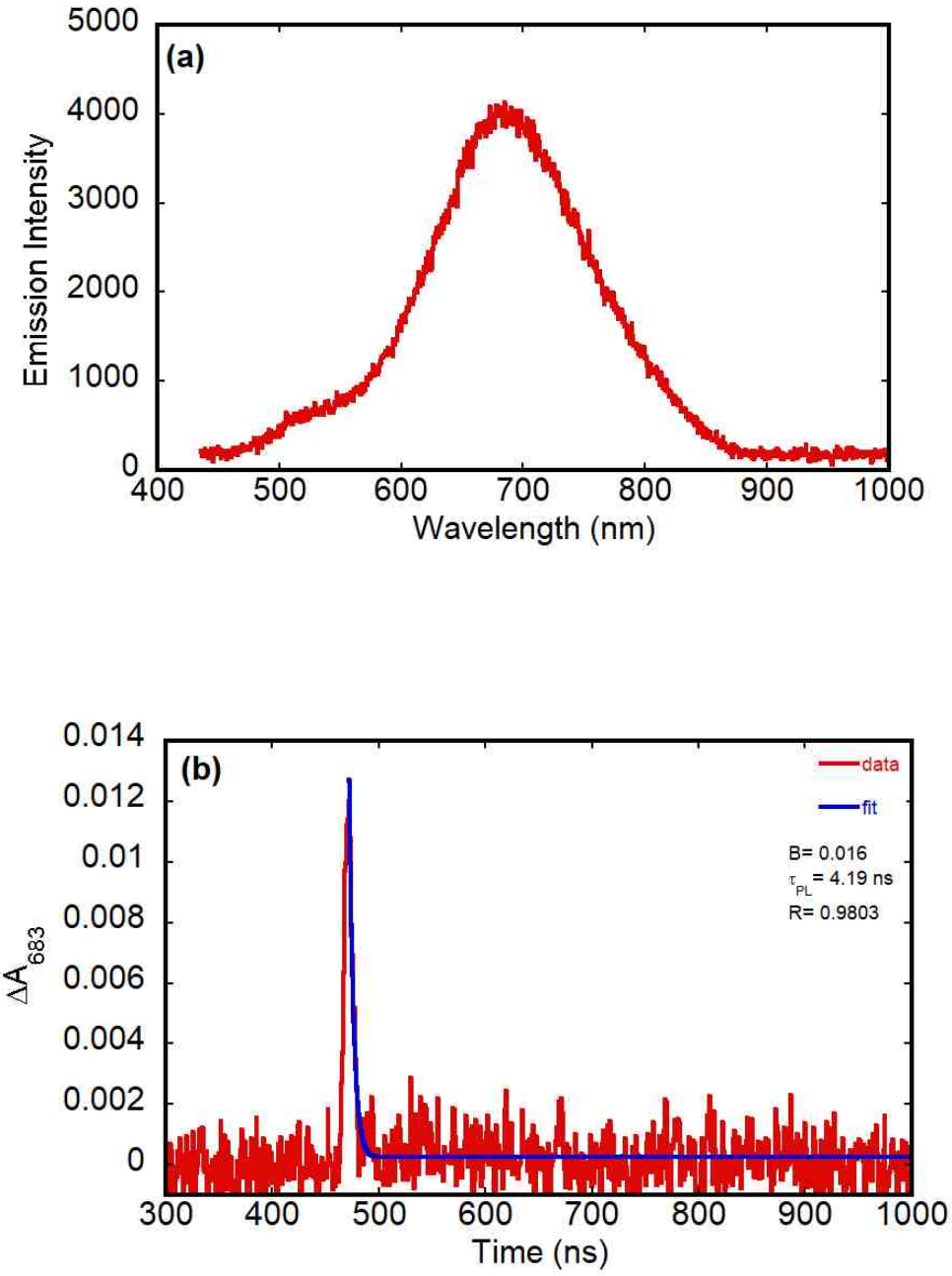

Figure 3.49: (a) Emission spectrum at 683 nm, excited @ 470 nm, power: 30 mW **(b)** kinetic emission trace at 683 nm excited at 470 nm for Pt(dbbpy)(qds) in degassed CH_2Cl_2 solution at 298 K.

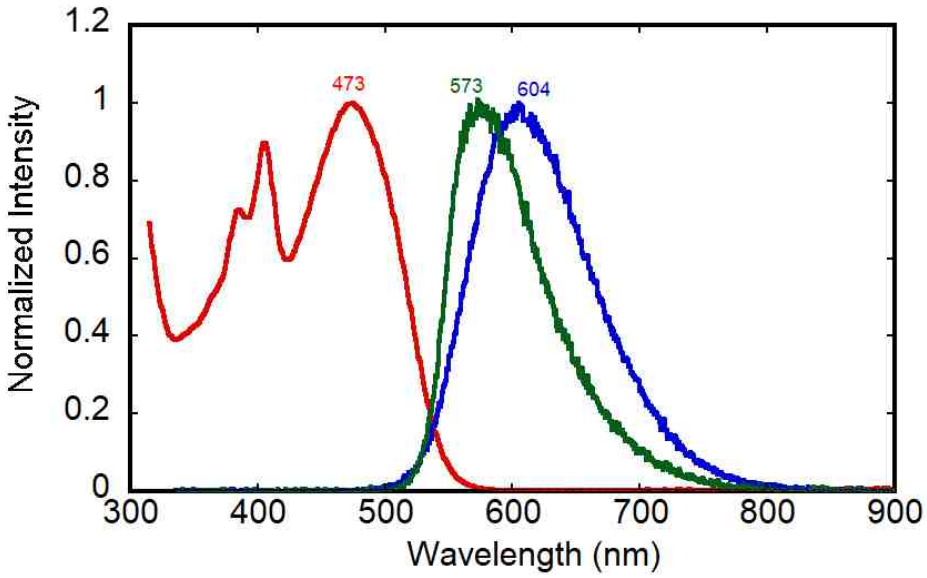

Figure 3.50: Overlay of normalized absorption spectrum (red), Normalized solid-state emission spectrum (green), and Normalized fluid solution emission spectrum (blue), excited @ 470 nm, power 30 Mw for Pt(dbbpy)(qdt) in degassed dichloromethane solution at 298 K.

respectively. The kinetic emission trace for Pt(dbbpy)(qdt) was monitored at 604 and 573 nm in fluid-state solution and solid-state respectively (Figure 3.51). The kinetic emission lifetimes (τ_{PL}) for Pt(dbbpy)(qdt) in fluid- and solid-state are 12 ± 2 and 6 ± 2 ns respectively. The emission lifetimes values in these two states are very different. It can be concluded that the solid-state emission has a shorter lifetime compared to the fluid state emission. The TA difference spectra for Pt(dbbpy)(qdt) in degassed dichloromethane solution obtained with a 470 nm pump pulse, starts at 0 ns and ends at 12 ns are presented in Figure 3.52 (b). Also depicted in Figure 3.52 (a) is the kinetic absorption trace for Pt(dbbpy)(qdt) in degassed CH_2Cl_2 solution at 298 K. The kinetic absorption trace was obtained by monitoring transient absorbance at 360 nm. The overall transient absorption profile decays with a lifetime (τ_{TA}) of 10 ± 2 ns.

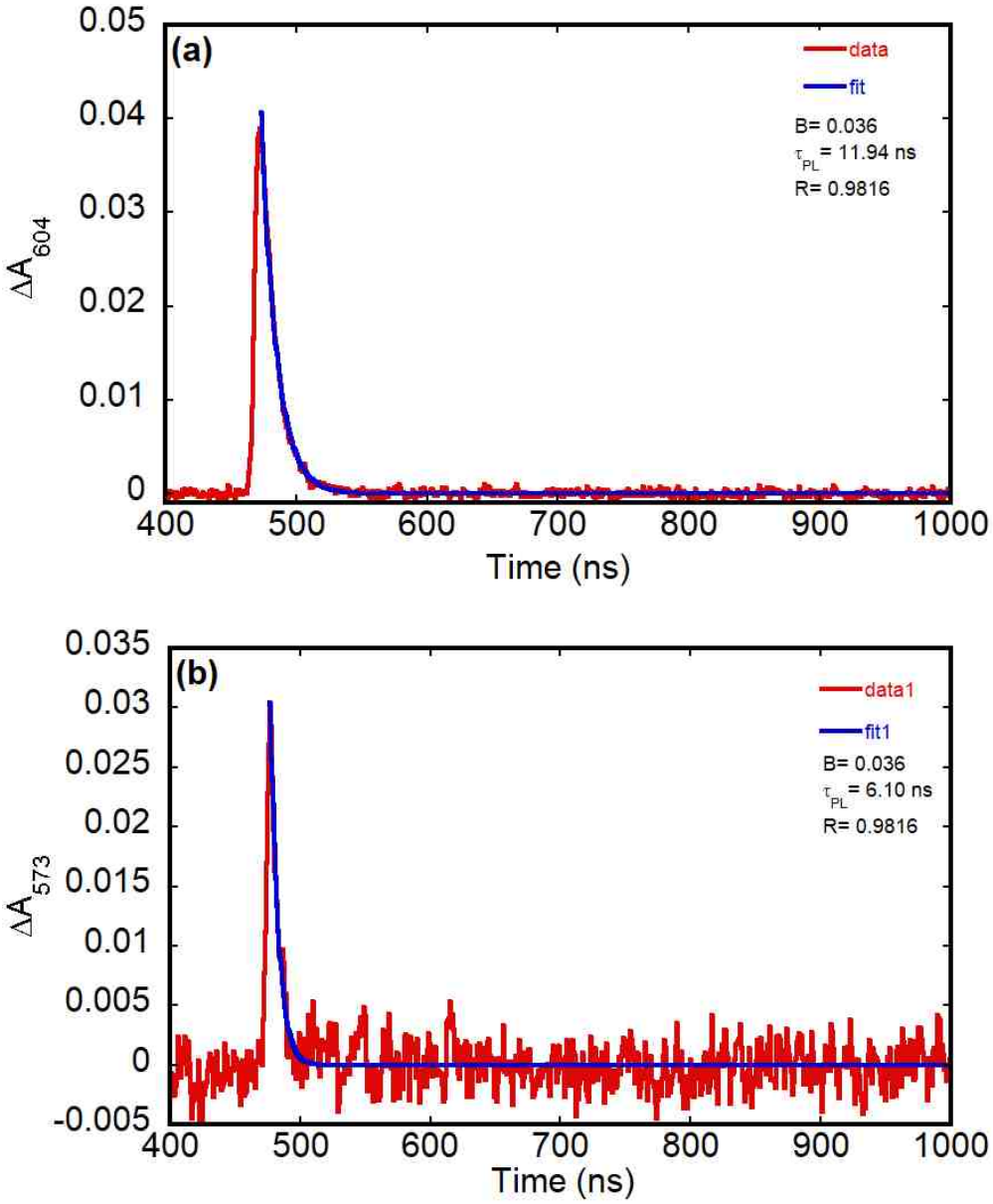

Figure 3.51: Kinetic emission trace **(a)** at 604 nm in fluid solution of degassed CH_2Cl_2 **(b)** at 573 nm in solid-state for Pt(dbbpy)(qdt), excited at 470 nm, power: 30 mW.

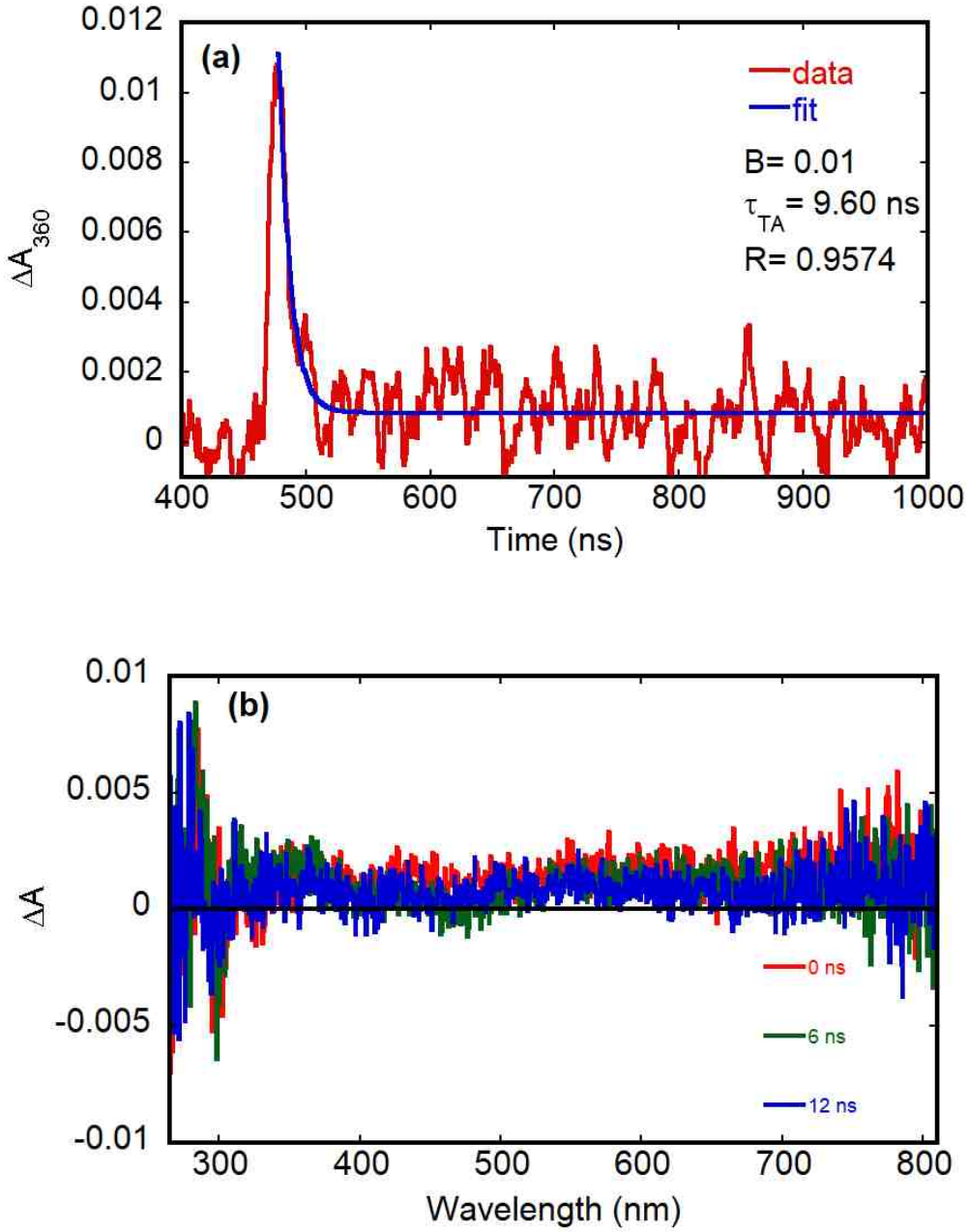

Figure 3.52: (a) Kinetic Absorption traces at 360 nm excited @ 470 nm, **(b)** Transient Absorption (TA) difference spectra @ 470 nm excitation, pump: 30 Mw, recorded at 0,6, and 12 ns.

3.2.9 [Pt(phen)(bdt)], [Pt(phen)(bds)] and [Pt(phen)(qdt)]

3.2.9.1 Electronic Absorption Spectroscopy

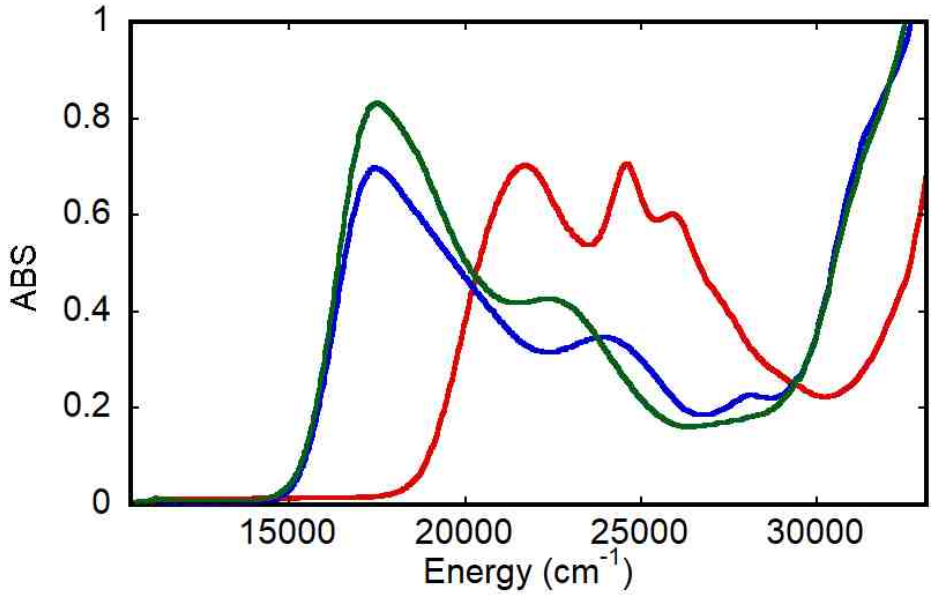

Figure 3.53: Overlay of electronic absorption spectra of Pt(phen)(bdt) (blue), Pt(dbbpy)(bds) (green), and Pt(dbbpy)(qdt) (red) in CH_2Cl_2 at 289 K.

The electronic absorption spectra of Pt(phen)(bdt) (blue), Pt(dbbpy)(bds) (green), and Pt(dbbpy)(qdt) (red) at room temperature solutions are presented in Figure 3.53. The lowest energy MMLL'CT absorption band for these complexes display almost symmetric absorption band at the visible region of the electromagnetic spectrum. The CT absorption band is very responsive to the nature of donor ligands, diimine and the polarity of the solvent. The lowest energy CT absorption maxima (λ_{max}^{Em}) for Pt(phen)(bdt), Pt(phen)(bds) and Pt(phen)(qdt) are 17510 cm^{-1} (571 nm), 17450 cm^{-1} (573 nm), and 21690 cm^{-1} (461 nm) respectively. From Figure 3.53, it can be observed that additional absorption bands are present at higher energies, but the absorption maxima are recorded only for the lowest-

energy band. From TD-DFT calculations, the lowest energy CT band for these complexes are assign as HOMO → LUMO. The HOMOs are admixed with Pt metal d-orbital character and dithiolate character for Pt(phen)(bdt), diselenolate character for Pt(phen)(bds), and quinoxalinedithiolate character for Pt(phen)(qdt). The quinoxaline ring has a higher electron withdrawing properties than the benzene ring due to the difference in electronegativity of the nitrogen atom compare to carbon atom, i.e. 3.04 for nitrogen atom and 2.55 for carbon atom. The electron withdrawing capability of quinoxalinedithiolate lowers the energy of the HOMO orbital of Pt(phen)(qdt) with respect to benzenoid-systems of Pt(phen)(bdt) and Pt(phen)(bds). This result in an increase in the HOMO-LUMO energy gap and hence a higher energy of the CT band maximum. The above reasons explain why the energy of the CT band maxima is higher in Pt(phen)(qdt) than in Pt(phen)(bdt) and Pt(phen)(bds).

3.2.9.2 Transient Absorption Spectra, Emission Spectra, and Lifetimes

The emission spectra for Pt(phen)(bdt) (blue), Pt(phen)(bds) (green) and Pt(phen)(qdt) (red) in degassed CH_2Cl_2 solution are depicted in Figure 3.54. The emission spectrum of Pt(phen)(bdt) was recorded at an absorption band of 716 nm with an excitation wavelength of 570 nm, while that of Pt(phen)(bds) and Pt(phen)(qdt) were measured at 720 and 620 nm absorption band with an excitation wavelength of 570 and 460 nm respectively. The emission maxima (λ_{max}^{Em}) for Pt(phen)(bdt), Pt(dbbpy)(bds) and Pt(dbbpy)(qdt) are 13970 cm^{-1} (716

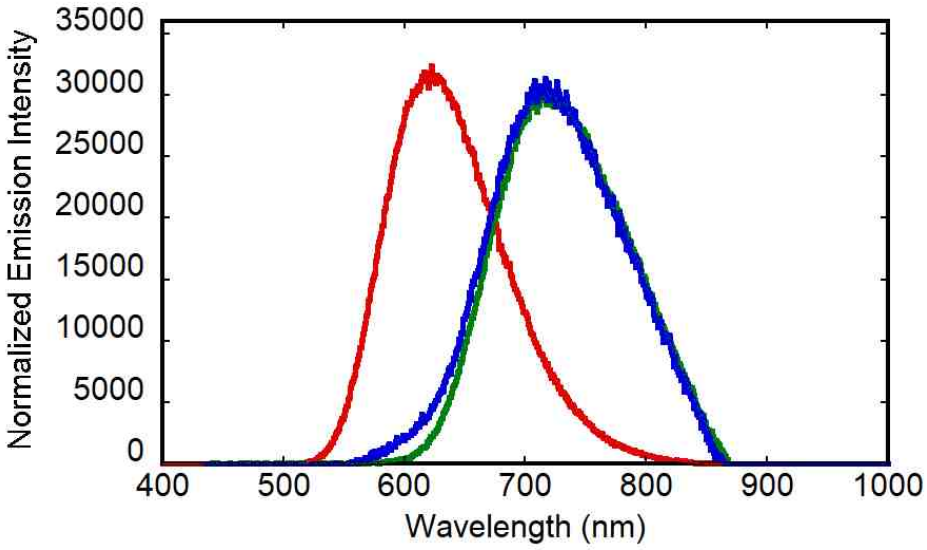

Figure 3.54: Overlay of normalized emission spectra for Pt(phen)(bdt) (blue) @ 716 nm excited at 570 nm, Pt(dbbpy)(bds) (green) @ 720 nm excited at 570 nm and Pt(dbbpy)(qdt) (red) @ 620 nm excited at 460 nm, power 30 Mw in degassed CH_2Cl_2 solution at 298 K.

nm), 13890 cm^{-1} (720 nm), and 16130 cm^{-1} (620 nm) respectively. The 298 K emission profiles for these complexes depicted in Figure 3.54 are symmetric with no shoulders separated from the spectra. The calculated stokes shift for Pt(phen)(bdt), Pt(phen)(bds), and Pt(phen)(qdt) are 3540, 3560 and 5560 cm^{-1} respectively.

Nanosecond TA spectroscopy was performed on Pt(phen)(bdt), Pt(phen)(bds), and Pt(phen)(qdt) complexes in deoxygenated dichloromethane solution at ambient temperature and the results are presented in Figures 3.55, 3.56, 3.57 3.58 and 3.59. Figure 3.55 depicts kinetic emission trace for (a) Pt(phen)(bds) at 720 nm with a 570 nm excitation pulse, (b) Pt(phen)(qdt) at 620 nm with 460 nm excitation pulse and (c) Pt(phen)(bdt) at 716 nm with 570 nm excitation pulse.

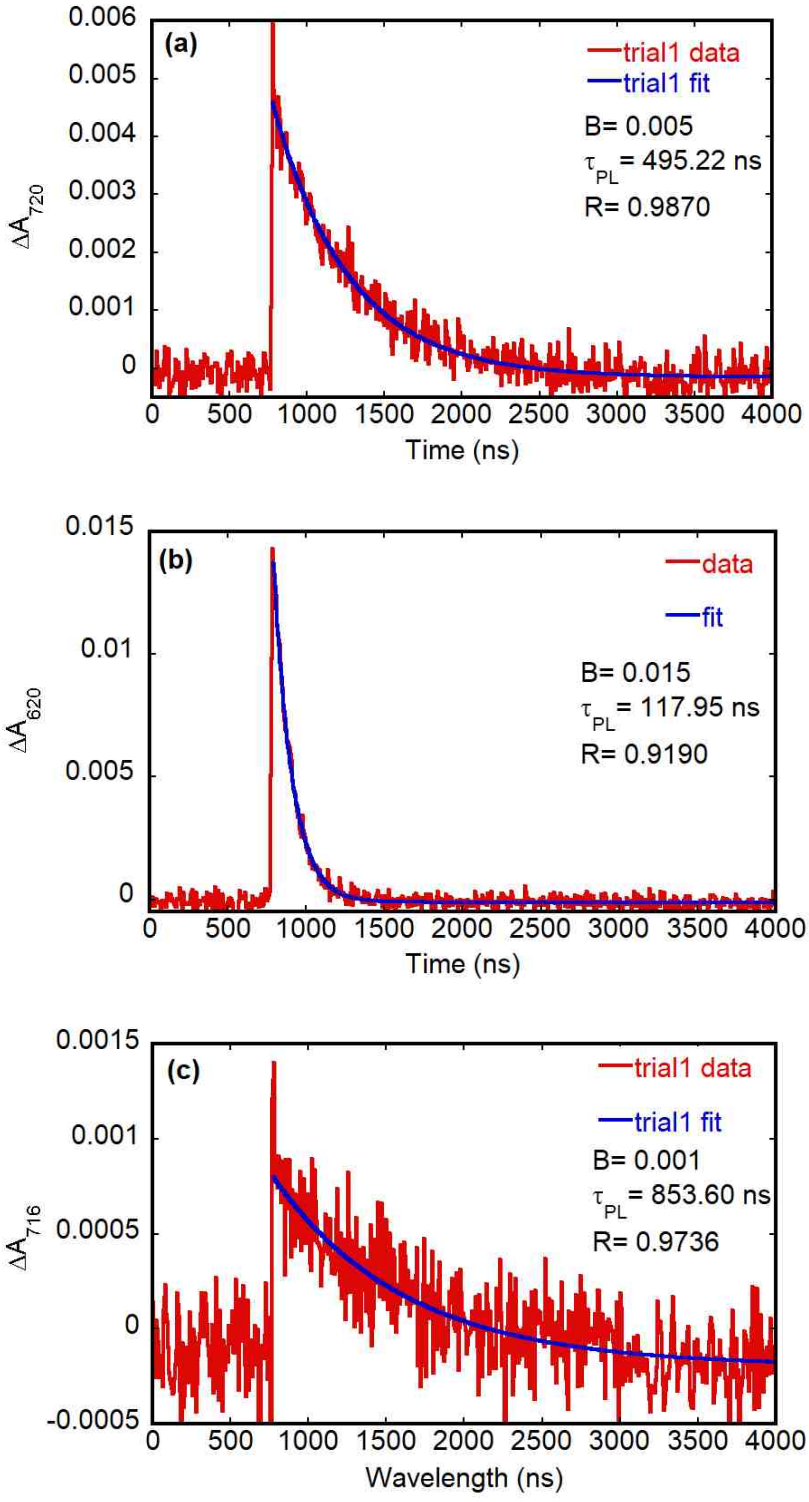

Figure 3.55: Kinetic emission trace for **(a)** Pt(phen)(bds) at 720 nm excited @ 570 nm **(b)** Pt(phen)(qdt) at 620 nm excited @ 460 nm **(c)** Pt(phen)(bdt) at 716 nm excited @ 570 nm in fluid solution of degassed CH_2Cl_2, excited at 470 nm, power: 30 mW.

The overall photoluminescence profile decays with a lifetime (τ_{PL}) of 854 ± 10, 495 ± 10, and 118 ± 10 ns for Pt(phen)(bdt), Pt(phen)(bds), and Pt(phen)(qdt) respectively. Pt(phen)(qdt) has the shortest emission lifetime followed by Pt(phen)(bds) and then Pt(phen)(bdt). The emission lifetime signifies the regeneration of the ground state after electron is transferred from the LL'CT excited state. Depicted in Figure 3.56 are the transient absorption (TA) map for Pt(phen)(bdt), Pt(phen)(bds), and Pt(phen)(qdt) in fluid solution of deoxygenated CH_2Cl_2 at 298 K. The TA spectrum of Pt(phen)(bds) was collected with a 570 nm excitation pulse, and it shows excited state absorption (ESA) with a broad positive signal at $\lambda < 420$ nm and $\lambda > 620$ nm. A ground state bleach (GSB) is observed from 420 to 620 nm with a more negative signal centered at 586 nm. The kinetic absorption trace for Pt(phen)(bds) depicted in Figure 3.57 (a) was monitored at a transient absorbance of 473 nm. The overall transient absorption profile decays with a lifetime (τ_{TA}) of 490 ± 10 ns. Figure 3.57 (b) depicts the kinetic trace for the growth process of the ground state bleach (GSB) with a lifetime of 482 ± 10 ns. The pre-exponential factors (B) which represent the amplitude of the curves under study at time zero is -0.019. The negative value of B signifies a growth process. The kinetic traces for the decay and growth processes of Pt(phen)(bds) (Figure 3.57) occur with very similar lifetimes, indicating that both excited state absorption (ESA) and ground state bleach (GSB) relaxes back to the ground state with the same time constant.

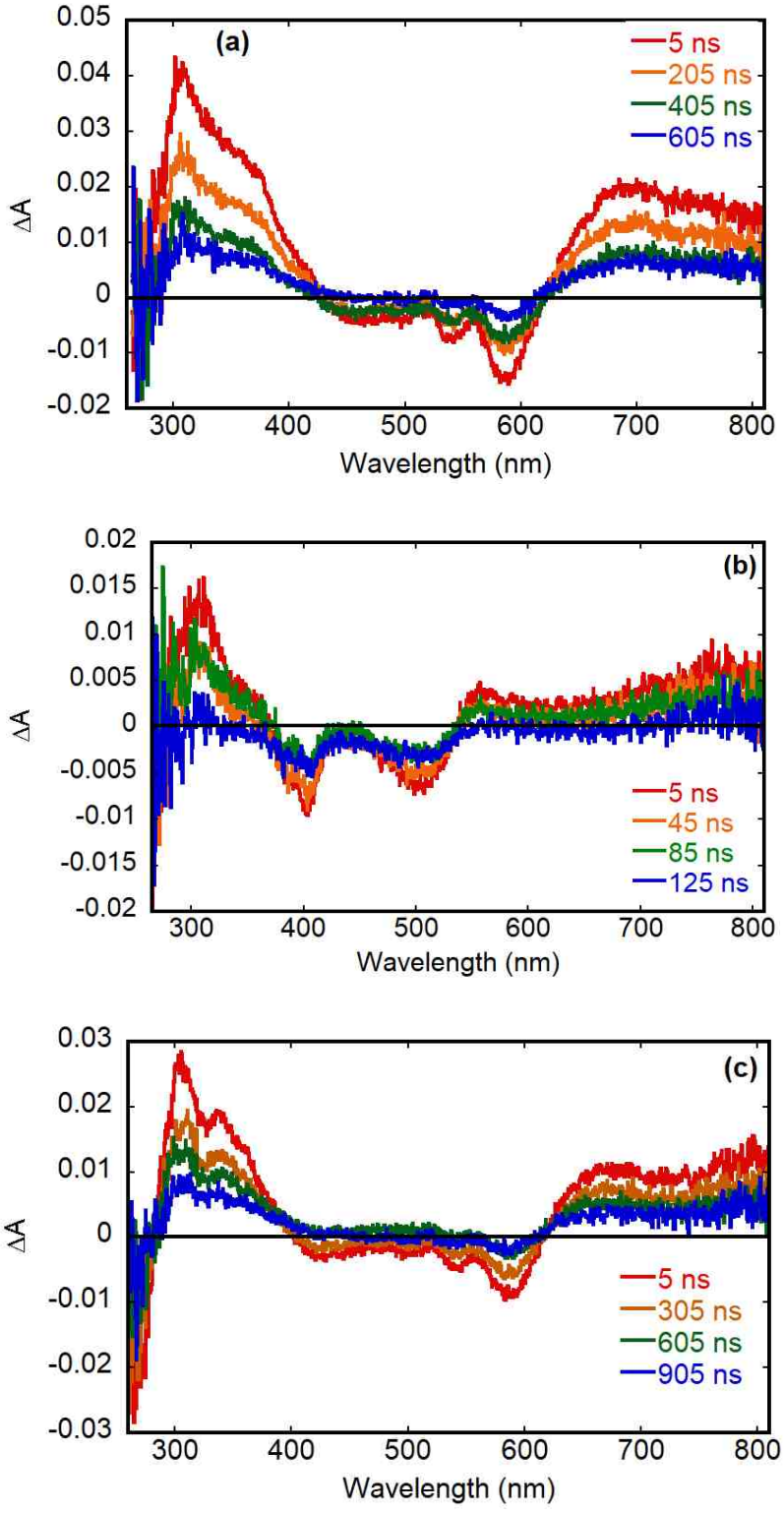

Figure 3.56: (a) TA map for (a) Pt(phen)(bds) excited @ 570 nm, start: 5 ns, end: 605 ns, step: 200 ns **(b)** Pt(phen)(qdt) excited @ 460 nm, start: 5 ns, end: 125 ns, step: 40 ns **(c)** Pt(phen)(bdt) excited @ 570 nm, start: 5 ns, end: 905 ns, step: 300 ns in fluid solution of degassed CH_2Cl_2, power: 35 mW.

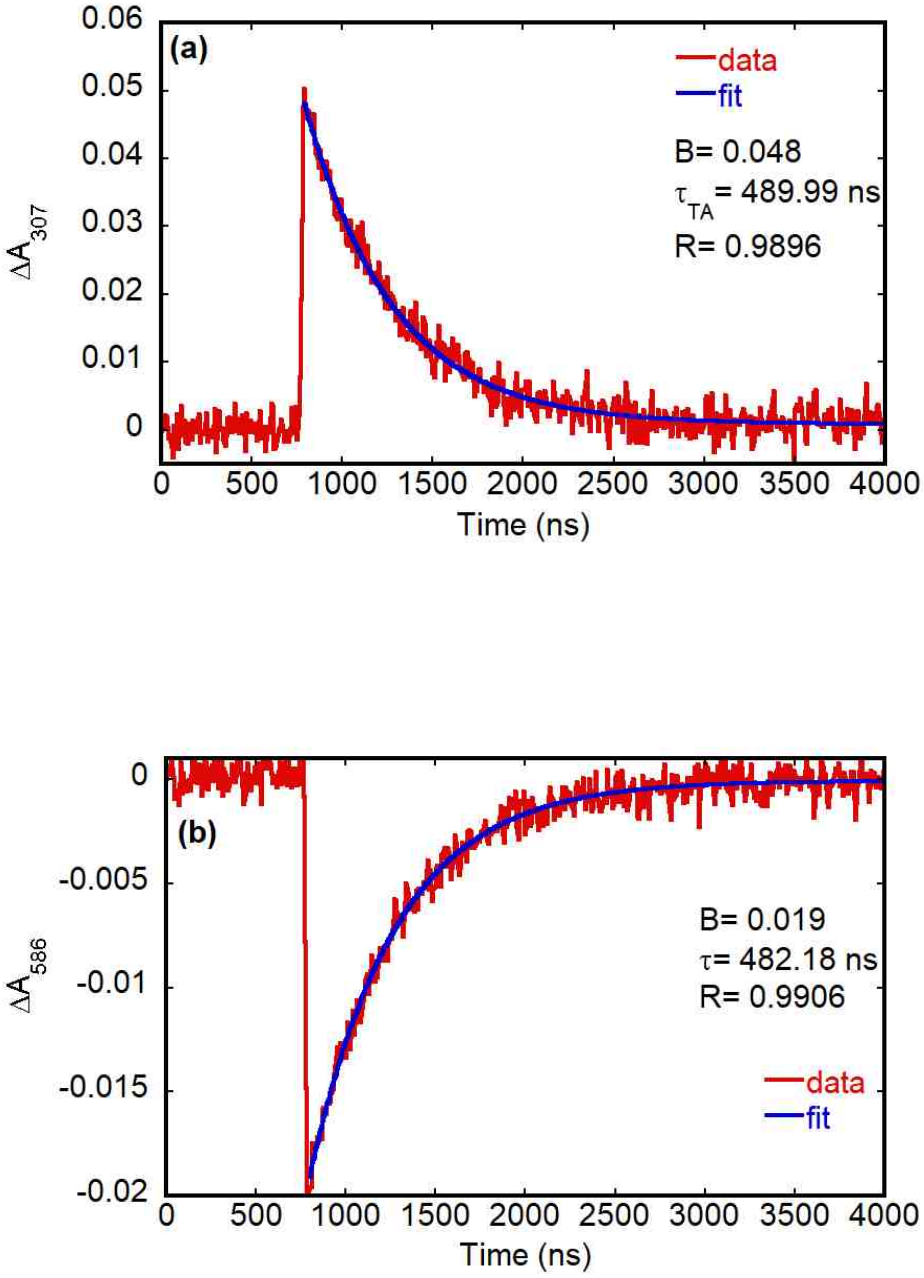

Figure 3.57: Kinetic Absorption traces for Pt(phen)(bds) **(a)** at 307 nm excited @ 570 nm, **(b)** at 586 nm excited @ 570 nm in fluid solution of degassed CH_2Cl_2, power: 35 mW.

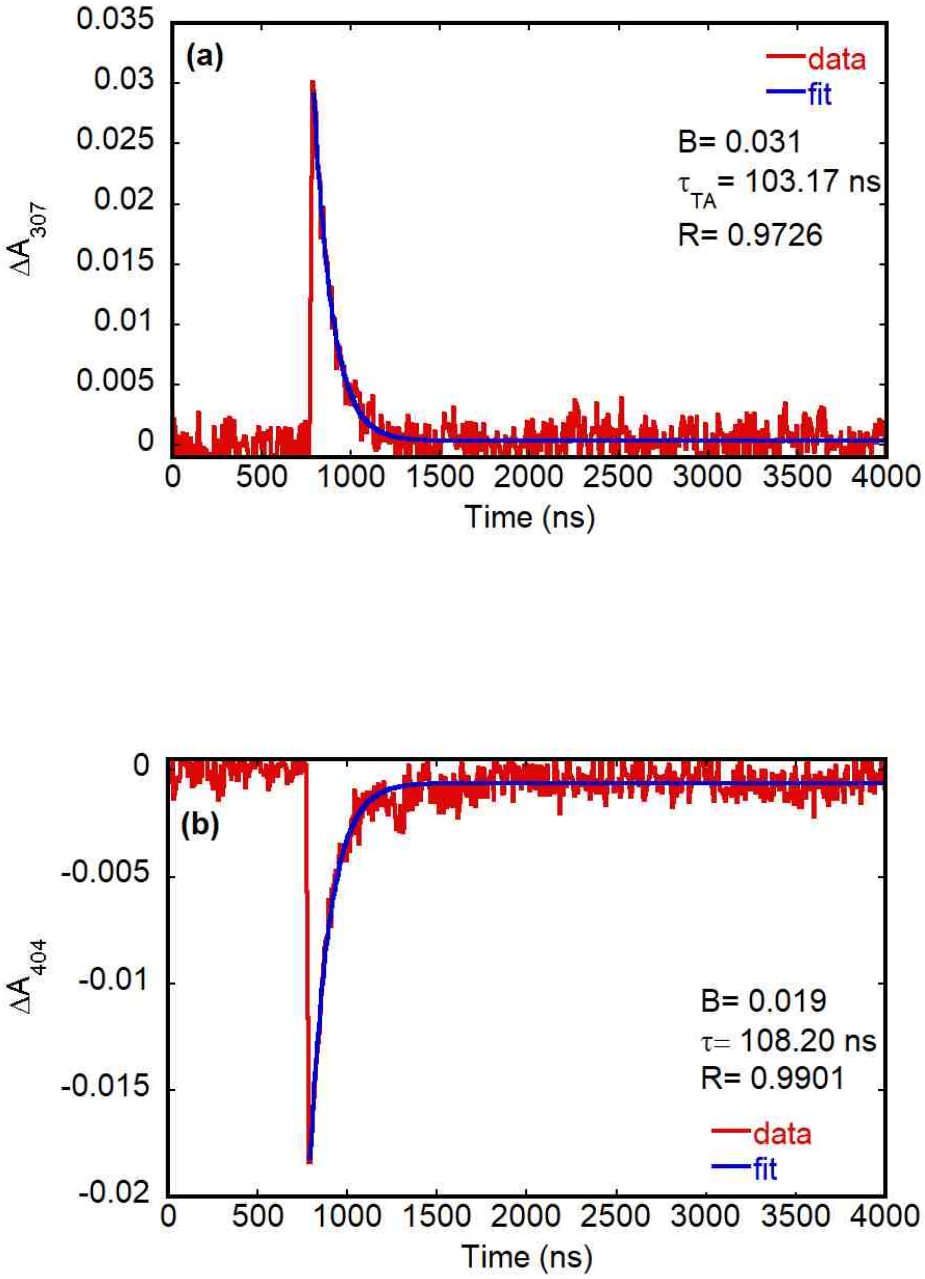

Figure 3.58: Kinetic Absorption traces for Pt(phen)(qdt) **(a)** at 307 nm excited @ 570 nm, **(b)** at 404 nm excited @ 460 nm in fluid solution of degassed CH_2Cl_2, power: 35 mW.

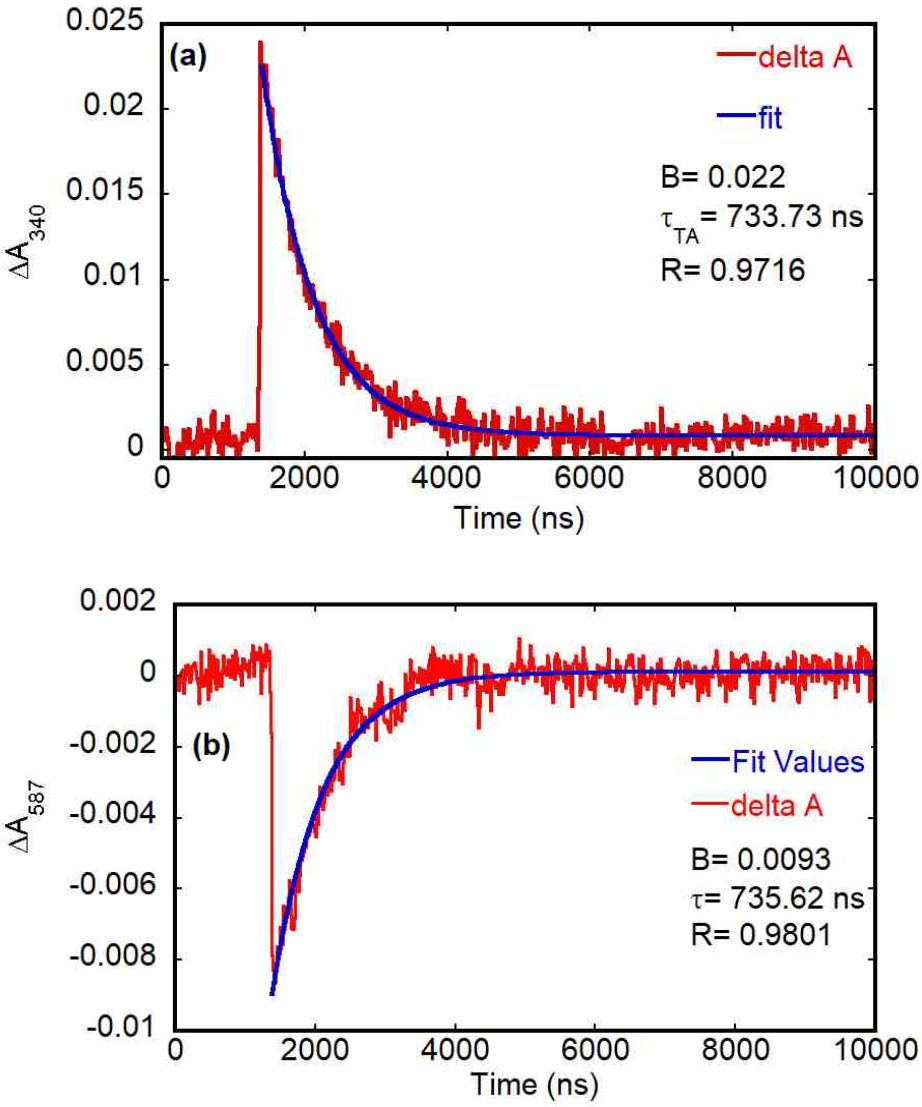

Figure 3.59: Kinetic Absorption traces for Pt(phen)(bdt) (a) at 340 nm excited @ 570 nm, (b) at 587 nm excited @ 570 nm in fluid solution of degassed CH_2Cl_2, power: 35 mW.

The pictorial presentation of the kinetic trace of Pt(phen)(qdt) is depicted in Figure 3.58. The lifetimes for the ESA decay (103 ± 10 ns) and GSB (108 ± 10 ns) growth processes are very comparable signifying very similar time constants relaxation back to the ground state. ESA decay and GSB growth processes for Pt(phen)(qdt) are short-lived compared to that of Pt(phen)(bds) which has a

longer lifetime.

The kinetic absorption trace for Pt(phen)(bdt) is presented in Figure 3.59. The ESA decay process for Pt(phen)(bdt), Figure 3.59 (a) was obtained by monitoring transient absorbance at 340 nm in fluid solution of degassed CH_2Cl_2 at 298 K. The overall transient absorption profile decays with a lifetime (τ_{TA}) of 734 ± 10 ns. GSB growth process spectrum was acquired by monitoring the transient absorbance at 587 nm. The growth process lifetime observed for Pt(phen)(bdt) is 736 ± 10 ns. Both the decay and growth processes occur with the same lifetimes, demonstrating the same relaxation back to the ground state.

By comparing the lifetimes of Pt(phen)(bds), Pt(phen)(qdt), and Pt(phen)(bdt) (see Table 3.5), it can be ascertained that Pt(phen)(qdt) has the shortest lifetime, followed by Pt(phen)(bds) and then Pt(phen)(bdt).

Table 3.5: Photophysical Properties of seven (7) Pt(diimine)(dichalcogenolene) Complexes.

Complex	λ_{max}^{Abs} (nm)	λ_{max}^{Abs} (cm^{-1})	λ_{max}^{Em} (nm)	λ_{max}^{Em} (cm^{-1})	$\Delta\tilde{\nu}$[a]	τ_{PL} (ns)[b]	$\tau_{trip\ abs}$ (ns)[c]	$\tau_{GS\ dep}$ (ns)[d]
Pt(NN)[d](pdt)	487	20530	642	15580	4950	105 ± 10	135 ± 10	133 ± 10
Pt(NN)[d](pds)	504	19840	630	15870	3970	5 ± 0.5	-	-
Pt(NN)[d](qdt)	473	21140	604	16560	4580	12 ± 2	12 ± 2	10 ± 2
Pt(NN)[d](qds)	485	20620	683	14640	5980	4 ± 2	-	-
Pt(NN)[e](bdt)	571	17510	716	13970	3540	854 ± 10	734 ± 10	736 ± 10
Pt(NN)[e](qdt)	461	21690	620	16130	5560	118 ± 10	103 ± 10	108 ± 10
Pt(NN)[e](bds)	573	17450	720	13890	3560	495 ± 10	490 ± 10	482 ± 10

[a] $\Delta\tilde{\nu}$ = stokes shift in cm^{-1}, [b]PL = photoluminescence, [c]Trip abs = triplet absorption, [d]GS dep = ground state depletion, ε_{max} = emission maxima, E_{abs} = Energy of the absorption maxima, λ_{abs} = wavelength of maximum absorption, $(NN)^d$ = (dbbpy), $(NN)^e$ = (phen)

3.2.10 [Pt(dbbpy)(mcp)]

3.2.10.1 Electronic Absorption Spectroscopy and Emission Spectrum

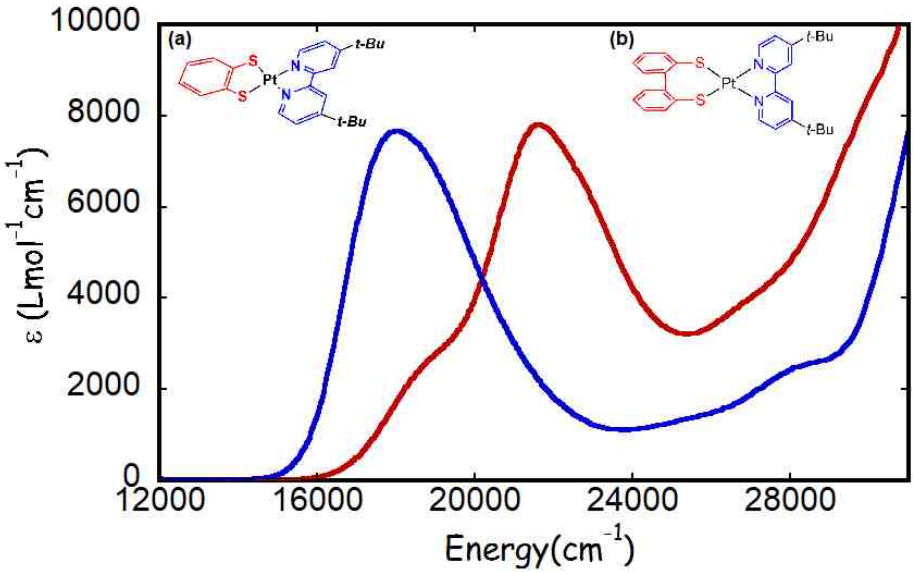

Figure 3.60: Overlay of electronic absorption spectra of Pt(dbbpy)(bdt) (blue), and Pt(dbbpy)(mcp) (red) in CH_2Cl_2 at 289 K. Inset: Compound structure: **(a)** for Pt(dbbpy)(bdt) and **(b)** for Pt(dbbpy)(mcp).

The electronic absorption spectrum of 4,4'-di-tert-butyl-2,2'-bipyridineplatinum(II)-(2,2'-dimercatpto-biphenyl), [Pt(dbbpy)(mcp)] in dichloromethane solution at 298 K is depicted in Figure 3.60. Also included in Figure 3.60 is the UV-vis spectrum of Pt(dbbpy)(bdt) for comparison. The CT absorption maxima and the molar extinction coefficient of Pt(dbbpy)(mcp) and Pt(dbbpy)(bdt) are 21600 cm^{-1} (463 nm), 7810 $M^{-1}cm^{-1}$ and 18350 cm^{-1} (545 nm), 7700 $M^{-1}cm^{-1}$ respectively. By changing the donor ligand of Pt(dbbpy)(bdt) from 1,2-benzenedithiol (bdt) to 2,2'-dimercatptobiphenyl (mcp) in Pt(dbbpy)(mcp), CT absorption maxima of Pt(dbbpy)(mcp) is blue shifted with respect to Pt(dbbpy)(bdt). From TD-DFT calculation, the MMLL'CT is designated as HOMO → LUMO. From Table 3.14,

the HOMO-LUMO energy gap calculated for Pt(dbbpy)(bdt) and Pt(dbbpy)(mcp) are 1.84 eV (14840 cm^{-1}) and 2.12 eV (17100 cm^{-1}) respectively. Based on the TD-DFT calculation, we can conclude that the CT absorption maxima for Pt(dbbpy)(mcp) would be blue shifted (higher energy) with respect to that of

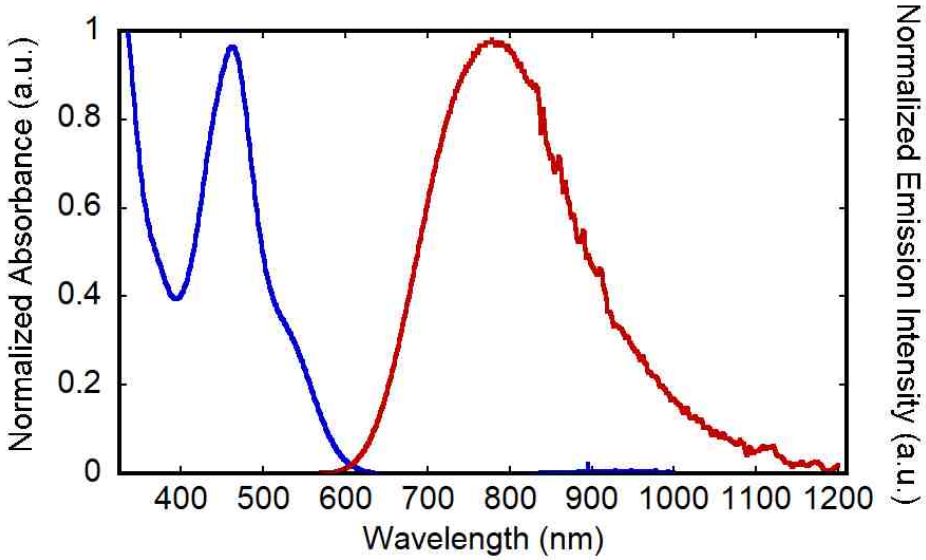

Figure 3.61: Overlay of Absorption (blue) and Emission (red) spectra of Pt(dbbpy)(mcp) in degassed CH_2Cl_2 solution at 298 K.

Pt(dbbpy)(bdt). The 298 K emission with excitation wavelength of 460 nm in deoxygenated dichloromethane fluid solution for Pt(dbbpy)(mcp) is presented in Figure 3.61. The room-temperature fluid solution emission spectrum for Pt(dbbpy)(mcp) has emission maxima (ε_{max}) at 785 nm (12740 cm^{-1}) and the calculated stokes shift is 8860 cm^{-1}.

3.2.10.2 X-ray Crystallography

The crystal structure of 4,4'-di-tert-butyl-2,2'-bipyridineplatinum(II)(2,2'-

dimercatpto-biphenyl), Pt(dbbpy)(mcp) was analyzed at the UNM X-ray Laboratory. A red rod-like specimen of $C_{31}H_{34}Cl_2N_2PtS_2$, approximate dimensions 0.220 mm x 0.326 mm x 0.538 mm, was used for the X-ray crystallographic analysis. The X-ray intensity data were measured on a Bruker Kappa APEX II CCD system equipped with a graphite monochromator and a Mo Kα fine-focus tube (λ = 0.71073 Å) operated at 1500 W power (50 kV, 30 mA). The temperature of the X-ray intensities was record at 100(2) K and the detector was located at 4.50 cm from the crystal. A total of 3763 frames were collected. The total exposure time was 4.18 hours. The frames were integrated with the Bruker SAINT software package using a narrow-frame algorithm. The integration of the data using a triclinic unit cell yielded a total of 55926 reflections to a maximum θ angle of 30.55° (0.70 Å resolution), of which 9266 were independent (average redundancy 6.036, completeness = 99.9%, R_{int} = 2.84%, R_{sig} = 2.09%) and 8725 (94.16%) were greater than $2\sigma(F^2)$. The final cell constants of a = 9.6715(3) Å, b = 13.0150(4) Å, c = 13.1340(4) Å, α = 89.8830(10)°, β = 80.7380(10)°, γ = 68.2900(10)°, volume = 1512.96(8) $Å^3$, are based upon the refinement of the XYZ-centroids of 9933 reflections above 20 σ(I) with 4.469° < 2θ < 61.10°. Data were corrected for absorption effects using the multi-scan method (SADABS). The ratio of minimum to maximum apparent transmission was 0.608. The calculated minimum and maximum transmission coefficients (based on crystal size) are 0.1750 and 0.4070.

The structure was solved and refined using the Bruker SHELXTL Software

Package, using the space group P -1, with Z = 2 for the formula unit, $C_{31}H_{34}Cl_2N_2PtS_2$. Non-hydrogen atoms were refined anisotropically. Hydrogen atoms were placed in geometrically calculated positions with U_{iso} = 1.2U_{equiv} of the parent atom (U_{iso} = 1.5U_{equiv} for methyl groups). One chlorine atom of the co-crystallized CH_2Cl_2 solvent molecule was found to be disordered over two positions. The occupancy of each position was allowed to refine freely, converging at 50/50. The final anisotropic full-matrix least-squares refinement on F^2 with 359 variables converged at R1 = 2.29%, for the observed data and wR2 = 6.21% for all data. The goodness-of-fit was 1.092. The largest peak in the final difference electron density synthesis was 1.004 $e^-/Å^3$ and the largest hole was 2.238 $e^-/Å^3$ with an RMS deviation of 0.133 $e^-/Å^3$. Based on the final model, the calculated density was 1.679 g/cm^3.

Results

Molecular Crystal Structure

The crystal structure of (dbbpy)Pt(mcp) is shown in Figure 3.62. Red rod-like crystals of (dbbpy)Pt(mcp) were grown in the presence of air by slow evaporation of saturated CH_2Cl_2 solution in the dark for 10 days at ambient temperature. Table 3.6 contains the crystallographic date for (dbbpy)Pt(mcp) complex. The comparison of calculated selected bond lengths (Å) with experimental values from X-ray analysis is given in Table 3.6. Figure 3.62 presents the ORTEP diagram for (dbbpy)Pt(mcp) complex showing the numbering scheme of all the atoms in the complex. The solvent molecule, dichloromethane (CH_2Cl_2)

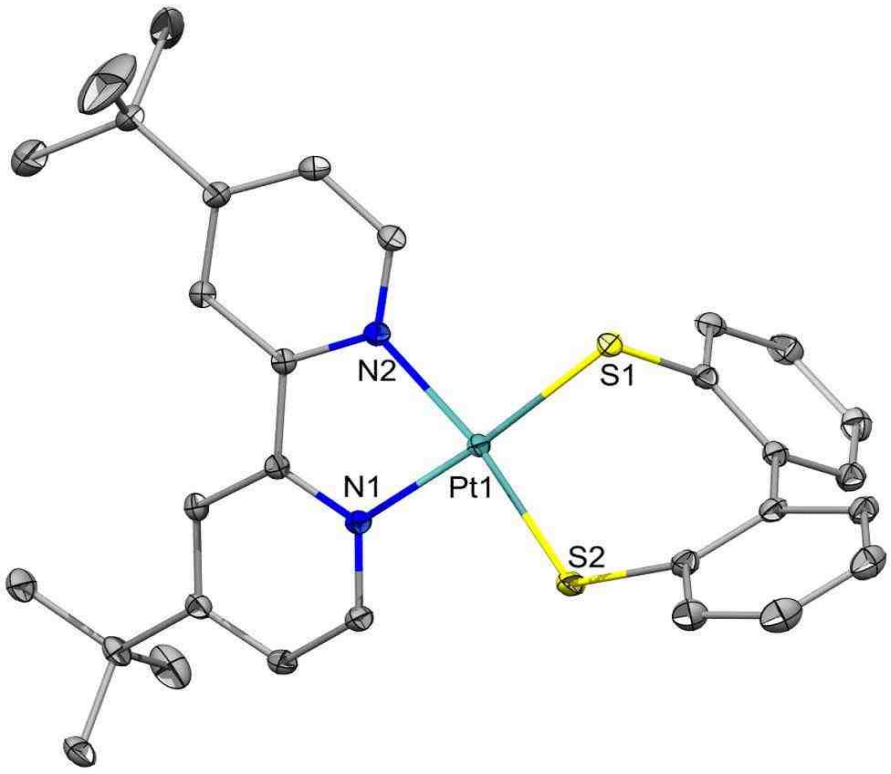

Figure 3.62: Crystal structure of (dbbpy)Pt(mcp).

cocrystallized with the (dbbpy)Pt(mcp) complex as shown in Figure 3.62**.** The selected bond lengths and angles for the complex are presented in Table 3.6 and Table 3.7 respectively. (dbbpy)Pt(mcp) complex possesses a distorted square planar coordination geometry with a C_2 symmetry. The plane of the molecule contains a five-membered ring and the out-of-plane contains a seven-membered ring. The coordination geometry about the Pt(II) ion can be described as a square planar that is distorted towards dithiolate sulfur atoms. Having dithiolate ligand with sulfur atoms on the two adjacent but attached phenyl groups ends up in a preferable formation of a cleft in which the Pt(II) center residues.[9] The experimental Pt-N distances of 2.062(2), and 2.046(2) Å are in close agreement with the calculated (2.113 Å). The average experimental Pt-N distance is the

Table 3.6: X-ray Crystallographic Data for (dbbpy)Pt(mcp).

Crystallographic Data	(dbbpy)Pt(mcp)●CH_2Cl_2
empirical formula	$C_{31}H_{34}Cl_2N_2PtS_2$ [a]
fw, $gmol^{-1}$	764.71
crystal system	triclinic
crystal habit	red rod
space group	P-1
a, Å	9.672(3)
b, Å	13.015(4)
c, Å	13.134(4)
α, deg	89.883(10)
β, deg	80.738(10)
γ, deg	68.290(10)
V, $Å^3$	1512.96
Z	2
T, K	100(2)
R1[b]	0.0229
wR2[b]	0.0621
GOF $(F^2)^b$	1.092

[a] A solvent molecule (CH_2Cl_2) was cocrystallized with the complex.

[b] R1 = $\sum ||F_0 - |F_c||/\sum |F_0|$ (55926 reflections collected, $I > 2\sigma(I)$);

wR2 =$[\sum[w|F_0^2 - F_c^2|^2]/w(F_0^2)^2]^{½}$; GOF = $[\sum[w|F_0^2 - F_c^2|^2]/(n-p)]^{½}$, where n and p represent the number of data and number of parameters refined respectively.

same as those observed for its (bpy)Pt(bdt) analog i.e. (2.050(4), and 2.049(5) Å)[10]. The Pt-N bond lengths are significantly longer than that found for its yellow Pt(bpy)Cl_2 derivative, i.e. 2.009(6) and 2.010(1) Å.[11,12] The observed Pt-S

distances, 2.290(6) and 2.272(7) Å) agree well with the calculated values found in Table 3.7. The Pt-S bond lengths are typically short, proposing a strong Pt-S interaction. These bond lengths are like other Pt(diimine)(dithiolate) complexes[60] such as Pt(bpm)(mnt), 2.244(2), and 2.254(2) Å, where mnt and bpm are maleonitriledithiolate and 2,2'-bipyrimidine respectively;[61] Pt(dpphen)(dtbdt), 2.2514(4), 2.244(4) Å, dtbdt = 3,5-di-*tert*-butylbenzene-1,2-dithiolate, dpphen = 4,7-diphenyl-1,10-phenanthroline,[2]

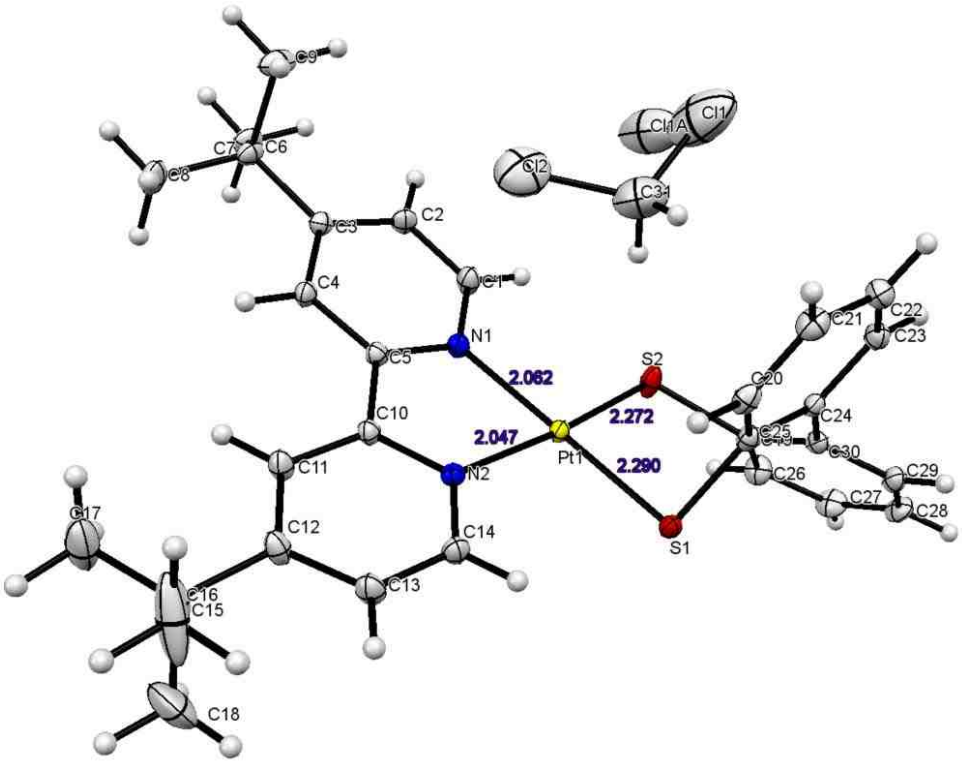

Figure 3.63: Molecular structure and atom numbering (ORTEP diagram) for (dbbpy)Pt(mcp). Thermal ellipsoids are at 50% probability level.

Pt(dmbpy)(met), 2.245(2), 2.244(2) Å,[15] (where dmbpy is 4,4'-dimethyl-2,2'-bipyridine, met = cis-1,2-dicarbomethoxyethylene-1,2-dithiolate). The Pt-S bond distances in (dbbpy)Pt(mcp) are shorter than that found in complexes with

phosphine ligands (e.g. Pt(dppe)(mnt), 2.303(2) and 2.296(2) Å), where dppe represents 1,2-bis(diphenylphospino).[15] The C-S bond lengths in Table 3.7 agree very well with the free ligand (2,2'-dimercatptobiphenyl), i.e. 1.764(8)- 1.783(8).[62] Both the experimental (78.8^0) and calculated (77.4^0) N-Pt-N bond angles are in

Table 3.7: Comparison of Calculated Selected Bond Lengths (Å) with experimental values from X-ray analysis for (dbbpy)Pt(mcp).

	Experimental	**Calculated**
Pt1-N1	2.062(2)	2.113
Pt1-N2	2.046(2)	2.113
Pt1-S1	2.290(6)	2.347
Pt1-S2	2.272(7)	2.347
N1-C1	1.341(3)	1.345
N1-C5	1.352(3)	1.345
N2-C14	1.341(3)	1.345
N2-C10	1.352(3)	1.357
S1-C19	1.776(3)	1.794
S2-C25	1.776(3)	1.794
C5-C10	1.471(3)	1.477
C19-C24	1.403(4)	1.413
C24-C30	1.484(4)	1.491
C25-C30	1.407(4)	1.413

close agreement. Additionally, the metal identity does not have a big structural

effect on dithiolate ligands due to the fact the C-S bond lengths are similar, i.e. 1.776(3) Å for (dbbpy)Pt(mcp), 1.761(6) Å for (bpy)Pt(bdt) and 1.762(2) Å for (bpy)Pd(bdt).[63]

Comparing the two complexes, Pt(dbbpy)(mcp) and Pt(bpy)(bdt), their structures are less distorted around the Pt center. The S1-Pt-S2, N1-Pt-N2, N1-Pt-S2, and N2-Pt-S1 bond angles are all close to a perfect square planar (90^0), for Pt(dbbpy)(mcp) being 92.2(2), 78.7(8), 93.9(6), and $95.5(6)^0$ respectively and Pt(bpy)(bdt) being 89.0(1), 80.1(2), 95.4(1), and $95.7(1)^0$ respectively.[61] The dihedral angle between N1-Pt-N2 and S1-Pt-S2 planes are 6.57 and 7.00^0 respectively for Pt(dbbpy)(mcp) and Pt(bpy)(bdt). These values are slightly closer to a perfect flat geometry with a 0^0 dihedral angle.[2]

The crystal structure of (dbbpy)Pt(mcp) was analysis for intermolecular interactions because of their effect on optical spectroscopy.[64] The two intermolecular interactions of square-planar Pt(II) complexes that are significant are Pt—Pt interaction and π-to-π interactions of the aromatic α-diimine ligands.[65,66] Due to the bulky tert-butyl groups, both Platinum chromophores lack close packing in the unit cell as depicted in Figure 3.63**.** Square planar Pt(II) complexes normally undergo molecular stacking in the solid state and the lack of stacking in (dbbpy)Pt(mcp) is very important. The Pt—Pt and π-to-π distances in a crystal packing arrangement are 3.24 and 3.51 Å respectively.[67,59,68] The Pt—Pt distance in Figure 3.63 is 5.670 Å, this value is significantly larger indicating that the presence of bulky tert- butyl groups on the ligand is averting the packing of the Pt chromophores in the crystal.[2]

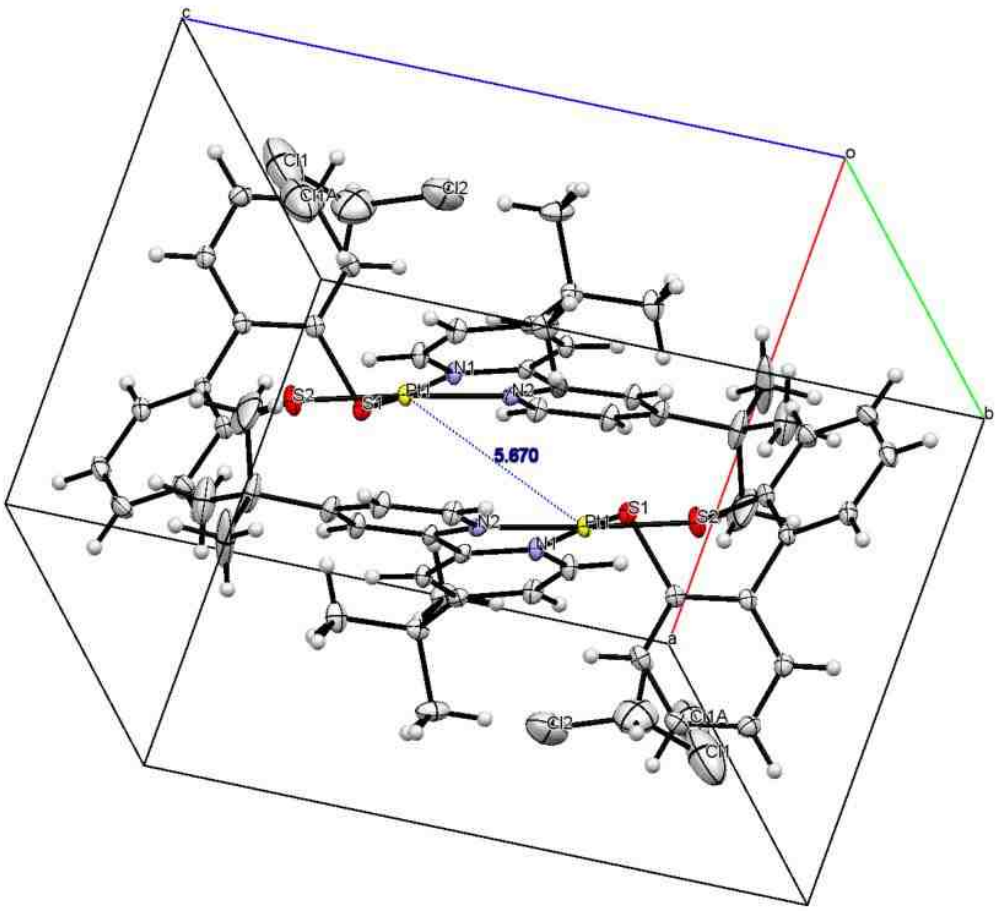

Figure 3.64: P**t**(dbbpy)(mcp) crystal packing arrangement.

3.2.11 [Pt(dbbpy)(tbp)$_2$] and [Pt(dbbpy)(tbt)$_2$]

3.2.11.1 Electronic Absorption Spectroscopy

The electronic absorption spectra of 4,4'-di-tert-butyl-2,2'-bipyridineplatinum(II)-(bis-4-tert-butylbenzenethiolate), [Pt(dbbpy)(tbt)$_2$] and 4,4'-di-tert-butyl-2,2'-bipyridineplatinum(II)(bis-4-tert-butylphenolate), [Pt(dbbpy)(tbp)$_2$] in dichloromethane at 298 K are presented in Figure 3.66. Also, presented pictorially in Figure 3.65, is the overlay of the UV-vis spectra of Pt(dbbpy)(bdt)

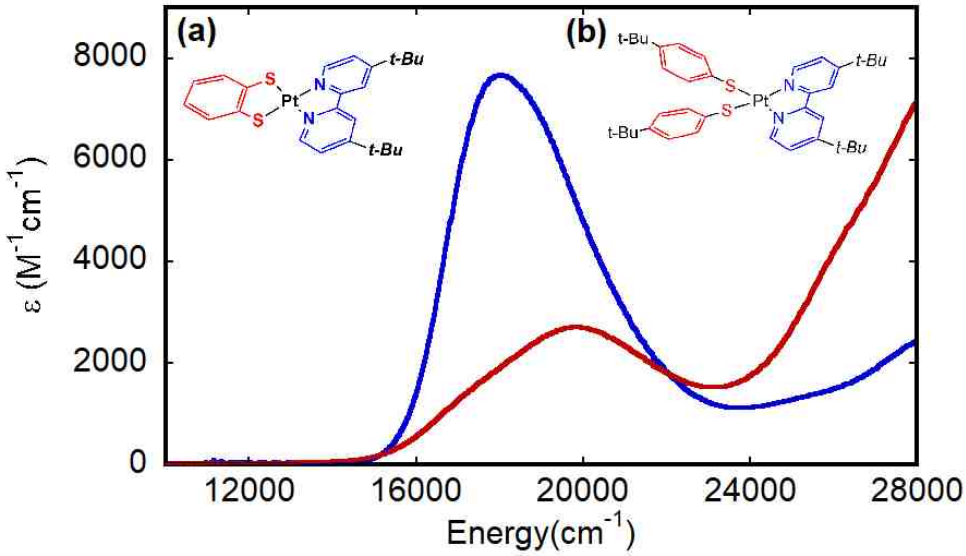

Figure 3.65: Overlay of electronic absorption spectra for Pt(dbbpy)(bdt) (blue), and Pt(dbbpy)(tbt)$_2$ (red) in CH_2Cl_2 at 289 K. Inset: Compound structure: **(a)** for Pt(dbbpy)(bdt) and **(b)** for Pt(dbbpy)(tbt)$_2$.

(blue), and Pt(dbbpy)(tbt)$_2$ (red) for comparison. The CT absorption maxima and the molar extinction coefficient for Pt(dbbpy)(tbt)$_2$ and Pt(dbbpy)(bdt) are 19850 cm^{-1} (504 nm), 2800 $M^{-1}cm^{-1}$ and 18350 cm^{-1} (545 nm), 7700 $M^{-1}cm^{-1}$ respectively. By changing the donor ligand of Pt(dbbpy)(bdt) from 1,2-benzenedithiol (bdt) to bis-4-tert-butylbenzenethiolate (tbt) in Pt(dbbpy)(tbt)$_2$, CT absorption maxima of Pt(dbbpy)(tbt)$_2$ is blue shifted by 1500 cm^{-1}. The molar extinction coefficient of Pt(dbbpy)(bdt) is about 2.75 times larger than that of Pt(dbbpy)(tbt)$_2$ which implies that it has greater absorption of light than that of Pt(dbbpy)(tbt)$_2$. The CT absorption maxima for Pt(dbbpy)(tbp)$_2$ is at 535 nm (18700 cm^{-1}) with the molar extinction coefficient of 680 $M^{-1}cm^{-1}$ (see Figure 3.66). The molar extinction coefficient for the lowest energy visible absorption

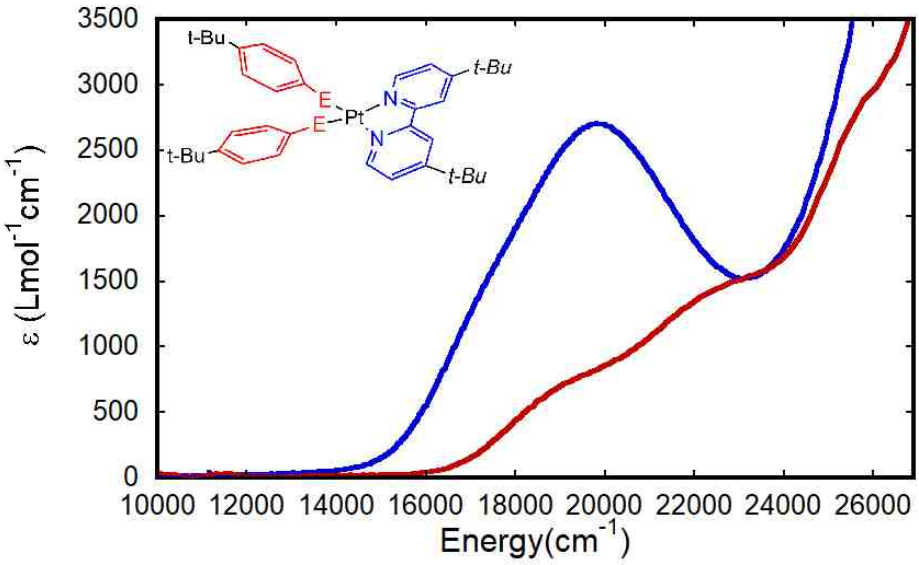

Figure 3.66: Overlay of electronic absorption spectra for Pt(dbbpy)(tbt)$_2$ (blue), and Pt(dbbpy)(tbp)$_2$ (red) in CH_2Cl_2 at 289 K. Inset: X=S for Pt(dbbpy)(tbt)$_2$ and X=O for Pt(dbbpy)(tbp)$_2$.

band for Pt(dbbpy)(tbt)$_2$ is about 4 times higher than that of Pt(dbbpy)(tbp)$_2$. The absorption maximum is recorded only for the lowest-energy band, even though additional absorption feature occurs at higher energies i.e. 22220 cm^{-1} (450 nm). The molar extinction coefficient for the lowest energy visible absorption band for Pt(diimine)(dichalcogenolene) complexes with bidentate dichalcogenide ligands are much greater than the complexes with monodentate ligands (Figure 3.65). The reason for much higher molar extinction coefficient for Pt(diimine)(dichalcogenolene) complexes with bidentate dichalcogenide ligands can be ascribed to better mixing of bidentate dichalcogenide ligands with Pt d-orbitals.[2] The photoluminescence properties of Pt(dbbpy)(tbp)$_2$ and Pt(dbbpy)(tbt)$_2$ were observed at room-temperature in a degassed

dichloromethane fluid solution at an excitation wavelength of 460 nm. The ambient temperature (298 K) emission and

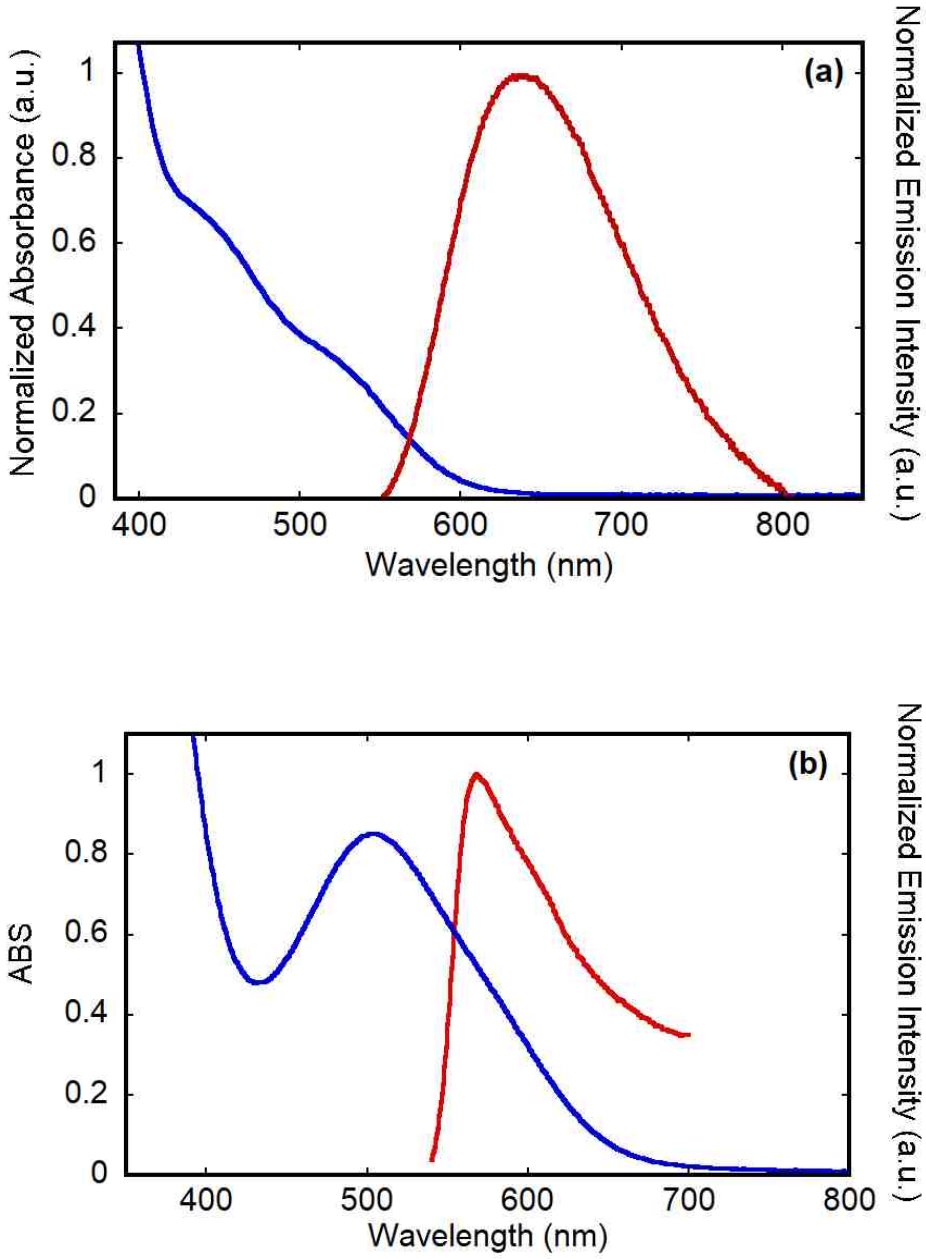

Figure 3.67: Overlay of Absorption (blue) and Emission (red) spectra for **(a)** Pt(dbbpy)(tbp)$_2$ and **(b)** Pt(dbbpy)(tbt)$_2$ in degassed CH_2Cl_2 solution at 298 K.

absorption spectra of Pt(dbbpy)(tbp)$_2$ and and Pt(dbbpy)(tbt)$_2$ are shown in Figure 3.67 (a) and (b) respectively. The emission maxima (λ_{max}^{Em}) for Pt(dbbpy)(tbp)$_2$ is at 690 nm (14490 cm^{-1}) and the stokes shift is 4210 cm^{-1}. Centered at 568 nm is the emission maximum band for Pt(dbbpy)(tbt)$_2$ with energy of 17610 cm^{-1}. The calculated stokes shifts is 2240 cm^{-1}. Pt(dbbpy)(tbp)$_2$ has a bigger stokes shift with respect to Pt(dbbpy)(tbt)$_2$ because the emission maximum (λ_{max}^{Em}) of Pt(dbbpy)(tbp)$_2$ occurs at a longer wavelength than that of Pt(dbbpy)(tbt)$_2$.

3.2.11.2 X-ray Crystallography

Pt(dbbpy)(tbt)$_2$

The crystal structure of 4,4'-di-tert-butyl-2,2'-bipyridineplatinum(II)(bis-4-tert-butylbenzenethiolate), [Pt(dbbpy)(tbt)$_2$] depicted in Figure 3.68 was analyzed at the UNM X-ray Laboratory. A black plate-like specimen of $C_{38}H_{50}N_2PtS_2$, approximate dimensions 0.078 mm x 0.178 mm x 0.228 mm, was coated with paratone oil and mounted on a MiTeGen micro loop that had been previously attached to a metallic pin using epoxy for the X-ray crystallographic analysis. The X-ray intensity data were measured on a Bruker Kappa APEX II CCD system equipped with a graphite monochromator and a Mo Kα fine-focus tube (λ = 0.71073 Å). The temperature of the X-ray intensities was record at 100(2) K and the detector was located at 4.50 cm from the crystal. A total of 1191 frames were collected. The total exposure time was 6.62 hours. The frames were integrated with the Bruker SAINT software package using a narrow-frame algorithm. The integration of the data using a monoclinic unit cell yielded a total of 36100

reflections to a maximum θ angle of 27.48° (0.77 Å resolution), of which 7851 were independent (average redundancy 4.598, completeness = 100.0%, R_{int} = 6.67%, R_{sig} = 5.64%) and 6010 (76.55%) were greater than $2\sigma(F^2)$. The final cell constants of a = 13.8008(9) Å, b = 16.7767(11) Å, c = 15.0744(10) Å, β = 100.954(4)°, volume = 3426.6(4) $Å^3$, are based upon the refinement of the XYZ-centroids of 6801 reflections above 20 σ(I) with 5.065° < 2θ < 53.73°. Data were corrected for absorption effects using the Multi-Scan method (SADABS). The ratio of minimum to maximum apparent transmission was 0.771.

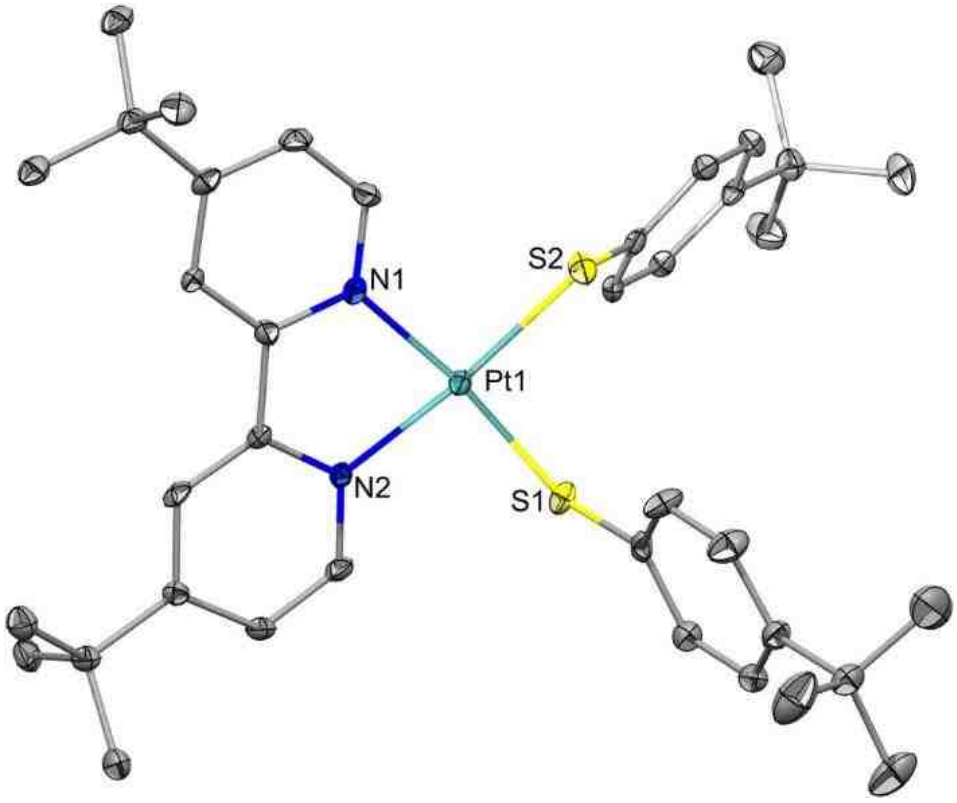

Figure 3.68: Crystal structure of (dbbpy)Pt(tbt)$_2$.

The calculated minimum and maximum transmission coefficients (based on crystal size) are 0.4440 and 0.7330. The structure was solved and refined using

the Bruker SHELXTL Software Package, using the space group P 2(1)/n, with Z = 4 for the formula unit, $C_{38}H_{50}N_2PtS_2$. Non-hydrogen atoms were refined anisotropically. Hydrogen atoms were placed in geometrically calculated positions with U_{iso} = 1.2U_{equiv} of the parent atom (U_{iso} = 1.5U_{equiv} for methyl). The final anisotropic full-matrix least-squares refinement on F^2 with 400 variables converged at R1 = 3.27%, for the observed data and wR2 = 6.62% for all data. The goodness-of-fit was 1.018. The largest peak in the final difference electron density synthesis was 1.321 $e^-/Å^3$ and the largest hole was -0.720 $e^-/Å^3$ with an RMS deviation of 0.136 $e^-/Å^3$. On the basis of the final model, the calculated density was 1.539 g/cm^3 and F(000), 1608 e^-.

Pt(dbbpy)(tbp)$_2$

The crystal structure of 4,4'-di-tert-butyl-2,2'-bipyridineplatinum(II)(bis-4-tert-butylphenolate), [Pt(dbbpy)(tbp)$_2$] depicted in Figure 3.69 was also analyzed at the UNM X-ray Laboratory. A red-orange block-like specimen of $C_{38}H_{50}N_2O_2Pt$, approximate dimensions 0.236 mm x 0.324 mm x 0.447 mm, was coated with Paratone oil and mounted on a MiTeGen Micro Loop that had been previously attached to a metallic pin using epoxy for the X-ray crystallographic analysis. The X-ray intensity data were measured on a Bruker Kappa APEX II CCD system equipped with a graphite monochromator and a Mo Kα fine-focus tube (λ = 0.71073 Å). A total of 1599 frames were collected. The total exposure time was 0.89 hours. The frames were integrated with the Bruker SAINT software package using a narrow-frame algorithm. The integration of the data using a monoclinic unit cell yielded a total of 56255 reflections to a maximum θ angle of 31.55° (0.68 Å resolution), of which

10877 were independent (average redundancy 5.172, completeness = 99.8%, R_{int} = 5.95%, R_{sig} = 5.35%) and 8224 (75.61%) were greater than $2\sigma(F^2)$. The final cell constants of a = 13.1875(6) Å, b = 17.1219(7) Å, c = 14.5282(6) Å, β = 96.474(2)°, volume = 3259.5(2) $Å^3$, are based upon the refinement of the XYZ-centroids of 9916 reflections above 20 σ(I) with 5.026° < 2θ < 54.40°. Data were corrected for absorption effects using the Multi-Scan method (SADABS). The ratio of minimum to maximum apparent transmission was 0.744. The calculated minimum and maximum transmission coefficients (based on crystal size) are 0.2470 and 0.4270.

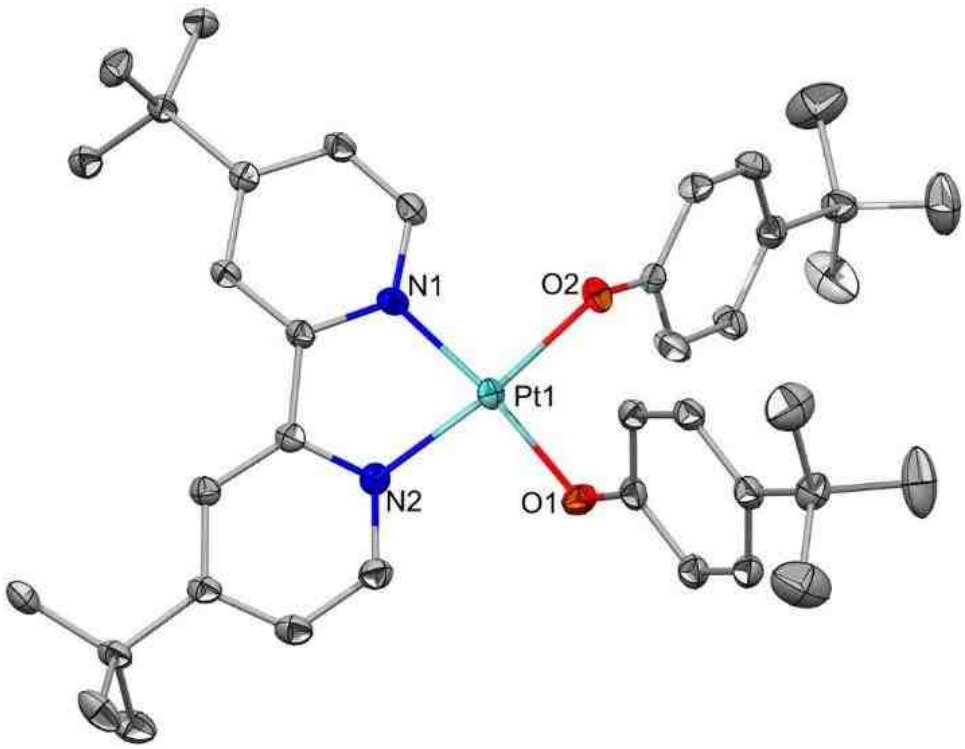

Figure 3.69: Crystal structure of (dbbpy)Pt(tbt)$_2$.

The structure was solved and refined using the Bruker SHELXTL Software Package, using the space group P2(1)/n, with Z = 4 for the formula unit,

$C_{38}H_{50}N_2O_2Pt$. Non-hydrogen atoms were refined anisotropically. Hydrogen atoms were placed in geometrically calculated positions with U_{iso} = 1.2U_{equiv} of the parent atom (U_{iso} = 1.5U_{equiv} for methyl). The final anisotropic full-matrix least-squares refinement on F^2 with 400 variables converged at R1 = 3.36%, for the observed data and wR2 = 7.52% for all data. The goodness-of-fit was 1.027. The largest peak in the final difference electron density synthesis was 1.468 $e^-/Å^3$ and the largest hole was -0.982 $e^-/Å^3$ with an RMS deviation of 0.143 $e^-/Å^3$. On the basis of the final model, the calculated density was 1.553 g/cm^3 and F(000), 1544 e^-.

Results

Molecular Crystal Structure

The crystal structures of $Pt(dbbpy)(tbt)_2$ and $Pt(dbbpy)(tbp)_2$ are shown in Figure 3.68. and 3.69 respectively. A black plate-like crystals of $Pt(dbbpy)(tbt)_2$ with an approximate dimensions of 0.078 mm x 0.178 mm x 0.228 mm were obtained by slow evaporation of saturated solution of dichloromethane (CH_2Cl_2) and hexane in a 1:1 mixture in the dark for 12 days. On the other hand, a red-orange block-like specimen of $Pt(dbbpy)(tbt)_2$ with an approximate dimensions of 0.236 mm x 0.324 mm x 0.447 mm were obtained in the presence of air by slow evaporation of 20% acetonitrile solution in dichloromethane. Both crystals were found to be stable in air at ambient temperature. Table 3.8 contains the crystallographic date for $Pt(dbbpy)(tbt)_2$ and $Pt(dbbpy)(tbp)_2$. The comparison of the calculated selected bond lengths (Å) with experimental values from X-ray analysis is given

in Table 3.9. Figures 3.70 and 3.71 present the ORTEP thermal ellipsoid plots for Pt(dbbpy)(tbt)$_2$ and Pt(dbbpy)(tbp)$_2$ respectively. The plot displays the key bond lengths around the central platinum atom and it shows the numbering

Table 3.8: X-ray Crystallographic Data for (dbbpy)Pt(tbt)$_2$ and (dbbpy)Pt(tbp)$_2$.

Crystallographic Data	**(dbbpy)Pt(tbt)$_2$**	**(dbbpy)Pt(tbp)$_2$**
empirical formula	**$C_{38}H_{50}N_2PtS_2$**	**$C_{38}H_{50}N_2PtO_2$**
fw, gmol^{-1}	794.01	761.89
crystal system	monoclinic	monoclinic
crystal habit	black plate	red-orange block
space group	P 2(1)/n	P 2(1)/n
a, Å	13.801 (9)	13.188(6)
b, Å	16.777(11)	17.122(7)
c, Å	15.074(10)	14.528(6)
α, deg	90	90
β, deg	100.95(4)	96.47(2)
γ, deg	90	90
V, Å^3	3426.6(4)	3259.5(2)
Z	4	4
T, K	100(2)	100(2)
R1[b]	0.0558	0.0336
wR2[a]	0.0662	0.0752
GOF *(F^2)*[a]	1.018	1.027

[a] R1 = $\sum ||F_0 - |F_c||/\sum |F_0|$ (55926 reflections collected, $I > 2\sigma(I)$);

wR2 =$[\sum[w|F_0^2 - F_c^2|^2]/w(F_0^2)^2]^{½}$; GOF = $[\sum[w|F_0^2 - F_c^2|^2]/(n-p)]^{½}$, where n and p represent the number of data and number of parameters refined respectively.

scheme of all the atoms present in the complex. No solvent molecule was observed to cocrystallized with the two complexes. Single-crystal X-ray diffraction

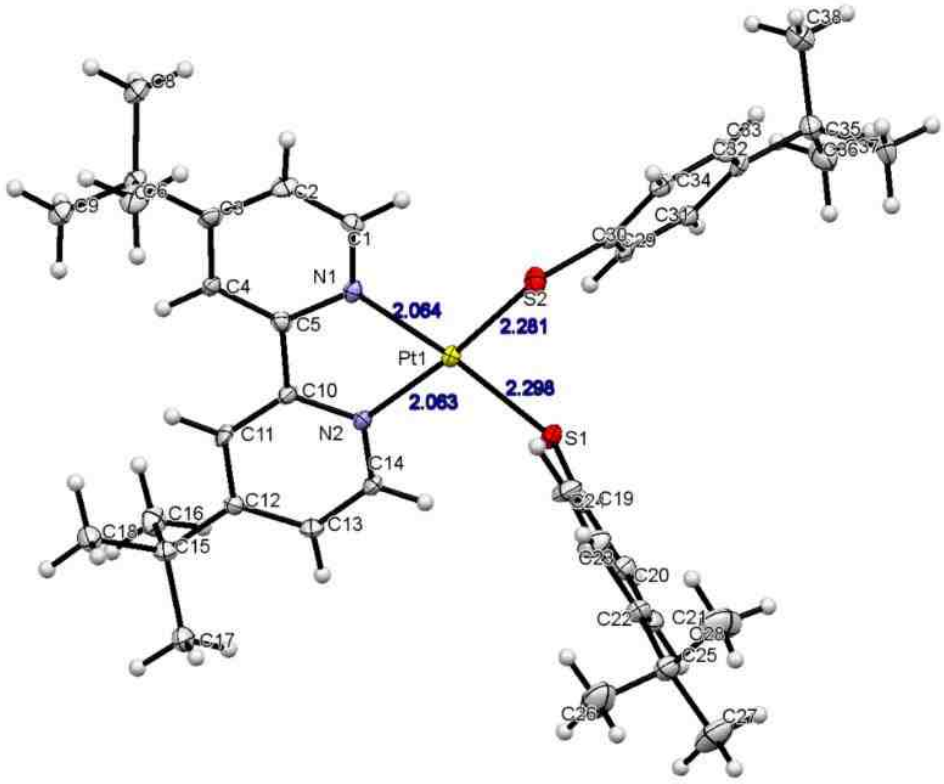

Figure 3.70: Crystal structure and atomic numbering system (ORTEP diagram) for (dbbpy)Pt(tbt)$_2$. Thermal ellipsoids are at 50% probability level.

studies of the two complexes confirmed slightly distorted square-planar geometry about the central platinum metal. The central metal, platinum in the two complexes possesses a square planar with some torsional deformation. The coordination geometry around the Pt(II) ion in Figures 3.68 and 3.69 depict slightly distorted square planar geometry with the four coordination sites been occupied by two nitrogen atoms from 4,4'-di-tert-butyl-2,2'-bipyridine (dbbpy), and two sulfur atoms or two oxygen atoms from 4-tert-butylbenzenethiolate and

4-tert-butylphenolate molecule's respectively. The dbbpy chelate results in a N2-Pt-N1 bond angles of $78.32(13)^0$ and $79.67(10)^0$ for $Pt(dbbpy)(tbt)_2$ and $Pt(dbbpy)(tbp)_2$ respectively, which are appreciably less than the perfect value of 90^0.[15] The asymmetric unit cells of the two complexes, i.e. $Pt(dbbpy)(tbt)_2$ and $Pt(dbbpy)(tbp)_2$ are each made up of one crystallographically independent molecule which consists of one Pt(II) atom, one dbbpy ligand, and two molecules

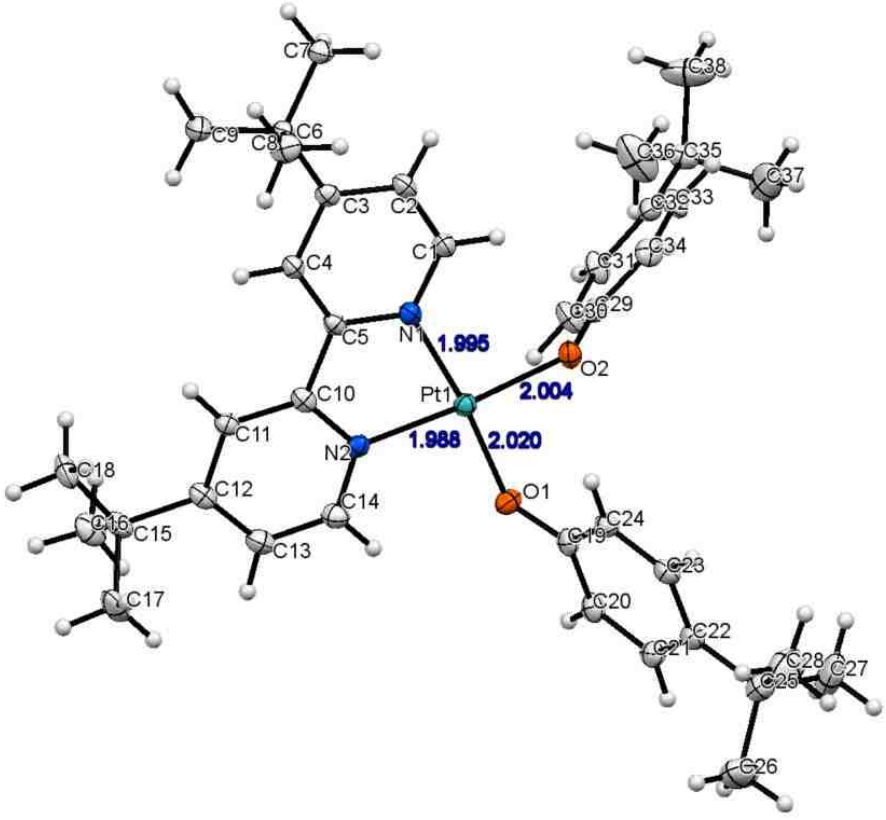

Figure 3.71: Crystal structure and atomic numbering system (ORTEP diagram) for $(dbbpy)Pt(tbp)_2$. Thermal ellipsoids are at 50% probability level.

of 4-tert-butylbenzenethiolate and 4-tert-butylphenolate for $Pt(dbbpy)(tbt)_2$ and $Pt(dbbpy)(tbp)_2$ respectively.[69] The selected bond lengths and angles for the complexes are presented in Table 3.9 and Table 3.10 respectively. Molecular

stacking was not observed in the crystal structure of the two complexes although Pt(II) complexes are known to form intermolecular stacking with Pt-Pt distance of 3.24 Å and π-π distance of 3.51 Å.[67,68] Pt—Pt interaction was not observed in these complexes because the average Pt—Pt bond distance is 10.86 Å as shown in Figure 3.72 is higher than the intermolecular staking Pt-Pt distance.

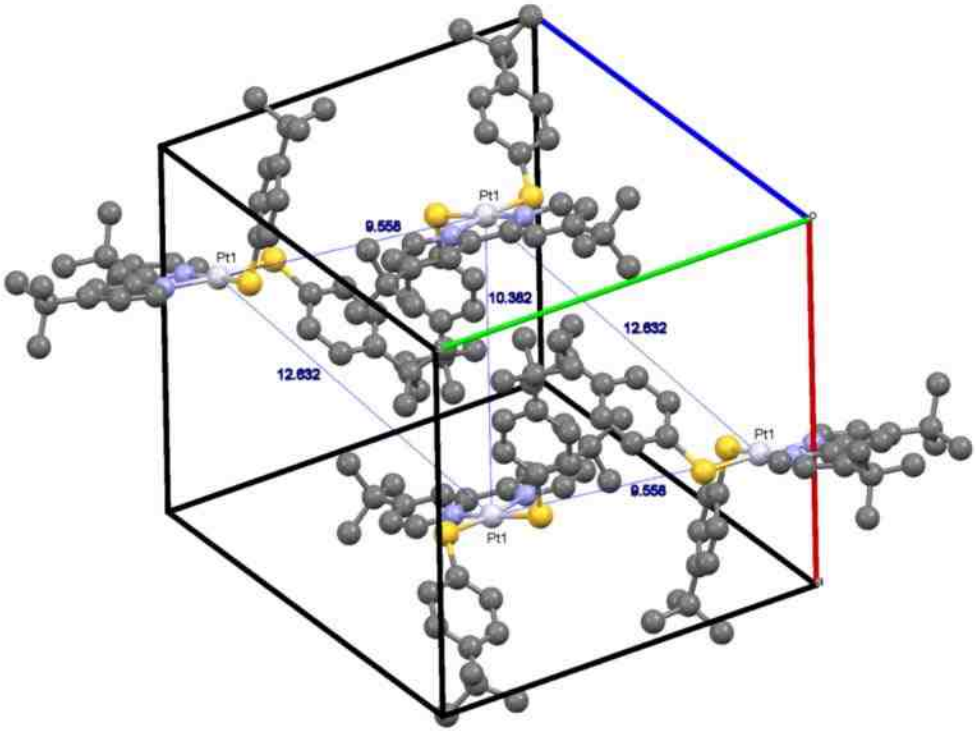

Figure 3.72: (dbbpy)Pt(tbt)$_2$ crystal packing arrangement.

Furthermore, π-to-π intermolecular interactions was not observed in the asymmetric unit cell due to the bulkiness of the tert-butyl groups on the dbbpy and phenolate/thiolate ligands. As depicted in Table 3.9**,** Pt-S, and Pt-N bond distances in Pt(dbbpy)(tbt)$_2$ are 2.299(10), 2.282(11) Å, and 2.064(3), 2.063(3) Å, respectively, compare well with theoretical values of 2.312 and 2.113 Å respectively for Pt-S and Pt-N. These experimental values are in the range of

typical bond lengths of Pt(diimine)(dithiolate) complexes. On the other hand, the Pt-O, and Pt-N bond distances in Pt(dbbpy)(tbp)$_2$ are 2.020(2), 2.004(2), and 1.995(2), 1.988(3) Å, respectively, compares well with the calculated values

Table 3.9: Comparison of Calculated Selected Bond Lengths (Å) with experimental values from X-ray analysis for (dbbpy)Pt(tbt)$_2$ and (dbbpy)Pt(tbp)$_2$. Where E = S for (dbbpy)Pt(tbt)$_2$ and E = O for (dbbpy)Pt(tbp)$_2$.

	(dbbpy)Pt(tbt)$_2$		**(dbbpy)Pt(tbp)$_2$**	
	Experimental	Calculated	Experimental	Calculated
Pt1-N1	2.064(3)	2.113	1.995(2)	2.019
Pt1-N2	2.063(3)	2.113	1.988(3)	2.017
Pt1-**E1**	2.299(10)	2.312	2.020(2)	2.008
Pt1-**E2**	2.282(11)	2.312	2.004(2)	1.999
N1-C1	1.344(5)	1.352	1.347(4)	1.355
N1-C5	1.366(5)	1.352	1.354(4)	1.359
N2-C10	1.359(5)	1.340	1.352(4)	1.343
N2-C14	1.340(5)	1.340	1.345(4)	1.340
E1-C19	1.759(4)	2.312	1.331(4)	1.346
E2-C29	1.756(4)	2.312	1.330(4)	1.330
C5-C10	1.477(5)	1.473	1.476(4)	1.469

of 2.008, 1.999, 2.019, and 2.017 Å respectively. The Pt-N bond length of Pt(dbbpy)(tbp)$_2$ agrees well with the analogous catecholate compound, 2,2'-bipyridineplatinum(II)(3,5-di-tert-butylcatechol), [(Pt(bpy)(Bu$_2$cat)], i.e. 1.978 and 1.992 Å. The Pt-O bond distances of Pt(dbbpy)(tbp)$_2$ are slightly longer than that

of Pt(bpy)(Bu_2cat) i.e. 1.982 and 1.984 Å. The dbbpy chelate ligands in Pt(dbbpy)$(tbp)_2$ and Pt(bpy)(Bu_2cat) results in N-Pt-N bond angles of 79.67(10) and 80.38^0 respectively, which is appreciably less than the idealized value of 90^0.

Table 3.10: Comparison of Calculated Selected Angles (deg) with experimental angles from X-ray analysis for (dbbpy)Pt$(tbt)_2$ and (dbbpy)Pt$(tbp)_2$. Where **E = S** for (dbbpy)Pt$(tbt)_2$ and **E = O** for (dbbpy)Pt$(tbp)_2$.

	(dbbpy)Pt$(tbt)_2$		**(dbbpy)Pt$(tbp)_2$**	
	Experimental	Calculated	Experimental	Calculated
N2-Pt1-N1	78.32(13)	77.39	79.67(10)	80.12
N2-Pt1-**E2**	171.15(10)	171.72	173.31(9)	175.57
N1-Pt1-**E2**	94.17(10)	171.72	94.20(9)	96.09
N2-Pt1-**E1**	94.99(9)	95.02	93.95(9)	89.84
N1-Pt1-**E1**	173.16(10)	95.02	173.41(9)	169.71
E2-Pt1-**E1**	92.62(4)	92.74	92.25(9)	93.84
C10-N2-Pt1	116.10(3)	115.70	116.90(19)	115.44
C5-N1-Pt1	116.3(3)	115.70	116.29(19)	115.24
C19-**E1**-Pt1	110.56(14)	111.65	124.50(2)	127.70
C29-**E2**-Pt1	113.13(15)	111.65	120.86(19)	124.24
C14-N2-Pt1	125.50(3)	125.28	124.40(2)	124.66
C1-N1-Pt1	125.90(3)	125.28	124.8(2)	125.69
C24-C19-**E1**	125.40(3)	124.19	124.6(3)	124.88
C30-C29-S2	125.7(3)	124.19	124.4(3)	119.21

On the other hand, O-Pt-O angles in Pt(dbbpy)$(tbp)_2$ and Pt(bpy)(Bu_2cat) are 92.25(9) and 84.23^0 respectively. These angles are very different from each other, and that of Pt(dbbpy)$(tbp)_2$ is very close to a perfect square planar geometry.[1] The S-Pt-S angles in Pt(dbbpy)$(tbt)_2$ and Pt(dpphen)(dtbdt) are 92.62(4) and $86.64(13)^0$ respectively where Pt(dpphen)(dtbdt) is (4,7-diphenyl-1,10-phenanthroline)(3,5-di-tert-butylbenzene-1,2-dithiolate). The S-Pt-S angle from Pt(dpphen)(dtbdt) is considerably smaller and is due to the slightly strained five-membered ring system of the complex.[2]

In comparison, the structure of Pt(dbbpy)$(tbt)_2$ is less distorted around the Pt(II) center than Pt(dpphen)(dtbdt). The S1-Pt-S2, N1-Pt-N2, N1-Pt-S2, and N2-Pt-S1 bond angles are all close to a perfect square planar (90^0) for Pt(dbbpy)$(tbt)_2$. The bond angles are 92.62(4), 78.32(13), 94.17(10), and $94.99(9)^0$ respectively and for Pt(dpphen)(dtbdt), the angles are 88.64(13), 80.30(4), 96.80(3), and $94.40(3)^0$ respectively.[2] Furthermore, the complex Pt(dbbpy)$(tbp)_2$ is less distorted around the Pt(II) center than Pt(bpy)(Bu_2cat). The O1-Pt-O2, O2-Pt-N2, O1-Pt-N1, and N1-Pt-N2 angles are close to 90^0 for Pt(dbbpy)$(tbp)_2$. The bond angles are 92.25(9), 94.20(9), 93.95(9), and 79.67(10) respectively and for Pt(bpy)(Bu_2cat) the angles are 84.23, 98.76, 96.61, and 80.38 respectively. The dihedral angle between the N1-Pt-N2 and O1-Pt-O2 planes are 5.54 and 3.10^0 respectively for Pt(bpy)(Bu_2cat) and Pt(dbbpy)$(tbp)_2$. These values are very close to a perfect flat geometry with a 0^0 dihedral angle.[1] Additionally, the dihedral angle between N1-Pt-N2 and S1-Pt-S2 planes are 4.89 and 4.33 for Pt(dbbpy)$(tbt)_2$ and Pt(dpphen)(dtbdt) respectively.

3.2.12 Pt(dpphen)(dichalcogenolene)

3.2.12.1 Electronic Absorption and Emission Spectroscopy

The electronic absorption spectra of 4,7-diphenyl-1,10-phenathrolineplatinum(II) – (2-selenylphenolate),[Pt(dpphen)(bSeO)], 4,7-diphenyl-1,10-phenathrolineplatinum(II)(2-mercaptophenolate),[Pt(dpphen)(bSO)], 4,7-diphenyl-1,10-phenathrolineplatinum(II)(toluene-3,4-dithiolate), [Pt(dpphen)(tdt)], 4,7-diphenyl-1,10-phenathrolineplatinum(II)(2-selenylbenzenethiolate), [Pt(dpphen)(bSSe)], 4,7-diphenyl-1,10-phenathrolineplatinum(II)(bis-4-tert-butylphenolate),[Pt(dpphen)$(tbp)_2$], and 4,7-diphenyl-1,10-phenathrolineplatinum(II)(1,2-benzenediselenolate),

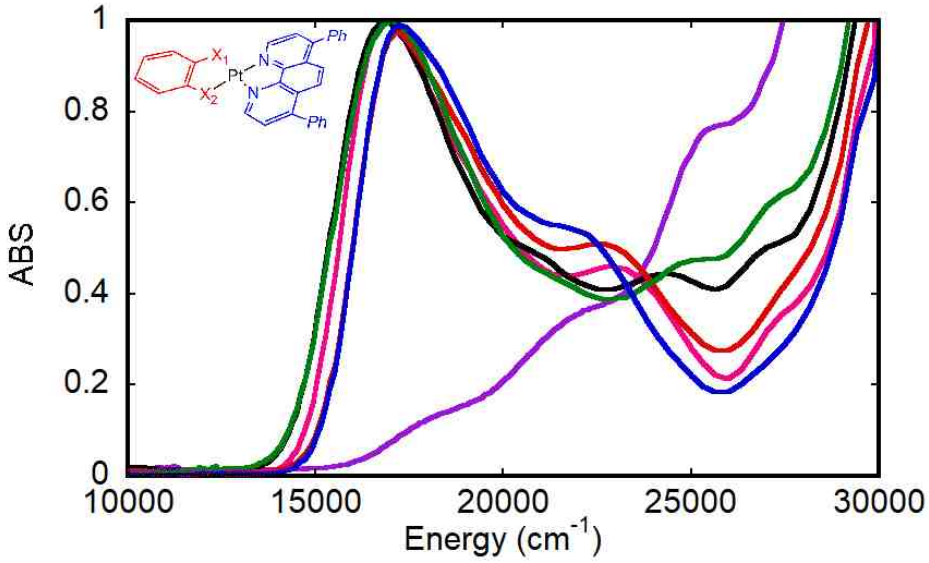

Figure 3.73: Electronic absorption overlay for Pt(dpphen)(bSeO) (black) and Pt(dpphen)(bSO) (green), Pt(dpphen)(bds) (blue), Pt(dpphen)(tdt) (pink), Pt(dpphen)$(tbp)_2$ (purple) and Pt(dpphen)(bSSe) (red), in CH_2Cl_2 at 298 K. Inset: Compound structure: X_1=X_2 =Se for Pt(dpphen)(bds), X_1=O, X_2 =Se for Pt(dpphen)(bSeO), X_1=O, X_2 =S for Pt(dpphen)(bSO), X_1=S, X_2 =Se for Pt(dpphen)(bSSe), tbp=4-*tert*-butylphenolate and tdt= toluene-3,4-dithiolate.

Table 3.11: Electronic Absorption and Emission Data for Pt(dpphen)(dichalcogenolene) Complexes.

Complex	λ_{max}^{Abs} (nm)	λ_{max}^{Abs} (cm^{-1})	λ_{max}^{Em} (nm)	λ_{max}^{Em} (cm^{-1})	Stokes shift (cm^{-1})
Pt(dpphen)(bSeO)	595	16800	855	11700	5100
Pt(dpphen)(bSO)	586	17070	860	11630	5440
Pt(dpphen)(bds)	580	17240	805	12420	4820
Pt(dpphen)(tbp)$_2$	575	17390	640	15630	1,760
Pt(dpphen)(tdt)	590	16950	-	-	
Pt(dpphen)(bSSe)	580	17230	-	-	

ε_{max} = emission maxima, E_{abs} = Energy of the absorption maxima, λ_{abs} = wavelength of maximum absorption.

[Pt(dpphen)(bds)], at ambient temperature in dichloromethane are depicted in Figure 3.73. The lowest energy charge transfer absorption maxima (λ_{abs}) for Pt(dpphen)(dichalcogelene) complexes are recorded in Table 3.11. The lowest energy CT absorption maxima recorded for Pt(dpphen)(bSeO) and Pt(dpphen)(bSO) are red shifted with respect to Pt(dbbpy)(SeO) and Pt(dbbpy)(SO) (see Figure 3.40 and 3.74). Also, red shifted in the charge transfer absorption maxima are Pt(dpphen)(bds) and Pt(dpphen)(bSSe) with respect to Pt(dbbpy)(bds) and Pt(dbbpy)(bSSe). The absorption maxima recorded for Pt(dpphen)(dichalcogelene) complexes are only for the lowest-energy band, despite the fact that additional absorption features occur at higher energies as depicted in Figure 3.73. The 298 K emission in deoxygenated dichloromethane fluid solution at 580 nm excitation wavelength and electronic absorption for Pt(dpphen)(bds) is depicted in Figure 3.74 (a). Pt(dpphen)(bds) is emissive in fluid solution at room temperature upon excitation into the lowest energy

absorption band with an emission maximum (λ_{max}^{Em}) at 805 nm (12420 cm^{-1}) and the calculated stokes shift is 4820 cm^{-1}. Figure 3.74 (b) depicts the absorption and emission spectra of $Pt(dpphen)(tbp)_2$ in degassed dichloromethane (CH_2Cl_2)

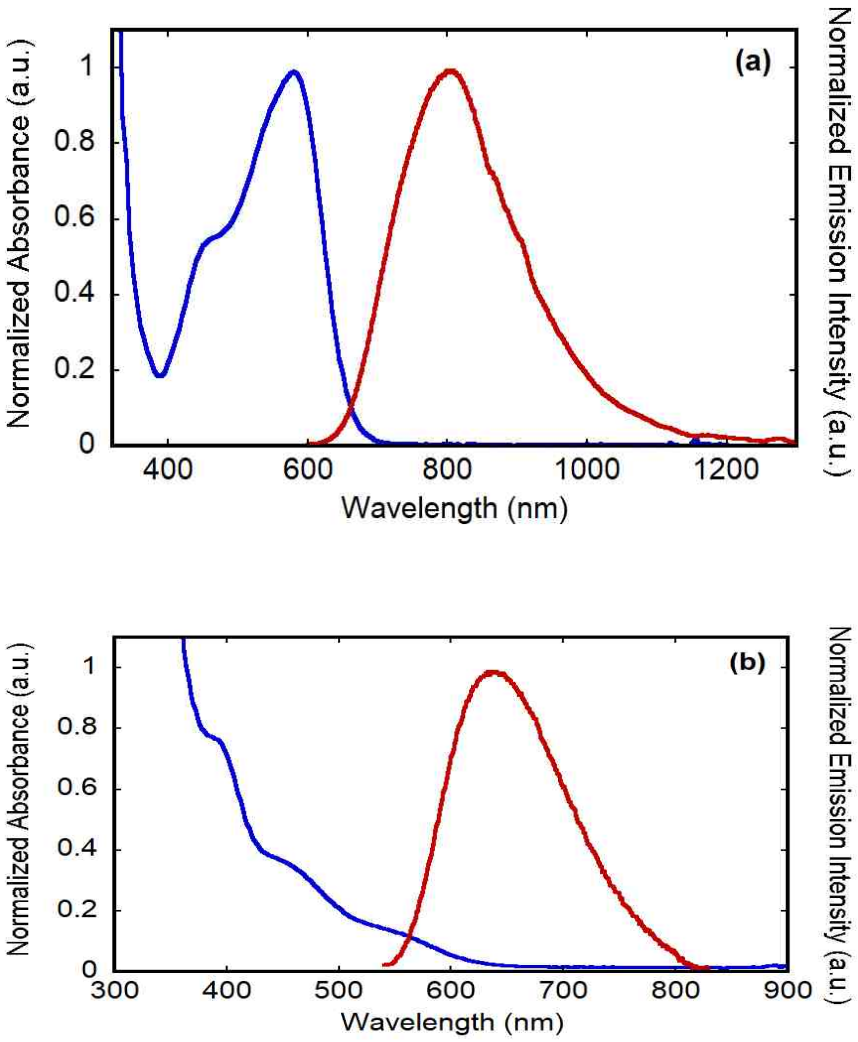

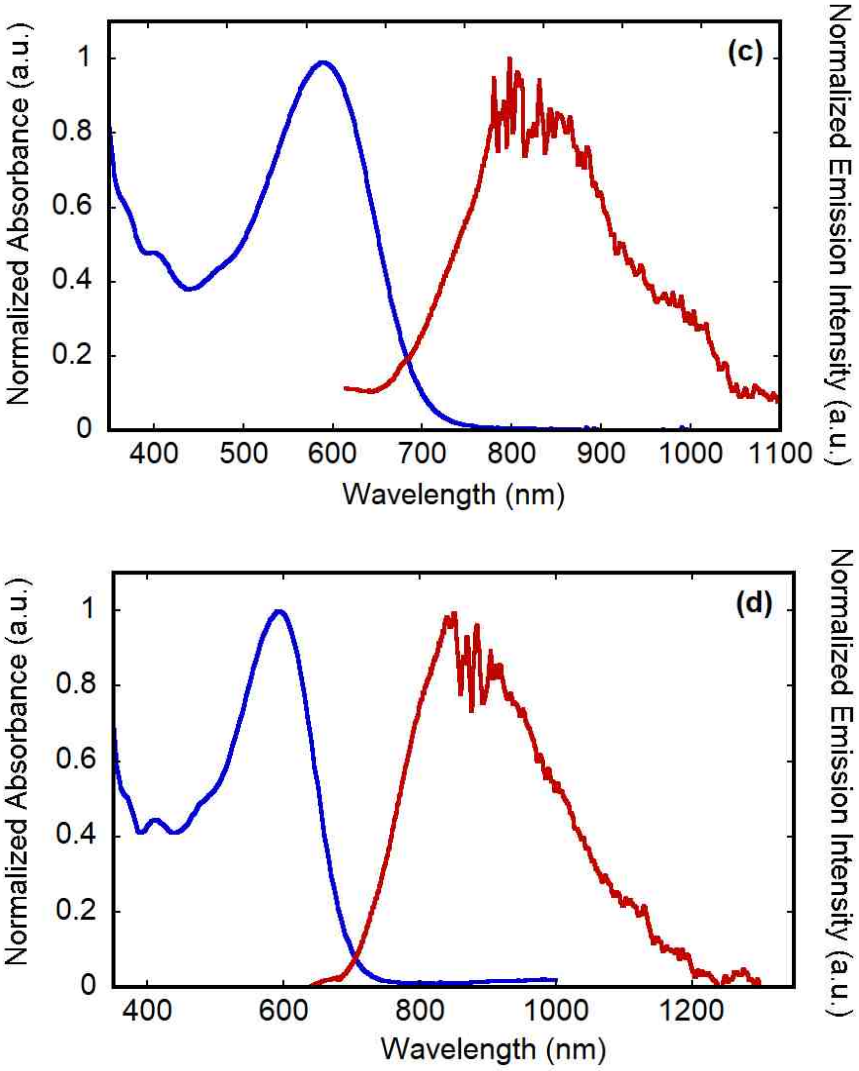

Figure 3.74: Overlay of Absorption (blue) and Emission (red) spectra for **(a)** Pt(dpphen)(bds), **(b)** Pt(dpphen)(tbp)$_2$, **(c)** Pt(dpphen)(bSO), and **(d)** Pt(dpphen)(bSeO) in degassed CH_2Cl_2 solution at 298 K.

fluid solution. The structureless emission spectrum of Pt(dpphen)(tbp)$_2$ with an excitation wavelength of 420 nm, has emission maxima (λ_{max}^{Em}) at 640 nm (15630 cm^{-1}) and a stokes shift of 1760 cm^{-1} (see Table 3.11). Figure 3.74 (c) and (d) shows the absorption and emission spectra of Pt(dpphen)(bSO) and Pt(dpphen)(bSeO) respectively, in degassed dichloromethane fluid solution at ambient temperature. Pt(dpphen)(bSO) and Pt(dpphen)(bSeO) depict a far-red

emission in fluid solution at room temperature upon excitation into the lowest energy absorption band. The wavelength of excitation into the lowest energy CT band was 590 nm. The recorded emission maxima (λ_{max}^{Em}) and stokes shift for Pt(dpphen)(bSO) are 860 nm (11630 cm^{-1}) and 5440 cm^{-1} respectively. Pt(dpphen)(bSeO) has emission (ε_{max}) of 855 nm (11700 cm^{-1}) and a calculated stokes shift of 5100 cm^{-1}. The emission spectra of Pt(dpphen)(bSO) and Pt(dpphen)(bSeO) shown in Figure 3.74 (c) and (d), contains both the visible and near-IR (NIR) region of the spectrum. The NIR region of the spectra were noisy due to low signal. From Table 3.11, can it can be ascertained that the more red-shifted the emission maxima (λ_{max}^{Em}), the greater the stokes shift. Pt(dpphen)(bSO) has the most red-shifted emission maxima (λ_{max}^{Em}) and the largest stokes shift. Pt(dpphen)$(tbp)_2$ has the least red-shifted emission maxima (λ_{max}^{Em}) and the smallest stokes shift.

3.2.12.2 X-ray Crystallography

Molecular Crystal Structures

Pt(dpphen)(bSeO)

The crystal structure of 4,7-diphenyl-1,10-phenathrolineplatinum(II)(2-selenylphenolate), [Pt(dpphen)(bSeO)] depicted in Figure 3.75 was analyzed at the UNM X-ray Laboratory. A dark purple rod-like specimen of $C_{34}H_{29}N_3O_2PtSe$, approximate dimensions 0.170 mm x 0.217 mm x 0.420 mm, was coated with Paratone oil and mounted on a MiTeGen MicroLoop that had been previously

attached to a metallic pin using epoxy for the X-ray crystallographic analysis. The X-ray intensity data were measured on a Bruker Kappa APEX II CCD system equipped with a graphite monochromator and a Mo Kα fine-focus tube (λ = 0.71073 Å).

A total of 597 frames were collected. The total exposure time was 7.46 hours. The frames were integrated with the Bruker SAINT software package using a narrow-frame algorithm. The integration of the data using a triclinic unit cell yielded a total of 21938 reflections to a maximum θ angle of 25.68° (0.82 Å resolution), of which 5289 were independent (average redundancy 4.148, completeness = 99.9%, R_{int} = 8.08%, R_{sig} = 8.84%) and 3670 (69.39%) were greater than $2\sigma(F^2)$. The final cell constants of a = 8.3518(10) Å, b = 13.4012(17) Å, c = 13.9475(17) Å, α = 67.523(4)°, β = 87.773(4)°, γ = 75.749(4)°, volume = 1395.4(3) $Å^3$, are based upon the refinement of the XYZ-centroids of 7916 reflections above 20 σ(I) with 5.041° < 2θ < 52.90°. Data were corrected for absorption effects using the Multi-Scan method (SADABS). The ratio of minimum to maximum apparent transmission was 0.226. The calculated minimum and maximum transmission coefficients (based on crystal size) are 0.1750 and 0.4110.

The structure was solved and refined using the Bruker SHELXTL Software Package, using the space group P -1, with Z = 2 for the formula unit, $C_{34}H_{29}N_3O_2PtSe$. Non-hydrogen atoms were refined anisotropically. Hydrogen atoms were placed in geometrically calculated positions with U_{iso} = 1.2U_{equiv} of the parent atom (U_{iso} = 1.5U_{equiv} for methyl). The final anisotropic full-matrix least-

squares refinement on F^2 with 331 variables converged at R1 = 6.84%, for the observed data and wR2 = 17.16% for all data. The goodness-of-fit was 1.050. The largest peak in the final difference electron density synthesis was 4.036 $e^-/Å^3$ and the largest hole was -2.588 $e^-/Å^3$ with an RMS deviation of 0.282 $e^-/Å^3$. On the basis of the final model, the calculated density was 1.870 g/cm^3 and F(000), 764 e^-.

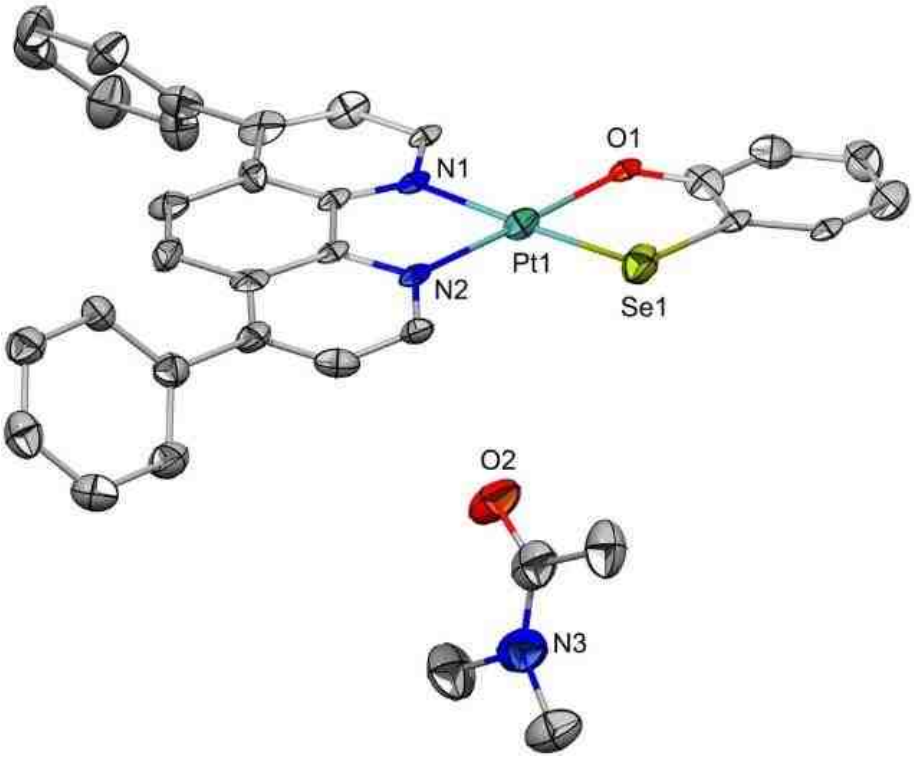

Figure 3.75: Crystal structure of (dpphen)Pt(bSeO).

Pt(dpphen)(bSO)

The crystal structure of 4,7-diphenyl-1,10-phenathrolineplatinum(II)(2-mercaptophenolate), [Pt(dpphen)(bSO)] depicted in Figure 3.76 was analyzed at

the UNM X-ray Laboratory. A dark purple rod-like specimen of $C_{30}H_{20}N_2OPtS$, approximate dimensions 0.162 mm x 0.253 mm x 0.331 mm. The X-ray intensity data were measured on a Bruker Kappa APEX II CCD system equipped with a graphite monochromator and a Mo Kα fine-focus tube (λ = 0.71073 Å). A total of 1119 frames were collected. The total exposure time was 4.66 hours. The frames were integrated with the Bruker SAINT software package using a narrow-frame algorithm. The integration of the data using a monoclinic unit cell yielded a total of 7141 reflections to a maximum θ angle of 30.99° (0.69 Å resolution), of which 7141 were independent (average redundancy 1.000, completeness = 98.6%, R_{int} = 2.54%, R_{sig} = 4.14%) and 5486 (76.82%) were greater than $2\sigma(F^2)$. The final cell constants of a = 13.5921(8) Å, b = 7.0984(4) Å, c = 23.5468(14) Å, β = 91.7830(10)°, volume = 2270.7(2) $Å^3$, are based upon the refinement of the XYZ-centroids of 6670 reflections above 20 σ(I) with 5.996° < 2θ < 61.70°. Data were corrected for absorption effects using the Multi-Scan method (SADABS). The ratio of minimum to maximum apparent transmission was 0.602. The calculated minimum and maximum transmission coefficients (based on crystal size) are 0.2300 and 0.4280. The structure was solved and refined using the Bruker SHELXTL Software Package, using the space group P 21/n, with Z = 4 for the formula unit, $C_{30}H_{20}N_2OPtS$. Non-hydrogen atoms were refined anisotropically. Hydrogen atoms were placed in geometrically calculated positions with $U_{iso} = 1.2U_{equiv}$ of the parent atom. The atoms Pt1, S1, O1 and C1-C6 were found to be disordered over two positions. The occupancies were allowed to freely refine and converged at 51/49. The final anisotropic full-matrix

least-squares refinement on F^2 with 374 variables converged at R1 = 3.88%, for the observed data and wR2 = 7.76% for all data. The goodness-of-fit was 1.147. The largest peak in the final difference electron density synthesis was 1.373 $e^-/Å^3$ and the largest hole was -1.376 $e^-/Å^3$ with an RMS deviation of 0.144 $e^-/Å^3$. On the basis of the final model, the calculated density was 1.906 g/cm^3 and (000), 1264 e^-.

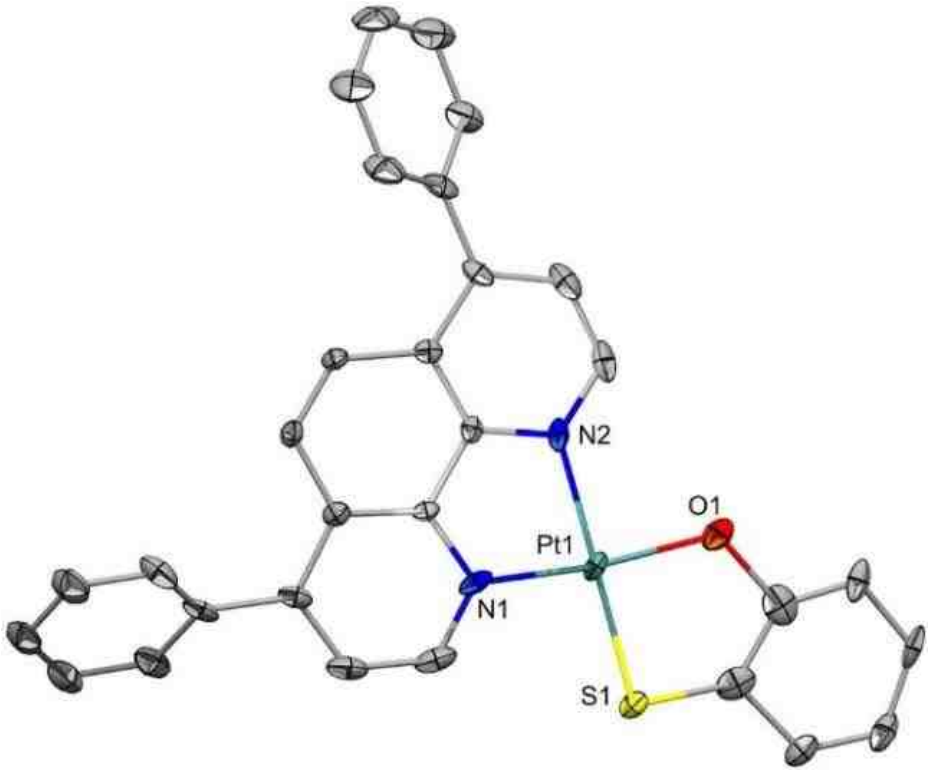

Figure 3.76: Crystal structure of (dpphen)Pt(bSO).

Results

Molecular Crystal Structure

The crystal structures of (dpphen)Pt(bSeO) and (dpphen)Pt(bSO) is shown in Figure 3.75 and 3.76 respectively. Dark purple rod-like crystals of

(dpphen)Pt(bSeO) with an approximate dimensions of 0.170 mm x 0.217 mm x 0.420 mm mm were obtained by slow evaporation of saturated solution of dichloromethane (CH_2Cl_2), hexane and dimethylacetamide in a 1:1:1 mixture in the dark for a month. On the other hand, a dark purple rod-like specimen of (dpphen)Pt(bSO) with an approximate dimension of 0.162 mm x 0.253 mm x 0.331 mm were obtained by slow evaporation of saturated solution of dichloro-

methane and benzene in the dark for 3 weeks.

Table 3.12: X-ray Crystallographic Data for (dpphen)Pt(bSeO) and (dpphen)Pt(bSO).

Crystallographic Data	**(dpphen)Pt(bSeO)●DMA**	**(dpphen)Pt(bSO)**
empirical formula	**$C_{34}H_{29}N_3O_2PtSe_2$**[a]	**$C_{30}H_{20}N_2OPtS$**
fw, $gmol^{-1}$	785.65	651.63
crystal system	triclinic	monoclinic
crystal habit	dark purple rod	dark purple rod
space group	P-1	P 2(1)/n
a, Å	8.352(10)	13.592(8)
b, Å	13.401(17)	7.098(4)
c, Å	13.948(17)	23.547(14)
α, deg	67.52(4)	90
β, deg	87.77(4)	91.78(10)
γ, deg	75.75(4)	90
V, $Å^3$	1395.4(3)	2270.7(2)
Z	2	4
T, K	100(2)	100(2)
R1[b]	0.1246	0.0388
wR2[b]	0.1716	0.0738

GOF *(F^2)*[b] 1.050 1.147

[a] A solvent molecule dimethylacetamide (DMA) cocrystallized with the complex.

[b] R1 = $\sum ||F_0 - |F_c||/\sum |F_0|$ (55926 reflections collected, *I* > 2σ(I));

wR2 =$[\sum[w|F_0^2 - F_c^2|^2]/w(F_0^2)^2]^{½}$; GOF = $[\sum[w|F_0^2 - F_c^2|^2]/(n-p)]^{½}$, where n and p represent the number of data and number of parameters refined respectively.

Table 3.12 contains the crystallographic date for Pt(dpphen)(bSeO) and Pt(dpphen)(bSO). The comparison of the calculated bond lengths (Å) with experimental values from X-ray analysis is given in Table 3.13. Figure 3.77 and 3.78 present the ORTEP thermal ellipsoid plots for Pt(dpphen)(bSeO) and Pt(dpphen)(bSO) respectively. The plot displays the key bond lengths around the

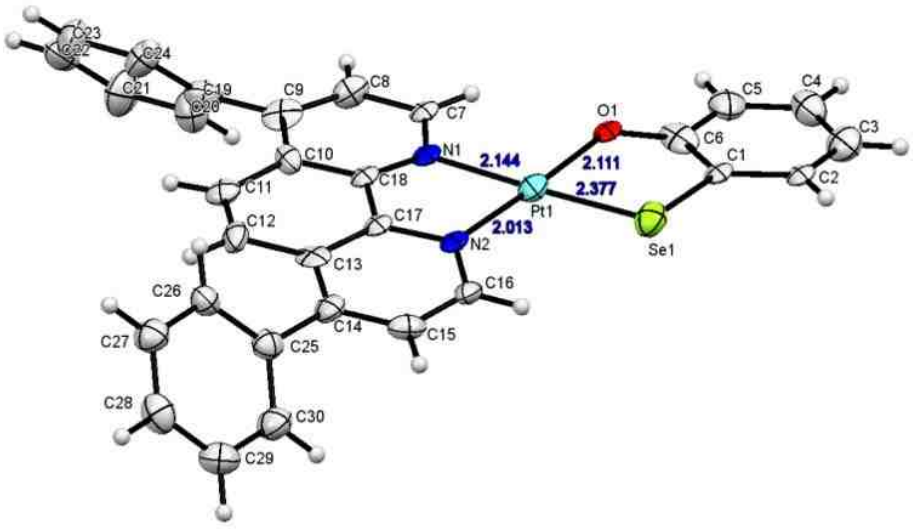

Figure 3.77: Crystal structure and atomic numbering system (ORTEP diagram) for (dpphen)Pt(bSeO). Thermal ellipsoids are at 50% probability level.

central platinum atom and it also shows the numbering scheme of all the non-hydrogen atoms present in the complex. N ,N'-dimethylacetamide (DMA) solvent molecule was observed to cocrystallized with Pt(dpphen)(bSeO) complex. The

central platinum metal in the two complexes possesses a square planar geometry with the structure of Pt(dpphen)(bSO) having more torsional deformation than Pt(dpphen)(bSeO). As depicted in Figure 3.79 both structures display an upward bend in the molecule about dichalogenolene donor atoms. The coordination geometry around the Pt(II) ion in Figures 3.75 and 3.76 depict slightly distorted square planar geometry with the four coordination sites been

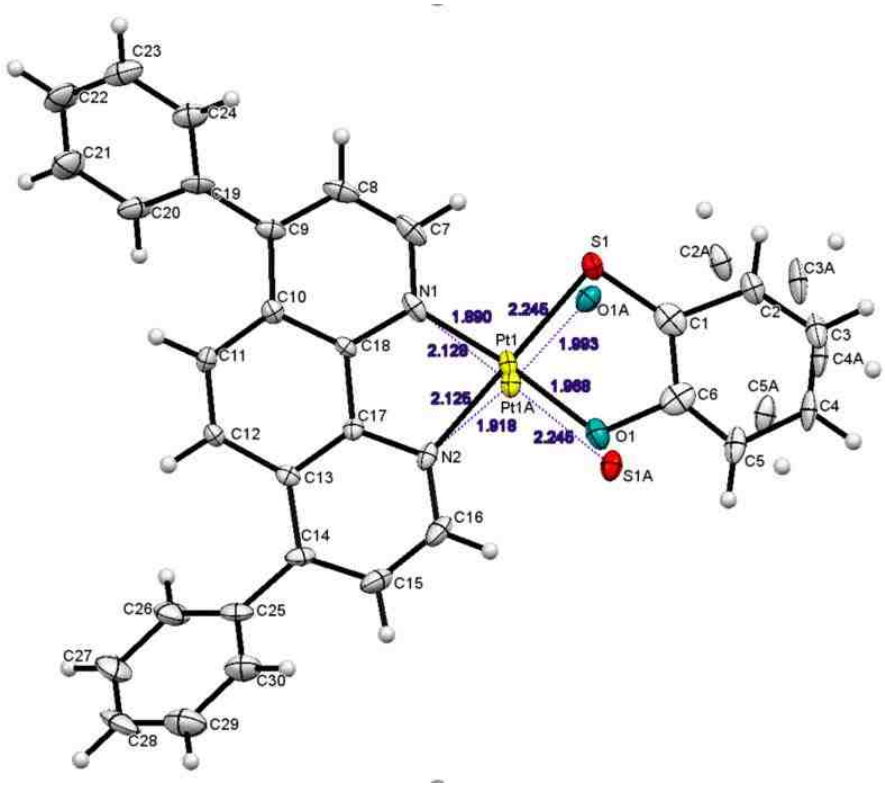

Figure 3.78: Crystal structure and atomic numbering system (ORTEP diagram) for (dpphen)Pt(bSO). Thermal ellipsoids are at 50% probability level.

occupied by two nitrogen atoms for 4,7-diphenyl-1,10-phenathroline (dpphen), a sulfur and oxygen atom in Pt(dpphen)(bSO), a sulfur and selenium atom in Pt(dpphen)(bSeO). The selected bond lengths and bond angles for Pt(dpphen)(bSO) and Pt(dpphen)(bSeO) are presented in Table 3.13 and 3.14

respectively. The dpphen chelate results in a N2-Pt-N1 bond angles of 80.6(16) and $81.2(4)^0$ for Pt(dpphen)(bSO) and Pt(dpphen)(bSeO) respectively, which are significantly less than the perfect value of 90^0 for an ideal square planar geometry. The asymmetric unit cells of the two complexes, i.e. Pt(dpphen)(bSO) and Pt(dpphen)(bSeO) are each made up of one crystallographically independent molecule which consists of one Pt(II) atom, one dpphen ligand, and one molecules of 2-mercaptophenolate and 2-selenylphenolate for Pt(dpphen)(bSO) and Pt(dpphen)(bSeO) respectively.

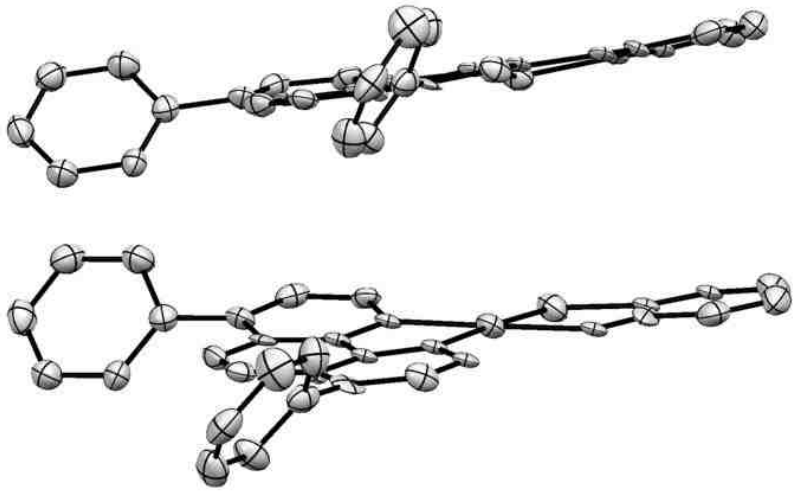

Figure 3.79: An ORTEP diagram of (dpphen)Pt(bSO) displaying the upward bending the molecule about the sulfur and oxygen atoms. H atoms are not included.

Molecular stacking was not observed in the crystal structure of the two complexes although Pt(II) complexes are known to form intermolecular stacking with Pt-Pt distance of 3.24 Å and π-π distance of 3.51 Å. The lack of Pt—Pt interaction in the crystal packing arrangement of Pt(dpphen)(bSO) complex (Figures 3.80), is noteworthy even though the average Pt—Pt bond distance (i.e.

3.65 Å) is slightly higher than the known Pt—Pt bond distance of Pt(II) complexes in the solid state. This increase in the Pt—Pt bond distance is a clear indication of the bulky substituents on the acceptor ligands preventing the molecular stacking of the chromophores in the crystal structure.[2] As summarized in Table 3.13, the Pt-N2, Pt-N1, and Pt-O1 bond lengths of Pt(dpphen)(bSeO) from the X-ray crystallography are 2.014(11), 2.144(11) and 2.112(9) Å

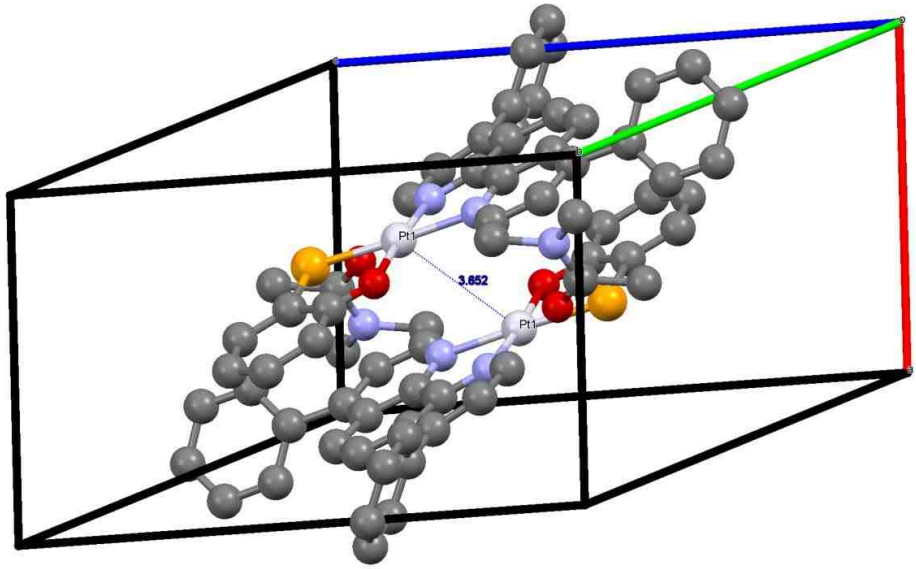

Figure 3.80: Pt(dpphen)(bSO) crystal packing arrangement.

respectively. These values compare well with the calculated values i.e. 2.060, 2.085 and 2.046 Å respectively from DFT.[1] The experimental values of Pt-N are in the range of bonds lengths common to other Pt(diimine)(dithiolate) complexes.[2] On the other hand, the Pt-O bond distance of Pt(dpphen)(bSeO) is slightly longer than that of Pt(bpy)(tbuCAT) i.e. 1.982, and 1.984 Å. The Pt-Se bond length of Pt(dpphen)(bSeO) is 2.377(17) Å and is comparable to that of

Pt(dbbpy)(bds) with Pt-Se bond lengths of 2.367 and 2.372 Å where bds is 1,2-benzenediselenolate.

Outlined in Table 3.13 are the Pt-N2, and Pt-N1 bond lengths for Pt(dpphen)(bSO) from the X-ray crystallography. The Pt-N2, and Pt-N1 bond lengths are 2.125(4), and 1.890(4) Å respectively. These values do not compare very well with the calculated values of 2.067, and 2.043 Å respectively. The difference in Pt-N bond length can be ascribed to the disorderliness in the

Table 3.13: Comparison of Calculated Selected Bond Lengths (Å) with experimental values from X-ray analysis for (dpphen)Pt(bSeO) and (dpphen)Pt(bSO). Where **E = Se** for (dpphen)Pt(bSeO) and **E = S** for (dpphen)Pt(bSO).

	(dpphen)Pt(bSeO)		**(dpphen)Pt(bSO)**	
	Experimental	Calculated	Experimental	Calculated
Pt1-N2	2.014(11)	2.060	2.125(4)	2.067
Pt1-N1	2.144(11)	2.085	1.890(4)	2.043
Pt1-O1	2.112(9)	2.046	1.969(10)	1.995
Pt1-**E1**	2.377(17)	2.449	2.245(4)	2.314
E1-C1	1.920(13)	1.878	1.645(6)	1.779
O1-C6	1.236(18)	1.311	1.504(11)	1.344
N1-C7	1.277(17)	1.337	1.333(6)	1.339
N1-C18	1.332(16)	1.345	1.372(4)	1.375
N2-C16	1.311(17)	1.349	1.328(6)	1.335
N2-C17	1.360(16)	1347	1.363(4)	1.365
C1-C6	1.400(2)	1.435	1.381(6)	1.411

C17-C18	1.456(19)	1.453	1.435(6)	1.428

crystal structure from both the donor (2-mercaptophenolate) and acceptor (dpphen) ligand. Furthermore, the experimental Pt-O bond length of 1.969(10) Å compares well with the calculated value of 1.994 Å. The experimental values of Pt-N bond lengths are not in the range of bond lengths common to another Pt(diimine)(dithiolate)[1] and Pt(diimine)(catecholate)[1]. The Pt-N bond lengths of

Pt(dpphen)(dtbdt) are 2.066(9) and 2.055(1) Å while that of Pt(bpy)(tbuCAT) are 1.978 and 1.992 Å.

On the other hand, the experimental Pt-N2, Pt-N1 and Pt-O bond lengths of Pt(dpphen)(bSeO) are 2.014(11), 2.144(11) and 2.112(9) Å respectively. These

Table 3.14: Comparison of Calculated Selected Angles (deg) with experimental angles from X-ray analysis for (dpphen)Pt(bSeO) and (dpphen)Pt(bSO). Where **E = Se** for (dpphen)Pt(bSeO) and **E = S** for (dpphen)Pt(bSO).

	(dpphen)Pt(bSeO)		**(dpphen)Pt(bSO)**	
	Experimental	Calculated	Experimental	Calculated
N2-Pt1-N1	81.2(4)	79.5	80.6(16)	79.5
N2-Pt1-O1	174.6(4)	172.9	92.8(3)	92.8
O1-Pt1-N1	93.7(4)	93.3	173.3(3)	172.3
N2-Pt1-**E1**	98.7(3)	101.6	178.8(2)	179.0
O1-Pt1-**E1**	86.5(2)	85.53	87.5(3)	86.2
N1-Pt1-**E1**	177.5(3)	178.9	99.1(16)	101.4

C1-**E1**-Pt1	93.5(4)	93.5	95.6(2)	96.6
C6-O1-Pt1	116.0(9)	120.67	118.4(6)	118.7
C7-N1-C18	125.9(12)	121.0	117.8(3)	117.8
C7-N1-Pt1	124.4(9)	125.5	123.9(3)	127.8
C16-N2-Pt1	127.9(9)	126.0	130.9(3)	126.7
C17-N2-Pt1	113.7(9)	114.0	110.7(3)	114.2
C16-N2-C17	118.2(12)	119.9	118.4(4)	119.14
C6-C1-C2	122.3(13)	120.11	105.6(6)	120.10

values compare well with the calculated values of 2.060, 2.085, and 2.046 Å respectively. The Pt-N diimine bond lengths are in the range of bond lengths common to other Pt(diimine)(dithiolate)[1]. The Pt-O bond distance of Pt(dpphen)(bSeO) is slightly longer than that found in Pt(bpy)(tbuCAT) i.e. 1.982, and 1.984 Å. The Pt-Se bond length in Pt(dpphen)(bSeO) complex is 2.377(17) Å and is comparable to that found in Pt(dbbpy)(bds) with Pt-Se bond lengths of 2.367 and 2.372 Å where bds is 1,2-benzenediselenolate. With regards to Pt-chalcogenolene bond distance (Pt—E) where E= O, S, Se, the bond length exhibits the trend of Se>S>O as presented in Table 3.13. The bond length of Pt-O (2.041 Å, the average of the two Pt-O bond distances) is shorter than that of Pt-S (2.245 Å) and Pt-Se (2.377 Å). The difference in these bond lengths can be ascribed to the fact that each chalcogenolene atom has different atomic radius with Se having the largest among the three and O having the smallest. The dpphen chelate ligands in Pt(dpphen)(bSeO) and Pt(dpphen)(bSO) complexes

result in N-Pt-N bond angles of 81.2(4) and 80.6(16)^0 respectively, which is appreciably less than the idealized value of 90^0. The O-Pt-Se and O-Pt-S bond angles are 86.5(2) and 87.5(3)^0 respectively. These bond angles are comparable to the S-Pt-S bond angle (86.64^0) of Pt(dpphen)(dtbdt)^2 but slightly higher than the bond angle of O-Pt-O (84.23^0) in Pt(bpy)(tbuCAT).[1]

In comparison, the distortion around the Pt(II) center in both Pt(dpphen)(bSO) and Pt(dpphen)(bSeO) are very similar. Their bond angles compare very well with that of Pt(dpphen)(dtbdt).[1] The S1-Pt-O1, N1-Pt-N2, N2-Pt-O1, and N1-Pt-S1 bond angles for Pt(dpphen)(bSO) are 87.5(3), 80.6(16), 92.8(3), and 99.1(16)^0 respectively, while that of Se1-Pt-O1, N1-Pt-N2, N1-Pt-O1, and N2-Pt-Se1 are 86.5(2), 81.2(4), 93.7(4), and 98.7(3)^0 respectively for Pt(dpphen)(bSeO). The S1-Pt-S2, N1-Pt-N2, N1-Pt-S2, and N2-Pt-S1 bond angles for Pt(dpphen)(dtbdt) are 88.64(13), 80.30(4), 96.80(3), and 94.40(3)^0 respectively. The bond angles of Pt(dpphen)(bSO) and Pt(dpphen)(bSeO) deviate slightly from the perfect square planar geometry. The dihedral angle between N1-Pt-N2 and S1-Pt-O1 planes is 1.38^0 for Pt(dpphen)(bSO), while that of Pt(dpphen)(bSeO) is 3.19^0 for the dihedral angle between N1-Pt-N2 and Se1-Pt-O1 planes. The dihedral angle measured for Pt(dpphen)(dtbdt) is 6.53^0 for the planes of N1-Pt-N2 and S1-Pt-S1.[2] Pt(dpphen)(bSO) and Pt(dpphen)(bSeO) dihedral angles values are very close to 0^0 indicating a perfect flat geometry.

3.3 Computational Studies for M(dichalcogenolene)(diimine) Complexes

3.3.1 Geometry Optimization Calculation

Geometry Optimization Calculation

To explicate the nature of the frontier molecular orbitals of M(diimine)(dichalcogenolene) complexes [M=Pt, Ni, and Pd] and to assist in our understanding of electronic spectra of complexes, ground-state electronic structure calculations were computed at the density functional theory (DFT; TDDFT) level using the Gaussian 09 revision C.01 software package.[70] The functional employed across these calculations are the B3LYP. The functional consist of non-local hybrid exchange functional as describe by Becke's three-parameter equation [52] and Lee-Yang-Parr correlation functional.[71] The ground-state geometry optimization for Pt(dbbpy)(mcp), Pt(dbbpy)(tbp)$_2$, Pt(dbbpy)(tbt)$_2$, Pt(dpphen)(bSO), Pt(dpphen)(bSeO), and Pt(dbbpy)(bds) were performed in the gas phase starting from the X-ray crystallographic data. Based on the optimized structures of these compounds, the backbone of the other structures was generated. The saddle points on the potential energy surface diagram from the optimum structures were validated by the absence of imaginary frequencies.

The basis set employed in the calculation includes 6-31G(d) on light atoms and LANL2DZ on Pt. Gaussian view and ChemCraft software were used to visualized and render the molecular orbitals and electron density difference map (EDDM). Excited state calculations were computed under CASSCF based on initial geometry and TD calculations with B3LYP hybrid functional, def2-TZVP[72] on all atoms, 6-31G(d) on light atoms and LANL2DZ on Pt. EMSL website was used to obtained def2-TZVP basis set.[73-74] For the TDDFT calculations, 20 lowest singlet

and triplet excited states of the closed shell complexes were computed in Gaussian. In other to eradicate the physically unrealistic low energy charge transfer states, the long-range-corrected B3LYP level theory was employed. The lowest energy and highest oscillator strength vertical transitions from both singlets and triplets were calculated and included in this analysis using the time dependent DFT (TD-DFT) methods equipped in the Gaussian 09[75-81]. In these studies, states with very weak oscillator strength and ambiguous assignments were disregarded since the experimental data displays no proof for these additional states. The electron density difference maps (EDDM) that resulted from the ORCA 2.8[63-70] software package was envisaged with ChemCraft program, were used to probe the nature of key calculated electronic transitions such as charge transfer (CT) transitions.

3.3.2 Molecular Orbitals of M(diimine)(dichalcogenolene) Complexes

M(diimine)(dichalcogenolene) complexes represent a family of complexes that furnish us with necessary data to switch between metals, diimines and dichalcogenolene ligands.

In all the M(diimine)(dichalcogenolene) complexes, Pt, Ni, and Pd, exist as Pt^{2+}, Ni^{2+}, and Pd^{2+} respectively with a d^8 electronic configuration. When these molecules form a square planar complex, their metal d electrons are distributed in other to form a stable configuration with a spin multiplicity of unity.

The frontier molecular orbital diagrams for the model complexes were generated from the optimized geometries. The peripheral alkyl groups in some of the model

complexes were removed in other to reduce the computation time. The computational results obtained with or without the peripheral alkyl groups are the same.[63,82]

In all the complexes, the highest occupied molecular orbitals (HOMOs) are ascribed as mainly dichalcogenolene/metal in character with the paramount molecular orbital contributions from the HOMO and HOMO-1 orbitals. Due to the noninnocent nature of the dichalcogenolene ligands, no pure metal d-orbitals were observed in the frontier molecular orbital. The HOMO is mainly made up of chalcogenolene atom (O, S or Se) out-of-plane, p_z orbitals, metal d_{xz} orbitals and

Table 3.15: The frontier MO energy of Pt(diimine)(dichalcogenolene) Complexes (B3LYP/LANL2DZ).

Complex	**E_{eV} HOMO**	**E_{eV} LUMO**	**E_{eV} HOMO-LUMO**
Pt(bpy)(bdt)	-4.69	-2.85	1.84
Pt(bpy)(bds)	-4.72	-2.85	1.87
Pt(bpy)(bSSe)	-4.70	-2.86	1.84
Pt(bpy)(bSO)	-4.57	-2.87	1.70
Pt(bpy)(bSeO)	-4.57	-2.88	1.69
Pt(dbbpy)(mcp)	-4.56	-2.41	2.12
Pt(bpy)(CAT)	-4.45	-2.89	1.56
Pt(dbbpy)(pdt)	-4.63	-2.50	2.13
Pt(dbbpy)(pds)	-4.65	-2.50	2.15
$Pt(dbbpy)(tbp)_2$	-4.41	-2.69	1.72
$Pt(dbbpy)(tbt)_2$	-4.24	-2.59	1.65
Pt(phen)(qdt)	-4.91	-2.79	2.12
Pt(phen)(bdt)	-4.43	-2.59	1.84
Pt(phen)(bds)	-4.51	-2.63	1.88

dpphenPt(bSeO)	-3.97	-2.67	1.30
dpphenPt(bSO)	-3.97	-2.67	1.30
Ni(dbbpy)(bdt)	-4.67	-2.85	1.82
Ni(dbbpy)(CAT)	-4.31	-2.88	1.43
Ni(dbbpy)(bds)	-4.73	-2.88	1.85
Ni(dbbpy)(bSSe)	-4.70	-2.87	1.83
Ni(dbbpy)(bSO)	-4.49	-2.88	1.61
Pd(dbbpy)(bdt)	-4.25	-2.35	1.90
Pd(dbbpy)(CAT)	-3.76	-2.39	1.37
Pddb(bpy)(bSO)	-4.01	-2.39	1.62
Pd(dbbpy)(bds)	-4.27	-2.31	1.96
Pd(dbbpy)(bSeO)	-4.02	-2.38	1.64

carbon p_z which results in an antibonding interaction on the chelating ring. These complexes form sulfonated and sulfinated derivatives when oxidized due to the fact that chalcogenolene atom out-of-plane p_z orbital forms a major part of the HOMO. Calculations shows that LUMO is not entirely localized on the diimine, a finite contribution from both the metal and chalcogenolene atom plays a vital role. The $2p_z$ nitrogen orbitals from the diimine forms antibonding interactions with the metal d_{xz}. The preceding discussion support the theory of π*-back-bonding, which implies that electron back-donation to diimine (bpy, dbbpy, phen, or dpphen) is decreased by the existence of dichalcogenolene ligands in comparison with other complexes that are made up mainly diimine.[82]

The bonding calculations indicate that the highest occupied molecular orbitals (HOMOs) is predominantly localized on dichalcogenolene, amalgamated with some metal d-orbitals character, and the Lowest unoccupied molecular orbitals

(LUMOs) are primarily on the diimine. The LUMOs in the M(diimine)(dichalcogenolene) series are characteristics of two diimine ligands namely bpy, phen and its substituted derivatives such as dbbpy and dpphen. The valence occupied orbital character is similar in character due to identity of dichalcogenolene ligand and Pt metal. The π*-accepting ability of the bpy and phen are almost identical from the energetics point of view and hence the HOMO-LUMO energy gap for these complexes are very similar assuming the same solvation energy difference between these two levels (see Table 3.15). Table 3.15 depicts the frontier MO energies of a series of M(diimine)(dichalcogenolene) complexes. The HOMO-LUMO energy gap calculated from DFT for these complexes ranges from 1.30 – 2.15 eV. The main aim of the theoretical studies by means of DFT is to ascertain the character of the electronic transitions in the M(diimine)(dichalcogenolene) complexes. To dissect the character of the vertical electronic transitions, I analyze the contributions from coligands and metal orbitals to the frontier molecular orbitals, singlet and triplet excited states.

3.3.3 The Analysis of Frontier MO for Pt(diimine)(dichalcogenolene) Complexes

3.3.3.1 [Pt(bpy)(bdt)]

The model Pt(dbbpy)(bdt) depicts frontier molecular orbitals where the HOMO and HOMO-1 are admixed with Pt d-orbital and dithiolate character, whereas the LUMOs are of bpy π* character. The lowest triplet and singlet vertical transitions for Pt(dbbpy)(bdt) are charge transfer (CT) transitions from the HOMO to LUMO.

These CT transitions have been previously ascribed to MMLL'CT. The bonding calculations indicate the presence of metal character in the LUMO as depicted in Figure 3.81. The lowest singlet (S_1) and triplet state (T_1) have calculated energies of 1.57 and 1.00 eV respectively with the singlet (S_1) having an oscillator strength of 0.1576 (see Table 3.16). The molecular orbitals involved in the lowest energy singlet transition (S_1) are HOMO and LUMO. The other higher singlet states, i.e. S_2, S_3 and S_4 have calculated energies and oscillator strength of 1.66, 2.15, 2.41 eV and 0.0031, 0.0095, 0.0106 respectively. The molecular orbitals involved in S_2, S_3 and S_4 are HOMO-1 to LUMO, HOMO to LUMO+1, and HOMO to LUMO+2 respectively. The HOMO and HOMO-1 have b_1 and a_2 symmetry

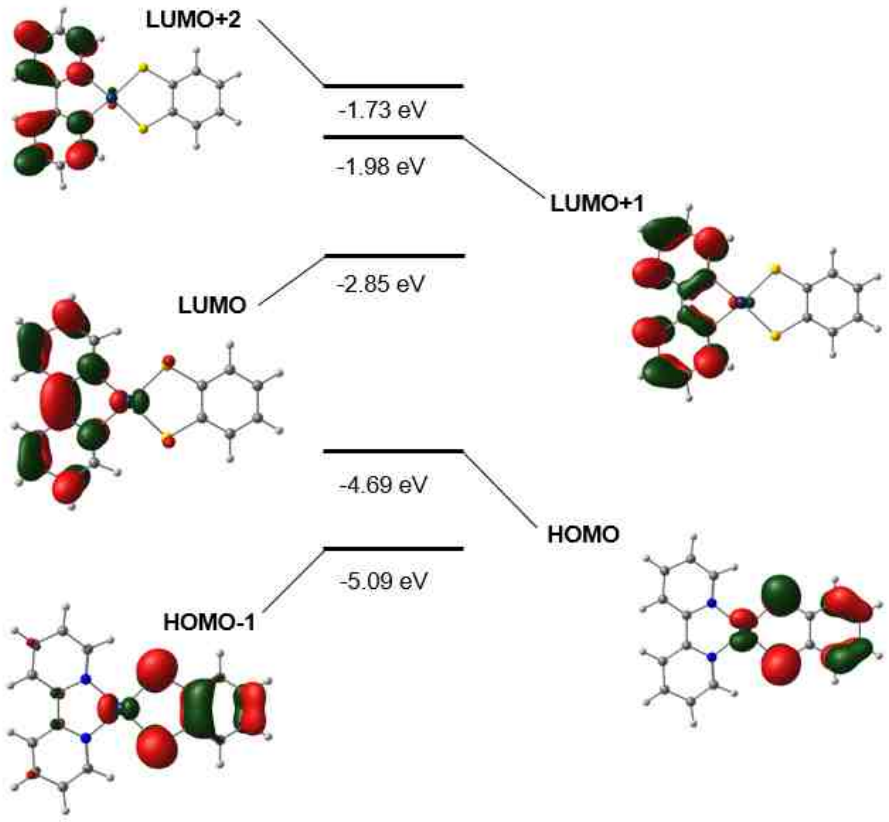

Figure 3.81: Frontier MOs and their respective energies of Pt(bpy)(bdt).

respectively while the LUMO's have b_1 symmetry characteristic of the diimine chelate moiety and they are optically active orbitals as specify by TD-DFT.[38] These symmetry assignments are depicted in Figure 3.82. MMLL'CT transition is a clear evident in the electron density difference maps (EDDMs) depicted in Figure 3.83. In the effective C_{2V} symmetry, Pt(bpy)(bdt) possess $a_2{}^2b_1{}^2b_1{}^0$ ground state configuration which is denoted by S_0. The filled $a_2{}^2$ (HOMO-1) donor orbital is predominately made up of antisymmetric combination (S_π^-) of sulfur out-of-plane S_{Px} orbital while the filled $b_1{}^2$ (HOMO) donor orbital is dominantly comprise of symmetric combination (S_π^+) of sulfur out-of-plane S_{Px} orbital depicted in Figure 3.82.[83-84] The lowest of antisymmetric combination (S_π^-) of sulfur out-of-

Table 3.16: Selected TD-DFT Calculated Energies and Compositions of the Lowest Lying Singlet and Triplet Energy States together with oscillator strengths for Pt(bpy)(bdt).

	Composition[a]	**ΔE[b]**	***f*[c]**	**Assignment**
Singlets				
S_1	HOMO→LUMO, 70%	1.57	0.1576	bdt/Pt→bpy/Pt (LMCT/LLCT)
S_2	HOMO-1→LUMO, 70%	1.66	0.0031	bdt/Pt→bpy/Pt (LMCT/LLCT)
S_3	HOMO→LUMO+1, 70%	2.15	0.0095	bdt/Pt→bpy (MMLL'CT)
S_4	HOMO→LUMO+2, 69%	2.41	0.0106	bdt/Pt→bpy (MMLL'CT)
Triplets				
T_1	HOMO→LUMO, 70%	1.00	0.0000	bdt/Pt→bpy/Pt (LMCT/LLCT)
T_2	HOMO-1→LUMO, 70%	1.57	0.0000	bdt/Pt→bpy/Pt (LMCT/LLCT)
T_3	HOMO→LUMO+1, 70%	2.02	0.0000	bdt/Pt→bpy (MMLL'CT)
T_4	HOMO→LUMO+2, 69%	2.24	0.0000	bdt/Pt→bpy (MMLL'CT)

[a] Electronic transitions compositions expressed in terms of ground-state Kohn-Sham molecular orbitals. [b] Transition energy expressed in eV. [c] Oscillator strength.

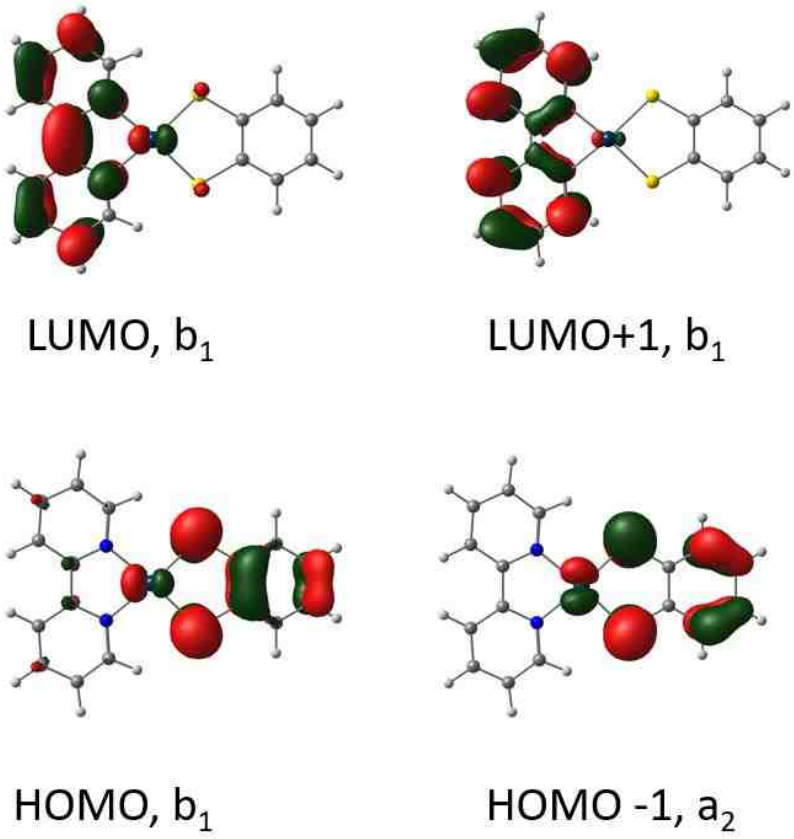

Figure 3.82: Frontier MOs of Pt(bpy)(bdt) with symmetry assignment.

plane S_{Px} orbital while the filled b_1^2 (HOMO) donor orbital is dominantly comprise of symmetric combination (S_π^+) of sulfur out-of-plane S_{Px} orbital depicted in Figure 3.82.[83-84] The lowest-energy absorption band is ascribed to HOMO → LUMO transition which is composed primarily of 70% $b_1 \rightarrow b_1$ tabulated in Table 3.16. This represent S_1 singlet excited state with a configuration of $a_2^2 b_1^1 b_1^1$; $^1A_1$. The second lowest-energy absorption band is assign to HOMO-1 → LUMO transition which is also composed mainly of 70% $a_2 \rightarrow b_1$ denoted as S_2 singlet

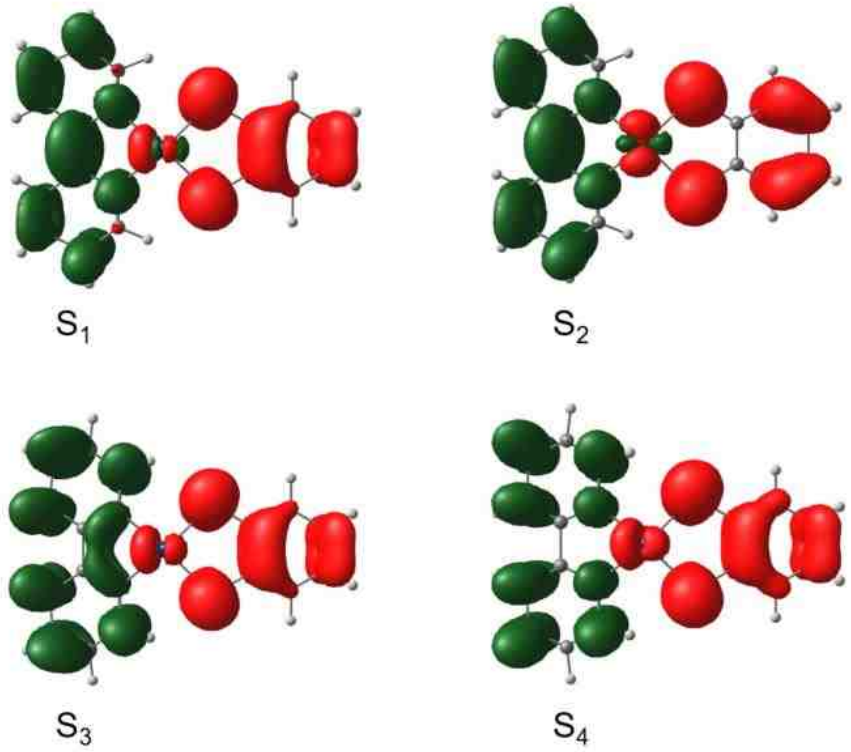

Figure 3.83: Calculated electron density difference map (EDDM) for Singlet States at an isodensity value of 0.0012 au. The red and green regions represent loss and gain of electron density respectively in a transition to the excited state.

excited state with $a_2^1 b_1^2 b_1^1$; $^1B_2$ configuration. The triplet excited states, T_1 ($^3A_1$) and T_2 ($^3B_2$) uses the same frontier molecular orbitals as their singlet (S_1 and S_2)

Table 3.17: Solvent effect on the experimental energy of the charge transfer maxima ($E_{MMLL'CT}$) and the HOMO-LUMO energy gap (ΔE) calculated by DFT for **Pt(dbbpy)(bdt).**

Solvent	**E_{eV} HOMO**	**E_{eV} LUMO**	**ΔE_{eV}[a]**	**$\Delta E(cm^{-1})$**	**$E_{MMLL'CT}$ (cm^{-1})[b]**
Benzene	-6.1941	-2.3323	3.8618	31148	15991
Chloroform	-6.3323	-2.3189	4.0134	32370	17391
DCM	-6.4252	-2.3154	4.1098	33148	18186
Acetone	-6.5002	-2.3151	4.1851	33755	18348

DMF	-6.5307	-2.3157	4.2150	33996	18692
DMSO	-6.5386	-2.3159	4.2227	34058	19048
Acetonitrile	-6.5291	-2.3159	4.2132	33982	19242
THF	-6.4017	-2.3159	4.0858	32954	17098

[a] HOMO-LUMO energy gap (∆E) calculated by DFT/PCM, [b] Experimental energy of the MMLL'CT band maxima.

counterpart.[83] Solvent effects on molecular properties was treated using polarizable continuum model (PCM), a continuum solvent model procedure that dominantly affects the HOMOs with large metal contributions. The LUMO contributions only changes by infinitesimal amount, with contributions mainly from the diimine chelate ligand.[82,85] These observations are presented in Table 3.17. The reliability of the DFT/PCM theory was examined by comparison of its predictions for Pt(dbbpy)(bdt) in eight different organic solvents with the experimental energies of the CT band maxima. From Table 3.17, it can be ascertained that the model of solvation increases the HOMO-LUMO gap by 0.35 eV (2800 cm-1) ranging from benzene to acetonitrile. The application of PCM was tested on Pt(diimine)(dichalcogenolene) complexes by using the equation, $E_{MMLL'CT} = f(\Delta E)$ on eight solvents namely acetonitrile, acetone, DMF, DMSO, tetrahydrofuran (THF), chloroform, dichloromethane (DCM), and benzene. The linear relationship between $E_{MMLL'CT}$ and ∆E is depicted in Figure 3.84 and a perfect correlation exists between nonpolar solvents as result of large transition moments these complexes possess. THF was excluded from the regression analysis due to specific parametrization on the level of polarizable continuum model.[82]

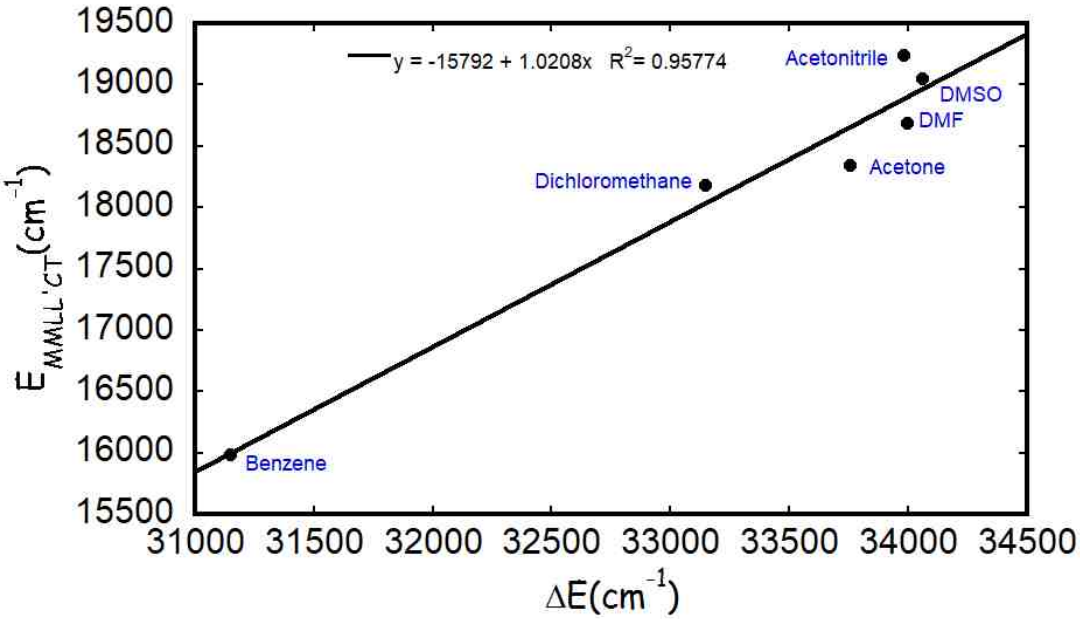

Figure 3.84: Linear correlation between experimental energy of the CT maxima ($E_{MMLL'CT}$) and the HOMO-LUMO energy gap (ΔE) calculated by DFT for Pt(dbbpy)(bdt).

3.3.3.2 Pt(bpy)(bds)

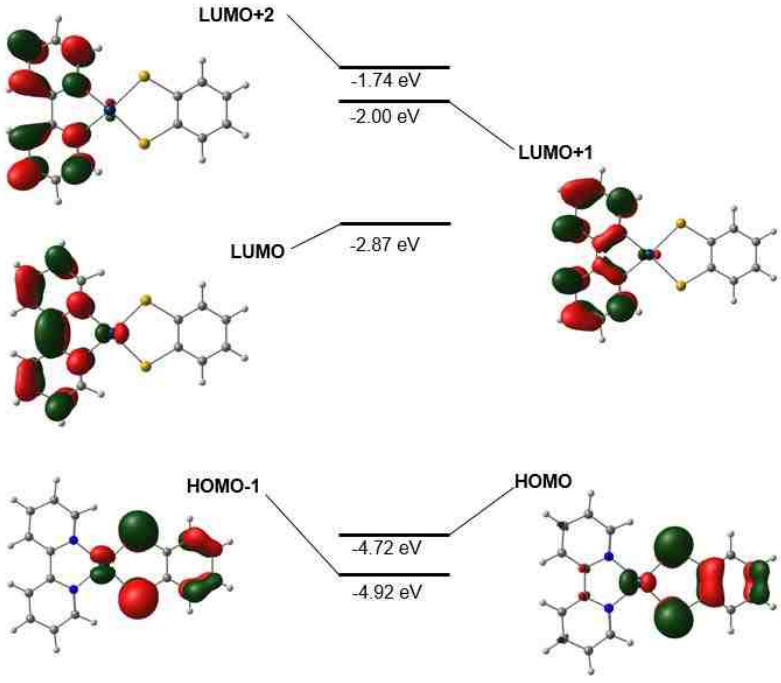

Figure 3.85 Frontier MOs and their respective energies of Pt(dbbpy)(bds).

The frontier molecular orbitals displayed by Pt(bpy)(bds) are like other Pt(diimine)(dichalcogenolene) models. Here, the chalcogenolene atom involved is Selenium (Se) instead of sulfur for Pt(bpy)(bdt). The MO diagram and energies for the frontier orbitals of Pt(dbbpy)(bds) is depicted in Figure 3.85. The frontier molecular orbital energies of Pt(bpy)(bds) are very close to that of Pt(bpy)(bdt). TD-DFT calculation predicts the lowest singlet and triplet vertical transitions for Pt(bpy)(bds) to be from the HOMO →LUMO. This vertical transition is assign as LMCT/LLCT instead of MMLL'CT due to the metal contributions to both the HOMO and LUMO molecular orbitals. The calculated S_1 and T_1 have energies of 1.49 and 1.04 eV respectively with the oscillator strength of S_1 given as 0.0039 (Table 3.18). The most probable vertical transition is S_2 with 1.55 eV and an

Table 3.18: Selected TD-DFT Calculated Energies and Compositions of the Lowest Lying Singlet and Triplet Energy States Together with Oscillator Strengths for Pt(bpy)(bds).

	Composition[a]	**ΔE[b]**	***f*[c]**	**Assignment**
Singlets				
S_1	HOMO→LUMO, 70%	1.49	0.0039	bds/Pt→bpy/Pt (LMCT/LLCT)
S_2	HOMO-1→LUMO, 70%	1.55	0.1390	bds/Pt→bpy/Pt (LMCT/LLCT)
S_3	HOMO→LUMO+1, 70%	2.14	0.0044	bds/Pt→bpy (MMLL'CT)
S_4	HOMO→LUMO+2, 60%	2.48	0.0273	bds/Pt→bpy (MMLL'CT)
Triplets				
T_1	HOMO→LUMO, 70%	1.04	0.0000	bds/Pt→bpy/Pt (LMCT/LLCT)
T_2	HOMO-1→LUMO, 70%	1.31	0.0000	bds/Pt→bpy/Pt (LMCT/LLCT)
T_3	HOMO→LUMO+1, 70%	2.02	0.0000	bds/Pt→bpy (MMLL'CT)
T_4	HOMO→LUMO+2, 69%	2.26	0.0000	bds/Pt→bpy (MMLL'CT)

[a] Electronic transitions compositions expressed in terms of ground-state Kohn-Sham molecular orbitals. [b] Transition energy expressed in eV. [c] Oscillator strength.

oscillator strength of 0.1390. The molecular orbitals involved in the second lowest

singlet (S_2) transitions are HOMO-1 and LUMO. The electronic transitions compositions of S_1 and S_2 are both made up of 70% of the HOMO →LUMO and the HOMO-1 →LUMO respectively. In effective C_{2V} symmetry, the HOMO's and LUMO's have the same symmetry assignment as that of Pt(bpy)(bdt) (see Figure 3.86)**.** The calculated electron density difference map (EDDM) for singlet states at an isodensity value of 0.0012 au is depicted in Figure 3.87. The red and green regions represent loss and gain of electron density respectively in a vertical electronic transition to the excited state. The EDDM's of S_1, S_2, S_3 and S_4 show clearly that the electron density is lost from the HOMO which is a mixture of 1,2-benzenediselenolate and Pt. The gain of electron density by the LUMO is represented as purely diimine for S_3, S_4 and S_1 and S_2 is a mixture of and diimine

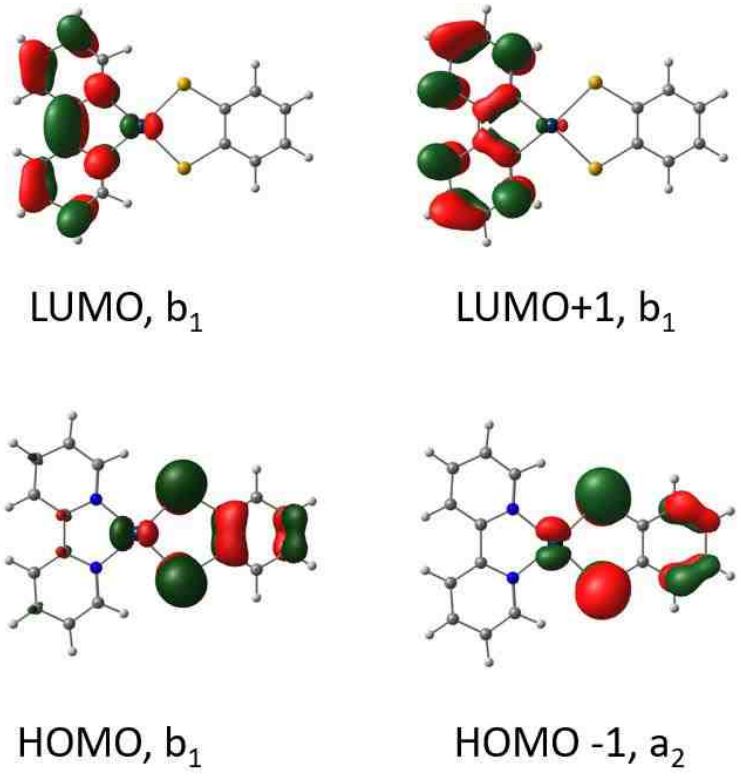

Figure 3.86 Frontier MOs of Pt(dbbpy)(bds) with symmetry assignment.

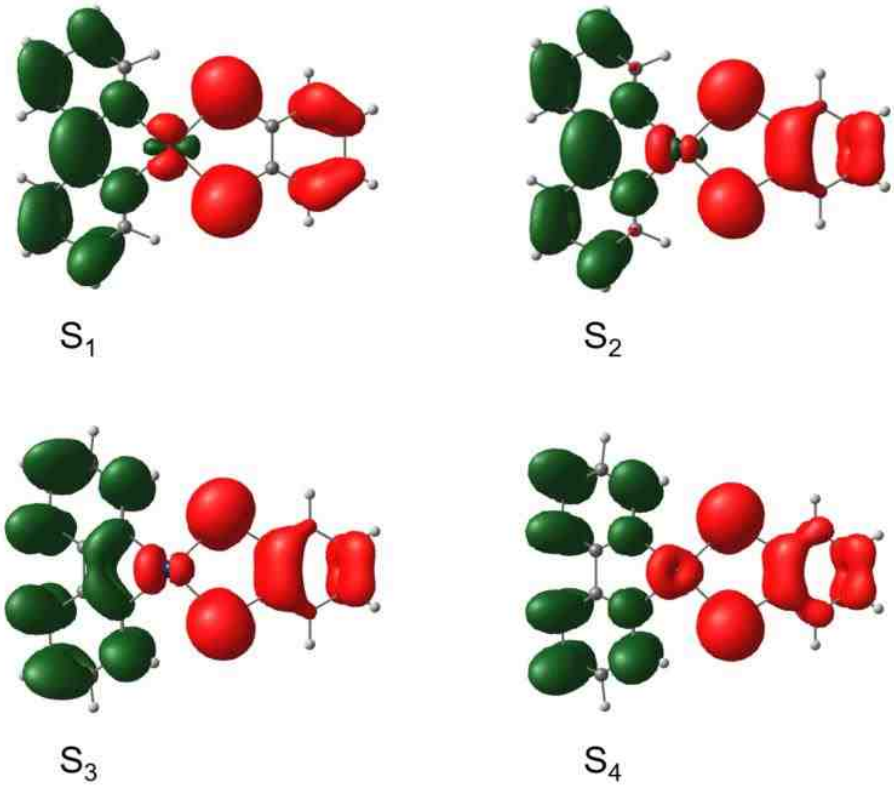

Figure 3.87: Calculated electron density difference map (EDDM) for Singlet States at an isodensity value of 0.0012 au. The red and green regions represent loss and gain of electron density respectively in a transition to the excited state.

and Pt (see Figure 3.87). Based on DFT/PCM theory, the HOMO-LUMO gap of Pt(dbbpy)(bds) was examined using polar and non-polar organic solvent. The results were then compared with the experimental energies of the CT band maxima (see Table 3.19).

Table 3.19: Solvent effect on the experimental energy of the charge transfer maxima ($E_{MMLL'CT}$) and the HOMO-LUMO energy gap (ΔE) calculated by DFT for **Pt(dbbpy)(bds).**

Solvent	**E_{eV} HOMO**	**E_{eV} LUMO**	**ΔE_{eV}[a]**	**$\Delta E(cm^{-1})$**	**$E_{MMLL'CT}(cm^{-1})$[b]**
Benzene	-6.4330	-2.3454	4.0876	32969	16011

Chloroform	-6.6083	-2.3282	4.2801	34521	17483
DCM	-6.7065	-2.3214	4.3851	35368	18311
Acetone	-6.7748	-2.3181	4.4567	35946	18528
DMF	-6.7999	-2.3173	4.4826	36155	18911
DMSO	-6.8061	-2.3171	4.4890	36206	19086
Acetonitrile	-6.7985	-2.3173	4.4814	36145	19306
THF	-6.6831	-2.3228	4.3603	35169	17283

[a] HOMO-LUMO energy gap (ΔE) calculated by DFT, [b] Experimental energy of the MMLL'CT band maxima.

Based on the results tabulated in Table 3.19**,** it can be deduced that a continuum solvent model procedure increases the HOMO-LUMO gap by 0.40 eV (3200 cm-1) ranging from non-polar benzene to polar acetonitrile. By using the equation, $E_{MMLL'CT} = f(\Delta E)$, a linear relationship between $E_{MMLL'CT}$ and ΔE was obtained (Figure 3.88).

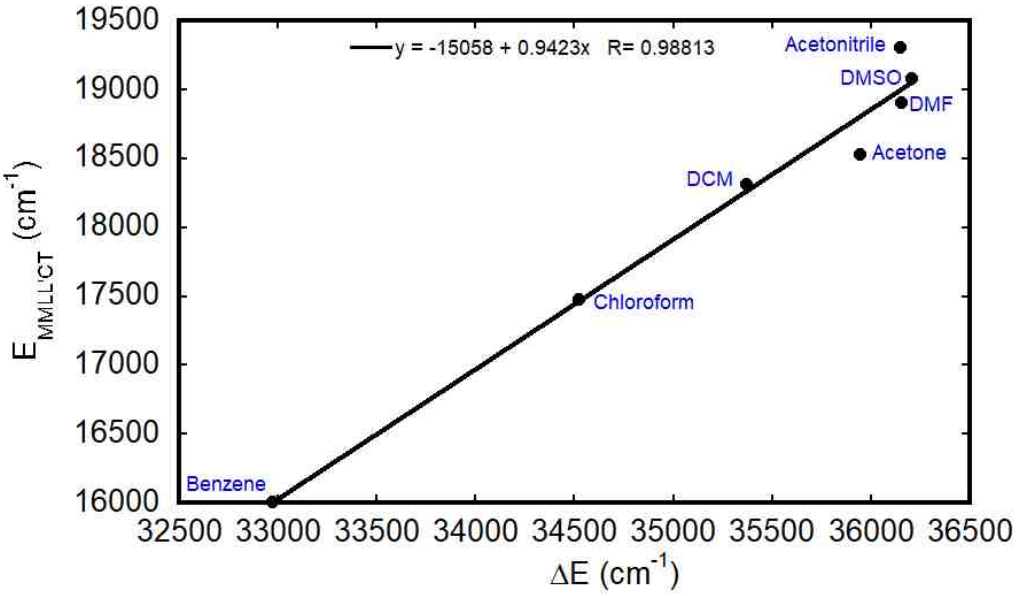

Figure 3.88: Linear correlation between experimental energy of the CT maxima ($E_{MMLL'CT}$) and the HOMO-LUMO energy gap (ΔE) calculated by DFT for Pt(dbbpy)(bds)

3.3.3.3 Pt(bpy)(bSSe)

Molecular orbital diagram and energies for the frontier orbitals of the

Pt(dbbpy)(bSSe) is depicted in Figure 3.89. In Pt(dbbpy)(bSSe), the chalcogenolene atoms involved are Selenium (Se) and Sulfur (S). The frontier molecular orbital energies of Pt(bpy)(bSSe) are very close to that of Pt(bpy)(bdt). From Table 3.20, the lowest energy singlet and triplet vertical transitions for Pt(bpy)(bSSe) are CT transitions from HOMO →LUMO and are assign as LMCT/LLCT. The calculated S_1 and T_1 have energies of 1.55 and 1.02 eV respectively with a high oscillator strength of S_1 given by 0.1008. The second singlet (S_2) and triplet (T_2) vertical transitions for Pt(bpy)(bSSe) are also CT from HOMO-1 →LUMO and are assign as LMCT/LLCT. From TDDFT, the calculated

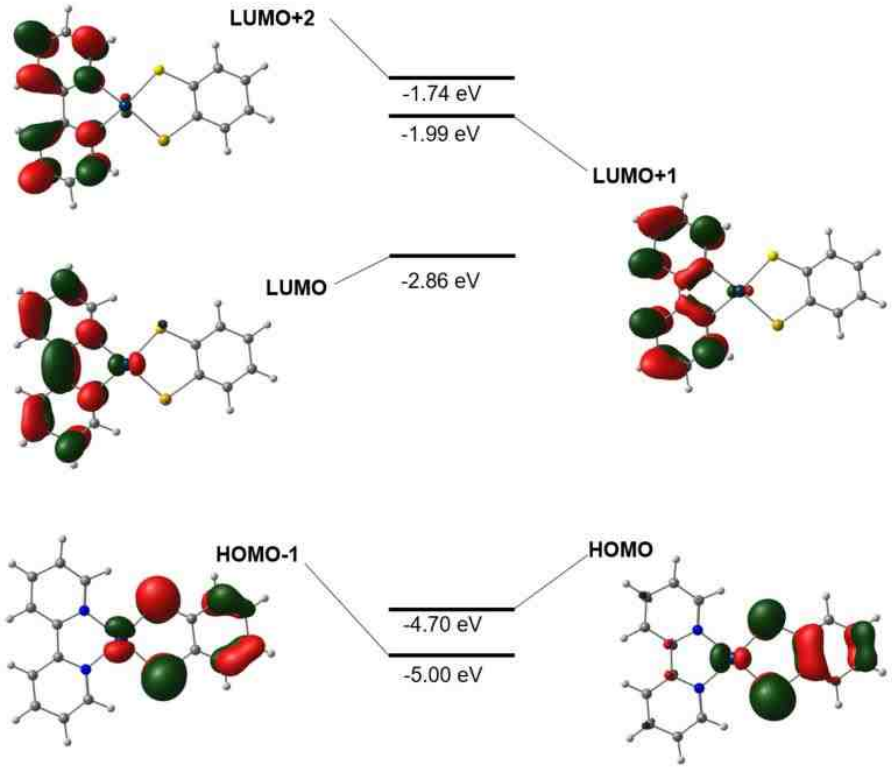

Figure 3.89 Frontier MOs and their respective energies of Pt(dbbpy)(bSSe).

S_2 and T_2 have energies of 1.59 and 1.39 eV respectively with an oscillator strength of S_2 given by 0.0510. The third singlet (S_3) and triplet state (T_3) are primarily ^{1}MMLL'CT and ^{3}MMLL'CT respectively in character, from the Pt(bSSe) HOMO to the bpy π*, LUMO+1. The vertical transition energies for S_3 and T_3 are 2.14 and 2.02 eV respectively with S_3 having an oscillator strength of 0.0066. The lowest lying singlet (S_1) and triplet (T_1) transitions are 61% and 70% HOMO to LUMO respectively. The second singlet (S_2) and triplet (T_2) are 61% and 70% HOMO-1 to LUMO respectively. Based on symmetry, HOMO-1 is assigned as a_2, HOMO is b_1, and LUMO is b_1 (Figure 3.90) with each frontier molecular orbital

Table 3.20: Selected TD-DFT Calculated Energies and Compositions of the Lowest Lying Singlet and Triplet Energy States Together with Oscillator Strengths for **Pt(bpy)(bSSe).**

	Composition[a]	**ΔE[b]**	***f*[c]**	**Assignment**
Singlets				
S_1	HOMO→LUMO, 61%	1.55	0.1008	bSSe/Pt→bpy/Pt (LMCT/LLCT)
S_2	HOMO-1→LUMO, 61%	1.59	0.0510	bSSe/Pt→bpy/Pt (LMCT/LLCT)
S_3	HOMO→LUMO+1, 70%	2.14	0.0066	bSSe/Pt→bpy (MMLL'CT)
S_4	HOMO→LUMO+2, 56%	2.39	0.0035	bSSe/Pt→bpy (MMLL'CT)
Triplets				
T_1	HOMO→LUMO, 70%	1.02	0.0000	bSSe/Pt→bpy/Pt (LMCT/LLCT)
T_2	HOMO-1→LUMO, 70%	1.39	0.0000	bSSe/Pt→bpy/Pt (LMCT/LLCT)
T_3	HOMO→LUMO+1, 70%	2.02	0.0000	bSSe/Pt→bpy (MMLL'CT)
T_4	HOMO→LUMO+2, 56%	2.39	0.0000	bSSe/Pt→bpy (MMLL'CT)

[a] Electronic transitions compositions expressed in terms of ground-state Kohn-Sham molecular orbitals. [b] Transition energy expressed in eV. [c] Oscillator strength.

admixed with varying degree of Pt d-orbital character. The calculated electron density difference map (EDDM) for singlet and triplet States at an isodensity

value of 0.0012 au are depicted in Figure 3.91. The red and green regions represent loss and gain of electron density respectively in a transition to the excited state. From the EDDM's in Figure 3.91, it is very clear that electron density is lost from the donor orbitals, in this case, 2-selenylbenzenethiolate admixed with some Pt d-orbital character. The acceptor orbitals that gain electron density in the EDDM's are bpy π* also admixed with Pt-d orbital character. This is very noticeable in S_1 and S_2 while in S_3 and S_4, the acceptor orbitals do not involve Pt-d orbital character.

DFT/PCM model was also applied to Pt(dbbpy)(bSSe) to revel solvation

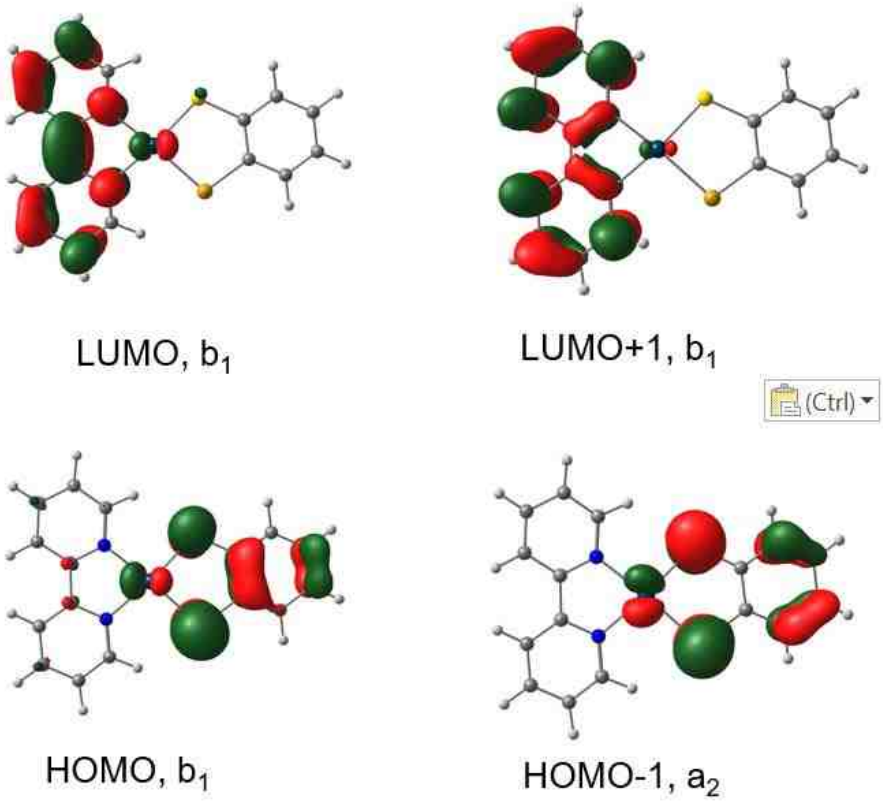

Figure 3.90: Frontier MOs of Pt(dbbpy)(bSSe) with symmetry assignment.

procedures. The solvent model procedure significantly affects the HOMO's, without or little changes in the LUMO's. The electronic behavior of Pt(dbbpy)(bSSe) was probed with eight widely used organic solvents ranging from acetonitrile, acetone, dimethyl formamide (DMF), dimethyl sulfoxide (DMSO), chloroform, tetrahydrofuran (THF), dichloromethane (DCM), and benzene with varying electric fields. The solvent model was tested using the equation $E_{MMLL'CT} = f(\Delta E)$ on the three solvent fields with different solvent polarity ranging from minor, medium and high. It was ascertained that an increase in the polarity of the field remarkably stabilizes the HOMOs and it results in an increase HOMO-LUMO gap. This result is manifested in the low

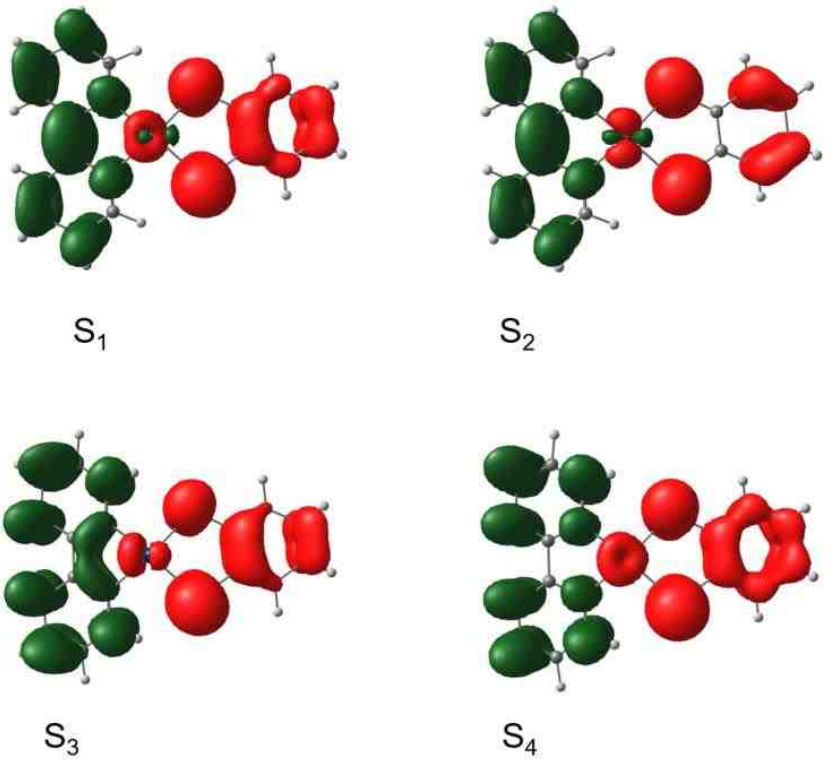

Figure 3.91: Calculated electron density difference map (EDDM) for Singlet States at an isodensity value of 0.0012 au. The red and green regions represent loss and gain of electron density respectively in a transition to the excited state.

energy MMLL'CT band in the UV- Vis spectrum as it turns to be blue shifted. These results are outlined in Table 3.21 and conferred pictorially in Figure 3.92. It

Table 3.21: Solvent effect on the experimental energy of the charge transfer maxima ($E_{MMLL'CT}$), calculated dipole moment (μ) and the HOMO-LUMO energy gap (ΔE) calculated by DFT for **Pt(dbbpy)(bSSe).**

Solvent	**E_{eV} HOMO**	**E_{eV} LUMO**	**ΔE_{eV}[a]**	**$\Delta E(cm^{-1})$**	**$E_{MMLL'CT}$ (cm^{-1})[b]**	**μ (debye)**
Benzene	-6.1642	-2.3451	3.8191	30803	15993	15.05
Chloroform	-6.3041	-2.3307	3.9734	32047	17421	16.60
DCM	-6.3988	-2.3268	4.0720	32843	18150	17.28
Acetone	-6.4758	-2.3263	4.1495	33468	18344	17.85
DMF	-6.5065	-2.3266	4.1799	33713	18775	17.97
DMSO	-6.5147	-2.3266	4.1881	33779	19050	18.08
Acetonitrile	-6.5049	-2.3266	4.1783	33700	19250	17.96
THF	-6.3748	-2.3274	4.0474	32644	17029	17.17

[a] HOMO-LUMO energy gap (ΔE) calculated by DFT, [b] Experimental energy of the MMLL'CT band maxima.

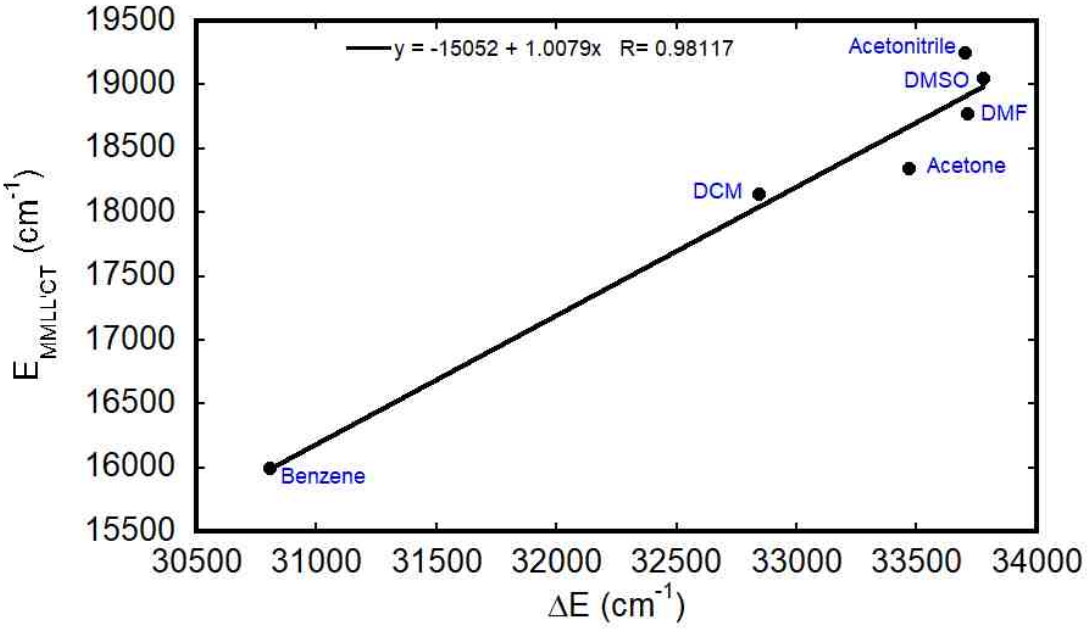

Figure 3.92: Linear correlation between experimental energy of the CT maxima ($E_{MMLL'CT}$) and the HOMO-LUMO energy gap (ΔE) calculated by DFT for Pt(dbbpy)(bSSe).

was observed from previous experiment that the solvent field stabilizes both metal and dithiolate ligand and destabilizes the orbitals of the diimine chelate ligand. The charge distribution in the ground state, i.e. solvation due to diploe-dipole interaction can be used to explain this trend. The dipole-dipole interaction tends to stabilize the part of the molecule with higher electron density and destabilizes the other part with a lower electron density. [64] In our case the Pt metal and 2-selenylbenzenetiolate possesses the higher electron density (Figure 3.91). From the above discussion, one can conclude that for solvent with minor polarity, the electronic description of Pt(diimine)(dichalcogenolene) model is almost the same as that calculated in the gas phase. A closer inspection of Table 3.21 indicates that the HOMO-LUMO gap increases by 0.37 eV (3000 cm^{-1}) from benzene to DMSO. A linear correlation exists between a plot of $E_{MMLL'CT}$ vs ΔE except for THF, which deviates appreciably from linearity (Figure 3.92).

Furthermore, from the summarized results in Table 3.21, the DFT/PCM calculation shows that the calculated dipole moment (μ) decreases steadily from polar to non-polar solvents i.e. 18.08 D for DMSO, 17.28 D for dichloromethane, 16.60 D for chloroform, and 15.05 D for benzene. The decrease in the calculated diploe moment of the molecule can be ascribe to the reduction of the ground state polarity of the complexes going from polar to non-polar solvents.[84]

3.3.3.4 Pt(bpy)(bSO)

Figure 3.94 depicts the energy diagram of the frontier molecular orbitals of Pt(dbbpy)(bSO), where sulfur (S) and oxygen (O) are the donor atoms of the

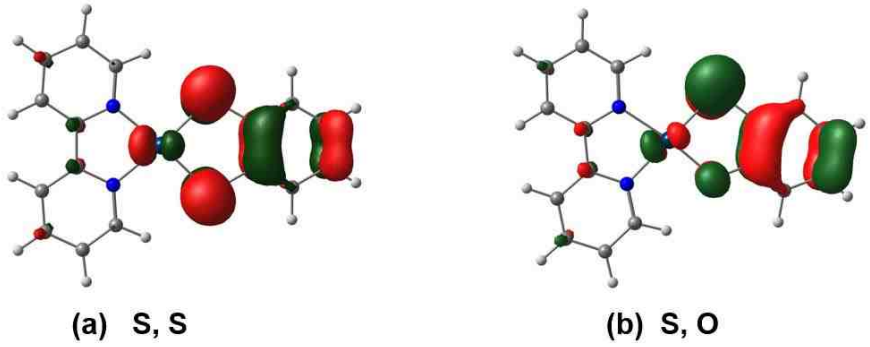

Figure 3.93: HOMO for (a) Pt(bpy)(bdt) and (b) Pt(bpy)(bSO).

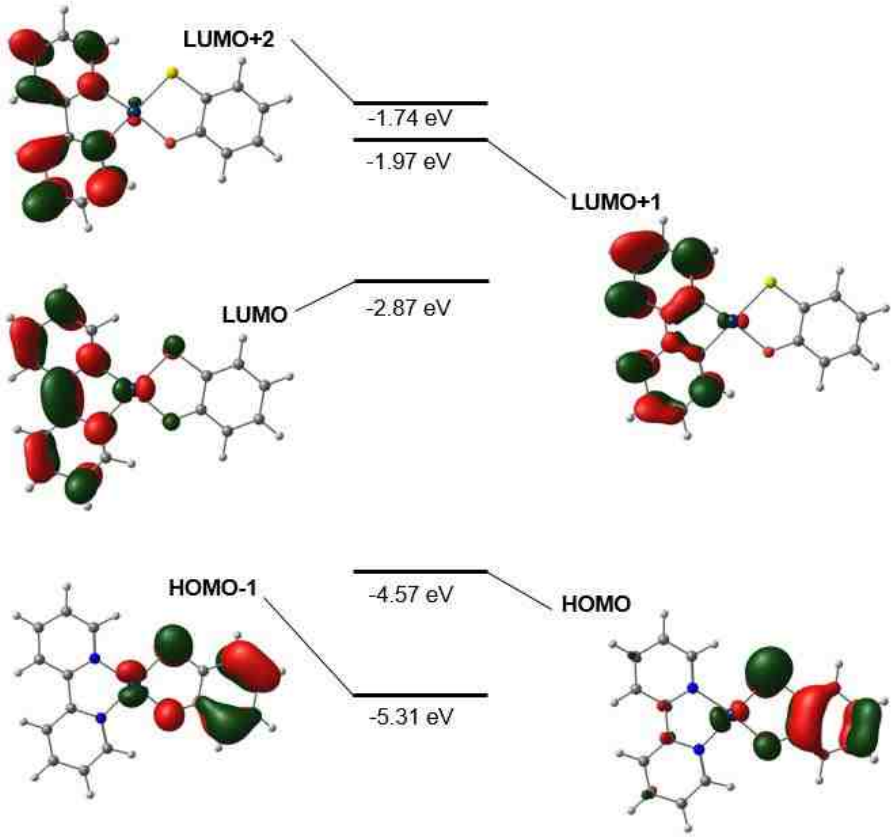

Figure 3.94: Frontier MOs and their respective energies of Pt(dbbpy)(bSO).

chalcogenolene. Pt(bpy)(bdt) possesses C_{2v} symmetry because it has the same chalcogenolene donor S atoms, and the atomic orbital (AO) compositions of the two S donor atoms are equivalent in the HOMO. In Pt(bpy)(bSO), the symmetry

is lowered to C_S because the chalcogenolene donor atoms involve are different i.e. S and O. The mirror plane in Pt(bpy)(bSO) lies in the plane of the molecule. In Pt(bpy)(bdt), the Pt d_{xz} dπ orbital is positioned along the plane of the mirror that is orthogonal to the molecular plane while in Pt(bpy)(bSO), Pt d_{xz} dπ orbital is rotated in the direction of the softer chalcogenolene S atom resulting in the atomic orbital composition of S donor being remarkably larger than that of O donor in the HOMO.[27] This observation is depicted in Figure 3.93. From Figure

Table 3.22: Selected TD-DFT Calculated Energies and Compositions of the Lowest Lying Singlet and Triplet Energy States Together with Oscillator Strengths for **Pt(bpy)(bSO).**

	Composition[a]	**ΔE^b**	***f*[c]**	**Assignment**
		Singlets		
S_1	HOMO→LUMO, 71%	1.47	0.1557	bSO/Pt→bpy/Pt (LMCT/LLCT)
S_2	HOMO-1→LUMO, 70%	1.87	0.0077	bSO/Pt→bpy/Pt (LMCT/LLCT)
S_3	HOMO→LUMO+1, 70%	2.04	0.0124	bSO/Pt→bpy (MMLL'CT)
S_4	HOMO→LUMO+2, 70%	2.32	0.0246	bSO/Pt→bpy (MMLL'CT)
		Triplets		
T_1	HOMO→LUMO, 71%	0.84	0.0000	bSO/Pt→bpy/Pt (LMCT/LLCT)
T_2	HOMO-1→LUMO, 69%	1.68	0.0000	bSO/Pt→bpy/Pt (LMCT/LLCT)
T_3	HOMO→LUMO+1, 70%	1.91	0.0000	bSO/Pt→bpy (MMLL'CT)
T_4	HOMO→LUMO+2, 70%	2.13	0.0000	bSO/Pt→bpy (MMLL'CT)

[a] Electronic transitions compositions expressed in terms of ground-state Kohn-Sham molecular orbitals. [b] Transition energy expressed in eV. [c] Oscillator strength.

3.94, it is evident that the HOMO is formed by a combination of mercaptopheno-late orbital and the metal dπ while in the case of the LUMO, the major contribution comes from the bpy and some Pt dπ character. The lowest energy singlet and triplet vertical transitions are from HOMO →LUMO. The calculated S_1 and T_1 energies are 1.47 and 0.84 eV respectively with a high oscillator strength

of S_1 given by 0.1557. The second singlet (S_2) and triplet (T_2) vertical transitions of Pt(bpy)(bSO) are also charge transfer from HOMO-1 →LUMO and are assign as LMCT/LLCT. From Table 3.22, the calculated S_2 and T_2 have energies of 1.87 and 1.68 eV respectively and the S_2 has an oscillator strength of 0.0077. The third singlet (S_3) and triplet state (T_3) are primarily ^{1}MMLL'CT and ^{3}MMLL'CT respectively in character, from the Pt/bSO HOMO to the bpy π* LUMO+1. The vertical transition energies for S_3 and T_3 are 2.04 and 1.91 eV respectively with

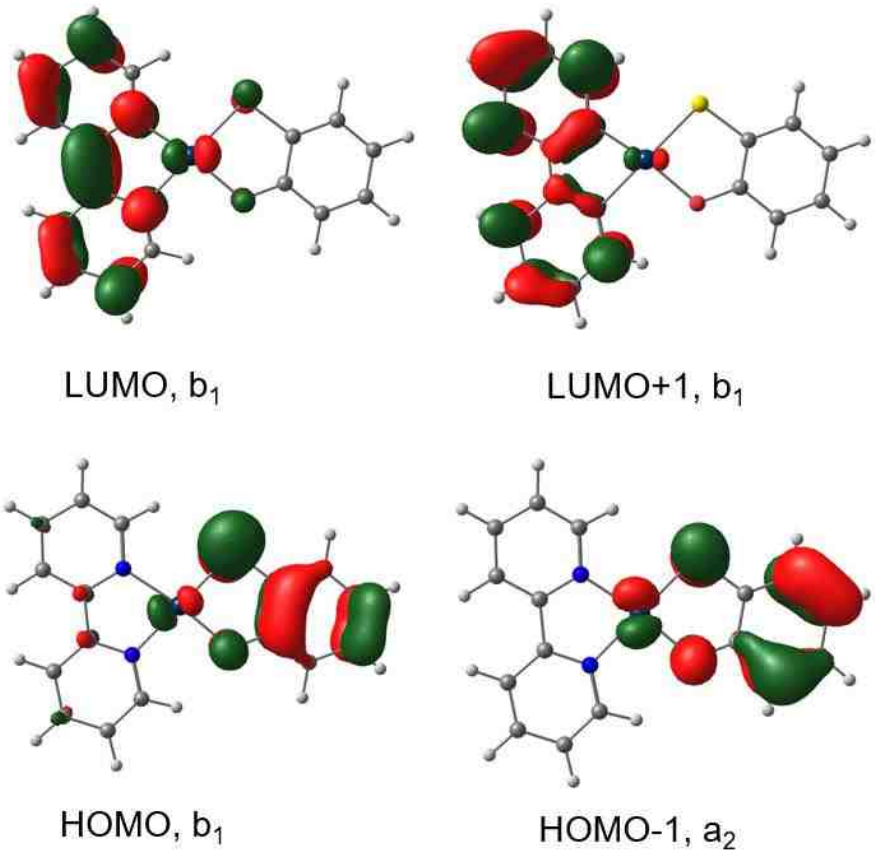

Figure 3.95: Frontier MOs of Pt(bpy)(bSO) with symmetry assignment.

S_3 having an oscillator strength of 0.0124. By inspecting Table 3.22**,** we observe that the lowest lying singlet (S_1) and triplet (T_1) transitions are made up of 71% HOMO→LUMO atomic orbital compositions. The second singlet (S_2) and triplet

(T_2) are 70% HOMO-1→LUMO atomic orbital compositions. From Figure 3.95, it can be observed that HOMO-1 has a_2 symmetry while HOMO, LUMO and LUMO+1 have b_1 symmetry. The calculated electron density difference map (EDDM) for the singlet states at an isodensity value of 0.0012 au are depicted in Figure 3.96. The red regions designate a loss of electron density while the green regions represent a gain of electron density in a transition to the excited state.

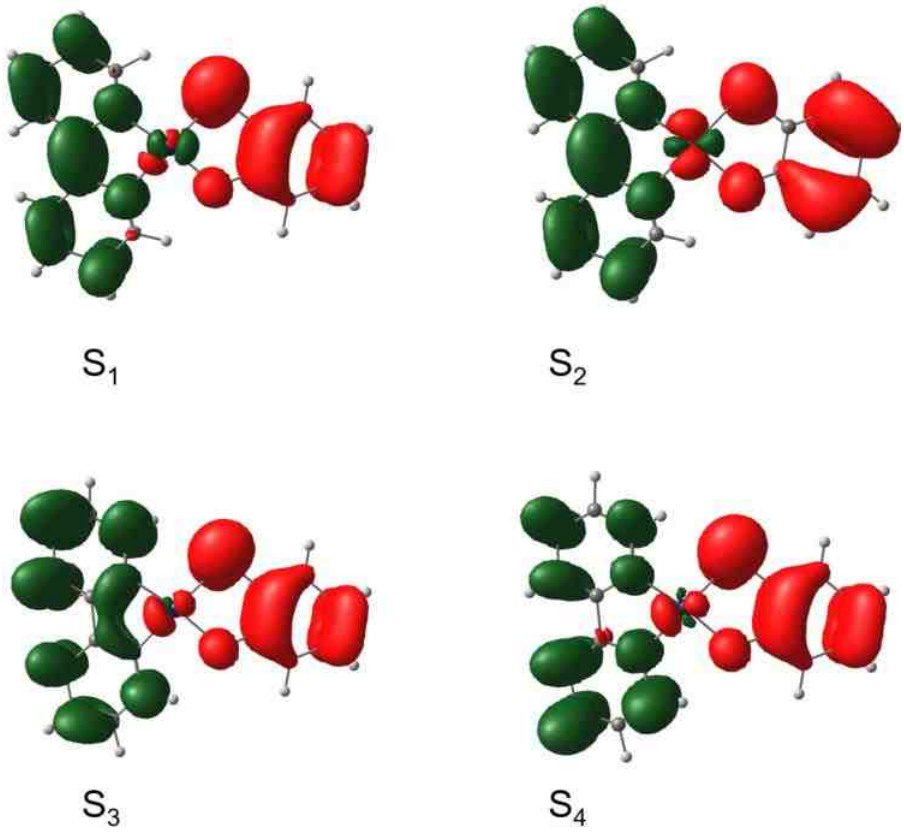

Figure 3.96: Calculated electron density difference map (EDDM) for Singlet at an isodensity value of 0.0012 au. The red and green regions represent loss and gain of electron density respectively in a transition to the excited state.

The pictorial representation of the calculated EDDMs (Figure 3.96) shows that the frontier MOs of Pt(bpy)(bSO) involve in the loss of electron density in a transition to the excited state is mercaptophenolate orbital admixed with some Pt

dπ orbital character. The MOs of Pt(bpy)(bSO) involve in the gain of electron density is the acceptor diimine chelate π* orbital with some Pt d-orbital character.

Table 3.23: Solvent effect on the experimental energy of the charge transfer maxima ($E_{MMLL'CT}$), calculated dipole moment (μ) and the HOMO-LUMO energy gap (ΔE) calculated by DFT for **Pt(dbbpy)(bSO)**.

Solvent	E_{eV} HOMO	E_{eV} LUMO	ΔE_{eV}[a]	$\Delta E(cm^{-1})$	$E_{MMLL'CT}$ (cm^{-1})[b]	μ (debye)
Benzene	-6.4330	-2.3454	4.0876	32969	16148	16.00
Chloroform	-6.6083	-2.3282	4.2801	34521	17332	17.49
DCM	-6.7065	-2.3214	4.3851	35368	17889	18.12
Acetone	-6.7748	-2.3181	4.4567	35946	17968	18.69
DMF	-6.7999	-2.3173	4.4826	36155	18396	18.78
DMSO	-6.8061	-2.3171	4.4890	36206	18745	18.92
Acetonitrile	-6.7984	-2.3173	4.4811	36142	18916	18.77
THF	-6.6831	-2.3228	4.3603	35168	16845	18.03

[a] HOMO-LUMO energy gap (ΔE) calculated by DFT, [b] Experimental energy of the MMLL'CT band maxima.

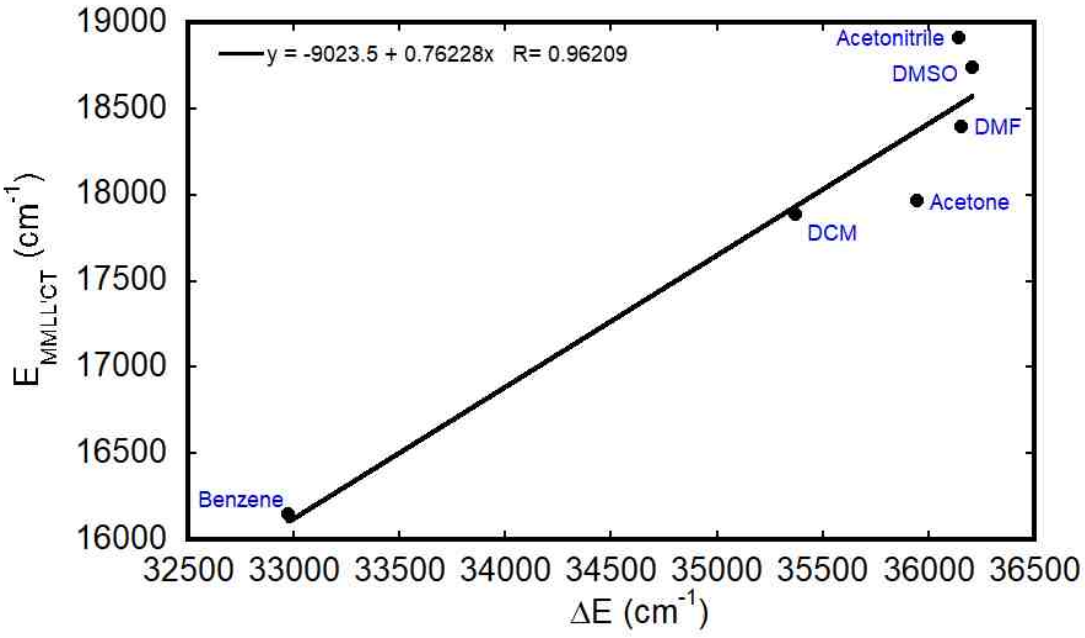

Figure 3.97: Linear correlation between experimental energy of the CT maxima ($E_{MMLL'CT}$) and the HOMO-LUMO energy gap (ΔE) calculated by DFT for Pt(dbbpy)(bSO).

The electronic behavior of Pt(bpy)(bSO) was also investigated using polar and non-polar solvents ranging from acetonitrile, acetone, dimethyl formamide (DMF), dimethyl sulfoxide (DMSO), chloroform, tetrahydrofuran (THF), dichloromethane (DCM), and benzene with different electric fields. A linear relationship was obtained (Figure 3.97) when the solvent model was tested using the equation $E_{MMLL'CT} = f(\Delta E)$. The reason for this linear relationship that exist between experimental energy of the CT maxima ($E_{MMLL'CT}$) and the HOMO-LUMO energy gap (ΔE) calculated by DFT is the same for other Pt(diimine)(dichalcogenolene) complexes. A closer inspection of Table 3.23 indicates that the HOMO-LUMO gap increases by 0.40 eV (3200 cm^{-1}) from benzene to DMSO.

DFT/PCM calculations shows that the calculated dipole moment (μ) decreases from polar to non-polar solvents i.e. 18.92 D for DMSO, 18.12 D for CH_2Cl_2, 17.49 D for chloroform, and 16.00 D for benzene. The reason for the decrease in the calculated dipole moment (μ) of Pt(bpy)(bSO) is the same for other Pt(diimine)(dichalcogenolene) complexes.

3.3.3.5 Pt(bpy)(bSeO)

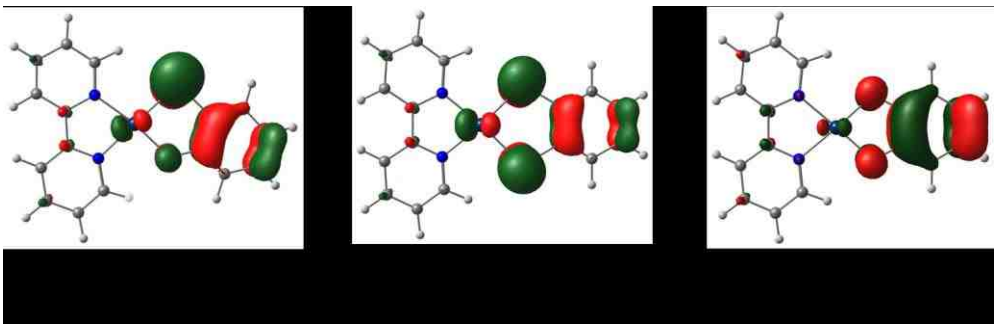

Figure 3.98: HOMO for (a) Pt(bpy)(bSeO), Pt(bpy)(bds) and (b) Pt(bpy)(CAT).

The pictorial presentation of the energy diagram of the frontier molecular orbitals of Pt(bpy)(bSeO) is depicted in Figure 3.99. The chalcogenolene donor atoms present in Pt(bpy)(bSeO) are selenium (Se) and oxygen (O). Based on the spectral similarities of Pt(diimine)(dichalcogenolene) complexes, an effective C_{2v} symmetry can be applied across this series since they possess parallel $a_2^2 b_1^2 b_1^0$ ground state configuration. In Pt(bpy)(bSeO), the atomic orbital

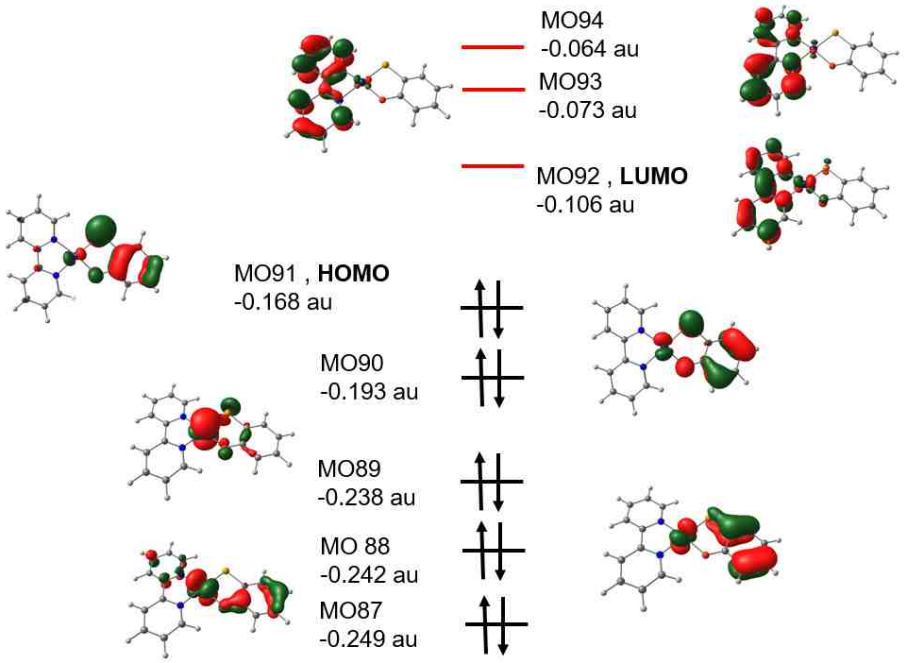

Figure 3.99: MO diagram and energies for the frontier MOs of Pt(dbbpy)(bSeO).

compositions of the two donor atoms in the HOMO are not equivalent due to the fact the two donor atoms are different i.e. Se and S (see Figure 3.89). The difference in the donor atoms of the molecule lowers the symmetry of the molecule from C_{2v} to C_s where the mirror plane acts as the molecular plane. Moreover, from Figure 3.98 (a), it can be discerned that the Pt dπ orbital is rotated toward the softer selenium (Se) donor atom. The result is observed in atomic orbital composition of Se being larger than that of O in the HOMO.[83] The

summarized result in Table 3.24 shows TD-DFT calculated energies and compositions of the lowest lying singlet and triplet energy states together with oscillator strengths for Pt(dbbpy)(bSeO). From Table 3.24, it can be ascertained that the lowest energy singlet (S_1) and triplet (T_1) vertical transitions are from HOMO to LUMO with vertical transition energies of 1.41 and 0.78 eV respectively.

Table 3.24: Selected TD-DFT Calculated Energies and Compositions of the Lowest Lying Singlet and Triplet Energy States Together with Oscillator Strengths for **Pt(bpy)(bSeO).**

	Composition[a]	**ΔE^b**	***f*[c]**	**Assignment**
Singlets				
S_1	HOMO→LUMO, 70%	1.41	0.1367	bSeO/Pt→bpy/Pt (LMCT/LLCT)
S_2	HOMO-1→LUMO, 69%	1.78	0.0142	bSeO/Pt→bpy/Pt (LMCT/LLCT)
S_3	HOMO→LUMO+1, 70%	2.01	0.0080	bSeO/Pt→bpy (MMLL'CT)
S_4	HOMO→LUMO+2, 70%	2.31	0.0231	bSeO/Pt→bpy (MMLL'CT)
Triplets				
T_1	HOMO→LUMO, 70%	0.78	0.0000	bSeO/Pt→bpy/Pt (LMCT/LLCT)
T_2	HOMO-1→LUMO, 64%	1.50	0.0000	bSeO/Pt→bpy/Pt (LMCT/LLCT)
T_3	HOMO→LUMO+1, 67%	1.82	0.0000	bSeO/Pt→bpy (MMLL'CT)
T_4	HOMO→LUMO+2, 58%	1.98	0.0000	bSeO/Pt→bpy (MMLL'CT)

[a] Electronic transitions compositions expressed in terms of ground-state Kohn-Sham molecular orbitals. [b] Transition energy expressed in eV. [c] Oscillator strength.

The HOMO →LUMO orbital compositions for both S_1 and T_1 is 70%. The lowest energy singlet (S_1) has a high oscillator strength of 0.1367. S_2 and T_2 vertical transitions for Pt(bpy)(bSeO) is also charge transfer from HOMO-1 →LUMO and is assign as LMCT/LLCT. Their calculated vertical transition energies are 1.78 and 1.50 eV respectively with S_2 having an oscillator strength of 0.0142. The HOMO-1 →LUMO orbital compositions for S_2 and T_2 are 69 and 64% respectively. The third singlet (S_3) and triplet states (T_3) are primarily ^{1}MMLL'CT and ^{3}MMLL'CT respectively in character. Their vertical transition energies are

calculated as 2.01 and 1.82 eV respectively, and the oscillator strength of S_3 given by 0.0080. The HOMO →LUMO+1 orbital composition for S_3 and T_3 are 70 and 67% respectively. The S_4 and T_4 are primarily ^{1}MMLL'CT and ^{3}MMLL'CT respectively in character with vertical transition energies of 2.31 and 1.98 eV. The calculated oscillator strength of S_4 is 0.0231. The HOMO →LUMO+2

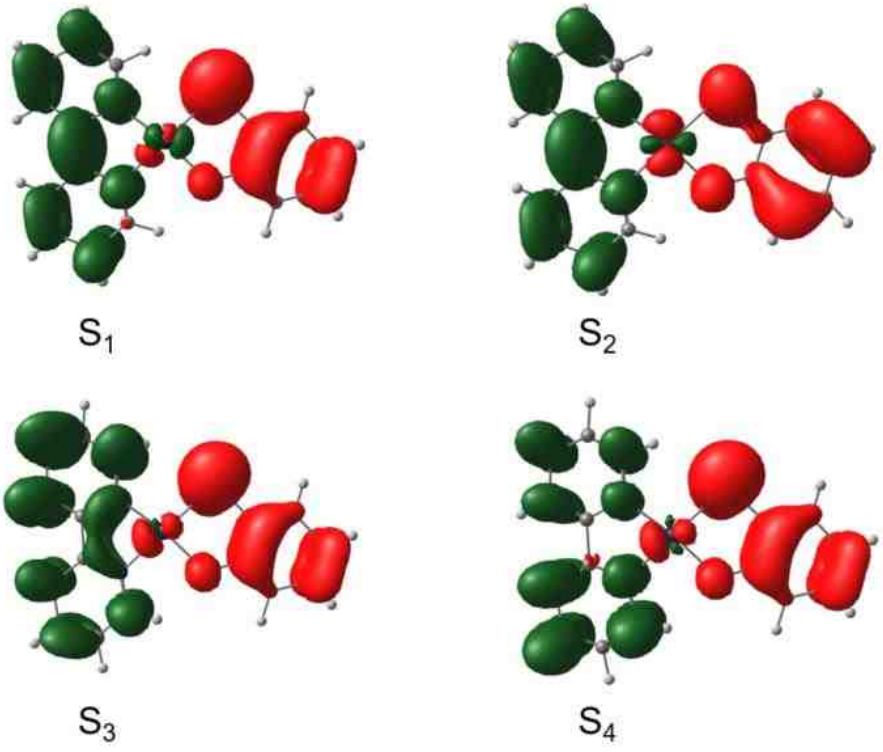

Figure 3.100: Calculated electron density difference map (EDDM) for Singlet States at an isodensity value of 0.0012 au. The red and green regions represent loss and gain of electron density respectively in a transition to the excited state.

orbital compositions for both S_4 and T_4 are 70 and 58% respectively. The pictorial presentation of the calculated electron density difference map (EDDM) for the singlet states at an isodensity value of 0.0012 au are shown in Figure 3.100. Moreover, inspecting Figure 3.100**,** we detect that the MOs responsible for the loss of electron density are the selenylphenolate orbital admixed with some Pt dπ

orbital character. The MOs of Pt(bpy)(bSeO) that gain electron density in a transition to the excited state are the π* orbitals of the diimine chelate with some Pt d-orbital character. The symmetry of the frontier molecular orbitals of Pt(bpy)(bSeO) are depicted in Figure 3.101**.** The HOMO, LUMO and LUMO+1 frontier molecular orbitals are assigned as b_1 while the HOMO-1 is denoted by a_1.

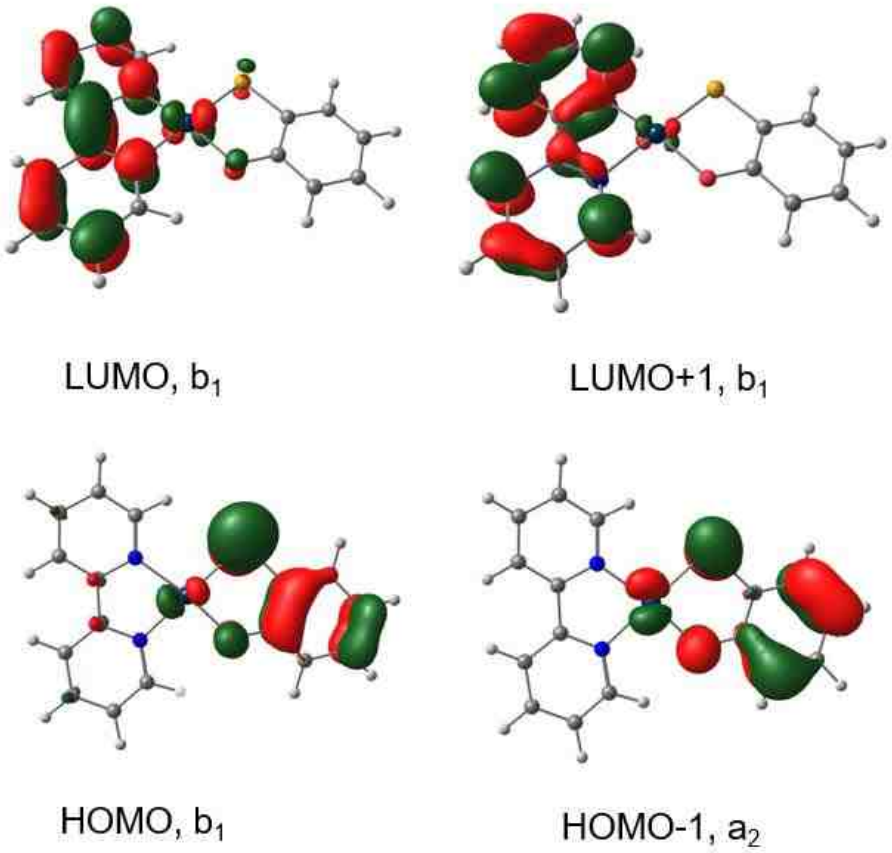

Figure 3.101: Frontier MOs of Pt(bpy)(bSeO) with symmetry assignment.

Table 3.25: Solvent effect on the experimental energy of the charge transfer maxima ($E_{MMLL'CT}$), calculated dipole moment (μ) and the HOMO-LUMO energy gap (ΔE) calculated by DFT for **Pt(dbbpy)(bSeO).**

Solvent	**E_{eV} HOMO**	**E_{eV} LUMO**	**ΔE_{eV}[a]**	**$\Delta E(cm^{-1})$**	**$E_{MMLL'CT}$ (cm^{-1})[b]**	**μ (debye)**
Benzene	-4.4300	-2.3347	2.0953	16899	16124	15.57

Chloroform	-4.6504	-2.3429	2.3075	18611	17231	17.10
DCM	-4.7783	-2.3320	2.4463	19730	17769	17.74
Acetone	-4.8708	-2.3293	2.5415	20520	17901	18.33
DMF	-4.9062	-2.3293	2.5769	20784	18538	18.42
DMSO	-4.9171	-2.3266	2.5905	20893	18602	18.56
Acetonitrile	-4.9062	-2.3293	2.5769	20784	18765	18.42
THF	-4.7457	-2.3347	2.4110	19446	16733	17.66

[a] HOMO-LUMO energy gap (ΔE) calculated by DFT, [b] Experimental energy of the MMLL'CT band maxima.

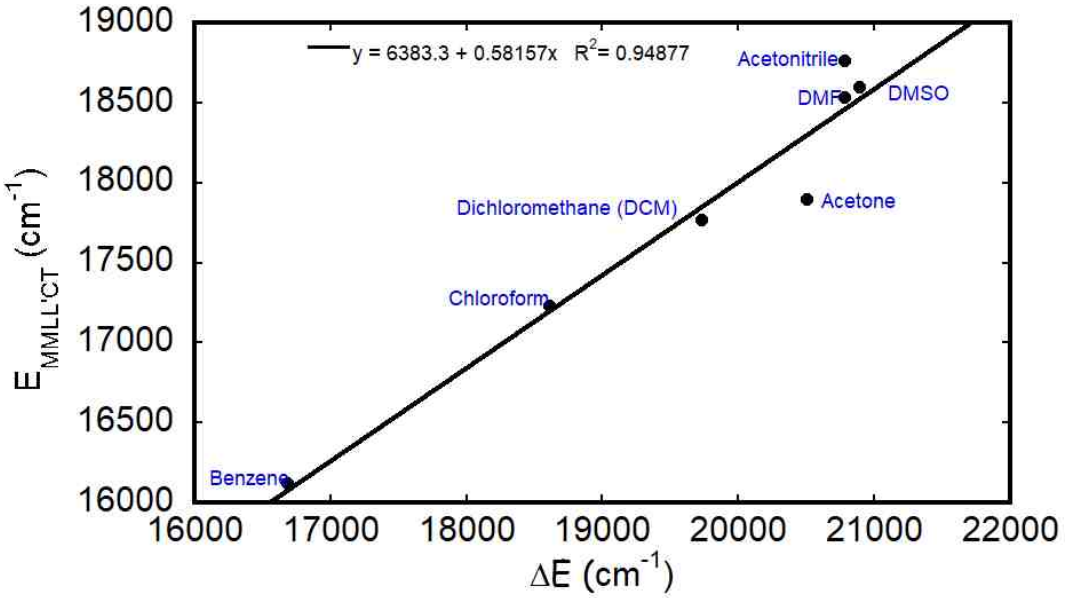

Figure 3.102: Linear correlation between experimental energy of the CT maxima ($E_{MMLL'CT}$) and the HOMO-LUMO energy gap (ΔE) calculated by DFT for Pt(dbbpy)(bSeO)

The electronic behavior of Pt(bpy)(bSeO) was tested using polar and non-polar solvents ranging from acetonitrile, acetone, dimethyl formamide (DMF), dimethyl sulfoxide (DMSO), chloroform, tetrahydrofuran (THF), dichloromethane (DCM), and benzene. It was observed that its electronic behavior follows the same trend displayed by other Pt(diimine)(dichalcogenolene) complexes. This conclusion was based on an increase in HOMO-LUMO gap because of an increase in the polarity of the field. Increasing the solvent polarity increases the polarity of the field and this in turn stabilizes the occupied orbitals. From the summarized result

in Table 3.25, the experimental energy of the CT band maxima ($E_{MMLL'CT}$) in benzene (minor polarity) is 16124 cm^{-1}, acetone (medium polarity) is 17901 cm^{-1} and in acetonitrile (high polarity) is 18765 cm^{-1}. The calculated HOMO-LUMO energy gap (ΔE) from DFT/PCM (Table 3.25) also shows that, ΔE, increases from non-polar to polar solvent. A closer inspection of Table 3.25 indicates that

Table 3.26: Calculated frontier MOs energies for Pt(dbbpy)(bSeO) in the gas phase, and under different electrostatic field of benzene, dichloromethane and dimethylsulfoxide (DMSO) using DFT/PCM.

MO	E_{au}[a] Gas Phase	E_{au}[a] Benzene	E_{au}[a] DCM	E_{au}[a] DMSO
LUMO+3	-0.0267	-0.0286	-0.0372	-0.0409
LUMO+2	-0.0643	-0.0479	-0.0464	-0.0460
LUMO+1	-0.0732	-0.0548	-0.0530	-0.0525
LUMO	-0.1061	-0.0868	-0.0857	-0.0855
HOMO	-0.1683	-0.1628	-0.1756	-0.1807
HOMO-1	-0.1927	-0.1863	-0.1988	-0.2037
HOMO-2	-0.2376	-0.2278	-0.2349	-0.2384

[a]Energy in Hartrees

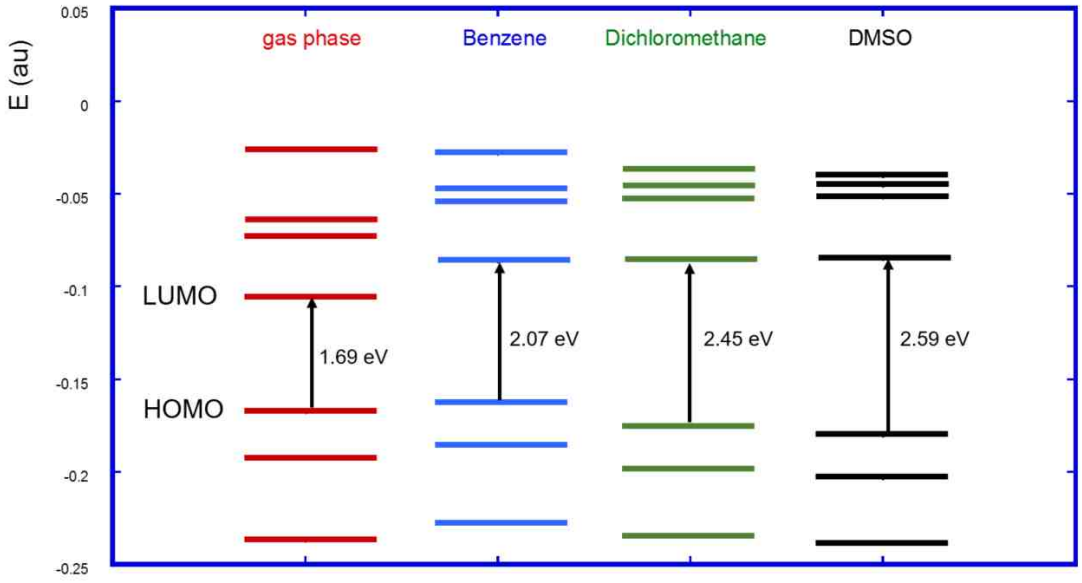

Figure 3.103: Energy diagram of calculated frontier MOs for Pt(dbbpy)(bSeO) in the gas phase along with the corresponding calculated MOs using DFT/PCM

under different electrostatic field of benzene, dichloromethane and dimethylsulfoxide (DMSO).

the HOMO-LUMO gap increases by 0.48 eV (3900 cm^{-1}) from benzene to acetonitrile. Based on the summarized results in Table 3.26 and the pictorial presentation in Figure 3.103, an increase in the solvent field polarity stabilizes the HOMO and the LUMO relatively stays the same. A plot of experimental energy of the CT maxima ($E_{MMLL'CT}$) vs the HOMO-LUMO energy gap (ΔE) shows a linear relationship which satisfy the equation $E_{MMLL'CT} = f(\Delta E)$. A pictorial presentation of this linear relationship is depicted in Figure 3.102. DFT/PCM calculations shows that the calculated dipole moment (μ) decreases from polar to non-polar solvents i.e. 18.56 D for DMSO, 17.74 D for dichloromethane, 17.10D for chloroform, and 15.57 D for benzene. The reason for the decrease in calculated dipole moment (μ) for Pt(bpy)(bSeO) is the same for other Pt(diimine)(dichalcogenolene) complexes.

3.3.3.6 Pt(bpy)(mcp)

The molecular orbital diagram and energies for the valence orbitals of Pt(dbbpy)(mcp) is depicted in Figure 3.104. In Pt(dbbpy)(mcp), the lowest triplet and singlet vertical transitions are charge transfer (CT) transitions from HOMO to LUMO. From Figure 3.104, the HOMO consists of a mixture of Pt dπ and dithiolate ligand character. The LUMO's on the other hand, has it major contributions from the dbbpy chelate ligand and the minor part coming from Pt dπ character. The lowest singlet (S_1) and triplet states (T_1) have calculated energies

of 1.51 and 1.41 eV respectively with S_1 having an oscillator strength of 0.0028 as summarized in Table 3.27. S_2, S_3 and S_4 have calculated energies and oscillator strength of 1.93, 2.21, 2.53 eV and 0.0847, 0.0000, and 0.0030 respectively. The molecular orbitals involve in S_2, S_3 and S_4 are HOMO-1→LUMO, HOMO-2→LUMO, and HOMO→LUMO+1 respectively. T_2, T_3 and T_4 have calculated energies of 1.66, 2.17, and 2.19 eV. The molecular orbitals involved in T_2, T_3 and T_4 are the same as its S_2, S_3 and S_4 counterparts. The S_1

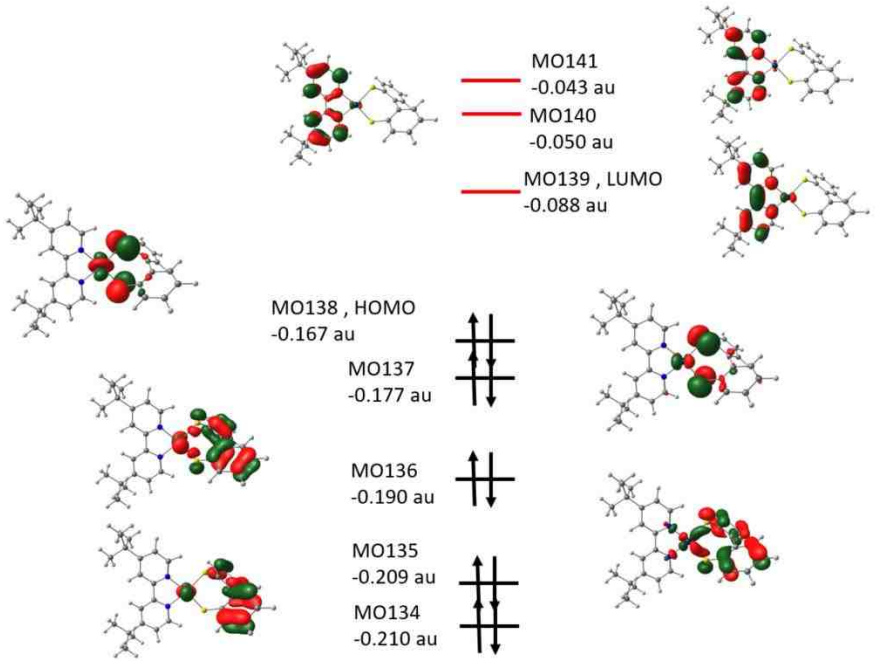

Figure 3.104: MO diagram and energies for the frontier MOs of Pt(dbbpy)(mcp).

Table 3.27: Selected TD-DFT Calculated Energies and Compositions of the Lowest Lying Singlet and Triplet Energy States Together with Oscillator Strengths for Pt(bpy)(mcp).

	Composition[a]	**ΔE[b]**	***f*[c]**	**Assignment**
Singlets				
S_1	HOMO→LUMO, 70%	1.51	0.0028	mcp/Pt→bpy/Pt (LMCT/LLCT)

S_2	HOMO-1→LUMO, 70%	1.93	0.0847	mcp/Pt→bpy (MMLL'CT)
S_3	HOMO-2→LUMO, 68%	2.21	0.0000	mcp/Pt→bpy (MMLL'CT)
S_4	HOMO→LUMO+1, 58%	2.53	0.0030	mcp/Pt→bpy/Pt (MMLL'CT)
Triplets				
T_1	HOMO→LUMO, 70%	1.41	0.0000	mcp/Pt→bpy/Pt (LMCT/LLCT)
T_2	HOMO-1→LUMO, 70%	1.66	0.0000	mcp/Pt→bpy (MMLL'CT)
T_3	HOMO-2→LUMO, 65%	2.17	0.0000	mcp/Pt→bpy (MMLL'CT)
T_4	HOMO→LUMO+1, 66%	2.19	0.0000	mcp/Pt→bpy/Pt (MMLL'CT)

[a] Electronic transitions compositions expressed in terms of ground-state Kohn-Sham molecular orbitals. [b] Transition energy expressed in eV. [c] Oscillator strength.

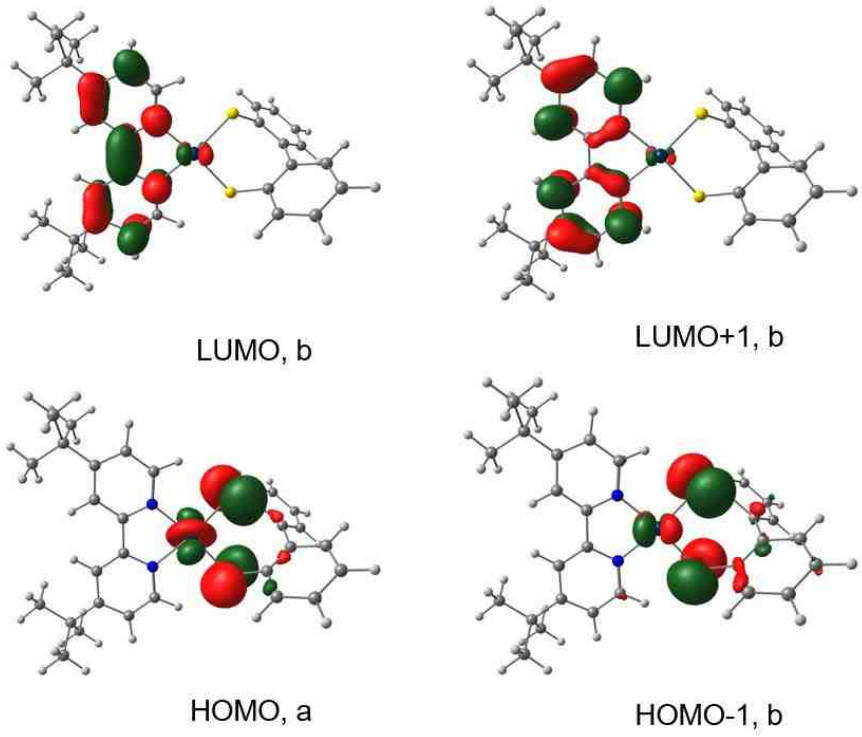

Figure 3.105 : Frontier MOs of Pt(dbbpy)(mcp) with symmetry assignment.

and T_1 are primarily composed of 70% HOMO→LUMO, S_2 and T_2 composed of 70% HOMO-1→LUMO. The MO compositions for the other states i.e. S_3, S_4, T_3 and T_4 are summarized in Table 3.27. HOMO-1, LUMO, and LUMO+1 all have b symmetry while the HOMO has a symmetry depicted in Figure 3.105. The ground state configuration for Pt(dbbpy)(mcp) denoted as S_0 is given by $b^2a^2b^0$ in a C_2

symmetry. The filled b^2 (HOMO-1) donor orbital is predominately made up of symmetric combination (S_π^+) of sulfur out-of-plane S_{Py} orbital while the filled a^2 (HOMO) donor orbital is dominantly comprised of antisymmetric combination (S_π^-) of sulfur out-of-plane S_{Py} orbital depicted in Figure 3.105. The first singlet excited state (S_1) has a configuration of $b^2a^1b^1$; ^{1}B and the second singlet excited state (S_2) has a configuration of $b^1a^2b^1$; ^{1}A. The triplet excited states T_1

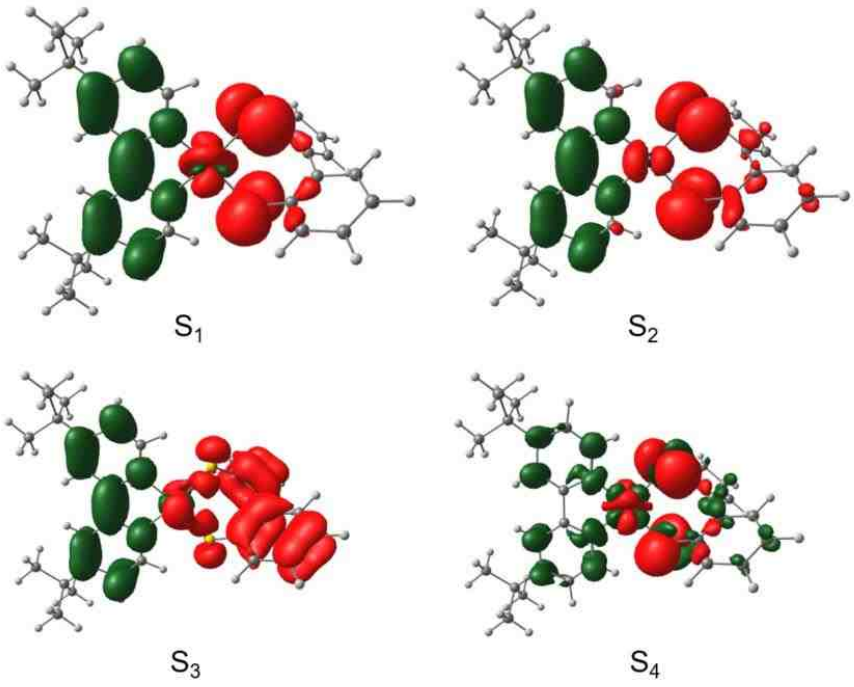

Figure 3.106: Calculated electron density difference map (EDDM) for Singlet States at an isodensity value of 0.0012 au. The red and green regions represent loss and gain of electron density respectively in a transition to the excited state.

and T_2 uses the same valence orbitals as its singlet counterpart and hence a configuration of ^{3}B and ^{3}A respectively. Presented pictorially in Figure 3.106 is the calculated electron density difference map (EDDM) for singlet states at an isodensity value of 0.0012 au. The red and green regions represent loss and gain of electron density respectively in a transition to the excited state.

By employing a wide range of solvents from non-polar to polar, we investigated the electronic behavior of Pt(dbbpy)(mcp) using different solvent electric fields. The use of equation $E_{MMLL'CT} = f(\Delta E)$, shows a linear relationship between experimental energy of the CT band maxima ($E_{MMLL'CT}$) and the HOMO-LUMO energy gap (ΔE) calculated by DFT/PCM. The results are summarized in Table

Table 3.28: Solvent effect on the experimental energy of the charge transfer maxima ($E_{MMLL'CT}$), calculated dipole moment (μ) and the HOMO-LUMO energy gap (ΔE) calculated by DFT for Pt(dbbpy)(mcp).

Solvent	**E_{eV} HOMO**	**E_{eV} LUMO**	**ΔE_{eV}[a]**	**$\Delta E(cm^{-1})$**	**$E_{MMLL'CT}$ (cm^{-1})[b]**	**μ (debye)**
Benzene	-4.8518	-2.3592	2.4926	20104	20000	14.88
Chloroform	-5.0749	-2.3538	2.7211	21947	21277	16.06
DCM	-5.2083	-2.3565	2.8518	23001	21645	16.66
Acetone	-5.3089	-2.3619	2.9470	23769	21978	17.08
DMF	-5.3470	-2.3647	2.9823	24053	21978	17.23
DMSO	-5.3579	-2.3647	2.9932	24142	22472	17.27
Acetonitrile	-5.3470	-2.3647	2.9823	24054	22727	17.22
THF	-5.1756	-2.3538	2.8218	22759	20824	16.52

[a] HOMO-LUMO energy gap (ΔE) calculated by DFT, [b] Experimental energy of the MMLL'CT band maxima.

3.28 and the pictorial presentation is depicted in Figure 3.107. From Table 3.28, it can be ascertained that the HOMO-LUMO gap increases by 0.49 eV (3950 cm^{-1}) from benzene to acetonitrile. From Table 3.29 and Figure 3.108, it can be observed that solvent field stabilizes the HOMOs and the LUMOs remain virtually unaffected. This observation can be explained in terms of solvation, mainly

dipole-diploe interactions. These interactions stabilize the part of the molecule that has a higher electron density in our case the dithiolate ligand and Pt metal center (see Figure 3.106), and destabilize the other part lower in electron density. Dipole moment (μ) increases from polar to non-polar solvents i.e. 14.88 D for

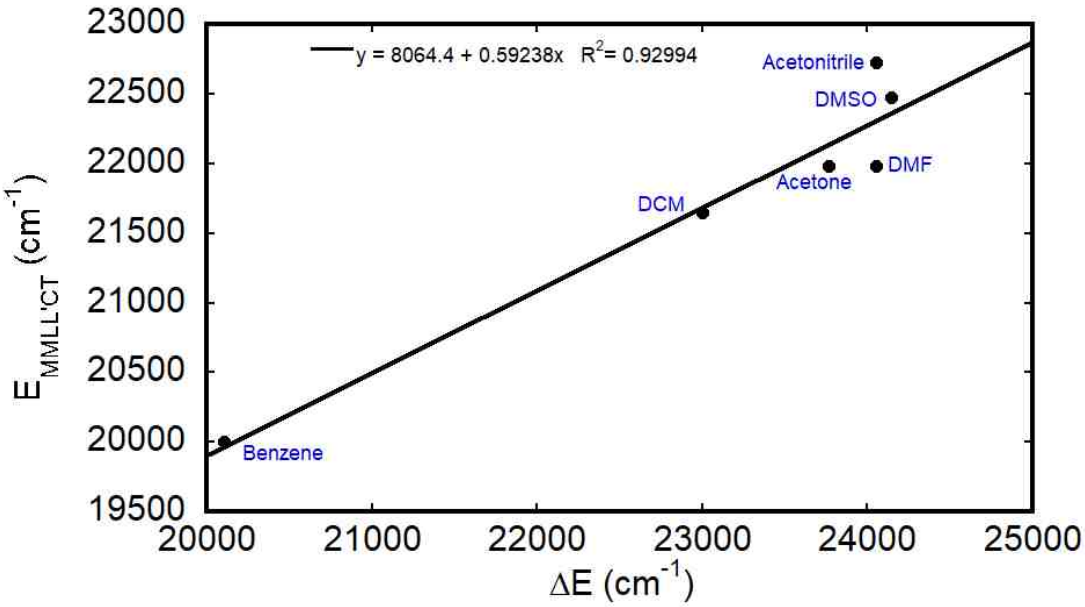

Figure 3.107: Linear correlation between experimental energy of the CT maxima ($E_{MMLL'CT}$) and the HOMO-LUMO energy gap (ΔE) calculated by DFT for Pt(dbbpy)(mcp).

Table 3.29: Calculated frontier MOs energies for Pt(dbbpy)(mcp) in the gas phase, and under different electrostatic field of benzene, dichloromethane and dimethylsulfoxide (DMSO) using DFT/PCM.

MO	**E_{eV} Gas Phase**	**E_{eV} Benzene**	**E_{eV} DCM**	**E_{eV} DMSO**
LUMO+3	-0.8544	-1.0912	-1.1048	-1.1075
LUMO+2	-1.1919	-1.1293	-1.2817	-1.2817
LUMO+1	-1.3796	-1.3115	-1.3687	-1.4857
LUMO	-2.4082	-2.3592	-2.3565	-2.3647
HOMO	-4.5579	-4.8518	-5.2083	-5.3579
HOMO-1	-4.8219	-5.1021	-5.4368	-5.5783
HOMO-2	-5.1811	-5.4749	-5.7987	-5.9348

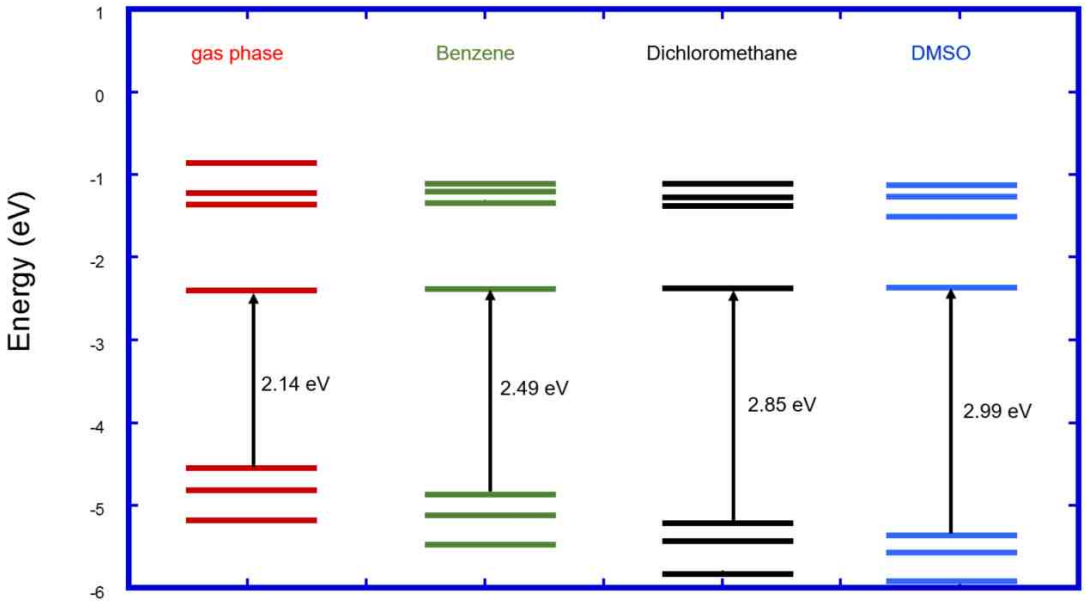

Figure 3.108: Energy diagram of calculated frontier MOs for Pt(dbbpy)(mcp) in the gas phase along with the corresponding calculated MOs using DFT/PCM.

benzene, 16.66 D for dichloromethane and 17.27 D for DMSO. The reason being the same as other Pt(diimine)(dichalcogenolene) complexes.

3.3.3.7 Pt(dbbpy)(pds) and Pt(dbbpy)(pdt)

The frontier molecular orbitals of Pt(dbbpy)(pds) and Pt(dbbpy)(pdt) depicted in Figure 3.109 have very similar energies. The valence MOs of these pairs i.e. Pt(dbbpy)(pds), Pt(bpy)(bds) and Pt(dbbpy)(pdt), Pt(bpy)(bdt) are slightly different due to the differences in the benzeniod and pyrazinic ring involved in the HOMO. The pyrazinic ring of Pt(dbbpy)(pds) and Pt(dbbpy)(pdt) have higher electron withdrawing properties than that of benzeniod-dithiolene/diselenol ring. The differences in electron withdrawing properties of these rings are due to the fact that nitrogen atom has a larger electronegativity value of 3.04 whereas carbon atom has a smaller value of 2.55.[85] TD-DFT calculations shows a notable

difference in energy of the valence orbital and related properties due to small structural variations of these rings. These computational results (see Figure 3.109) also shows that the HOMO which is predominantly S/Se atoms also has a significant contribution from the pyrazinic ring. TD-DFT calculation shows that the lowest singlet and triplet vertical transitions for Pt(dbbpy)(pds) is HOMO→ LUMO

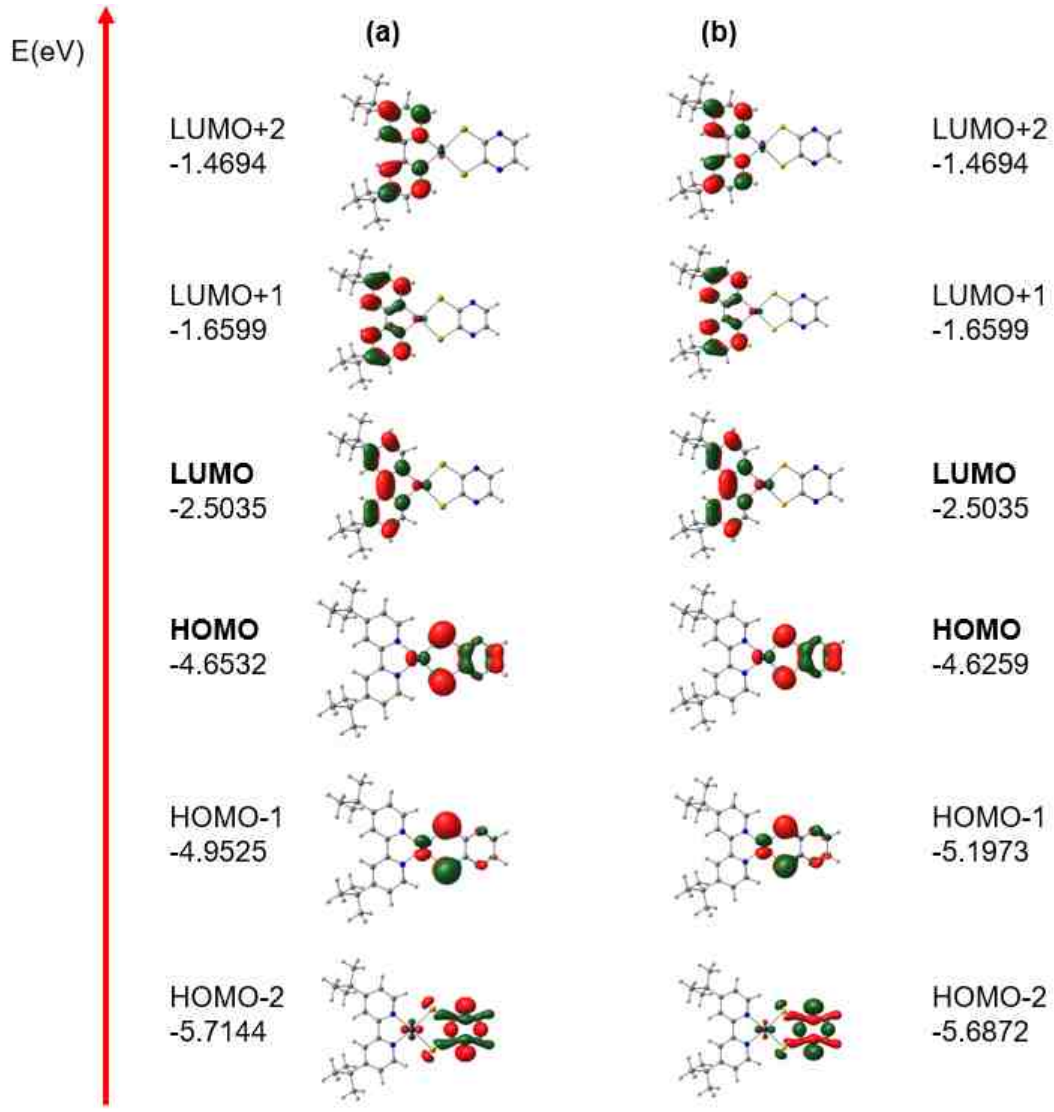

Figure 3.109: Diagram of the relative energy levels of (a) Pt(dbbpy)(pds) and (b) Pt(dbbpy)(pdt) showing the most notable frontier molecular orbitals.

and assigned as MMLL'CT. The calculated S_1 and T_1 have energies of 1.75 and 1.42 eV respectively with 0.1209 oscillator strength for S_1 (see Table 3.30). The second lowest singlet (S_2) transition is HOMO-1 to LUMO. The electronic transitions compositions of S_1 and S_2 are both made up of 70% of the HOMO →LUMO and the HOMO-1→LUMO respectively. The computed energies for S_2 and T_2 are 1.85 and 1.74 eV respectively, with 0.0035 oscillator strength for S_2.

Table 3.30: Selected TD-DFT Calculated Energies and Compositions of the Lowest Lying Singlet and Triplet Energy States Together with Oscillator Strengths for Pt(dbbpy)(pds).

	Composition[a]	**ΔE[b]**	***f*[c]**	**Assignment**
Singlets				
S_1	HOMO→LUMO, 70%	1.75	0.1209	pds/Pt→bpy (MMLL'CT)
S_2	HOMO-1→LUMO, 70%	1.85	0.0035	pds/Pt→bpy/Pt (MMLL'CT)
S_3	HOMO→LUMO+1, 70%	2.43	0.0111	pds/Pt→bpy (MMLL'CT)
S_4	HOMO-2→LUMO, 61%	2.61	0.0054	pds/Pt→bpy (MMLL'CT)
Triplets				
T_1	HOMO→LUMO, 70%	1.42	0.0000	pds/Pt→bpy/Pt (MMLL'CT)
T_2	HOMO-1→LUMO, 70%	1.74	0.0000	pds/Pt→bpy/Pt (MMLL'CT)
T_3	HOMO→LUMO+1, 70%	2.32	0.0000	pds/Pt→bpy (MMLL'CT)
T_4	HOMO-2→LUMO, 68%	2.50	0.0000	pds/Pt→bpy (MMLL'CT)

[a] Electronic transitions compositions expressed in terms of ground-state Kohn-Sham molecular orbitals. [b] Transition energy expressed in eV. [c] Oscillator strength.

S_3 and T_3 have electronic transition compositions of 70% and are mainly HOMO→LUMO+1 with energies of 2.43 and 2.32 eV respectively. S_3 has an oscillator strength of 0.0111. Based on C_{2V} symmetry, the HOMO, LUMO, LUMO+1 are assigned as b_1, whereas HOMO-1 is given a_2 symmetry assignment (Figure 3.110). The calculated electron density difference map (EDDM) for singlet states at an isodensity value of 0.0012 au are depicted in

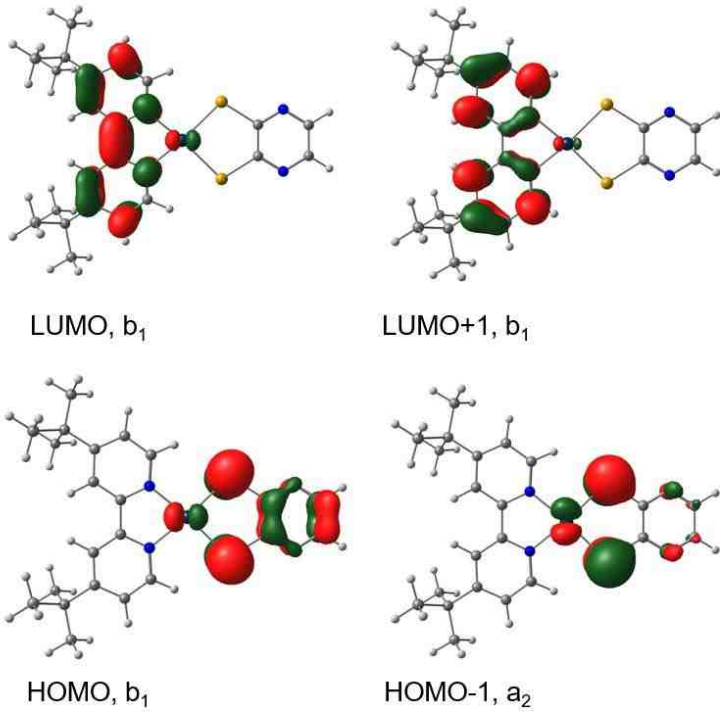

Figure 3.110: Frontier MOs of Pt(dbbpy)(pds) with symmetry assignment.

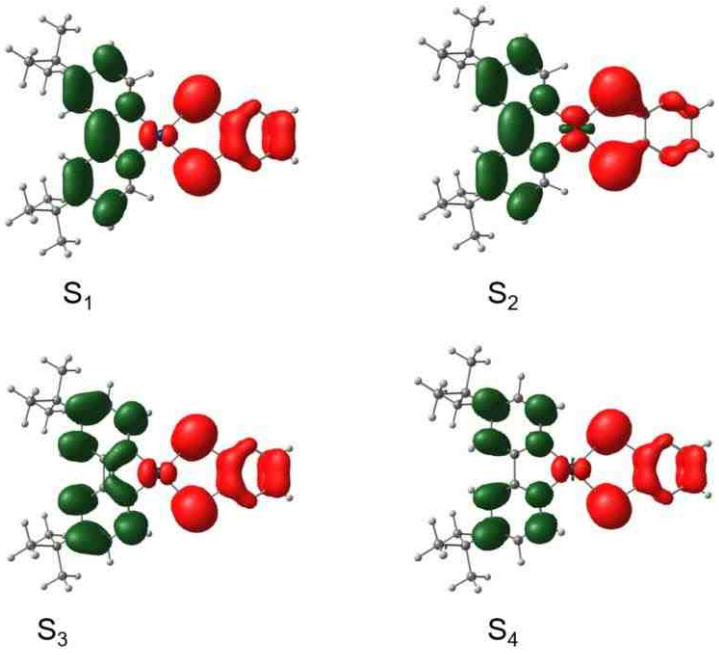

Figure 3.111: Calculated electron density difference map (EDDM) for Singlet States at an isodensity value of 0.0012 au for Pt(dbbpy)(pds). The red and green regions represent loss and gain of electron density respectively in a transition to the excited state.

Table 3.31: Solvent effect on the experimental energy of the charge transfer maxima ($E_{MMLL'CT}$), calculated dipole moment (μ) and the HOMO-LUMO energy gap (ΔE) calculated by DFT for Pt(dbbpy)(pds).

Solvent	**E_{eV} HOMO**	**E_{eV} LUMO**	**ΔE_{eV}[a]**	**$\Delta E(cm^{-1})$**	**$E_{MMLL'CT}$ (cm^{-1})[b]**	**μ (debye)**
Benzene	-4.9552	-2.4327	2.5225	20345		17.07
Chloroform	-5.1702	-2.3973	2.7729	22365	19615	18.64
DCM	-5.2926	-2.3837	2.9089	23462	20002	19.43
Acetone	-5.3824	-2.3756	3.0068	24251	20405	19.97
DMF	-5.4151	-2.3728	3.0423	24538	20747	20.17
DMSO	-5.4232	-2.3728	3.0504	24603	20951	20.22
Acetonitrile	-5.4151	-2.3756	3.0395	24515		20.16
THF	-5.2627	-2.3864	2.8763	23199	19229	20.25

[a] HOMO-LUMO energy gap (ΔE) calculated by DFT, [b] Experimental energy of the MMLL'CT band maxima.

Figure 3.111. The red and green regions represent loss and gain of electron density respectively in a vertical electronic transition to the excited state. The EDDM's of S_1, S_2, S_3 and S_4 show clearly that the electron density is lost from

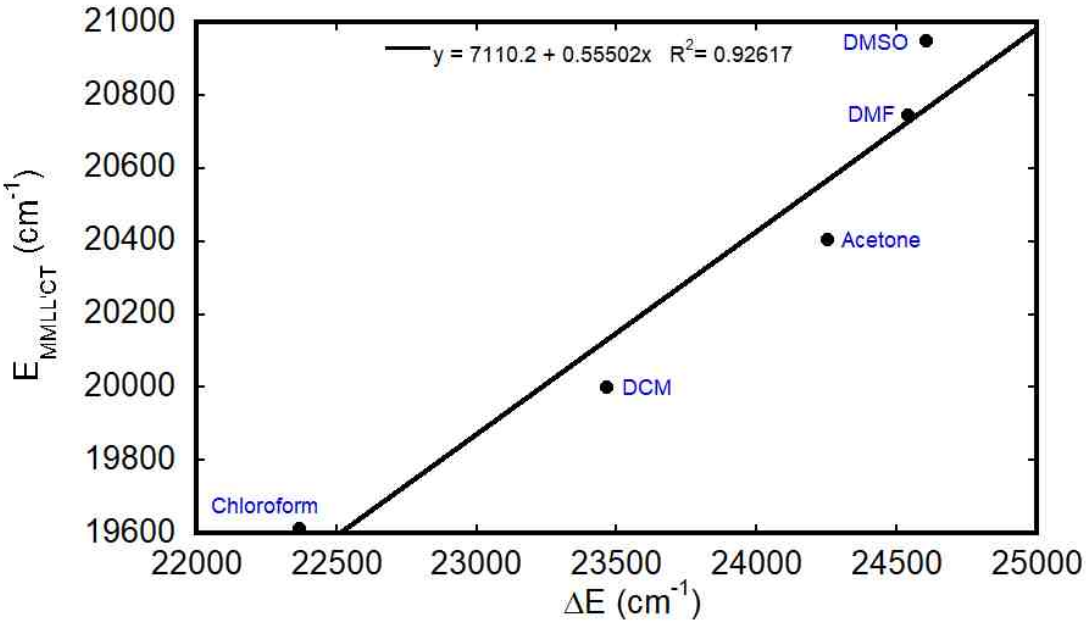

Figure 3.112: Linear correlation between experimental energy of the CT maxima ($E_{MMLL'CT}$) and the HOMO-LUMO energy gap (ΔE) calculated by DFT for Pt(dbbpy)(pds).

pyrazine diselenolate ring and Pt metal. The gain of electron is observed by the acceptor ligand i.e. diimine for S_1, S_3, and S_4. For S_2, the acceptor orbital is a mixture of diimine and Pt as shown in Figure 3.111. The HOMO-LUMO energy gap of Pt(dbbpy)(pds) was examined using polar and non-polar organic solvent.

Table 3.32: Calculated frontier MOs energies for Pt(dbbpy)(pds) in the gas phase, and under different electrostatic field of benzene, dichloromethane and dimethylsulfoxide (DMSO) using DFT/PCM.

MO	E_{eV} Gas Phase	E_{eV} Benzene	E_{eV} DCM	E_{eV} DMSO
LUMO+3	-1.0259	-1.2354	-1.3116	-1.2925
LUMO+2	-1.4667	-1.3742	-1.4749	-1.4776
LUMO+1	-1.6708	-1.5755	-1.5021	-1.5728
LUMO	-2.5089	-2.4327	-2.3837	-2.3728
HOMO	-4.6504	-4.9552	-5.2926	-5.4232
HOMO-1	-4.9634	-5.2817	-5.6300	-5.7661
HOMO-2	-5.7144	-6.0681	-6.4137	-6.5226

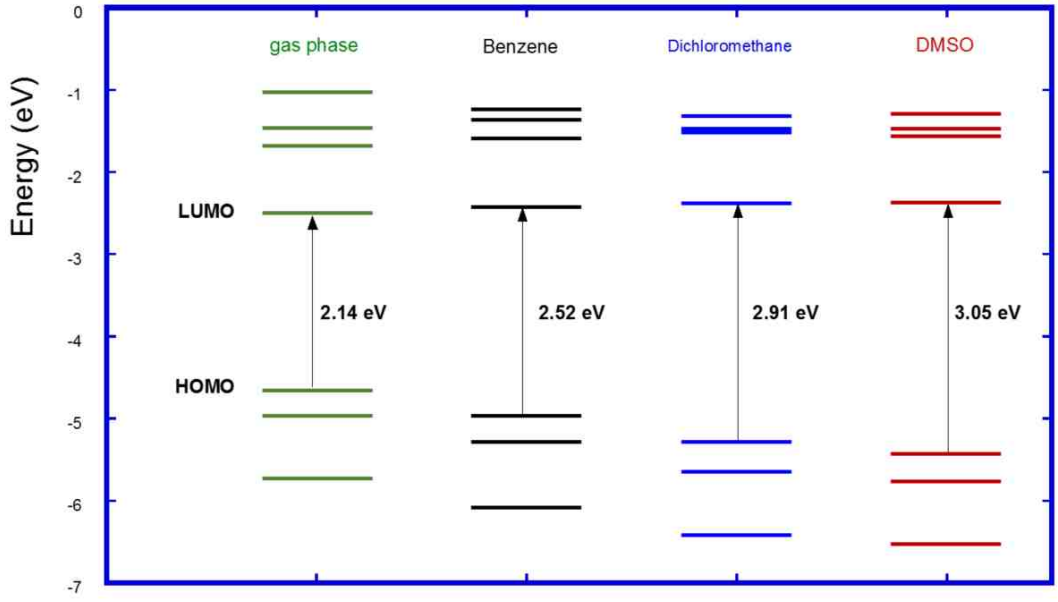

Figure 3.113: Energy diagram of calculated frontier MOs for Pt(dbbpy)(pds) in the gas phase along with the corresponding calculated MOs using DFT/PCM under different electrostatic field of benzene, dichloromethane and dimethylsulfoxide (DMSO).

The result matches well with other Pt(diimine)(dichalcogenolene) complexes. From the results tabulated in Table 3.31, it can be concluded that a continuum solvent model procedure increases the HOMO-LUMO energy gap by 0.52 eV (4200 cm-1) from benzene to acetonitrile. The experimental energy of the CT band maxima ($E_{MMLL'CT}$) in benzene and acetonitrile were not recorded due to solubility issues. A linear relationship was observed when $E_{MMLL'CT}$ was plotted against ΔE by using the equation $E_{MMLL'CT} = f(\Delta E)$ as presented in Figure 3.112. The results summarized in Table 3.31 shows that the calculated dipole moment (μ) increase from non-polar to polar solvents for the same reasons shown by other Pt(diimine)(dichalcogenolene) complexes. Solvatochromism was further evaluated by considering the frontier MOs of Pt(dbbpy)(pds) using DFT/PCM calculations. The results are tabulated in Table 3.32 and the pictorial presentation shown in Figure 3.113. Based on the result in Figure 3.113, it is evident that an increase in the solvent field polarity stabilizes the HOMO and leaves the LUMO unchanged.

3.3.3.8 Pt(dbbpy)(tbp)$_2$ and Pt(dbbpy)(tbt)$_2$

The valence molecular orbitals of Pt(dbbpy)(tbp)$_2$ and Pt(dbbpy)(tbt)$_2$ are depicted in Figure 3.114. The frontier MOs of Pt(dbbpy)(tbp)$_2$ and Pt(dbbpy)(tbt)$_2$ are slightly different due to the differences in the donor ligands involved in the HOMOs. The acceptor ligand is the same for the two complexes. In Pt(dbbpy)(tbp)$_2$, it uses phenolate (tbp) as the donor ligand whereas Pt(dbbpy)(tbt)$_2$ uses thiolate (tbt) as the donor ligand. The HOMO is mainly

comprised of thiolate(π)/S(p)/Pt(d) and phenolate(π)/O(p)/Pt(d) orbitals for Pt(dbbpy)(tbt)$_2$ and Pt(dbbpy)(tbp)$_2$ respectively.[50,86] The LUMOs for the two complexes are predominantly localized on the π* (diimine) ligand with a significant contribution from Pt d orbital. Figure 3.114 shows that the HOMO is composed mainly of phenolate/thiolate as the dominant contributors and the Pt dπ as the minor contributor. Table 3.33 summarized the selected TD-DFT calculated energies and compositions of the lowest lying singlet and triplet

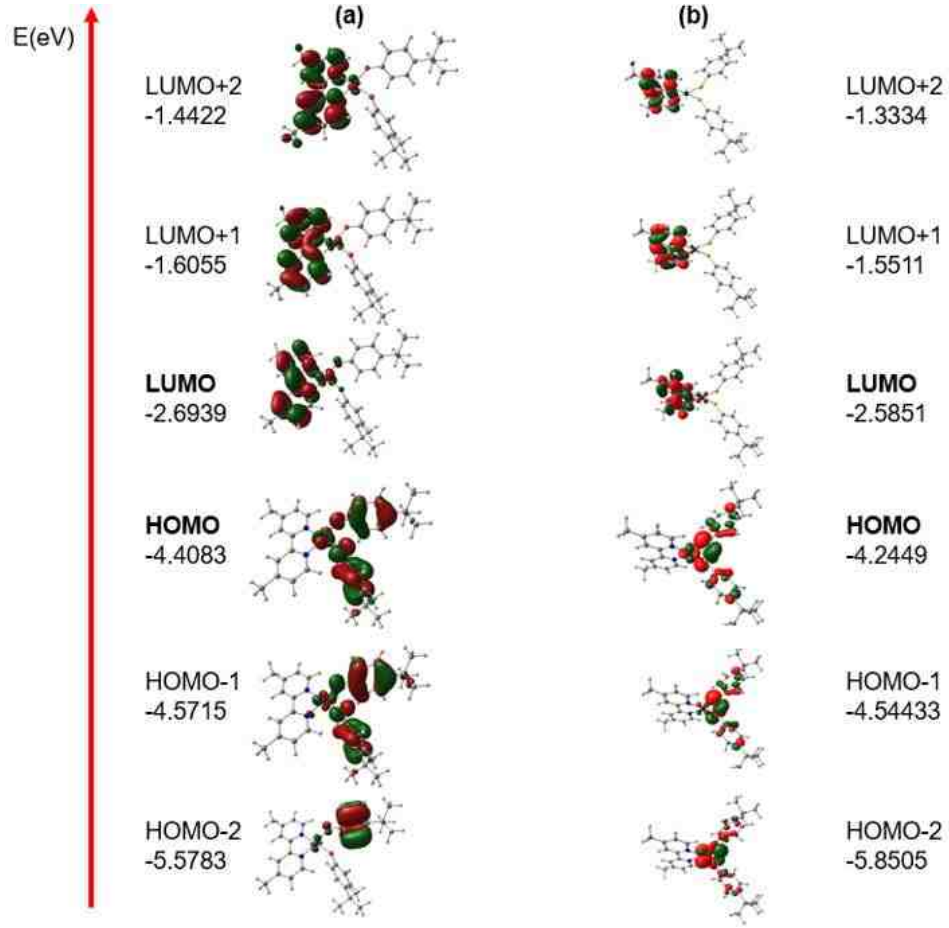

Figure 3.114: Diagram of the relative energy levels of **(a)** Pt(dbbpy)(tbp)$_2$ and **(b)** Pt(dbbpy)(tbt)$_2$ showing the most notable frontier molecular orbitals.

energy states together with oscillator strengths for Pt(dbbpy)(tbp)$_2$. The lowest singlet (S_1) and triplet (T_1) vertical transitions is HOMO → LUMO with transition energies of 1.18 and 0.45 eV respectively. The oscillator strength for the S_1 state

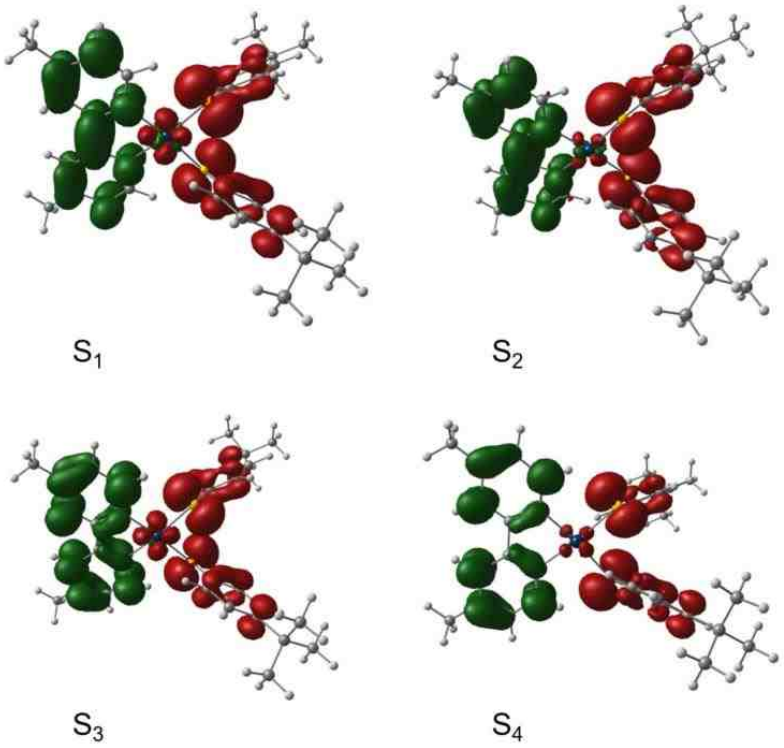

Figure 3.115: Calculated electron density difference map (EDDM) for Singlet States at an isodensity value of 0.0012 au. The red and green regions represent loss and gain of electron density respectively in a transition to the excited state for Pt(dbbpy)(tbt)$_2$.

Table 3.33: Selected TD-DFT Calculated Energies and Compositions of the Lowest Lying Singlet and Triplet Energy States together with oscillator strengths for Pt(dbbpy)(tbp)$_2$.

	Composition[a]	**ΔE[b]**	***f*[c]**	**Assignment**
	Singlets			
S_1	HOMO→LUMO, 67%	1.18	0.0045	tbp/Pt→dbbpy/Pt (LMCT/LLCT)
S_2	HOMO-1→LUMO, 67%	1.41	0.0397	tbp/Pt→dbbpy (MMLL'CT)
$_3$	HOMO→LUMO+1, 68%	2.26	0.0029	tbp/Pt→dbbpy/Pt (MMLL'CT)
S_4	HOMO-2→LUMO, 70%	2.34	0.0065	tbp/Pt→dbbpy (MMLL'CT)
Triplets				

T_1	HOMO→LUMO, 70%	0.45	0.0000	tbp/Pt→dbbpy/Pt (LMCT/LLCT)
T_2	HOMO-1→LUMO, 70%	0.84	0.0000	tbp/Pt→dbbpy (MMLL'CT)
T_3	HOMO→LUMO+1, 69%	2.03	0.0000	tbp/Pt→dbbpy/Pt (MMLL'CT)
T_4	HOMO-2→LUMO, 70%	2.06	0.0000	tbp/Pt→dbbpy (MMLL'CT)

[a] Electronic transitions compositions expressed in terms of ground-state Kohn-Sham molecular orbitals. [b] Transition energy expressed in eV.

Table 3.34: Selected TD-DFT Calculated Energies and Compositions of the Lowest Lying Singlet and Triplet Energy States together with oscillator strengths for $Pt(dbbpy)(tbt)_2$.

	Composition[a]	**ΔE[b]**	***f*[c]**	**Assignment**
Singlets				
S_1	HOMO→LUMO, 70%	1.08	0.0034	tbt/Pt→dbbpy/Pt (LMCT/LLCT)
S_2	HOMO-1→LUMO, 70%	1.44	0.0319	tbt/Pt→dbbpy/Pt (LMCT/LLCT)
S_3	HOMO→LUMO+1, 70%	2.14	0.0013	tbt/Pt→dbbpy (MMLL'CT)
S_4	HOMO→LUMO+2, 69%	2.49	0.0069	tbt/Pt→dbbpy (MMLL'CT)
Triplets				
T_1	HOMO→LUMO, 70%	0.50	0.0000	tbt/Pt→dbbpy/Pt (LMCT/LLCT)
T_2	HOMO-1→LUMO, 70%	1.02	0.0000	tbt/Pt→dbbpy/Pt (LMCT/LLCT)
T_3	HOMO→LUMO+1, 70%	2.04	0.0000	tbt/Pt→dbbpy (MMLL'CT)
T_4	HOMO→LUMO+2, 70%	2.18	0.0000	tbt/Pt→dbbpy (MMLL'CT)

[a] Electronic transitions compositions expressed in terms of ground-state Kohn-Sham molecular orbitals. [b] Transition energy expressed in eV. [c] Oscillator strength.

is 0.0045. It is assigned as tbp/Pt→dbbpy/Pt (LMCT/LLCT). For $Pt(dbbpy)(tbt)_2$, the donor ligand involved is a thiolate (tbt). From the tabulated results in Table 3.34, the most probable vertical transition is S_2 with a transition energy of 1.41 eV and an oscillator strength of 0.0397. This transition is composed of 67% HOMO-1→LUMO and assigned as tbt/Pt→dbbpy (MMLL'CT). Its triplet counterpart (T_2) has a transition energy of 0.84. The vertical transition energies, composition and transition assignment of S_3, T_3, S_4, and T_4 are tabulated in Table 3.33 for $Pt(dbbpy)(tbp)_2$. Table 3.34 outlined the selected TD-DFT calculated energies and compositions of the lowest lying singlet and triplet energy states

together with oscillator strengths for $Pt(dbbpy)(tbt)_2$. TD-DFT calculation shows that the lowest singlet and triplet vertical transitions for $Pt(dbbpy)(tbt)_2$ is of 70% HOMO →LUMO and is assigned as tbt/Pt→dbbpy/Pt (LMCT/LLCT). The calculated S_1 and T_1 have energies of 1.08 and 0.50 eV respectively with 0.0034 oscillator strength for S_1. The computed energies for S_2 and T_2 are 1.44 and 1.02 eV respectively, with 0.0319 oscillator strength for S_2. S_2 has most probable vertical transition based on the oscillator strength. Its electronic transition composition is 70% HOMO-1→LUMO same as T_2 and assigned as tbt/Pt→dbbpy/Pt (LMCT/LLCT). S_3 and T_3 have vertical transition energies of 2.14 and 2.04 eV respectively with 70% composition of HOMO→ LUMO+1 and

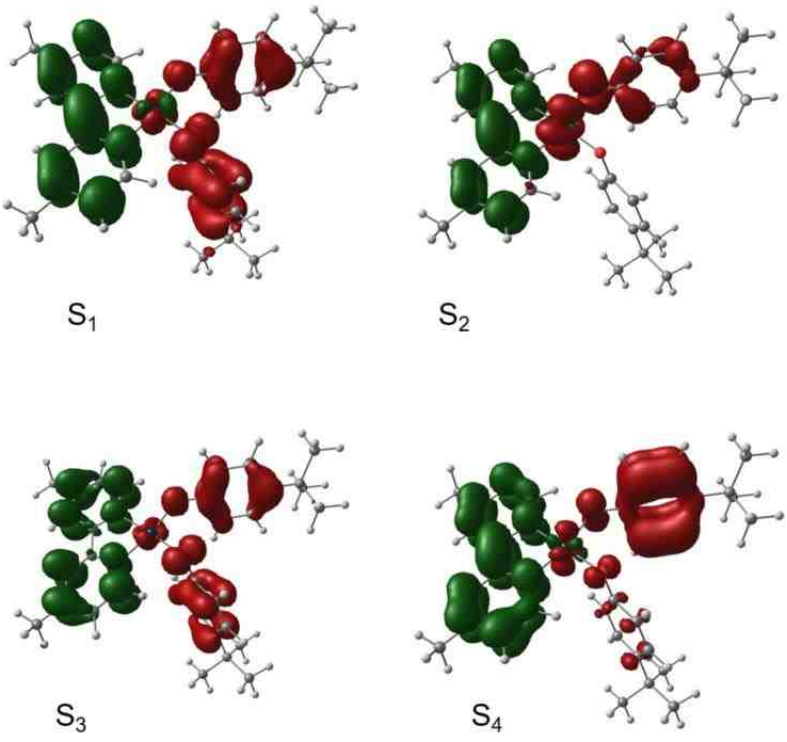

Figure 3.116: Calculated electron density difference map (EDDM) for Singlet States at an isodensity value of 0.0012 au. The red and green regions represent loss and gain of electron density respectively in a transition to the excited state for $Pt(dbbpy)(tbp)_2$.

denoted as tbt/Pt→dbbpy (MMLL'CT). Figure 3.115 and Figure 3.116 present the calculated electron density difference map (EDDM) for singlet states at an isodensity value of 0.0012 au. The EDDM's of S_1, S_2, S_3 and S_4 clearly shows that electron density is lost mainly from thiolate/phenolate and Pt d(π) metal orbitals. The gain of electron density is observed primarily by the diimine acceptor orbitals.

3.3.3.9 Pt(dpphen)(bSO) & Pt(phen)(bdt)

Figure 3.117 depicts the energy diagram of the frontier molecular orbitals of the

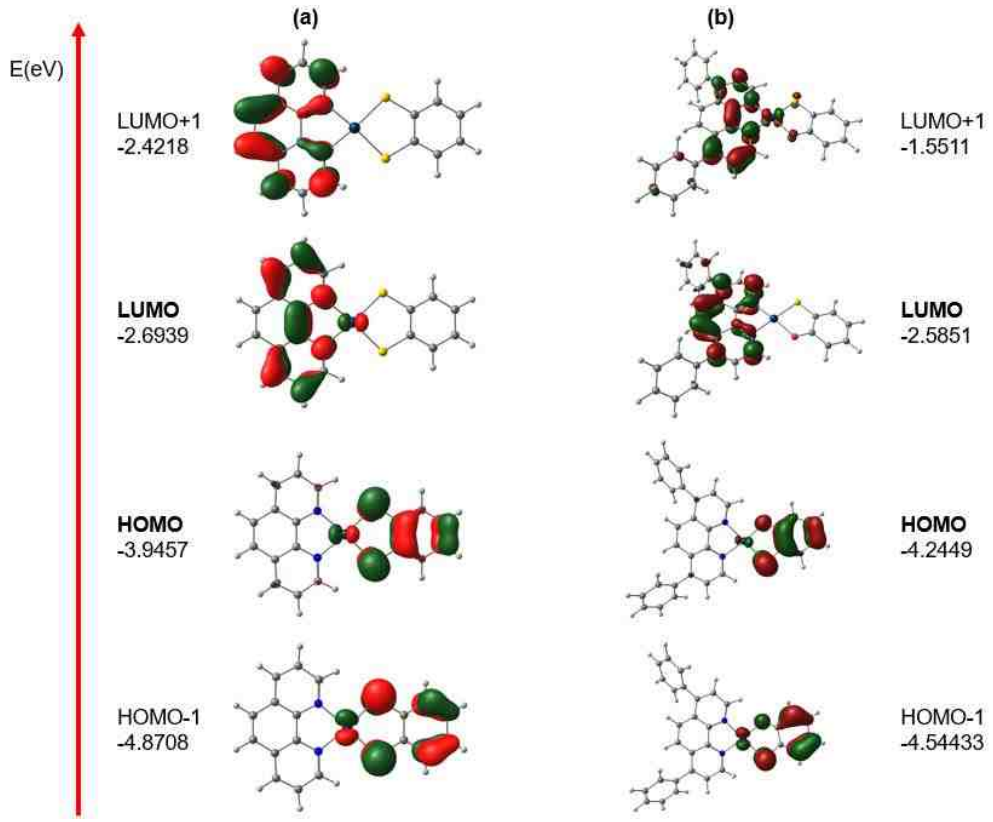

Figure 3.117: Diagram of the relative energy levels of **(a)** Pt(phen)(bdt) and **(b)** Pt(dpphen)(bSO) showing the most notable frontier molecular orbitals.

(a) Pt(phen)(bdt) and **(b)** Pt(dpphen)(bSO) where sulfur (S) and oxygen (O) are the donor atoms for Pt(dpphen)(bSO) and only S chalcogenolene atoms for Pt(phen)(bdt). In Pt(phen)(bdt), C_{2v} symmetry is observed because it has the same chalcogenolene S donor atoms, and the atomic orbital compositions of the two S donor atoms are equivalent in the HOMO. In Pt(dpphen)(bSO), the symmetry is lowered to C_S because different chalcogenolene donor atoms are involved i.e. S and O. The observed mirror plane in Pt(dpphen)(bSO) lies in the molecular plane. In Pt(phen)(bdt), the Pt d_{xz} dπ orbital is positioned along the plane of the mirror that is orthogonal to the molecular plane while in Pt(dpphen)(bSO), Pt d_{xz} dπ orbital is rotated in the direction of the softer chalcogenide S atom resulting in the atomic orbital composition of S donor being

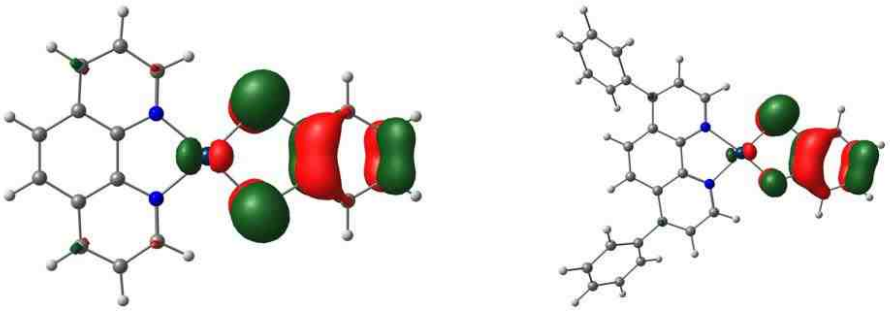

Figure 3.118: HOMO for (a) Pt(phen)(bdt) and (b) Pt(dpphen)(bSO).

remarkably larger than that of O donor in the HOMO.[7] The pictorial presentation depicted in Figure 3.118 shows these remarkable changes in the HOMOs of these complexes. TD-DFT calculations of Pt(phen)(bdt) and Pt(dpphen)(bSO) shows a significant difference in energy of the frontier molecular orbitals and related properties due to small structural variations of the donor ligands (see

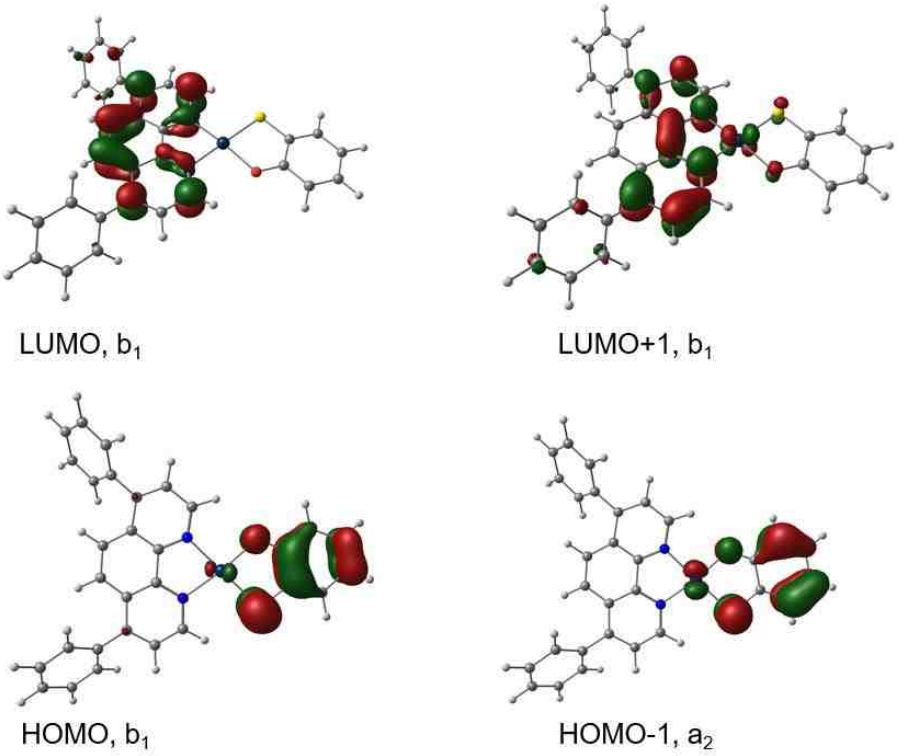

Figure 3.119: Frontier MOs of Pt(dpphen)(bSO) with symmetry assignment.

Table 3.35: Selected TD-DFT Calculated Energies and Compositions of the Lowest Lying Singlet and Triplet Energy States together with oscillator strengths for **Pt(dpphen)(bSO).**

	Composition[a]	**ΔE[b]**	***f*[c]**	**Assignment**
Singlets				
S_1	HOMO→LUMO, 36% HOMO→LUMO+1, 60%	1.28	0.0298	bSO/Pt→bpy (MMLL'CT)
S_2	HOMO→LUMO, 60% HOMO→LUMO+1, 36%	1.42	0.1767	bSO/Pt→bpy (MMLL'CT)
S_3	HOMO-1→LUMO, 70%	1.86	0.0115	bSO/Pt→bpy/Pt (LMCT/LLCT)
S_4	HOMO-1→LUMO+1, 70%	2.04	0.0546	bSO/Pt→bpy (MMLL'CT)
Triplets				
T_1	HOMO→LUMO, 72%	0.52	0.0000	bSO/Pt→bpy (MMLL'CT)
T_2	HOMO→LUMO+1, 70%	1.04	0.0000	bSO/Pt→bpy (MMLL'CT)
T_3	HOMO-1→LUMO, 69%	1.66	0.0000	bSO/Pt→bpy/Pt (LMCT/LLCT)
T_4	HOMO-1→LUMO+1, 70%	2.18	0.0000	bSO/Pt→bpy (MMLL'CT)

[a] Electronic transitions compositions expressed in terms of ground-state Kohn-Sham molecular orbitals. [b] Transition energy expressed in eV. [c] Oscillator strength.

Figure 3.117). From Figure 3.117, it is evident that the HOMO of Pt(dpphen)(bSO) and Pt(phen)(bdt) are made of mercaptophenolate and dithiolate orbitals respectively and the Pt dπ. In the case of the LUMO, the major contribution comes from the phen (dpphen) and some Pt dπ orbital character. In an effective C_2v symmetry, the HOMO, LUMO, and LUMO+1 have b_1 symmetry while the HOMO has a a_2 symmetry (see Figure 3.119). TDDFT results for Pt(dpphen)(bSO) are summarized in Table 3.35 and are schematically depicted in Figure 3.117. The lowest singlet energy state(S_1) is dominated by two

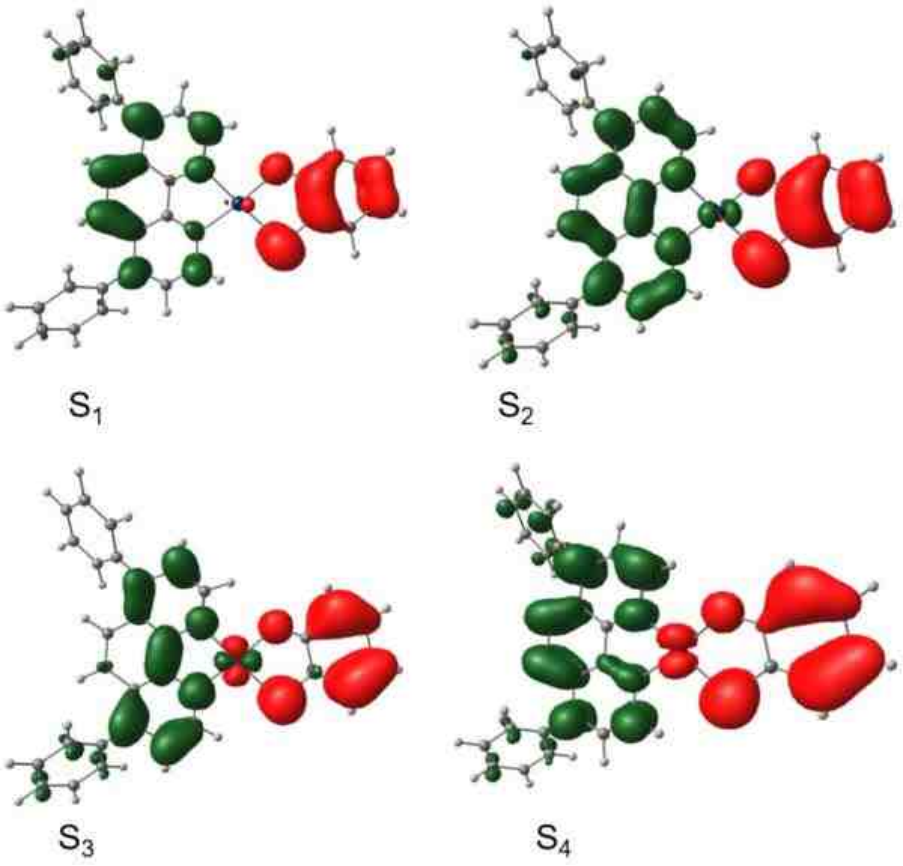

Figure 3.120: Calculated electron density difference map (EDDM) for Singlet States at an isodensity value of 0.0012 au. The red and green regions represent loss and gain of electron density respectively in a transition to the excited state for Pt(dpphen)(bSO).

electronic transitions composition namely HOMO→LUMO, 36% and HOMO→LUMO+1, 60%. The lowest triplet energy state(T_1) is composed mainly of HOMO→LUMO, 72%. The calculated S_1 and T_1 vertical transition energies are 1.28 and 0.52 eV respectively with the oscillator strength of S_1 given as 0.0298. The most probable vertical transition is S_2 with 1.42 eV and an oscillator strength of 0.1767. The second lowest singlet energy state(S_2) is dominated by two electronic transitions composition namely HOMO→LUMO, 60% and HOMO→ LUMO+1, 36%. The second lowest triplet energy state(T_2) is composed mainly of HOMO→LUMO+1, 70% and has a vertical excitation energy of 1.04. S_3 and S_4 have vertical transition energies and oscillator strength of 1.86, 2.04 ev and 0.0115 and 0.0546 respectively. The calculated energies and electronic transition compositions of the other states are all tabulated in Table 3.35. The EDDM's of S_1, S_2, S_3 and S_4 of Pt(dpphen)(bSO) are depicted in Figure 3.120. Its pictorial presentation shows clearly that the electron density is lost from the HOMOs and the gain of electron density is observed by the LUMOs.

3.3.3.10 Pt(dpphen)(bSeO)

Figure 3.121 depicts the energy diagram of the frontier molecular orbitals of the **(a)** Pt(phen)(bds) and **(b)** Pt(dpphen)(bSeO) where selenium (S) and oxygen (O) are the donor atoms of Pt(dpphen)(bSeO) and only Se chalcogenolene atoms for Pt(phen)(bds). In Pt(phen)(bds), C_{2v} symmetry is observed because it has the same chalcogenolene Se donor atoms, and the atomic orbital compositions of

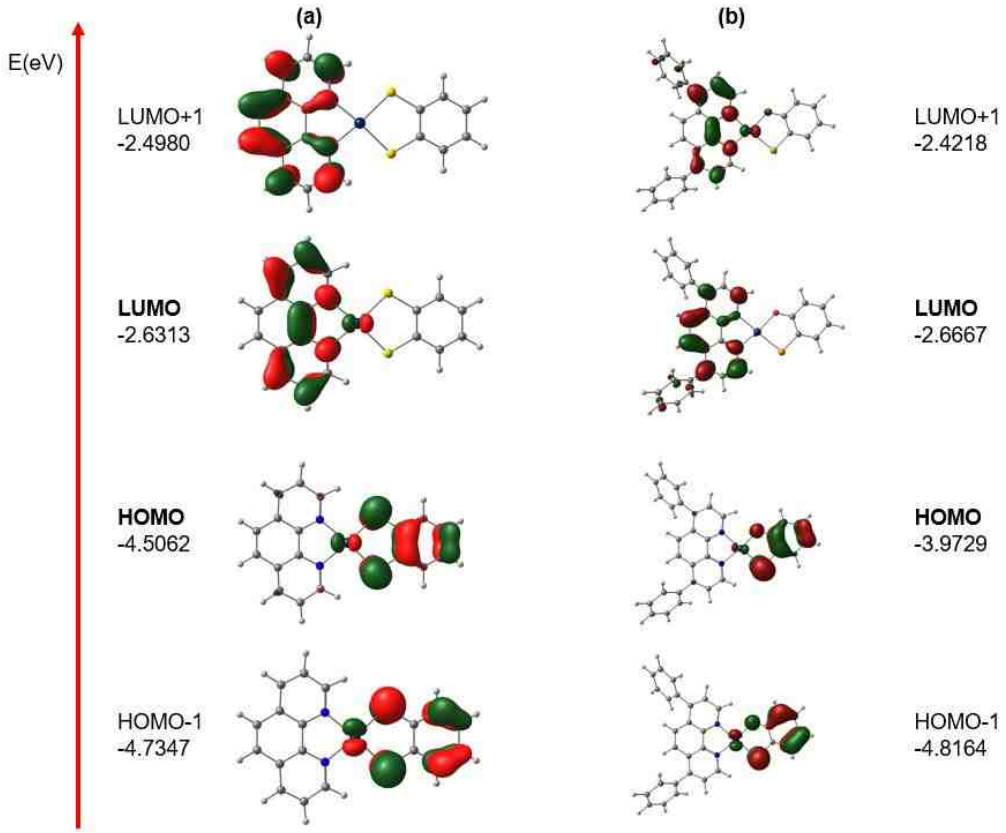

Figure 3.121: Diagram of the relative energy levels of **(a)** Pt(phen)(bds) and **(b)** Pt(dpphen)(bSeO) showing the most notable frontier molecular orbitals.

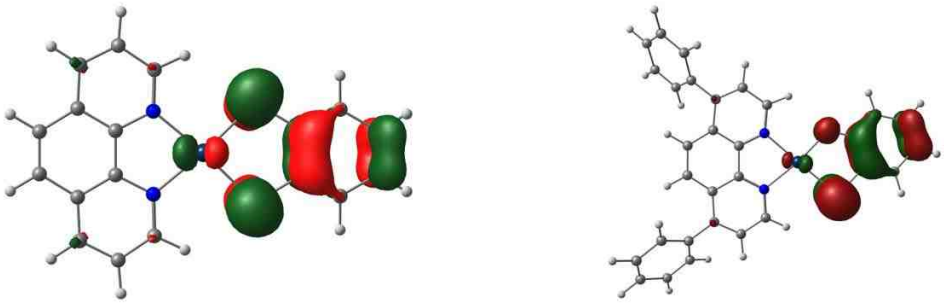

(a) Se, Se **(b) Se, O**

Figure 3.122: HOMO for (a) Pt(phen)(bds) and (b) Pt(dpphen)(bSeO).

the two Se donor atoms are equivalent in the HOMO. In Pt(dpphen)(bSeO), the symmetry is C_S because different chalcogenolene donor atoms are involved i.e. Se and O. The observed mirror plane in Pt(dpphen)(bSeO) lies in the plane of

the molecule. In Pt(phen)(bds), the metal Pt d_{xz} dπ orbital is positioned along the plane of the mirror that is orthogonal to the molecular plane whereas in Pt(dpphen)(bSeO), Pt d_{xz} dπ orbital is rotated in the direction of the softer chalcogenolene Se atom resulting in the atomic orbital composition of Se donor atom being exceptionally larger than that of O donor atom in the HOMO.[30] These observations are presented in Figure 3.122. Due to structural changes in the donor ligands of these two complexes, the TD-DFT calculations of Pt(phen)(bdt) and Pt(dpphen)(bSO) show remarkable difference in the valence orbitals energies (see Figure 3.121). TD-DFT results presented in Figure 3.121 shows

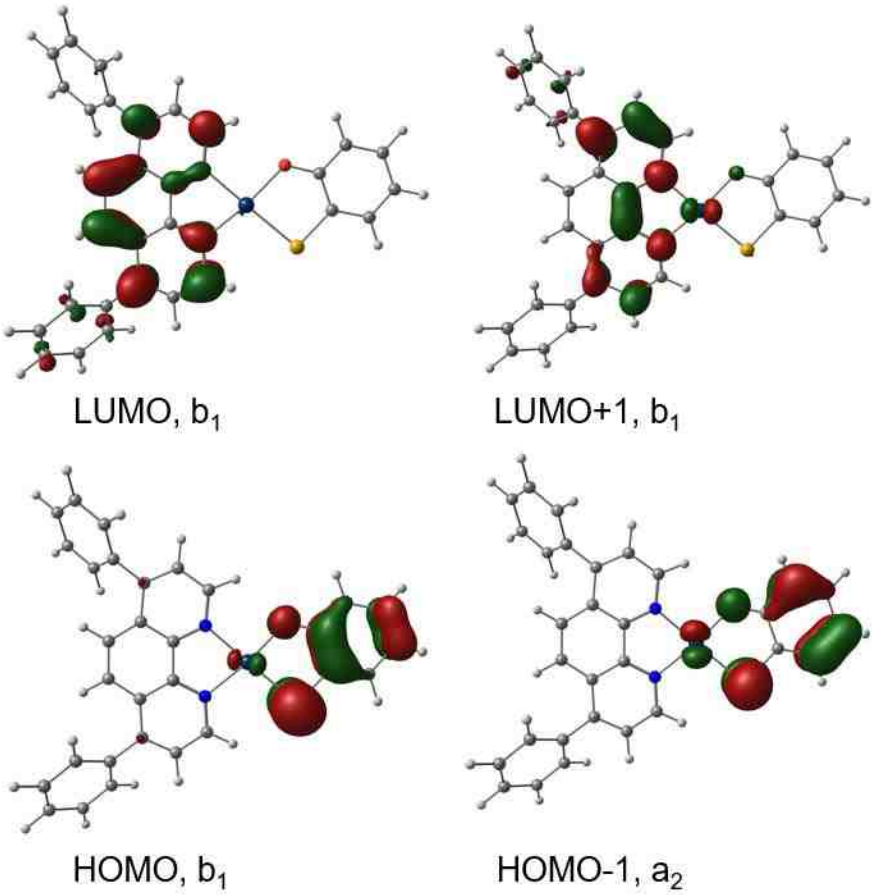

Figure 3.123: Frontier MOs of Pt(dpphen)(bSeO) with symmetry assignment.

that the HOMO of Pt(dpphen)(bSeO) and Pt(phen)(bds) are made of selenylphenolate and diselenolate orbitals respectively and some Pt metal dπ orbital. The LUMO electronic composition is mainly π* orbitals of phen or dpphen. Figure 3.123 shows that in an effective C_{2v} symmetry, the HOMO, LUMO, and LUMO+1 can have b_1 symmetry whereas the HOMO has a_2 symmetry. The selected TD-DFT calculated energies and compositions of the lowest lying singlet and triplet energy states together with their oscillator strengths for Pt(dpphen)(bSeO) is depicted in Table 3.36. By closely observing Table 3.36, it can be ascertained that the S_1 state is composed of two electronic transitions composition namely HOMO→LUMO, 53% and HOMO→LUMO+1, 47%. The lowest triplet energy state(T_1) is composed mainly of HOMO→LUMO,

Table 3.36: Selected TD-DFT Calculated Energies and Compositions of the Lowest Lying Singlet and Triplet Energy States together with oscillator strengths for Pt(dpphen)(bSeO).

	Composition[a]	**ΔE[b]**	***f*[c]**	**Assignment**
Singlets				
S_1	HOMO→LUMO, 53% HOMO→LUMO+1, 47%	1.27	0.0345	bSeO/Pt→bpy (MMLL'CT)
S_2	HOMO→LUMO, 48% HOMO→LUMO+1, 52%	1.42	0.1578	bSeO/Pt→bpy (MMLL'CT)
S_3	HOMO-1→LUMO, 70%	1.81	0.0177	bSeO/Pt→bpy/Pt (LMCT/LLCT)
S_4	HOMO-1→LUMO+1, 70%	1.99	0.0580	bSeO/Pt→bpy (MMLL'CT)
Triplets				
T_1	HOMO→LUMO, 72%	0.57	0.0000	bSeO/Pt→bpy (MMLL'CT)
T_2	HOMO→LUMO+1, 70%	1.07	0.0000	bSeO/Pt→bpy (MMLL'CT)
T_3	HOMO-1→LUMO, 69%	1.59	0.0000	bSeO/Pt→bpy/Pt (LMCT/LLCT)
T_4	HOMO-1→LUMO+1, 70%	2.10	0.0000	bSeO/Pt→bpy (MMLL'CT)

[a] Electronic transitions compositions expressed in terms of ground-state Kohn-Sham molecular orbitals. [b] Transition energy expressed in eV. [c] Oscillator strength.

72%. The calculated S_1 and T_1 transition energies are 1.27 and 0.57 eV respectively with the oscillator strength of S_1 given by 0.0345. The second lowest singlet state (S_2), which is the most probable has a vertical transition energy of 1.42 eV with oscillator strength of 0.1578. Its two electronic transitions composition are HOMO→LUMO, 48% and HOMO→LUMO+1, 52%. The T_2 is composed mainly of HOMO→LUMO+1, 70% and has a vertical excitation energy of 1.07 eV. S_3 and S_4 have vertical transition energies and oscillator strength of 1.81, 1.99 eV and 0.0177 and 0.0580 respectively. The calculated energies and

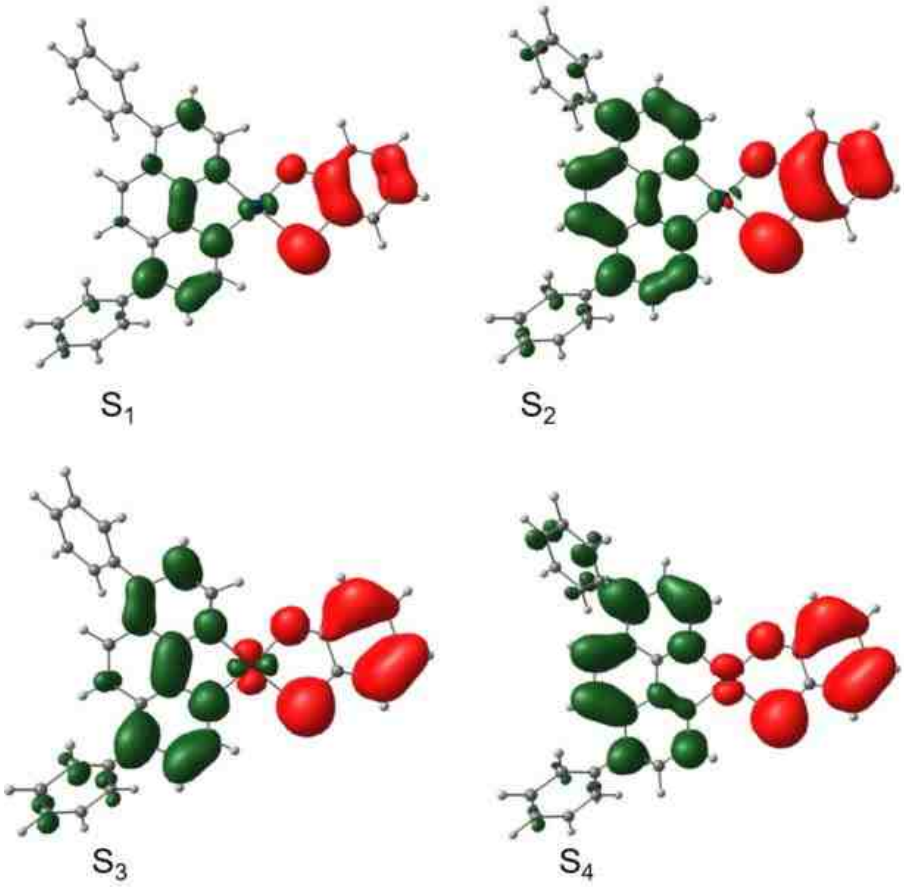

Figure 3.124: Calculated electron density difference map (EDDM) for Singlet States at an isodensity value of 0.0012 au. The red and green regions represent loss and gain of electron density respectively in a transition to the excited state for Pt(dpphen)(bSeO).

electronic transition compositions of the other states are recorded in Table 3.36. The EDDM's of S_1, S_2, S_3 and S_4 of Pt(dpphen)(bSeO) are depicted in Figure 3.124. Its pictorial presentation shows clearly that the electron density is lost from the HOMOs and the gain of electron density is observed by the LUMOs.

3.3.4 The Analysis of the Frontier MOs of Ni(diimine)(dichalcogenolene) and Pd(diimine)(dichalcogenolene) Complexes

3.3.4.1 Ni(bpy)(bdt)

The frontier molecular orbitals displayed by Ni(bpy)(bdt) are similar to that of Pt(bpy)(bdt). Here, the transition metal involved is Ni^{2+} instead of Pt^{2+} for Pt(bpy)(bdt). The MO diagram for Ni(bpy)(bdt) is depicted in Figure 3.125. The basic characteristics of the frontier molecular orbitals of Ni(bpy)(bdt) are like that of Pt(bpy)(bdt). The frontier molecular orbital energies of Ni(bpy)(bdt) are very close to that of Pt(bpy)(bdt). From TD-DFT, the calculated HOMO-LUMO energy gap (ΔE) are 1.82 eV (14679 cm^{-1}) and 1.84 eV (14841 cm^{-1}) for

Table 3.37: HOMO-LUMO energy gap (∆E) and MMLL'CT band maxima for M(diimine)(dichalcogenolene) Complexes [M=Pt, Ni].

Complex	ΔE_{eV}[a]	∆E(cm^{-1})[a]	$E_{MMLL'CT}$(cm^{-1})[b]
Pt(bpy)(bdt)	1.84	14841	18350
Ni(bpy)(bdt)	1.82	14679	18954
Pt(bpy)(CAT)	1.56	12582	16920
Ni(bpy)(CAT)	1.43	11534	17447

[a] HOMO-LUMO energy gap (∆E) calculated by TD-DFT, [b] Experimental energy of the MMLL'CT band maxima in dichloromethane.

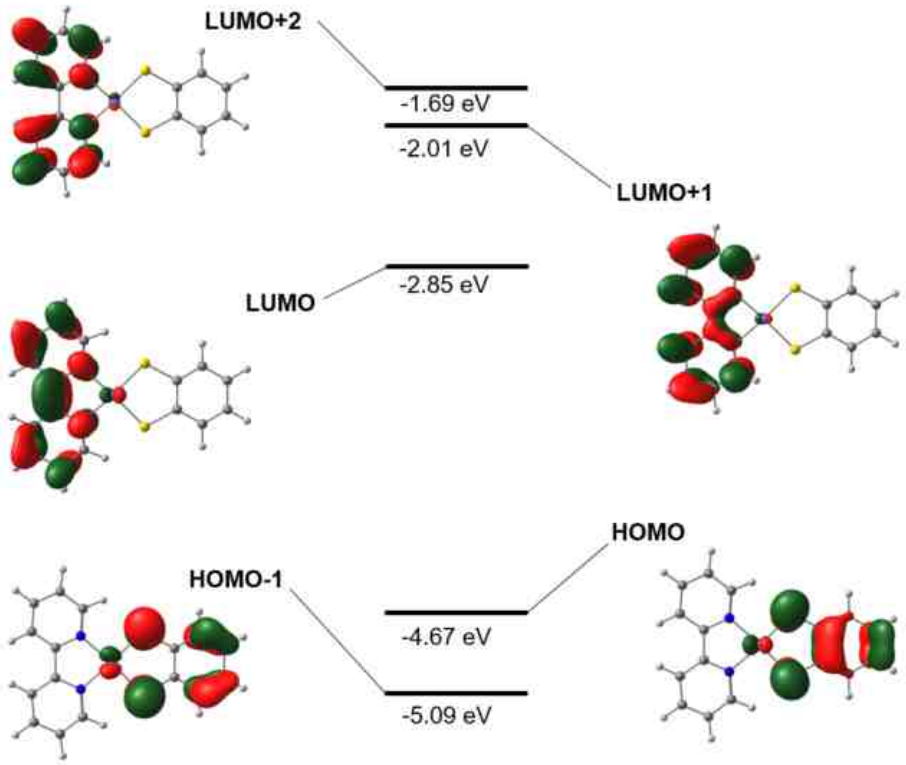

Figure 3.125: Frontier MOs and their respective energies of Ni(bpy)(bdt).

Ni(bpy)(bdt) and Pt(bpy)(bdt) respectively (see Table 3.37). In the Ni(diimine)(dichalcogenolene) series, TD-DFT calculation predicts the lowest

Table 3.38: Selected TD-DFT Calculated Energies and Compositions of the Lowest Lying Singlet and Triplet Energy States Together with Oscillator Strengths for **Ni(bpy)(bdt).**

State	Composition[a]	ΔE[b]	*f*[c]	Assignment
Singlets				
S_1	HOMO→LUMO, 71%	1.48	0.1248	bdt/Ni→bpy/Ni (LMCT/LLCT)
S_2	HOMO-1→LUMO, 68%	1.60	0.0015	bdt/Ni→bpy/Ni(LMCT/LLCT)
S_3	HOMO-2→LUMO+3, 64%	1.82	0.000	bdt//Ni →bpy(MMLL'CT)
Triplets				
T_1	HOMO→LUMO, 70%	1.02	0.0000	bdt//N →bpy/Ni (LMCT/LLCT)
T_2	HOMO-1→LUMO, 69%	1.49	0.0000	bdt//Ni →bpy/Ni(LMCT/LLCT)

T_3	HOMO-2→LUMO+3, 71%	0.89	0.0000	bdt//Ni →bpy (MMLL'CT)
T_4	HOMO-3→LUMO+3, 50% HOMO-1→LUMO+3, 43%	0.93	0.0000	bdt//Ni →bpy (MMLL'CT)

[a] Electronic transitions compositions expressed in terms of ground-state Kohn-Sham molecular orbitals. [b] Transition energy expressed in eV. [c] Oscillator strength.

singlet (S_1) and triplet (T_1) vertical transitions of Ni(bpy)(bdt) to be HOMO →LUMO. T_2/S_2 is assigned as HOMO-1 →LUMO, T_3 = HOMO-2 →LUMO+3 and T_4 = HOMO-3 →LUMO+3/ HOMO-1 →LUMO+3. S_1 and T_1 vertical transitions are LMCT/LLCT instead of MMLL'CT due to the metal contributions in both the HOMO and LUMO. The calculated S_1 and T_1 have energies 1.48 and 1.02 eV

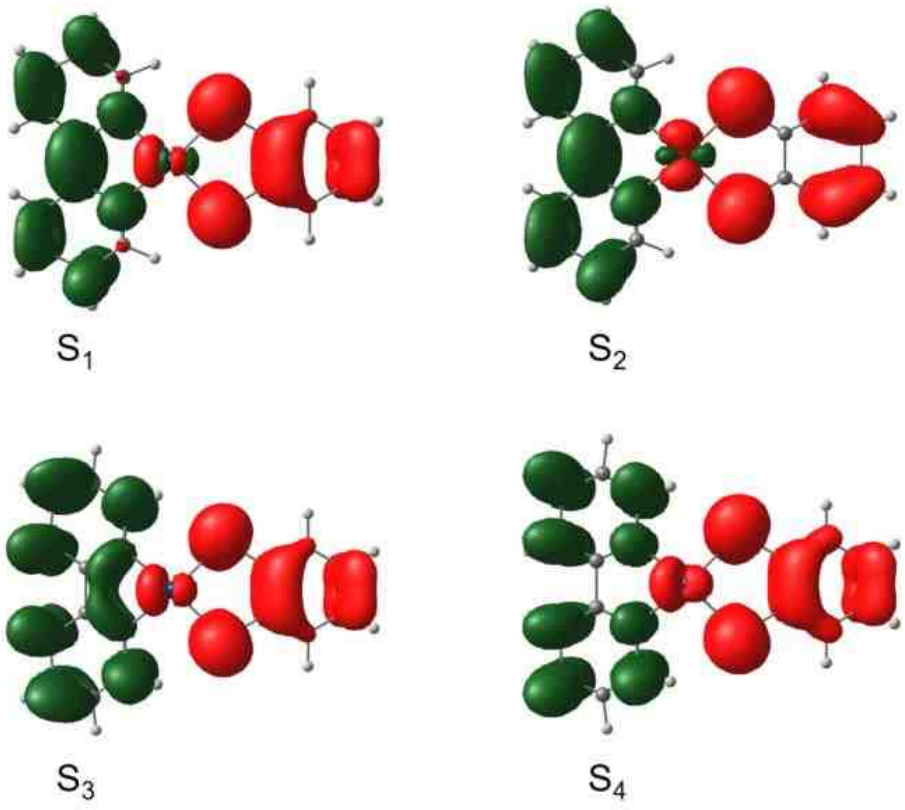

Figure 3.126 Calculated electron density difference map (EDDM) for singlet states at an isodensity value of 0.0012 au. The red and green regions represent loss and gain of electron density respectively in a transition to the excited state.

respectively with the oscillator strength of S_1 given as 0.1248 (Table 3.38). By comparing the oscillator strength of S_1 vertical transitions of Ni(bpy)(bdt) and Pt(bpy)(bdt), Ni(bpy)(bdt) has a more probable S_1 vertical transition than that of Pt(bpy)(bdt) due to the larger magnitude of its oscillator strength (see Table 3.38 and Table 3.18). The electronic transitions compositions of S_1, S_2, S_3, T_1, T_2, T_3, and T_4 are tabulated in Table 3.38. In effective C_{2V} symmetry, the HOMO's and

LUMO's have the same symmetry assignment as Pt(bpy)(bdt) depicted in Figure 3.86. The calculated electron density difference map (EDDM) for the singlet states at an isodensity value of 0.0012 au are depicted in Figure 3.126. The red and green regions represent loss and gain of electron density respectively in a vertical electronic transition to the excited state.

3.3.4.2 Ni(bpy)(bds)

The MO diagram and energies for the frontier orbitals of Ni(bpy)(bds) are comparable to that of Pt(bpy)(bds) [see Figure 3.81]. The selected TD-DFT

Table 3.39: Selected TD-DFT Calculated Energies and Compositions of the Lowest Lying Singlet and Triplet Energy States Together with Oscillator Strengths for **Ni(bpy)(bds).**

State	Composition[a]	ΔE[b]	f[c]	Assignment
Singlets				
S_1	HOMO→LUMO, 70%	1.48	0.1091	bds/Ni→bpy/Ni(LMCT/LLCT)
S_2	HOMO-1→LUMO, 69%	1.44	0.0018	bds/Ni→bpy/Ni(LMCT/LLCT)
S_3	HOMO-2→LUMO+3, 60%	1.76	0.0002	bds/Ni →bpy(MMLL'CT)
Triplets				
T_1	HOMO→LUMO, 70%	1.07	0.0000	bds/Ni→bpy/Ni(LMCT/LLCT)
T_2	HOMO-1→LUMO, 70%	1.33	0.0000	bds/Ni→bpy/Ni(LMCT/LLCT)

T_3	HOMO-2→LUMO+3, 72%	0.79	0.0000	bds/Ni →bpy (MMLL'CT)
T_4	HOMO-3→LUMO+3, 41% HOMO-1→LUMO+3, 50%	0.83	0.0000	bds/Ni →bpy (MMLL'CT)

[a] Electronic transitions compositions expressed in terms of ground-state Kohn-Sham molecular orbitals. [b] Transition energy expressed in eV. [c] Oscillator strength.

calculated energies and composition of the lowest lying singlets (S_1, S_2, and S_3) and triplet excited states (T_1, T_2, T_3 and T_4) together with their vertical excitation energies and oscillator strengths for Ni(bpy)(bds) are displayed in Table 3.39. The most probable vertical excitation is HOMO →LUMO with oscillator strength of 0.1091, whereas Pt(bpy)(bds) has the most probable vertical excitation from HOMO-1 →LUMO with an oscillator strength of 0.1390 (see Table 3.18). The calculated electron density difference map (EDDM) for the singlet excited states are very comparable to that of Pt(bpy)(bds).

3.3.4.3 Ni(bpy)(bSSe) & Ni(bpy)(bSO)

Figure 3.127 depicts the MO diagram and energies of the valence orbitals of Ni(bpy)(bSO). The frontier molecular orbitals displayed by Ni(bpy)(bSSe) and Ni(bpy)(bSO) are like that of Pt(bpy)(bSSe) and Pt(bpy)(bSO) respectively. In Ni(bpy)(bSSe) and Ni(bpy)(bSO), the HOMO's are denoted mainly by bSSe/Ni and bSO/Ni in character respectively, with the major contribution coming from HOMO and HOMO-1 molecular orbitals. No pure Nickel d-orbitals orbitals were observed due to the noninnocent nature of the mercaptophenolate (bSO) and selenylbenzenethiolate (bSSe) ligands. Ni(bpy)(bSSe) and Ni(bpy)(bSO) have C_s symmetry because the chalcogenolene donor atoms involve are different i.e.

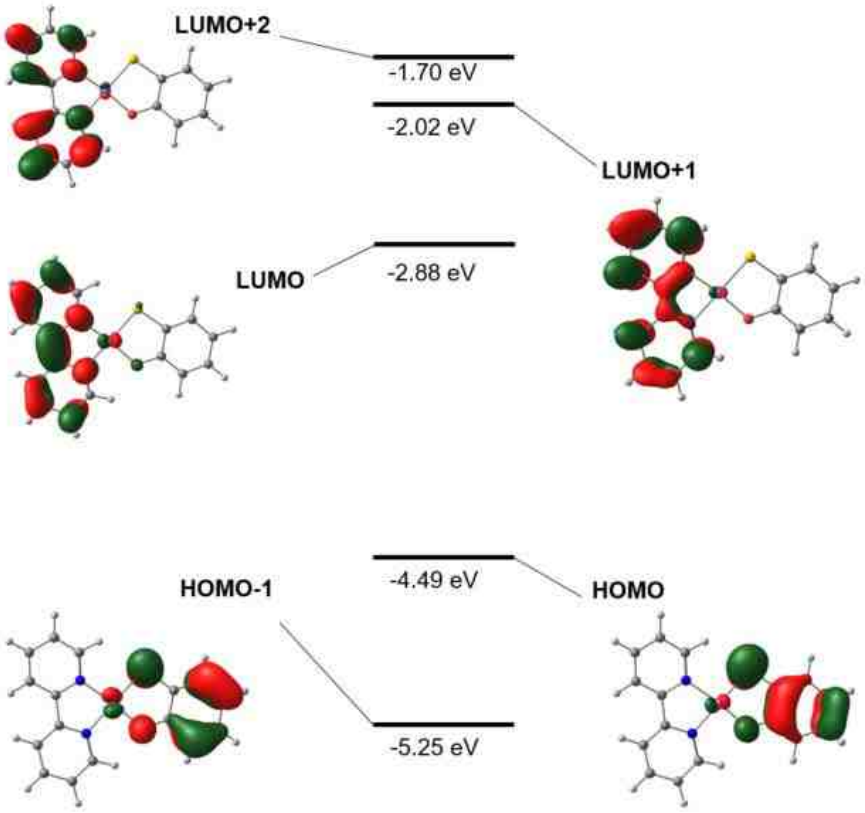

Figure 3.127: Frontier MOs and their respective energies of Ni(bpy)(bSO).

Table 3.40: Selected TD-DFT Calculated Energies and Compositions of the Lowest Lying Singlet and Triplet Energy States Together with Oscillator Strengths for **Ni(bpy)(bSSe).**

State	Composition[a]	ΔE[b]	*f*[c]	Assignment
Singlets				
S_1	HOMO→LUMO, 66%	1.47	0.0933	bSSe/Ni→bpy/Ni(LMCT/LLCT)
S_2	HOMO-1→LUMO, 64%	1.53	0.0250	bSSe/Ni→bpy/Ni(LMCT/LLCT)
S_3	HOMO-2→LUMO+3, 66%	2.09	0.0001	bSSe/Ni →bpy(MMLL'CT)
Triplets				
T_1	HOMO→LUMO, 70%	1.05	0.0000	bSSe/Ni→bpy/Ni(LMCT/LLCT)
T_2	HOMO-1→LUMO, 70%	1.41	0.0000	bSSe/Ni→bpy/Ni(LMCT/LLCT)
T_3	HOMO-2→LUMO+3, 71%	0.84	0.0000	bSSe/Ni →bpy (MMLL'CT)

T_4	HOMO-3→LUMO+3, 30% HOMO-1→LUMO+3, 50%	0.88	0.0000	bSSe/Ni →bpy (MMLL'CT)

[a] Electronic transitions compositions expressed in terms of ground-state Kohn-Sham molecular orbitals. [b] Transition energy expressed in eV. [c] Oscillator strength.

sulfur (S) and selenium (Se) for Ni(bpy)(bSSe), and sulfur (S) and oxygen (O) for Ni(bpy)(bSO). The HOMO's and LUMO's of Ni(bpy)(bSSe) and Ni(bpy)(bSO) have the same symmetry assignment of that of Pt(bpy)(bSSe) and Pt(bpy)(bSO) [see Figures 3.90 and 3.95]. Displayed in Tables 3.40 and 3.41 are the selected TD-DFT calculated energies and composition of the lowest lying singlets (S_1, S_2, and S_3) and triplet excited states (T_1, T_2, T_3 and T_4) together with their vertical

Table 3.41: Selected TD-DFT Calculated Energies and Compositions of the Lowest Lying Singlet and Triplet Energy States Together with Oscillator Strengths for **Ni(bpy)(bSO).**

State	**Composition[a]**	**ΔE^b**	***f*[c]**	**Assignment**
		Singlets		
S_1	HOMO→LUMO, 71%	1.32	0.1218	bSO/Ni→bpy/Ni (LMCT/LLCT)
S_2	HOMO-1→LUMO, 66%	1.86	0.0000	bSO/Ni→bpy/Ni(LMCT/LLCT)
S_3	HOMO-2→LUMO+3, 67%	1.78	0.0047	bSO/Ni →bpy(MMLL'CT)
		Triplets		
T_1	HOMO→LUMO, 70%	0.83	0.0000	bSO/Ni →bpy/Ni (LMCT/LLCT)
T_2	HOMO-1→LUMO, 69%	1.67	0.0000	bSO/Ni →bpy/Ni(LMCT/LLCT)
T_3	HOMO-2→LUMO+3, 69%	0.74	0.0000	bSO/Ni →bpy (MMLL'CT)
T_4	HOMO-3→LUMO+3, 41% HOMO-1→LUMO+3, 42%	0.82	0.0000	bSO/Ni →bpy (MMLL'CT)

[a] Electronic transitions compositions expressed in terms of ground-state Kohn-Sham molecular orbitals. [b] Transition energy expressed in eV. [c] Oscillator strength.

excitation energies and oscillator strengths for Ni(bpy)(bSSe) and Ni(bpy)(bSO) respectively. The lowest energy singlet (S_1) and triplet (T_1) vertical transitions are

from HOMO →LUMO. The electronic transitions compositions of S_1 are 71% and 70% respectively for Ni(bpy)(bSSe) and Ni(bpy)(bSO). From Table 3.40, the calculated S_1 and T_1 energies for Ni(bpy)(bSSe) are 1.47 and 1.05 eV respectively with oscillator strength of S_1 given as 0.0933. The calculated S_1 and T_1 energies of Ni(bpy)(bSSe) are comparable to that of Pt(bpy)(bSSe) [see

Table 3.20]. Also, the calculated S_1 and T_1 energies of Ni(bpy)(bSO) are 1.32 and 0.83 eV respectively with a high oscillator strength of S_1 given by 0.1218 (Table 3.41).

3.3.4.4 Pd(bpy)(bdt), Pd(bpy)(bds), Pd(bpy)(bSeO), Pd(dbbpy)(bSO), & Pd(dbbpy)(CAT)

The model Pd(diimine)(dichalcogenolene) complexes depict frontier MOs where the highest occupied MOs (HOMO) are admixed with Pd d-orbital and dichalcogenolene character (Figures 3.128 and 3.129). TD-DFT calculations performed on these model systems reveal that the major contribution comes from the HOMO and HOMO-1. Also, no pure Pd d-orbitals orbitals were observed due observed due to the noninnocent nature of the dichalcogenolene ligands. Although, the lowest occupied MOs (LUMO) are calculated to be primarily localized on the diimine acceptor ligand, a finite contribution of Pd metal and dichalcogenolene ligand still exists. The HOMO and HOMO-1 have b_1 and a_2 symmetry respectively while the LUMO and LUMO+1 have b_1 symmetry characteristic of the diimine chelate moiety in an effective C_{2V} environment.

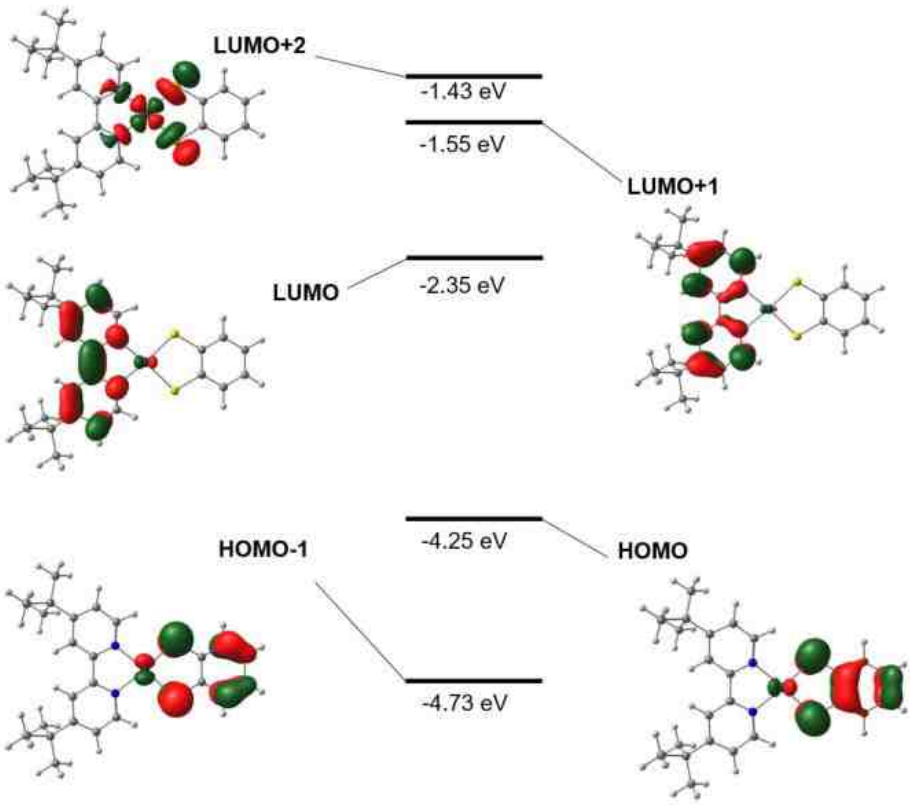

Figure 3.128: Frontier MOs and their respective energies of Pd(dbbpy)(bdt).

Summarized in Tables 3.42, 3.43, C2, C3, and C4 (appendix C) are the selected TD-DFT calculated energies and composition of the lowest lying singlets (S_1, S_2, and S_3) and triplet excited states (T_1, T_2, T_3 and T_4) together with their vertical excitation energies and oscillator strengths for Pd(diimine)(dichalcogenolene) model systems. The TD-DFT calculated lowest triplet and singlet vertical transitions for all Pd(diimine)(dichalcogenolene) model systems are charge transfer (CT) transitions from the HOMO to LUMO. The CT transition is denoted as MMLL'CT because is mainly composed of mixed metal/dichalcogenolene to diimine character. A closer examination of Tables 3.42, 3.43, C2, C3, and C4 revealed that the vertical transitions from HOMO to LUMO are composed of only

70% of MMLL'CT band for all Pd(diimine)(dichalcogenolene) model systems. The

Table 3.42: Selected TD-DFT Calculated Energies and Compositions of the Lowest Lying Singlet and Triplet Energy States together with oscillator strengths for **Pd(dbbpy)(bdt).**

State	Composition[a]	ΔE[b]	*f*[c]	Assignment
Singlets				
S_1	**HOMO→LUMO, 71%**	**1.52**	**0.0988**	**bdt/Pd→dbbpy (MMLL'CT)**
S_2	HOMO-1→LUMO, 66%	1.79	0.0000	bdt/Pd→dbbpy/Pd (LMCT/LLCT)
S_3	HOMO-2→LUMO+3, 70%	1.85	0.0012	bdt/Pd→dbbpy/Pd (MMLL'CT)
S_4	HOMO-1→LUMO+2, 69%	2.18	0.0082	bdt/Pd→dbbpy (MMLL'CT)
Triplets				
T_1	HOMO→LUMO, 70%	1.26	0.0000	bdt/Pd→dbbpy (MMLL'CT)
T_2	HOMO→LUMO+2, 69%	1.51	0.0000	bdt/Pd→dbbpy/Pd (LMCT/LLCT)
T_3	HOMO-1→LUMO, 70%	1.78	0.0000	bdt/Pd→dbbpy/Pd (MMLL'CT)
T_4	HOMO-1→LUMO+2, 67%	1.85	0.0000	bdt/Pd→dbbpy (MMLL'CT)

[a] Electronic transitions compositions expressed in terms of ground-state Kohn-Sham molecular orbitals. [b] Transition energy expressed in eV. [c] Oscillator strength.

energies of Pd(diimine)(dichalcogenolene) model systems calculated from TD-DFT agree only moderately with the experimental values (see Table C1 from Appendix C). The difference in energies between experimental and TD-DFT calculated values can be ascribed to solvatochromism of these complexes. The experimental energies of the CT band are blue shifted moving from nonpolar solvents (benzene, toluene) to polar solvents (acetonitrile, DMSO) (see Figure C6 from Appendix C). Another reason for the differences in energies between the experimental and calculated values is that, TD-DFT does not consider spin-orbit coupling due to metal atom. However, qualitatively the calculated and experimental energies agree to some extent by displaying a few low energy transitions of weak intensity which form part of the broad MMLL'CT band.

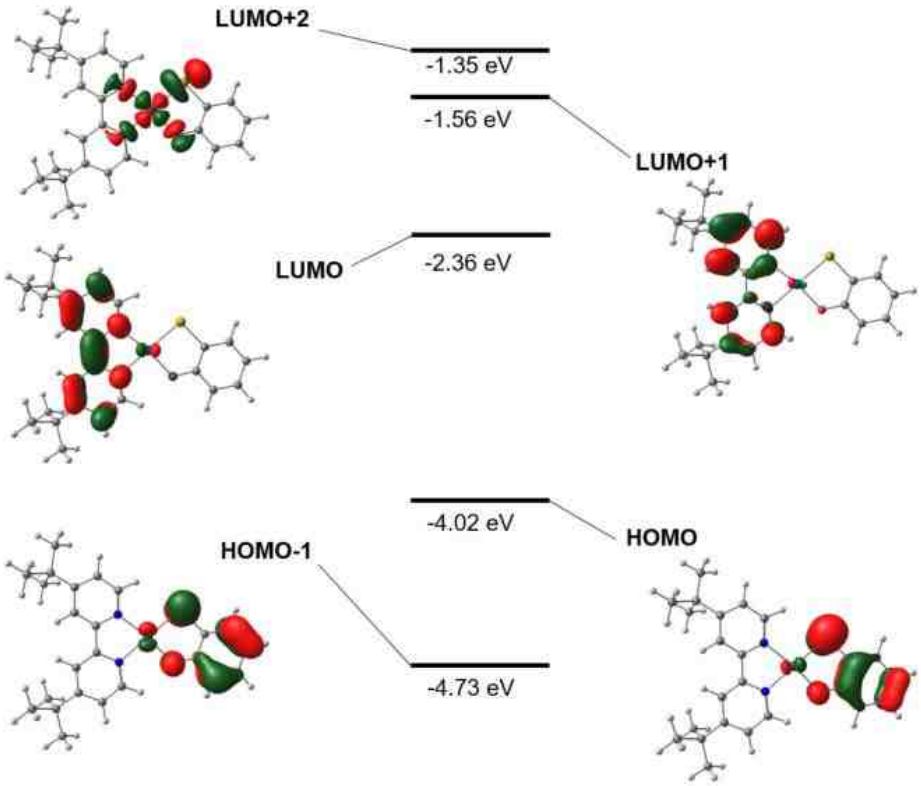

Figure 3.129 Frontier MOs and their respective energies of Pd(dbbpy(bSeO).

Table 3.43: Selected TD-DFT Calculated Energies and Compositions of the Lowest Lying Singlet and Triplet Energy States together with oscillator strengths for Pd(dbbpy)(bSeO).

State	Composition[a]	ΔE[b]	*f*[c]	Assignment
Singlets				
S_1	**HOMO→LUMO, 71%**	**1.30**	**0.0969**	**bSeO/Pd→dbbpy/Pd (MMLL'CT)**
S_2	HOMO→LUMO+2, 70%	1.64	0.0000	bSeO→dbbpy/Pd (LMCT/LLCT)
S_3	HOMO-1→LUMO, 70%	1.85	0.0028	bSeO/Pd→dbbpy/Pd (MMLL'CT)
S_4	HOMO→LUMO+1, 70%	1.93	0.0082	bSeO/Pd→dbbpy (MMLL'CT)
Triplets				
T_1	HOMO→LUMO, 70%	0.98	0.0000	bSeO →dbbpy/Pd (MMLL'CT)
T_2	HOMO→LUMO+2, 69%	1.40	0.0000	bSeO→dbbpy/Pd (LMCT/LLCT)
T_3	HOMO-1→LUMO, 70%	1.77	0.0000	bSeO/Pd→dbbpy/Pd (MMLL'CT)

T_4	HOMO→LUMO+1, 70%	1.87	0.0000	bSeO→dbbpy/Pd (MMLL'CT)

[a] Electronic transitions compositions expressed in terms of ground-state Kohn-Sham molecular orbitals. [b] Transition energy expressed in eV. [c] Oscillator strength.

The EDDMs of S_1, S_2, S_3 and S_4 for Pd(dbbpy)(bdt) and Pd(dbbpy)(bSeO) are depicted in Figures C7 and C8 respectively (Appendix C), show clearly that the electron density is lost from the HOMO which is a mixture of dichalcogenolene and Pd metal. The gain of electron density by the LUMO is represented as purely diimine for S_1, S_3 and S_4. EDDM for S_2 shows that the acceptor orbitals are a mixture of and diimine and Pd.

A closer inspection of M(diimine)(dichalcogenolene) model systems reveal that the oscillator strength displayed by platinum complexes are much higher than that of nickel and palladium model complexes. (Tables 3.16, 3.38, and 3.42). This observation indicates the major involvement of the metal in the MMLL'CT transitions. This trend is ascribed to a better metal-ligand (M-L) overlap generated by the 5d-, 4d- and 3d-orbitals of Pt, Pd, and Ni respectively. Pt 5d-orbital has the greatest radial extensive orbital nature than that of Pd and Ni. This results in better π-delocalization in Pt(diimine)(dichalcogenolene) complexes. In M(diimine)(dichalcogenolene) complexes, the metal increases the molar absorptivity (ε) and decreases the energy of MMLL'CT absorption band of the order Pt(II) > Pd(II) > Ni(II) (Figures C1, C9 – C12, and Table C5 in Appendix C). This trend strongly confirms metal d-orbital involvement in the CT to diimine excited state.[17] The dichalcogenolene ligands involvement in the charge-transfer to diimine excited state was confirmed by measuring the MMLL'CT absorption band maxima for Pd(dbbpy)(dichalcogenolene) complexes (Figure C2 in

Appendix C). Pd(dbbpy)(bdt) has the longest MMLL'CT absorption band maxima (21000 cm^{-1}) followed by Pd(dbbpy)(bSO) (19375 cm^{-1}), and then Pd(dbbpy)(tbuCAT) (17170 cm^{-1}) (Table C1 in Appendix C).

3.3.5 The Analysis of Singlet and Triplet excited states of Pt(diimine) (dichalcogenolene).

Figure 3.130 depicts the energy level ordering for the singlet ground state (S_0), singlet excited states (S_1 and S_2) and triplet excited states (T_1, and T_2) for O,O; O,S; S,S; S,Se; and Se,Se complexes. The ground-state UV-vis absorption spectra for O,O; O,S; S,S; S,Se; and Se,Se complexes, display a broad LL'CT band with very similar absorption maxima which ranges from 16920 (O,O) to 18350 cm^{-1} (S,S). These results are tabulated in Table 3.4 and presented pictorially in Figure 3.40. Due to their ground-state electronic absorption spectra similarities, these complexes possess indistinguishable ground-state electronic configuration, i.e. $a_2^2 b_1^2 b_1^0$ in an effective C_{2v} symmetry. Thus, these complexes have S_0 ground state with the same energy (see Figure 3.130).[5] The singlet excited states, S_1 and S_2 are composed of $a_2^2 b_1^1 b_1^1$; $^1A_1$ and $a_2^1 b_1^2 b_1^1$; $^1B_2$ respectively. It's triplet counterpart are T_1 ($^3A_1$) and T_2 ($^3A_2$) states. S_1/T_1 state represent HOMO → LUMO vertical transition whereas S_2/T_2 represent HOMO-1 → LUMO vertical transition. Based on TD-DFT spectroscopic calculations (Figure 3.130), the T_2 state lies below S_1 state for S,S; S,Se; and Se,Se whereas for O,O and O,S, the T_2 state lies above S_1 state. Figure 3.131 depicts a Jablonski diagram showing photophysical processes for O,O; O,S; S,S; S,Se; and Se,Se

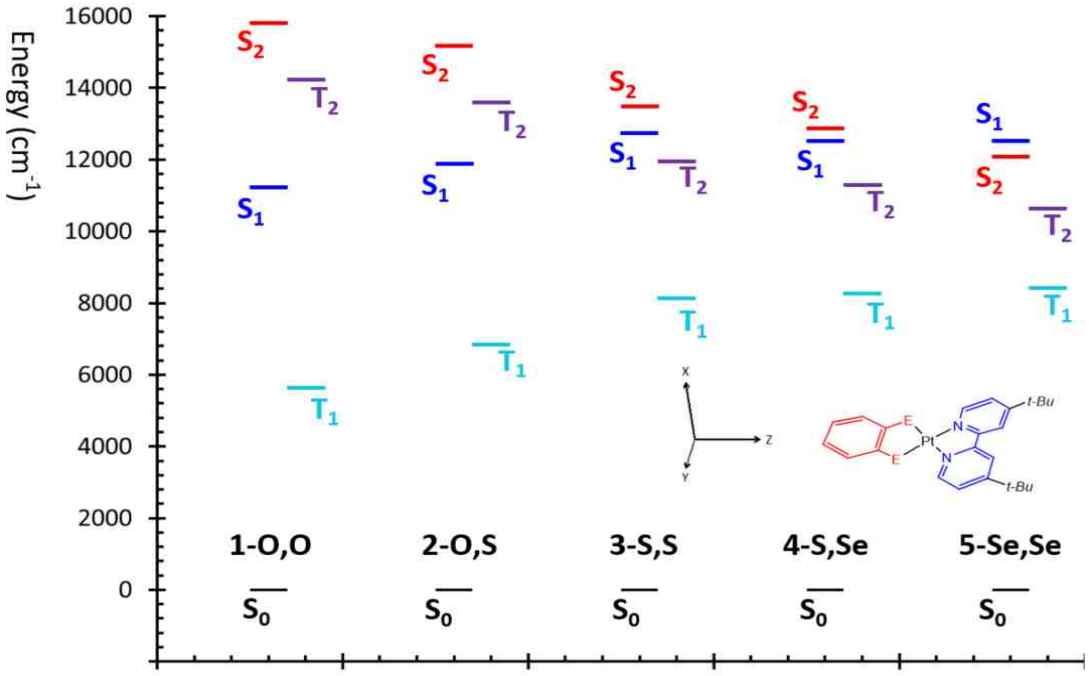

Figure 3.130: Energy level arrangement for the Singlet ground state (S_0), Singlet excited states (S_1 and S_2) and Triplet excited states (T_1, and T_2) for O,O, O,S, S,S, S,Se, and Se,Se complexes based on TD-DFT calculation. O,O = Pt(dbbpy)(tbuCAT), O,S = Pt(dbbpy)(bSO), S,S = Pt(dbbpy)(bdt), S,Se = Pt(dbbpy)(bSSe) and Se,Se = Pt(dbbpy)(bds)[51]

complexes. The diagram also shows the arrangement of the S_0, S_1, S_2, T_1 and T_2 states. Upon photoexcitation into the low-energy LL'CT band, a charge separated excited state (ES), (dithiolene$^{\bullet+}$)Pt(diimine$^{\bullet-}$) is created along the molecular z-axis with an open shell D-A biradical character. Photoluminescence is observed for S,S upon photoexcitation into the LL'CT band and is long-lived. For O,O; no emission was observed upon photoexcitation in the LL'CT band because it relaxes rapidly from $S_1 \rightarrow S_0$ through internal conversion (IC) with k_{IC} of 0.63 ns. In the two-level approximation, spin-orbit coupling (SOC) controls the rate constant for intersystem crossing (k_{ISC})

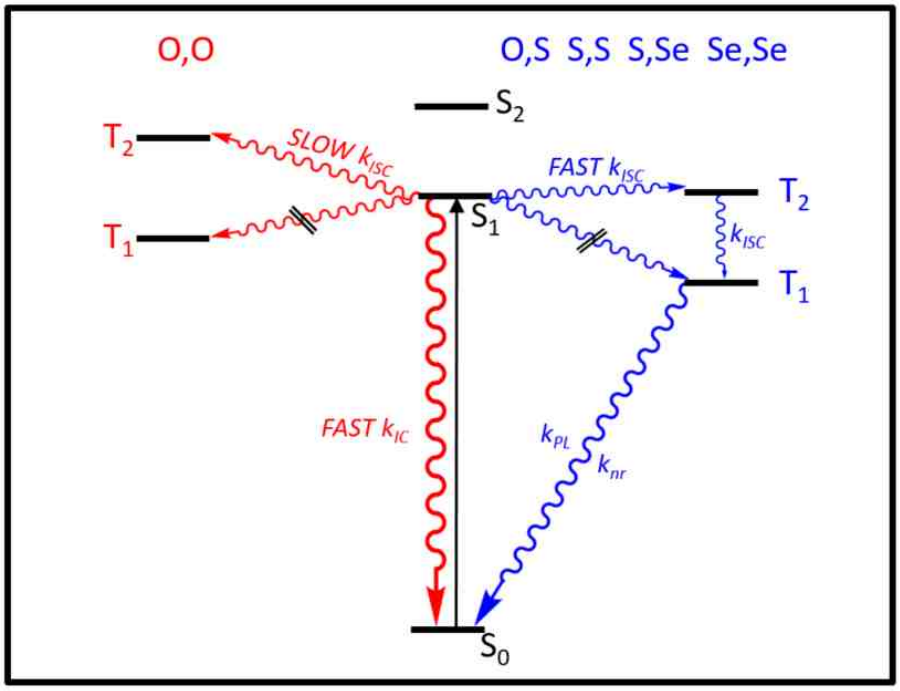

Figure 3.131: Jablonski diagram showing photophysical processes for the none-emissive O,O (left) and emissive complexes (O,S S,S S,Se Se,Se) (right). ISC from S_1 to T_1 by spin-orbit coupling (SOC) promotion is symmetry-forbidden and ISC from S_1 to T_2 by SOC promotion, is symmetry-allowed. k_{ISC}, k_r, and k_{nr} represent the rates for inter-system crossing (ISC), radiative and non-radiative process respectively.[51]

$$k_{ISC} \propto \langle S_n|L_x|T_n\rangle^2 / \Delta E_{ST}^2 \quad \text{.....(1)}$$

$$\langle S_1|L_i|T_1\rangle = \langle A_1|L_i|A_1\rangle = 0 \text{.....(2)}$$

$$\langle A_1|L_x|B_2\rangle \neq 0 \text{.....(3)}$$

where L_i are the orbital angular momentum operators, which transform as a_2, b_1, and b_2 in C_{2v} symmetry. Intersystem crossing (ISC) from $S_1 \rightarrow T_1$ and $T_1 \rightarrow S_0$ are symmetry-forbidden (equation 2) and its observed rates are often small. On the other hand, ISC from $S_1 \rightarrow T_2$ is symmetry-allowed due to equation 3 and the observed rate is the highest when the energies of T_2 and S_1 are very close (see equation 1).[51] From Jablonski diagram in Figure 3.131, photophysical pathways

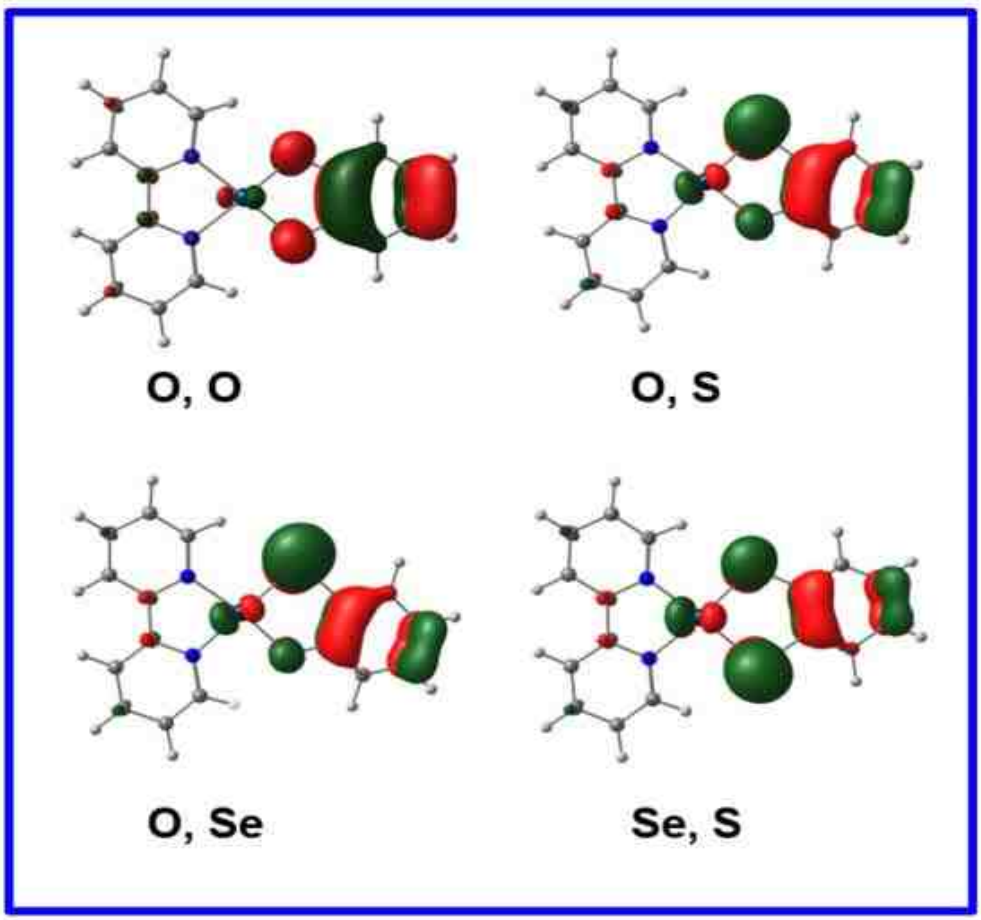

Figure 3.132: Highest Molecular Orbitals (HOMO) for O,O; O,S; O,Se; and Se,S.

leading to ground-state recovery can occur both from the triplet and singlet manifold. Pt(dbbpy)(tbuCAT) has the fastest ground-state recovery rate of 0.63 ns which occurs through IC from $S_1 \rightarrow S_0$. This pathway does not compete with $S_1 \rightarrow T_1$ for ground-state recovery because the $S_1 \rightarrow T_1$ ISC is symmetry-forbidden. Ground-state recovery is also possible through $S_1 \rightarrow T_2$ ISC pathway (symmetry-allowed) but this does not occur because the observed rate (k_{ISC}) is slow (Figure 3.131). This observation was based on TD-DFT spectroscopic calculations (see Figure 3.130) which confirm that the T_2 state of O,O is about 1500 cm-1 above S_1.

Pt(dbbpy)(bSO), Pt(dbbpy)(bdt), Pt(dbbpy)(bSSe), and Pt(dbbpy)(bds) are all emissive, proposing that their T_2 state lie below S_1. Their photophysical pathways leading to ground-state recovery occurs through fast ISC via SOC-allowed $S_1 \rightarrow T_2$, followed by internal conversion (IC) from $T_2 \rightarrow T_1$ and then $T_1 \rightarrow S_0$. The spin-orbit coupling (SOC) allowed $S_1 \rightarrow T_2$ ISC is arbitrated by the amount of Pt d-orbital contribution in the HOMO, HOMO-1 and LUMO (equation 4). In low symmetry Pt(dbbpy)(bSO) and Pt(dbbpy)(bSeO) complexes, it is demonstrated

$$\langle Pt(xz)|L_x|Pt(xy)\rangle \neq 0 \quad \text{.....(4)}$$

by the rotation of Pt(dπ) HOMO toward the Pt-S and Pt-Se bond respectively in O,S, and O,Se (Figure 3.132), resulting in adequate mixing of some metal dxy orbital character into the HOMO (equation 5). This results in an increased in non-radiate rate (k_{nr}) leading to ground-state recovery.

$$\langle \Psi_{T1}|L_x|\Psi_{S0}\rangle \propto \langle Pt(xy)|L_x|Pt(xz)\rangle \neq 0 \quad \text{.....(5)}$$

The Pt(dπ) orbital rotation is less in S,Se compared to O,S; and O,Se; due to indistinguishable Pt-S and Pt-Se covalencies in S,Se assuming C_{2v} symmetry. Thus, the lifetimes (τ) observed for these pairs S,Se; S,S; and O,S; O,Se; are similar (see Table 3.4).[51] The donor atom SOC can be used to predict the excited-state processes in S,S; S,Se; and Se,Se complexes. The ligand SOC mechanism can be used to modulate the T_1 lifetmes, i.e. the rate of ground-state recovery from $T_1 \rightarrow S_0$. In C_{2v} symmetry, ISC from $T_1 \rightarrow S_0$ induced by direct SOC is symmetry-forbidden. The symmetry-forbiddeness can be control by incorporating spin-vibronic and vibronic SOC, which operate by coupling states of different spin multiplicity. Vibrations due to out-of-plane a_2, and b_1 are effective in

mixing the out-of-plane Ep_x orbitals with in-plane Ep_y and Ep_z orbitals. Thus,

$$\langle Ep_x | \mathbf{L_z} | E'p_y \rangle \neq 0 \quad \text{.....(5)}$$

$$\langle Ep_x | \mathbf{L_y} | E'p_z \rangle \neq 0 \quad \text{.....(6)}$$

equation 5 and 6 are formed as a result of linear combination of atomic orbital (LCAO)-expanded matrix elements, where E=S and E'=Se. Equations 5 and 6 should be nonzero and a donor atom SOC addition to $T_1 \rightarrow S_0$ ISC. Since selenium has a larger SOC constant (ζ_O = 154, ζ_S = 365, ζ_{Se} = 1659 cm^{-1}) than that of sulfur (~4.5 times), a shorter T_1 lifetimes should be anticipated by a plot T_1 lifetimes verses selenium ligation. This prediction was observed experimentally for S,S; S,Se; and Se,Se complexes (Table 3.4).[51]

3.3.6 The Analysis of Singlet and Triplet excited states of Ni(diimine)(dichalcogenolene)

Figure 3.133 depicts the energy level ordering for the singlet ground state (S_0), singlet excited states (S_1 and S_2) and triplet excited states (T_1, T_2, T_3, T_4 and T_5) for O,O; O,S; S,S; S,Se; and Se,Se complexes. Ni(diimine)(dichalcogenolene) complexes have indistinguishable ground-state electronic configuration of the type $a_2^2 b_1^2 b_1^0$ in an effective C_{2v} symmetry due to their ground-state electronic absorption spectra similarities. Thus, these complexes possess S_0 ground state with the same energy (Figure 3.133). The energy level arrangement for the singlet and triplet states of Ni(diimine)(dichalcogenolene) are very similar to that of Pt(diimine)(dichalcogenolene) [see Figure 3.130]. Based on time dependent (TD) DFT calculations, the lowest singlet (S_1) and triplet (T_1) vertical transitions in

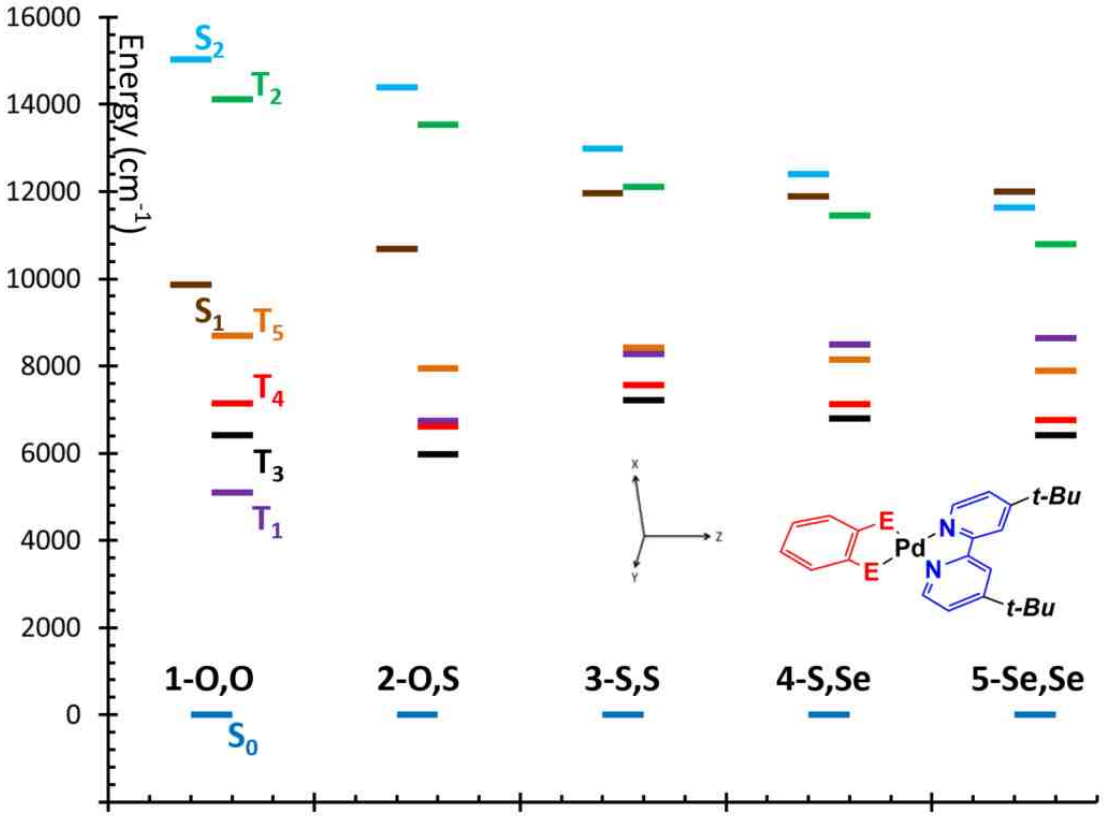

Figure 3.133: Energy level arrangement for the Singlet ground state (S_0), Singlet excited states (S_1 and S_2) and Triplet excited states (T_1, T_2, T_3, T_4 and T_5) for O,O; O,S; S,S; S,Se; and Se,Se complexes based on TD-DFT calculation. O,O = Ni(dbbpy)(tbuCAT), O,S = Ni(dbbpy)(bSO), S,S = Ni(dbbpy)(bdt), S,Se = Ni(dbbpy)(bSSe) and Se,Se = Ni(dbbpy)(bds).

Ni(diimine)(dichalcogenolene) complexes are assigned HOMO →LUMO. T_2/S_2 vertical transition is assigned as HOMO-1 →LUMO, whereas T_3 and T_4 vertical transitions are assigned as HOMO-2 → LUMO+3 and HOMO-3 → LUMO+3/ HOMO-1 →LUMO+3 respectively. As it is designated in Figure 3.133, the T_2 state lies below S_1 state for S,Se and Se,Se, while for O,O; S,S; and O,S the T_2 state lies above S_1 state.

3.3.7 The Linear Relationship between Photoluminescence rates, Calculated SOC and ^{13}C-NMR chemical shifts

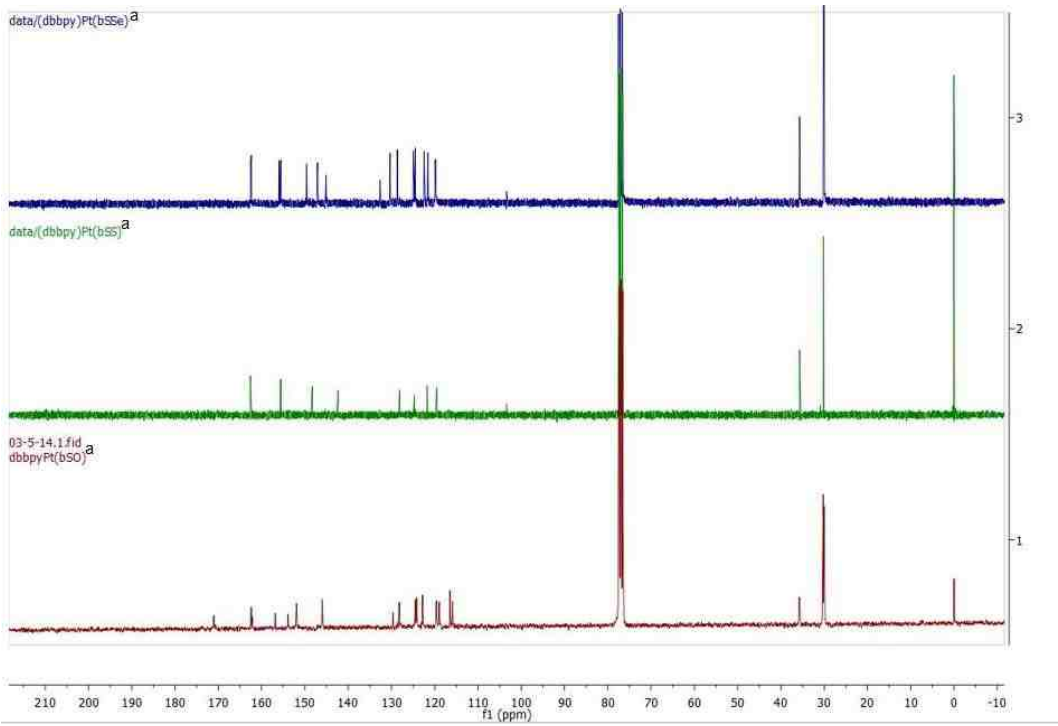

Figure 3.134: Overlay of ^{13}C -NMR for Pt(dbbpy)(bdt), Pt(dbbpy)(bSSe) and Pt(dbbpy)(bSO).[a] ^{13}C-NMR was taken in chloroform-d with the solvent peak at 77.23 ppm with a triplet multiplicity.

Heteroatom effects has modulated the excited-state lifetimes by not less than three orders of magnitude. Table 3.44 summarizes the non-radiative decay rates (k_{nr}) in S,S; S,Se; Se,O; S,O; and Se,Se series. The differences in ^{13}C-NMR chemical shift for Pt(diimine)(dichalcogenolene) complexes are tabulated in Table 3.44 and the overlay of ^{13}C-NMR spectra are presented pictorially in Figures 3.134 and 3.135. Figure 3.136 depicts the structure of Pt(diimine)(dichal-cogenolene) complex used in the donor ligand ^{13}C-NMR chemical shifts (δ) assignment. A closer inspection of the non-radiative decay rates (k_{nr})

summarized in Table 3.44 suggests that Se,Se does not follow the linear trend

Table 3.44: ^{13}C-NMR chemical shift (δ) and triplet absorption lifetime for Pt(diimine)(dichalcogenolene) complexes.

Complex	Non-Radiative Lifetime (ns)	Δδ (ppm)	$\Delta\delta^2$ (ppm)^2
S,S	600	0.00	0.00
S,Se	550	10.85	117.72
Se,O	70	41.04	1684.28
S,O	46	41.59	1729.73
Se,Se	154	0.00	0.00

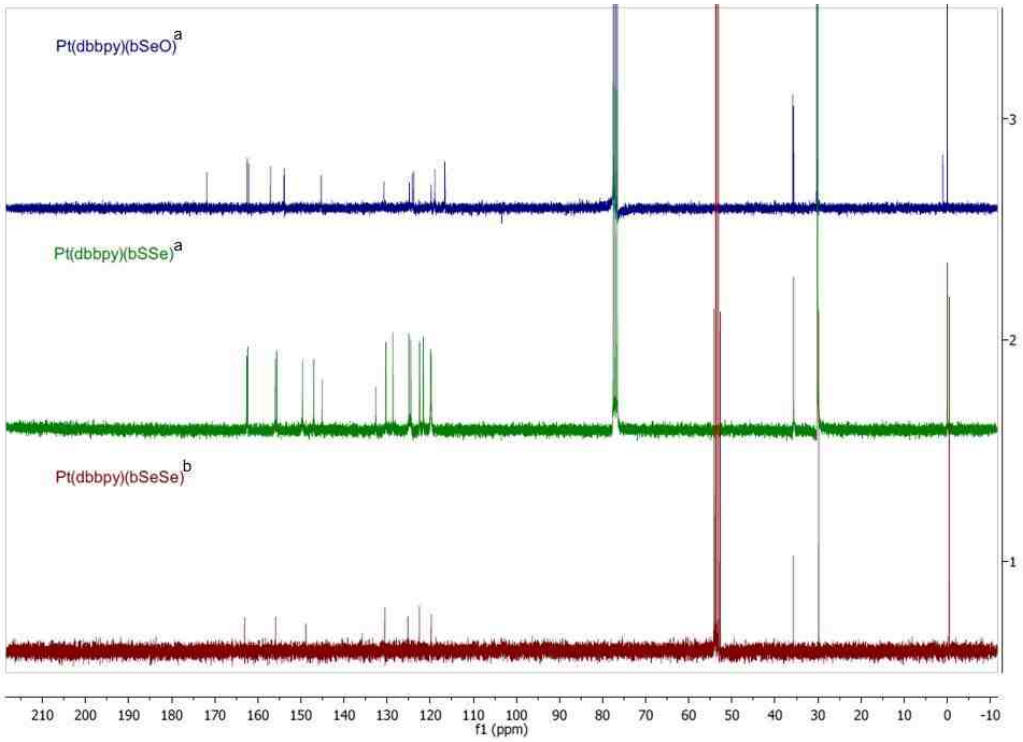

Figure 3.135: Overlay of ^{13}C -NMR for Pt(dbbpy)(bSeSe), Pt(dbbpy)(bSSe) and Pt(dbbpy)(bSeO). [a] ^{13}C-NMR was taken in chloroform-d with the solvent peak at 77.23 ppm with a triplet multiplicity . [b] ^{13}C NMR was taken in dichloromethane-d_2 with the solvent peak at 53.5 ppm with a quintet multiplicity.

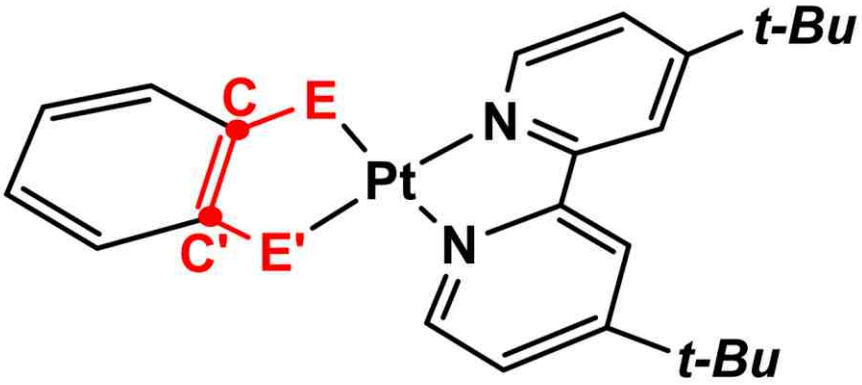

Figure 3.136: Structure of Pt(diimine)(dichalcogenolene) complex used in ^{13}C-E-E'-^{13}C' ligand ^{13}C-NMR chemical shifts (δ) assignment.

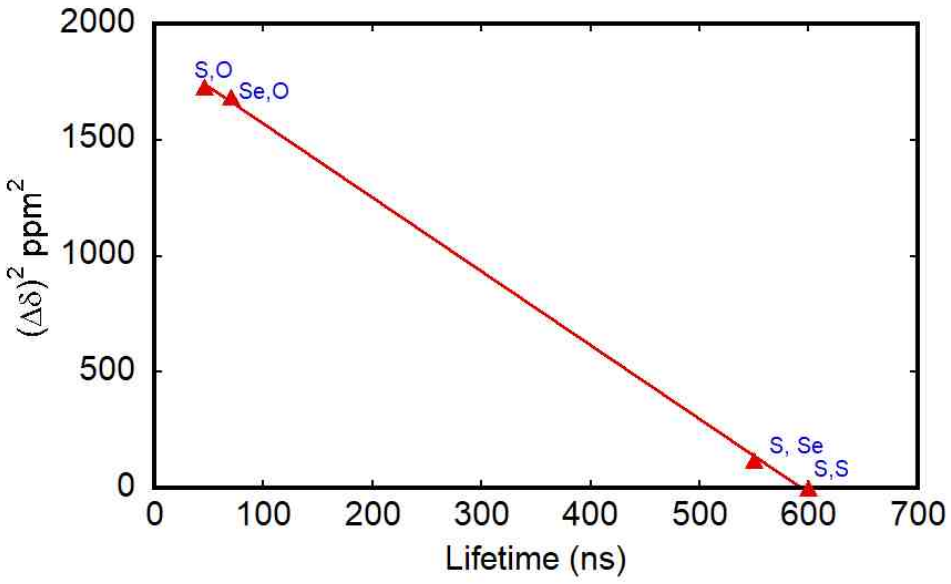

Figure 3.137: Linear correlation between the squares of the differences in ^{13}C-E-E'-^{13}C' ligand ^{13}C NMR chemical shifts $(\Delta\delta)^2$ and the observed lifetimes. E=E'=S for Pt(dbbpy)(bdt), E=S, E'=Se for Pt(dbbpy)(bSSe), E=S, E'=O for Pt(dbbpy)(bSO) and E=Se, E'=O for Pt(dbbpy)(bSeO)

exhibited by S,S; S,Se; Se,O; and S,O due to the fact that it possesses shorter lifetime. The shorter lifetime observed for $T_1 \rightarrow S_0$ ground-state recovery is suggested to result from vibronic SOC contributing to T_1 depoulation.[44-48] A linear

correlation was found to exist between the squares of the differences in ^{13}C-E-E'-^{13}C' ligand ^{13}C NMR chemical shifts $(\Delta\delta)^2$ and the observed lifetimes (see Figure 3.137). This same relationship was found to exist between $<T_1|L_i|S_0>^2$ and T_1 ground-state recovery lifetimes. The computed $<T_1|L_i|S_0>$ matrix elements from SOC calculations shows an exceptional linear relationship with the $T_1 \rightarrow S_0$ lifetime. Anisotropic covalency in the E-Pt-E' bonding scheme induced orbital rotation in the HOMO (Pt d_{xy} and d_{zx}) and intensified SOC. The Pt d-orbital rotation is the source of non-zero $<T_1|L_i|S_0>$ matrix elements. For O,O, there is no d-orbital rotation and $<T_1|L_i|S_0> = 0$.

3.3.8 Conclusion

Square planar d^8 Pt(diimine)(dichalcogenolene) complexes have been explored extensively due to their electrochromic and photoluminescence (PL) properties. It's PL properties was obtained from the low energy, long-lived, LL'CT charge separated biradical character [(dichalcogenolene)$^{\bullet+}$Pt(diimine)$^{\bullet-}$].[37] Even though modulation of excited state (ES) properties of Pt(II) diimine dithiolate chromophores have been explored extensively through systematic ligand variation, no detailed studies have focused on how the combination of donor atom SOC and metal-ligand (M-L) anisotropic covalency can be used in a predictive way to control their electrochromic and ES lifetime.

The donor-acceptor (D-A) ES properties of Pt(diimine)(dichalcogenolene) were controlled through anisotropic covalency contributions obtained from the mixed ligand donor domain of O,S; O,Se; and S,Se. The anisotropic covalency in the metal-ligand (M-L) bonding scheme was used to forecast ES processes in these

Pt(II) chromophores.[51] The donor atom SOC-induced ISC between S-T states was used to modulate ES properties by the introduction of mixed donor ligands pairs (O,S; O,Se; and S, Se) with different SOC constants into the bonding scheme. The results obtained from these experiments, i.e. electronic absorption spectroscopy, emission spectroscopy, photoluminescence lifetimes, and transient absorption difference spectra for Pt(diimine)(dichalcogenolene) complexes were used to determine how M-L anisotropic covalency and SOC modulate the excited-state electronic structure and T_1 ground-state recovery lifetimes. The relative energies of lowest singlet and triplet excited states calculated by TD-DFT were adjusted by using photoluminescence spectra and electronic absorption spectra. Our data obtained from these experiments shows that M-L anisotropy covalency and ligand SOC attune the ES lifetimes by not less than three orders of magnitude. The plot of squares of the differences in ^{13} C-E-E'-^{13}C' ligand ^{13}C NMR chemical shifts $(\Delta\delta)^2$ for the series S,S; S,Se; Se,O; and S,O against the observed lifetimes, displays a linear relationship between these two parameters. Also, a linear relationship was observed when $\langle T_1|L_i|S_0\rangle^2$ was plotted against the ES lifetime. Based on these results, ^{13}C-NMR can be used a prognostic way to ascertain the ES lifetime and $\langle T_1|L_i|S_0\rangle$ matrix elements.

3.2.9 Reference

(1) Best, J.; Sazanovich, I. V.; Adams, H.; Bennett, R. D.; Davies, E. S.; Meijer, A. J. M.; Towrie, M.; Tikhomirov, S. A.; Bouganov, O. V.; Ward, M. D.; Weinstein, J. A. *Inorg. Chem.* **2010**, 49, 10041–10056.

(2) Cummings, S. D.; Eisenberg, R. *J. Am. Chem. Soc.* 1**996**, 118, 1949-1960.

(3) Weinstein, J. A.; Blake, A. J.; Davies, E. S.; Davis, A. L.; George, M. W.; Grills, D. C.; Lileev, I. V.; Maksimov, A. M.; Matousek, P.; Mel′nikov, M. Y.; Parker, A. W.; Platonov, V. E.; Towrie, M.; Wilson, C.; Zheligovskaya, N. N. *Inorg. Chem.* **2003**, 42, 7077.

(4) Harriman, A.; Ziessel, R. Chem. *Commun.* **1996**, 1707.

(5) Gray, H. B.; Winkler, J. R. *Annu. Rev. Biochem.* 1**996**, 65, 537.

(6) Juris, A.; Balzani, V.; Barigelletti, F.; Campagna, S.; Belser, P.; von Zelewsky, A. *Coord. Chem. Rev.* **1988,** 84, 85.

(7) Meyer, T. *J. Acc. Chem. Res.* **1989**, 22, 163.

(8) Pelizzetti, E.; Serpone, N. Eds.; D. Reidel Publishing: Dordrecht, **1985**.

(9) Prasad, P. N.; Williams, D. J. Introduction to Nonlinear Optical Effects in Molecules and Polymers; Wiley-Interscience: New York, **1991**.

(10) Balzani, V.; Juris, A.; Venturi, M.; Campagna, S.; Serroni, S. *Chem. Rev.* **1996**, 96, 759.

(11) Sauvage, J. P.; Collin, J. P.; Chambron, J. C.; Guillerez, S.; Coudret, C.; Balzani, V. *Chem. Rev.* **1994**, 94, 993.

(12) Ballardini, R.; Balzani, V.; Credi, A.; Gandolfi, M. T.; Venturi, M. *Acc. Chem. Res.* **2001**, 445.

(13) Blaskie, M. W.; McMillin, D. R. *Inorg. Chem.* **1980**, 19, 3519.

(14) Zuleta, J. A.; Chesta, C. A.; Eisenberg, R. *J. Am. Chem. Soc.* **1989**, 111, 8916.

(15) Bevilacqua, J. M.; Eisenberg, R. *Inorg. Chem.* **1994,** 33, 2913-2923.

(16) Connick, W. B.; Geiger, D.; Eisenberg, R. *Inorg. Chem.* **1999**, 38, 3264.

(17) Cummings, S. D.; Eisenberg, R. *Inorg. Chem.* **1995**, 34, 2007.

(18) McMillin, D. R.; McNett, K. M. *Chem. Rev*. **1998**, 98, 1201.

(19) Miller, M. T.; Gantzel, P. K.; Karpishin, T. B. *Inorg. Chem.* **1998**, 37, 2285.

(20) Miller, M. T.; Gantzel, P. K.; Karpishin, T. B. *J. Am. Chem. Soc.* **1999**, 121, 4292.

(21) Peck, B. M.; Ross, G. T.; Edwards, S. W.; Meyer, G. J.; Meyer, T. J.; Erickson, B. W. *Int. J. Peptide Protein Res.* **1991**, 38, 114.

(22) Yersin, H.; Humbs, W. *Inorg. Chem.* **1999**, 38, 5820.

(23) Shavaleev, N. M.; Accorsi, G.; Virgili, D.; Bell, Z. R.; Lazarides, T.; Calogero, G.; Armaroli, N.; Ward, M. D. *Inorg. Chem.* **2005**, 44, 61.

(24) Zuleta, J. A.; Bevilacqua, J. M.; Eisenberg, R. *Coord. Chem. Rev.* **1991**, 111, 237.

(25) Zuleta, J. A.; Bevilacqua, J. M.; Rehm, J. M.; Eisenberg, R. *Inorg. Chem.* **1992**, 31, 1332.

(26) Zuleta, J. A.; Bevilacqua, J. M.; Proserpio, D. M.; Harvey, P. D.; Eisenberg, R. *Inorg. Chem.* **1992**, 31, 2396.

(27) Connick, W. B.; Gray, H. B. *J. Am. Chem. Soc.* **1997**, 119, 11620.

(28) Fleeman, W. L.; Connick, W. B. C. *The Spectrum* **2002**, 15, 14.

(29) Pettijohn, C. N.; Jochnowitz, E. B.; Chuong, B.; Nagle, J. K.; Vogler, A. *Coord. Chem. Rev.* **1998**, 85.

(30) Crites Tears, D. K.; McMillin, D. R. *Coord. Chem. Rev.* **2001**, 211, 195.

(31) Chassot, L.; von Zelewsky, A.; Sandrini, D.; Maestri, M.; Balzani, V. *J. Am. Chem. Soc.* **1986**, 108, 6084.

(32) Chang, C. C.; Pfennig, B.; Bocarsly, A. B. *Coord. Chem. Rev.* **2000**, 208, 33.

(33) Cummings, S. D.; Cheng, L.-T.; Eisenberg, R. *Chem. Mater.* **1997**, 9, 440.

(34) Base, K.; Tierney, M. T.; Fort, A.; Muller, J.; Grinstaff, M. W. *Inorg. Chem.* **1999**, 38, 287.

(35) Chan, S. C.; Chan, M. C. W.; Wang, Y.; Che, C. M.; Cheung, K. K.; Zhu, M. E.; Frechet, J.-M. J. *J. Am. Chem. Soc.* **2004**, 126, 15388.

(36) Geary, E. A. M.; Yellowlees, L. J.; Jack, L. A.; Oswald, I. D. H.; Parsons, S.; Hirata, N.; Durrant, J. R.; Robertson, N. *Inorg. Chem.* **2005**, 44, 242

(37) Zhang, Y.; Ley, K. D.; Schanze, K. S. *Inorg. Chem.* **1996**, 35, 7102.

(38) Kumar, L.; Puthraya, K. H.; Srivastava, T. S. *Inorg. Chim. Acta* **1984**, 86, 173.

(39) Balzani, V.; Scandola, F. *Supramolecular Photochemistry*; Ellis Horwood: Chichester, UK, **1991**.

(40) Pelizzetti, E.; Serpone, N. *Homogeneous and Heterogeneous Photocatalysis*; Pelizzetti, E., Serpone, N., Ed.; D. Reidel Publishing: Dordrecht, Holland, **1985**.

(41) Cheng, L.-T.; Tam, W.; Eaton, D. F. *Organometallics* **1990**, *9*, 2856-2857.

(42) Prasad, P. N.; Reinhardt, B. A. *Chem*. *Mater*. **1990**, *2*, 660-669.

(43) Friedman, A. E.; Chambron, J.-C.; Sauvage, J.-P.; Turro, N. J.; Barton, J. K. *J*. *Am*. *Chem*. *Soc*. **1990**, *112*, 4960.

(44) Zuleta, J. A.; Burberry, M. S.; Eisenberg, R. *Coord. Chem. Rev*. **1990,** 97, 47.

(45) Base, K.; Grinstaff, M. W.; *Inorg. Chem.* **1998**, 37,1432.

(46) Lee, W. W. S.; Wong, K. Y.; Li, X. M. *Anal. Chem.* **1993**, 65, 255-258.

(47) Liu, H. Q.; Cheung, T. C.; Che, C.-M. *Chem. Commun.* **1996**, 1039- 1040.

(48) Kunugi, Y.; Mann, K. R.; Miller, L. L.; Exstrom, C. L. *J. Am. Chem. Soc.* **1998**, 120, 589-590.

(49) Mansour, M. A.; Connick, W. B.; Lachicotte, R. J.; Gysling, H. J.; Eisenberg, R. *J. Am. Chem. Soc. 1**998***, 120, 1329- 1330.

(50) Paw, W.; Lachicotte, R. J.; Eisenberg, R. *Inorg. Chem.* **1998**, 37, 4139.

(51) Yang, J.; Kersi, D. K.; Giles, L. J.; Stein, B. W.; Feng, C.; Tichnell, C. R.; Shultz, D. A.; Kirk, M. L. *Inorg. Chem.* **2014**, 53, 4791-4793.

(52) Lazarides, T.; McCormick, T. M; Wilson, K. C.; Lee, S.; McCamant, D. W.; Eisenberg, R. *J*. *Am*. *Chem*. *Soc*. **2011**, *133*, 350-364.

(53) Paw, W.; Cummings, S. D.; Mansour, M. A.; Connick, W. B.; Geiger, D. K.; Eisenberg, R. *Coordination Chemistry Reviews*, **1998**, 171, 125-150.

(54) Witold, P. *Coordination Chemistry Reviews*, **1998**, 171, 125-150.

(55) Bachman, R. E.; Dibrov, S. M., *Inorganica Chimica Acta.,* **2004,** 1198-1204.

(56) Conry, R. R.; Tipton, A. A. *J. Biol. Inorg. Chem.* **2001**, 6, 359-366.

(57) William, B. C.; Gary, B. H. *JACS* **1997**, 119, 11620-11627.

(58) Canty, A. J.; Skelton, B. W.; Traill, P. R.; White, A. H. *J. Chem.* **1992**, *45*, 417.

(59) Connick, W. B.; Henling, L. M.; Marsh, R. E.; Gray, H. B. *Inorg. Chem.* **1996**, *35*, 6261.

(60) Zuo, J.-L.; Xiong, R.-G.; You, X.-Z.; Huang, X.-Y. *Inorg. Chim. Acta* **1995**, *237*, 177.

(61) Matsubayashi, G.; Yamaguchi, Y.; Tanaka, T. *J. Chem. Soc., DaltonTrans.* **1988**, 2215.

(62) Nejman, P. S.; Fernandez-Morton, B.; Black, N.; Cordes, D. B.; Slawin, M. Z. A.; Kilian, P.; Woollins, J. D. *Journal of Organometallic Chemistry*, **201**5, 776, 7-16.

(63) Makedonas, C.; Mitsopoulou, C. A.; Lahoz, F. J.; Balana, A. I. *Inorg. Chem.* **2003**, *42*, 8853-8865.

(64) Janiak, C. J. *J. Chem. Soc., Dalton Trans*. **2000**, 3885-3896.

(65) Flleman, W. L.; Connick, W. B. *Comments Inorg Chem*, **2002**, *23*, 205-230.

(66) Smucker, B. W.; Hudson, J. M.; Omary, M. A.; Dunbar, K. R. *Inorg. Chem.* **2003**, *42*, 4714-4723.

(67) Connick, W. B.; Marsh, R. E.; Schaefer, W. P.; Gray, H., B. *Inorg. Chem.* **1997**, *36*, 913.

(68) Osborn, R. S.; Rogers, D. *J. Chem. Soc., Dalton. Trans.* **1974**, 1002-1004.

(69) Heidari, B.; Shafaatian, B. *Journal of Organometallic Chemistry*, **2015**, 780, 34-42.

(70) Gaussian 09, Revision C.1, M. J. Frisch, G. W. Trucks, H. B. Schlegel, G. E.Scuseria, M. A. Robb, J. R. Cheeseman, G. Scalmani, V. Barone, B. Mennucci, G. A. Petersson, H. Nakatsuji, M. Caricato, X. Li, H. P. Hratchian, A. F. Izmaylov, J. Bloino, G. Zheng, J. L. Sonnenberg, M. Hada, M. Ehara, K. Toyota, R. Fukuda, J. Hasegawa, M. Ishida, T.

Nakajima, Y. Honda, O. Kitao, H. Nakai, T. Vreven, J. A. Montgomery, Jr., J. E. Peralta, F. Ogliaro, M. Bearpark, J. J. Heyd, E. Brothers, K. N. Kudin, V. N. Staroverov, R. Kobayashi, J. Normand, K. Raghavachari, A. Rendell, J. C. Burant, S. S. Iyengar, J. Tomasi, M. Cossi, N.Rega, J. M. Millam, M. Klene, J. E. Knox, J. B. Cross, V. Bakken, C. Adamo, J. Jaramillo, R. Gomperts, R. E. Stratmann, O. Yazyev, A. J. Austin, R. Cammi, C. Pomelli, J. W. Ochterski, R. L. Martin, K. Morokuma, V. G. Zakrzewski, G. A. Voth, P. Salvador, J. J. Dannenberg, S. Dapprich, A. D. Daniels, Ö. Farkas, J. B. Foresman, J. V. Ortiz, J. Cioslowski, and D.J. Fox, Gaussian, Inc., Wallingford CT, 2009.

(71) Neese, F. *Ab initio, Density Functional and Semiempirical Program Package version* **2009**, 2.

(72) Weigend, F.; Ahlrichs, R., *Phys. Chem. Chem. Phys*. **2005**, 7, 3297.

(73) Feller, D., *J. Comp. Chem*. **1996**, 17, 1571.

(74) Schuchardt, K. L.; Didier, B.T.; Elsethagen, T.; Sun, L.; Gurumoorthi, V.; Chase, J.; Li, J.; Windus, T. L., *J. Chem. Inf. Model*. **2007**, 47, 1045.

(75) Bauernschmitt, R.; Ahlrichs, R., *Chem. Phys. Lett.* **1996**, 256, 454.

(76) Casida, M. E.; Jamorski, C.; Casida, K. C.; Salahub, D. R., *J. Chem. Phys.***1998**,108, 4439.

(77) Stratmann, R. E.; Scuseria, G. E.; Frisch, M. J., *J. Chem. Phys.*, **1998**, 109, 8218.

(78) Caillie, C. V.; Amos, R. D., *Chem. Phys. Lett.* **1999**, 308, 249.

(79) Caillie, C. V.; Amos, R. D., *Chem. Phys. Lett.* **2000**, 317, 159.

(80) Furche, F.; Ahlrichs, R., *J. Chem. Phys.* **2002**, 117, 7433.

(81) Scalmani, G.; Frisch, M. J.; Mennucci, B.; Tomasi, J.; Cammi, R.; Barone, V., *J. Chem. Phys.* **2006**, 124, 1.

(82) Joshi, H. K.; Cooney, J. A.; Inscore, F. E.; Gruhn, N. E.; Lichtenberger, D. L.; Enemark, J. H. *PNAS,* **2003,** 100(7), 3719-3724.

(83) Tomasi, J.; Mennucci, B.; Cammi, R.; Cheeseman, J. R.; Frisch, M. J., Devlin, F. J.; Gabriel, S.; Stephens, P. J., *J. Phys. Chem. A,* **2002**, 106, 6102-6113.

(84) Makedonas, C.; Mitsopoulou, C. A., *Inorganica Chimica Acta,* **2007**, 360, 3997-4009.

(85) Bruno, G.; Almeida, M.; Artizzu, F.; Dias, J. C.; Mercuri, M. L.; Pilia, L.; Rovira, C.; Ribas, X.; Serpe, A.; Deplano, P. *Dalton Trans.*, **2010**, 39, 4566-4574.

(86) Parker, S. F.; Refson, K.; Bennett, R. D.; Best, J.; Mel'nikov, M. Y.; Weinstein, J. A., *Inorg. Chem.*, **2012,** 51, 9748-9756.

Chapter 4: Solvent Effects on the Electronic Absorption of Pt(II), Pd(II), and Ni(II) Diimine Complexes

4.1 Introduction

Solvatochromism is the tendency of an organic compound to change color due to changes in solvent polarity. Negative solvatochromism is referred to as hypsochromic shift (blue shift) with increasing solvent polarity while positive solvatochromism correspond to bathochromic shift. The differences in diploe moment between the ground and excited state give rise to the sign of solvatochromism. Because the polarities of the ground and excited states of the organic molecules are different, changing the solvent polarity will lead to stabilization of the ground and excited state differently. As a result, changes in intensity, position, and shape of the absorption or/and emission spectra can be used as a direct measure of specific interactions between the solute and solvent molecules.[1,9,14-20]

Solvatochromic shift is defined as the change of optical transition energies of the solute. This shift results from the difference in solute-solvent interactions of the solute's ground and excited state. In a polar protic or aprotic solvent, significant part of the shift is caused by changes in the solute charge density that occurs on optical excitation. This result can be explained from the classical physics point of view, in that the charge density of the solute polarizes the solvent and this polarization in turn acts back on the solute. Solvation energy is the interaction energy between the reaction field of the polarization and the charge density. The difference in solvation energies between the solute's ground and excited states

result in solvatochromic shift.

Nonpolar solvents do not possess a permanent dipole moment and the charge density of the solute mostly polarized the electron clouds of the solvent. In addition, the inductive interaction, i.e. the dispersive solute-solvent interaction plays a major role in nonpolar solvents. From quantum mechanical uncertainty principle, molecules with no permanent diploe moment will possess a fluctuating dipole moment that can polarize its neighbor and resulting in a van der Waals interaction between the two nonpolar molecules in their electronic ground states.

The redistribution of charges generates conformational changes in the excited state when a photon excites a molecule, and this can lead to an increase or decrease in the dipole moment of the excited state. The diploe moment of an electronically excited state of a molecule is an important property that can supply information on the geometrical and electronic structure of the molecule in the short-lived state. Elucidating the nature of the excited states, determining the course of photochemical transformation and designing nonlinear optical materials can be achieved from the knowledge of the excited state dipole moment.[3]

Spectral shift originated either externally by electrochromism or internally by solvatochromism are used as the basis in determining singlet excited-state dipole moments. The solvatochromic technique furnishes key information about electronic transitions which is useful for assigning $n \rightarrow \pi^*$ or $\pi \rightarrow \pi^*$ transitions. It is an accepted way to ascertain the dipole moments in the ground and excited states for short-lives states based on a linear correlation between the wave

numbers of electronic absorption spectra of the solute and solvent polarity function of the dielectric constant (ε) and the refractive index (n) of the solvent.[4]

4.2 Solvent Effects on UV-Vis Absorption Spectra

Spectra band positions, shapes and intensities are always modified when the absorption/emission spectra are taken in solvent with different polarity or dielectric constant. Generally, spectral shifts are ascribed to solute-solvent and solute-solute interactions generated from hydrogen bonding or bulk properties. The other factors that also influence spectra shifts are acid-base chemistry and charge-transfer interactions.

Spectral shifts magnitude in solvents with different polarities depends mainly on the strength of the intermolecular hydrogen bonds(s) between the –OH or –NH groups of the solvent molecules and the substituent groups of the spectral active molecule. For molecular systems that do not possess intramolecular hydrogen bonds, spectral shifts depend mainly on the solvent polarity. In molecular systems with intramolecular hydrogen bonding, the $\pi \rightarrow \pi^*$ bands are bathochromically (red) shifted with an increase in solvent polarity. These shifts are ascribed to hydrogen-bonding interaction between the solute molecule and the solvent molecule. The spectral shifts that results from the absence of intermolecular hydrogen bonds are very small and the shifts are well understood in terms of solvent polarity function. M(diimine)(dichalcogenolene) complexes exhibit inverted solvatochromism, with bathochromic (red) band shift in the low solvent polarity region of the UV-Vis spectra and blue (hypsochromic) band shift in the high solvent polarity region of the absorption spectra.[29,30] Inverted

solvatochromism is attributed to a solvent-indcuced change in the ground state structure of M(diimine)(dichalcogenolene) complexes from a less dipolar to a stronger dipolar ground state structure.[5,29-30]

4.3 Specific Solvent Effects on UV-Vis Absorption Spectra

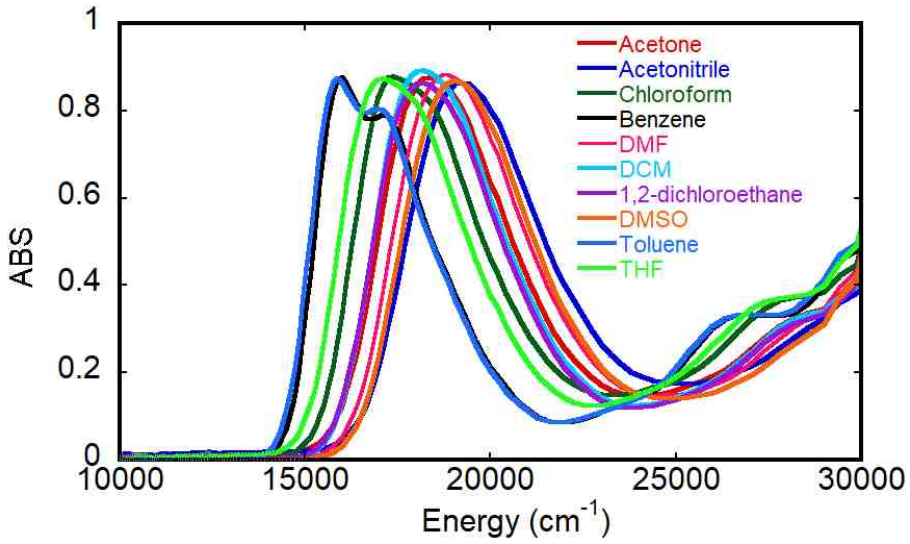

Figure 4.0: Overlay of Pt(dbbpy)(bSSe) absorption spectra in ten different solvents.

Due to the high solubility of these colored complexes in a variety of organic solvent, it grants access to detailed investigation of its solvatochromism. Absorption spectra were obtained in at least 6 different organic solvents. The solvents range from polar aprotic solvents such as dichloromethane (DCM), 1,2-dichloroethane (DCE), tetrahydrofuran (THF), acetone, dimethylformamide (DMF), dimethyl sulfoxide (DMSO), acetonitrile (MeCN) to non-polar solvents such as benzene, toluene and chloroform. The absorption maxima were recorded for only the lowest-energy band, although additional absorption bands at higher energies are present in these complexes. The position of the lowest-

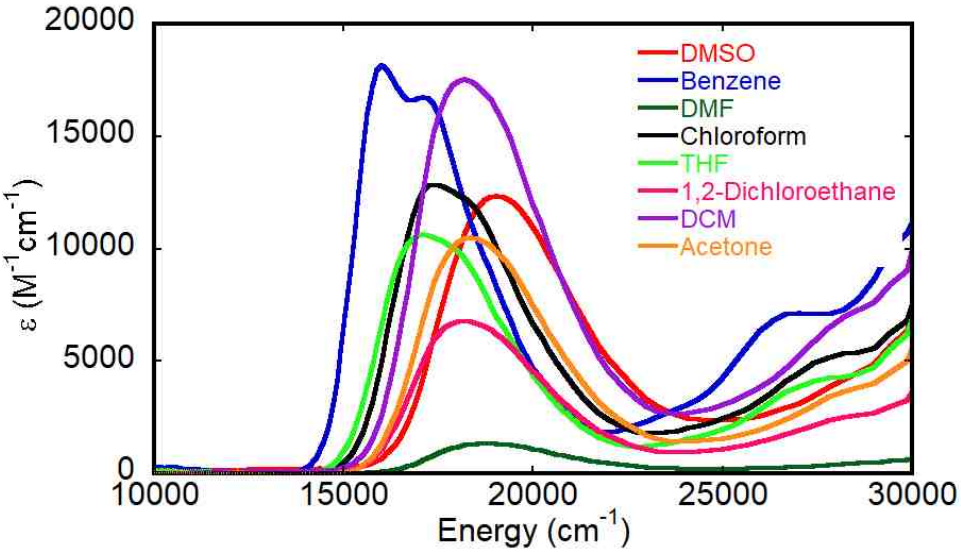

Figure 4.1: Charge-transfer-to-diimine absorption band for Pt(dbbpy)(bSSe) in 8 different solvents with their respective molar extinction coefficient.

energy charge transfer band maxima for all these complex is solvent dependent. The absorption spectra in ten different solvents are depicted in Figure 4.0, exhibiting solvatochromism of the lowest-energy band which shifts from 630 nm (15871 cm^{-1}) in toluene to 519 nm (19250 cm^{-1}) in acetonitrile. A study of this solvatochromic effect was carried out in 10 different polar aprotic and non-polar solvents, and the solvent-induced shifts in energy were recorded. The energy of the charge-transfer-to-diimine absorption band maxima correlate well with the E^*_{MLCT} solvent polarity scale presented in Figure 4.0, and the slope signify that this transition involves a remarkable change in dipole moment between a less polar excited state and a more polar ground state of M(diimine)(dichalcogenolene) complexes.[6,9-19] All the complexes under study shows a single charge-transfer-to-diimine absorption band in all the solvents used with the exception of Pt(dbbpy)(bSSe), Pt(dbbpy)(bdt) and Pt(dbbpy)(bds). In benzene and toluene,

the CT absorption band is considerably broadened and is split into two bands. The charge transfer (CT) band shows a decrease in molar extinction coefficient with an increase in solvent polarity depicted in Figure 4.1. The molar extinction coefficient of Pt(dbbpy)(bSSe) absorption band in toluene is 18200 $M^{-1}cm^{-1}$, 6800 $M^{-1}cm^{-1}$ in 1,2-dichloroethane, and 1400 $M^{-1}cm^{-1}$ in DMF. Figure B1-B11 (see appendix B) shows a series of M(diimine)(dichalcogenolene) complexes with dithiolate, diselenolate, mercaptophenolate, selenylbenzenethiolate, selenylphenolate and cateholate exhibit solvatochromic shift in different solvent. The designation for the solvatochromic transition in these complexes are in accordance with that put forward by Dance and Vogler as LLCT.[10,12-15] However, MO calculations depict significant metal base participation in the HOMO. The justification for the solvent dependence of the solvatochromic transition is explained in terms of significant change in dipole moment between the excited and ground states. The large change in dipole moment leads to different solvation of the ground and excited states with increasing solvent polarity. The LL'CT absorption band for these complexes shows a shift to higher energy as the solvent polarity increases, suggesting that the ground state is more polar then the excited state and upon photo excitation, the dipole moment of the ground state is significantly reduced or even reversed.[7,10-12]

The fact that Pt(dbbpy)Cl_2 does not exhibit the intense solvatochromic band whereas Pt(dbbpy)(dichalcogenolene) complexes do, with dithiolate, diselenolate, mercaptophenolate, selenylbenzenethiolate, selenylphenolate and cateholate as the dichalcogenolene ligand, indicate that the HOMO has a

remarkable ligand character. Solvatochromic transition also occurs in complexes with nonchelating thiolate ligands such as Pt(dbbpy)$(PhSH)_2$ and this further concludes the assignment of this transition as {d(Pt)/p(S)- π*-(diimine)} charge transfer. The absorption spectra of O- and Se- containing analogues provide additional support.[7,26-29]

4.4 Linear and Multilinear Relationship between the energy of CT band maxima, solvent polarity parameters, calculated dipole moment and HOMO-LUMO energy gap

A study of this solvatochromism was conducted in 10 different organic solvents and the solvent-induced shifts in energy for these complexes were measured. A linear correlation was observed when the plot of the energies of the CT band maxima against the solvent polarity parameter using the E^*_{MLCT} solvent scale derived by Kosower's Z and Lee's depicted in Figure 4.3. The data for all the complexes fit well with $r^2 \geq 90\%$ using this scale and the slopes of these plots have comparable magnitude. Similar slopes were obtained when the energies of the CT band maxima were plotted against the calculated dipole moment.[20-25] The slope suggests a significant dipole moment change in the polar ground state and a less polar excited state. A linear correlation was also observed when the energies of the CT band maxima were plotted against the calculated dipole moment presented in Figure 4.2. The ground-state dipole moments of these complexes were computed by quantum chemical calculations using B3LYP/6-31 g* basis sets. Figure 4.3 shows a plot of the energy of the CT band maxima versus the E^*_{MLCT} solvent parameter for series of M(diimine)(dichalcogenolene)

Table 4.1: Charge Transfer (CT) Absorption Maxima and Solvatochromic Shifts of Pt(diimine)(dichalcogenolene) Complexes.

Compound	λ_{max}^{Abs} CH_2Cl_2, 298 K	Solvatochromic Shift (10^4)[a]	Solvatochromic Shift (10^4)[b]
Pt(dbbpy)(bdt)	550	0.10	0.10
Pt(dbbpy)(bds)	546	0.11	0.11
Pt(dbbpy)(bSeO)	563	0.33	0.07
Pt(dbbpy)(bSO)	559	0.34	0.07
Pt(dbbpy)(mcp)	462	0.33	0.10
Pt(dbbpy)(bSSe)	551	0.10	0.10
Pt(dbbpy)(qdt)	470	0.38	0.12
Pt(dbbpy)(pds)	500	0.37	
Pt(dbbpy)(tbuCAT)	590	0.44	
Pt(dbbpy)(PhSH)	500	0.28	
Pt(dbbpy)(CAT-VZ)	541	0.34	
Pt(dpphen)(tbuCAT)	615	0.33	
Pt(dpphen)(bds)	579	0.31	
Pt(dpphen)(bSeO)	595	0.23	
Pt(dpphen)(bSO)	585	0.29	
Pt(dpphen)(bSSe)	580	0.29	
Pt(dpphen)(tdt)	590	0.30	

[a] Unitless slope from plot of E_{abs} vs Pt(NN)(SS) empirical solvent parameter. [b] Unitless slope from plot of E_{abs} vs Calculated Dipole Moment(Debye).

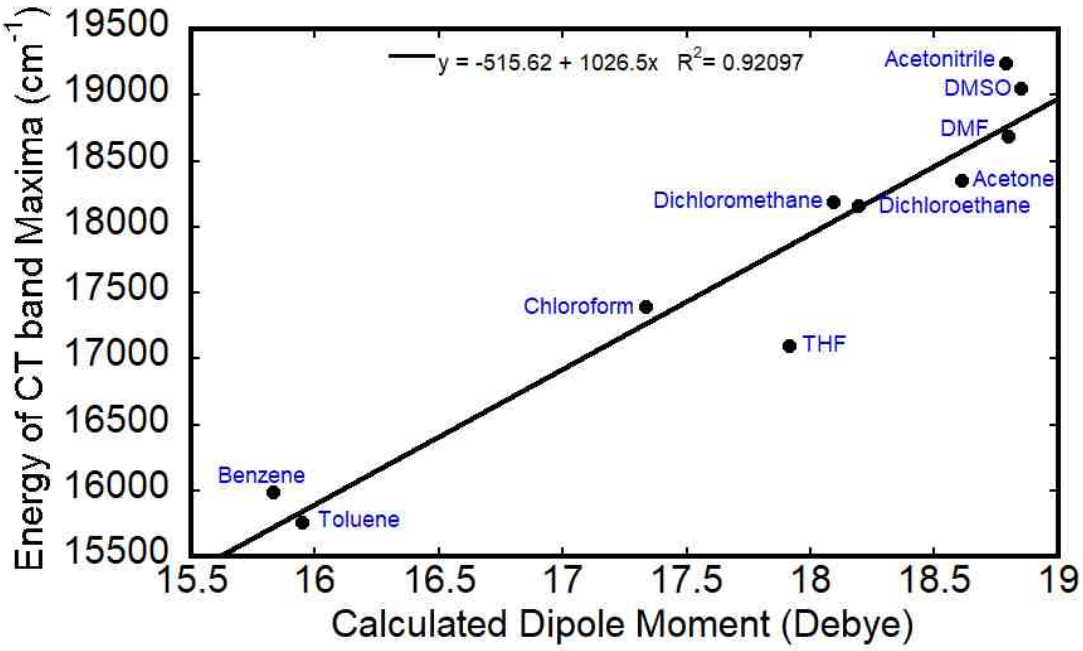

Figure 4.2: A linear correlation between the energy of the CT band maxima and the calculated dipole moment for Pt(dbbpy)(bdt).

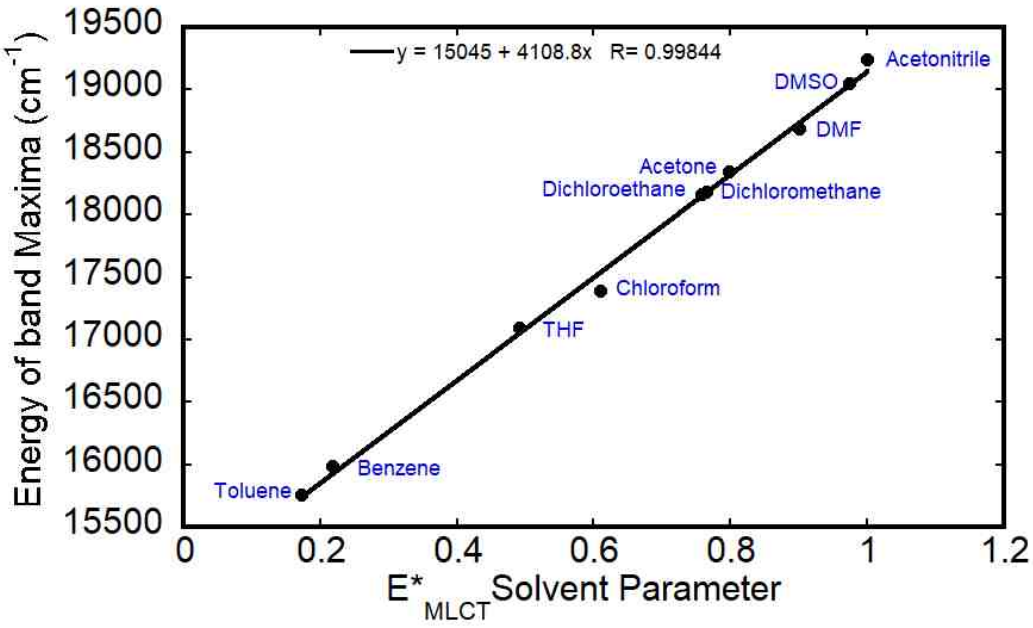

Figure 4.3: A plot of the energy of the CT band maxima versus the E^*_{MLCT} solvent parameter for Pt(dbbpy)(bdt).

complexes with dithiolate, diselenolate, mercaptophenolate, selenylbenzenethiolate, selenylphenolate and cateholate as dichalcogenolene ligand. Figures B11-B15 (see appendix B) depict a plot of the energy of the CT band maxima versus the calculated dipole moment for (dbbpy)Pt(bds), (dbbpy)Pt(bdt), (dbbpy)Pt(bSSe), (dbbpy)Pt(mcp) and (dbbpy)Pt(pds).[30-37]

4.5 Conclusion

A series of M(diimine)(dichalcogenolene) complexes was tested against the electric field of ten widely used organic solvents, acetone, acetonitrile, dimethyl sulfoxide (DMSO), dichloromethane (DCM), chloroform, tetrahydrofuran (THF), toluene, dichloroethane (DCE), dimethylformamide (DMF) and benzene. First and foremost, it was observed that an increase of the polarity of the field remarkably stabilizes the occupied orbitals (HOMO) and destabilizes the virtual ones. The HOMO- LUMO gap increases due to stabilization of the occupied molecular orbitals. The LL'CT band is blue shifted due to an increase in the energy gap between these ten widely used organic solvents, acetone, acetonitrile, dimethyl sulfoxide (DMSO), Dichloromethane (DCM), chloroform, tetrahydrofuran (THF), toluene, dichloroethane (DCE), dimethylformamide (DMF) and benzene. First and foremost, it was observed that an increase of the polarity of the field remarkably stabilizes the occupied orbitals (HOMO) and destabilizes the virtual ones. The HOMO- LUMO gap increases due to stabilization of the occupied molecular orbitals. The LL'CT band exhibit inverted solvatochromism, with a bathochromic (red) band shift in the low solvent polarity region of the UV-

Vis spectra and blue (hypsochromic) band shift in the high solvent polarity region of the absorption spectra.[8] From TD-DFT calculations, it was ascertained that HOMO orbitals are localized on both the metal and the dichalcogene ligand and the LUMO is of diimine character. The solvent field stabilizes the orbitals that are localized on the dichalcogene ligand and metal and destabilizes the orbitals which posses mainly diimine character. The EDDM plots of these model systems shows that electron density is always lost from the HOMO and gained by the LUMO during the vertical transition. The observed trend in the increasing energy of LL'CT band as the solvent polarity increases can be explained based on charge distribution in the ground state. In other words, solvation, mainly dipole-dipole interactions, which turns to stabilizes these orbitals which are localized to part of the molecule that possesses higher electron density and destabilizes the all other parts. A linear relationship was observed when a plot of the energy of the LL'CT band maxima versus E^*_{MLCT} solvent parameter. The same trend was observed when the energy of the LL'CT band maxima was plotted against the calculated dipole moment.

4.6 References

(1) Reichardt, C.; Welton, T. **2010**. Solvents and solvent effects in organic chemistry (4th, updated and enl. ed.). Weinheim, Germany: Wiley-VCH. p. 360.

(2) Renger, T.; Grundkotter, B.; Madjet, M.; Muh F. *PNAS* ***2008***,105, 13235-13240.

(3) Joshi, S.; Pant, D. *International Journal of Chemical and Biological Engineering*, **2012**, 6, 225-229.

(4) Tememee, N.; Al-Ani, S.; AbdAlfahdaw, A. *Journal of Science and Technology*, **2013**, 9, 34-42.

(5) Homocianu, M.; Airinei, A.; Dorohoi, D. *Journal of Advanced Research in Physics*, **2011**, 2(1), 011105.

(6) Cummings, S.; Eisenberg, R. *Inorganic Chemistry*, **1995**, 34, 2007-2014.

(7) Zuleta, J.; Bevilacqua, J.; Proserpio, D.; Harvey, P.; Eisenberg, R. *Inorganic Chemistry*, **1992**, 31, 2396-2404.

(8) Catalan, Javier *Dyes and Pigments,* **2012,** 95, 180-187.

(9) Juan **A.** Zuleta, J. A.; Bevilacqua, J. M.; Proserpio, D. M.; Harvey, P. D; Eisenberg, R. *Inorganic Chemistry*, **1992**, 31, 2396-2404.

(10) Makedonas, C.; Mitsopoulou, C. A. *Inorganica Chimica Acta* 2007, 360, 3997–4009.

(11) Makedonas, C.; Mitsopoulou, C. A.; Lahoz, F.J.; Balana, A. I. *Inorg. Chem.* **2003**, 42, 8853-8865.

(12) Makedonas, C.; Mitsopoulou, C. A.; Lahoz, F. J.; Balana, A. I. *Inorg. Chem.* **2003**, *42*, 8853-8865.

(13) Cummings, S.; Eisenberg, R. *J. Am. Soc.*, **1996**, 118, 1949-1960.

(14) Bevilacqua, J.; Zuleta, J.; Eisenberg, R. *Inorganic Chemistry*, **1994**, 32, 3689.

(15) Zuleta, J. A.; Burberry, M. S.; Eisenberg, R. *Coord. Chem. ReV.* **1990**, *97*, 47-64.

(16) Zuleta, J. A.; Chesta, C. A.; Eisenberg, R. *J. Am. Chem. Soc.* **1989**, *111*, 8916-8917.

(17) Huertas, S.; Hissler, M.; McGarrah, J. E.; Lachicotte, R. J.; Eisenberg R. *Inorg. Chem.* **2001**, *40*, 1183-1188.

(18) Hissler, M.; McGarrah, I. E.; Connick, W. B.; Geiger, D. K.; Cummings, S. D.; Eisenberg, R. *Coord. Chem. Re*V. **2000**, *208*, 115-137.

(19) Connick, W. B.; Geiger, D.; Eisenberg, R. *Inorg. Chem.* **1999**, *38*, 3264-3265.

(20) Mansour, M. A.; Lachicotte, R. J.; Gysling, H. J.; Eisenberg, R. *Inorg. Chem.* **1998**, *37*, 4625-4632.

(21) Paw, W.; Lachicotte, R. J.; Eisenberg, R. *Inorg. Chem.* **1998**, *37*, 4139-4141.

(22) Paw, W.; Cummings, S. D.; Mansour, M. A.; Connick, W. B.; Geiger, D. K.,Eisenberg, R. *Coord. Chem. Rev.* **1998**, *171*, 125-150.

(23) Paw, W.; Eisenberg, R. *Inorg. Chem.* **1997**, *36*, 2287-2293.

(24) Cummings, S. D.; Cheng, L.-T.; Eisenberg, R. *Chem. Mater.* **1997**, *9*, 440-450.

(25) Kosower, E. *J*. *Am*. *Chem*. *Soc*. **1958**, *80*, 3253-3260.

(26) Manuta, D. M.; Lees, A. J. *Inorg. Chem.* **1986**, *25*, 1354-1359.

(27) Reichardt, C. *Angew. Chem., Int. Ed. Engl.* **1965**, *4*, 29-39.

(28) Cummings, S. D.; Eisenberg, R. *J*. *Am*. *Chem*. *Soc*. **1997**, *118*, 1949.

(29) Bourhill, G.; Brédas, J. L.; Cheng, L. T.; Marder, S. R.; Meyers, F.; Perry, J. W.; Tiemannn B. G., *J. Am. Chem. Soc.,* **1994**,116, 2619– 2620.

(30) Blanchard-Desce, M.; Alain, V.; Bedworth, P. V.; Marder, S. R.; Fort, A.;Runser, C.; Barzoukas, M.; Lebus, S.; Wortmann, R., *Chem. Eur. J.,* **1997**, 3, 1091–1104.

(31) Chan, C.-W.; Che, C.-M.; Cheng, M.-C.; Wang, Y. *Inorg. Chem.* **1992**, 31, 4874-4878.

(32) Miller, T. R.; Dance, *G. J. Am. Chem.* SOC. **1973**, 95, 6790.

(33) Vogler, A.; Kunkely, H.; Hlavatsch, J.; Merz, A. *Inorg. Chem.* **1984**, 23, 506.

(34) Truesdell, K. A.; Crosby, G. A. *J. Am. Chem.* Soc., **1985**,107, 1788.

(35) Highland, R. G.; Crosby, G. A. *Chem. Phys. Leu.* **1985**, 119, 454.

(36) Highland, R. G.; Brummer, J. G.; Crosby, G. A. *J. Chem. Phys.* **1986**, 90, 1593.

(37) Crosby, G. A.; Highland, R. G.; Truesdell, K. A. *Coord. Chem. Rev.* **1990**, 8916.

Appendix A

Additional Information for Chapter 2

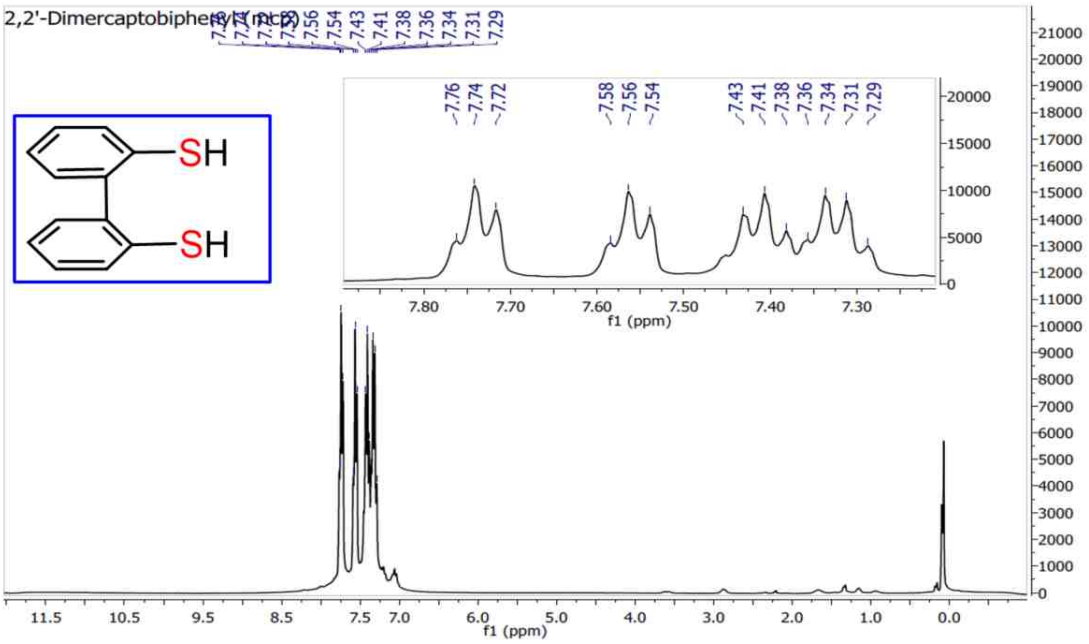

Figure A1: ^{1}H NMR of 2,2'-Dimercaptobiphenyl (mcp). Solvent: $CDCl_3$.

Table A1: Experimental energy of the MMLL'CT band maxima for Pd(diimine)(dichalcogelene) and Ni(dbbpy)(dichalcogelene).

Complex	λ_{max} (nm)	$E_{MMLL'CT}$ (cm^{-1})
Pd(phen)(bdt)	535	18700
Pd(phen)(bSO)	566	17670
Pd(phen)(bSSe)	524	19070
Pd(phen)(dtbCAT)	611	16360
Pd(dpphen)(tbCAT-Vz)	589	16980
Pd(dbbpy)(bdt)	478	20900
Pd(dbbpy)(bSO)	516	19370
Ni(dbbpy)(bdt)	530	18870
Ni(dbbpy)(dtbCAT)	571	17500

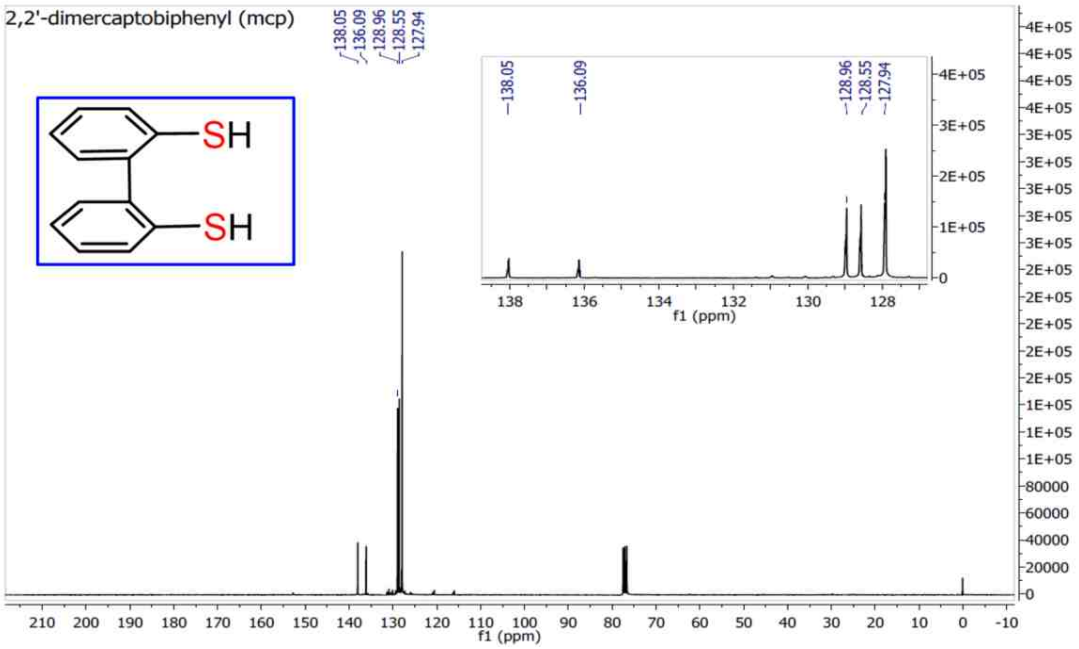

Figure A2: ^{13}C NMR of 2,2'-Dimercaptobiphenyl (mcp). Solvent: $CDCl_3$. Solvent peak: 77.2 ppm.

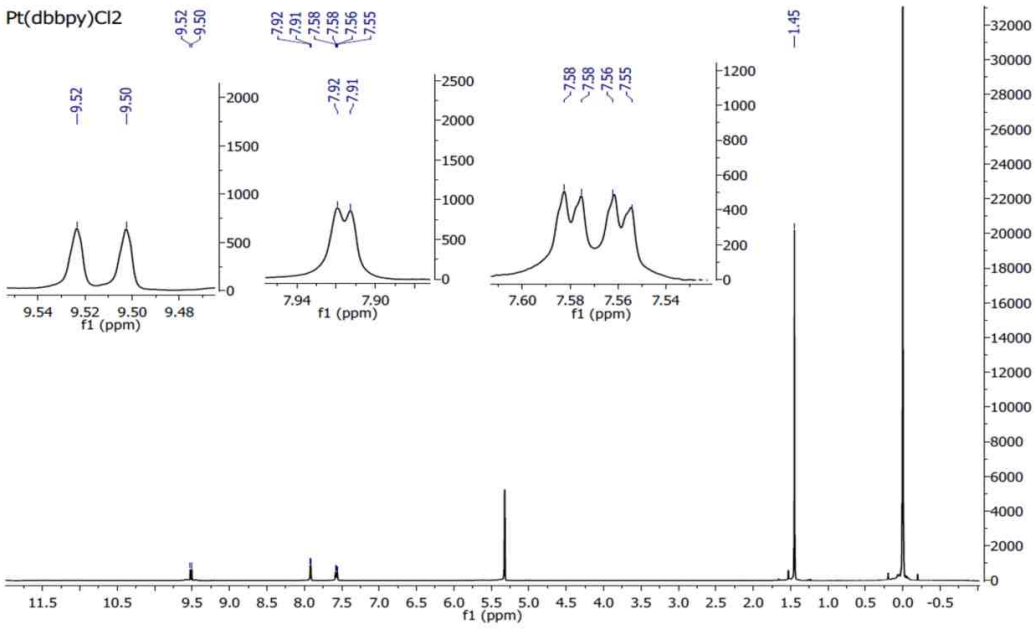

Figure A3. ^{1}H NMR of 4,4'-di-tert-butyl-2,2'-bipyridineplatinum(II) dichloride [Pt(dbbpy)Cl_2]. Solvent: CD_2Cl_2. Solvent peak: 5.32 ppm.

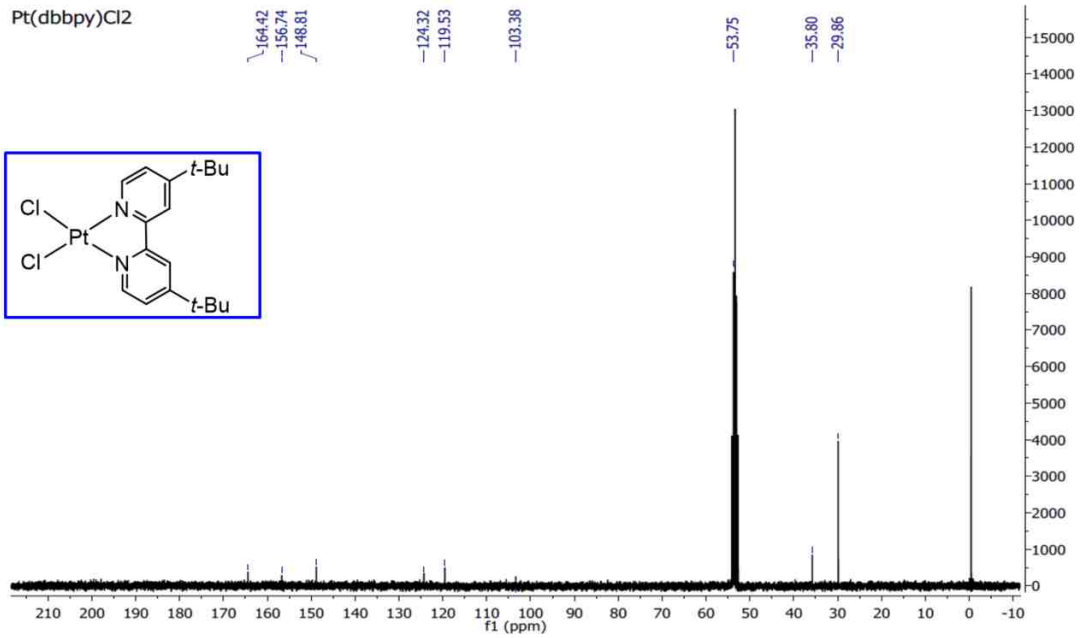

Figure A4: ^{13}C NMR of 4,4'-di-tert-butyl-2,2'-bipyridineplatinum(II) dichloride [Pt(dbbpy)Cl_2]. Solvent: CD_2Cl_2. Solvent peak: 54.0 ppm.

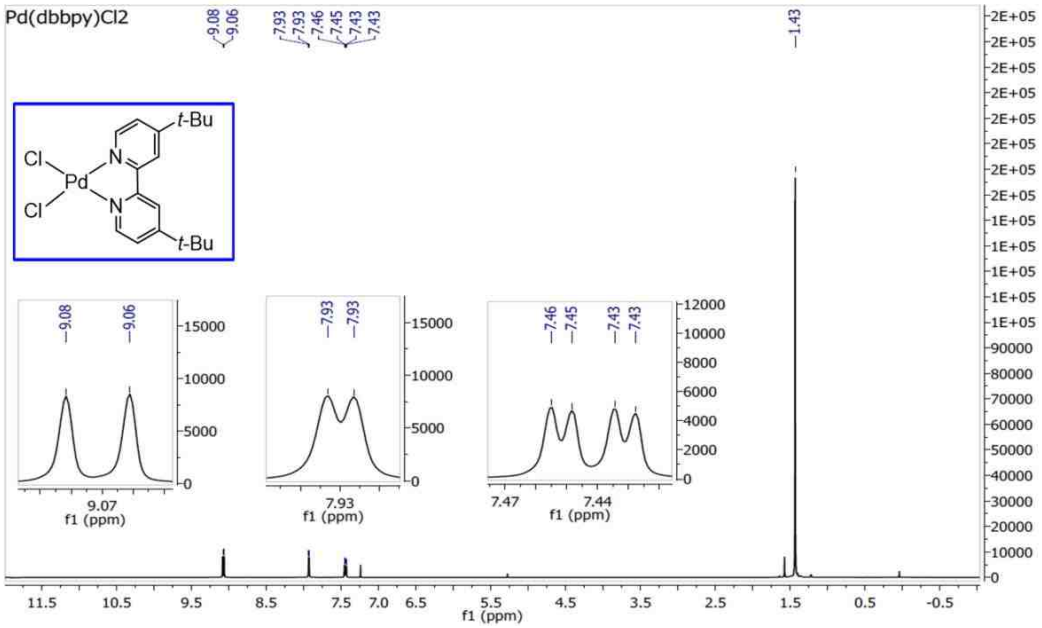

Figure A5: ^{1}H NMR of 4,4'-di-tert-butyl-2,2'-bipyridinepalladium(II) dichloride [Pt(dbbpy)Cl_2]. Solvent: $CDCl_3$. Solvent peak: 7.24 ppm.

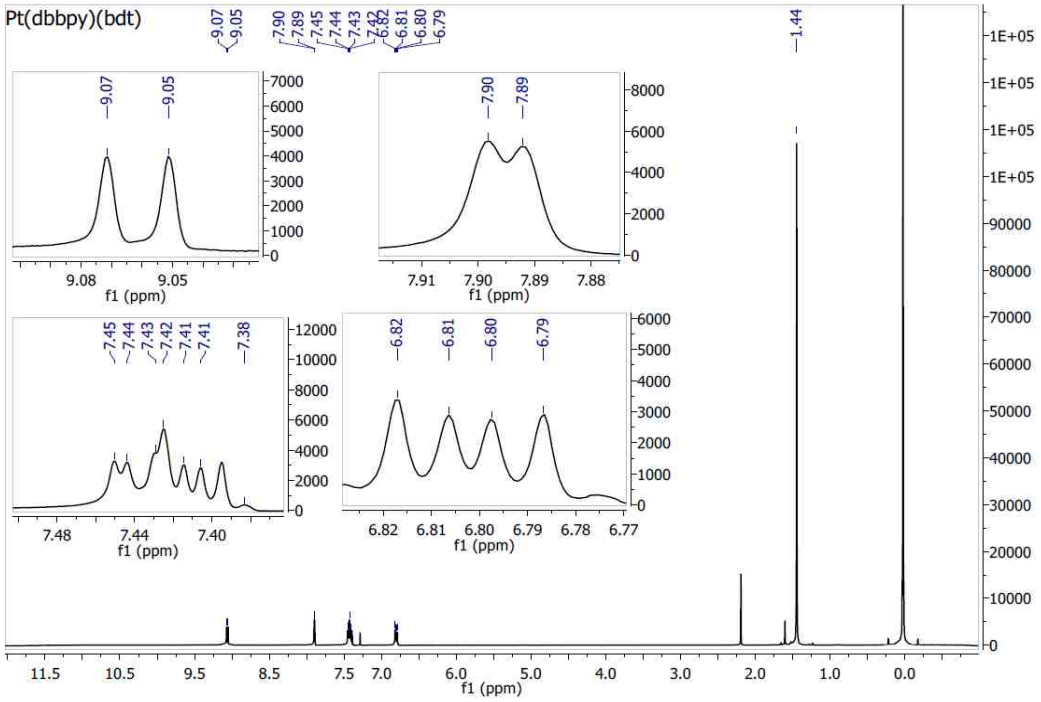

Figure A6: ^{1}H NMR of 4,4'-di-*tert*-butyl-2,2'-bipyridineplatinum(II)(benzene-dithiolate), [Pt(dbbpy)(bdt)]. Solvent: $CDCl_3$. Solvent peak: 7.23 ppm.

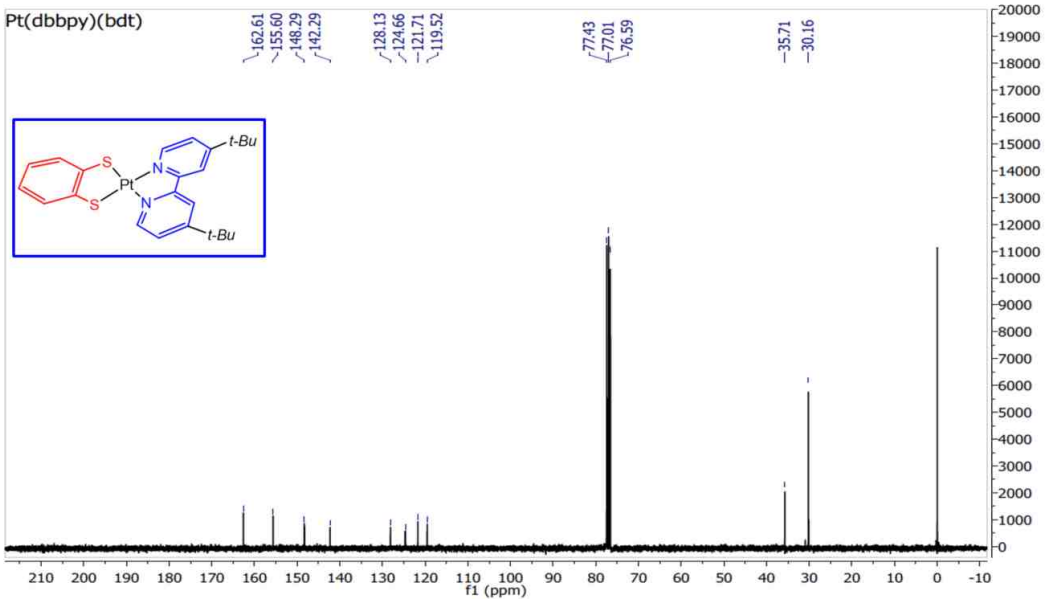

Figure A7: ^{13}C NMR of 4,4'-di-*tert*-butyl-2,2'-bipyridineplatinum(II) (benzenedithiolate), [Pt(dbbpy)(bdt)]. Solvent: $CDCl_3$. Solvent peak: 77.2 ppm.

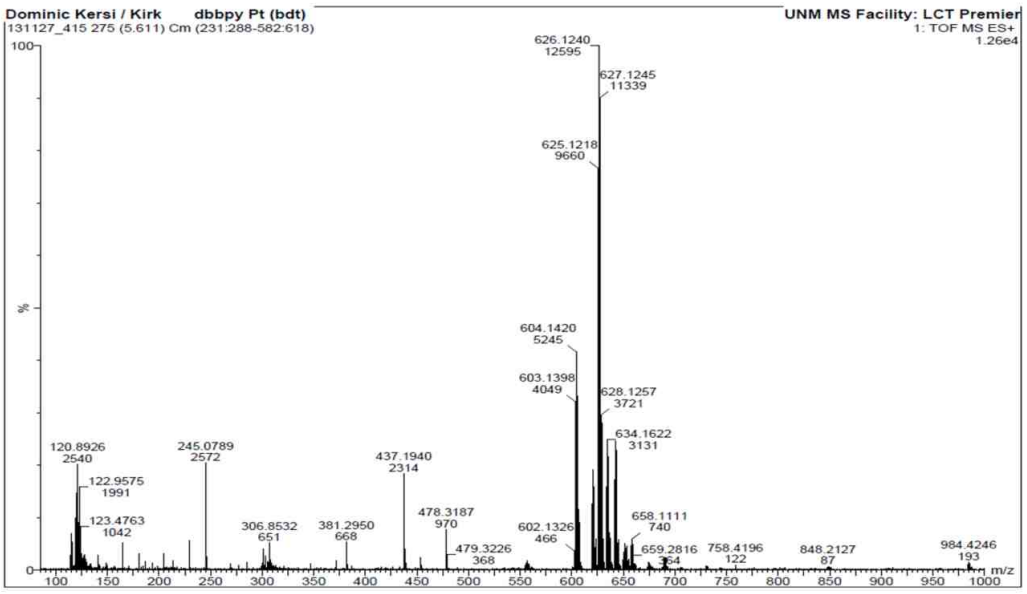

Figure A8: MS (ESI) of 4,4'-di-*tert*-butyl-2,2'-bipyridineplatinum(II)(benzene-dithiolate), [Pt(dbbpy)(bdt)].

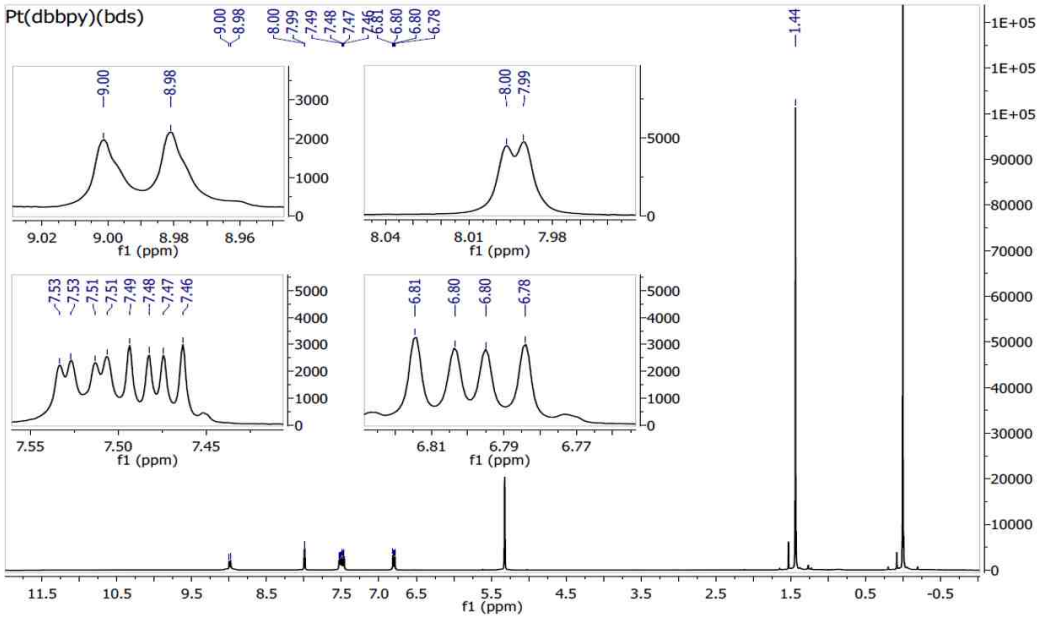

Figure A9: ^{1}H NMR of 4,4'-di-*tert*-butyl-2,2'-bipyridineplatinum(II) benzenedise-lenolate), [Pt(dbbpy)(bds)]. Solvent: CD_2Cl_2. Solvent peak: 5.32 ppm.

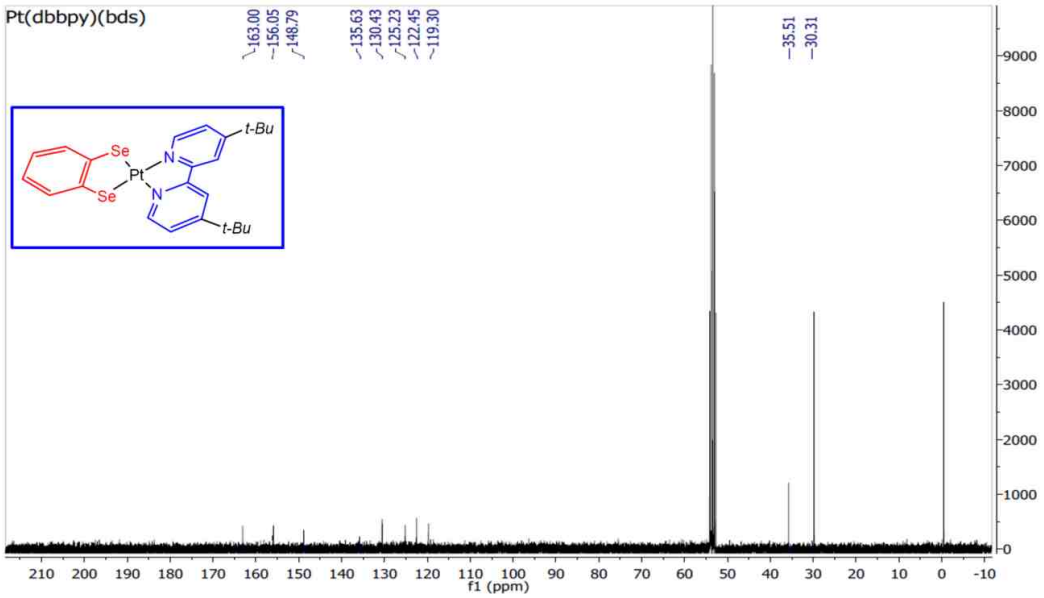

Figure A10: ^{13}C NMR of 4,4'-di-*tert*-butyl-2,2'-bipyridineplatinum(II)(benzene-diselenolate), [Pt(dbbpy)(bds)]. Solvent: CD_2Cl_2. Solvent peak: 53.5 ppm.

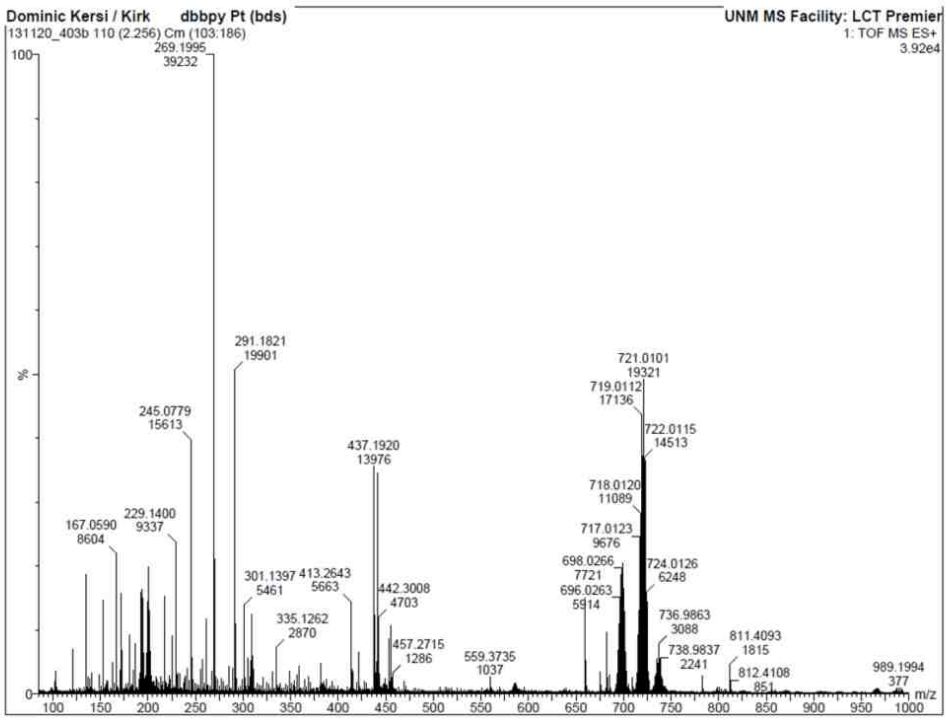

Figure A11: MS (ESI) of 4,4'-di-*tert*-butyl-2,2'-bipyridineplatinum(II)(benzene-diselenolate), [Pt(dbbpy)(bds)].

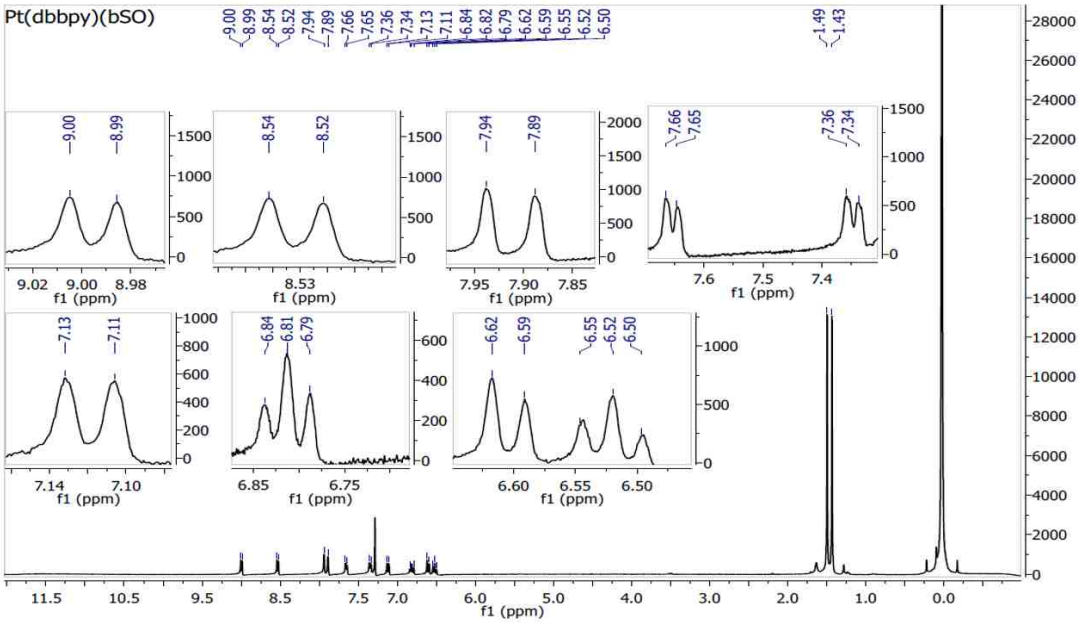

Figure A12: ^{1}H NMR of 4,4'-di-*tert*-butyl-2,2'-bipyridineplatinum(II) (2-mercaptophenolate), [Pt(dbbpy)(bSO)]. Solvent: $CDCl_3$. Solvent peak: 7.23 ppm.

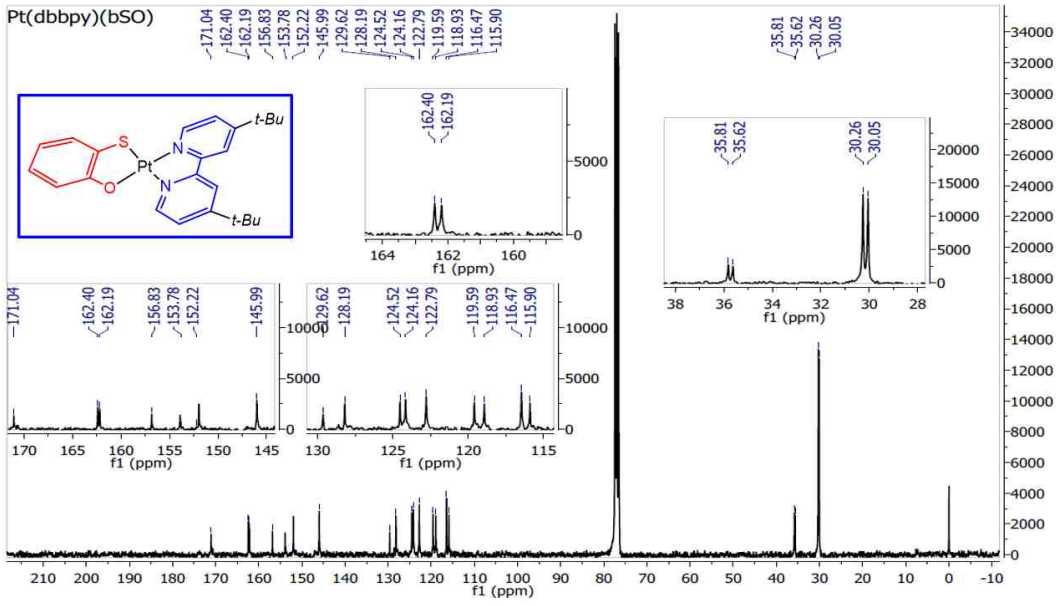

Figure A13: ^{13}C NMR of 4,4'-di-*tert*-butyl-2,2'-bipyridineplatinum(II) (2-mercaptophenolate), [Pt(dbbpy)(bSO)]. Solvent: $CDCl_3$. Solvent peak: 77.2 ppm.

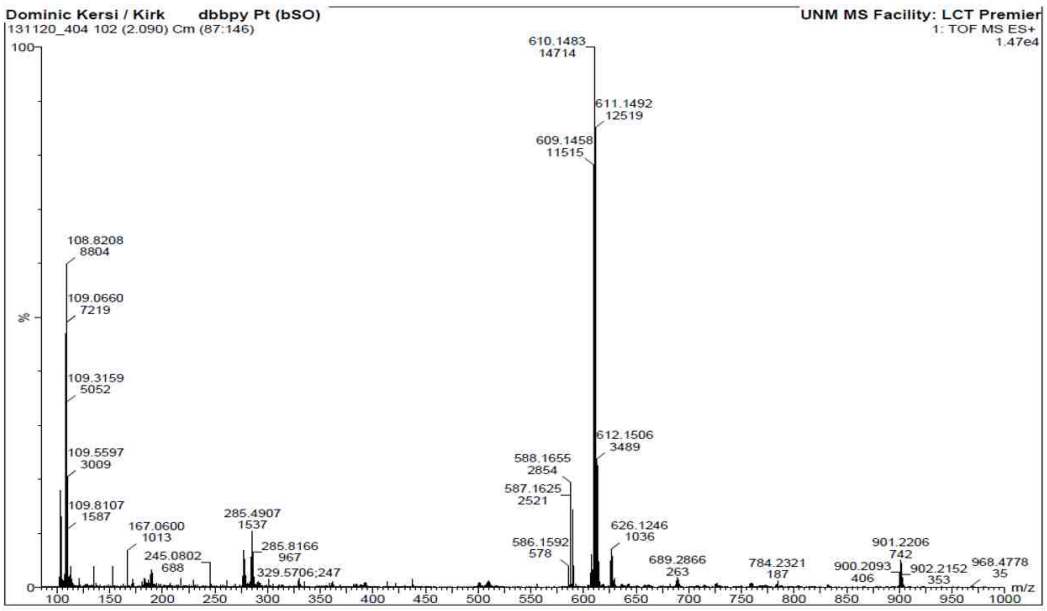

Figure A14: MS (ESI) of 4,4'-di-*tert*-butyl-2,2'-bipyridineplatinum(II)(2-mercapto-phenolate), [Pt(dbbpy)(bSO)].

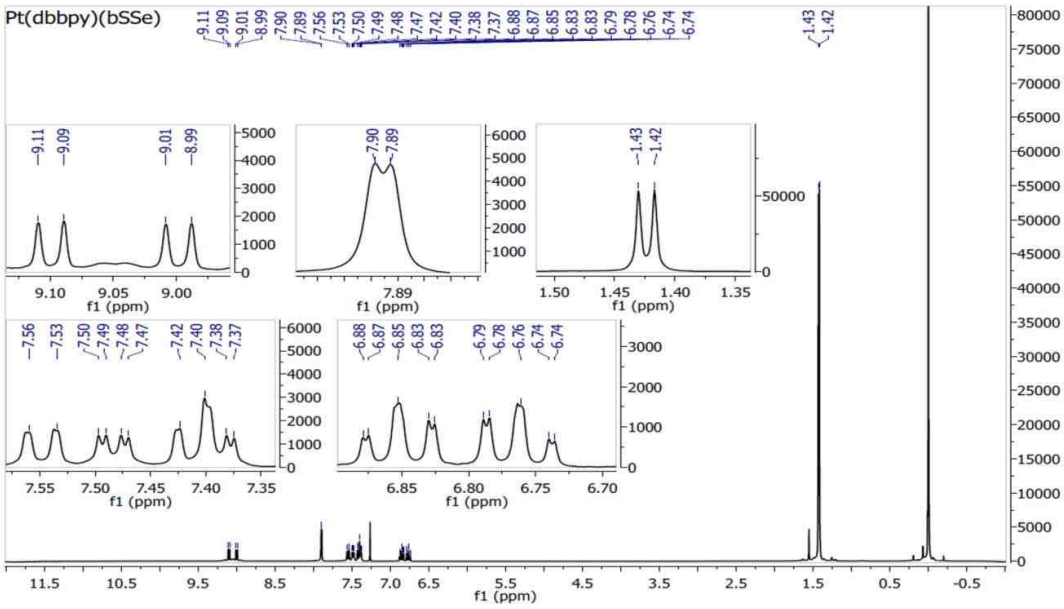

Figure A15: ^{1}H NMR of 4,4'-di-*tert*-butyl-2,2'-bipyridineplatinum(II) (2-selenylbenzenethiolate), [Pt(dbbpy)(bSSe)]. Solvent: $CDCl_3$. Solvent peak: 7.23 ppm.

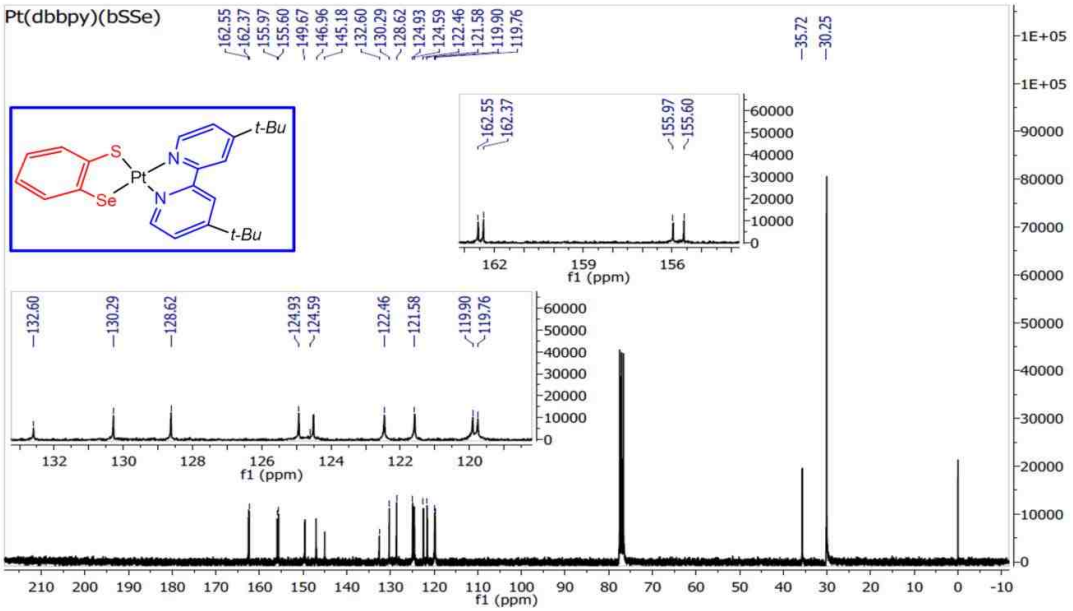

Figure A16: ^{13}C NMR of 4,4'-di-*tert*-butyl-2,2'-bipyridineplatinum(II(2-selenylbenzene- thiolate), [Pt(dbbpy)(bSSe)]. Solvent: $CDCl_3$. Solvent peak: 77.2 ppm

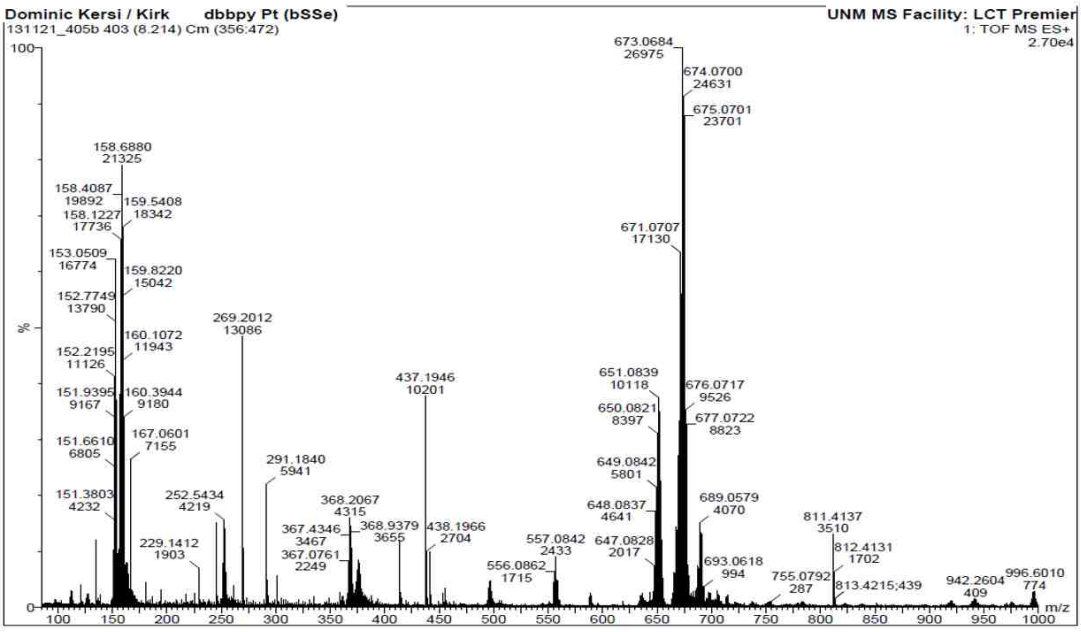

Figure A17: MS (ESI) of 4,4'-di-*tert*-butyl-2,2'-bipyridineplatinum(II) (2-selenylbenzene- thiolate), [Pt(dbbpy)(bSSe)].

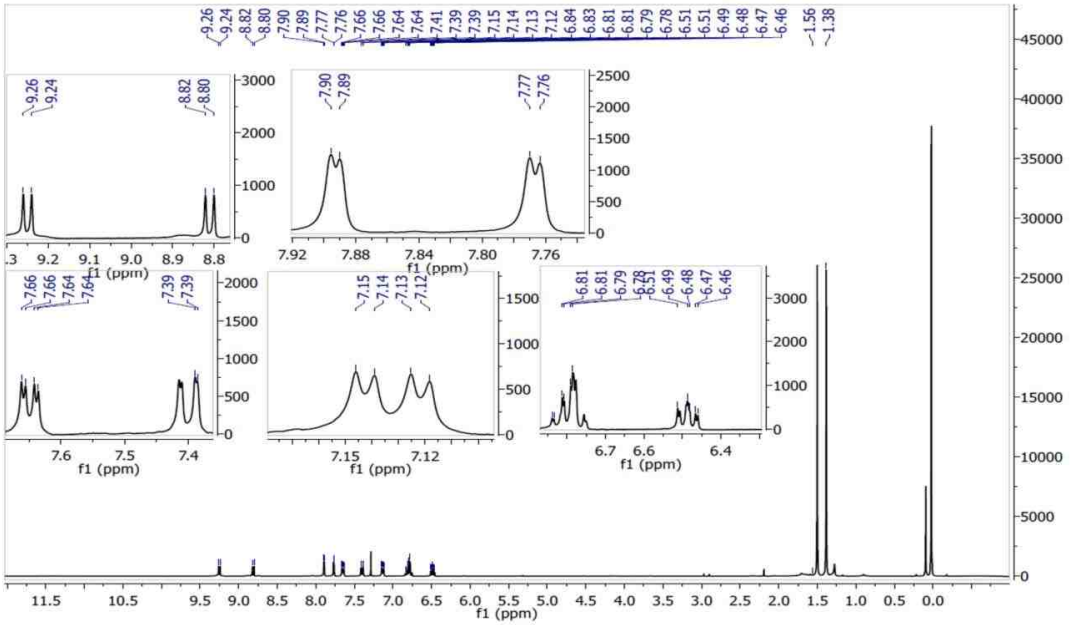

Figure A18: ^{1}H NMR of 4,4'-di-*tert*-butyl-2,2'-bipyridineplatinum(II)(2-selenylphenolate), [Pt(dbbpy)(bSeO)]. Solvent: $CDCl_3$. Solvent peak: 7.23 ppm.

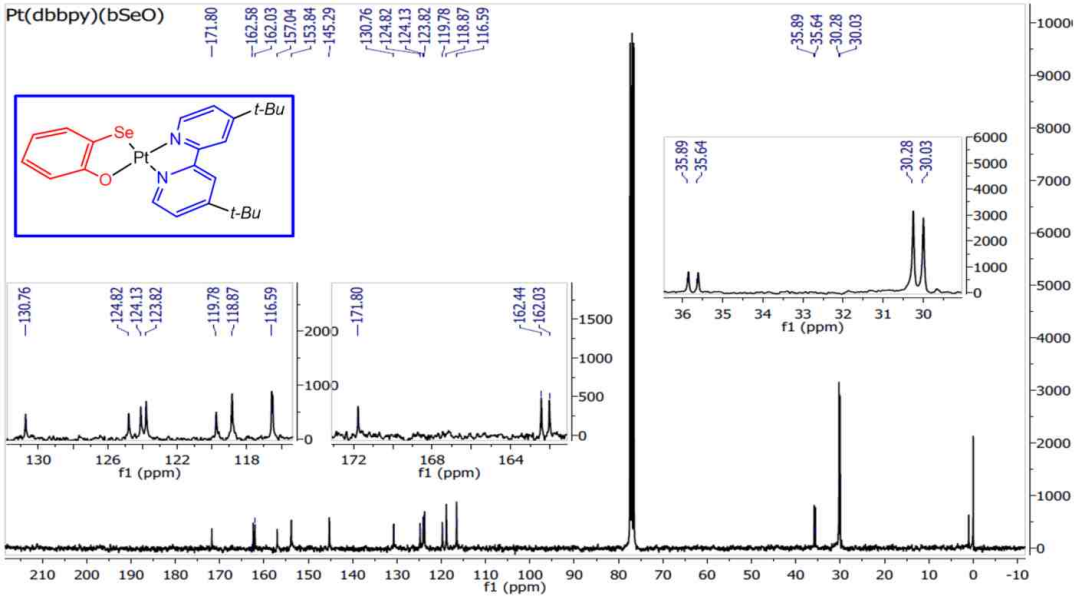

Figure A19: ^{13}C NMR of 4,4'-di-*tert*-butyl-2,2'-bipyridineplatinum(II)(2-selenylphenolate), [Pt(dbbpy)(bSeO)]. Solvent: $CDCl_3$. Solvent peak: 77.2 ppm.

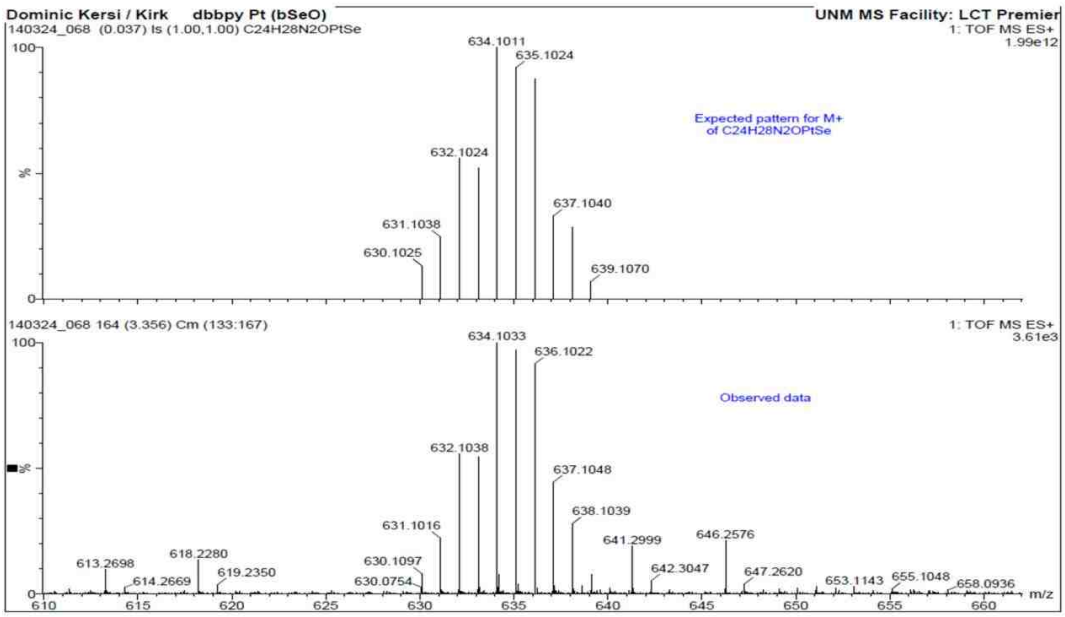

Figure A20: MS (ESI) of 4,4'-di-*tert*-butyl-2,2'-bipyridineplatinum(II)(2-selenylphenolate), [Pt(dbbpy)(bSeO)].

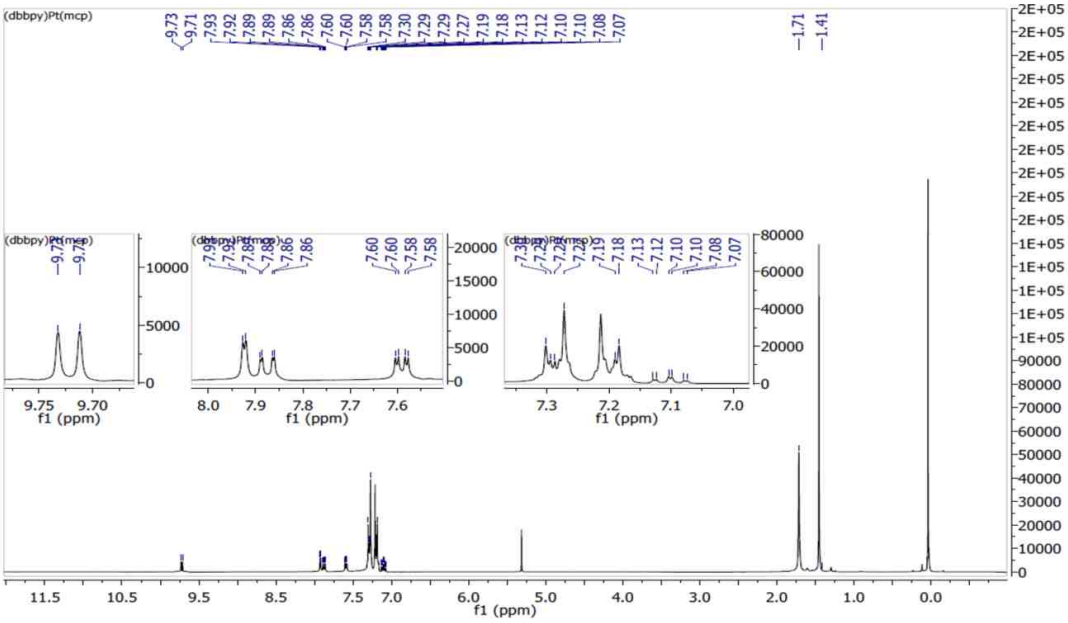

Figure A21: ^{1}H NMR of 4,4'-di-*tert*-butyl-2,2'-bipyridineplatinum(II) (2,2'-dimercaptobiphenyl) [Pt(dbbpy)(mcp)]. Solvent: $CDCl_3$. Solvent peak: 7.23 ppm.

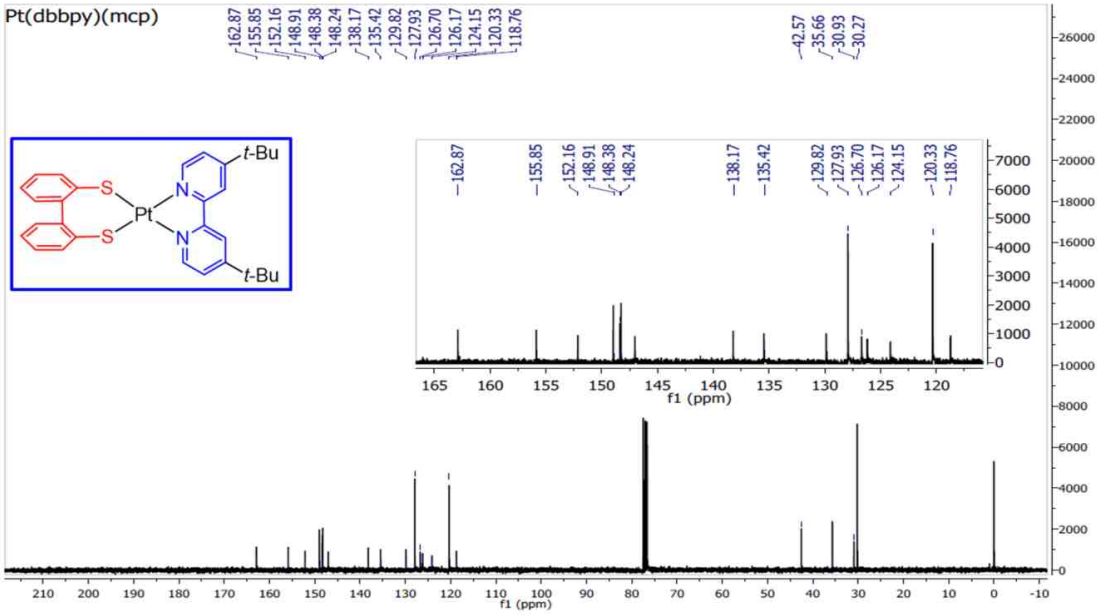

Figure A22: ^{13}C NMR of 4,4'-di-*tert*-butyl-2,2'-bipyridineplatinum(II) (2,2'-dimercaptobiphenyl) [Pt(dbbpy)(mcp)]. Solvent: $CDCl_3$. Solvent peak: 77.2 ppm.

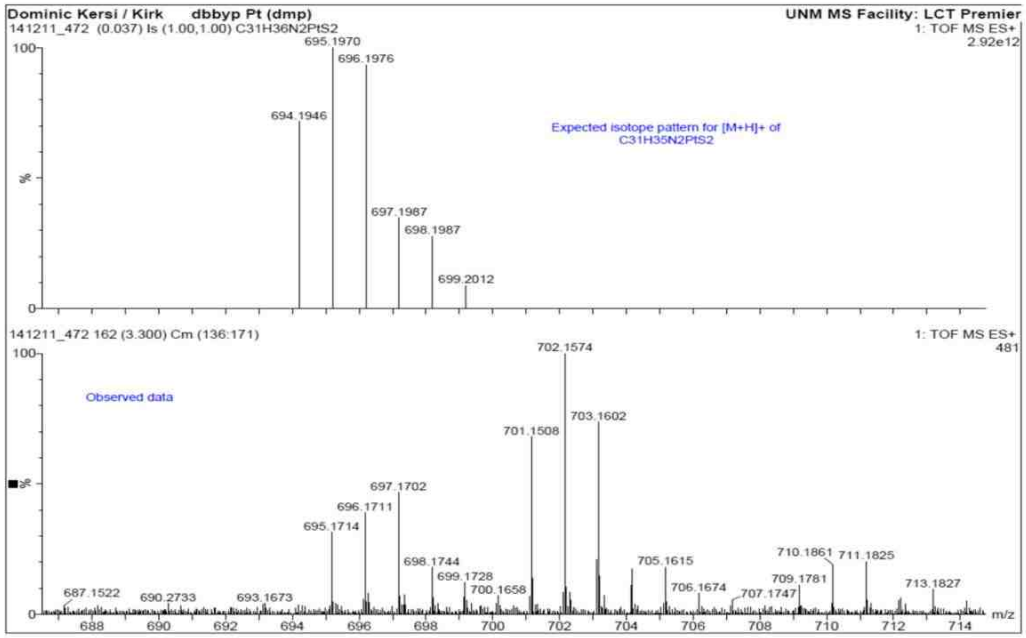

Figure A23: MS (ESI) of 4,4'-di-*tert*-butyl-2,2'-bipyridineplatinum(II) (2,2'-dimercaptobiphenyl) [Pt(dbbpy)(mcp)].

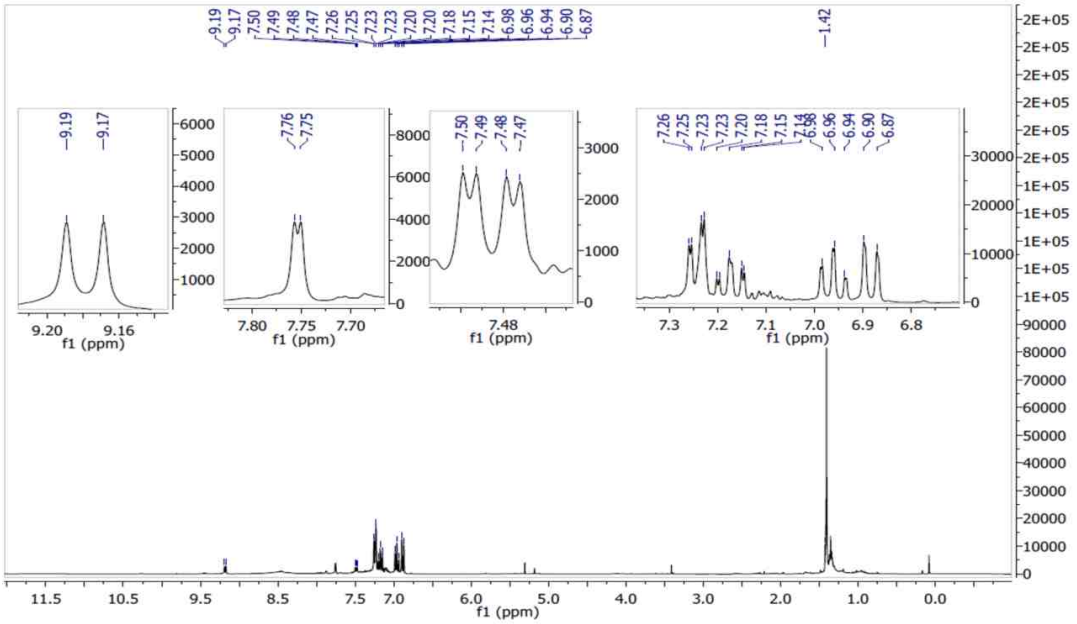

Figure A24: ^{1}H NMR of 4,4'-di-*tert*-butyl-2,2'-bipyridineplatinum(II) (2,2'-dihydroxybiphenyl) [Pt(dbbpy)(hbp)]. Solvent: $CDCl_3$. Solvent peak: 7.23 ppm.

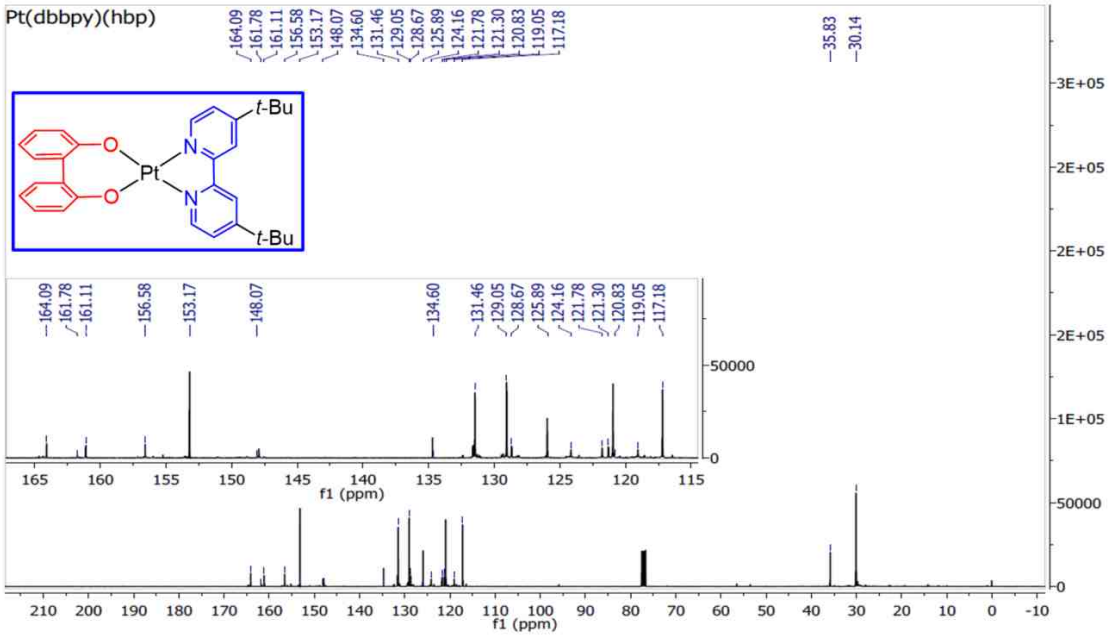

Figure A25: ^{13}C NMR of 4,4'-di-*tert*-butyl-2,2'-bipyridineplatinum(II)(2,2'-dihydroxybiphenyl) [Pt(dbbpy)(hbp)]. Solvent: $CDCl_3$. Solvent peak: 77.2 ppm.

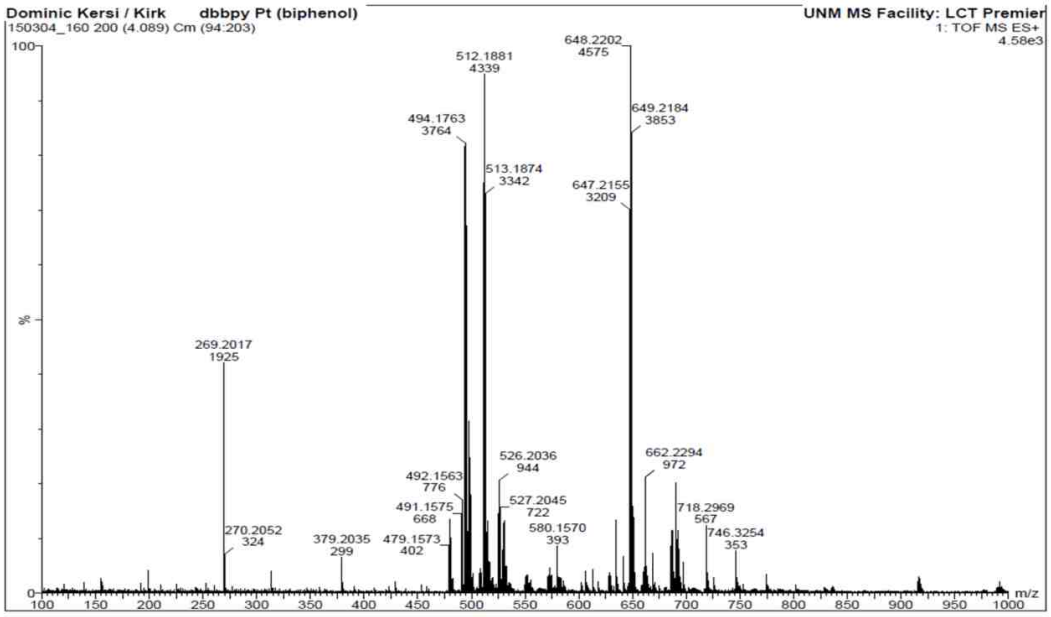

Figure A26: MS (ESI) of 4,4'-di-*tert*-butyl-2,2'-bipyridineplatinum(II)(2,2'-dihydroxybiphenyl) [Pt(dbbpy)(hbp)].

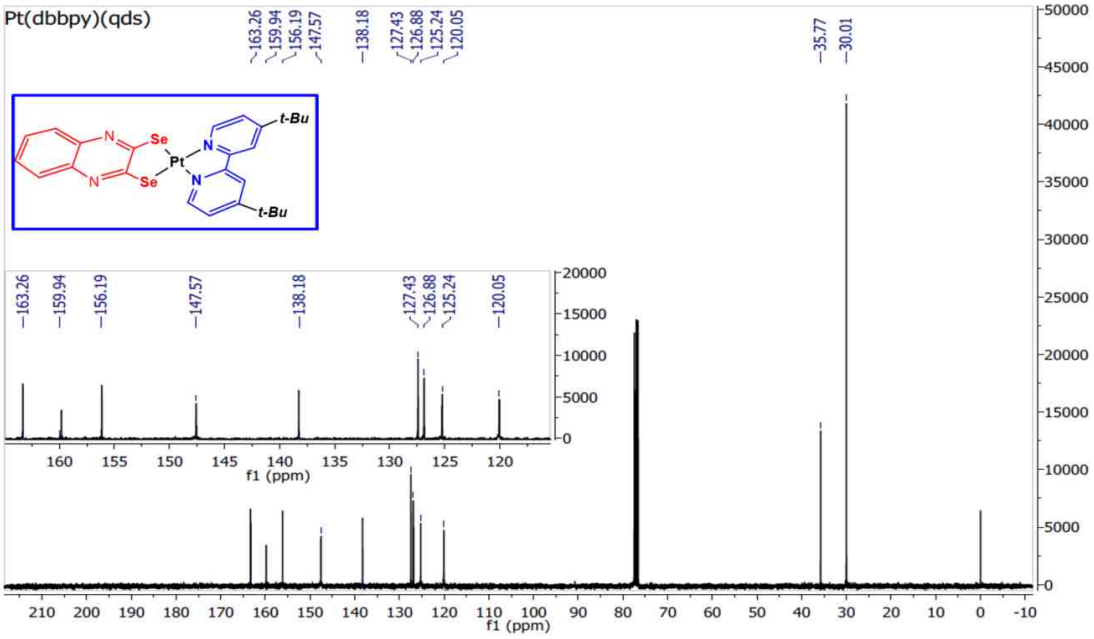

Figure A27: ^{13}C NMR of 4,4'-di-*tert*-butyl-2,2'-bipyridineplatinum(II)(quinoxaline-2,3-diselenolate) [Pt(dbbpy)(qds)]. Solvent: $CDCl_3$. Solvent peak: 77.2 ppm.

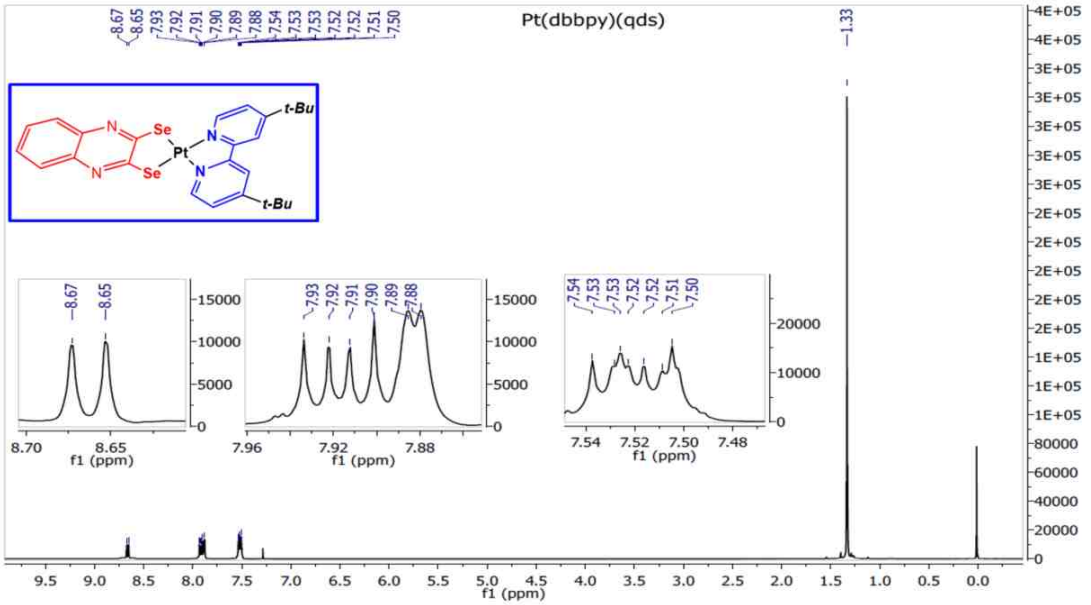

Figure A28: ^{1}H NMR of 4,4'-di-*tert*-butyl-2,2'-bipyridineplatinum(II) (quinoxaline-2,3-diselenolate) [Pt(dbbpy)(qds)]. Solvent: $CDCl_3$. Solvent peak: 7.23 ppm.

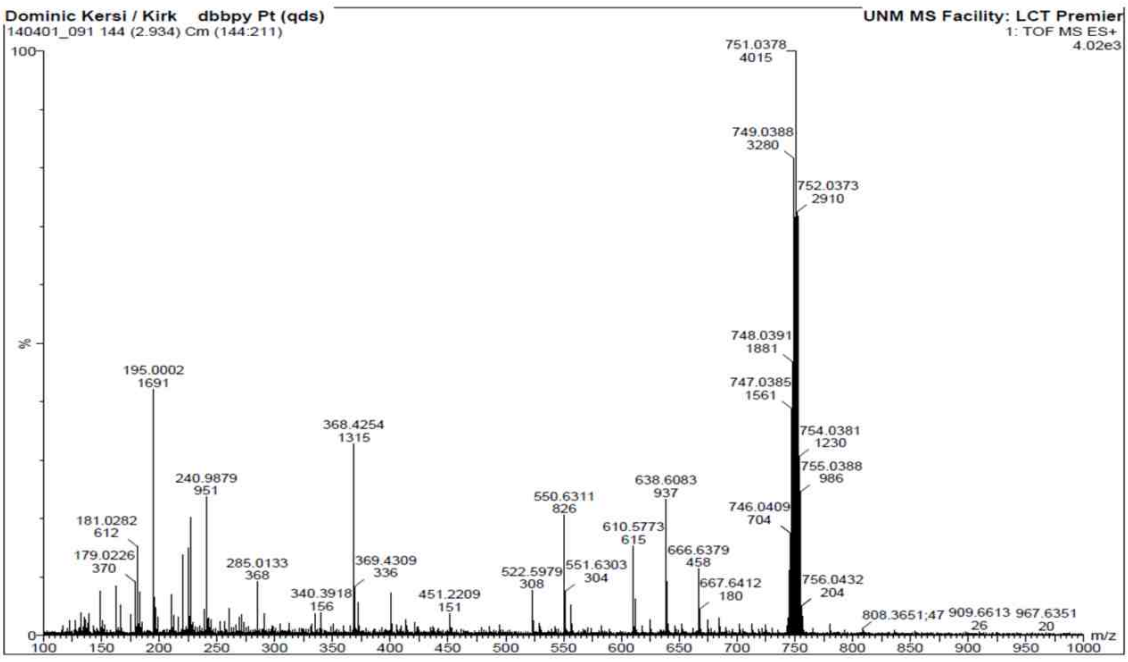

Figure A29: MS (ESI) of 4,4'-di-*tert*-butyl-2,2'-bipyridineplatinum(II)(quinoxaline-2,3-diselenolate) [Pt(dbbpy)(qds)].

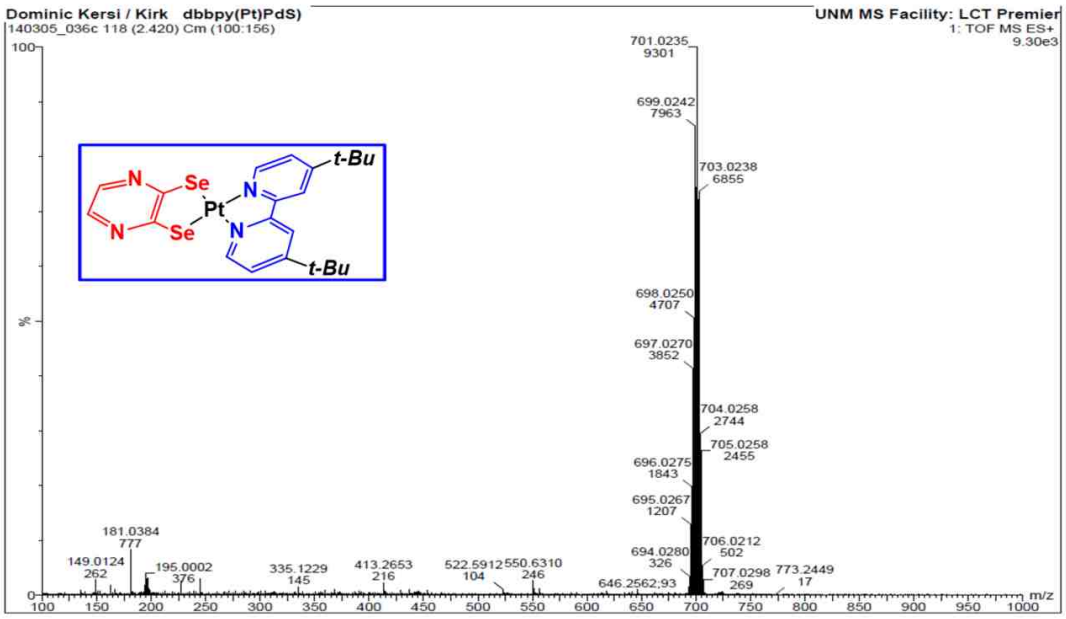

Figure A30. MS (ESI) of 4,4'-di-*tert*-butyl-2,2'-bipyridineplatinum(II)(pyrazine-2,3-diselenolate) [Pt(dbbpy)(pds)].

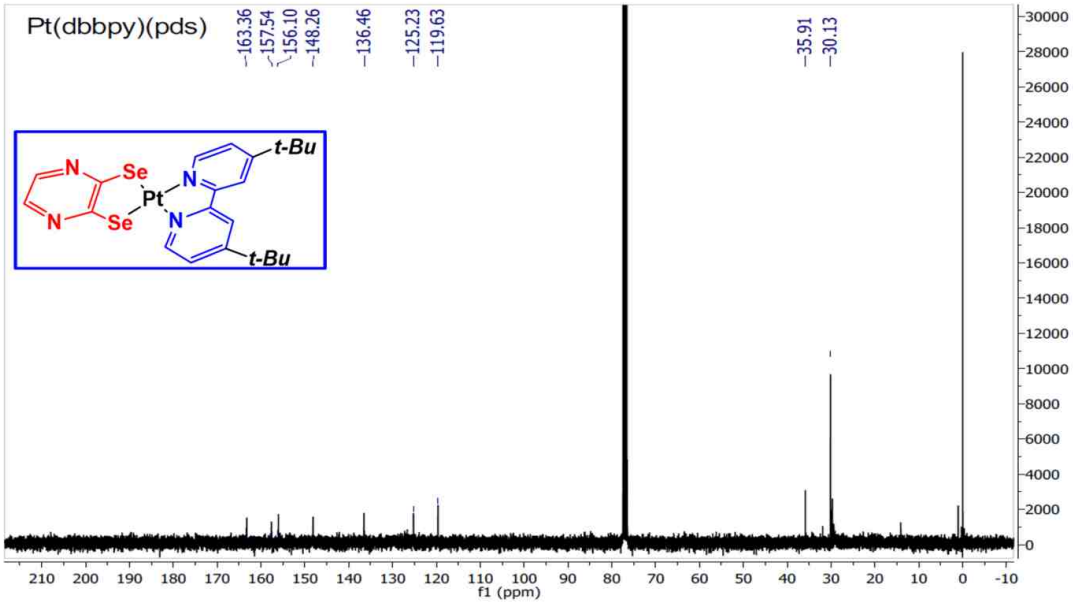

Figure A31: ^{13}C NMR of 4,4'-di-*tert*-butyl-2,2'-bipyridineplatinum(II)(pyrazine-2,3-diselenolate) [Pt(dbbpy)(pds)]. Solvent: $CDCl_3$. Solvent peak: 77.2 ppm.

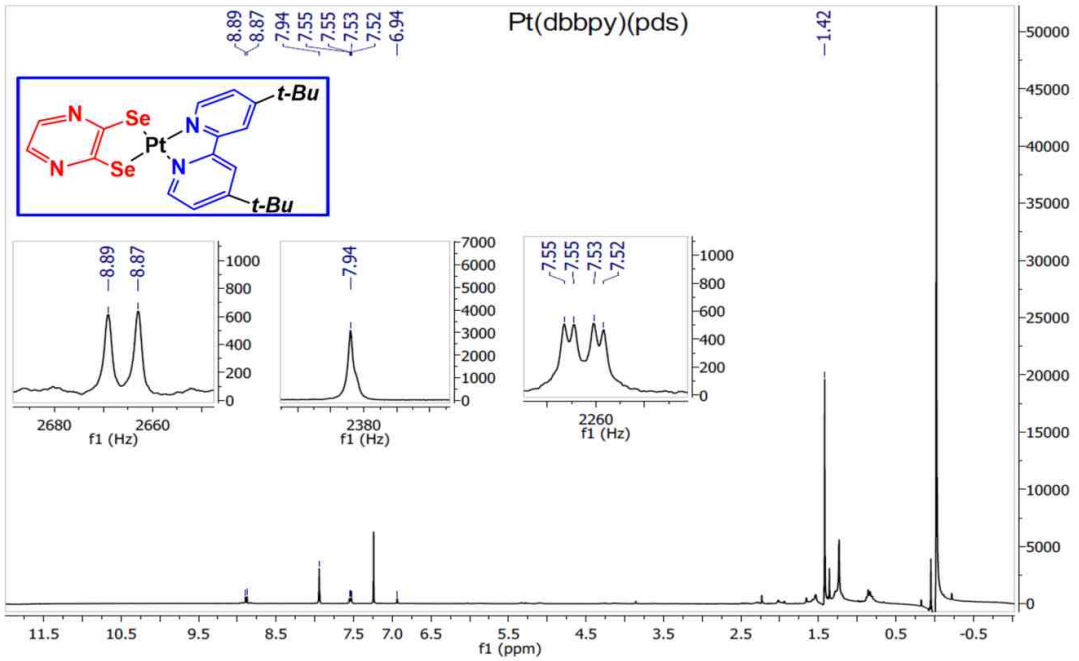

Figure A32: ^{1}H NMR of 4,4'-di-*tert*-butyl-2,2'-bipyridineplatinum(II)(pyrazine-2,3-diselenolate) [Pt(dbbpy)(pds)]. Solvent: $CDCl_3$. Solvent peak: 7.23 ppm.

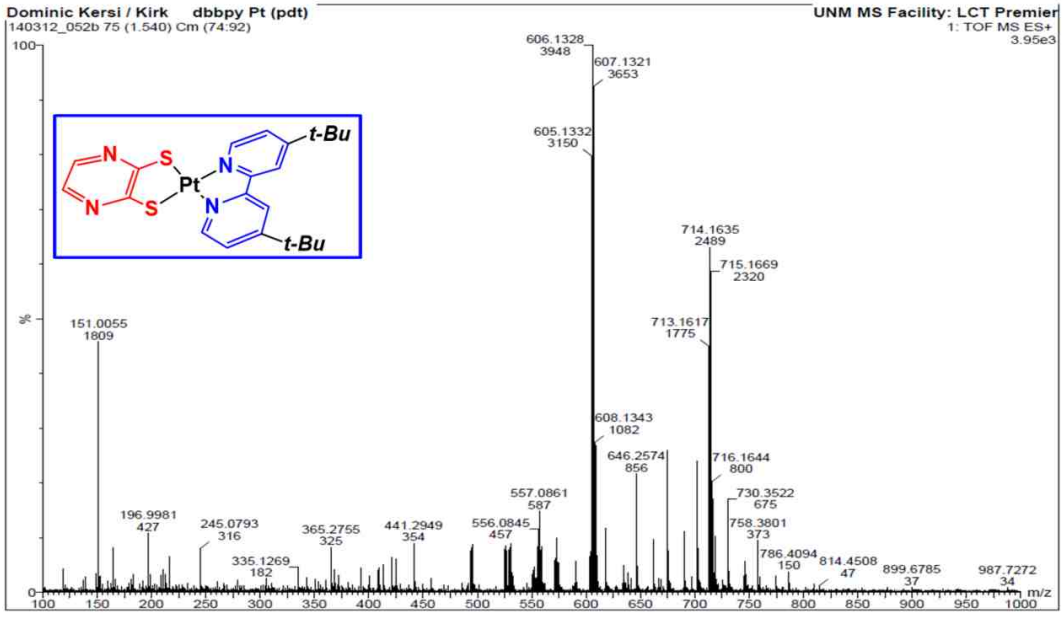

Figure A33: MS (ESI) of 4,4'-di-*tert*-butyl-2,2'-bipyridineplatinum(II)(pyrazine-2,3-dithiolate) [Pt(dbbpy)(pdt)].

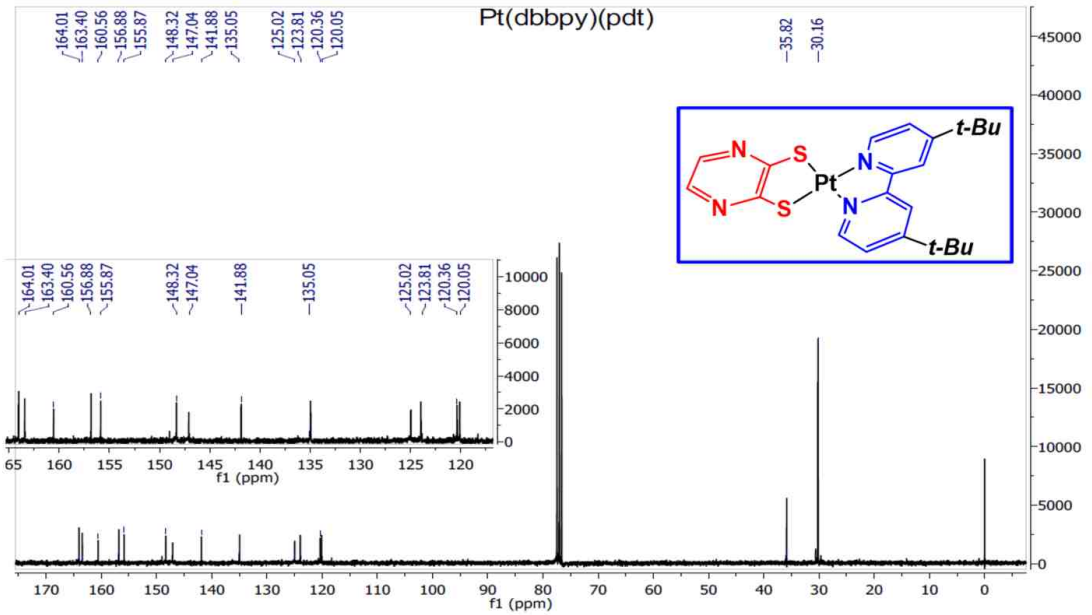

Figure A34: ^{13}C NMR of 4,4'-di-*tert*-butyl-2,2'-bipyridineplatinum(II)(pyrazine-2,3-dithiolate) [Pt(dbbpy)(pdt)]. Solvent: $CDCl_3$. Solvent peak: 77.2 ppm.

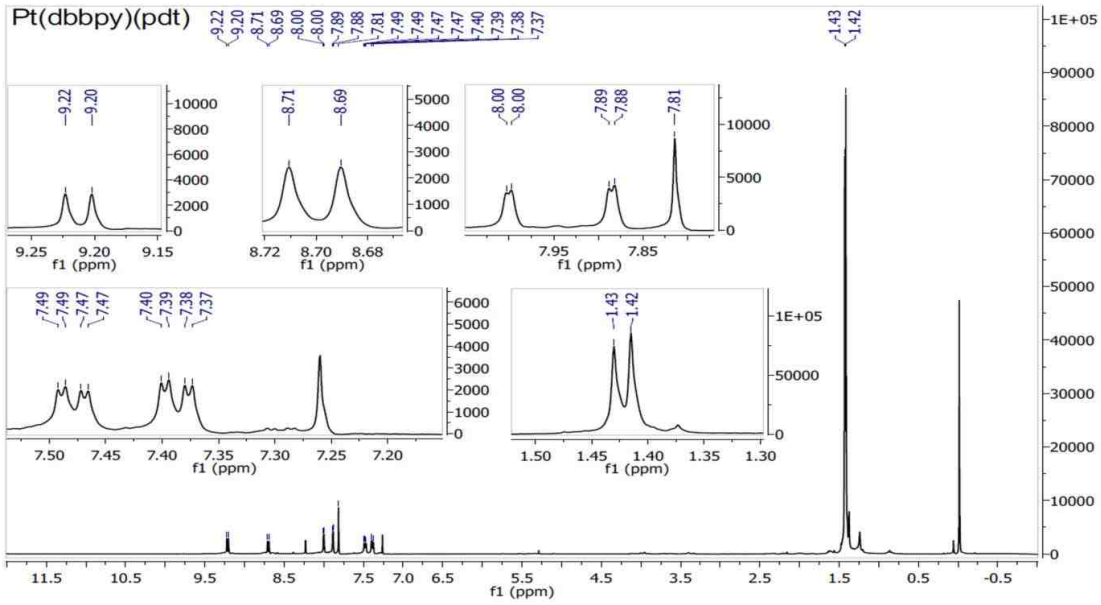

Figure A35: ^{1}H NMR of 4,4'-di-*tert*-butyl-2,2'-bipyridineplatinum(II) (pyrazine-2,3-dithiolatete) [Pt(dbbpy)(pdt)]. Solvent: $CDCl_3$. Solvent peak: 7.23 ppm.

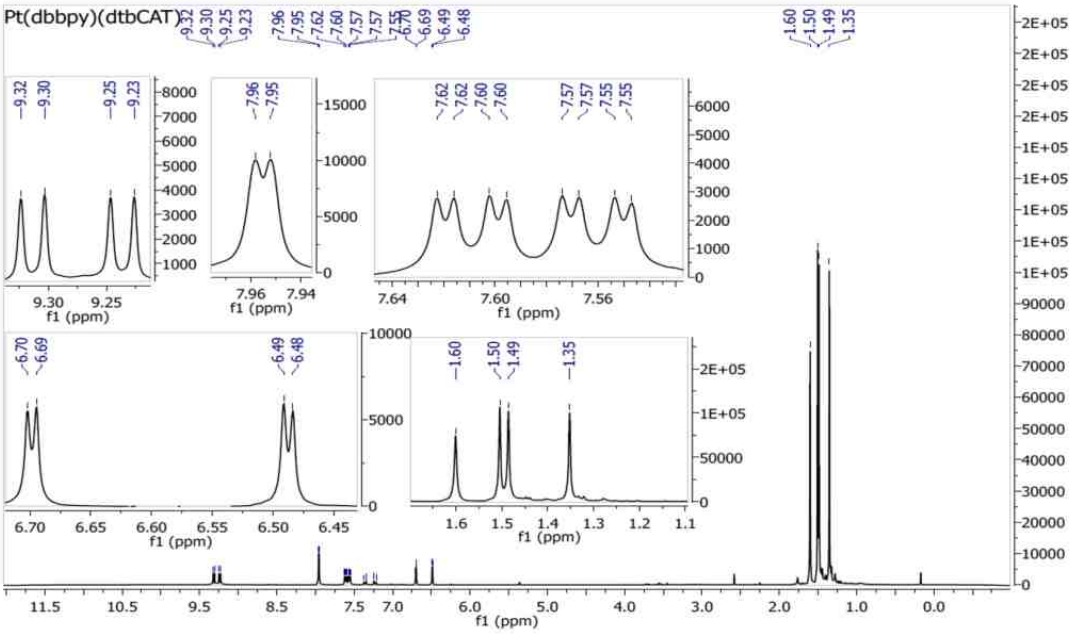

Figure A36: ^{1}H NMR of 4,4'-di-*tert*-butyl-2,2'-bipyridineplatinum(II) (3,5-di-*t*-butylbenzene catecholate) [Pt(dbbpy)(dtbCAT)]. Solvent: $CDCl_3$. Solvent peak: 7.23 ppm.

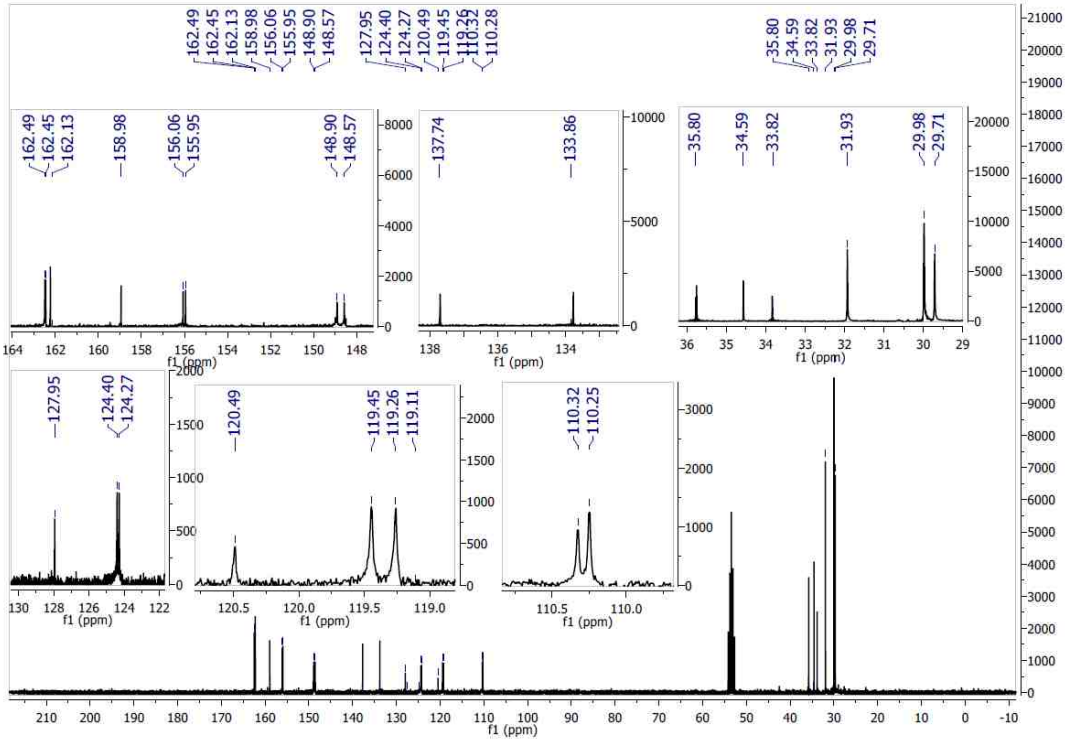

Figure A37: ^{13}C NMR of 4,4'-di-*tert*-butyl-2,2'-bipyridineplatinum(II)(3,5-di-*t*-butylbenzene catecholate) [Pt(dbbpy)(dtbCAT)]. Solvent: $CDCl_3$. Solvent peak: 77.2 ppm.

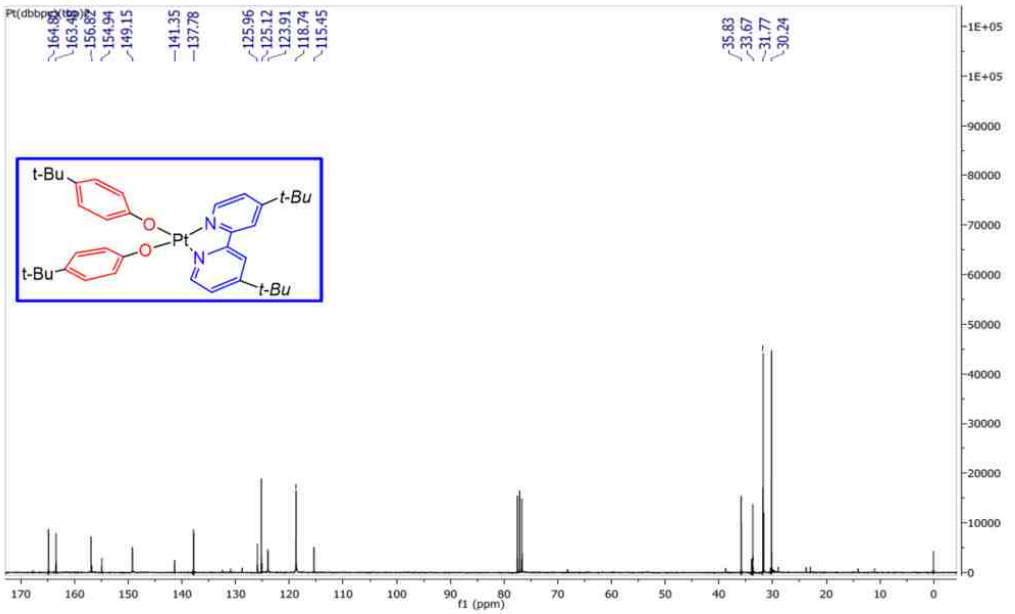

Figure A38: ^{13}C NMR of 4,4'-di-*tert*-butyl-2,2'-bipyridineplatinum(II)(bis-4-*tert*-butylphenolate), [Pt(dbbpy)(tbp)$_2$]. Solvent: $CDCl_3$. Solvent peak: 77.2 ppm.

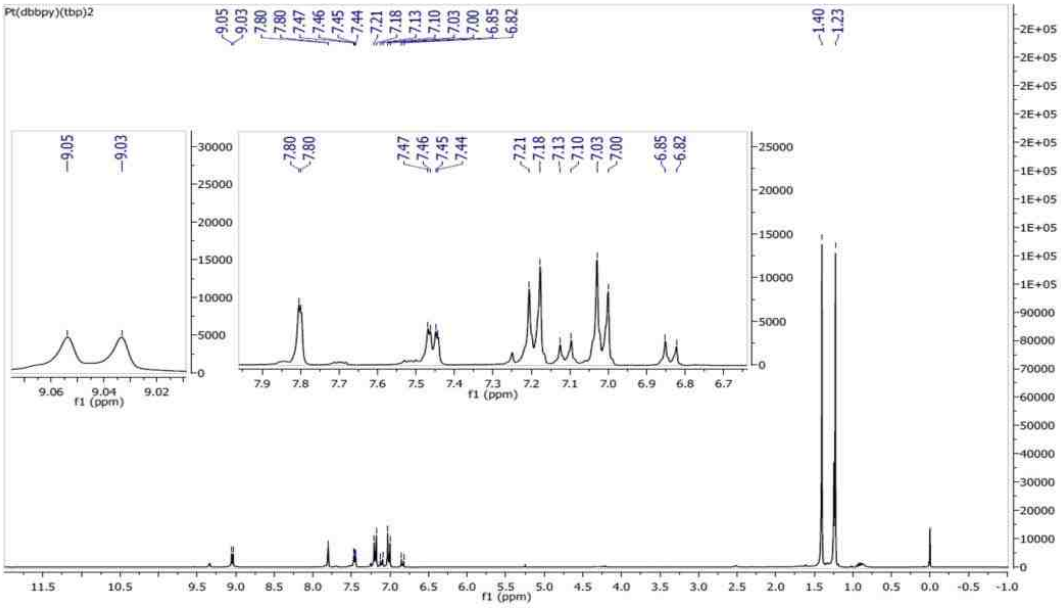

Figure A39: ^{1}H NMR of 4,4'-di-*tert*-butyl-2,2'-bipyridineplatinum(II) (bis-4-*tert*-butylphenolate), [Pt(dbbpy)(tbp)$_2$]. Solvent: $CDCl_3$. Solvent peak: 7.23 ppm.

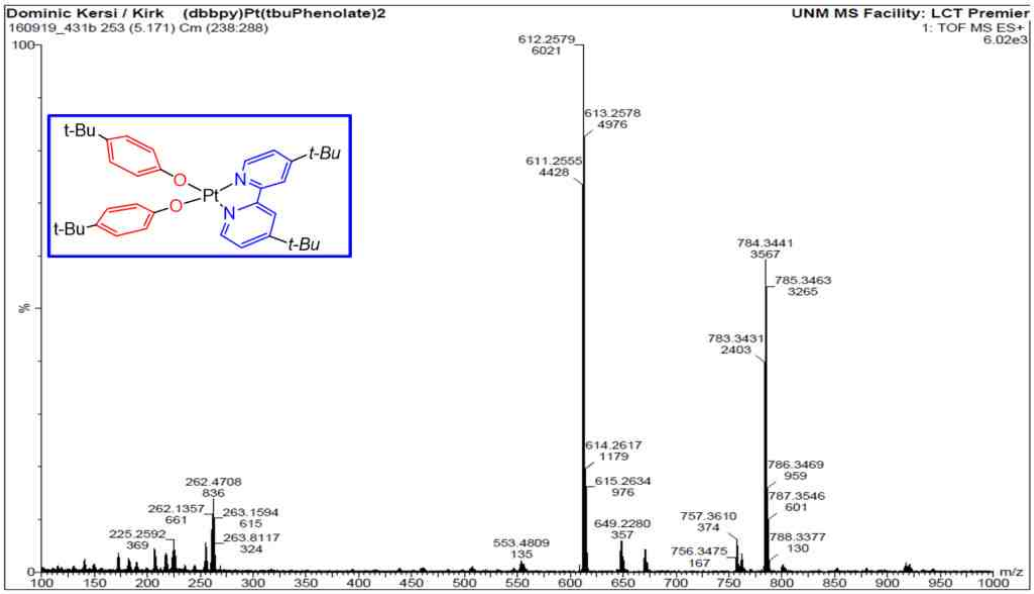

Figure A40: MS (ESI) of 4,4'-di-*tert*-butyl-2,2'-bipyridineplatinum(II) (bis-4-*tert*-butylphenolate), [Pt(dbbpy)(tbp)$_2$].

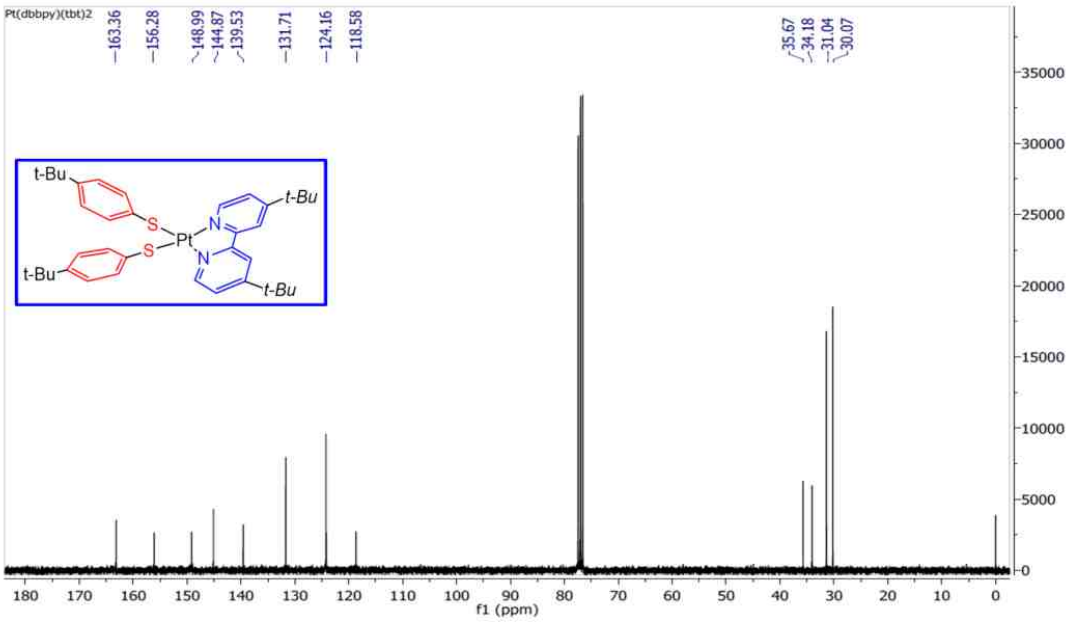

Figure A41: ^{13}C NMR of 4,4'-di-*tert*-butyl-2,2'-bipyridineplatinum(II)(bis-4-*tert*-butylbenzenethiolate), [Pt(dbbpy)(tbt)$_2$]. Solvent: $CDCl_3$. Solvent peak: 77.2 ppm.

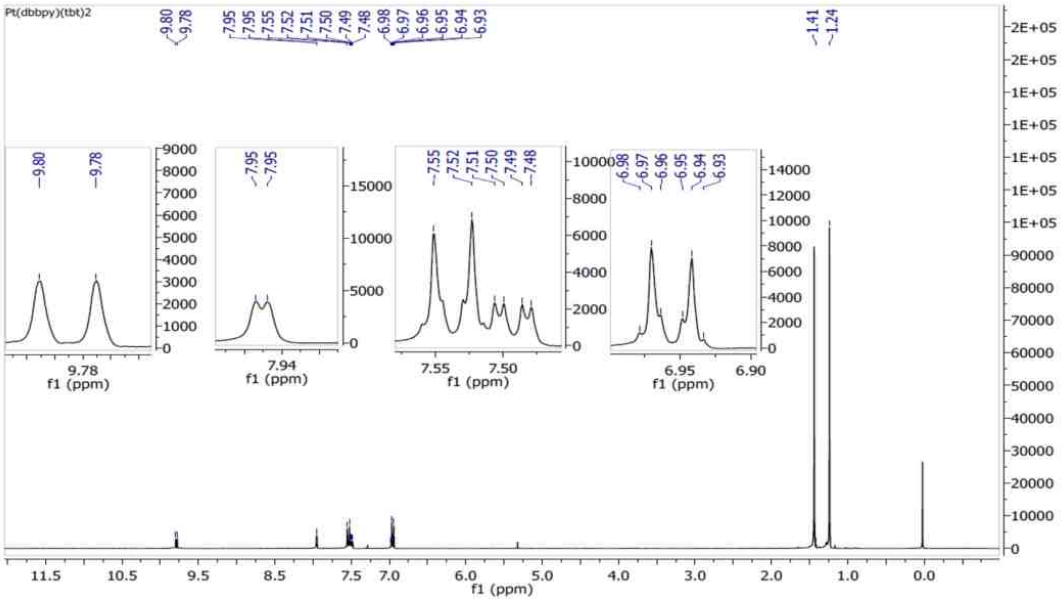

Figure A42: ^{1}H NMR of 4,4'-di-*tert*-butyl-2,2'-bipyridineplatinum(II) (bis-4-*tert*-butylbenzenethiolate), [Pt(dbbpy)(tbt)$_2$]. Solvent: $CDCl_3$. Solvent peak: 7.23 ppm.

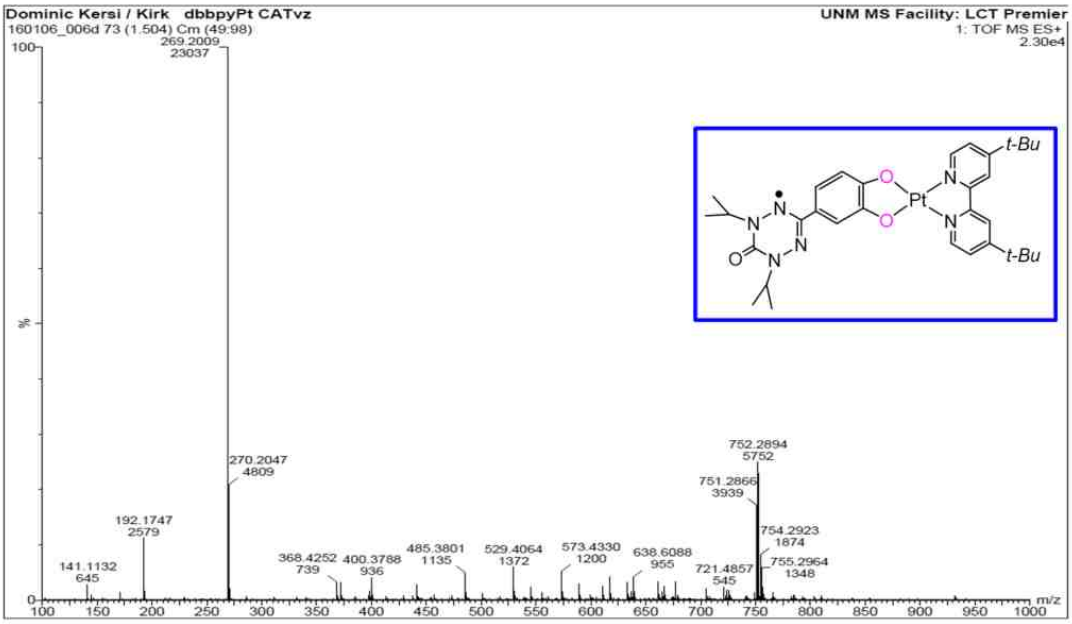

Figure A43: MS (ESI) of 4,4'-di-*tert*-butyl-2,2'-bipyridineplatinum(II) (1,5-diisopropyl-3-(3',4'-dihydroxyphenyl)-2-yl-6-oxoverdazyl, [Pt(dbbpy)(CAT-Vz)]

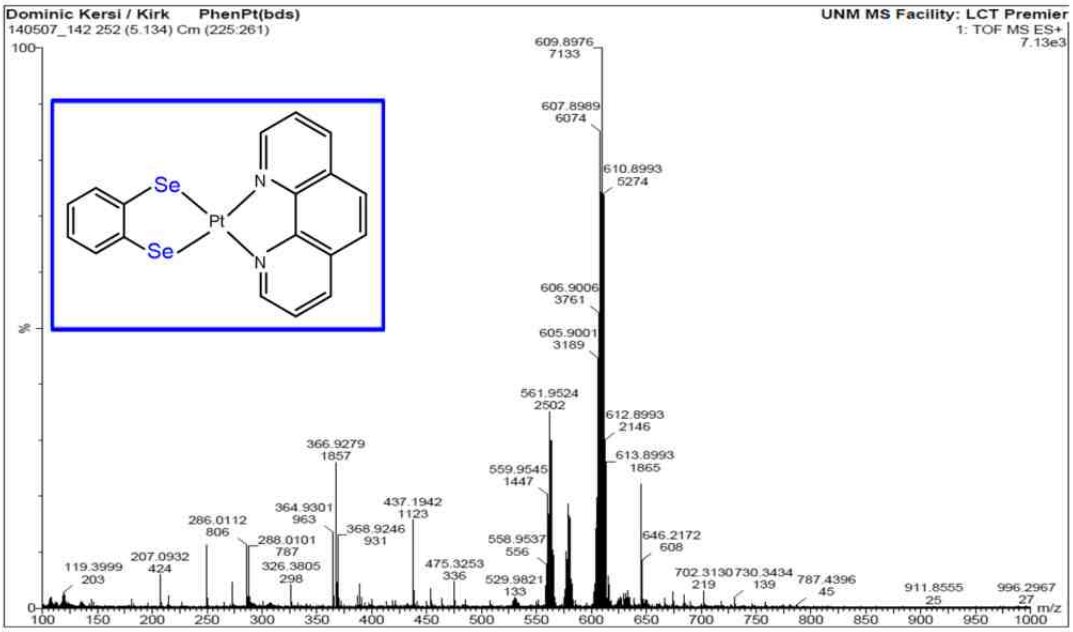

Figure A44: MS (ESI) phenathrolineplatinum(II)(benzenediselenolate), Pt(dpphen)(bds).

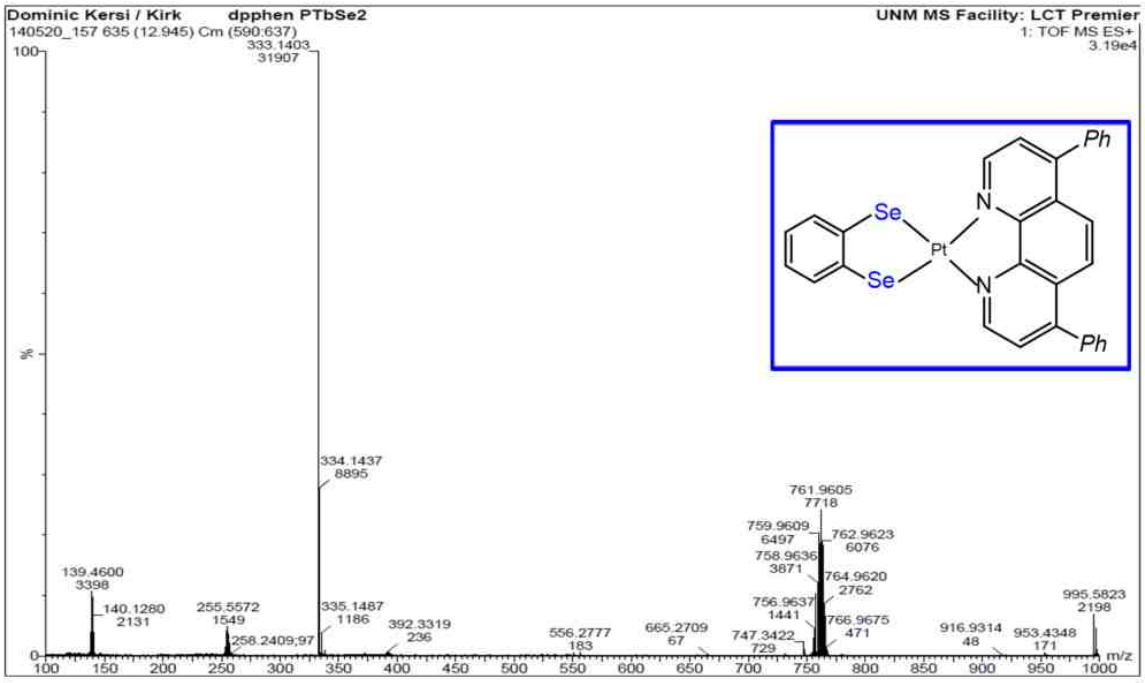

Figure A45: MS (ESI) 4,7-diphenyl-1,10-phenathrolineplatinum(II)(benzenediselenolate),[Pt(dpphen)(bds)].

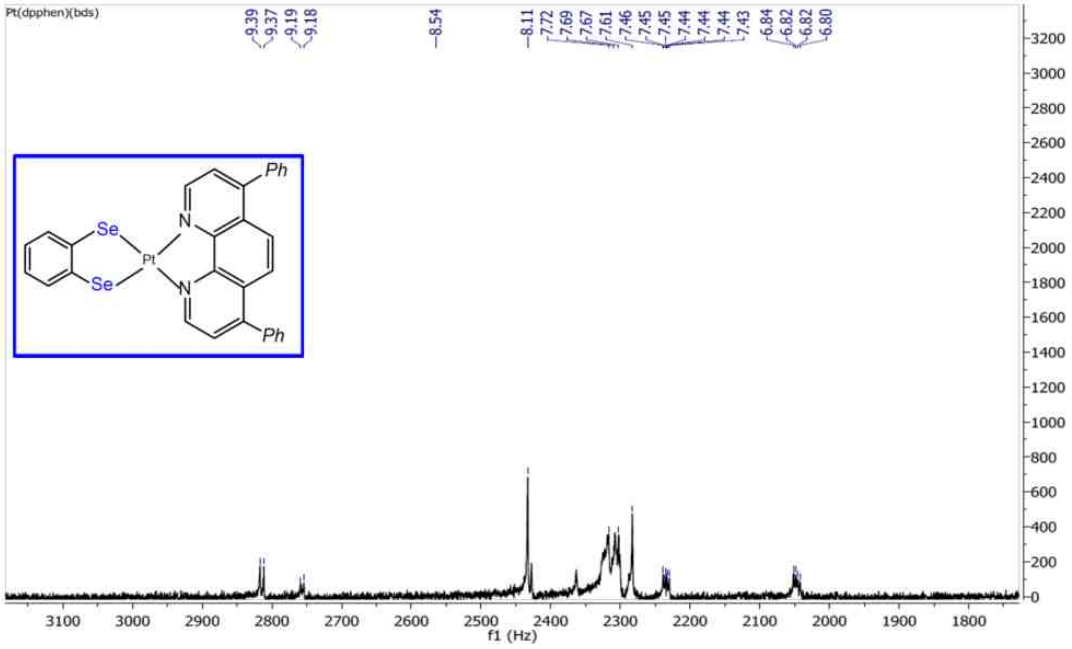

Figure A46: ^{1}H NMR of 4,7-diphenyl-1,10-phenathrolineplatinum(II) benzenediselenolate), [Pt(dpphen)(bds)]. Solvent: DMSO-d_6. Solvent peak: 2.50 ppm.

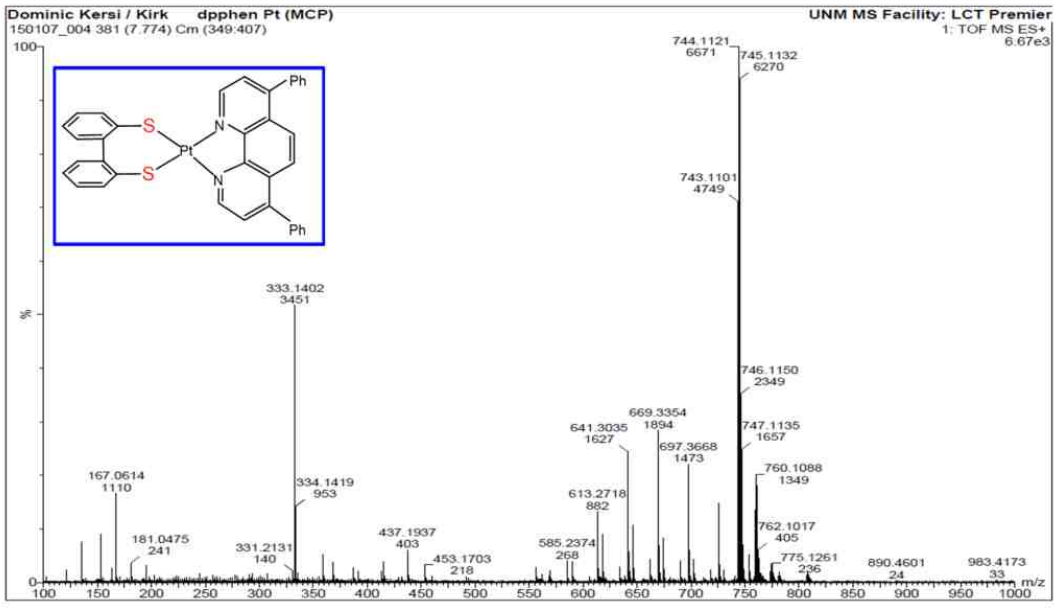

Figure A47: MS (ESI) ^{1}H NMR of 4,7-diphenyl-1,10-phenathrolineplatinum(II) (2,2'-di-mercaptobiphenyl), [Pt(dpphen)(mcp)].

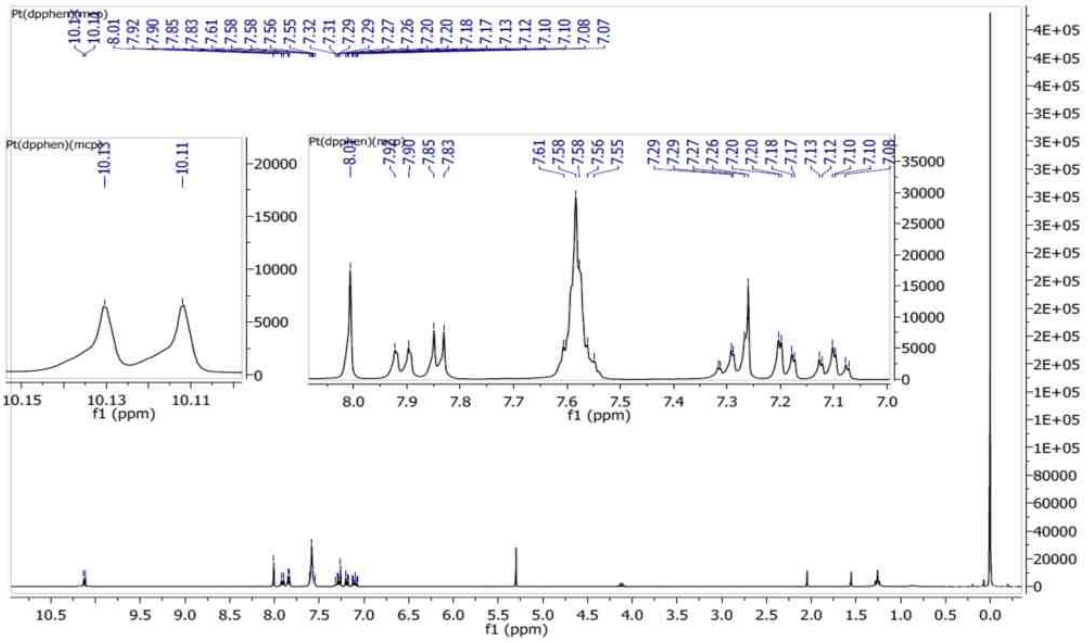

Figure A48: ^{1}H NMR of 4,7-diphenyl-1,10-phenathrolineplatinum(II)(2,2'-dimer-captobiphenyl), [Pt(dpphen)(mcp)]. Solvent: $CDCl_3$. Solvent peak: 7.23 ppm.

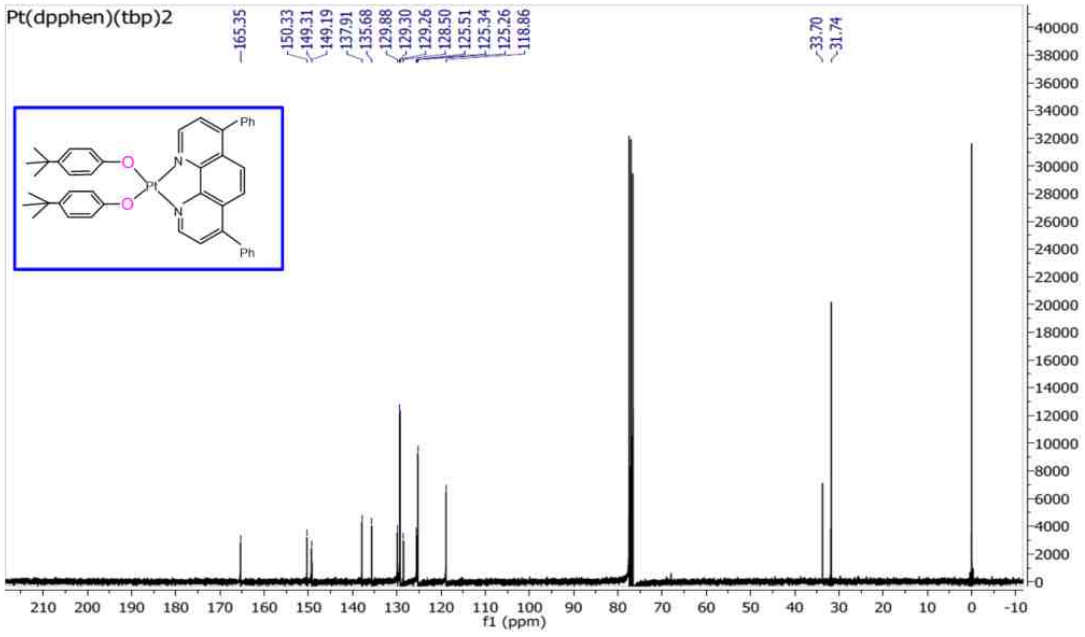

Figure A49: ^{13}C NMR of 4,7-diphenyl-1,10-phenathrolineplatinum(II) (bis-4-*tert*-butylphenolate), [Pt(dpphen)(tbp)$_2$]. Solvent: $CDCl_3$. Solvent peak: 77.2 ppm.

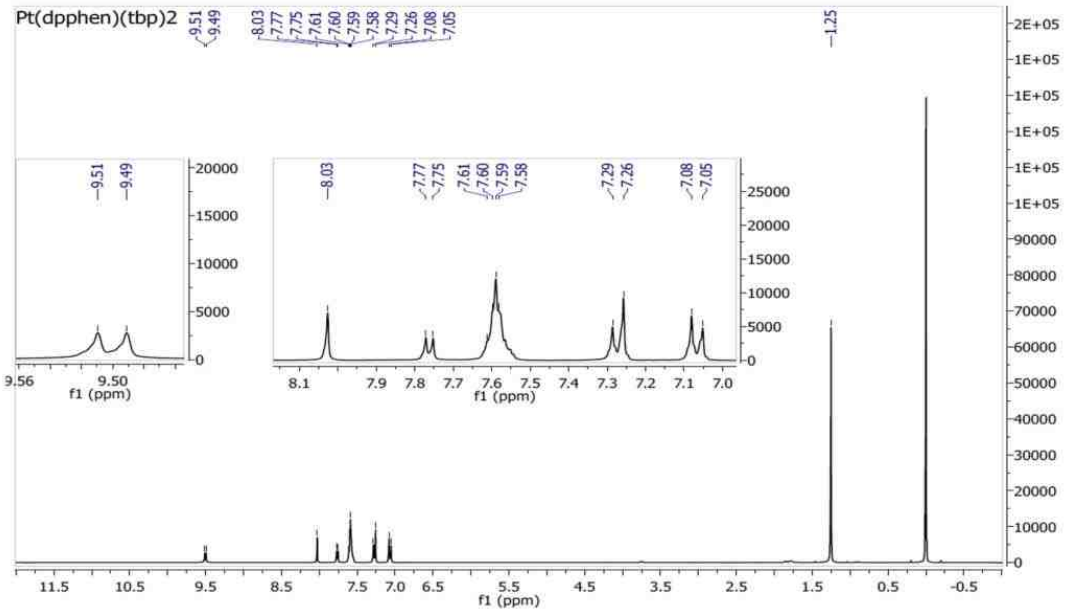

Figure A50: ^{1}H NMR of 4,7-diphenyl-1,10-phenathrolineplatinum(II) (bis-4-*tert*-butylphenolate), [Pt(dpphen)(tbp)$_2$]. Solvent: $CDCl_3$. Solvent peak: 7.23 ppm.

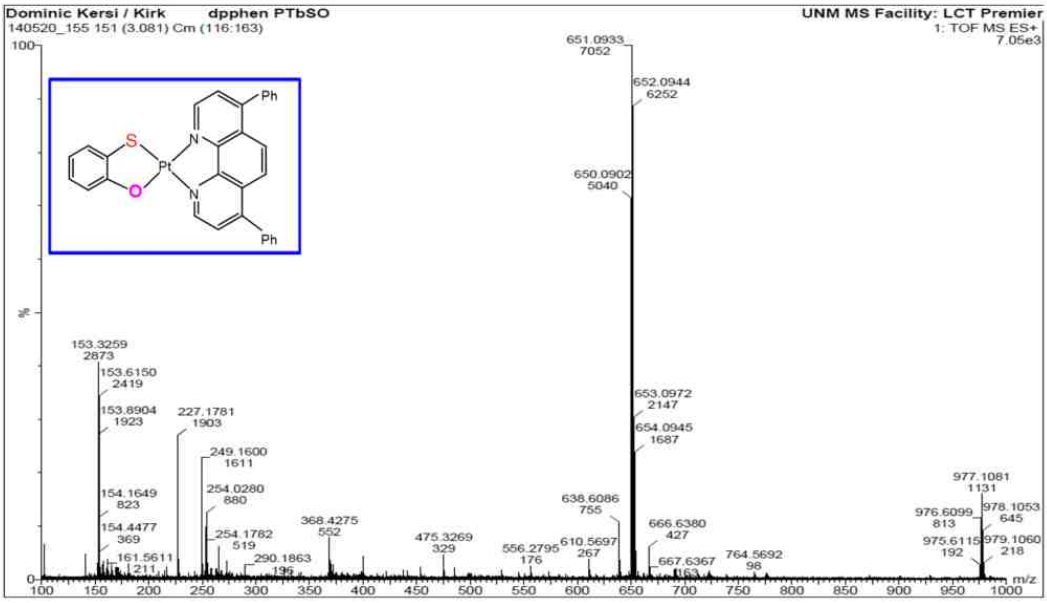

Figure A51: MS (ESI) of 4,7-diphenyl-1,10-phenathrolineplatinum(II)(2-mercaptophenolate), [Pt(dpphen)(bSO)].

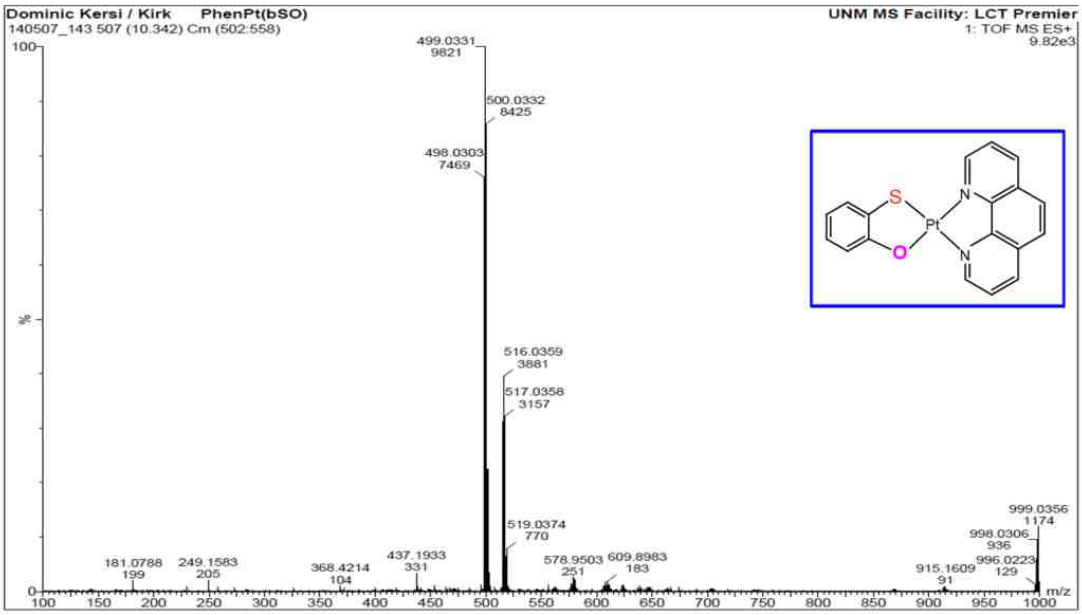

Figure A52: MS (ESI) of 1,10-phenathrolineplatinum(II)(2-mercaptophenolate), [Pt(dpphen)(bSO)].

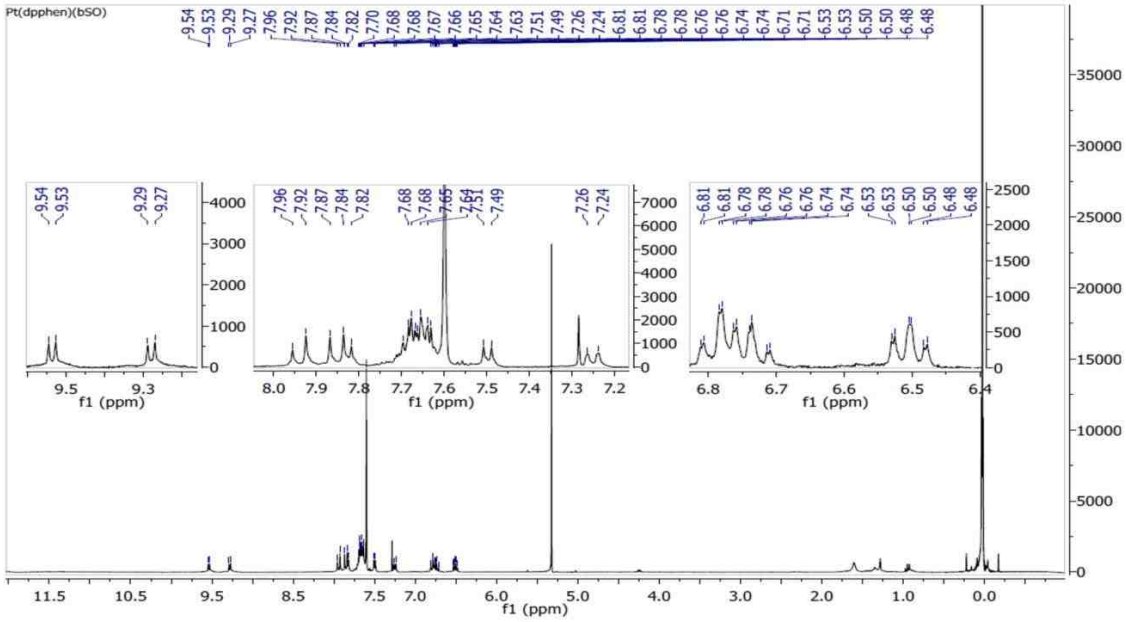

Figure A53: ^{1}H NMR of 4,7-diphenyl-1,10-phenathrolineplatinum(II) (2-mercaptophenolate), [Pt(dpphen)(bSO)]. Solvent: $CDCl_3$. Solvent peak: 7.23 ppm.

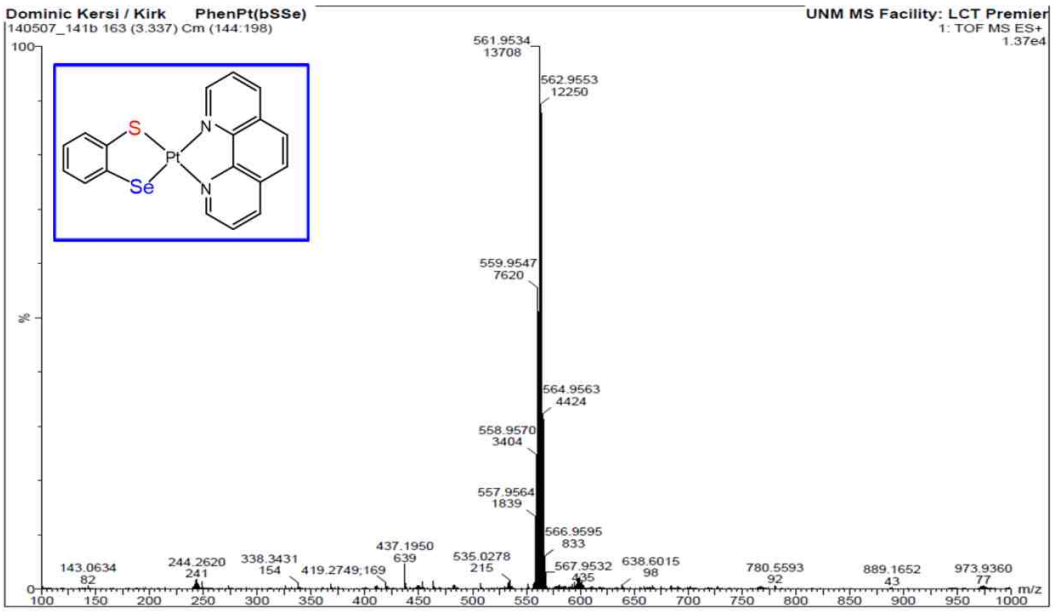

Figure A54: MS (ESI) of 10-phenathrolineplatinum(II)(2-selenylbenzenethiolate), [Pt(phen)(bSSe)].

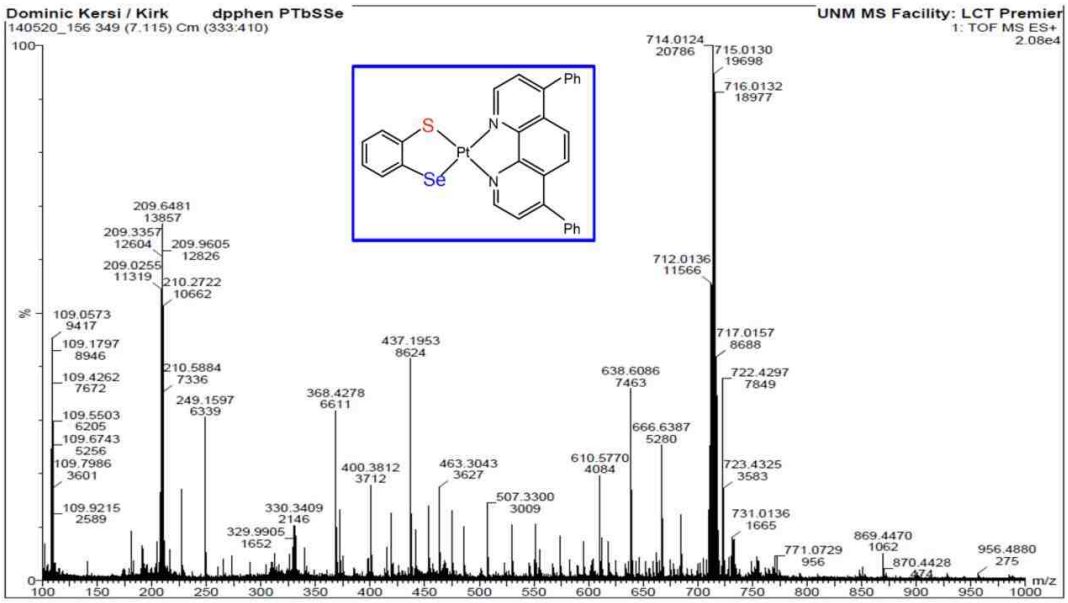

Figure A55: MS (ESI) of 4,7-diphenyl-1,10-phenathrolineplatinum(II)(2-selenylbenzenethiolate), [Pt(dpphen)(bSSe)].

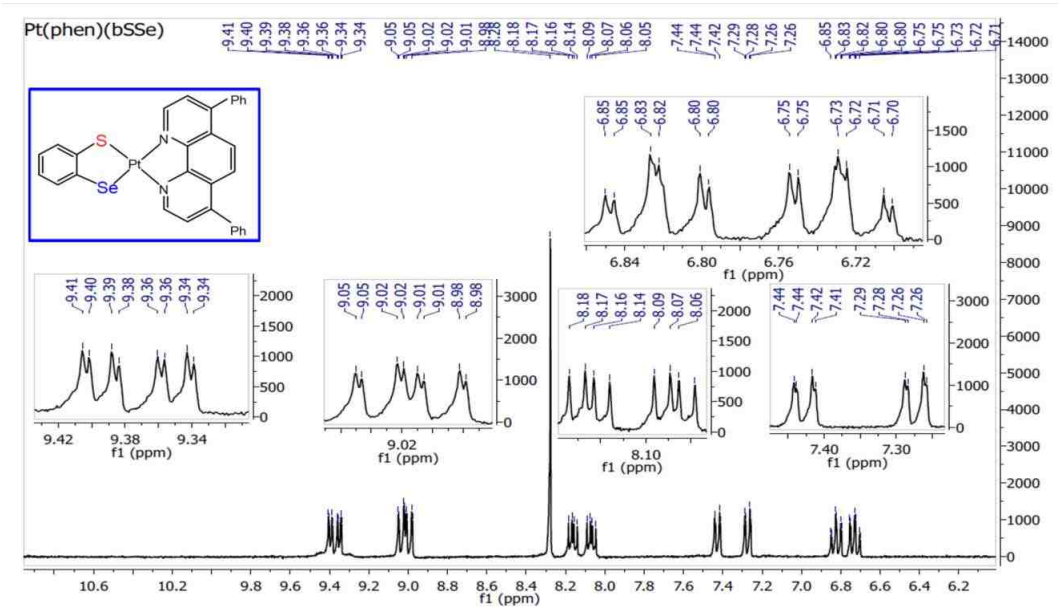

Figure A56: ^{1}H NMR of 10-phenathrolineplatinum(II)(2-selenylbenzenethiolate), [Pt(phen)(bSSe)]. Solvent: DMSO-d_6. Solvent peak: 2.50 ppm

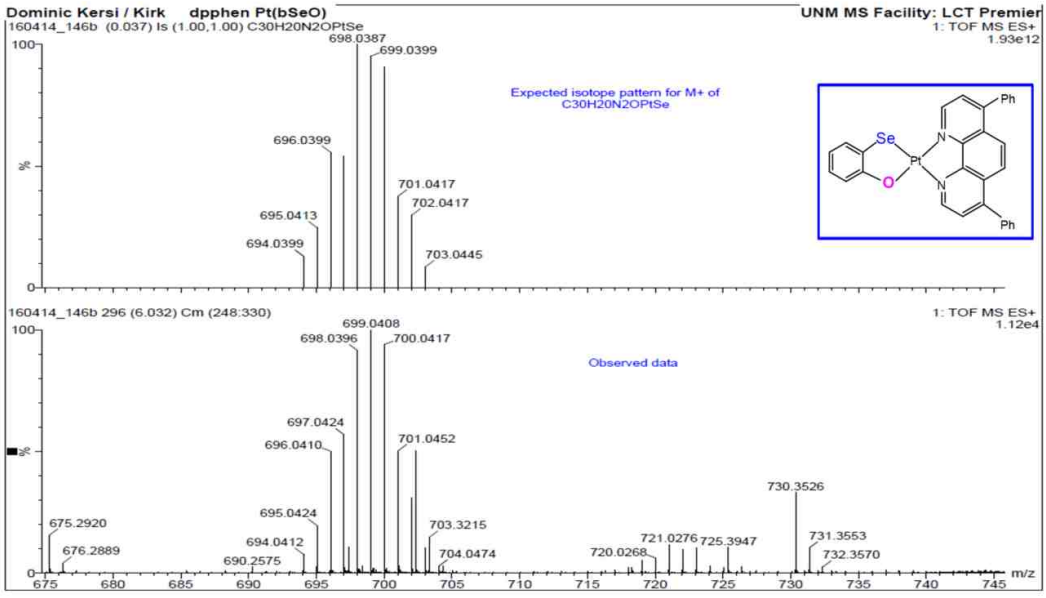

Figure A57: MS (ESI) of 4,7-diphenyl-1,10-phenathrolineplatinum(II)(2-selenyl-phenolate), [Pt(dpphen)(bSeO)].

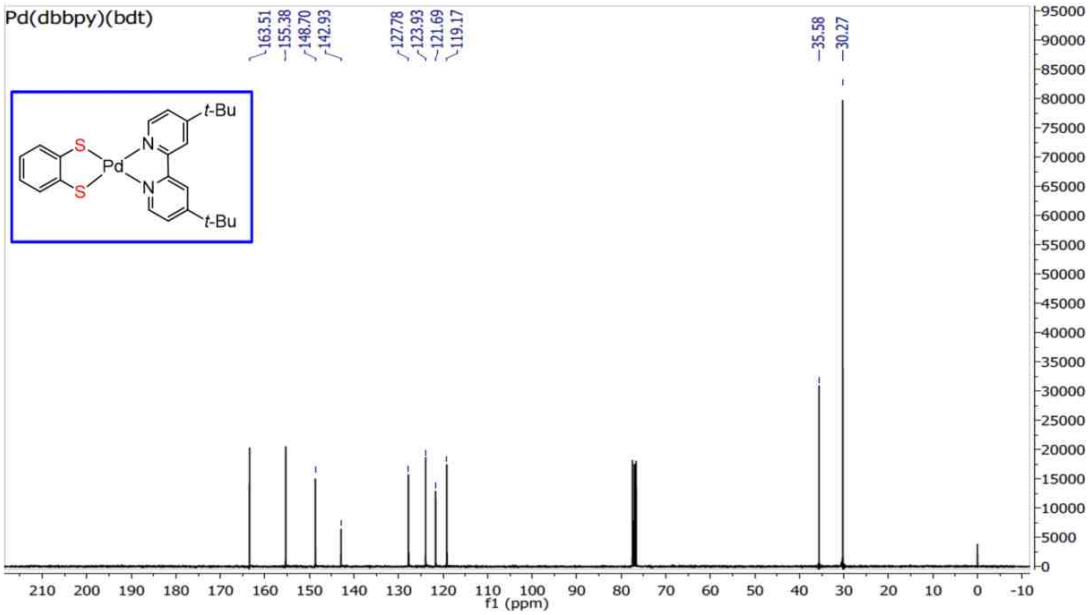

Figure 58: ^{13}C NMR of 4,4'-di-*tert*-butyl-2,2'-bipyridinepalladium(II)(benzenedithiolate), [Pd(dbbpy)(bdt)]. Solvent: $CDCl_3$. Solvent peak: 77.2 ppm.

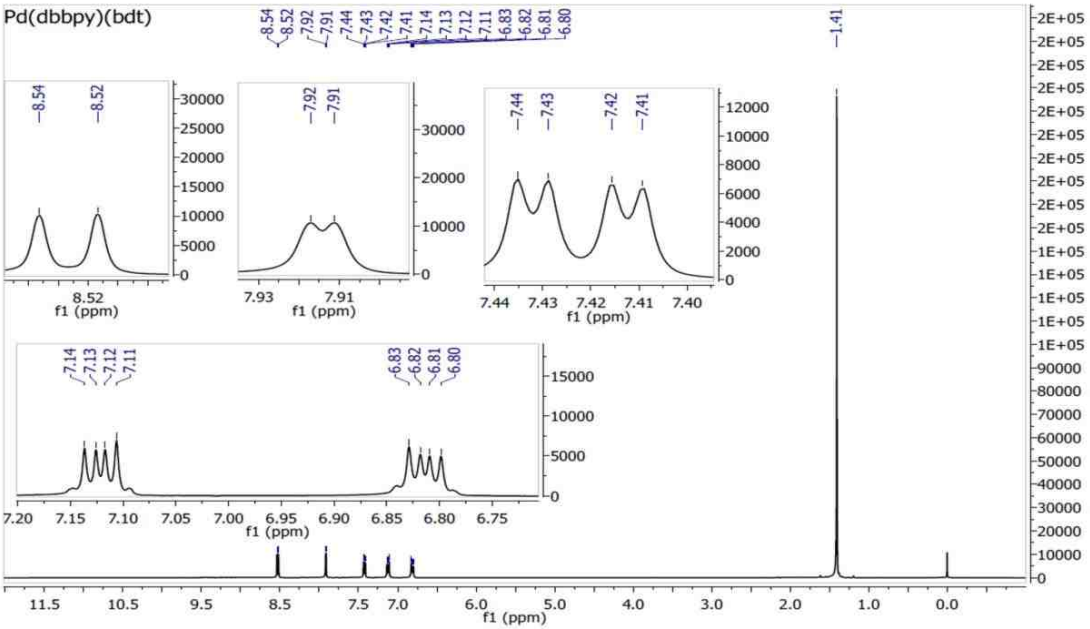

Figure 59: ^{1}H NMR of 4,4'-di-*tert*-butyl-2,2'-bipyridinepalladium(II)(benzenedithiolate), [Pd(dbbpy)(bdt)]. Solvent: $CDCl_3$. Solvent peak: 7.23 ppm.

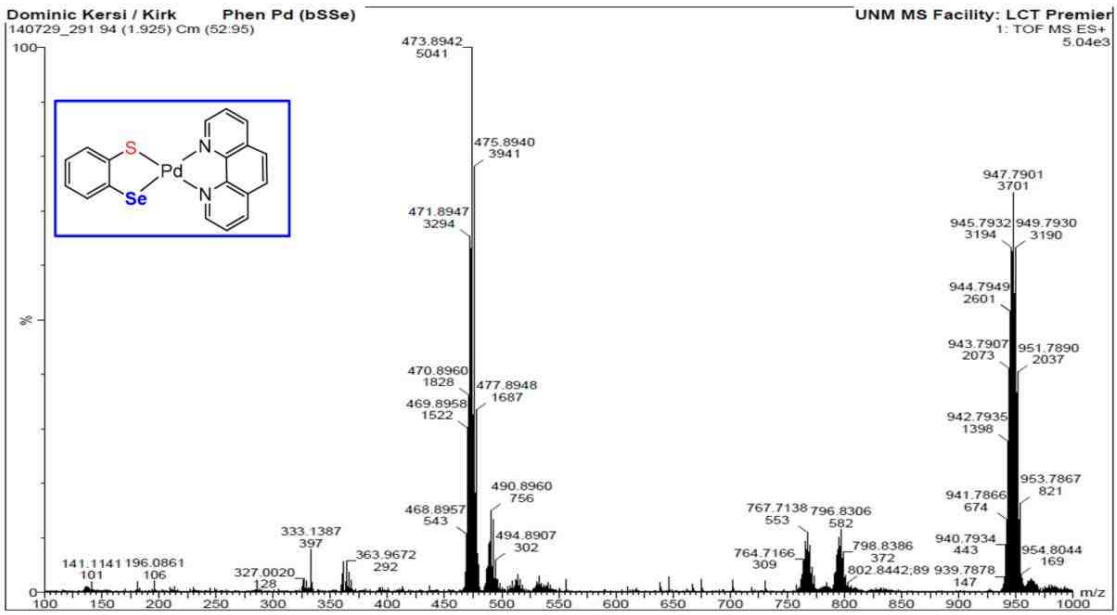

Figure A60: MS (ESI) of 10-phenathrolinepalladium(II)(2-selenylbenzenethiolate), [Pd(phen)(bSSe)].

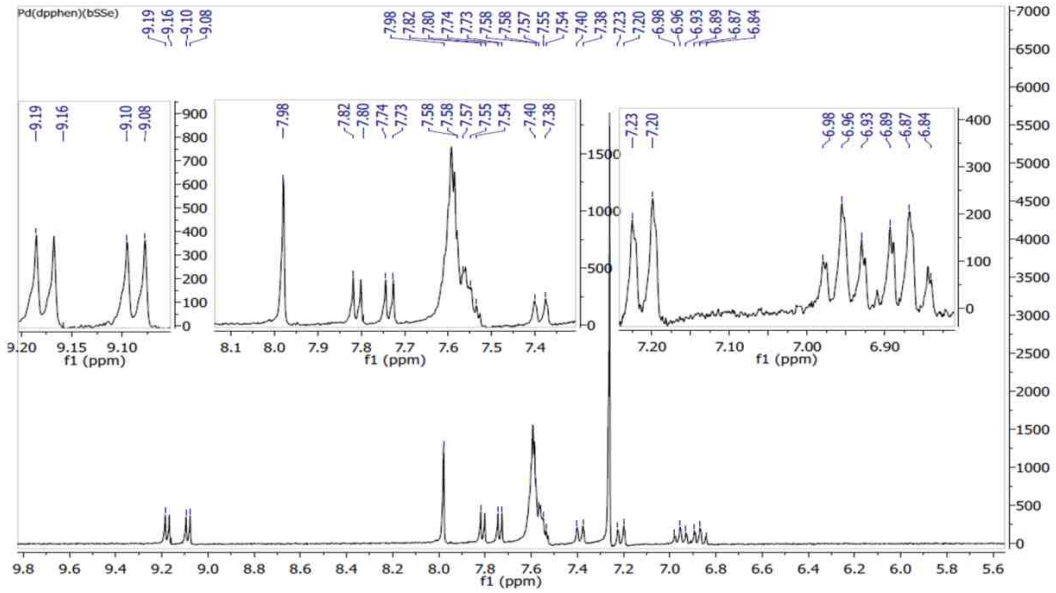

Figure A61: ^{1}H NMR of 4,7-diphenyl-1,10-phenathrolinepalladium (II)(2-selenylbenzenethiolate), [Pd(dpphen)(bSSe)]. Solvent: $CDCl_3$. Solvent peak: 7.23 ppm.

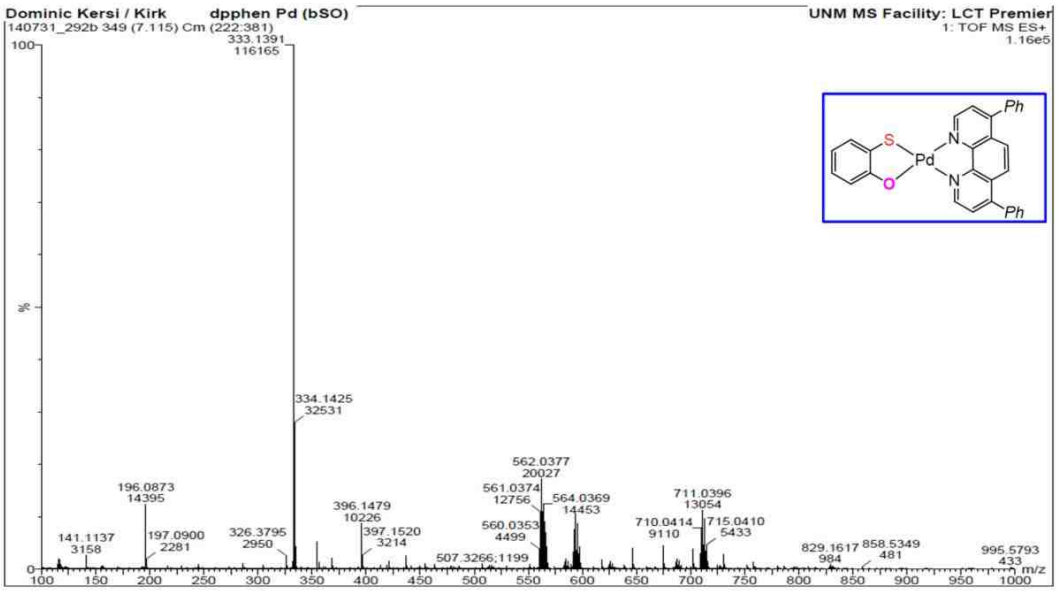

Figure A62: MS (ESI) of 4,7-diphenyl-1,10-phenathrolinepalladium(II)(2-mercaptophenolate), [Pd(dpphen)(bSO)].

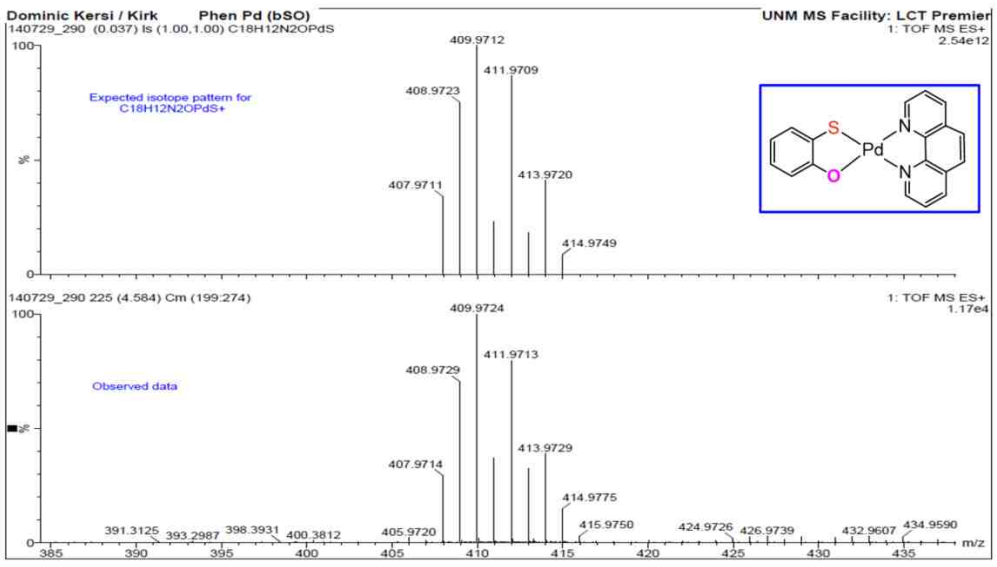

Figure A63: MS (ESI) of 1,10-phenathrolinepalladium(II)(2-mercaptophenolate), [Pd(phen)(bSO)].

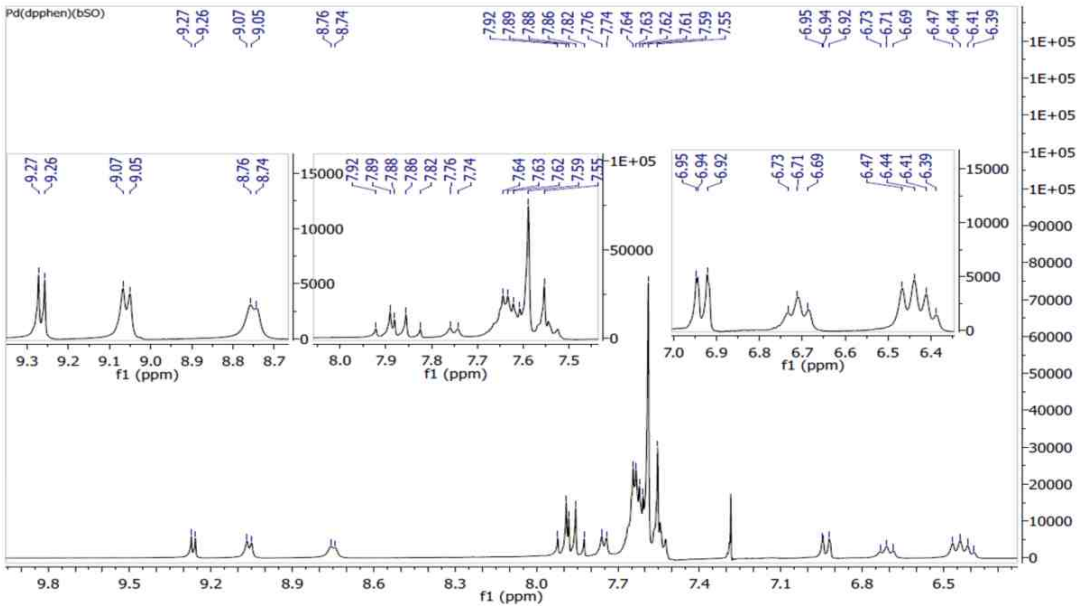

Figure A64: ^{1}H NMR of 4,7-diphenyl-1,10-phenathrolinepalladium(II)(2-mercaptophenolate), [Pd(dpphen)(bSO)]. Solvent: $CDCl_3$. Solvent peak: 7.23 ppm.

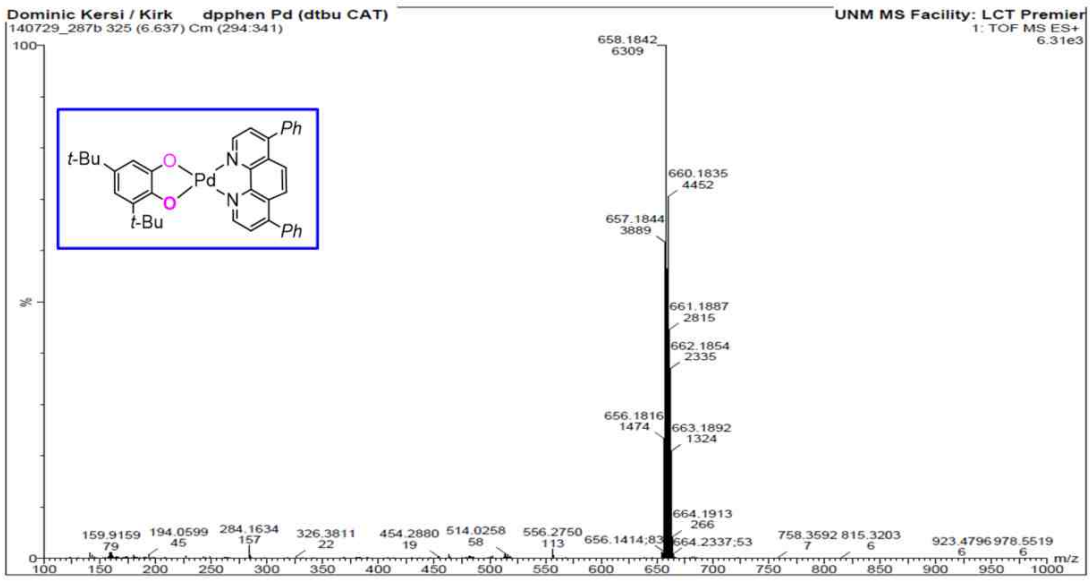

Figure A65: MS (ESI) of 4,7-diphenyl-1,10-phenathrolinepalladium(II) (3,5-di-*t*-butylbenzene catecholate), [Pd(dpphen)(dtbCAT)].

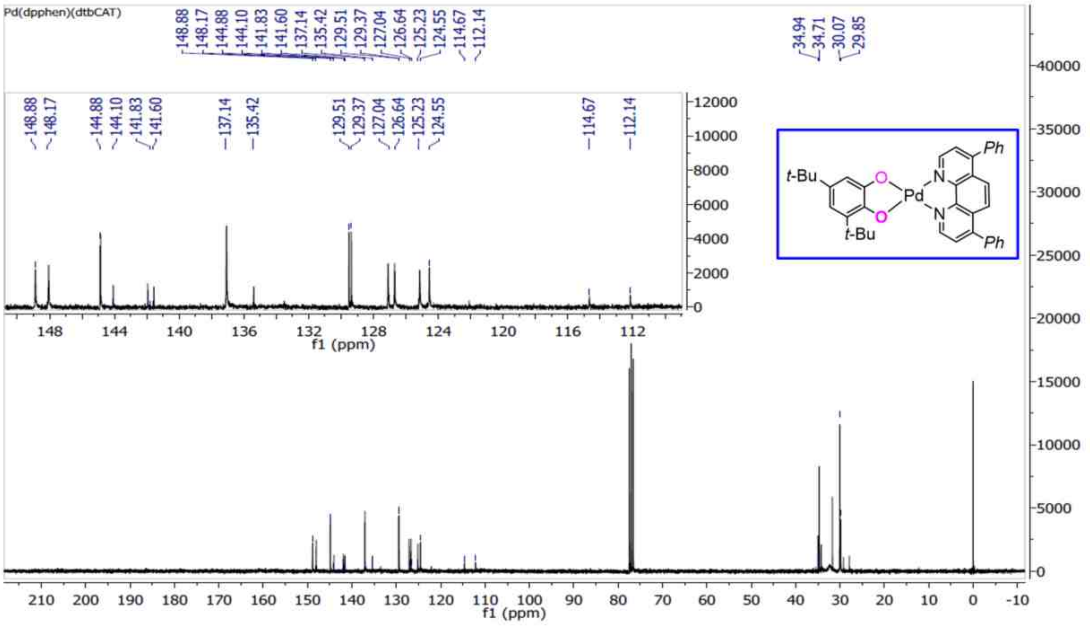

Figure A66: ^{13}C NMR of 4,7-diphenyl-1,10-phenathrolinepalladium(II) (3,5-di-*t*-butylbenzene catecholate), [Pd(dpphen)(dtbCAT)]. Solvent: $CDCl_3$. Solvent peak: 77.2 ppm.

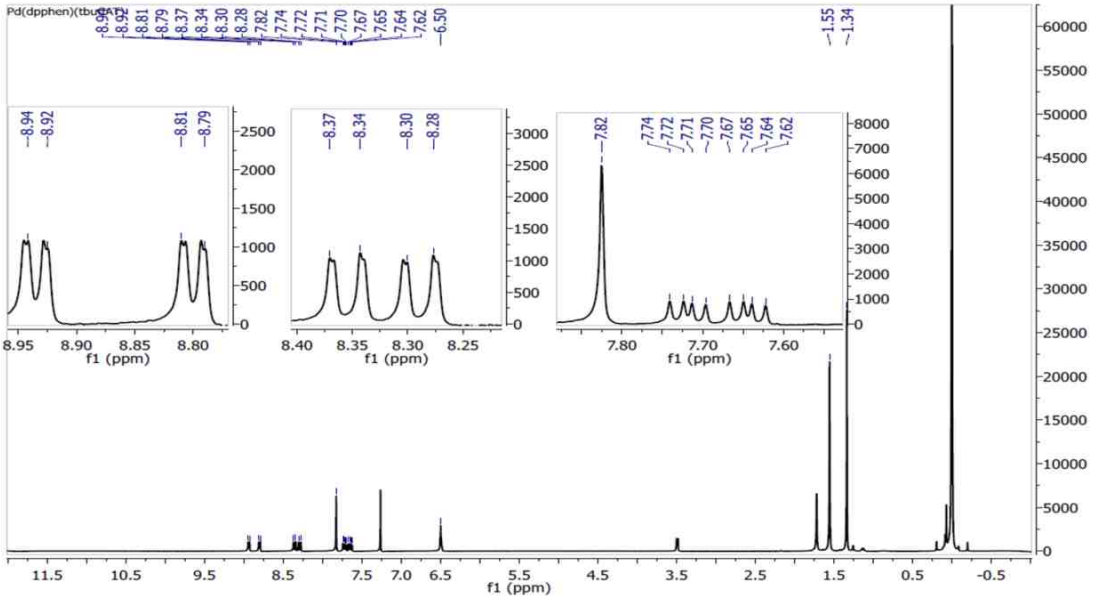

Figure A67: ^{1}H NMR of 4,7-diphenyl-1,10-phenathrolinepalladium(II) (3,5-di-*t*-butylbenzene catecholate), [Pd(dpphen)(dtbCAT)]. Solvent: $CDCl_3$. Solvent peak: 7.23 ppm.

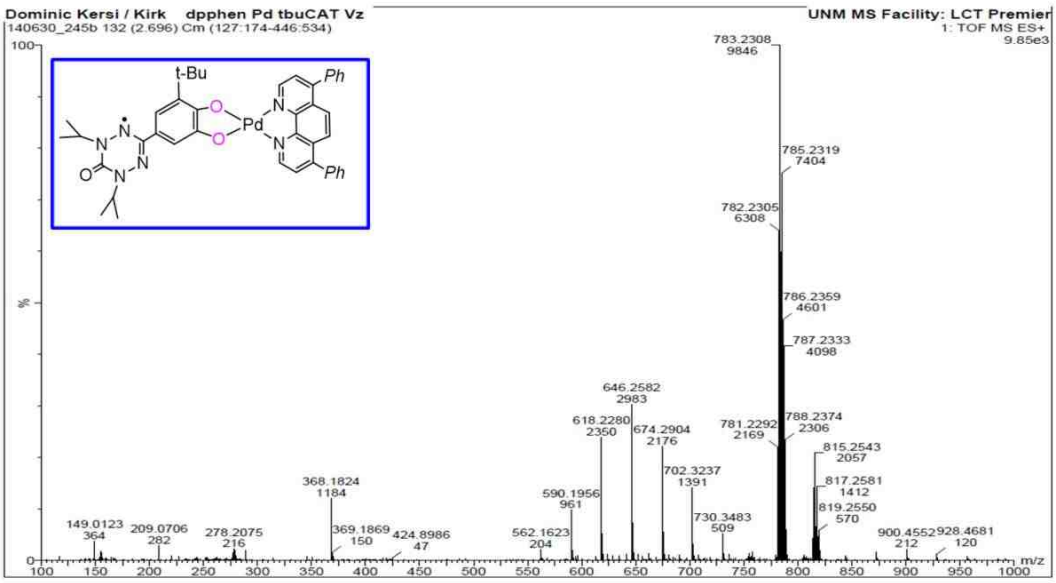

Figure A68: MS (ESI) of 4,7-diphenyl-1,10-phenathrolinepalladium(II) (1,5-diisopropyl-3-(3',4'-dihydroxy-5'-*t*-butylphenyl)-2-yl-6-oxoverdazyl, [Pd(dpphen)(tbCAT-Vz)].

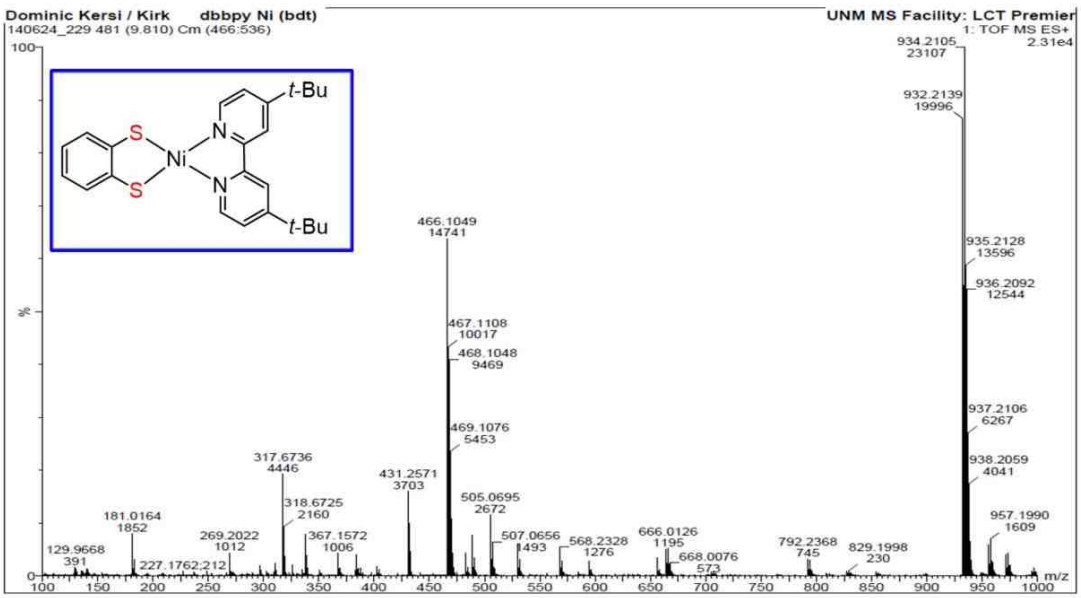

Figure A69: MS (ESI) 4,4'-di-*tert*-butyl-2,2'-bipyridinenickel(II)(benzenedithiolate), [Ni(dbbpy)(bdt)].

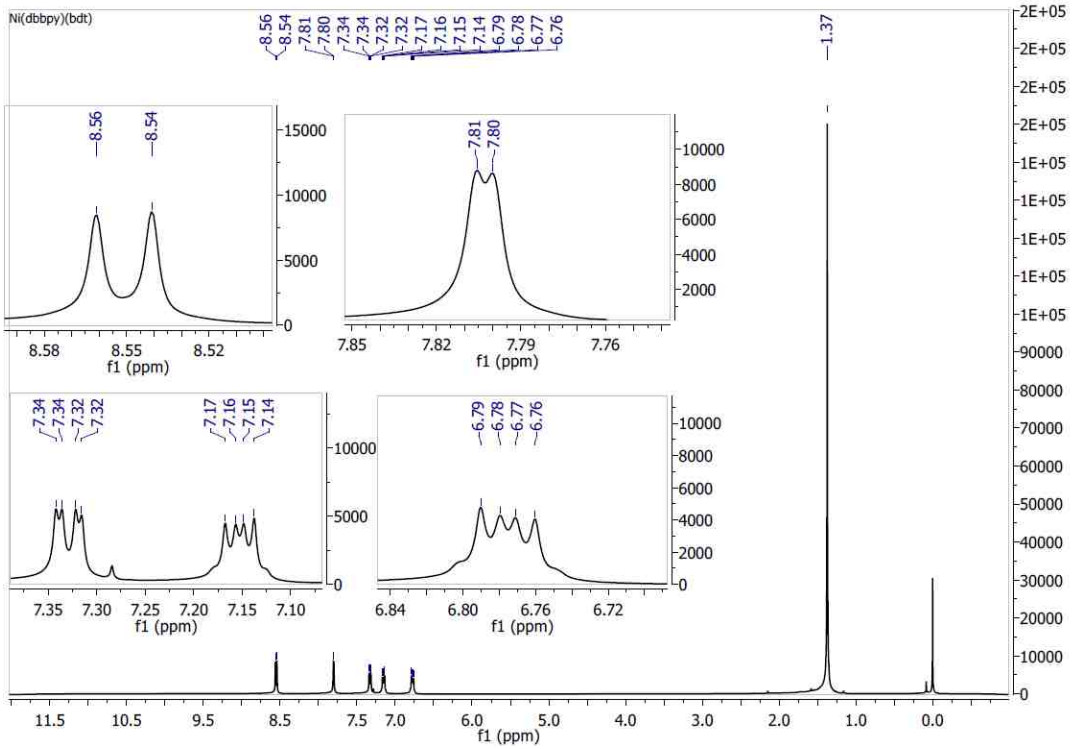

Figure A70: ^{1}H NMR of 4,4'-di-*tert*-butyl-2,2'-bipyridinenickel(II)(benzenedithiolate),[Ni(dbbpy)(bdt)]. Solvent: $CDCl_3$. Solvent peak: 7.23 ppm

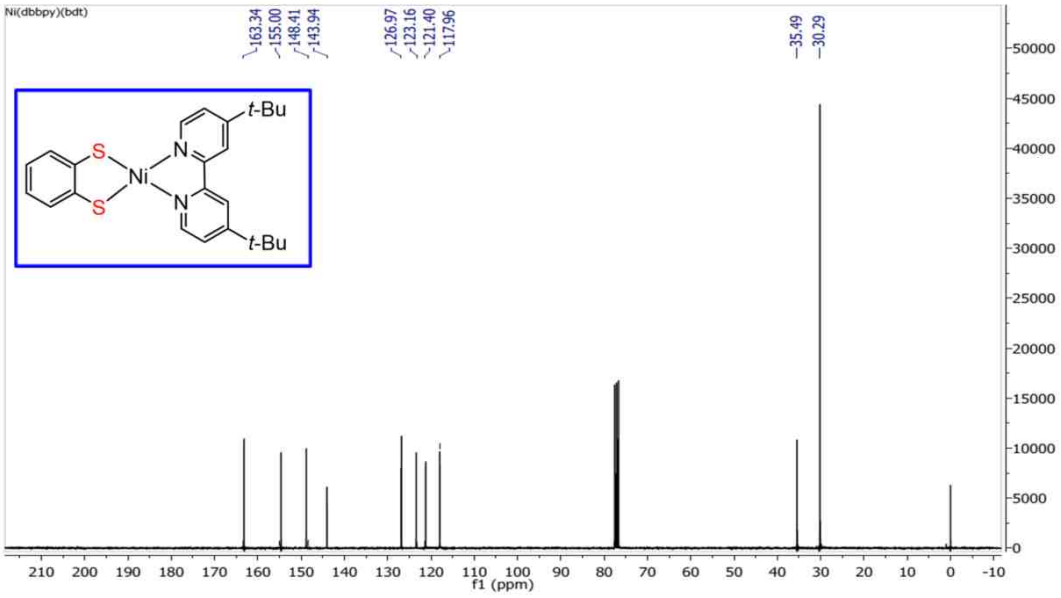

Figure A71: ^{13}C NMR of 4,4'-di-*tert*-butyl-2,2'-bipyridinenickel(II)(benzenedithiolate), [Ni(dbbpy)(bdt)]. Solvent: $CDCl_3$. Solvent peak: 77.2 ppm.

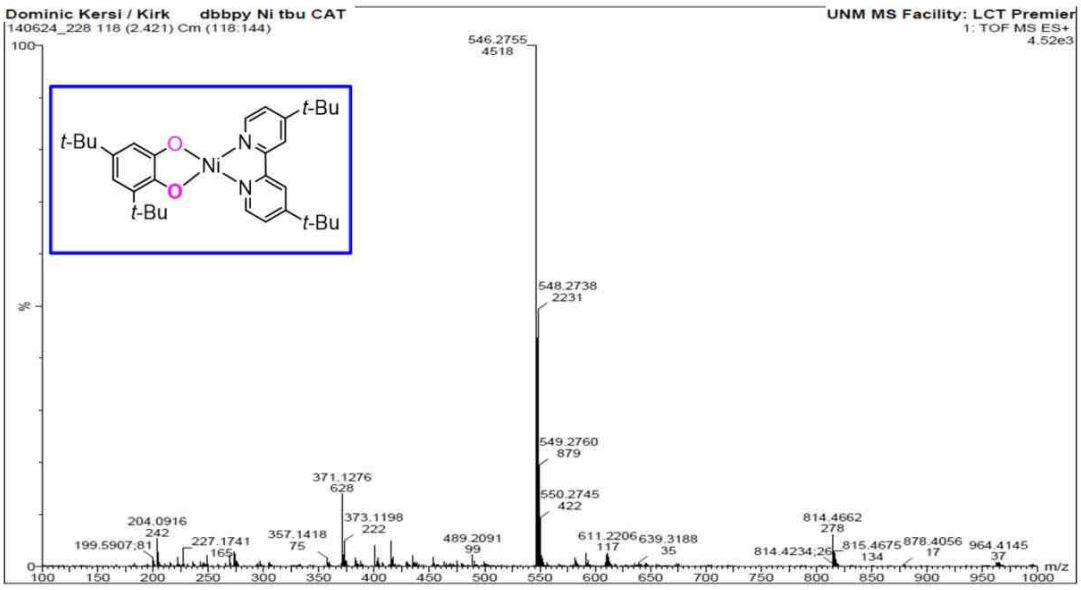

Figure A72: MS (ESI) 4,4'-di-*tert*-butyl-2,2'-bipyridinenickel(II)(3,5-di-*t*-butylbenz-enecatecholate), [Ni(dbbpy)(dtbCAT)].

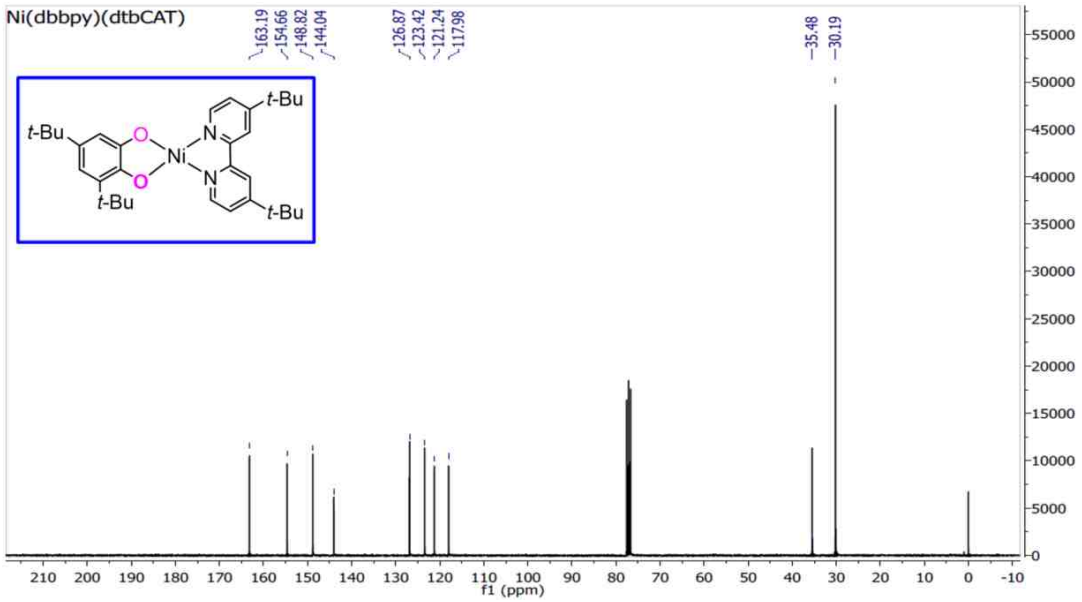

Figure A73: ^{13}C NMR of 4,4'-di-*tert*-butyl-2,2'-bipyridinenickel (II) 3,5-di-*t*-butyl-benzenecatecholate),[Ni(dbbpy)(dtbCAT)]. Solvent: $CDCl_3$. Solvent peak: 77.2 ppm.

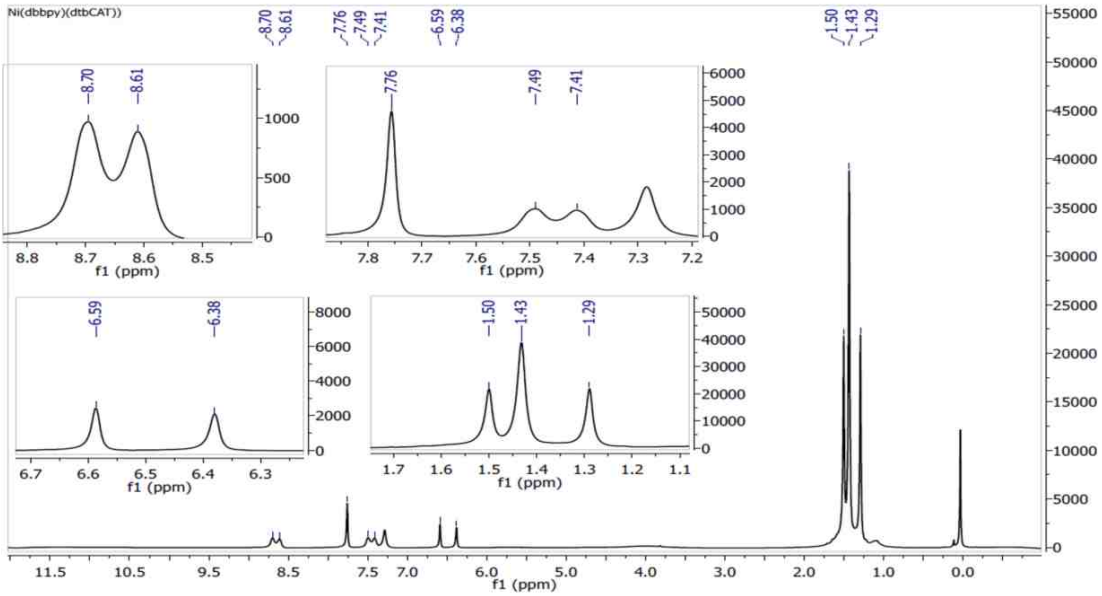

Figure A74: ^{1}H NMR of 4,4'-di-*tert*-butyl-2,2'-bipyridinenickel(II)(3,5-di-*t*-butylbenzene catecholate), [Ni(dbbpy)(dtbCAT)]. Solvent: $CDCl_3$. Solvent peak: 7.23 ppm.

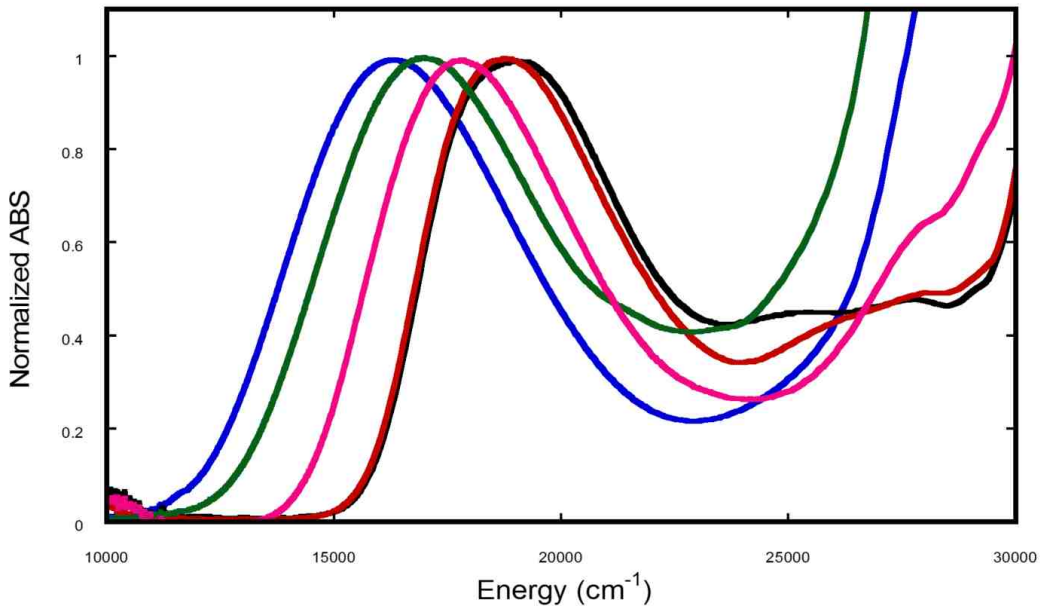

Figure A75: Electronic Absorption spectra Overlay for Pd(phen)(bdt) (red), Pd(phen)(bSO) (pink), Pd(phen)(bSSe) (black), Pd(phen)(dtbCAT) (blue), Pd(dpphen)(tbCAT-Vz) (green).

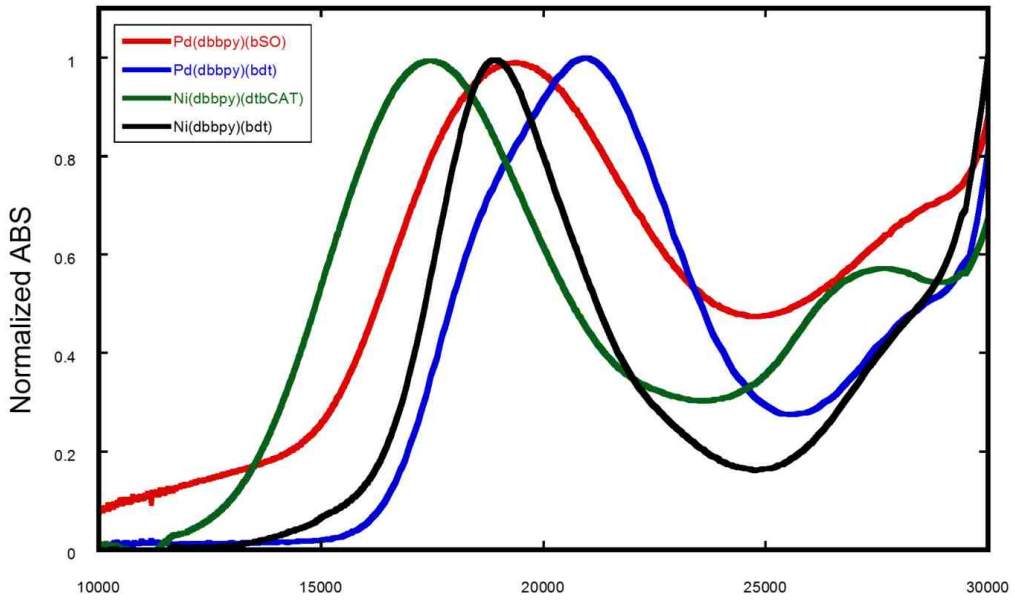

Figure A76: Electronic Absorption Overlay for Pd(dbbpy)(bSO) (red), Pd(dbbpy)(bdt) (blue), Ni(dbbpy)(dtbCAT) (green), Ni(dbbpy)(bdt) (black).

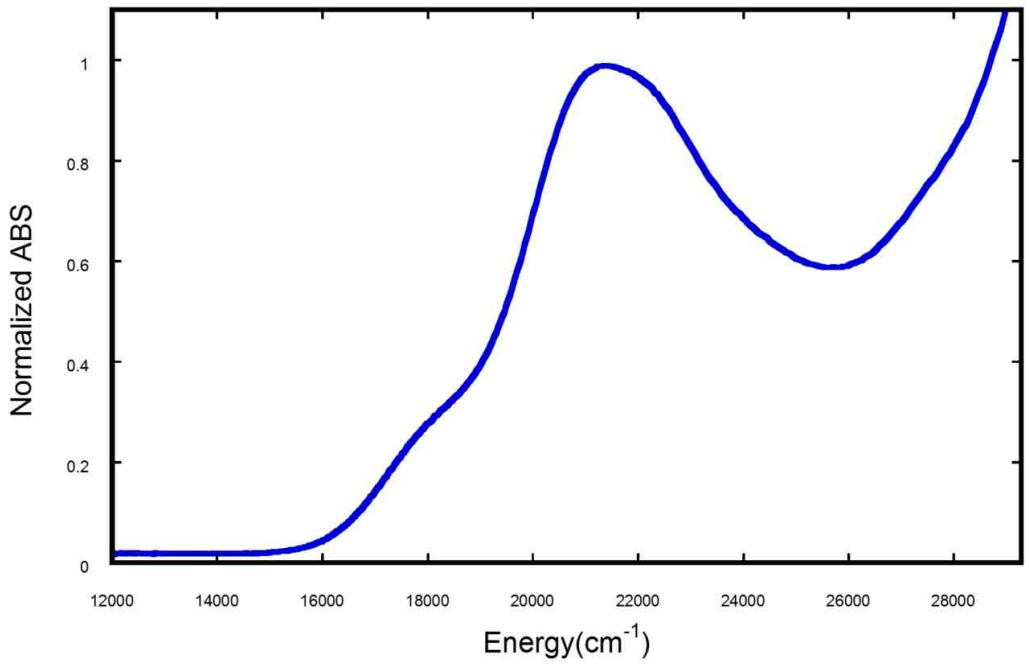

Figure A77: Electronic Absorption spectrum of Pt(dpphen)(mcp) in CH_2Cl_2 at ambient temperature (298 K).

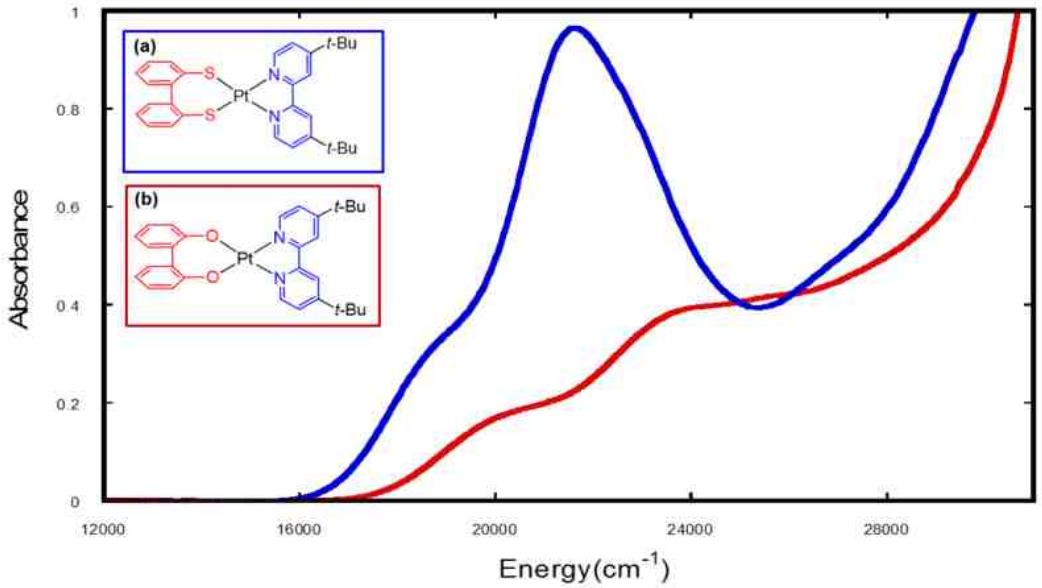

Figure A78: Electronic Absorption spectra Overlay for (a) Pt(dbbpy)(mcp) (blue), and (b) Pt(dbbpy)(hbp) (red) in CH_2Cl_2 at room temperature.

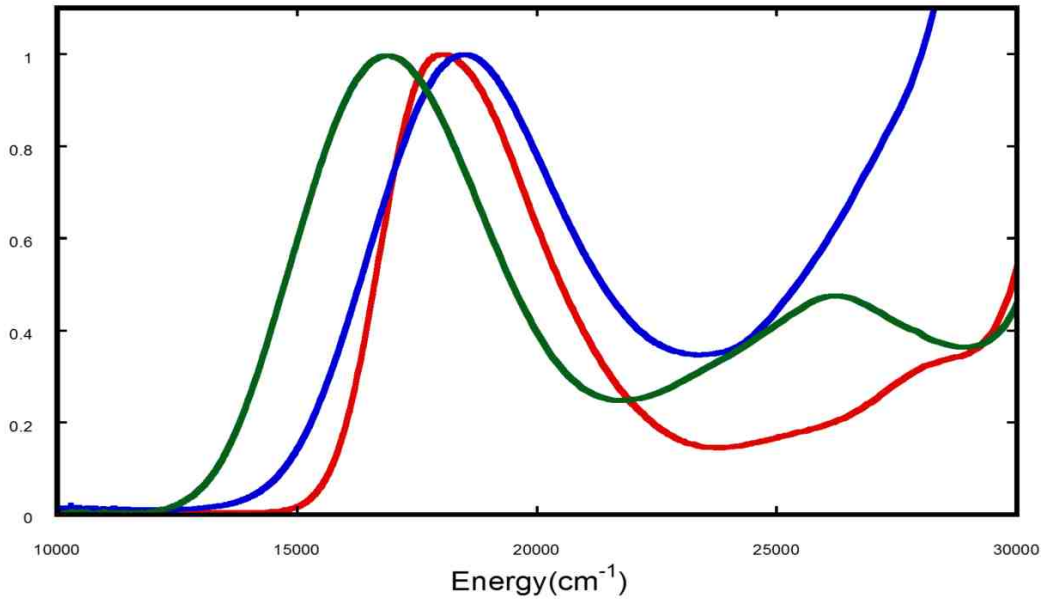

Figure A79: Electronic Absorption spectra Overlay for Pt(dbbpy)(CAT-Vz) (blue), Pt(dbbpy)(bdt) (red), and Pt(dbbpy)(dtbCAT) (green) in CH_2Cl_2 at room temperature.

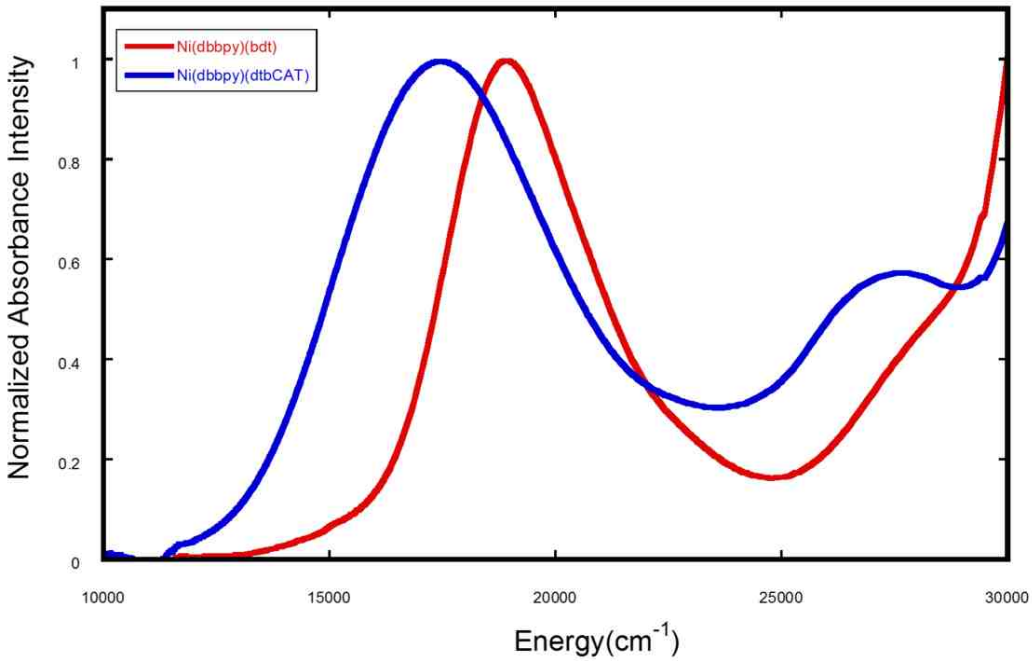

Figure A80: Electronic Absorption spectra Overlay for (dbbpy)(dtbCAT) (blue), and Ni(dbbpy)(bdt) (red) in CH_2Cl_2 at room temperature.

Appendix B

Additional Information for Chapter 4

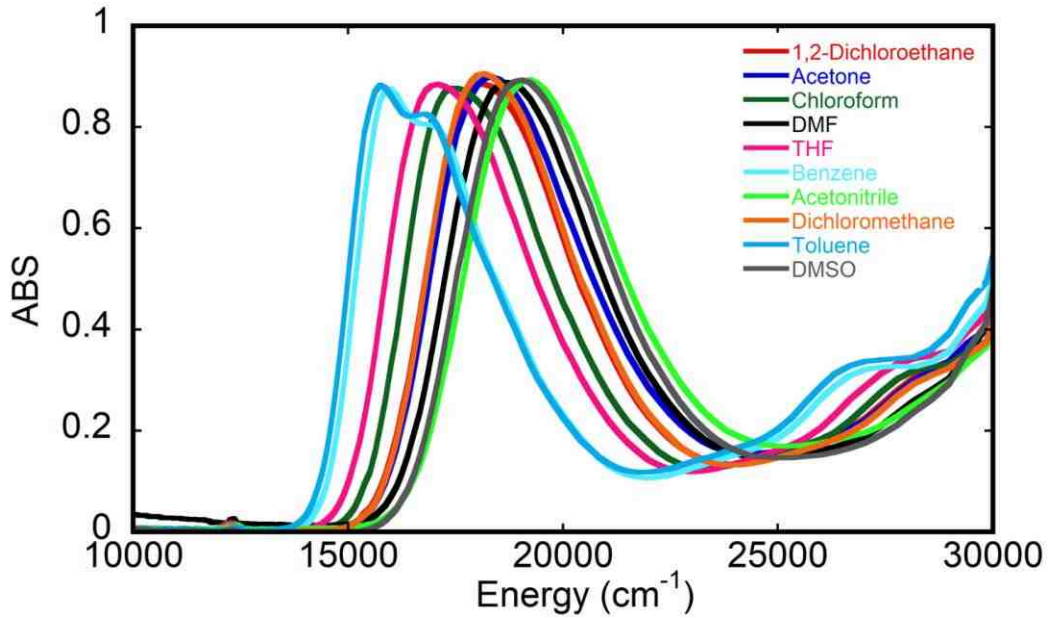

Figure B1: Overlay of Pt(dbbpy)(bdt) EA in ten different solvents.

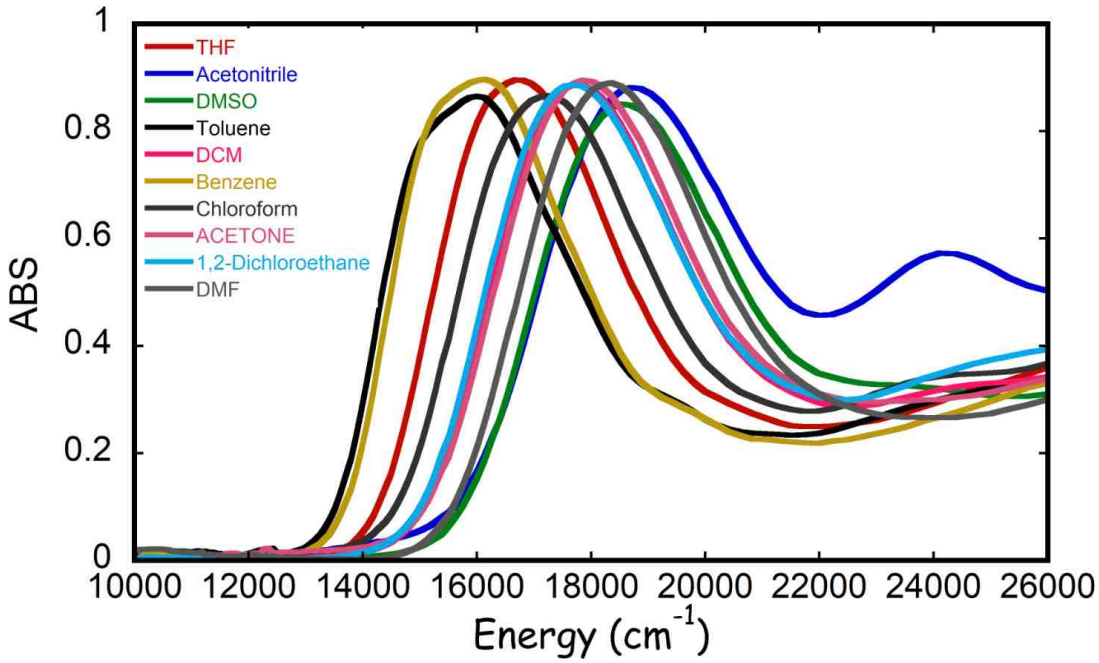

Figure B2: Overlay of Pt(dbbpy)(bSeO) EA in 10 different solvents.

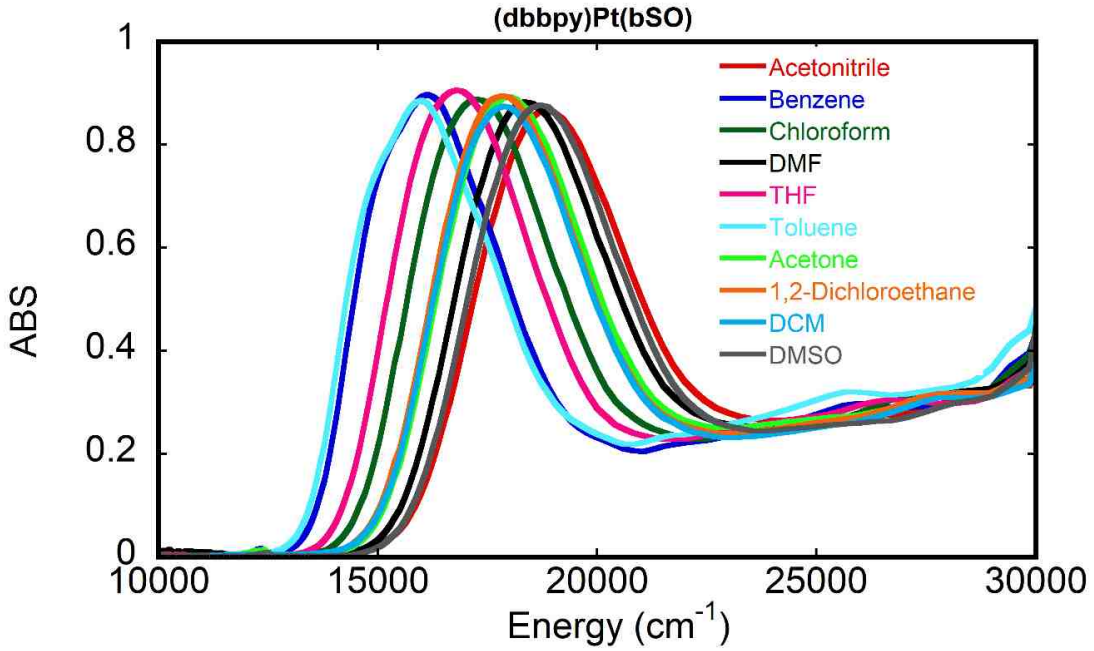

Figure B3: Overlay of Pt(dbbpy)(bSO) EA in ten different solvents.

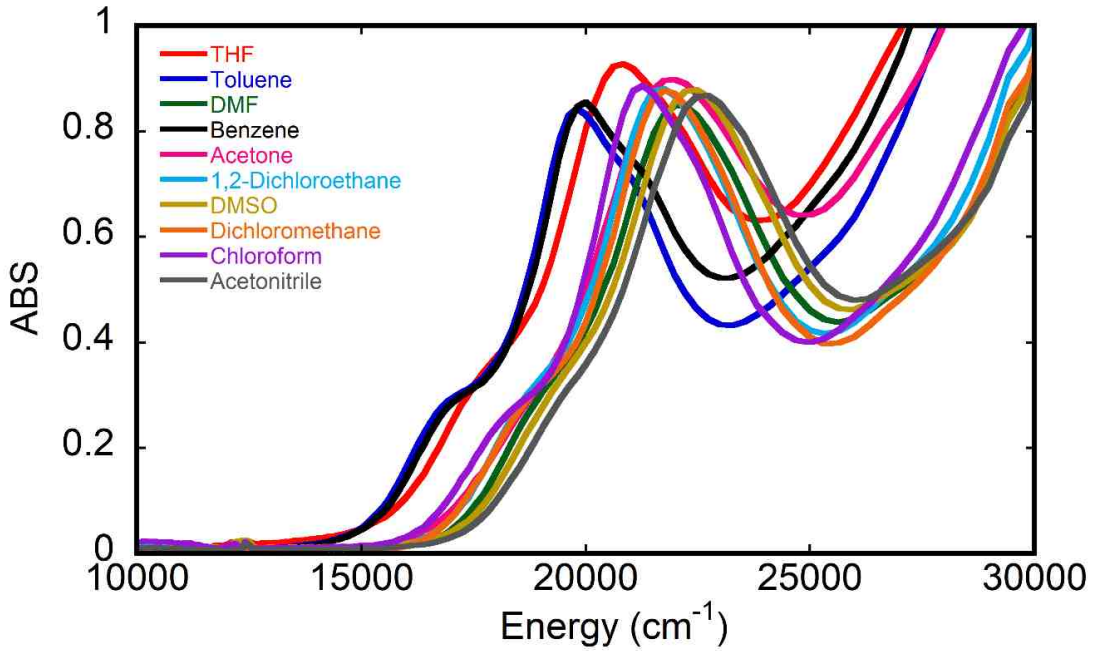

Figure B4: Overlay of Pt(dbbpy)(mcp) absorption spectra in ten different solvents.

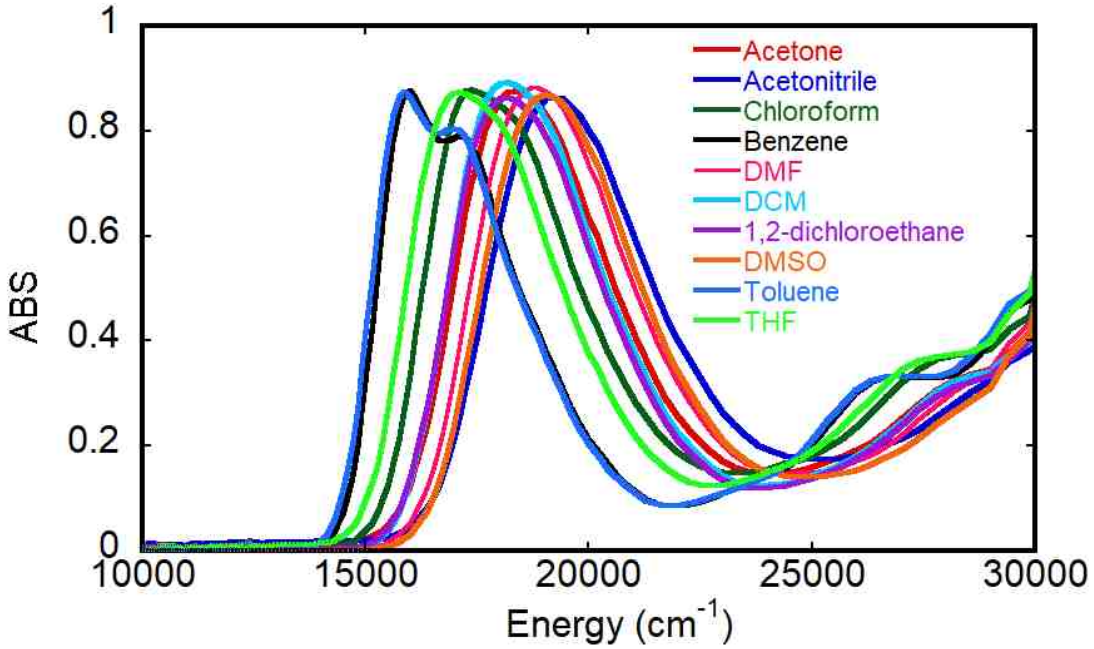

Figure B5: Overlay of Pt(dbbpy)(bSSe) EA in 10 different solvents.

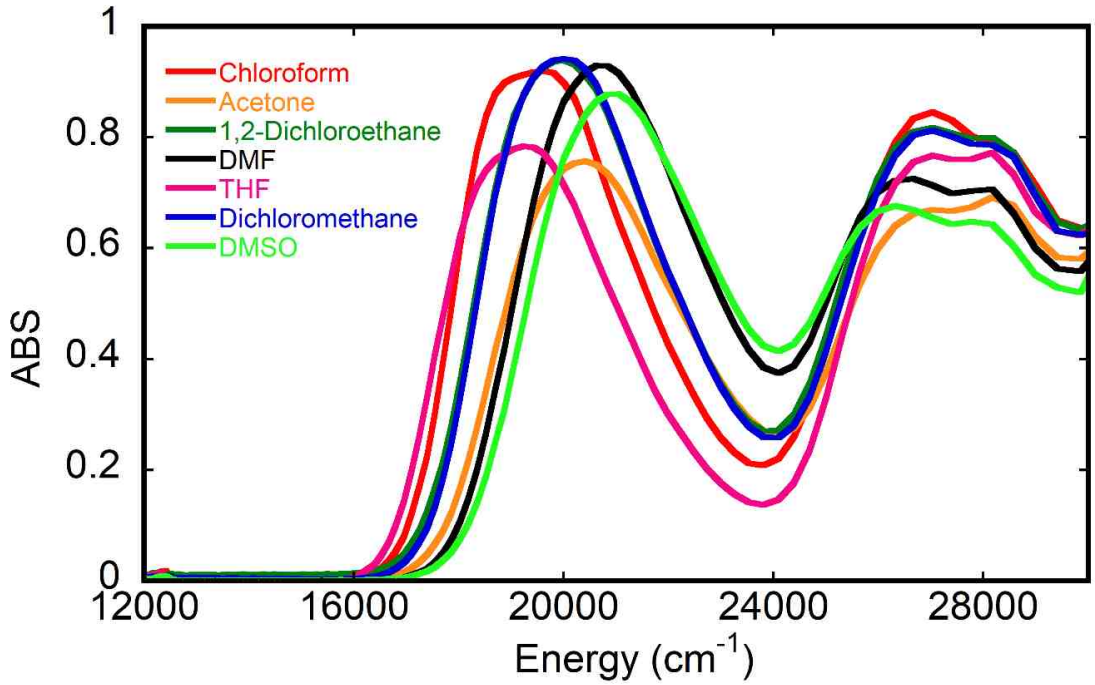

Figure B6: Overlay of Pt(dbbpy)(pds) EA in 7 different solvents.

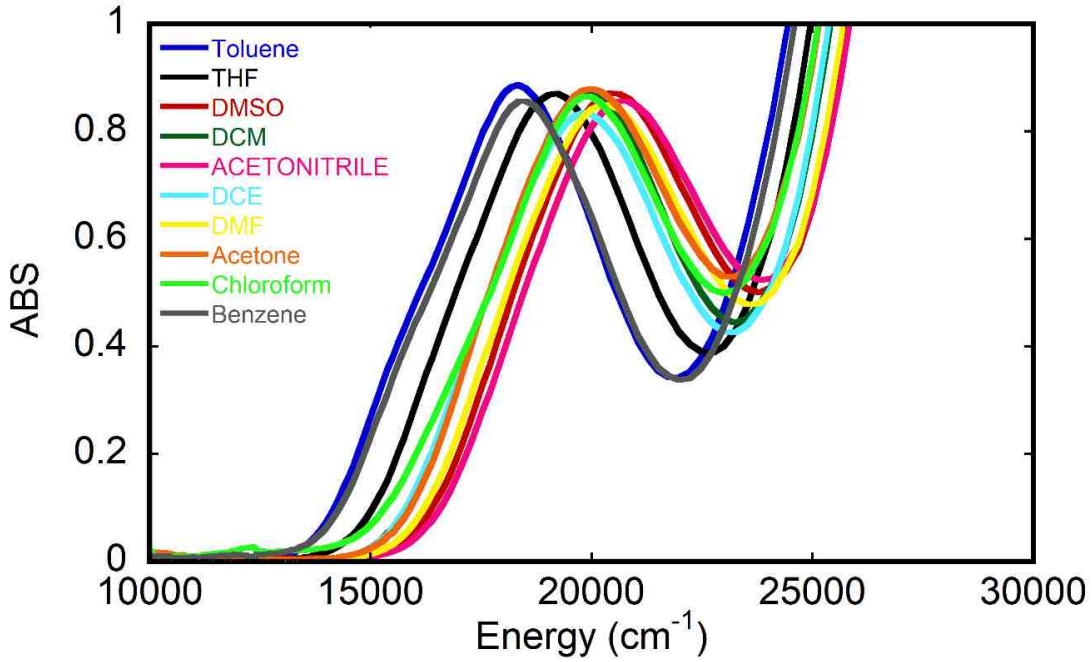

Figure B7: Overlay of Pt(dbbpy)$(PhSH)_2$ EA in 10 different solvents.

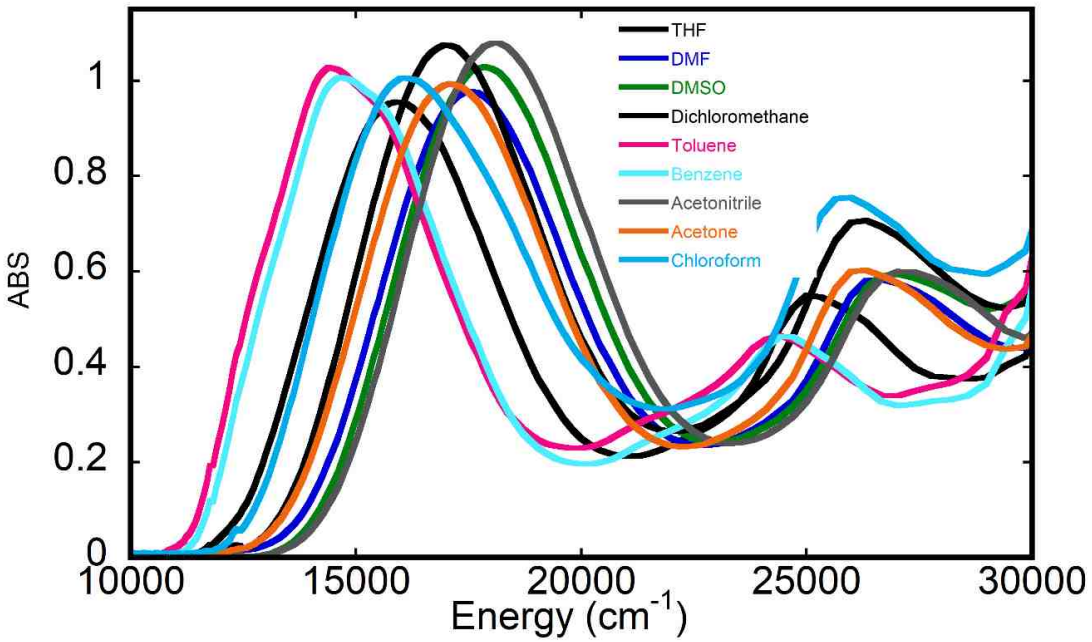

Figure B8: Overlay of Pt(dbbpy)(tbuCAT) absorption spectra in ten different solvents.

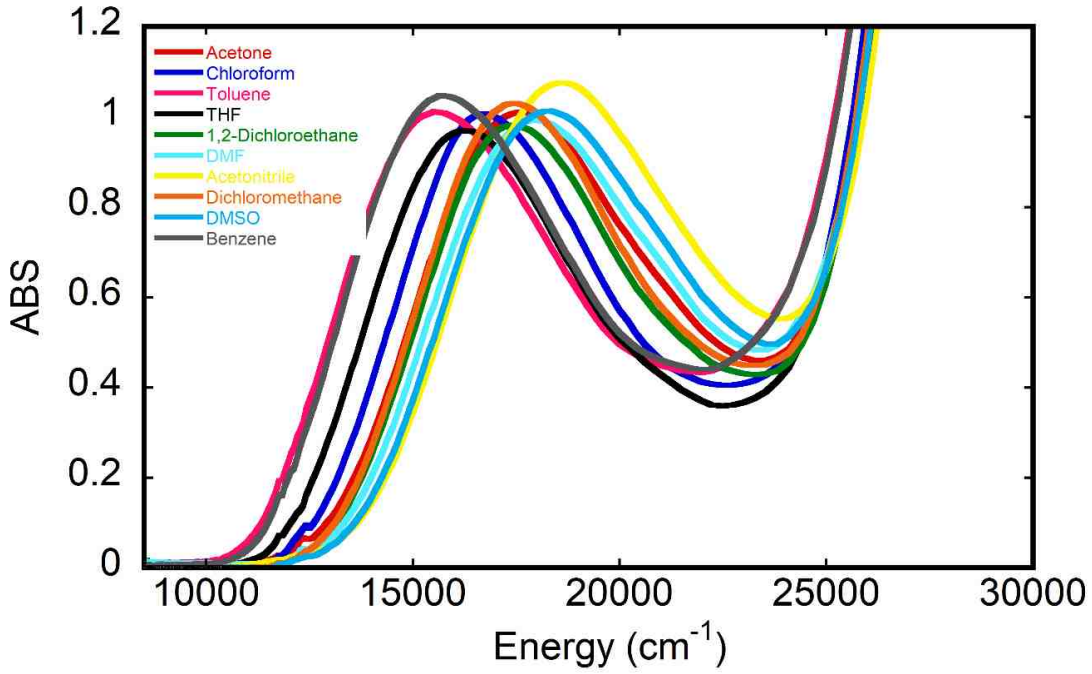

Figure B9: Overlay of Pd(dpphen)(tbuCAT-VZ) EA in ten different solvents.

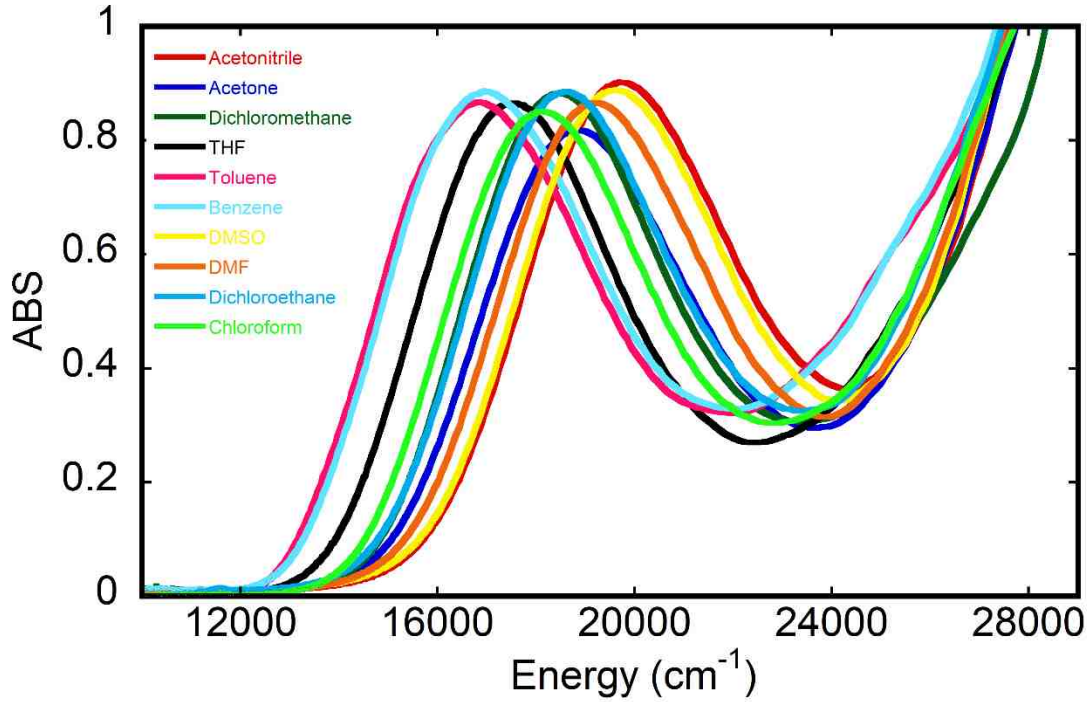

Figure B10: Overlay of Pt(dbbpy)(CAT-VZ) EA in ten different solvents.

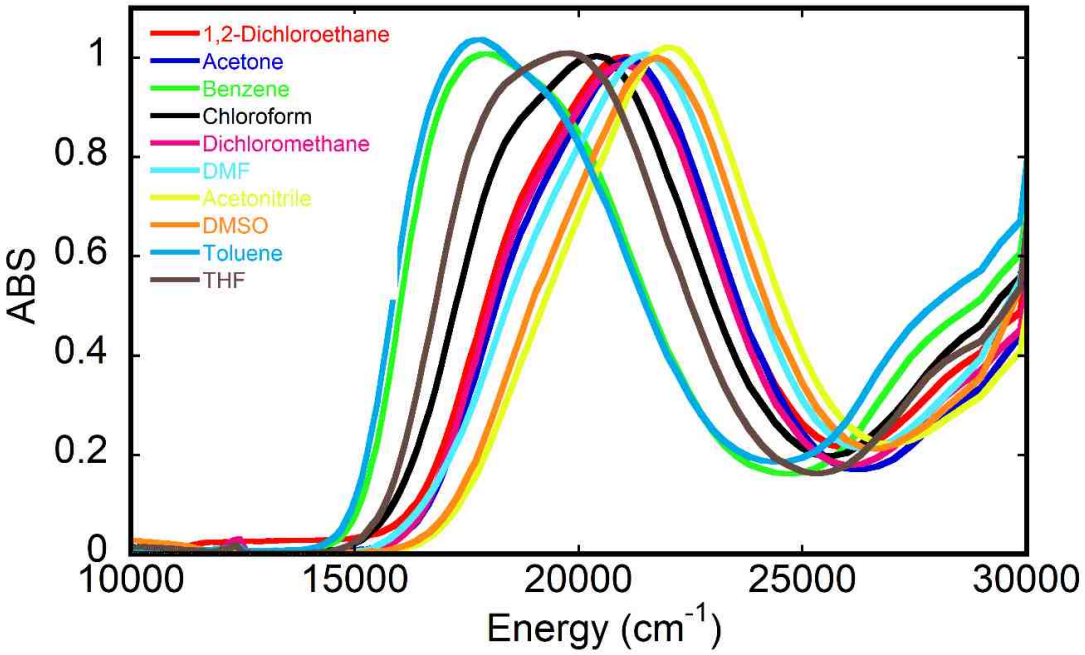

Figure B11: Overlay of Pd(dbbpy)(bdt) EA in ten different solvents.

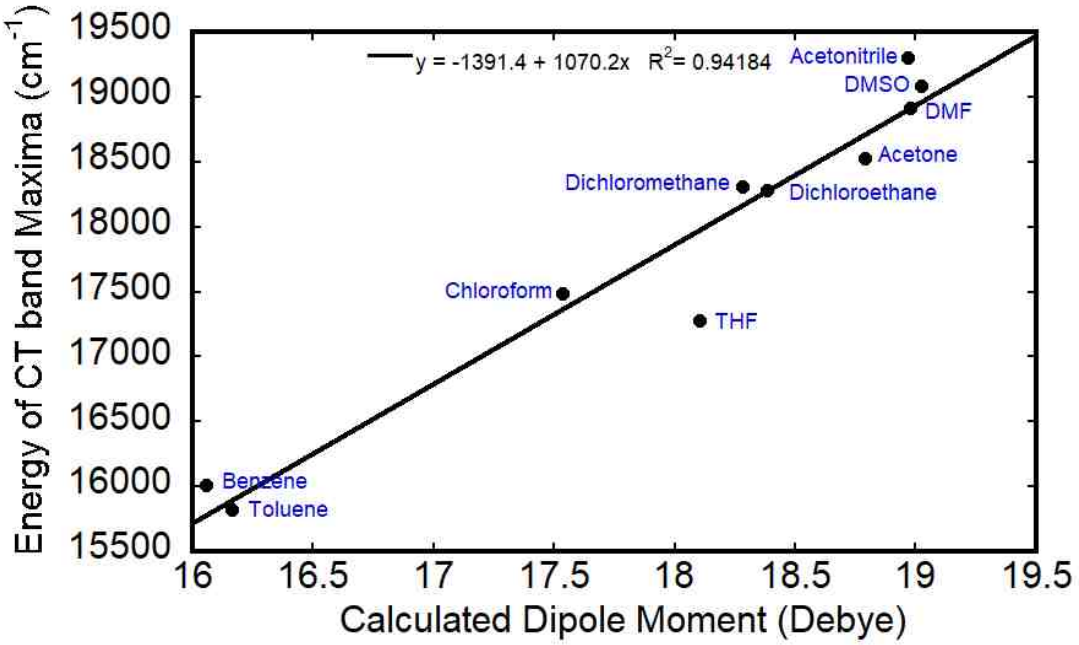

Figure B12: A linear correlation between the energy of the CT band maxima and calculated dipole moment for Pt(dbbpy)(bds).

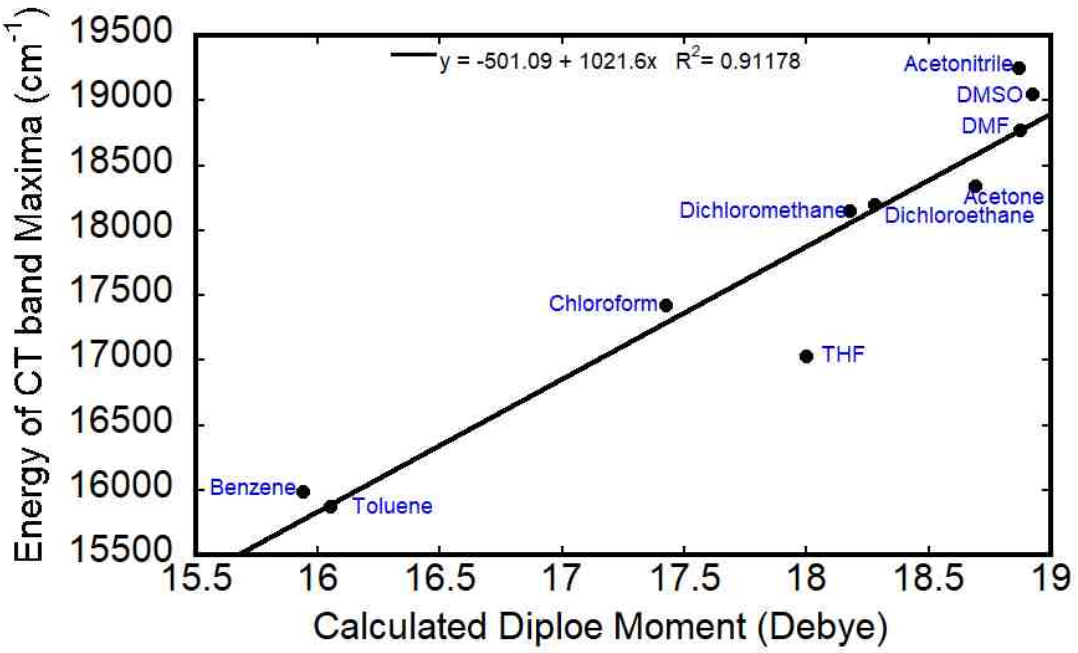

Figure B13: A linear correlation between the energy of the CT band maxima and calculated dipole moment for Pt(dbbpy)(bSSe).

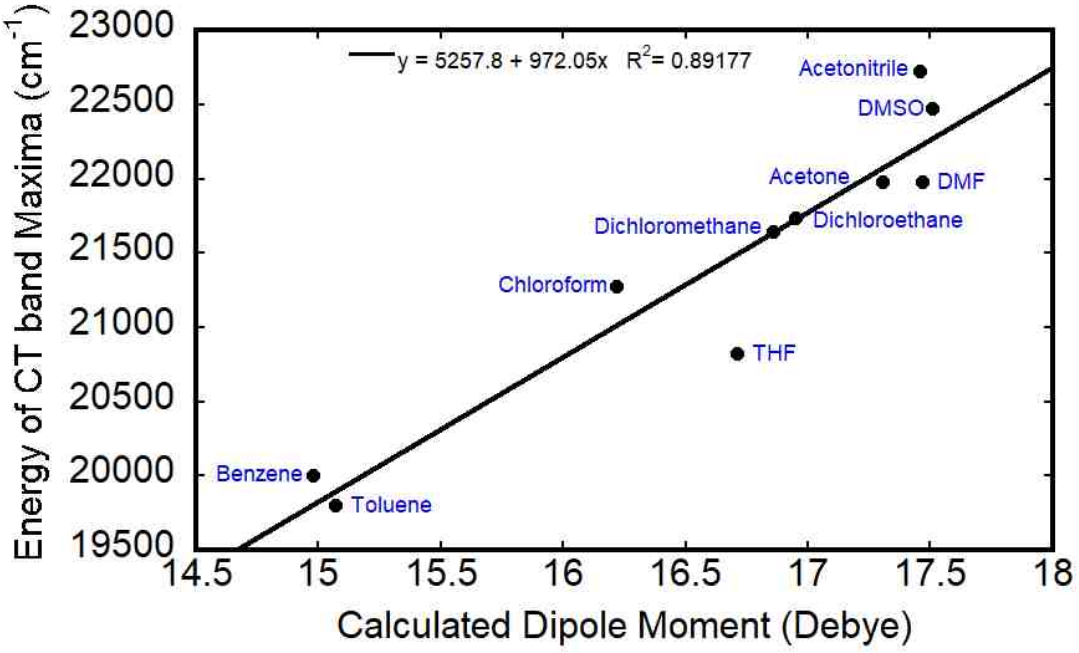

Figure B14: A linear correlation between the energy of the CT band maxima and calculated dipole moment for Pt(dbbpy)(mcp).

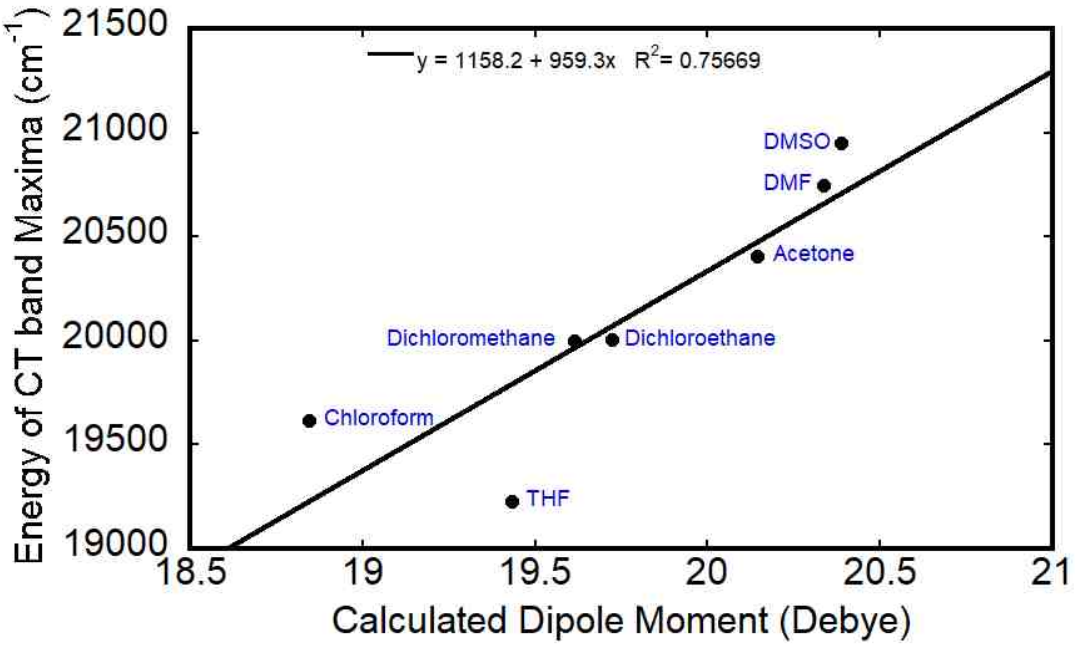

Figure B15: A linear correlation between the energy of the CT band maxima and calculated dipole moment for Pt(dbbpy)(pds).

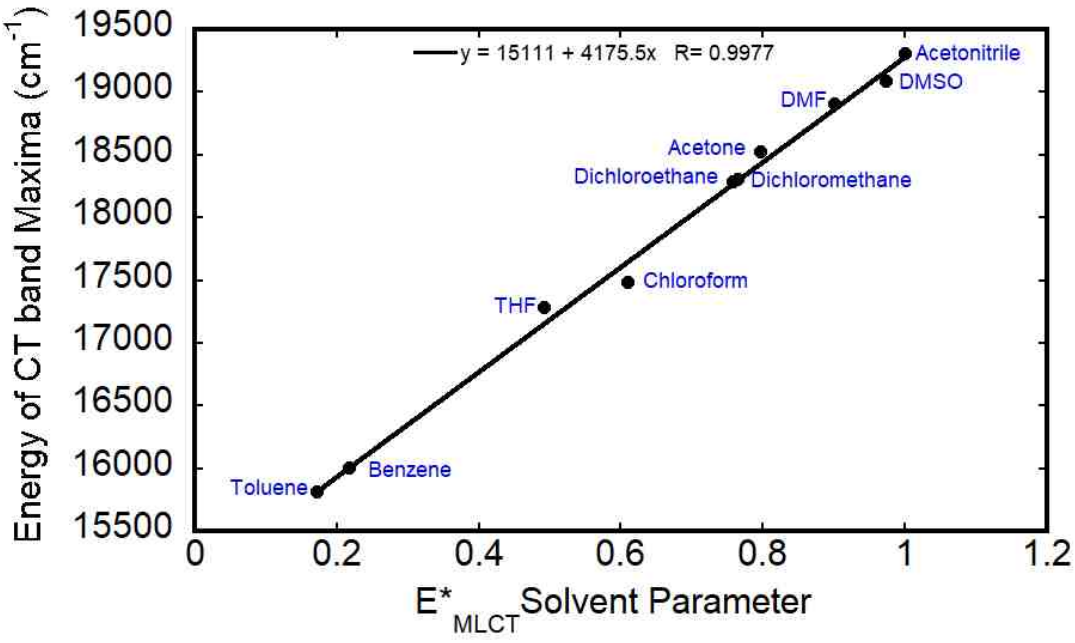

Figure B16: A plot of the energy of the CT band maxima versus the E^*_{MLCT} solvent parameter for Pt(dbbpy)(bds).

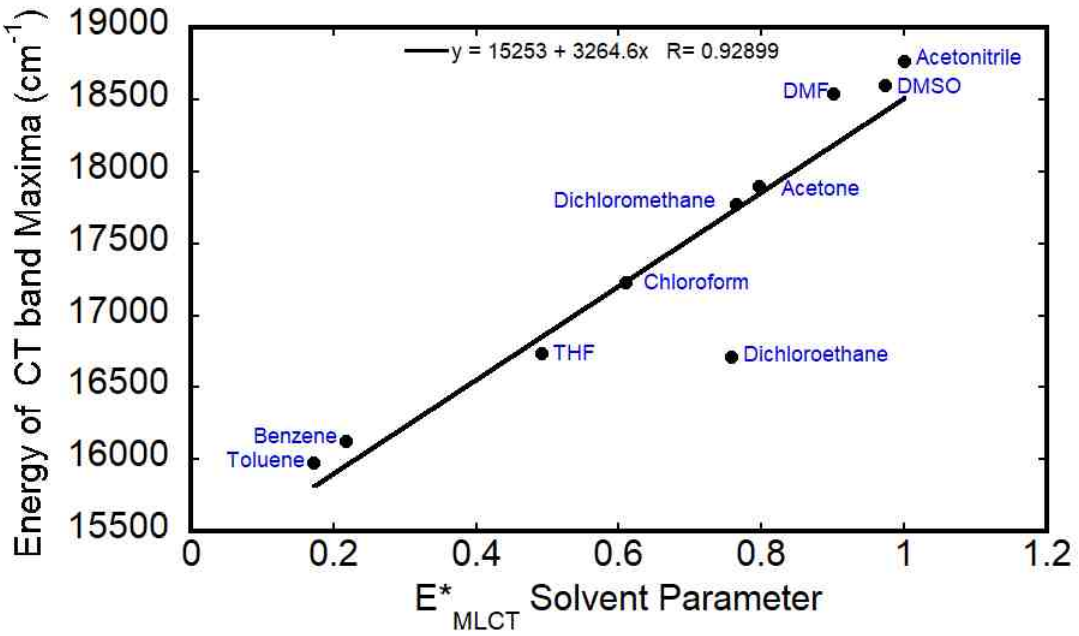

Figure B17: A plot of the energy of the CT band maxima versus the E^*_{MLCT} solvent parameter for Pt(dbbpy)(bSeO).

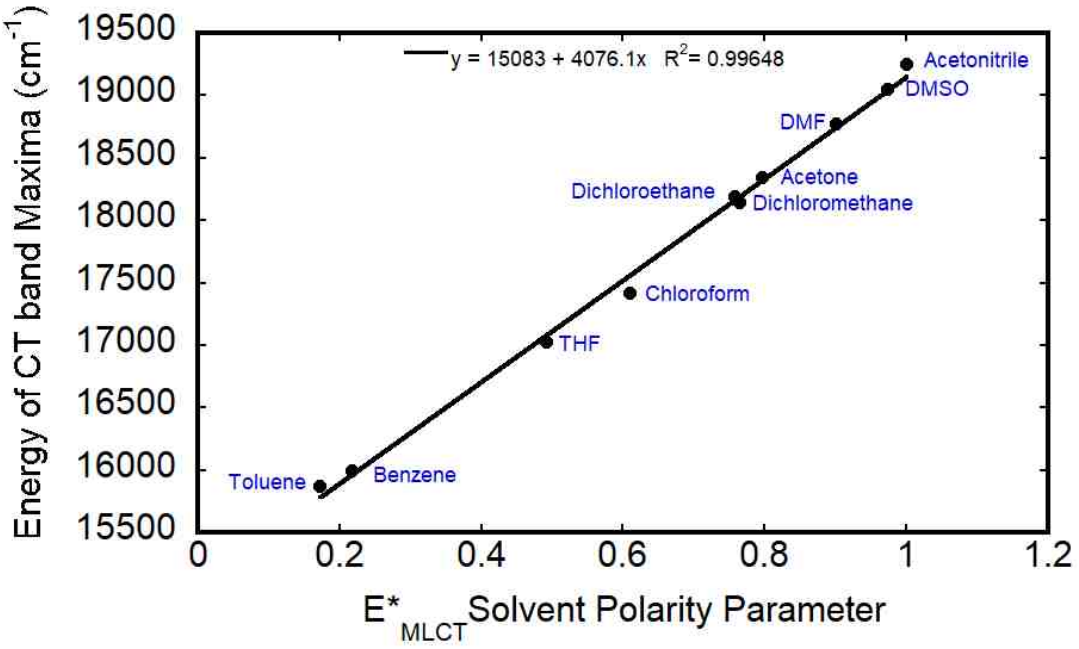

Figure B18: A plot of the energy of the CT band maxima versus the E^*_{MLCT} solvent parameter for Pt(dbbpy)(bSSe).

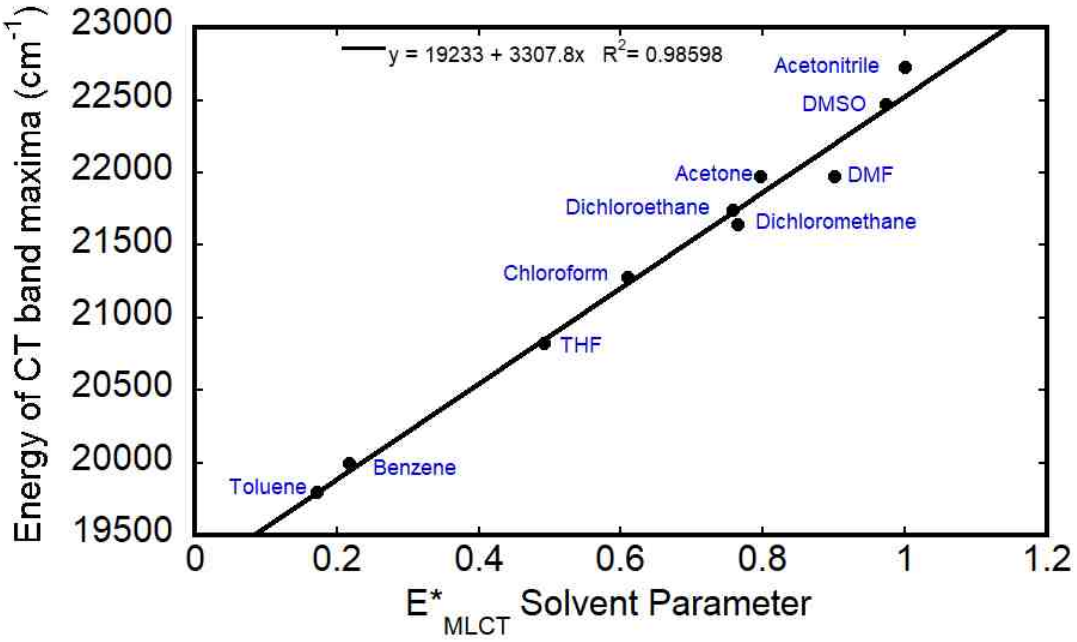

Figure B19: A plot of the energy of the CT band maxima versus the E^*_{MLCT} solvent parameter for Pt(dbbpy)(mcp).

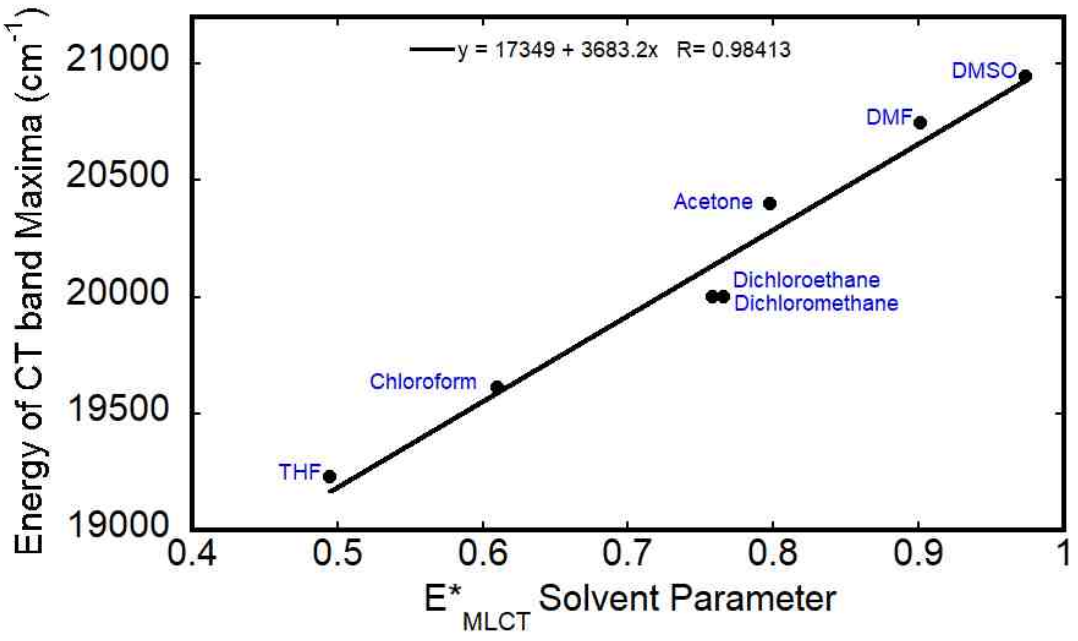

Figure B20: A plot of the energy of the CT band maxima versus the E^*_{MLCT} solvent parameter for Pt(dbbpy)(pds).

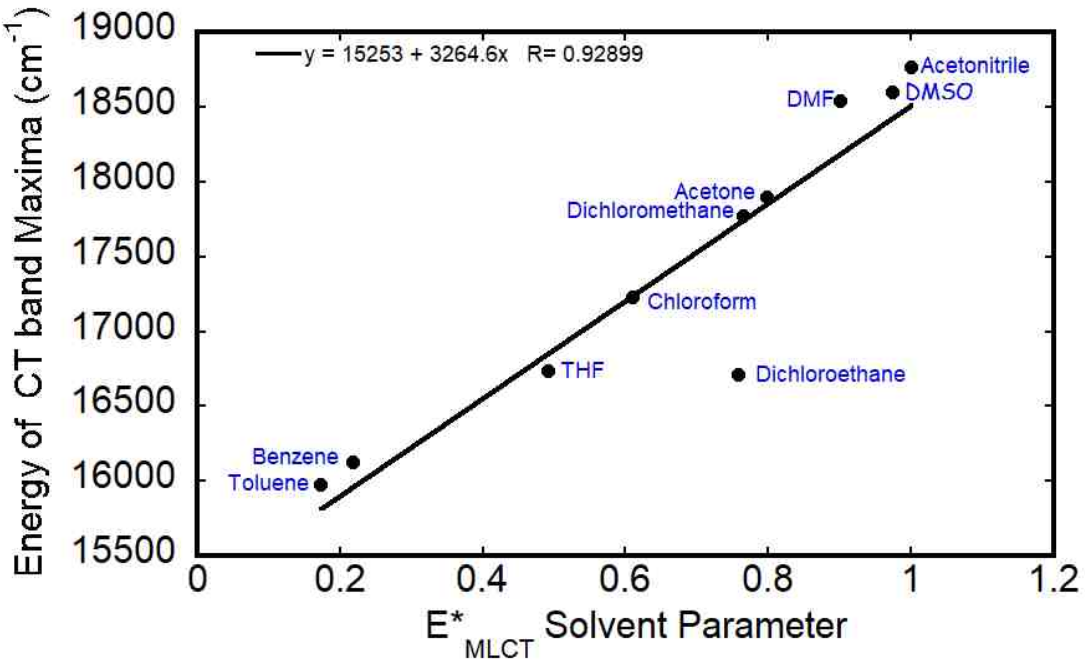

Figure B21: A plot of the energy of the CT band maxima versus the E^*_{MLCT} solvent parameter for Pd(dpphen)(tbuCAT-VZ).

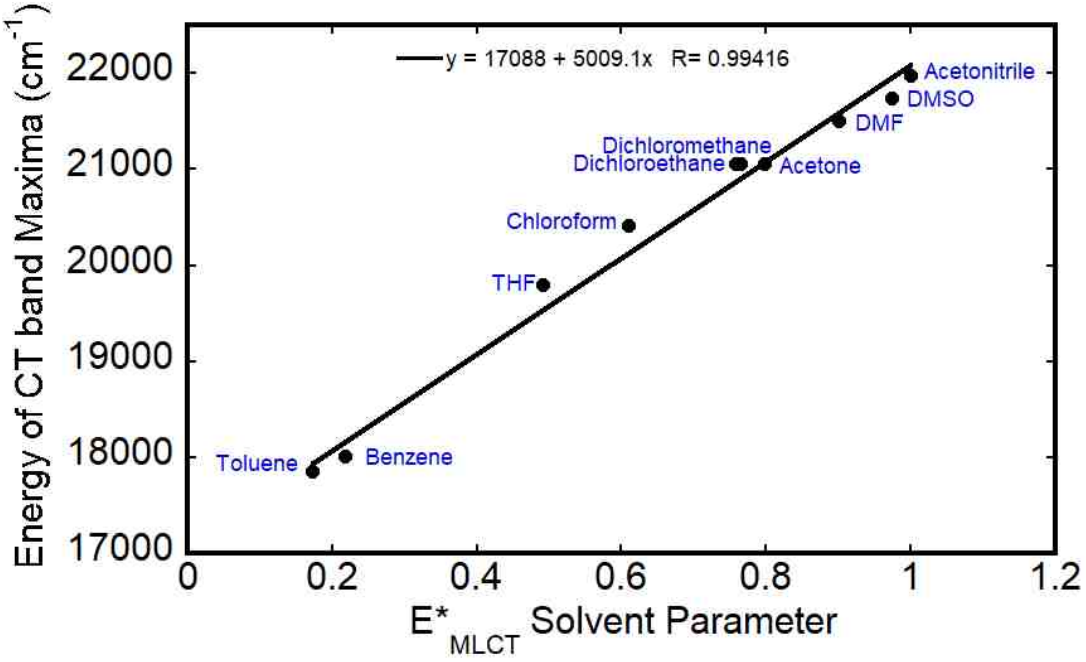

Figure B22: A plot of the energy of the CT band maxima versus the E^*_{MLCT} solvent parameter for Pd(dbbpy)(bdt).

Appendix C

Additional Information for Chapter 3

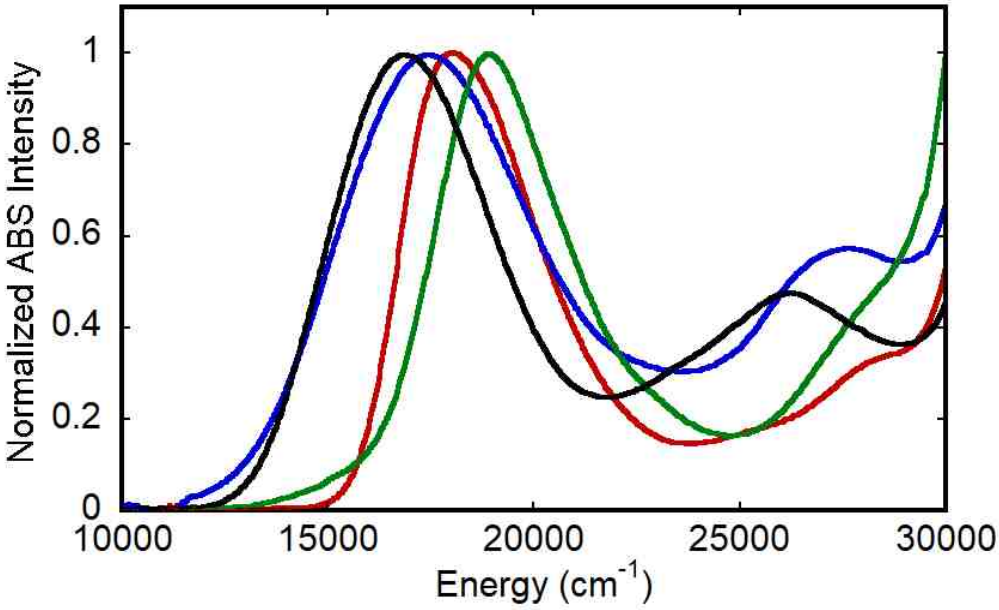

Figure C1: Electronic absorption overlay of Pt(dbbpy)(tbuCAT) (black), Pt(dbbpy)(bdt) (red), Ni(dbbpy)(dtCAT) (blue) and Ni(dbbpy)(bdt) (green) in CH_2Cl_2 at 298 K.

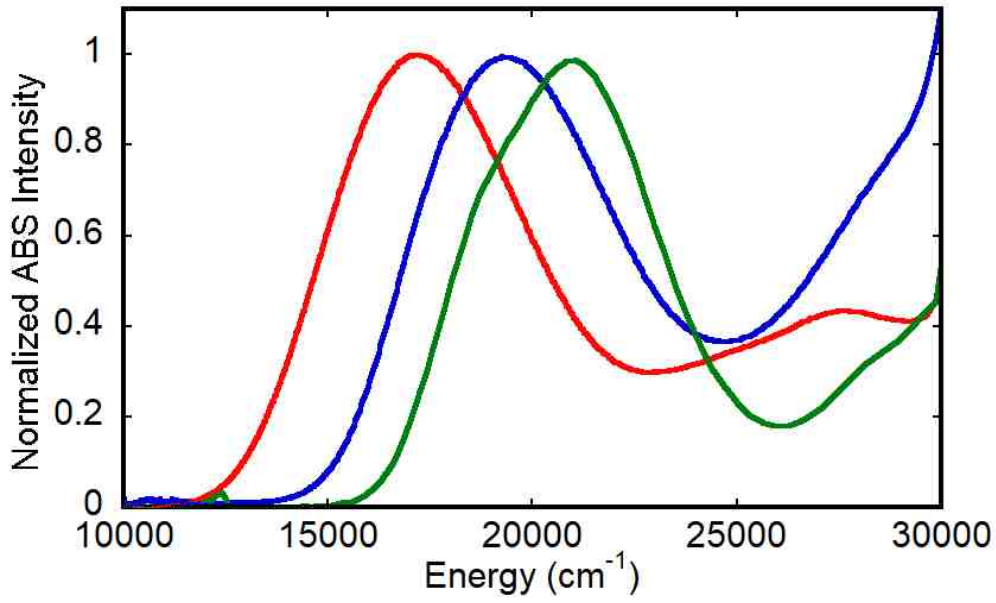

Figure C2: Electronic absorption overlay for Pd(dbbpy)(tbuCAT) (red), Pd(dbbpy)(bdt) (green) and Pd(dbbpy)(bSO) (blue) in CH_2Cl_2 at 298 K.

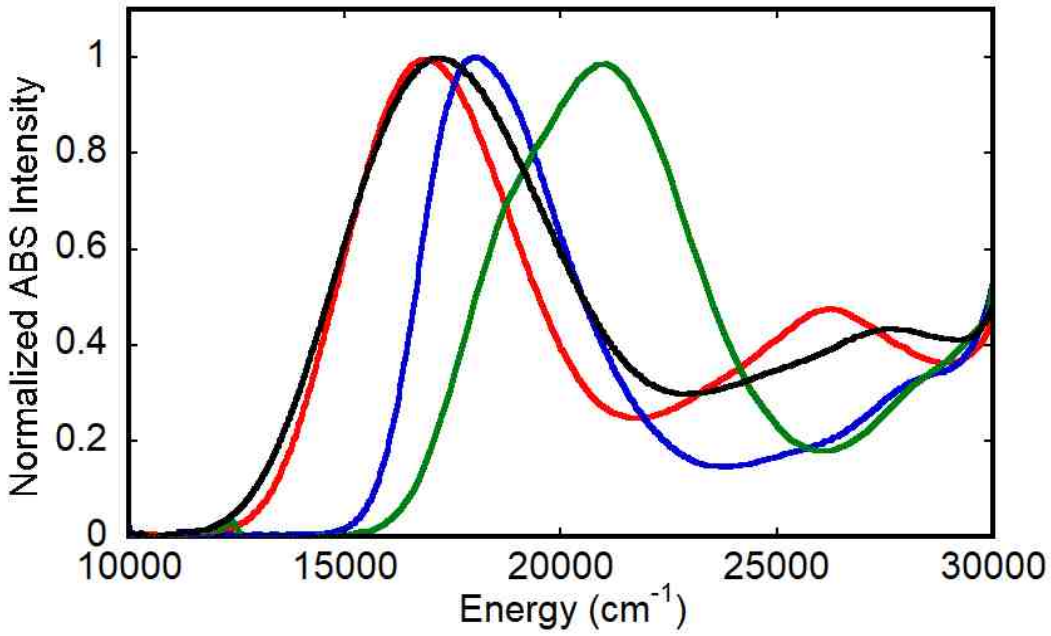

Figure C3: Electronic absorption overlay for Pt(dbbpy)(dtCAT) (red), Pt(dbbpy)(bdt) (blue), Pd(dbbpy)(tbuCAT) (black) and Pd(dbbpy)(bdt) (green) in CH_2Cl_2 at 298 K.

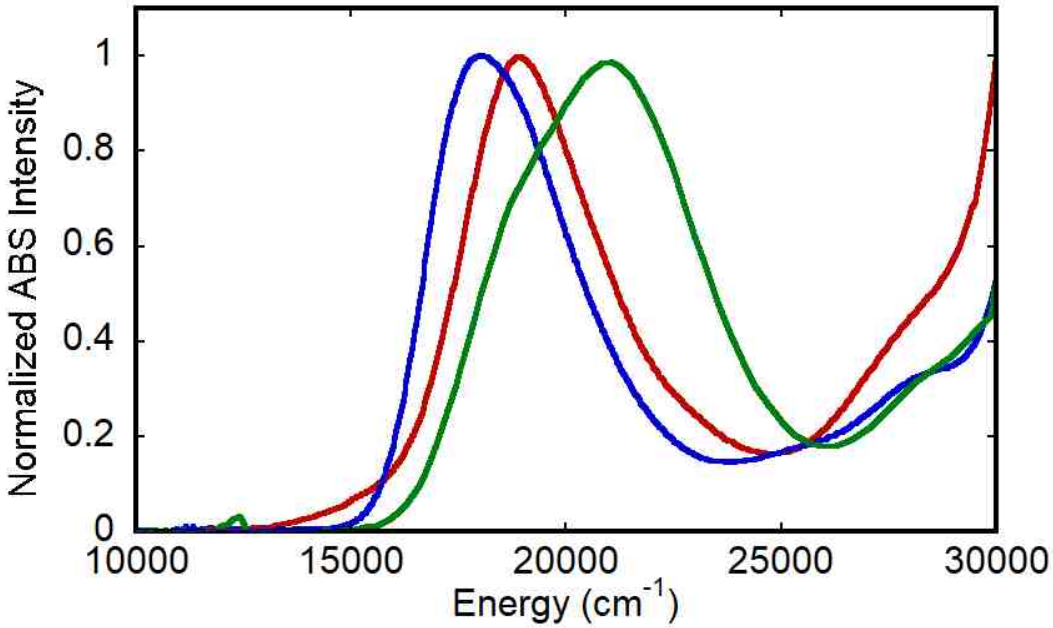

Figure C4: Electronic absorption overlay for Pt(dbbpy)(bdt) (blue), Ni(dbbpy)(bdt) (red), and Pd(dbbpy)(bdt) (green) in CH_2Cl_2 at 298 K.

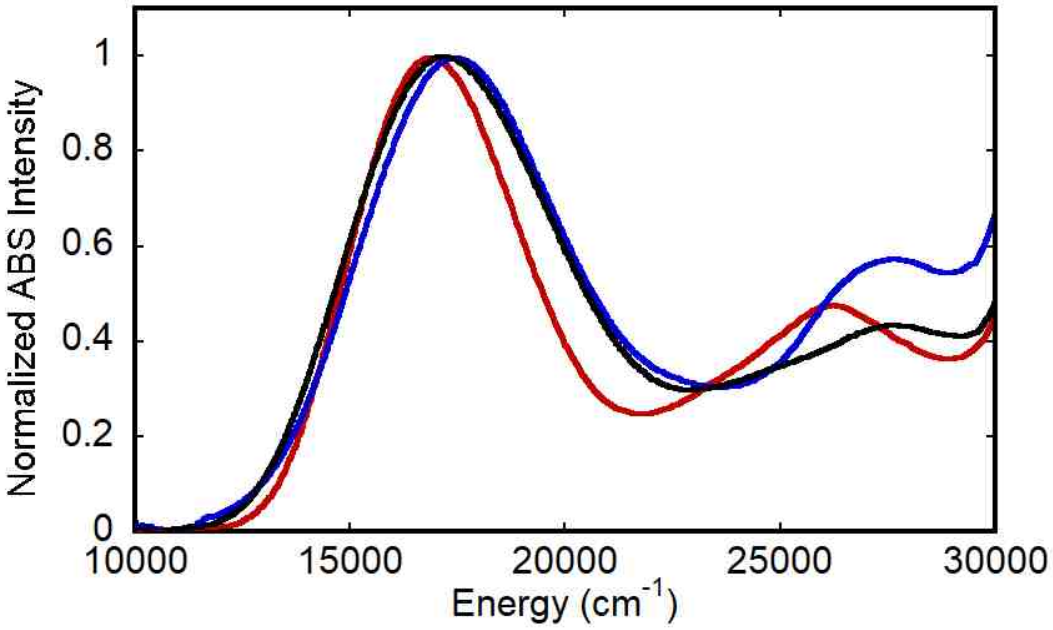

Figure C5: Electronic absorption overlay for Pt(dbbpy)(tbuCAT) (red), Ni(dbbpy)(tbuCAT) (blue), and Pd(dbbpy)(tbuCAT) (black) in CH_2Cl_2 at 298 K.

Table C1: Calculated transition energy and MMLL'CT band maxima for M(diimine)(dichalcogenolene) Complexes [M=Pt, Pd and Ni].

Complex	ΔE^a	ΔE^b	$E_{MMLL'CT}{}^c$	$E_{MMLL'CT}{}^d$
Pt(dbbpy)(bdt)	1.57	12663	2.28	18350
Ni(dbbpy)(bdt)	1.48	11937	2.35	18954
Pd (dbbpy)(bdt)	1.52	12260	2.61	21052
Pt(dbbpy)(CAT)	1.39	11211	2.10	16920
Ni(dbbpy)(CAT)	1.22	9840	2.16	17447
Pd (dbbpy)(CAT)	1.13	9114	2.13	17170

[a] TD-DFT calculated transition energy in eV. [b]TD-DFT calculated transition energy in cm^{-1}. [c] Experimental absorption maximum for the main band in CH_2Cl_2 in eV. [d] Experimental absorption maximum for the main band in CH_2Cl_2 in cm^{-1}.

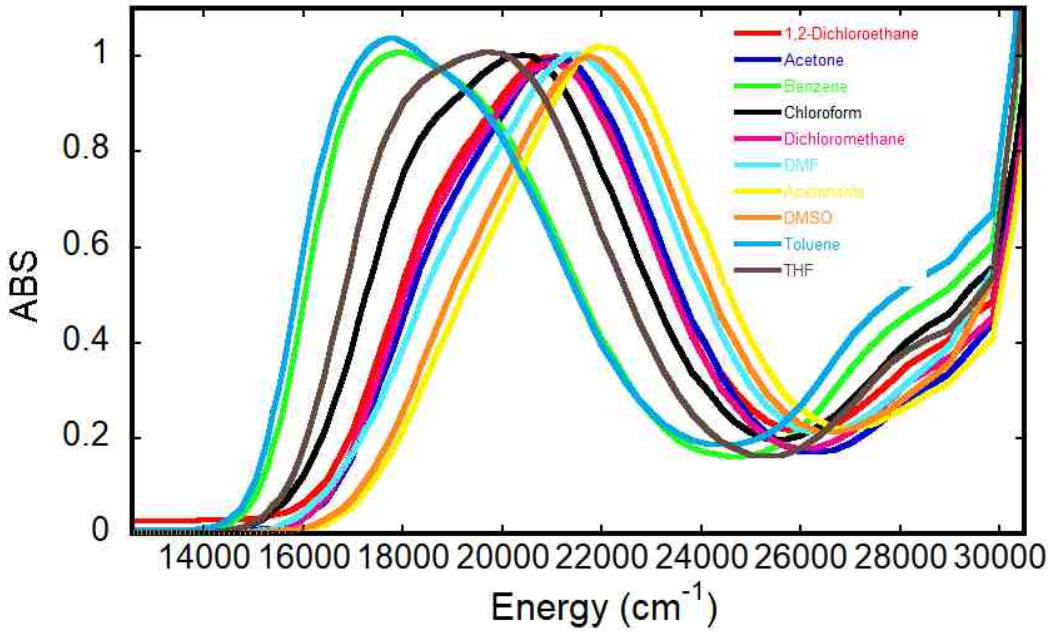

Figure C6: Overlay of Pd(dbbpy)(bdt) EA in ten different solvents.

Table C2: Selected TD-DFT Calculated Energies and Compositions of the Lowest Lying Singlet and Triplet Energy States together with oscillator strengths for Pd(dbbpy)(bSO).

State	Composition[a]	ΔE[b]	*f*[c]	Assignment
Singlets				
S_1	**HOMO→LUMO, 71%**	**1.29**	**0.1024**	**bSO→dbbpy/Pd (MMLL'CT)**
S_2	HOMO→LUMO+3, 70%	1.67	0.0000	bSO→dbbpy/Pd (LMCT/LLCT)
S_3	HOMO-1→LUMO, 69%	1.89	0.0010	bSO/Pd→dbbpy/Pd (MMLL'CT)
S_4	HOMO→LUMO+1, 70%	1.93	0.0100	bSO/Pd→dbbpy (MMLL'CT)
Triplets				
T_1	HOMO→LUMO, 70%	0.96	0.0000	bSO →dbbpy (MMLL'CT)
T_2	HOMO→LUMO+3, 69%	1.44	0.0000	bSO→dbbpy/Pd (LMCT/LLCT)
T_3	HOMO-1→LUMO, 70%	1.82	0.0000	bSO/Pd→dbbpy/Pd (MMLL'CT)
T_4	HOMO→LUMO+1, 70%	1.86	0.0000	bSO→dbbpy/Pd (MMLL'CT)

[a] Electronic transitions compositions expressed in terms of ground-state Kohn-Sham molecular orbitals. [b] Transition energy expressed in eV. [c] Oscillator strength.

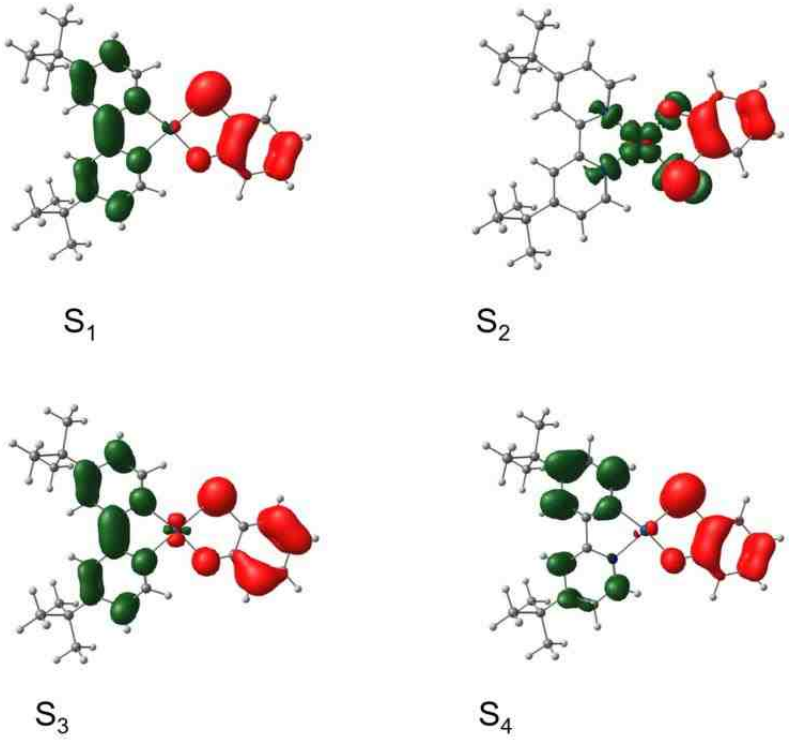

Figure C7: Calculated electron density difference map (EDDM) for Singlet State at an isodensity value of 0.0012 au Pd(dbbpy)(bdt). The red and green regions represent loss and gain of electron density respectively in a transition to the excited state.

Table C3: Selected TD-DFT Calculated Energies and Compositions of the Lowest Lying Singlet and Triplet Energy States together with oscillator strengths for Pd(dbbpy)(CAT).

State	Composition[a]	ΔE[b]	*f*[c]	Assignment
Singlets				
S_1	**HOMO→LUMO, 71%**	**1.13**	**0.1202**	**CAT/Pd→dbbpy/Pd (MMLL'CT)**
S_2	HOMO→LUMO+3, 70%	1.67	0.0000	CAT→dbbpy/Pd (LMCT/LLCT)
S_3	HOMO→LUMO+1, 70%	1.72	0.0162	CAT/Pd→dbbpy/Pd(MMLL'CT)
S_4	HOMO-1→LUMO, 67%	1.89	0.0000	CAT/Pd→dbbpy/Pd (MMLL'CT)
Triplets				
T_1	HOMO→LUMO, 71%	0.65	0.0000	CAT→dbbpy (MMLL'CT)
T_2	HOMO→LUMO+3, 69%	1.47	0.0000	CAT→dbbpy/Pd (LMCT/LLCT)
T_3	HOMO→LUMO+1, 70%	1.64	0.0000	CAT/Pd→dbbpy/Pd (MMLL'CT)
T_4	HOMO-1→LUMO, 69%	1.80	0.0000	CAT/Pd→dbbpy/Pd (MMLL'CT)

[a] Electronic transitions compositions expressed in terms of ground-state Kohn-Sham molecular orbitals. [b] Transition energy expressed in eV. [c] Oscillator strength.

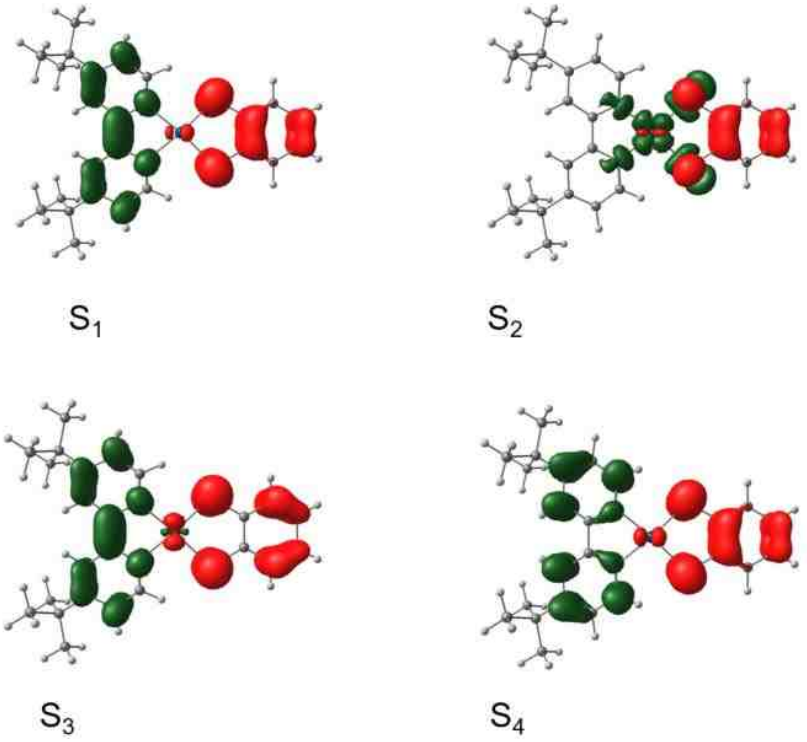

Figure C8: Calculated electron density difference maps (EDDMs) for singlet states at an isodensity value of 0.0012 au for Pd(dbbpy)(bSeO). The red and green regions represent loss and gain of electron density respectively in the transition to the excited state.

Table C4: Selected TD-DFT Calculated Energies and Compositions of the Lowest Lying Singlet and Triplet Energy States together with oscillator strengths for Pd(dbbpy)(bds)

	Composition[a]	**ΔE^b**	***f*[c]**	**Assignment**
Singlets				
S_1	**HOMO→LUMO, 71%**	**1.55**	**0.0953**	**bds/Pd→dbbpy (MMLL'CT)**
S_2	HOMO-1→LUMO, 70%	1.70	0.0014	bds/Pd→dbbpy (LMCT/LLCT)
S_3	HOMO-1→LUMO, 70%	1.81	0.0000	bds/Pd→dbbpy/Pd (MMLL'CT)
S_4	HOMO→LUMO+1, 70%	2.06	0.0002	bds/Pd→dbbpy/Pd (MMLL'CT)
Triplets				
T_1	HOMO→LUMO, 70%	1.31	0.0000	bds/Pd →dbbpy (MMLL'CT)
T_2	HOMO→LUMO+2, 69%	1.53	0.0000	bds/Pd→dbbpy (LMCT/LLCT)
T_3	HOMO-1→LUMO, 70%	1.63	0.0000	bds/Pd→dbbpy/Pd (MMLL'CT)
T_4	HOMO-1→LUMO+2, 68%	1.70	0.0000	bds/Pd→dbbpy/Pd (MMLL'CT)

[a] Electronic transitions compositions expressed in terms of ground-state Kohn-Sham molecular orbitals. [b] Transition energy expressed in eV. [c] Oscillator strength.

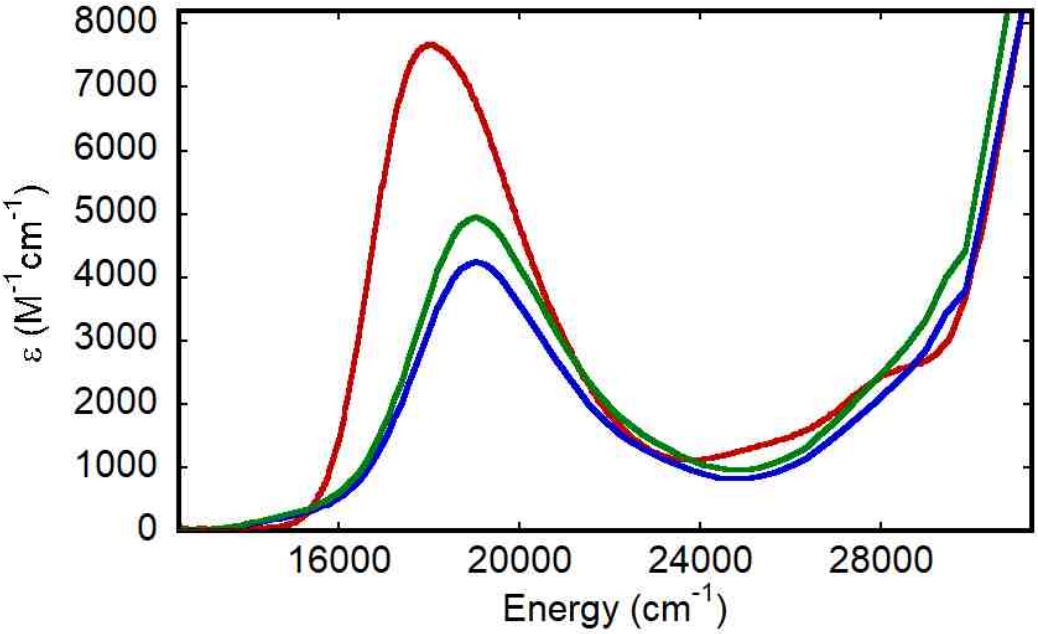

Figure C9: Electronic absorption overlay of Pt(dbbpy)(bdt) (red), Pd(dbbpy)(bdt) (green), and Ni(dbbpy)(bdt) (blue) in CH_2Cl_2 at 298 K.

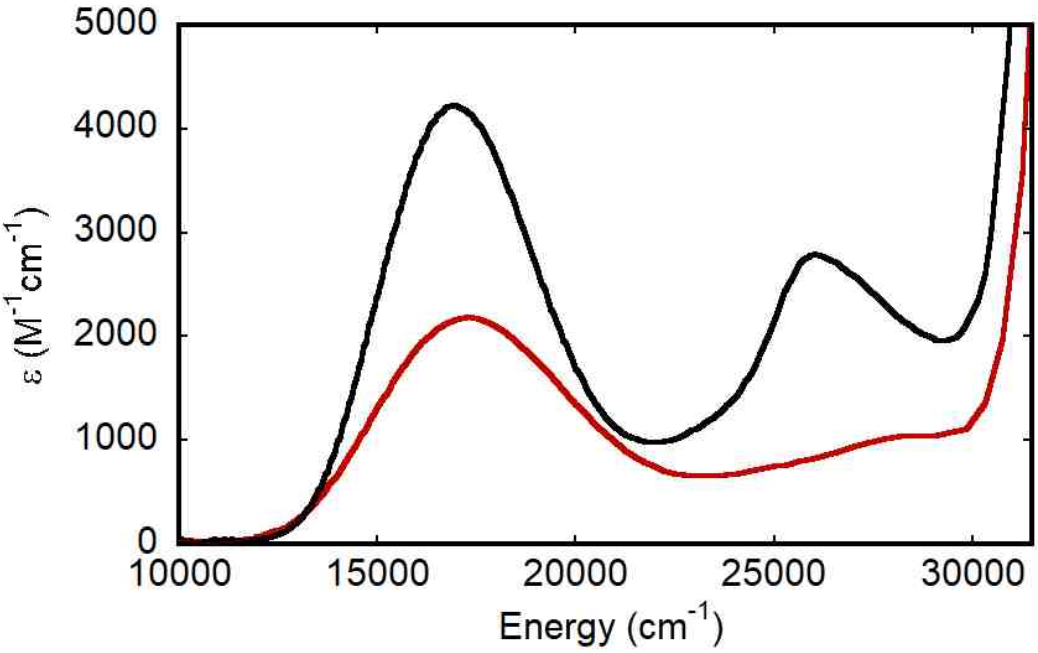

Figure C10: Electronic absorption overlay of Pt(dbbpy)(tbuCAT) (black), and Pd(dbbpy)(tbuCAT) (red), in CH_2Cl_2 at 298 K.

Table C5: MMLL'CT absorption band maxima and their respective molar extinction coefficient of M(diimine)(dichalcogenolene) complexes [M=Pt, Pd and Ni]

Complex	$E_{MMLL'CT}$[a]	ε[b]
Pt(dbbpy)(bdt)	18350	7710
Ni(dbbpy)(bdt)	18954	4285
Pd (dbbpy)(bdt)	21052	4950
Pt(dbbpy)(tbuCAT)	16920	4260
Ni(dbbpy)(tbuCAT)	17447	
Pd (dbbpy)(tbuCAT)	17170	2208
Pt(dpphen)(tbuCat)	16255	6304
Pd(dpphen)(tbuCat)	16480	3320

[a] Experimental absorption maximum for the main band in CH_2Cl_2 in cm^{-1}. [b] Molar extinction coefficient in $M^{-1}cm^{-1}$.

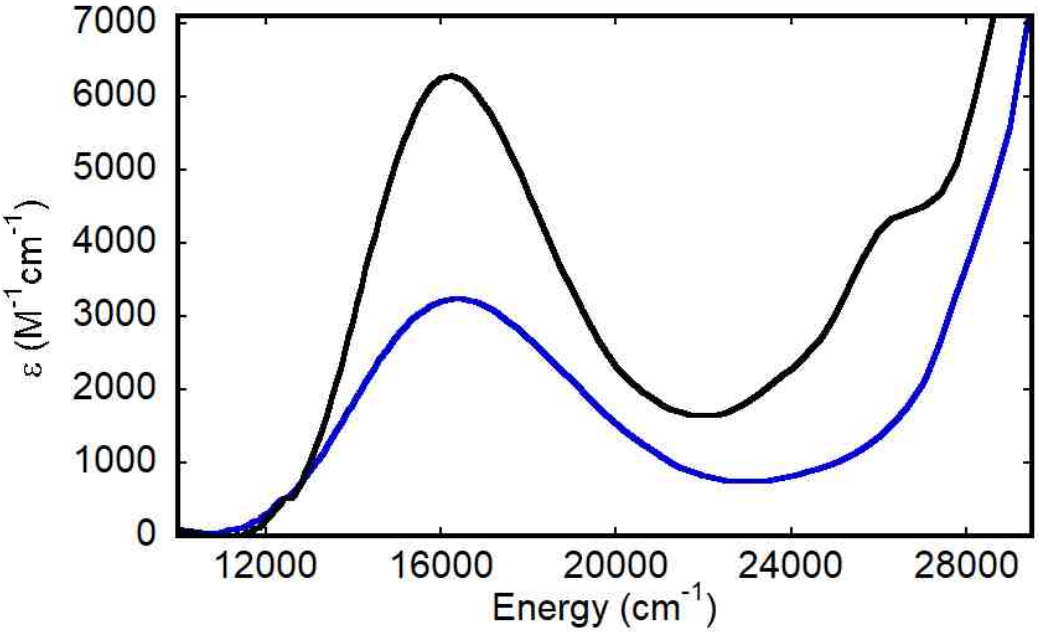

Figure C11: Electronic absorption overlay of Pt(dpphen)(tbuCAT) (black), and Pd(dpphen)(tbuCAT) (blue), in CH_2Cl_2 at 298 K.